

The ethics of egg manipulation

Cell research reopens the debate on embryo destruction, egg donation and what is natural.

Many couples are faced with the unpleasant choice between not having a child of their own and risking the passing on of a debilitating disease. Yet research into reproductive technologies to lessen the chances of having unhealthy babies has been hampered by public attitudes to interfering with the course of life.

Mutations in the DNA of mitochondria — energy-producing organelles in a cell — are linked to a growing list of diseases, and treatment options tend to be limited to the alleviation of symptoms. In theory, the mutations could be picked up by the early screening of embryos, but efforts to do so have been of limited value, in part because little is known about how much mitochondrial damage is needed to cause disease.

Now, a paper published online by *Nature* this week (M. Tachibana *et al.* *Nature* doi:10.1038/nature08368; 2009) offers a way to eliminate the problem. The technique involves taking the nuclear DNA from one egg cell and transferring it to another egg that has had its nucleus removed. The newly 'reconstructed' egg will then contain mitochondria only from the new egg cell, leaving behind any defective mitochondria from the original cell. It can then be used for *in vitro* fertilization.

But the work presented this week is done in monkeys. Demonstrating that it can be done safely in humans will require research that is likely to be contentious — and, in many countries, legally or practically impossible.

One major roadblock is that human embryos will need to be created solely for research, which many people feel violates the sanctity of human life. That argument was used by the administration of former US President George Bush to restrict such studies, and even now the National Institutes of Health and other US agencies cannot fund them. Still, this obstacle it hasn't stopped research from being

funded by non-federal sources, such as the state of California. Nor has it kept embryos from being created then destroyed in the course of commercial fertility treatments.

A more serious roadblock is the difficulty in obtaining the human eggs needed for both donor and recipient cells in the nuclear-transfer procedure. The egg-donation procedure is uncomfortable and somewhat risky, and some bioethicists argue that compensating women who undergo it is tantamount to a form of coercion. Paid egg donation for research is prohibited by most state and federal funding agencies in the United States and elsewhere (with the notable exception of New York state, which allows it).

As a result, egg cells are generally available only from women who are willing to give them altruistically — a comparatively small number, made smaller by the fact that women can get thousands of dollars for donating to a fertility clinic. Thus, research in some fields, such as somatic-cell nuclear transfer, or cloning, has slowed almost to a halt.

More states should take New York's lead, and allow researchers to pay for egg donation. The potential for coercion, although real, is manageable. And the technique's move to the clinic would certainly be faster, and arguably more ethical, if donors were paid (C. Thompson *Regen. Med.* **2**, 203–209; 2007).

Yet another argument raised when such research has been attempted in the past — for example when researchers tried to replenish damaged mitochondrial DNA in one egg with healthy mitochondrial DNA from another — is that such a three-parent union is 'unnatural'. Yet similar concerns greeted *in vitro* fertilization when it was being pioneered in the 1970s, and the technique is now widely accepted. Blanket bans can impede progress and encourage unethical practices. With appropriate oversight, research into other reproductive technologies has the potential to give more couples the chance of having a healthy baby. ■

All the news you need

This issue marks an evolution in *Nature's* news coverage. On page 1062, we are launching News Briefing — a two-page digest of the key events shaping the scientific enterprise in the past week. With coverage encompassing policy decisions, funding announcements, market trends and business deals, News Briefing offers a complete overview of the developments that affect anyone working in science. The section also features a calendar to highlight important events, reports and initiatives occurring in the forthcoming week.

Science is inextricably linked with the messy details of politics and commerce, and it is vital for today's researchers to be aware of how political and business decisions can steer their research programmes — and indeed how their research can affect society. Similarly, policy-makers require the perspective that science can provide on the likely outcomes of their decisions. Yet it is all too

easy to miss something important in the torrent of news that pours down on us every day.

By gathering all of the important events in one place, News Briefing aims to plug that gap. In doing so, it complements Research Highlights, which for the past four years has brought you our editors' selections of the most interesting research results from beyond the pages of *Nature*. Both sections will guide you to longer analytical pieces and exclusives in the main news section or online at www.nature.com/news. Apart from breaking daily news stories, our news website also carries stories from the print edition before they make it onto paper, getting analysis and information to our subscribers as soon as possible.

The introduction of News Briefing to our family of daily online coverage and weekly analysis means that *Nature* now provides a complete overview of the important events shaping our readers' lives. As ever, we would welcome any feedback on the changes, which should be sent to nature@nature.com. ■

RESEARCH HIGHLIGHTS

Walking in circles

Curr. Biol. doi:10.1016/j.cub.2009.07.053 (2009)

Books, movies and hiker-lore all predict that, unaided by landmarks or celestial objects, people tend to walk in circles. But few have tested whether this happens and, if so, why.

Jan Souman at the Max Planck Institute for Biological Cybernetics in Tübingen, Germany, and his team tracked people's movement through unfamiliar terrains — Bienwald Forest in Germany and the Tunisian Sahara Desert — using the Global Positioning System.

During outings on cloudy days (blue trails pictured in inset), and one on a moonless night, subjects tended to walk in loose, meandering circles, which suggests that external information is key to maintaining course. Blindfolded walkers often veered into tighter circles of less than 20 metres in diameter.

Common explanations for circular walking invoke physiology — handedness or body asymmetries, for example. But the authors found little evidence that people turn consistently in one direction, suggesting a more random process.



J. SOUMAN/MAX PLANCK INST. BIOL. CYBERNETICS

PHYSIOLOGY

Smooth transitions

J. Clin. Invest. doi:10.1172/JCI38864 (2009)

A pair of short RNA strands known as microRNAs may represent a therapeutic target for some forms of arterial disease.

The smooth muscle cells of arteries can switch between two phenotypes: contractile and synthetic; accumulation of the latter is associated with atherosclerosis. In a search for microRNAs that might control this switch in mice, Thomas Braun and Thomas Boettger at the Max Planck Institute for Heart and Lung Research in Bad Nauheim, Germany, and their collaborators came across two microRNAs — 143 and 145 — that are expressed in smooth muscle cells throughout the body (coloured blue in the heart pictured below). Their sequences are necessary for normal development of contractile smooth muscle cells.

The researchers performed an *in vivo* analysis of the proteins regulated by the microRNAs. Among them was ACE, a protein targeted by a major class of blood-pressure medication.

CANCER BIOLOGY

A nasty cut

Cell **138**, 673–684 (2009)

Cancer progression is often aided by increased expression of particular genes called oncogenes. Although this is often associated with changes in DNA,

Christine Mayr and David Bartel of the Whitehead Institute for Biomedical Research in Cambridge have shown that alterations to the messenger RNAs of several oncogenes can also contribute.

These alterations mostly occur as a result of alternative processing in the 3'UTR, an RNA region that doesn't encode protein. The processing involves the way that the end of an RNA strand is cut and the position at which a string of adenine bases is added, resulting in 3'UTRs of different lengths. Shorter than usual 3'UTRs make the mRNA more stable, typically allowing it to produce ten times the normal amount of the oncogene's protein. This overexpression is only partly explained by the loss of sites on the RNA that are recognized for silencing by microRNAs.

ECOLOGY

Winter warmer

J. Ecol. doi:10.1111/j.1365-2745.2009.01544.x (2009)

Many studies of Arctic warming have focused on summer temperatures, but a new study suggests that vegetation can be damaged by unseasonably warm winter weather.

Stef Bokhorst of the University of Sheffield, UK, and his colleagues looked at how the mountain crowberry (*Empetrum hermaphroditum*), the dominant shrub in northwestern Scandinavia, fared after a sudden, rapid warming in the region in December 2007. The following summer, many of the shrubs had

dead shoots, and overall vegetation growth across an area of 1,424 square kilometres was 26% lower than in the previous year.

An ecosystem-manipulation experiment that heated the ground produced a similar drop-off in shoot growth.

MODEL ORGANISMS

A new kind of knock out

Dis. Models Mech. doi:10.1242/dmm.003087 (2009)

A new tool to insert, delete and invert genes in a precise fashion could allow more sophisticated animal models of human diseases to be produced.

Francis Stewart at the Technical University of Dresden in Germany and his colleagues validated the potential of a previously discovered enzyme called Dre recombinase that cuts and rearranges DNA at specific target sites called *rox*. They show that it can be used to create mice in which specific gene sequences are disrupted.

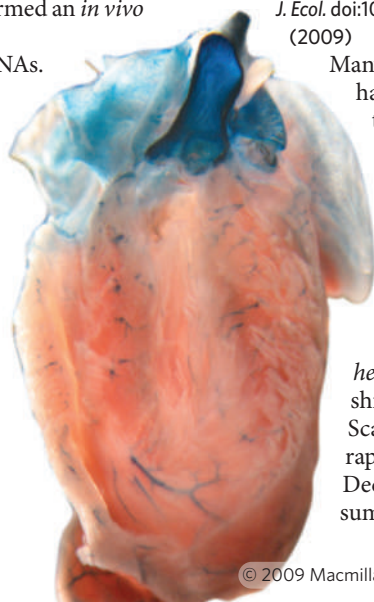
The Dre-*rox* system does not cross-react with a commonly used system for genetically engineering mice called Cre-*loxP*, the authors found. Thus, the two systems could be used in combination to create knock-out mice with independent controls for multiple genes.

NANOTECHNOLOGY

Origami bridge

Nature Nanotechnol. doi:10.1038/nnano.2009.220 (2009)

The miniaturization of electronic circuitry is limited by the size of features that can be etched into a surface using conventional lithography. Bridging the gap to the molecular world of self-assembling structures has been a major challenge in nanotechnology.



AM. SOC. CLIN. INVEST.

Paul Rothemund of the California Institute of Technology in Pasadena, Gregory Wallraff of the IBM Almaden Research Center in San Jose, California, and their colleagues now show that DNA, folded origami-style into triangles measuring 127 nanometres on each side, can slot neatly into matching depressions carved onto a silica surface.

In principle, each chunk of DNA origami can be attached to an individual molecule such as a conducting nanowire or a fluorescent protein. As a result, these structures offer a way to control the positioning and orientation of single molecules using straightforward lithographic techniques.

BIOLOGY

Following in the wake

Phys. Rev. Lett. **103**, 078102 (2009)

Fish can sense subtle differences in water pressure and velocity using the lateral line, a collection of sense organs that run the length of their bodies. So far, most research into this capability has been limited to the sensing of simple oscillating objects. Jan-Moritz Franosch of the Technical University of Munich in Germany and his colleagues now show how fish detect more complex disturbances — the orientation of ring-shaped vortices left in the wake of other fishes.

The authors modelled the stimulus expected from a vortex ring passing a fish's lateral line and compared this with recorded neuronal responses from a fish fixed in place and subjected to passing vortices. The recordings fit the model's predictions. Information on the orientation of vortices should allow fish to track the movement of other animals — and perhaps a meal — the authors argue.

PHYSICS

Trip the light magnetic

Science **325**, 973–976 (2009)

Researchers have coaxed the tiny particles known as quantum dots to change their magnetic properties simply by shining light on them. The finding is another development in the quest to produce 'spintronic' devices that rely on particles' spin states, rather than their charge, to convey information.

By adding manganese to a chemical suspension, or colloid, of cadmium selenide quantum dots, Daniel Gamelin at the University of Washington in Seattle and his co-workers were able to manipulate the particles' magnetism in new ways. Earlier work had had to be done at ultracold temperatures; the colloidal suspension permitted the particles to power up strong magnetic fields, retaining magnetic signatures even at room temperature.

The researchers say that future steps might include incorporating colloids into nanoparticle manufacturing technologies to see what other effects occur.

PLANT BIOLOGY

The other garden path

Cell **138**, 738–749 (2009)

There is more than one way to flower. In the thale cress, *Arabidopsis thaliana*, the well characterized *FT* gene encodes a pro-flowering protein that travels from leaf to shoot in response to changes in day length.

Now, Detlef Weigel and his colleagues at the Max Planck Institute for Developmental Biology in Tübingen, Germany, show that another pathway regulated by microRNAs

— molecules that prevent translation of messenger RNAs into proteins — can stimulate flowering independently of daylight cues.

They find that levels of microRNA-156 decline as the plant ages, paralleling a rise in expression of the genes it seems to silence. The products of these genes, called SPLs, set off floral development.

GEOSCIENCE

Ground down

Nature Geosci. doi:10.1038/ngeo616 (2009)

Glaciers are often said to be better than rivers at eroding the land, in part because of the dramatic landscapes they leave behind. But Michele Koppes of the University of British Columbia in Vancouver, Canada, and David Montgomery at the University of Washington in Seattle challenge this belief.



By compiling global data on erosion rates from glacial and non-glacial environments, they show that both ice and water flows can erode rock at up to 10 millimetres per year in areas of rapid tectonic uplift.

It seems that tectonics controls erosion rates from both rivers and glaciers, they say, and claims that glaciers erode faster are largely explained by incomplete data.

E. WELTY/AURORA PHOTOS

JOURNAL CLUB

Paul Riley
University College London

A molecular cardiologist looks into getting to the heart of his inner fish.

Newts do it, fish do it, but sadly humans and other mammals cannot repair or regenerate damaged heart tissue as adults.

Despite the modern-day promotion of healthier lifestyles (such as bans on smoking in public places and pro-fitness campaigns in the run-up to London 2012),

cardiovascular disease is still on the up worldwide and, not unlike swine flu, is a true pandemic that respects no borders. As a result, and for some time now, I and others have been asking how we might become more newt-like or fish-like and repair our own hearts after a heart attack.

We have favoured looking at small resident progenitor cells which, when stimulated, might make new heart muscle and blood vessels. But a study by Bernhard Kühn and his colleagues at the Children's Hospital Boston in Massachusetts shows us another

way (K. Bersell *et al.* *Cell* **138**, 257–270; 2009).

They simply asked whether or not existing heart muscle can be instructed to divide and make more of the same. Apparently it can, with the help of the epidermal growth factor neuregulin (famed for its role in the nervous system), and its Erb4 receptor. While under the influence of neuregulin, some mature heart cells in mice disassemble their scaffold, re-enter the cell cycle, divide and regenerate injured muscle.

Of course, the devil is in the detail: the trick, it seems, is to

have not only plenty of neuregulin, but also more heart muscle cells with one nucleus instead of two, because only the former responded to the growth factor. Unfortunately, this presents something of a conundrum where mammals are concerned. Mammalian heart-muscle cells generally become binuclear shortly after birth. Thus, for a complete fix, we are left heading back in the direction of the drawing board.

Discuss this paper at <http://blogs.nature.com/nature/journalclub>

NEWS BRIEFING

● POLICY

Stem cells: Restrictions on human embryonic stem-cell research in **Japan** were relaxed on 21 August, after updated government guidelines came into effect. But some scientists fear the new rules have come too late to regain lost ground in the field. For more, see page 1068.

Nuclear monitoring: Iran last week allowed inspectors from the **International Atomic Energy Agency** to visit a heavy-water nuclear reactor near the city of Arak, and agreed to changes that will ease monitoring at a uranium-enrichment facility at Natanz. The country last year withdrew access to the 40-megawatt Arak reactor, which is currently under construction and could enter operation as early as 2014. When completed, it will burn uranium fuel, producing electricity and a range of nuclear isotopes, including plutonium. Iran denies that the reactor has a military purpose.

Chemical regulation: The costs of complying with European Union legislation on chemical safety (REACH) are much greater than thought, according to a study released by toxicologists. Industry may have to spend €9.5 billion (US\$13.6 billion) on **toxicity testing** — six times more than expected — and the number of animals used in the tests could rise by 20 times to 54 million. The chemical industry challenged the numbers as worst-case estimates. For more, see pages 1065 and 1080.

Pandemic flu: People infected with the H1N1 swine flu virus who are otherwise healthy should not routinely be given **antiviral drugs**, the World Health Organization (WHO) warned last week. Its recommendations are at odds with current practice in many countries, where oseltamivir (Tamiflu) is routinely given out to all those suspected of having contracted H1N1. Although those with



It may have been watched by millions, but the launch of South Korea's first space rocket on 25 August was only a 'partial success', according to the country's science ministry. The two-stage Naro-1 blasted off from Naro Space Center, some 485 kilometres south of Seoul but, as *Nature* went to press, it had failed to put its observation satellite into its intended orbit. A second rocket launch from South Korean territory is planned for spring 2010.

"uncomplicated illness" should not get oseltamivir or zanamivir (Relenza), the WHO did recommend giving drugs to those presenting with severe illness, to children under five and to pregnant women (see <http://tiny.cc/WHOHI1N1>).

Renewable energy: On 20 August, **Australia's** parliament approved laws that require the country to produce 20% of its electricity from renewable sources by 2020 — up from around 8% today. The renewable-energy target is expected to spur billions of dollars of investment in wind, solar and hydroelectric power, although methane waste gas from coal mining was also classified as a renewable-energy source under the bill. The measures were delinked from a broader legislative package, defeated on 12 August, that proposed a cap-and-trade scheme to limit greenhouse-gas emissions from industry (see *Nature* 458, 554–555; 2009).

● EVENTS

Fraud trial: After almost three-and-a-half years, the trial of **Korean** stem-cell researcher **Woo Suk Hwang** may be drawing to

a close. On 24 August, in a final evidence hearing, prosecutors requested a four-year prison term for Hwang, who is charged with fraud, embezzlement of state funds and violation of the country's bioethics law. His papers claiming that he had created cloned human embryonic stem cells were shown to be fabrications in January 2006. A court decision is expected in mid-October.

Research voyage: A US research vessel left Oregon on 22 August for Canadian waters to conduct **seismic studies** imaging seafloor structures, after a Canadian court declined to halt the cruise. As *Nature* went to press, environmental groups seeking to block the use of air guns during the tests (see *Nature* 460, 939; 2009) were expected to return to court on 25 August to try to divert the RV *Marcus Langseth* from her mission.

SOUND BITES

"We won't be correcting the atlas."

Daniel Gutknecht, Swiss Federal Office of Topography

The Swiss government last week approved expanding the country's border into Italy, because melting glaciers in the Alps have altered the watershed that marks the border. (AP)

● BUSINESS

Stem cells: Six months after giving it the green light, the US Food and Drug Administration (FDA) halted plans for the world's **first clinical trial** of a therapy generated from human

JUNG YEON-JE/AFP/GETTY IMAGES

embryonic stem cells. The product's manufacturer, **Geron** in Menlo Park, California, had hoped to start human testing of its potential treatment for spinal-cord injury this summer (see *Nature* 457, 516; 2009). Geron says the hold order came after it submitted additional data from studies testing dose escalation, and from investigations of the product's use for other neurodegenerative diseases. It added that it was working closely with the FDA to review the data.

Drug development: Eli Lilly abandoned development of its **osteoporosis** drug arzoxifene, after results from an advanced clinical trial suggested it did not offer sufficient benefit over currently available treatments. The company, headquartered in Indianapolis, Indiana, had hoped arzoxifene would be a successor to its blockbuster osteoporosis treatment raloxifene (Evista), which will lose its patent protections by 2014. Meanwhile, **Amgen**, of Thousand Oaks, California, has received more positive news for its new-mode-of-action osteoporosis treatment, denosumab. The monoclonal antibody gained recommendations from an advisory committee at the Food and Drug Administration on 14 August, and awaits full approval.

● FACILITIES

Medical collaboration: The University of California, San Diego (UCSD) and the Indian Institute of Technology Kharagpur signed a pact last week to develop allied

NUMBER CRUNCH

16.99°C

The average surface temperature of the world's oceans in June and July 2009 — the warmest measured since records began in 1880.

(NOAA)

research, teaching and medical programmes. The agreement also calls for a joint **Indian-US medical centre** in Kharagpur. India will fund the 300-bed facility, with UCSD collaborating on clinical care and research. Researchers will study drug development, bioengineering and imaging technologies at the two campuses. The chance to test therapies on different populations makes the collaboration particularly attractive for physicians.

Isotope shortage: A nuclear reactor in Petten, the **Netherlands**, that supplies radioactive isotopes for use in medical imaging reopened

last week after a month's scheduled maintenance — partly alleviating a global shortage of the isotopes (see *Nature* 460, 312–313; 2009). But the reactor is due to shut down again next March for six months of repairs. **Canada's** Chalk River, Ontario, reactor — whose closure precipitated the isotope crisis — will not reopen until 2010.



Tobacco regulation: Lawrence Deyton (pictured) was appointed to direct the new **Center**

for Tobacco Products in Silver Spring, Maryland, part of the Food and Drug Administration (FDA). Deyton, who will start his new job on 14 September, is a physician at George Washington University's School of Medicine and Health Sciences in Washington DC, and a public health officer at the US Department of Veterans Affairs. He has also led research on allergy and infectious diseases at the National Institutes of Health. The FDA won powers to regulate tobacco for the first time in its 103-year history under legislation passed by Congress in June (see *Nature* 459, 901; 2009).

● ENVIRONMENT

Mercury contamination: A quarter of fish sampled from 291 streams across the **United States** between 1998 and 2005 contained levels of mercury higher than those deemed safe for human consumption, according to a non-

THE WEEK AHEAD

29 AUGUST-1 SEPTEMBER

The European Molecular Biology Organization holds its first annual conference in Amsterdam.
www.the-embo-meeting.org

30 AUGUST-3 SEPTEMBER

The seventh World Congress on Alternatives and Animal Use in the Life Sciences meets in Rome.
www.aimgroup.eu/2009/WC7

31 AUGUST-4 SEPTEMBER

The World Meteorological Organization hosts the third World Climate Conference in Geneva.
www.wmo.int/wcc3

31 AUGUST

The ten-person presidential panel deliberating NASA's future, chaired by Norman Augustine, is expected to publish its final report.

1 SEPTEMBER

The UK Royal Society will release a report on climate geoengineering options — the first such review from a major scientific academy.

peer-reviewed report from the US Geological Survey (USGS). More than two-thirds contained levels exceeding the Environmental Protection Agency's level of concern for the protection of fish-eating mammals, says the USGS. Coal-fired power plants are the main source of mercury reaching US waterways.

BUSINESS WATCH

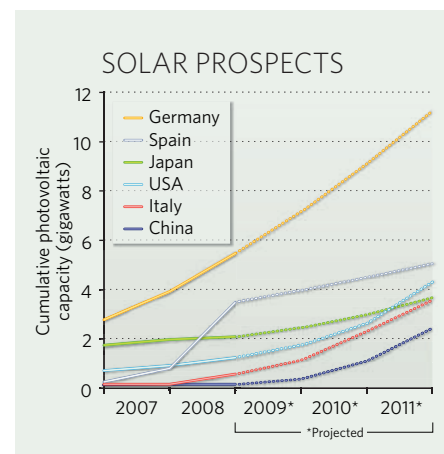
Despite the economic crisis, countries are still installing solar capacity at a rapid rate, as the cost of solar panels plummeted in the first half of 2009 (see also *Nature* 460, 677; 2009).

Prices of photovoltaic panels have dropped by almost 50% since September 2008, says Jenny Chase of New Energy Finance, a London-based global consultancy firm. The glut of cheap panels saw many solar companies reporting reduced revenues in the past financial quarter.

Chase says that Italy, a relative newcomer to solar power, is likely to be the second largest installer of photovoltaics in 2010. And Germany's solar capacity, which far exceeds that of other countries, should continue to increase (see chart).

Only Spain is slowing down. Generous feed-in tariffs, which guarantee a set price for each unit of electricity supplied by a solar provider, saw the country install 2.7 gigawatts of solar capacity in 2008; the Spanish government has now capped the amount of solar power eligible for this tariff at 0.5 gigawatts.

As the recession continues to bite, venture-capital investment in solar companies has fallen. Analyst Dallas Kachan, managing director of Cleantech Group, headquartered in Brighton, Michigan, says that solar investment sank from a high of US\$1.2 billion in the third quarter of 2008 to \$115 million in the second quarter of 2009.



Chemical-safety costs uncertain

Researchers and regulators disagree on how REACH legislation will affect costs and loss of animal lives.

Europe's chemical regulator has questioned a study suggesting that industry will have to spend €9.5 billion (US\$13.6 billion) — six times more than expected — on toxicity testing over the next decade, to comply with European Union (EU) legislation on chemical safety. The tests would require an estimated 54 million animals — a situation dismissed as a “worst-case scenario” by the European Chemical Industry Council (Cefic), a Brussels-based organization representing the European chemical industry.

The EU's REACH (Registration, Evaluation, Authorisation and Restriction of Chemicals) legislation, which came into force in 2007, is the world's most extensive attempt at improving the safe use of chemicals. It requires the registration and submission of toxicity data for all chemicals sold in the EU in quantities of more than one tonne per year by 2018.

But a study by Thomas Hartung, former head of the European Centre for the Validation of Alternative Methods (ECVAM) in Ispra, Italy, and Costanza Rovida, a consultant chemist in Varese, Italy, says that Europe lacks enough laboratories to carry out all the tests that the legislation demands. This will render the legislation unfeasible, concludes the study, which will be presented at the World Congress on Alternatives and Animal Use in the Life Sciences in Rome that begins on 30 August.

REACH's aim “will not be achieved” using traditional toxicity testing methods, says Hartung, now at Johns Hopkins University in Baltimore, Maryland. “The problem is that REACH will exceed the test capacities in Europe,” he says. “This will cause delays in testing, and [regulators] will not get all the data needed to take the decisions that are necessary.”

Hartung calls for a moratorium on the requirement to test chemicals' effects on reproductive systems in two generations of animals. These two-generation studies account for the lion's share of the increase in costs and test animals, the study says. The Organisation for Economic Co-operation and Development (OECD) is drawing up guidance for an extended one-generation reproductive toxicity test. The aim of this scheme is that tests beyond the first generation would be conducted only if a specific cause for concern arose in the first-generation offspring.



REACH rules will necessitate tests on millions of animals.

The OECD will hold a meeting in October to discuss outstanding technical issues, including what would be considered as a trigger for additional tests. Draft guidelines are expected to be submitted for approval in March 2010. If they get the green light, the guidelines would be published around September 2010, and could then be instituted before testing begins in December 2010.

European enlargement

In a written response to *Nature*, the European Chemicals Agency, in Helsinki, which administers the REACH system, disputes many of the figures put forth in the new study. The agency expects slightly more than 9,000 chemicals to be registered under REACH by its 1 December 2010 deadline for substances produced or imported in quantities of more than 1,000 tonnes a year, and 30,000 chemicals by 2018. It says it does not expect the costs and use of laboratory animals to differ significantly from the original estimates, which were based on an expectation that 8,730 chemicals would be registered by the 2010 deadline.

Hartung says that his estimates of cost and

numbers of animals used are based on an expectation that at least 68,000 chemicals will be registered by 2018, given the growth in the EU's chemical industry over the past 15 years and the addition of 15 more countries to the EU since 1995.

Cefic says it does not think that this growth will result in drastically more substances being registered. The council also expects around 30,000 chemicals to be registered by December 2018. “We are convinced that the situation in the article will not be reached because there will be fewer substances to be registered,” says Erwin Annys, the council's director of chemicals policy.

However, Manfred Liebsch, a toxicologist at the Federal Institute for Risk Assessment in Berlin, says the study's figures are “realistic”. “I support the aims of REACH, but if there are delays in testing, it will not be doing its job of providing safety to people and the environment,” he says. “Something must be changed.”

BASF, the chemical company headquartered in Ludwigshafen, Germany, says “it is not able to give valid feedback on the estimated numbers of needed studies and costs yet”, because discussions on toxicity data are ongoing. “It's not clear yet if all needed animal tests requested by REACH can be finalized in time,” the company says. “It seems there is not enough testing capacity available globally.”

“The article gives the impression that the data requirements for REACH can only be fulfilled by additional testing. This is not correct. So it is difficult to say how accurate the conclusions are,” says Claudius Griesinger, a neuroscientist and project manager at the ECVAM. “Only practice will show what data are currently available.”

Hartung calls for increased funding of new toxicology testing methods, saying that alternatives to animals experiments must be found if REACH is to succeed. He says the biggest advances are currently taking place in the United States, in particular the Environmental Protection Agency's ToxCast programme, which is developing ways to forecast the potential toxicity of chemicals using high-throughput screening bioassays developed in the pharmaceutical industry to discover new drugs. ■

Natasha Gilbert

See Opinion, page 1080.

P. GOETGHELUCK/SPL

China boosts pandemic surveillance

China is stepping up disease surveillance, drug stockpiling and vaccine development as fear of a second wave of pandemic influenza H1N1 intensifies. Chinese vice-premier Li Keqiang described the country's expanded pandemic plan last week in Beijing at a meeting convened by China's health ministry, the World Health Organization (WHO) and the London-based medical journal *The Lancet*. Experts warn, however, that the lack of systematic screening of patients with severe respiratory conditions, and inadequate health care in the country's rural areas, may stifle the efforts.

As of 24 August, mainland China had confirmed 3,103 cases of H1N1 flu, 75% of which were in five provinces. The only reported severe case, identified on 8 August, involves a 17-year-old in Guangdong province who also has Brugada syndrome, a genetic disease with an increased risk of sudden heart failure.

The epidemiology of H1N1 flu in China is similar to that elsewhere, says Yu Hongjie, deputy director of the disease control and emergency response office at the Beijing-based Chinese Center for Disease Control and Prevention (CDC). But of the 1.3 billion people in China, 300 million are children, elderly or pregnant, or have chronic diseases or reduced immune function — and are at high risk of developing severe or fatal disease if infected. “This is a daunting challenge and will be a test case for the country's surveillance strategies and health-care system,” says Ira Longini, a biostatistician and epidemiologist at the University of Washington in Seattle.

Initially, China focused on screening those entering the country and on monitoring patients with respiratory illness who had visited areas with confirmed H1N1 cases or had been in contact with diagnosed patients. Healthy people in close contact with H1N1 patients were quarantined.

“China has been very open from the beginning and has done an excellent job in containing the outbreak,” says Keiji Fukuda, the WHO's assistant director-general for health security and environment. But the containment strategy has become inadequate as the virus continues to spread, he says. The emphasis on detection, laboratory confirmation and investigation of all cases, even mild ones, is resource-intensive, leaving little capacity to investigate severe cases and other exceptional events.

Since 8 July, China has switched to testing patients with influenza-like illness for H1N1



As temperatures fall, China hopes to keep the expected winter resurgence of H1N1 flu under control.

infection in the 556 ‘sentinel’ hospitals and 411 virology laboratories across the country, says Yu. The government is closely monitoring local outbreaks and unusual disease clusters.

Some experts, such as Tomimasa Sunagawa, an epidemiologist at the National Institute of Infectious Diseases in Tokyo, are “curious” about the small number of confirmed and severe cases of H1N1 infection in mainland China — compared with about 6,000 confirmed and 13 severe cases in Japan, and 8,210 confirmed and 31 severe cases in Hong Kong, as of 20 August. Chen Zhu, China's health minister, says that early diagnosis and intervention in mild H1N1 infection may have resulted in the small number of severe cases reported in mainland China.

“Although the purpose of surveillance is to follow the trajectory of the pandemic, rather than to pick up every infected individual, identifying severe cases is an important component of influenza surveillance,” says Robert Fontaine, a Beijing-based epidemiologist with the US Centers for Disease Control and Prevention who consults for the Chinese CDC. One approach, he says, might be to collect throat swabs from a fraction of the patients with severe respiratory conditions and test them for H1N1.

Others fear that it may be hard to monitor H1N1 infection in the rural areas. Since 2005, China has seen 36 human cases of the avian influenza H5N1 virus, with an average of eight

days between disease onset and hospitalization — largely because doctors in village and county clinics are unable to make the diagnosis. In addition, doctors in underdeveloped regions may be offering inadequate or dangerous treatments for symptoms related to H1N1 infection; many clinics and hospitals in China, especially in rural areas, use dexamethasone, a potent immunosuppressant, to treat acute fever. “This could be very dangerous for patients with H1N1 infection,” Fontaine says.

Wang Yu, director of the Chinese CDC, acknowledges these challenges, but says the central government is making every effort to raise pandemic awareness and the standard of diagnosis and treatment by rural doctors.

Meanwhile, China is trying to produce as much H1N1 vaccine as possible. At the Beijing meeting, Liang Xiaofeng, director of the national immunization programme at the Chinese CDC, disclosed preliminary results of vaccine trials involving more than 13,000 healthy volunteers, including the health minister. Preliminary data from nearly 4,000 people suggest that the vaccine is safe and has elicited significant immune responses after the first injection.

“The results are encouraging,” says Longini. “But it's still very early days.” If the findings are confirmed, says Chen, China will produce 65 million doses of vaccine by the end of the year and another 65 million by next spring. ■

Jane Qiu

See <http://www.nature.com/swineflu> for more on swine flu.

LIU YING/XINHUA NEWS AGENCY/EYEVINE



SANOFI-AVENTIS IN R&D SHAKE-UP
Research chief Paul Chew talks about the drug company's future.
www.nature.com/news

SANOFI-AVENTIS

US plans for science outreach to Muslim world

The administration of US President Barack Obama is ramping up plans to develop scientific and technological partnerships with Muslim-majority countries.

The move follows a June speech by Obama at Cairo University in Egypt, when he promised to appoint regional science envoys, launch a fund to support technological development and open centres of scientific excellence in Africa, the Middle East and southeast Asia. So far, the science-envoy plan is closest to getting off the ground, say White House officials, who see it as part of a broader drive to improve relations with the Islamic world.

"Polling consistently shows that science and technology is an area

where the United States is widely respected for its leadership," says a top administration official, speaking on condition of anonymity. "This is a key part of the comprehensive partnerships we are pursuing with Muslim-majority communities." The effort is being led by the National Security Council and the Office of Science and Technology Policy.

The White House plans for leading US scientists to visit a Muslim-majority region for several weeks, to canvass local researchers, community leaders and others for ideas that would shape scientific initiatives.

Various US embassies have already identified themes of interest, officials say. Lebanon, for

instance, has expressed an interest in technology development focused on the environment, and Bangladesh wants to initiate mentoring programmes for young scientific professionals. The first science envoy is expected to be announced "shortly", according to the administration official.

"They [the administration] clearly have the door open for ideas, and we have ideas," says John Boright, director of international affairs at the National Academy of Sciences in Washington DC, an independent advisory group.

Boright was part of a delegation that visited Syria this spring to

discuss science and technology exchanges. Syrian researchers told it that their greatest need was for more training for nurses and medical technicians. Setting up a training centre along those lines might be "low-hanging fruit" for the White

House to pluck off, Boright says.

In the longer term, the White House will need to work within or around science initiatives that are

already underway, such as the Masdar eco-city in the United Arab Emirates and the King Abdullah University of Science and Technology, due to open next month in Saudi Arabia.

Alexandra Witze

"This is a key part of the partnerships with Muslim-majority communities."

Fossil protection law comes under fire

Chinese palaeontologists met government officials in Beijing last week to lobby for strict federal control of fossil specimens. The researchers are working to get changes incorporated into a draft law released in March by the Legislative Office of the State Council, which advises China's leaders, and the Ministry of Land and Resources.

As China has experimented with private enterprise, poor farmers have burrowed into hillsides, uncovering fossils from the Cretaceous to the Jurassic that have rewritten the palaeontological literature. With international traders paying tens of thousands of dollars for important finds, provincial officials have fought with the federal government for control over permits to dig and regulate the bounty.

Yet many scientists inside and outside China fear that the proposed federal law may foster the rampant trade in illegal fossil specimens. Zhou Zhonghe, director of the Institute of Vertebrate Paleontology and Paleoanthropology in Beijing, and other researchers have proposed several changes. These would include giving the land and resources ministry authority over vertebrate

fossil collections, and setting up a national panel of palaeontologists to regulate the collections on a nationwide level. "I think many of our suggestions will be adopted," Zhou says.

The law isn't expected to be finalized until early next year. The process is being watched closely by researchers worldwide who collaborate with Chinese palaeontologists. "I am in complete support of the Chinese government and academic institutions trying to clarify the laws to protect their tremendous fossil

heritage," says palaeontologist Mark Norell of the American Museum of Natural History in New York.

Palaeontologist Gao Keqin, of Peking University, remains deeply concerned. He says that recent versions of the draft law would not prevent provincial officials from blocking research by demanding large sums from scientists.

"The current situation is problematic because local jurisdictions with rightful interests but only a vague understanding of the scientific value of fossils can

unilaterally stop legitimate scientific exploration," says James Clark, a palaeontologist at George Washington University in Washington DC.

Many provinces built palaeontological museums in the hope of tapping the tourist trade, but fossil smugglers often use them as a front to buy and sell specimens. "Fossils require an institution with staff educated in curation and preservation," says Clark. "But few places in China have these facilities."

"I hope the new law will let us protect the fossil heritage," says Zhou. ■
Rex Dalton



Fossils found in Chinese rock formations have fuelled a cottage industry in illegal trading of specimens.

M. LEONG/REDUX/EYEVINE

Japan relaxes human stem-cell rules

But scientists fear it is too late to regain lost ground.

A long-sought loosening of Japan's guidelines on human embryonic stem-cell research came into effect on 21 August. But some say the new rules are too little, too late for a struggling field that was once a source of national pride.

On the surface the previous guidelines, set in 2001, were permissive. They allowed scientists to derive new human embryonic stem (ES) cell lines and research both home-grown and imported cell lines. But that could be done only after the research was approved, and the approval process was the stumbling block. Proposed projects needed to be approved twice — first by a local institutional review board and then by a science-ministry committee. And researchers working on human ES cells had to use separate facilities from other stem-cell research.

The upshot was a slowing down of research, some say. Roughly 50 groups have passed the application process, says Hirofumi Suemori of Kyoto University's Institute for Frontier Medical Sciences. But that is only about a quarter of the number that he estimates originally wanted to use human ES cells, based on the number of groups that work with mouse ES cells or request materials derived from human ES cells.

Some charge that the regulations cost the country leadership in the field. It was Shinya Yamanaka of Kyoto University who, in 2006, created induced pluripotent stem (iPS) cells for the first time (K. Takahashi and S. Yamanaka *Cell* **126**, 663–676; 2006) — produced from normal adult cells, iPS cells have the potential, like ES cells, to generate any cell type in the body. But it soon became clear that expertise with ES cells was essential for advancing iPS-cell technology, and further experiments such as comparing the properties of iPS cells and ES cells were done outside Japan. Even in the United States, where until this year federal funding was limited to ES-cell lines derived by August 2001, ES-cell research moved ahead, says Suemori. "Researchers there were able to press forward, and with that as the foundation, they also stole the lead in iPS-cell research," he says.

The Japanese government has been slowly trying to change the restrictions. In April, a new



Until April, Japanese scientists had to run separate facilities for human embryonic and other stem cells.

section in the explanatory material for the old guidelines erased the requirement for separate facilities. The latest guidelines also remove the secondary approval step for working with ES cells: a local review committee must still approve the work, but researchers then need only notify the science ministry of this.

Yet some burdensome restrictions remain, says Suemori. For example, the notification must include "word-for-word" minutes of the local review committee's meeting.

And the two-stage approval process remains for deriving new cell lines. Norio Nakatsuji, director of Kyoto University's Institute for Integrated Cell-Material Sciences, who created all five of Japan's human

ES-cell lines, has given up plans to make any more. "I would summarize the change as being from absurd to excessively strict," he says. "These irrational guidelines have done and will probably continue to do great damage to all related research fields in Japan."

Last December, Yamanaka was widely quoted for remarks made at a science-ministry assembly in which he appraised Japan's 2008 record against

other iPS-cell research groups, mostly in the United States: "One win, and about 10 losses," he said.

The new regulations were pushed through by the Council for Science and Technology Policy, a 15-person group chaired by the prime minister that stands as the country's highest science-policy body. Junichi Iwata, of the science ministry's life-science division, says the changes were targeted at the use of human ES cells and

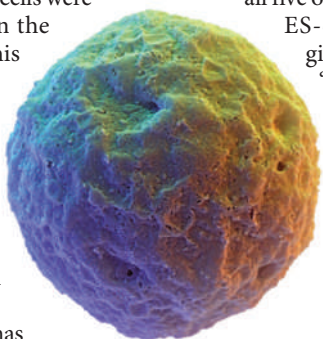
not their derivation, explaining that only two groups are licensed to derive such cells.

Asked why the reform didn't go further in addressing researchers' criticisms, he says: "The new guidelines just went into effect, so we'll see how things go. If need be, we'll change them again."

But it might be too late to make a difference. Most of Japan's stem-cell researchers have already been pushed into iPS-cell research through targeted funding programmes and are unlikely to go back to the ES-cell basics. "I do not expect a dramatic increase in ES-cell research," says Shin-Ichi Nishikawa, a stem-cell researcher at the RIKEN Center for Developmental Biology in Kobe.

Suemori likewise sees little change and fading hope. "It will be very difficult for us to catch up now," he says.

David Cyranoski



Future hope: a human embryonic stem cell.

FDA narrows drug label usage

The US Food and Drug Administration (FDA) has altered the usage labels on two cancer drugs on the basis of a re-evaluation of clinical data.

The agency introduced the change last month after its Oncologic Drugs Advisory Committee (ODAC) recommended that the drugs Erbitux and Vectibix — approved in 2004 and 2006, respectively, for patients with advanced-stage colorectal cancer — should now be prescribed only to individuals with a certain gene variant. To reach the decision, the agency reviewed seven randomized clinical trials, all of which showed that only the 60% or so of patients whose tumours harbour the non-mutated or ‘wild-type’ form of a gene called *K-RAS* responded positively to the drugs.

Ideally, the FDA would want to do these kinds of genetic-marker tests for patient response in a well-designed, forward-looking experiment, says ODAC consultant Richard Simon, chief of the National

Cancer Institute’s biometric research branch in Rockville, Maryland. “But cancer biology is very complex, and I think we’re going to find that it’s not always possible to have [all the answers] figured out beforehand.”

Erbitux is made by ImClone Systems and marketed by Bristol-Myers Squibb, both based in New York. Vectibix is made by Amgen, headquartered in Thousand Oaks, California.

Analysts and scientists are split on whether to expect after-the-fact label adjustments for other drugs. “The FDA will certainly become more open to these types of changes over time,” says Bruce Booth, a pharmaceutical analyst with Atlas Venture in Boston, Massachusetts.

ODAC member Gary Lyman of the Duke Comprehensive Cancer Center in Durham, North Carolina, says that revisiting drug efficacies could become so widespread that the FDA should at least encourage companies to bank tissues from finished trials for unanticipated post-hoc tests.

David Reese, Amgen’s executive director of oncology, says that some of the retrospective analyses would not have been possible had the company not banked tissues. “Obtaining tissues and having [them] available in the future is really critical,” he says.

But David Harrington, a statistician

at the Dana-Farber Cancer Institute in Boston, Massachusetts, and another ODAC member, says future calls for retrospective analyses will probably be considered on a case-by-case basis. “It was the striking nature of the data that led to the recommendation” to change Erbitux and Vectibix labelling, he says, “and it’s unlikely to happen very often in the future”.

Indeed, many argue that the conditions surrounding the label change were unique and won’t set a precedent. The American Society of Clinical Oncology and the National Comprehensive Cancer Network had already recommended that doctors test for *K-RAS* variants before treatment. Moreover, the drug companies themselves had asked for restricted use after learning

about the *K-RAS* results. In announcing the change, the FDA affirmed that both drugs are “not recommended for the treatment of colorectal cancer with [*K-RAS*] mutations”.

Doctors are now advised — but not compelled — to test for *K-RAS* before administering the drugs, notes Stephen Little, chief executive of DxS, a diagnostics company in Manchester, UK, that markets a *K-RAS* mutation test kit. He says that most drug companies now conduct diagnostic screening during clinical development.

In Europe, Erbitux’s label changed more than a year ago to reflect the *K-RAS* status, and Vectibix won approval only for those patients with non-mutated *K-RAS*. “Europe has been more inclined to look at retrospective data if otherwise those data are robust and reflect the general population in that trial,” says Hagop Youssoufian, senior vice-president of clinical research and development at ImClone in Branchburg, New Jersey.

Both drugs are currently being tested for use in combination with chemotherapy; data on this will be presented next month at a joint meeting in Berlin of the European Cancer Organisation and the European Society for Medical Oncology. These tests include two phase III trials, of roughly 1,200 patients each, that show Vectibix in combination with chemotherapy kept tumours in check for significantly longer in cancer patients with wild-type *K-RAS*, and a similar trial — details of which are not yet public — involving Erbitux. ■

Elie Dolgin

“Obtaining tissues and having them available in the future is critical.”

Canada assumes weighty mantle

Instrument to help redefine the kilogram makes a transatlantic move.

In the mission to define the kilogram more sensibly, only two of the instruments known as 'watt balances' have proven good enough to tackle the job. And one of them is currently in pieces, having been sold and shipped from the United Kingdom — the birthplace of this type of device — to Canada.

The move has some UK scientists saddened by their loss, and Canadians excited by their gain. It also has metrologists around the world holding their breath. "Taking it all apart, shipping it, putting it back together — the worrisome thing is that something will break," says Richard Steiner, who works with the other top watt balance at the US National Institute for Standards and Technology (NIST) in Gaithersburg, Maryland. "It's very fragile, and a lot of it is pretty old." The Canadian lab expects to receive the package by the end of August.

The kilogram is the only unit of measure still defined by a single object — a lump of platinum-iridium held in a vault near Paris. Over time, as atoms accrete or fall off this particular kilogram, its mass changes. Metrologists are thus aiming to redefine the kilogram on the basis of something more stable — such as Planck's constant, the value that quantifies the relationship between the energy and frequency of light, and which can be related to mass through equations of quantum physics and electromagnetism.

The best way to pin down the value of

Planck's constant is with a precision watt balance. Canada's device, which is about the size of a minivan, contains a metre-long balance beam, with a precisely known mass at one end and a 30-centimetre-wide metal coil in a magnetic field at the other. Running a current through the coil creates an electromagnetic force that balances the gravitational force on the other side. Further measurements are made to eliminate hard-to-measure factors and produce a value for Planck's constant.

The watt balance was thought up in 1975 at the National Physical Laboratory (NPL) in Teddington, UK. Ian Robinson, who helped to develop that first instrument and worked with its successor for more than 30 years, disassembled his life's work this summer. More than 500 items, including the 1-tonne magnet, were stowed in some 50 wooden crates to be shipped. Robinson packed the precision coil himself: "If anyone was going to bust it," he says, "it had to be me."

NPL research director Kamal Hossain says they decided to discontinue the watt-balance work because they already had some good results from the device and wanted to focus on more practical areas, such as nanometrology.

"It was a bit of a surprise when the NPL decided to roll this up," says Alan Steele, head of metrology for the Institute for National

Measurement Standards in Ottawa, Ontario. The machine will both stretch the metrological science done in the lab and give Canada an entrée into the kilogram scene.

Pursuit of accuracy

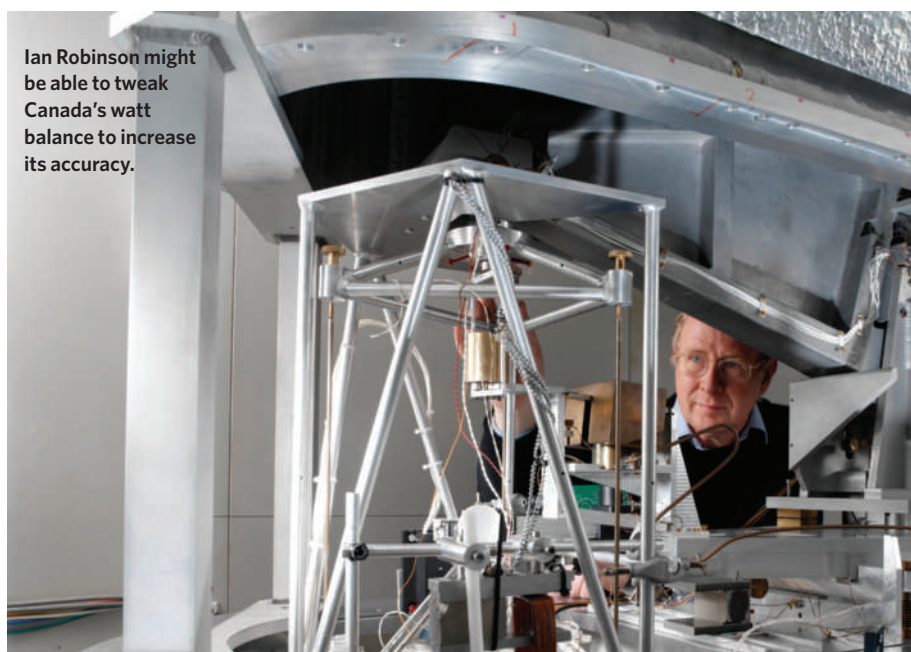
Another approach to redefining the kilogram involves more accurately calculating the Avogadro constant — the number of atoms or molecules in one mole of a substance — by determining the number of atoms in a near-perfect silicon sphere. Should the watt-balance project win out, national labs with watt balances will have an advantage in measuring exact masses and maintaining mass standards. Watt balances are being built and tested in Switzerland and France, but have not produced published results to prove their precision.

Thus far, the NIST watt balance and the one from the NPL do not quite agree on the value of Planck's constant. Although each has an uncertainty of tens of parts in a billion, the difference between the two most recently published values is ten times larger than that. The team working on the silicon-sphere approach, meanwhile, say they have data that are in fairly good agreement with NIST's value for Planck's constant, although these have not yet been published. The goal is to iron out discrepancies in time to redefine the kilogram in 2011.

Steele says his team plans to start reassembling the watt balance this October, with Robinson's help. They hope that the Ottawa lab, which is vibration-free and shielded from magnetic interference, will prove an ideal spot for the sensitive instrument. Moving the device should help to create a third, independent, set of data to help pin down Planck's constant, says Steele: "The equipment is so complex, just taking it apart and reassembling it is equivalent to doing a novel experiment." Robinson says he has possibly identified a small flaw in the experiment that he intends to fix once it is reassembled. If that creates agreement with the NIST value, then consensus should be easy.

Robinson, whose work was plagued by magnetic interference from a train line near the NPL, agrees that the Canadian lab is a real improvement. Although he says he is sad not to be able to continue his work in Britain, he adds that the important thing is that someone — anyone — will keep it running: "The main thing is that it doesn't get thrown away."

Nicola Jones



Ian Robinson might be able to tweak Canada's watt balance to increase its accuracy.

NPL



LAST CHANCE CLINIC

Some diseases defy diagnosis. **Brendan Maher** meets two people who hope that the US National Institutes of Health can help.

Dunham Aurelius is eager to take his shirt off and show his scars. One, a centimetre wide and roughly 20 long runs up his lower back and is from the placement of a steel rod to straighten his spine at the age of 14. Two others, looking like bullet wounds, are above his left buttock. But it's not his scars, nor his barrel-chested physique that have earned him the nickname 'ultimate fighting champion'. His urologist bestowed that title because of the fact that since the age of 22, Aurelius has passed a dozen and a half kidney stones — many, he's proud to say, without assistance. Aurelius is 39, a sculptor and a former triathlete with curly blond locks and a surfer's drawl. His wife, Michelle Barry Aurelius, jokes that he's like a human oyster. But the stones he grows are no smoothened pearls. At the cinema in 2008, Aurelius stepped out to use the bathroom. When he returned, he handed her the four-millimetre wide 'barnacle' of calcium phosphate his body had just expelled. She had noticed he was quiet that evening.

On a February morning this year, Aurelius and Barry are waiting in a hospital room in the sprawling Clinical Center on the campus of the US National Institutes of Health (NIH) in Bethesda, Maryland. They have travelled here from their home in Santa Fe, New Mexico, so that a small team of clinicians and research scientists can try to diagnose the mysterious disease that has dealt Aurelius more urological pain than most should have to bear. When William Gahl, the team's lead investigator and clinical director at the NIH's National Human Genome Research Institute (NHGRI) enters Aurelius' room at 9:50 a.m., he has a gaggle of clinical-genetics fellows in tow. He rattles through an introduction to Aurelius, and then stops himself. "Why don't you tell us," Gahl says, picking his words carefully, "why are you different from the average person?"

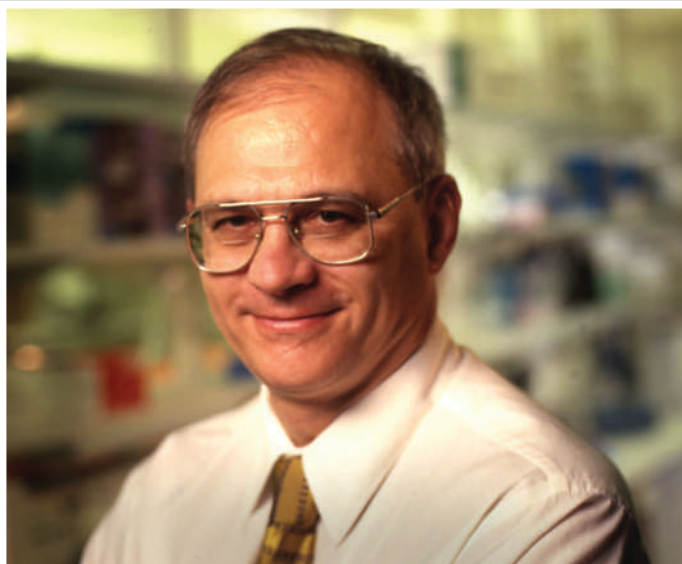
"There's nothing so complicated for a patient as not being able to put a name to their disease."

— Carl May

Elsewhere in the Clinical Center, another far-from-average person is awaiting time with Gahl. Sally Massagee, a 54-year-old certified public accountant from Hendersonville, North Carolina, is watching a neuromuscular specialist remove three deep-red slivers of muscle from her bicep. Although she was nervous going into the biopsy, Massagee jokes that she can spare the tissue. A little more than a decade ago, she started putting on weight. By the spring of 2007 she had gained nearly five kilograms on a compact 1.68-metre frame — all of it muscle. People around her thought she was training for competitive bodybuilding, but pain stopped her doing any exercise but tennis. Eventually she outgrew her clothes.

Massagee and Aurelius have few, if any, symptoms in common. What they do both have is a spot in the NIH's Undiagnosed Diseases Program, an effort to identify and characterize previously unknown diseases by drawing on the institution's 6,000 clinical and biomedical experts and the medical technologies at their fingertips. Gahl, a medical geneticist specializing in metabolic disorders, started the programme in May 2008 with \$280,000 in pilot funding from the NIH's Office of Rare Diseases. It received \$1.9 million more in its first year, and has been approved as a fully fledged NIH programme at \$3.5 million per year for the next five. Patients such as Aurelius and Massagee (pictured above) hope that this financial and academic wealth can finally provide the diagnosis that has eluded all the other specialists they have consulted over the years. "There's nothing so complicated for a patient as not being able to put a name to their disease," says Carl May, a professor of medical sociology at Newcastle University, UK, who has studied doctor-patient relationships in chronic disease. "If we can't put a name to it, it's hard for others to see or understand, and most importantly to believe, that something is legitimate or warranted."

M. BARRY AURELIUS; NIH; S. R. MASSAGEE



E. BRANSON/NIH

The researchers want a diagnosis, too — but their motives are somewhat different. For them, Aurelius, Massague and the other individuals are also a research opportunity, the chance to discover a new disease and potentially one that can be characterized at a genetic level. This could provide a new foothold in understanding human biology and perhaps the origins of other, more common diseases. Such diagnoses can result in high-profile publications and spur the development of new fields. As Clemens Bergwitz at the Massachusetts General Hospital in Cambridge puts it, the programme allows scientists to “make use of the human mutation pool”.

That approach is not new: throughout much of medical history clinicians with just the right background have stumbled on just the right patients to come up with a new diagnosis. Gahl says that one way of thinking about the Undiagnosed Diseases Program “is to reduce that need for serendipity” by setting out to find the unusual cases and throw at them everything research has to offer, including individualized sequencing of candidate genes and a genome-wide scan of genetic variations. “The sort of modern twist to this classic approach is the molecular-biology techniques available,” says NIH endocrinologist Michael Collins, who has been working on Aurelius’s case.

Aurelius and Massague spotlight the relationship between subject and scientist at its most focused, modern and expensive. The question is: what, if anything, will each side gain?

Stony symptoms

Aurelius reclines in a hospital bed while Gahl runs through his medical history. The stones are generally calcium phosphate. The largest two-to-three-centimetre stone was removed by surgery, which resulted in a perforated colon and left Aurelius with the bullet-hole scars in his back. He has regular gastrointestinal discomfort, and Aurelius says that he has very high calcium and vitamin D levels in his blood. Gahl asks how calcium in food affects him. “I avoid it in most cases. It makes me feel distended. If I had a bowl of ice cream I’d be miserable.”

“Ever take a vitamin D pill?” Gahl asks.

“No, but we could try it!” says Aurelius. Like others involved in the programme, Aurelius is happy to be a part of it even though he knows the chances of a diagnosis, let alone a treatment, are low. It means he hasn’t been given up on. “Most doctors would throw their hands up,” Aurelius says, describing his quest over the years. Gahl, no enemy of

Team leader William Gahl and nurse practitioner Colleen Wahl work on finding new diagnoses.

truth in levity, replies: “We may too, but we’ll do it behind closed doors, after you’re gone.”

After Aurelius is sent off for a bone-density scan and an ultrasound on his kidneys, the closed-door discussion begins. Gahl meets with a group of experts working on the case: Collins, nurse practitioner Colleen Wahl, pathologist Panagiota Andreopoulou, and attending genetics fellow Galina Nesterova. The meeting moves quickly as they bandy about the names of genes that might be responsible for Aurelius’s unusual blood test results.

At first the talk centres on a protein called fibroblast growth factor 23 (FGF23), which lowers phosphorus absorption and, through a series of regulatory loops, helps to cap the production of active vitamin D. Too much vitamin D can result in high calcium levels in the blood and urine — hypercalciuria — which leads to kidney stones. Nesterova, who worked as a nephrologist in Russia before coming to the United States, has another idea. She suggests looking at two genes, *CYP27B1* and *CYP24A1*, that activate and deactivate vitamin D, respectively. Her hunch is based in part on some ongoing work with two sisters with elevated vitamin D levels and highly calcified kidneys, who she also suspects of having mutations in these or related genes.

Collins is sceptical, not wanting to close the door on alternative explanations. Aurelius has low blood phosphorus levels, and Collins wonders whether the underlying problem could lie in the kidneys: if they are excreting too much phosphorus, this would feed back to the body, instructing it to manufacture more active vitamin D. He posits a mutation in one of the genes for a sodium/phosphate transporter, called *SLC34A3*, in the kidney tubule wall that may be causing Aurelius to dump out phosphorous.

“It’s neat that in-house, we’ve got Mike,” says Gahl later, referring to Collins. “He knows 100 times as much about this as me.” Collins was first introduced to Aurelius’s case through a monthly meeting for the Undiagnosed Diseases Program in which upwards of 50 basic- and clinical-research scientists sit and listen to presentations on potential patients to decide who should be invited into the programme. During the screening process they try to pull out diseases with simple genetic roots, ones probably caused by a single mutated gene, or a deletion or duplication of a large chunk of DNA. Maybe there is a mention of a family history in a chart, or signs that the symptoms are related to an organ system in a way that suggests a single unifying cause. Complex disorders

L. SPILLERS



Experts gather for monthly meetings at the NIH Clinical Center (left) to discuss which patients to admit.

with roots in multiple genes have to take a back seat, says Gahl: "This is triage, and triage means you go after what you can do." Since its inception, the programme has received more than 2,100 inquiries from doctors around the world, reviewed more than 900 full applications and, so far, seen little more than half of the 160 patients that, like Massagee and Aurelius, have been invited to come for an intensive week of tests and consultations.

As Nesterova and Collins spar collegially, Gahl finds a possible way to settle the debate. "Let's get the FGF23 back and have a plan then," he says, referring to a test already requested that will measure the amount of the hormone in Aurelius's blood. A high concentration might change the types of genes that they would test, probably striking *SLC34A3* from the list.

Less than an hour after talking vitamin D metabolism, Gahl is discussing muscle physiology and genetic tests he hopes to run on Massagee's blood. Like Aurelius, Massagee has already been through three and a half days of testing and has just a few more appointments to go. One of these is a wrap-up interview with Gahl and a different team of specialists, including Justin Kwan, the doctor who did the muscle biopsy, and clinician Irini Manoli from the NHGRI.

Accompanied by her husband, Massagee is dressed in velour tracksuit pants and an oversized man's dress shirt. She looks fatigued, but alert, her brown eyes peeking out over her puffy, muscle-tightened cheeks. When in 2008 doctors at Duke University Medical Center in Durham, North Carolina, did a magnetic resonance imaging test to try to diagnose her condition, they were shocked to see that even the orbital muscles that control her eye movements seemed to have doubled in size. Massagee says that when she had been exercising, the muscles had tone, and she believes many of the specialists she saw suspected she was taking steroids. Now the muscles are rock-hard, painful and toneless, weighing her down and leaving her exhausted.

Massagee's case has also drawn in experts from across the NIH, including Alexandra McPherron of the National Institute of Diabetes and Digestive and Kidney Diseases. For her PhD thesis, McPherron characterized a protein that doubled the skeletal muscle of mice when it was mutated (A. C. McPherron, A. M. Lawler and S.-J. Lee *Nature* **387**, 83–90; 1997) and she's worked on it ever since. Later named myostatin, the protein was found to be the molecular culprit behind heavily muscled cattle, sheep, dogs and in one

reported case of a human — a baby boy born in Germany with massive muscles in his thighs and upper arms (M. Schuelke *et al.* *N. Engl. J. Med.* **350**, 2682–2688; 2004). So, when a muscle-laden woman was accepted to the Undiagnosed Diseases Program, myostatin — and McPherron — were on Gahl's mind. He sent over photos of Massagee and eventually went to visit McPherron in her office. "I've never met a patient before," McPherron says. But she agreed to get involved with this one.

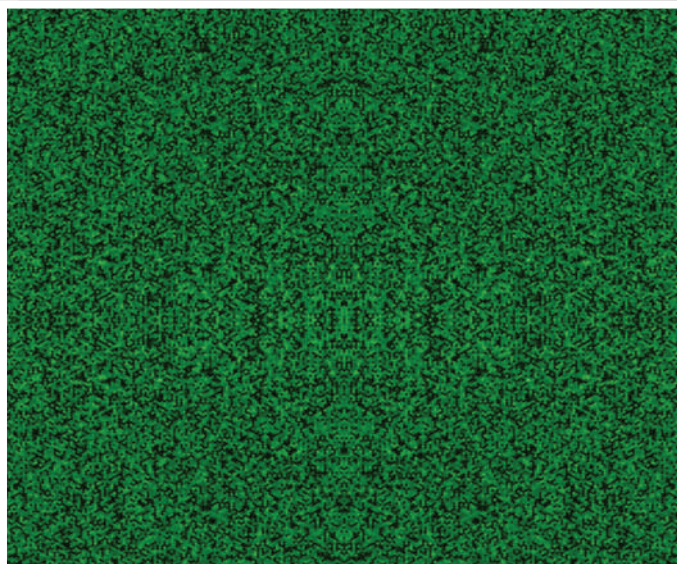
A question of need

Humans present experimental challenges that McPherron's mice do not. "The big question," she says, "was, do I want a muscle biopsy?" McPherron would need some tissue to do a thorough analysis of Massagee's myostatin expression levels. She knew the discomfort involved, but the only material already available was old and not prepared in a way that would allow protein extraction and RNA analysis. "I was hemming and hawing," she says, but when the rest of the team decided to go for it anyway, she decided she should be there to see Massagee and to carry the tissue back to the lab herself. The main results Gahl's team wanted would be coming from the biopsy tissue, both from McPherron's lab and from the laboratory at the Armed Forces Institute of Pathology (AFIP) in Washington DC that would be doing a full histopathological work-up.

There are other tests to run. Gahl explains to Massagee the purpose of a 'million SNP array', an assay that is used commonly in research genetics but rarely in clinical diagnostics. The array looks for single nucleotide polymorphisms (SNPs), spots in the genome that differ between individuals with relatively well known frequency. The SNPs serve as landmarks and if one that is expected to neighbour another is missing or doubled up, it can show where DNA has been deleted or duplicated, perhaps pointing to the genetic root of a disease. Gahl's team does an assay for everyone who enters the Undiagnosed Diseases Program, and often for their family members too.

Gahl appears to take a certain pleasure in explaining the method, but he seems to lose Massagee while trying to explain such concepts as 'loss of heterozygosity'. Still, he is patient with her, mirroring her wonder over how some tests work and assuring her that it is pointless for the time being to worry about what the results might mean for her children. "We're operating on best guesses and a lot of ignorance," he says.

"The physician in me is interested in helping people. The scientific part of us goes after the new disease areas."
— William Gahl



M. BARRY AURELIUS

But of course the patients do worry. Just days before Aurelius and his wife arrived in Bethesda, they found out that she was pregnant. Although extremely early in the pregnancy, they told the doctors in case there was anything they should know. The results of genetic tests take on greater significance when another generation could inherit the result. Aurelius explained the frustration of not knowing what to expect from his body or for his children. "Everything's good with me, but I have this alien disease. I keep wondering what's going to happen."

At the end of a week of tests, Massagee and Aurelius are discharged and return to their homes to await their results. "It's going to be nice to be able to walk out of here, if not with a diagnosis, with at least the next step," says Aurelius. Massagee effuses gratitude and says how wonderful everyone at the NIH has been.

"At its best it is a wonderful place," Gahl says, adding dryly, "at its worst it's a government organization."

Over the next few months, work starts on the data from Massagee and Aurelius. The test for the FGF23 levels in Aurelius's blood comes back normal. Nesterova had already begun to sequence *CYP27B1* and *CYP24A1*, and in May she finds that one copy of Aurelius's *CYP24A1* is missing three base pairs. This 'microdeletion' is not currently listed in any databases of known human variation, suggesting that it may be a novel change. It could be disabling or at least limiting Aurelius's ability to deactivate vitamin D, explaining his high levels of the vitamin. Then again, it could be harmless. "It's hard to put the weight of significance on these findings, for now," Nesterova says.

Collins still favours his hypothesis about the sodium/phosphate transporter, and at his urging Aurelius consents to send DNA samples to a programme, run by Bergwitz, that is sequencing genes that code for various versions of the transporter. Others with mutations in these genes have low phosphate levels and bone disorders such as rickets. "Our interest is to find more mutations," Bergwitz says, ones that create different symptoms. These could reveal what parts of the genes and their corresponding protein actually do, be it ion-pumping mechanics or insertion into cell membranes.

The million-SNP arrays come back with reams of data. Thomas Markello, who runs the studies for the programme, says that they spit out many hits but little in the way of answers. Raw data suggest that each person has between 3 and 10 positions in the genome in which both copies of

The DNA of sculptor Dunham Aurelius was analysed with a 'million SNP' array.

"It's going to be nice to be able to walk out of here, if not with a diagnosis, with at least the next step." —

Dunham Aurelius

a given genetic region are deleted, plus 50–200 instances each of single-copy gene deletions and duplications, any of which — or none of which — could be involved. "This is not what most physicians are used to seeing," Markello says. So far, the SNP arrays have helped with just one diagnosis. But this is a research programme, and part of the research is to determine how useful these techniques can be. Moreover, the data and samples, stored at the NHGRI, may still prove informative for future studies. Markello calls the programme "training wheels" for using whole-genome sequencing in the clinic, in which the number of genetic differences found in a given individual will go up many orders of magnitude but their clinical significance will be even harder to tease out. In the near future, he says, those in the programme will have their entire genome sequenced.

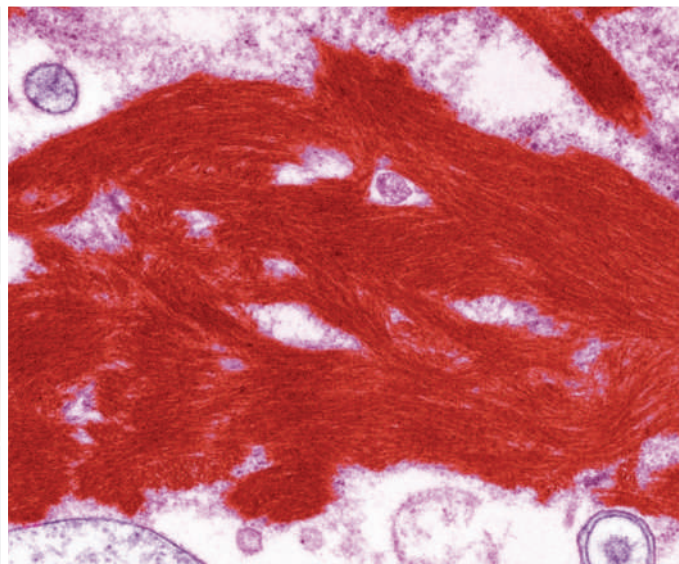
Hints of progress

On 8 April, Massagee e-mailed Manoli, her main contact point at the programme. Massagee was more fatigued than ever, having to stop what she was doing every 20 minutes and take a break. Work was becoming difficult, and she couldn't walk more than a block without losing her breath. Manoli called her back that day to ask if she could come back to Bethesda for more testing. Although the full report from the AFIP had not yet come back, the pathologists had found hints that proteins were building up in the walls of the blood vessels that feed Massagee's muscles.

On her second visit to the NIH, Massagee got her diagnosis. She had amyloid light-chain, or AL, amyloidosis, a rare disorder that is tied to the bone marrow's abnormal production of immune cells that make immunoglobulin proteins. Excess immunoglobulin accumulates into the proteinaceous build-ups that were lining some of her blood vessels.

Around 1,200 to 3,200 cases of AL amyloidosis are reported each year in the United States. Amyloid can build up in pretty much any tissue or organ, but Massagee's presentation in skeletal muscle is especially rare. The researchers do not know why the immunoglobulin caused her muscles to bulk up. But happily for Massagee, her heart muscles seemed to be unaffected and there was no serious damage to her kidneys, which can lead to death. Manoli contacted Morie Gertz, who studies the disease at the Mayo Clinic in Rochester, Minnesota, and pushed for a swift appointment. Gertz's team saw Massagee the following week to determine whether she would be a good candidate for a clinical trial

T.C. MARKELLO



Sally Massagee and her husband found out she had a type of amyloidosis, which causes protein build-up in tissues.

to treat the disease with chemotherapy and autologous bone-marrow transplantation.

She was. On 19 June, Massagee underwent the bone-marrow transplantation procedure. Afterwards she developed a condition called peri-engraftment syndrome, a poorly understood complication of autologous transplants that made her very sick. But now she says she's feeling stronger every day. Her doctors are uncertain whether treatment of the haematological condition will reverse the build up of muscle. But Massagee says that her muscles feel softer to the touch already, and that she considers the NIH programme to have saved her life.

Gahl's team was also pleased to get a diagnosis, even if it was one that is not new to medicine. None of their hunches about the involvement of myostatin came true. But McPherron is keeping Massagee's muscle sample in the freezer. She hopes to use it to investigate how the accumulation of immunoglobulin led to such an overgrowth of muscle. One idea is that the build up, or an inflammatory response to it, activated the satellite stem cells that normally divide to create new muscle tissue. But anything McPherron could do with it would be extremely preliminary.

"Our time will come with respect to new diseases," says Gahl. "We're very pleased to find different presentations of known disease, and I wouldn't discount the learning process." The team has made other such diagnoses. Gahl says that they have recognized a handful of cases of multiple sclerosis for patients enrolled in the programme and they were able to diagnose an atypical case of lymphoma simply from a chart review. But these are the happy endings. There are still upwards of 50 open cases in Gahl's files. May, the sociologist at Newcastle University, says that the doctors involved in the Undiagnosed Diseases Program are unusual in this sense because they know that the vast majority of their cases will never be solved. "There is a conflict there between having someone who is an interesting case and somebody who is going to be evidence of one's failure."

Gahl brings up one other statistic, and it's clear that it weighs heavily on him. Twelve of the patients who applied to the programme have died so far. One of these, a young woman called Summer Stiers, had serious symptoms affecting many of her organ systems and was the subject of several news stories earlier this year. The tests that Gahl's team ran when she was at the NIH generated few concrete leads. Stiers decided, with her local doctors' acquiescence,

to discontinue the regular dialysis and other treatments that had been keeping her alive. She died within three days. Stiers had called Gahl a few days before this, in part to make final arrangements for her body to be shipped to the NIH for further study. Even at the end of her quest for a diagnosis, she wanted to help.

Aurelius, in Santa Fe, is still anxiously awaiting news. Nesterova contacted him in July to tell him that she wished to publish an abstract about the *CYP24A1* microdeletion for a meeting on metabolic disorders in San Diego, California, this month. She suspects that it is responsible for his symptoms; if it is, it could mean the identification of an entirely new genetic disease. Although excited by this possibility, Nesterova is reluctant to become too confident until she can do more follow-up work to show definitively that the mutation affects the function or levels of the protein it encodes. Her colleagues have been sequencing the gene in 100 healthy controls to see whether the deletion is simply a harmless variant. "She's cautious and thorough," Aurelius says.

Despite being happy that someone is still working on his case, Aurelius says the pace still feels slow. "At the end of the day what I want to stop is the kidney stones because I don't want to have renal failure," he says. Another stone is currently growing in his left kidney. Aurelius and his wife are preparing for the birth of their child in late October, and he continues with his sculptures — large, craggy, organic-looking pieces in bronze and wood that unmistakably evoke the calcium phosphate stones that have caused him so much pain. He is even planning a show for the Clinical Center starting in November. He's promised that a portion of the proceeds from any sales will go to a patients' fund at the NIH. "It's rare in life when you feel like someone gives so much to you — taking me out there for a week, getting all these doctors together. It's important to give back to that."

And Gahl, like the other doctors in the programme, continues to wrestle with his dual motivations for it. "The physician in me is interested in helping people," he says. "The scientific part of us goes after the new disease areas. That's very stimulating — to be the first to discover something. I think all of us feel that way". Even if they don't find either diagnosis or new disease, the Undiagnosed Diseases Program offers at least an extension of hope for those who enter it.

"I'm astounded at how appreciative they are of our failed efforts," says Gahl.

Brendan Maher is Nature's biology features editor.

S. R. MASSAGEE

S. GSCHWEISSNER/SPL

The bot that plays ball

He looks like a child and plays like a child. But can the iCub robot reveal how a child learns and thinks? **Nicola Nosengo** reports.

Giulio Sandini cannot help smiling as his child reaches out a hand and tries to grasp the red ball that Sandini keeps waving before his eyes. “He is getting really good at it,” he says, with the proud tone of any father. True, most fathers would expect more from their three-year-old than the ability to grasp a ball. But Sandini is indulgent: although the object of his affection has the wide eyes and rounded cheeks of a little boy, he is, in fact, a robot.

His name is iCub or, as the team calls him, iCub Number 1. Together with his brothers now in laboratories around the world, this little robot may help researchers to understand how humans learn and think. Grasping a ball is only a first step, says Sandini, director of the robotics and cognitive-sciences department at the Italian Institute of Technology (IIT) in Genova, and head of the child-robot project since it started in 2004. Sandini is confident that iCub will learn more and more tricks — until, in the end, he is even able to communicate with humans.

“We wanted to create a robot with sufficient movement capabilities to replicate the learning process a real child goes through” as it develops from a dependent, speechless newborn

into a walking, talking being, Sandini says. So he and his colleagues have not only given iCub the hands, limbs and height of a toddler, they have also tried to give him the brain of one — a computer that runs algorithms allowing iCub to learn and develop as he interacts with his surroundings.

In a child, says Luciano Fadiga, a neurophysiologist at Italy’s University of Ferrara who is part of the team that developed iCub, those interactions are essential for shaping the rapidly growing brain. Before children can grasp a moving ball, for example, they must learn to coordinate head

and eye movements to keep the ball in their visual field; use visual clues to predict the ball’s trajectory and guide their hand; and close their fingers on the ball with the right angle and strength. None of these abilities is there at birth, and children cannot grasp appropriately until they reach around one year of age. “Many theories try to explain what happens in the brain as it learns all this stuff,” says Fadiga, “and the only way to test them is to see what works best in an artificial system.”

Such testing is certainly not new. Cognitive scientists have been using computer models to simulate mental processes since the 1950s, including algorithms that mimic learning. But

many of these simulations have focused on the high-level, conscious reasoning used to solve logical puzzles, play chess or make medical diagnoses. And many others — notably ‘neural network’ models — have simulated neurons. But Sandini and Fadiga are among the many researchers who have come to

think that both types of simulations leave out something essential: the body.

“There is ever-growing evidence from neuroscience that visuo-motor processing, and manipulation in particular, are crucial for higher cognitive development, including social behaviour and language,” Sandini says.

It was this line of thinking that led Sandini and his co-workers to their central hypothesis — that the best way to model the human mind would be to create a humanoid robot that is controlled by realistic learning algorithms, then let it explore the world as a child would. They gathered together scientists from 11 European universities and research institutions to form the RobotCub project, and began work with €8.5 million (US\$12 million) in funding from the European Union. The IIT is the project’s leading partner, and it is here that iCubs are born.

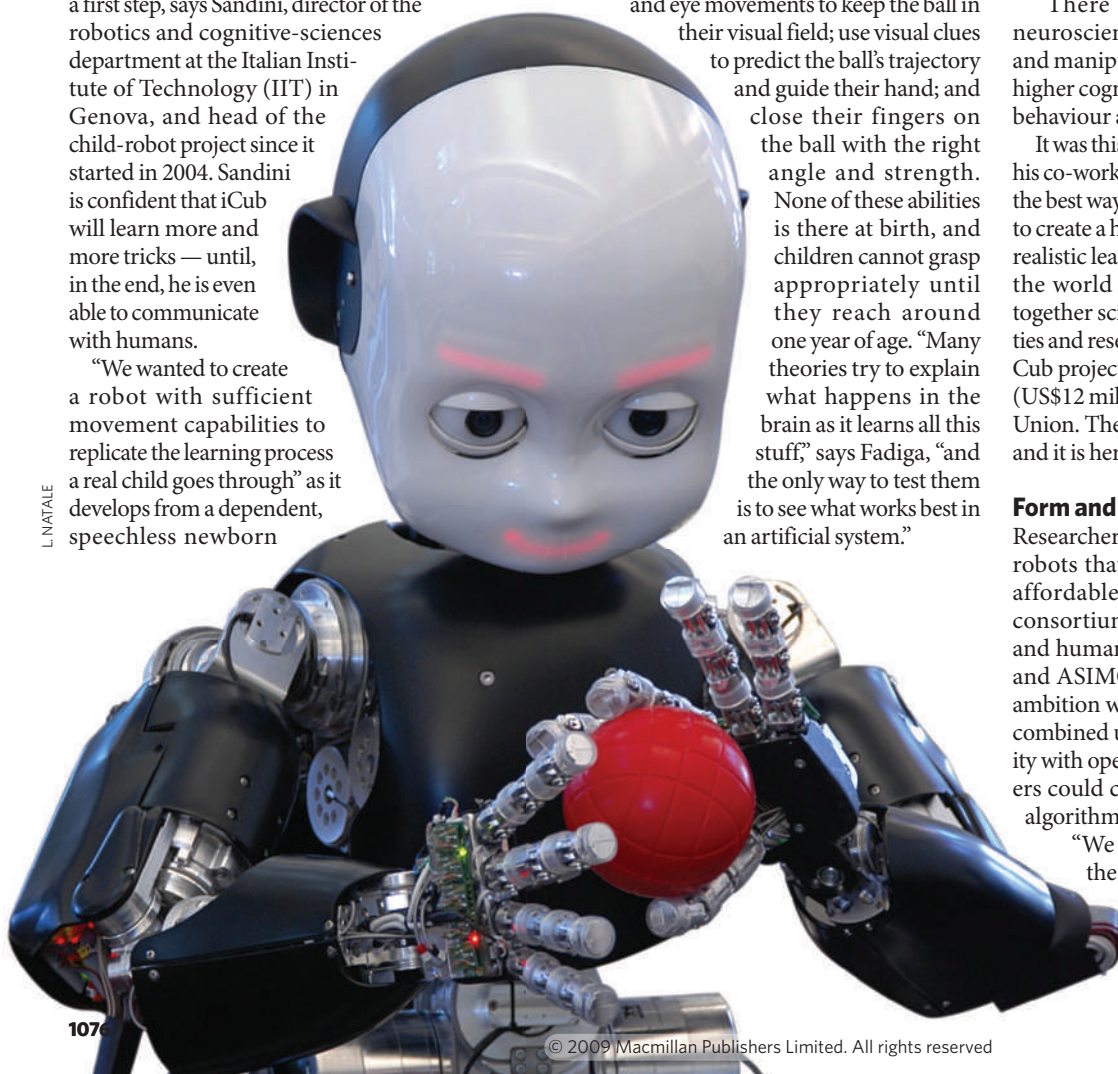
Form and function

Researchers can already choose from a list of robots that includes Khepera, a simple and affordable wheeled robot built by a Swiss consortium and used to study locomotion, and humanoid robots such as HRP-2, PINO and ASIMO, all built in Japan. But Sandini’s ambition was to create a humanoid robot that combined unprecedented mechanical versatility with open-source software, so that researchers could change both the hardware and the algorithms as needed.

“We started from the hand, and built the rest of the robot around it,” Sandini says. With seven degrees of freedom in the arm and nine in the hand, and its mechanical shoulders, elbows, wrists and fingers

“This is not a car you just buy and start to drive around; we’re in totally new ground.”

— Paul Verschure



L. NATALE

controlled by electric motors, iCub's arm is by itself a robotic marvel that took years to perfect. Next, iCub needed human-like senses. Project engineers gave him stereoscopic vision through two cameras mounted on moving ocular bulbs, complete with eyelids that close every now and then. And they gave him touch through sensors on his arms that can detect pressure applied from outside. They are also developing an artificial skin that will allow the robot to detect an object's shape and surface properties.

L. NATALE

Other team members tried to figure out what should happen inside iCub's brain. They decided to give him a few innate abilities similar to those seen in newborns, such as recognizing a face as being human and detecting objects against a background. Everything else would have to be learned. After reviewing evidence from neuroscience, psychology and animal studies, they came up with a three-level software architecture, mostly designed by Giorgio Metta of the IIT and by David Vernon of the Khalifa University of Science, Technology and Research in Sharjah, United Arab Emirates.

A. MALDONADO HERRERA

The first level gathers information on what iCub sees and feels. It collects raw signals from the cameras and other sensory systems, and channels them through a set of filters to determine which signals are most salient — a process similar to the human attention system. The second level is a kind of traffic director called the 'modulation' system. Loosely based on the functions of the hippocampus, basal ganglia and amygdala, this system takes in data from the lower level as the robot tries to grasp a ball, say, compares those data to combinations of action and sensory information iCub has encountered before, then decides what the robot should do next. In doing so, the modulation system is driven by some basic motivations, corresponding to a child's curiosity for new stimuli and tendency to engage in social interactions.

The third level uses prior experience to play 'what if?' with the current situation. What will happen if I move towards the ball with this force and this angle? What if the ball moves in the meantime? This information goes back down to the middle level to help determine the robot's next action.

It was only after almost three years of effort that the team finally activated its first complete robot. Their artificial child could now move, see and touch, which was all the researchers technically needed. But, in a symbolic gesture of whimsy, they decided they should also make it look like a child. The undeniably cute result was a semi-transparent mask with luminous colour light-emitting diodes under the surface to outline eyebrows and a mouth, allowing the robot to smile and frown. This engaging face

may have more uses than just making the robot look good in promotional pictures, says Fadiga. "In the future, some groups plan to try iCub with children who are autistic, testing their reactions to his expressions and movements".

iCub Number 1 was never meant to be an only son. After the first robot became operational, the consortium issued an open call for proposals to conduct experiments. The six winners, chosen by an independent panel appointed by the consortium and the European Union, have received their own iCub for free. And anyone else can order one for the cost of producing it, some €180,000–200,000. "It was part of the deal with the European Union that we should provide a number of robots to interested groups," Sandini says. This way, the team hopes to create a de facto standard in robotics, facilitating data exchange. "There is a desperate need for standardization in our field," says Paul Verschure, a technology professor at the Catalan Institute of Advanced Research in Barcelona, Spain, and one of those selected to receive an iCub. "People use a variety of platforms, they rarely publish every detail of their algorithms, and replication of experiments is minimal."

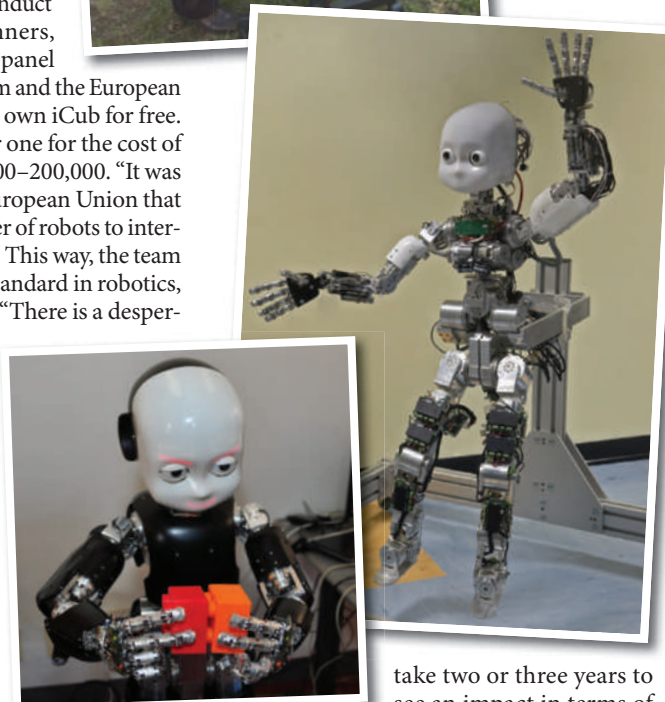
Small has its place

However, not even the most ardent enthusiasts believe that iCub will send all other robots into retirement. "Simpler and more affordable robots will remain important," says Chad Jenkins, a computer scientist at Brown University in Providence, Rhode Island. Jenkins chaired the robotics workshop at the International Joint Conference on Artificial Intelligence in Pasadena, California, at which iCub made his American debut in July. "They may be more limited in the long run, but they are easier to use in small-scale experiments."

Indeed, most of the researchers who have got their hands on an iCub find that programming him is a hard job, and it is likely to take some time before meaningful results can be seen. "Nobody expected anything different," says Verschure, "this is not a car you just buy and start to drive around; we're in totally new ground." Sandini agrees that the robot is still a work in progress, and predicts that it will



Giulio Sandini (left) and Giorgio Metta gradually pieced together a robot with an unprecedented level of dexterity and coordination.



take two or three years to see an impact in terms of

publications in major journals. But, he adds, a better measure of success will be if neuroscientists and psychologists start to see the robots as useful experimental tools. "Engineers creating an intelligent robot and neuroscientists studying the brain are asking the same questions, only with different words," Sandini says. "How can this particular task be performed with limited computational power?"

Convincing neuroscientists may be the hardest part, though, particularly those who question iCub's theoretical background. Although he sees many interesting ideas in iCub, Alfonso Caramazza, director of the Cognitive Neuropsychology Laboratory at Harvard University, says that "the claims being made about shared intentions and language in robots still seem light years away from being realized". In particular, he says, "to account for cooperation and communication you also need symbolic thought, and I do not see how such mechanisms can emerge from mere sensory-motor processes in a robot".

Sandini and Fadiga reply that a complete explanation of higher cognitive functions is a problem for any area of neuroscience, not just robotics. Furthermore, iCub's emphasis on perception and manipulation may one day lead to a better understanding of what 'symbolic thought' really is.

The final word, of course, will come from the robots themselves. Eight iCubs have left Genova since late last year for laboratories in Europe and Turkey, and ten more are being built. Add the two kept by Sandini's team, and the family will comprise 20 brothers by the end of the year.

Great expectations

Most of the researchers will first try iCub in experiments they were already performing with simpler robots. In Barcelona, for example, Verschure's group plans to see how a computer model of a cerebellum it has been working on for years performs in an iCub. "The cerebellum is a crucial organ for motion, it sets the timing and pace of our movements," Verschure says. "But the timing of actions depends on the body's shape. For example, the speed at which I can move my arm is limited by its length and weight. So it makes no sense to study the cerebellum outside the body."

At Imperial College London, Murray Shanahan, professor of cognitive robotics, is teaching his iCub to do very basic motor tasks, such as making circular hand movements, using a 'spiking' neural network. These artificial neurons not only 'fire', but the intensity of their firing changes over time. "It is a more biologically plausible model than typical networks," Shanahan says, "one in which the temporal dynamics of neurons is also modelled." Once validated, the spiking-network concept will be used to simulate more complex tasks.

The IIT's two robots will be used to study the development of goal-oriented behaviour. Researchers will start by teaching them to recognize a specific object such as a hammer among many different objects, then to grasp the hammer by the handle and not by the head, and finally to swing it appropriately while hitting a nail, something it may learn by imitation. But to prove that it has really developed

an internal representation of what a hammer is for, the robot will have to be able to use it in cooperation with humans. Fadiga says that in two or three years he hopes to get to the point at which "I pick a nail, I put it on the wall, there is a hammer on a table nearby. The robot sees all this and, without any further input, grasps the hammer and hands it to me".

As happens in every family, the brothers face different expectations. At Britain's University of Plymouth

cup on yellow cup," says Cangelosi.

In the very long term, the project aims to give the robot the ability to communicate with humans using natural language, with basic but appropriate grammar — but with no language rules coded anywhere in its software. Language, the researchers hope, will gradually emerge as an extension of visual and motor abilities, providing a strong proof of principle that the same may have happened in humans during evolution.

But some question whether iCub can live up to such expectations. Oliviero Stock, a senior

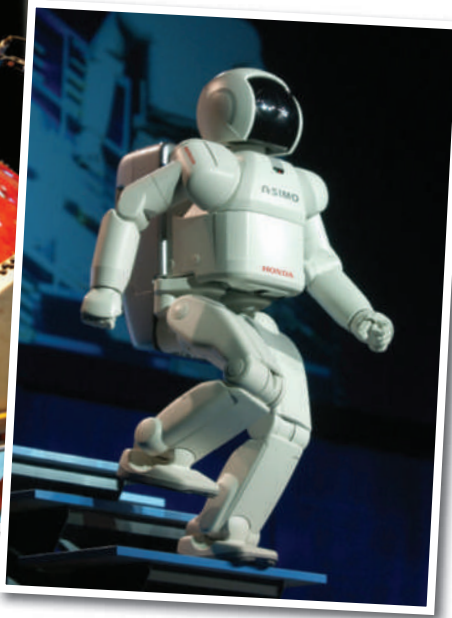
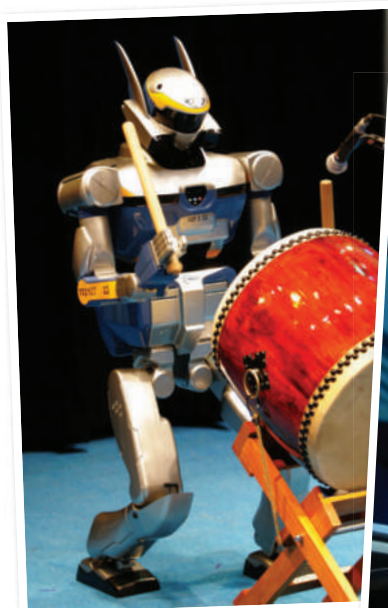
researcher at the Bruno

Kessler Foundation in Trento, Italy, and a leading expert in the application of artificial intelligence to linguistics, says that the 'bottom up' approach that iCub adopts can go only so far when it comes to language. "People in the field are coming to terms with the fact that to explain language, you have to presume some innate abilities for it, for grammar, and syntax in particular," he says. "I doubt that such a system can do more than utter single words without some kind of a priori linguistic skills, call it a language instinct if you want. That's what probably happens in humans too."

The idea of an innate predisposition for language in humans was famously introduced in the 1950s by Noam Chomsky, who wrote of a "universal grammar" that children seem to be primed for. Although hotly debated, this has become the dominant view in linguistics. iCub might now provide a way to put it to a rigorous test.

While grown-ups have been arguing passionately about their robots' talents, the iCub brothers have been having a good time, as would be expected from children during the summertime. In late July the Italian brothers spent two weeks on Italy's Liguria coast, where 37 roboticists from many parts of Europe and the United States had convened for a summer school, arranged by Sandini and his colleagues to give them a chance to try their algorithms on an iCub. In pictures posted on the Internet, the robots can be seen wearing hats, grasping the usual ball, and even assembling LEGO bricks. Their actions are not exactly masterful, Sandini admits. But, ever the encouraging father, he says it is only a matter of time.

Nicola Nosengo is a freelance science writer based in Rome.



The Japanese robots HRP-2 (left) and ASIMO are able to do a range of tasks, from making music to walking on uneven surfaces.

and at the Institute for Cognitive Sciences and Technologies in Rome, researchers led respectively by Angelo Cangelosi and Stefano Nolfi are undertaking what is probably the most ambi-

tious of the iCub projects: studying how children learn language. "We believe that manipulation and communication co-evolve during the first three years" says Cangelosi. "Children learn relations among objects by touching them, and learn to express the same relations with language."

To test this idea, he and his colleagues will treat the robot pretty much like a real child. While showing it a blue cup, for example, they will say 'blue cup', and so on, so that in time iCub can make associations between the sounds he hears and the data coming in through the visuo-motor system. "By the third year of the project, he should be able to use transitive and intransitive verbs in simple sentences, such as 'put red

"Engineers creating an intelligent robot and neuroscientists studying the brain are asking the same questions."

— Giulio Sandini

CORRESPONDENCE

Italy leads the way in supporting African biotechnology

SIR — In your News story 'African science drops down G8 agenda' (*Nature* **460**, 16; 2009), you express concern about the lack of interest that has been shown by the G8 countries in the development of science in Africa. But there are bright spots: for example, a laboratory of international standard recently opened in South Africa as a direct result of G8 discussions, with Italy taking the lead towards its rapid realization.

In the final declaration of the 2005 G8 summit in Gleneagles, heads of state and government considered the possibility of establishing an African branch of the International Centre for Genetic Engineering and Biotechnology (ICGEB, www.icgeb.org) to do research into diseases afflicting the continent. Action followed promptly, and the new ICGEB component was inaugurated in Cape Town in September 2007, joining others in Trieste and Delhi. In less than two years, the difficulties inherent in establishing a new research institution were overcome; these included meeting complex legal requirements as a result of the intergovernmental nature of our organization.

This achievement was possible because of generous funding and support by the South African and Italian governments. Today, more than 50 scientists are working in the new laboratories, producing high-level biomedical science, sparking collaboration with other research institutes in Africa and training young scientists from the whole continent.

ICGEB is also implementing an important project from Cape Town, which is funded by the Bill and Melinda Gates Foundation and aimed at building technical and scientific capabilities in sub-Saharan Africa for the effective regulation of biotechnology in agriculture.

Although ICGEB activities in Africa are still limited, they are actually happening. Regrettably, these activities are not as adequately noticed as they should be, perhaps because of a preference for highlighting projects rather than facts.

Francisco E. Baralle International Centre for Genetic Engineering and Biotechnology, AREA Science Park, Padriciano 99, 34149 Trieste, Italy
e-mail: baralle@icgeb.org

Investors likely to venture back as crisis subsides

SIR — As an investor and an independent adviser to corporate management, I am not convinced by John Browning's arguments that venture funding is unlikely to bounce back, as suggested by his Essay 'The incredible shrinking venture capital' (*Nature* **460**, 459; 2009).

Earlier trends indicate that venture-capital funding will probably rebound after the current financial crisis subsides. Until last year, venture-capital investments in US companies had increased annually for 12 years, except during the dot-com bubble of 1999–2001. The biotechnology sector, in particular, reported a substantial positive trend in these investments during the same period: their annual funding grew even when quarterly funding fell for one or two quarters by more than 30% relative to the previous quarter.

Meanwhile, most of the technologies that are crucial to solving societal problems — drugs, solar energy, biofuels and nanotechnology — will address huge markets and require large amounts of high-risk capital. Those that succeed will either be acquired or be taken public.

For every ten investments that a venture-capital firm makes, it needs only one or two big

winners to offset the three or four investments that fail and the remainder that seem to go nowhere.

J. Leslie Glick 12306 Ashville Drive, Tampa, Florida 33626, USA
e-mail: jlglick@ix.netcom.com

Czech bibliometric system fosters mediocre research

SIR — Following your News story 'Czech researchers angry over government changes' (*Nature* **460**, 157; 2009), we would like to point out that ill-conceived bibliometrics can be used as an excuse for deep cuts in basic research funding and the diversion of funds to 'applied' research.

The innovative evaluation system endorsed by the Czech government's research and development council ascribes a certain number of points to every paper, patent, technology and piece of software. However, it does not properly take into account the originality of the result or the publication medium, nor does it consider the different financial requirements of different branches of science.

This system effectively penalizes inter-institutional cooperation and promotes inflation of mediocre science. It discredits the whole concept of evaluation of science based on scientometrics.

It does not soothe our pain that publication of this letter will confer as many points on our institutions as a paper in *Progress in Polymer Science* or three in *The American Bankruptcy Law Journal*.
Jan Konvalinka, Helena Illnerová, Pavel Hobza, Václav Hořejší, Antonín Holý, Pavel Jungwirth, Václav Pačes Academy of Sciences of the Czech Republic
e-mail: konval@uochb.cas.cz
Pavel Martásek First Faculty of Medicine, Charles University, Prague, Czech Republic
Jiří Zlatuška Faculty of Informatics, Masaryk University, Brno, Czech Republic

Non-scientists could still contribute to reform of the ERC

SIR — The mid-term review of the European Research Council (ERC), the European homologue of the US National Science Foundation, draws attention to some of the council's bureaucratic shortcomings.

Towards a World-class Frontier Research Organisation (<http://tinyurl.com/noa7ra>), published in July, highlights the ERC's initial successes. But it points out that the council's long-term sustainability depends on a drastic reduction in red tape, better governance structures, more autonomy under a better-suited legal framework and several other reforms.

The reviewers argue that ERC steering bodies should not include too many non-scientists, nor be run by them. But an over-enthusiastic exclusion of non-scientists risks conveying a 'closed shop' impression. It would fly in the face of the principle of diversity management, in which different competencies and backgrounds are deployed to run a complex, multi-faceted societal enterprise such as the ERC.

Such a scheme would also undermine the professionalization that is proclaimed in the report, as well as closing doors to the taxpayer and people outside the inner rank and file. We must presume that this is not the reviewers' intention, but the point nevertheless calls for clarification, not least to enhance the impact of an otherwise strong report.

Wilhelm Krull VolkswagenStiftung, Kastanienallee 35, 30519 Hanover, Germany
e-mail: krull@volkswagenstiftung.de
Jakob Edler Manchester Institute of Innovation Research, University of Manchester, Manchester M13 9PL, UK
Michael Stampfer Vienna Science and Technology Fund, Währinger Strasse 3/15a, 1090 Vienna, Austria

Contributions may be submitted to correspondence@nature.com.

OPINION

Chemical regulators have overreached

The costs — both in animal lives and euros — of the European REACH legislation on chemical testing are escalating. **Thomas Hartung** and **Costanza Rovida** argue for a suspension of certain toxicity tests.

More than 100,000 synthetic chemicals are used in consumer products. In 1981, both the United States and the European Union (EU) introduced comprehensive safety evaluations for novel chemicals coming on to the market. However, existing chemicals represent about 97% of those in use today and 99% of the production volume. Safety testing data are needed for most of these 'old' chemicals. Over the next decade, the EU's 2006 Registration, Evaluation, Authorisation and Restriction of Chemicals (REACH) regulation aims to assess the toxicity of all chemicals sold in Europe in quantities of more than one tonne per year.

As toxicologists, we support the aims of REACH — it is the biggest investment into consumer safety ever. However, we feel that legislators have underestimated the scale of the challenge. Our report¹, released today by the Trans-Atlantic Think Tank for Toxicology at John Hopkins University in Baltimore, Maryland, is the first analysis of REACH costs to be published in 5 years. It is based, among other things, on the pre-registration of chemicals, which ended in 2008. It was expected that 27,000 companies would submit 180,000 pre-registrations on 29,000 substances. Instead, some 65,000 companies made more than 2.7 million pre-registrations for in excess of 140,000 substances. REACH aims to complete data collection on these substances by 2018. In recent decades Europe has tested some 200–300 new chemicals each year, making REACH an unprecedented challenge. Toxicologists do not have the appropriate tools — whether high-throughput methods or acceptable alternatives to animal testing — to meet these expectations.

Official estimates

When REACH was negotiated, between 2001 and 2005, several attempts were made to estimate the costs of the regulation, both financially and in terms of the number of animals used for toxicity testing. Officially, the EU is relying on estimates suggesting probable costs² of €1.6 billion (US\$2.3 billion) — range of estimate €1.2 billion–€2.4 billion — and 2.6 million animals³ (range of estimate 2.1 million–3.9 million). These estimates are based on data on chemical production from 1991 to 1994.

Our report relies on several new public sources of information that allow these

estimates to be reassessed. Among the factors that have increased costs and animal numbers are changes to the final legislation, such as the inclusion of reaction intermediates, and changes to the guidance for industry on how to test. The EU also now contains 27 members (plus three non-EU countries that adhere to REACH), compared with the 12 members on which the 1994 data were based. Factors that could, in principle, reduce the costs of REACH include progress in the availability of alternative methods to animal testing and availability of safety data from other sources, such as voluntary industry databases.

The latest published list of REACH chemicals contains 143,835 substances that are supposed to be fully registered, each requiring a chemical-safety report. However, this figure is likely to be an overestimate because of redundancies or mistakes made in deposition. The final number will be somewhere between 143,835 and the official estimate of 29,342 substances². We have re-evaluated the estimates for the

SUMMARY

- Complying with REACH may use 20 times more animals and cost 6 times as much as previously estimated.
- Regulatory toxicology has neither the high-throughput methods nor alternatives to animal testing to cope.
- A moratorium on reproductive toxicology tests would be wise, until alternatives are approved.

number of *in vivo* tests required by REACH. The plausibility of our assumptions and calculations was checked by eight experts from industry, academia and regulatory authorities¹.

We focused on the expansion of the EU and how that affects chemical production. Since 1994, the chemical industry in Europe has grown by about 5% per year, almost doubling its production and sales size by 2008, and the expansion of the EU further increases chemical production volume by 18%. This growth leads to an estimate of 68,000 chemicals falling under REACH, and this is the lower (optimistic) estimate in our study (see Fig. 1).

Optimistic assumptions

These 68,000 chemicals were then modelled under REACH testing requirements. Total chemical production or marketing volume in Europe determines the testing requirements, which are then modified by the specific toxicity and usage profiles of the substances. In all cases, our modelling used the most optimistic assumptions (minimal animal numbers per test and neglecting the triggering of additional tests). We ignored the need for confirmatory retesting as well as tests that have not yet been defined for endocrine disruption, respiratory irritation, respiratory sensitization and developmental neurotoxicity. We also considered alternative approaches (including computational toxicology) far enough along in the validation and acceptance process to have an impact on the execution of REACH.

Our results suggest that generating data to comply with REACH will require 54 million vertebrate animals and cost €9.5 billion over the next 10 years. This is 20 times more animals and 6 times the costs of the official estimates. By comparison, some 90,000 animals are currently used every year for testing



Figure 1 | Numbers too large to handle. Estimates for the numbers of chemicals (a) and of animals (b) expected to be needed for compliance with REACH legislation. Our best-case estimates¹ of 68,000 substances and 54 million animals are far above the official EU estimates.

new chemicals in Europe, costing the industry some €60 million per year. Without a major investment into high-throughput methodologies, the feasibility of the programme is under threat — especially given that our calculations represent a best-case scenario. In 15 months' time, industry has to submit existing toxicity data and animal-testing plans for the first of three groups of old chemicals.

Disaster prevention

Our modelling shows that the studies contributing most to animal use and costs are from reproductive-toxicity testing — the effects of the chemicals on reproductive functions — representing about 90% of projected animal use and 70% of projected costs (see Fig. 2).

In the short term, we recommend that testing requirements for reproductive toxicity are urgently reviewed with the goal of prioritizing the most suspicious chemicals, reviewing test strategies and allowing more time to carry out the programme.

Much of the projected increase in animal use is the result of the two-generation study for reproductive toxicity, in which toxic effects are studied in the offspring of exposed rats and then in a second generation. The EU animal estimate³ did not include offspring (despite their inclusion in EU animal-use statistics). This method consumes an average of 3,200 rats per chemical compared with 784 animals for a one-generation study with costs increasing five-fold. Moreover, changes to REACH introduced the unusual requirement of repeating the two-generation study in a second species, further increasing animal use and costs.

There are many limitations associated with the two-generation study in a second species (not least an increase in false positives) despite marginal gains in safety information⁴. A high number of false positives (perhaps as much as 40–60%) after REACH testing might lead to the expensive withdrawal of widely used chemicals, and cause unnecessary fears in consumers⁵. Over the past 25 years, only 2–3 industrial chemicals a year have been tested in two-generation studies — with REACH the challenge will be to test several hundred chemicals per year. We urgently need alternatives.

Despite concerted efforts, no acceptable alternatives to reproductive-toxicity testing have emerged, or are likely to be validated by 2018. Computational approaches are also limited by the complexity of reproductive toxicity and because half of the REACH chemicals are mixtures, inorganic, salts or contain metal atoms, rendering toxicity less predictable.

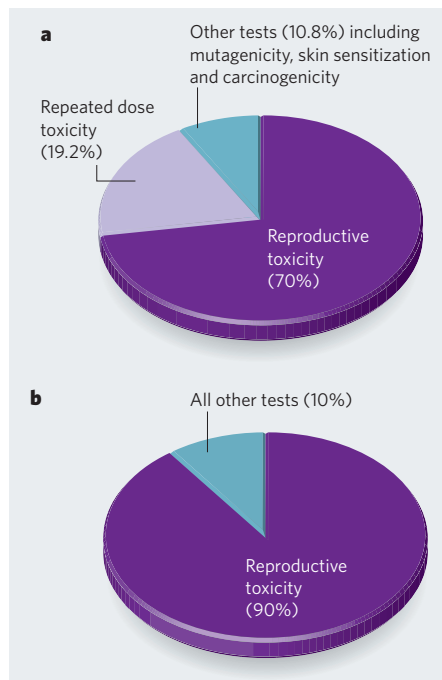


Figure 2 | The biggest piece of pie. Reproductive-toxicity testing makes a huge contribution to the estimated costs (a) and the number of animals used (b) for compliance with REACH legislation.

The only real alternative is an extended one-generation study, guidelines for which are under development by the Organisation for Economic Co-operation and Development (OECD). This approach extends the observation period for the first-generation offspring with additional testing on developmental neuro- and immunotoxicity if triggered by test results.

We favour replacing the two-generation study with the OECD test, which would, in our estimation, reduce animal use for this test by 40–60% and overall animal use by REACH by 15%. We recommend a moratorium on reproductive-toxicity testing, or at least limiting testing to the most suspicious substances, until the OECD guidelines are completed and alternative strategies for screening lots of chemicals are available. There are political as well as technical barriers to overcome, however — two EU member states are against the extended one-generation study unless the additional testing is mandatory, which would eliminate any cost or animal saving.

In the medium term, a different approach is needed. An initiative similar to the €50-million partnership between the European Commission and the cosmetic industry (Colipa), for research into alternatives for systemic

toxicity, is needed for reproductive toxicity. Colipa includes trans-Atlantic partners and the strong integration of computational and high-throughput approaches. The only serious EU investment into reproductive toxicity is the ReProTest project, which ends this year and should be continued.

In the longer term, regulatory toxicology needs to move into the twenty-first century⁵ — many core methods have remained largely unchanged for 40 years. The US Environmental Protection Agency understands this need. It introduced a new toxicity-testing strategy in March. The aim is to move to high-throughput methods based on identified pathways of toxicity with human cells, fish eggs, invertebrate species and computational methods. Instead of exposing animals to high doses and observing a multitude of possible effects, precise questions can be asked about whether sensitive physiological processes are disturbed.

REACH is not the only chemical testing programme coming online — others are planned in the United States, Japan and Canada — but it is the biggest and the first to come into effect. Lessons learned from REACH should be heeded by the others. Our report might be bad news for REACH as currently imagined, but it is also an opportunity. Given the EU's expansion, the growth in financial costs and animal use was inevitable — and would have been revealed in time as indicated by the pre-registration data. We are showing the challenges that lie ahead. Armed with this knowledge of the shortcomings of the current approach, regulators and industry can work together to protect consumer safety without using an excessive number of animals for toxicity testing.

Thomas Hartung is the Doerenkamp-Zbinden Chair for Evidence-based Toxicology at the Johns Hopkins University Bloomberg School of Public Health, Baltimore, Maryland 21205, USA, and a professor at the University of Konstanz, Germany. **Costanza Rovida** is a chemist working as a private consultant in Varese, Italy. e-mail: thartung@jhsph.edu

- Rovida, C. & Hartung, T. *Re-evaluation of Animal Numbers and Costs for In Vivo Tests to Accomplish REACH Legislation Requirements for Chemicals* Transatlantic Think Tank for Toxicology (2009); available at www.altex.ch or <http://altweb.jhsph.edu>.
- Pedersen, F., de Bruijn, J., Munn, S. & van Leeuwen, K. *Assessment of Additional Testing Needs Under REACH — Effects of (Q)SARs, Risk Based Testing and Voluntary Industry Initiatives*. Joint Research Centre Report EUR 20863 (2003).
- van der Jagt, K., Munn, S., Tørsløv, J. & de Bruijn, J. *Alternative Approaches can Reduce the Use of Test Animals Under REACH*. JRC Report EUR 21405 EN (2004).
- Janer, G., Hakker, B. C., Slob, W., Vermeire, T. & Piersma, A. H. *Reprod. Toxicol.* **24**, 97–102 (2007).
- Hartung, T. *Nature* **460**, 208–212 (2009).

Join the discussion at <http://tinyurl.com/nctlwu>.

BOOKS & ARTS

Bridging the gender gap in Indian science

A set of biographies reveals the trials and triumphs of India's women researchers, says **Asha Gopinathan**.

Lilavati was the clever daughter of the twelfth-century Indian mathematician Bhaskara II. A well-known mathematician in her own right, she inspired generations of Indian women. Bhaskara's famous book on mathematics was named after her, and he addressed many of its verses to her. *Lilavati's Daughters* spotlights women based in India who have pursued research in science, engineering and mathematics from the late nineteenth century to today.

A collection of 98 short biographies, the book stems from a project initiated by the Women in Science panel of the Indian Academy of Sciences, Bangalore, to provide young girls with inspiring role models (see www.ias.ac.in/womeninscience). The diverse personal stories span many disciplines and regions of India — and are inspiring.

The earliest chronological entry is for Anandibai Joshi, the first Indian woman to go abroad and study to become a doctor. From 1883 to 1886 she attended the Women's Medical College in Philadelphia and was awarded an MD degree for her thesis *Obstetrics Among Aryan Hindoos*. Unfortunately, she contracted tuberculosis and had to return to India. She received no treatment: Western doctors refused to treat a brown woman and Indian doctors would not help her because she had broken societal rules. Joshi died in 1887 at 22 years of age.

Thankfully, not all the women in the book had such tragic lives, although many had to overcome obstacles to achieve success. Physicist Anna Mani, who worked with the Nobel laureate C. V. Raman, was not awarded a doctorate despite publishing several single-author papers. Yet she went on to become the deputy director-general of the Indian Meteorological Department and, after retirement, set up a factory to manufacture instruments to measure wind speed and solar energy.

Many of those highlighted were the first to break into male-dominated professions: Asima Chatterjee was the first Indian woman to be awarded a DSc; E. K. Janaki Ammal was elected a fellow of the Indian Academy of Sciences the year it was founded; Kamala Sohonie was the first female director of the Institute of Science, Mumbai; and Bimla Buti is a former director of plasma physics at the International Centre for Theoretical Physics in Trieste, Italy.

It is interesting that many of these women



Attending a science summer school encouraged geneticist Sudha Bhattacharya to become a researcher.

scientists came from ordinary middle-class families. Most grew up not in the nation's big cities but in rural areas, where getting an education in any discipline, let alone in science, is difficult. In rural Punjab, mathematician R. J. Hans-Gill had to pretend to be a boy and wear a turban to attend school — a secret that was kept between her family and the headmaster. Biologist Chitra Mandal was accompanied to school in rural Bengal by her grandmother because the teacher would not let the four-year-old in without someone to look after her.

Almost all of the women speak of the premium their families placed on education and the support and encouragement each received from family members. Mothers are

especially significant — poorly educated ones as well as some who were scientists themselves. Dedicated teachers, both at school and college, were also influential. They spotted and nurtured talent and lit sparks of curiosity in the minds of these young girls. In post-independence India, government schemes such as the National Science Talent Search scholarship have helped many women, including geneticist Sudha Bhattacharya, now a professor at Jawaharlal Nehru University in New Delhi, to pursue their dreams by allowing them to study at a good university and to meet eminent scientists and peers from

across the country during summer camps.

The road to the top is never smooth. Many of the women acknowledge sexism in their professions, a lack of institutional support, double standards in measuring their achievements, social bias due to caste, self-imposed limitations, negative stereotypes surrounding single women and the multiple roles that married women with families have to juggle. They have used many strategies for survival. But most important is their passion for their work.

The motivations of these female scientists are often surprising. Not everyone in the book aspired to win the Shanti Swarup Bhatnagar Prize for Science and Technology: only a handful has won this coveted award. Instead, they have put their energies into teaching and communicating science, taking their research out of the lab to change people's lives.

Each of these essays is special. They tell of vibrant women who combine a tough life in the sciences with other interests such as cricket, dance, music or literature. Had I received this book as a young girl, I would have been captivated. I hope that *Lilavati's Daughters* will be translated into many languages and grace libraries worldwide. It is a wonderful resource for both mentors and mentees. ■

Asha Gopinathan is a neuroscientist based in Trivandrum, Kerala, and a member of the International Network of Women Engineers and Scientists.

e-mail: dendron.15@gmail.com

Lilavati's Daughters: The Women Scientists of India

Edited by Rohini Godbole and Ram Ramaswamy

Indian Academy of Sciences: 2008.
369 pp. 300 rupees, \$25 (pbk)
See <http://tinyurl.com/liladaug>

The many faces of mathematics

Mathematicians: An Outer View of the Inner World

by Mariana Cook

Princeton University Press: 2009.
208 pp. \$35, £24.95

Recountings: Conversations with MIT Mathematicians

by Joel Segel

AK Peters: 2009. 330 pp. \$49

The question of how one makes a great scientific discovery, or teaches others to do so, is central to two recent books that portray mathematicians. In *Mathematicians*, Mariana Cook photographs more than 90 living mathematicians, each portrait accompanied by an explanation of how they became interested in their subject. Many cite an early introduction to problem solving, often before the age of ten, by a family member. For others, it was a teacher who piqued their interest in mathematics. Later influences came from mentors or leaders in the field — Alexander Grothendieck is named by several as having suggested what they should work on.

Collaboration, such as that between Benedict Gross and Don Zagier on their eponymous formula or between Isadore Singer and Michael Atiyah on their index theorem, can be decisive in achieving a successful research career. Also important is sustained concentration on a problem: Jean-Pierre Serre says his best work is done at night when half-asleep. A background in music is another frequent theme: Timothy Gowers and Persi Diaconis both come from families of professional musicians, and Noam Elkies and Manjul Bhargava note an early interest in the patterns of Western and Indian classical music, respectively.

Recountings tells of the influential US mathematics department at the Massachusetts Institute of Technology (MIT) through interviews with a dozen faculty members by author Joel Segel. The book was compiled after the sudden early death of Gian-Carlo Rota, MIT professor of applied mathematics and philosophy, when his colleague Gilbert Strang became concerned that reflections on mathematics and the story of the department might be lost with the passing of other senior faculty members. Also interviewed is Zipporah Levinson, the widow of Norman

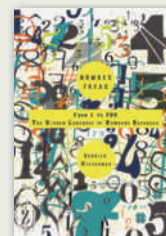
Levinson, a past department chairman who is revered both for his mathematics and for his able running of the department.

The interest in teaching among these senior faculty members is broad and deep. Many textbooks have arisen from MIT courses, such as George Thomas's classic text *Calculus and Analytic Geometry* (Addison-Wesley, 1952). The collective pride is palpable as many remember the day in 1959 when maths courses became catalogued as equivalent to others at MIT — no longer carrying an 'M' prefix to indicate that maths was a service department for the others. The professors share their strategies for achieving research success, from working on prize problems to developing an intuitive feel for proofs. They explain how new research directions have come from interactions with students and colleagues or from writing a review article.

Bertram Kostant's account is particularly inspiring and appears in both books. His interest in science began with his chemistry teacher, Mr Lieberman at Stuyvesant High School in New York, and listing the formulae in chemical reactions. Wherever Kostant went — from college at Purdue University, by way of the University of Chicago, the Institute for Advanced Study in Princeton, the University of California, Berkeley, to MIT — he found himself in the midst of a maths department at a high point. He was also tied to history. At Purdue he was taught by Arthur Rosenthal, a German refugee who had previously taught physicist Werner Heisenberg and had studied under C. L. F. Lindemann — who proved that π is not an algebraic number.

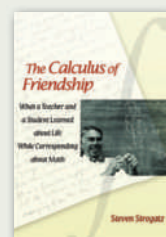
Years later at Princeton, Kostant drove Albert Einstein home just a week before Einstein's sudden death. Lingered in the car, Einstein asked Kostant what he worked on. "Lie groups," he replied, to which Einstein responded, "Oh, that will be very important." The great man's prophetic reply shows that his legendary intuition extended from physics to mathematics. On a different scale, the insights in these two books will inspire mathematicians and scientists to come.

Eric L. Altschuler is assistant professor in the Department of Physical Medicine and Rehabilitation at the University of Medicine & Dentistry of New Jersey, New Jersey 07103, USA. e-mail: eric.altschuler@umdnj.edu



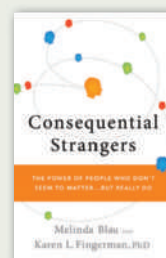
In *Number Freak* (Perigee Books, 2009), Derrick Niederman tells the stories behind the numerals 1 to 200. Each number gets

an entry, detailing its significance from ancient myth to mathematical reality. For instance, the prime number 17 is considered unlucky in Italy and was detested by the Pythagoreans compared with its neighbours 16 and 18; yet the choreographer George Balanchine saw its beauty in a double-diamond configuration of 17 dancers in his ballet *Serenade*.



An intimate view of mentorship is revealed by US mathematician Steven Strogatz in *The Calculus of Friendship* (Princeton University

Press, 2009), a compilation of letters exchanged with his high-school maths teacher over 30 years. Through their correspondence they share problems in calculus, chaos theory and major life events, from professional and sporting successes to family bereavements and divorce. The book touchingly charts their changing roles and relationship, from student to professor, teacher to retirement.



Numerous contacts with neighbours or workmates have a profound effect on our success, happiness and health, according to journalist Melinda Blau

and psychologist Karen Fingerman. In *Consequential Strangers* (W. W. Norton, 2009), they explain how casual acquaintances are most likely to tip you off about a new job or provide a creative solution to a problem. Even though wide social networks can encourage bullying, lying and gossip, they enable people to become more conscious of their shared humanity.



Timothy Gowers: music inspired maths.

M. COOK

NUMERICAL READING

Q&A: Science pop songsters

The US band They Might Be Giants has played rock to adults for more than two decades — and to children since 2002. Next week it releases the album *Here Comes Science*, with educational tunes about the elements and evolution. **John Linnell**, who fronts the band with John Flansburgh, explains why a science-friendly thread runs through their music.

Your 1987 remake of the 1959 children's song 'Why Does the Sun Shine?' is still popular. Why did you cover it?

We have songs about science and also about the pro-science culture of our childhood — the post-war science boosterism that was going on. The science record that we covered that track from was part of the post-Sputnik period in US history when there was a lot of interest in getting kids into science.

Was science a missed calling?

I would have been a crummy scientist but I would have been enthusiastic. I like science a lot and it's something that I think about all the time, almost as an amateur. It was a nice convergence of personal interests and a logical next step that we did an album about science.

How does this follow on from your previous records for children?

We put out *Here Come the ABCs* as a placeholder. We were not overly concerned about teaching kids the alphabet because they are going to learn the alphabet anyway. It was a pretext for entertainment. The follow-up with the numbers was an obvious choice — although we were resistant to doing the *Here Come the 123s* because it was so obvious. Science was a departure from that pattern. And that was really exciting. We got to do something personal to us with the full promotional machinery of the Disney corporation behind it.

From the first song, 'Science is Real', this album seems to be making a statement. Why is that important?

It seems that science has suffered in this country recently, so it was political in a way. There has been some scepticism about science in the past 25 years that has been unfortunate. There's a decadent quality to that — that the culture has lost its way.

Your lyrics talk about evolution being real and how stories about angels and unicorns are just that, stories. Did



John Linnell (above left) and John Flansburgh of They Might Be Giants hope their next album for children (inset) will help boost interest in science.

you worry that this might alienate some listeners?

John Flansburgh took the bull by the horns by writing that song and

addressing that situation, which is that religion cannot take the place of science. It's not something you can tiptoe around. It's important that everybody gets what the discussion is about. If we're talking about the history of Earth, we can't rely on religious tradition to tell us all the information. He says it in the song: as beautiful as the stories are, they don't tell us everything we need to know. It's an old complaint on the part of scientists, but it bears repeating.

Did you hire a fact-checker?

We did. Eric Siegel from the New York Hall of Science listened to everything and gave us very useful information, only some of which we entirely comprehended. He was pointing out, also, things in the videos that were misleading or not making the point in the right way.

In the new album you write a musical retraction: 'Why Does the Sun Really Shine?' Why set the record straight?

We overstated the case in saying that the original song is fatally flawed, because a lot of the information in it is good. The Sun does convert hydrogen into helium and there's a nuclear reaction and that's the source of the explosive radiative energy coming out of the Sun. The only thing that was seriously wrong with the original song is that the Sun is not gas, it's plasma. It's one of those modern distinctions that was lost on the writers in the fifties.

What's next?

I wish we could do a second volume of the science because there's a lot more stuff we haven't covered. I don't know, maybe that's going to be our next move. We could spend a lot more time on science. ■

Interview by **Brendan Maher**, *Nature's* Biology Features Editor.

***Here Comes Science* will be released digitally on 1 September, and as a CD/DVD set on 22 September on Idlewild/Disney Sound.**

STEM CELLS

The promises and perils of p53

Valery Krizhanovsky and Scott W. Lowe

Five studies show that disabling p53, an essential tumour-suppressor protein, improves the efficiency of stem-cell production. Are these results a 'heads up' that cancer cells and stem cells are disturbingly similar?

Mutations that inactivate the p53 tumour-suppressor-protein network occur in most human cancers and, consequently, the roles and regulation of p53 activity in tumour formation are the topic of intense research. Inherited germline mutations in the *p53* gene promote cancer in mice and humans, and *p53* loss interacts with various mutant genes to transform normal cells into tumour cells. p53 is a stress-response protein, which suppresses tumour formation by triggering programmed cell death (apoptosis); by activating cell-cycle checkpoints that prevent damaged cells from proliferating; or by promoting senescence (permanent cell-cycle arrest). Thus, inactivation of p53 facilitates the expansion of aberrant cells and leads to rampant genome instability. Five papers^{1–5} in this issue describe how disruption of the p53 network also enhances the production of induced pluripotent stem (iPS) cells*. Although these observations catapult p53 into the centre of stem-cell research, time will tell whether they represent a promise or a warning.

iPS cells were first produced three years ago⁶ by the enforced expression of genes encoding four transcription factors (c-Myc, Klf4, Sox2 and Oct4) in mouse fibroblast cells. These cells have the same capabilities as embryonic stem (ES) cells isolated from early mammalian embryos — they can self-renew, and are able to give rise to all tissue types of the body. ES cells hold promise as a potential treatment for various diseases; and because iPS cells can be produced from adult cells from any individual, the availability of these cells can, in principle, solve the ethical issues associated with ES-cell use and may also circumvent the need for immunologically matched cell donors. Still, despite much enthusiasm, it is not known whether iPS cells will be an effective treatment for human diseases. In fact, even embryo-derived ES cells have been tested in only a few settings, and their effectiveness and safety are not well established.

Methods for producing iPS cells have so far been inefficient. They initially involved expression of the tumour-promoting oncogene *c-myc*, and random insertion of foreign DNA, including DNA from viruses used as vectors, into the

*This article and the papers concerned^{1–5} were previously published online.

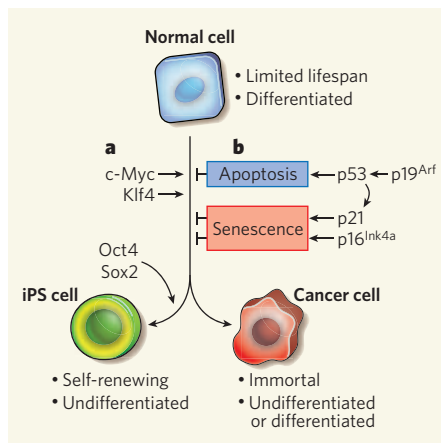


Figure 1 | Overlapping mechanisms control iPS-cell and cancer-cell production. Normal fibroblasts, which are mature, differentiated cells, can be reprogrammed into induced pluripotent stem (iPS) cells or tumour cells by a combination of defined factors. **a**, The transcription factors c-Myc and Klf4 promote reprogramming of fibroblasts into iPS cells in a manner that conceptually parallels their roles in transforming normal cells into tumour cells. Oct4 and Sox2, although overexpressed in cancers, are currently thought to function specifically to promote iPS-cell formation. **b**, Conversely, the p53 tumour-suppressor protein, which can be induced by p19^{Arf}, directly or indirectly limits the reprogramming of fibroblasts into iPS cells^{1–5} or into transformed cancer cells by inducing apoptosis, or cellular senescence through its target protein, the cell-cycle inhibitor p21. Another cell-cycle inhibitor, p16^{Ink4a}, also promotes cellular senescence directly to limit both processes. The *Ink4a/Arf* locus (not shown), which encodes p19^{Arf} and p16^{Ink4a}, is silenced during iPS reprogramming^{2,4}.

recipient genome — techniques that could lead to cancer. Subsequently, in a flurry of activity, researchers identified ways to produce iPS cells without *c-myc*⁷, devoid of viral integration⁸, or using only proteins for reprogramming⁹. Indeed, the 'factorology' of iPS-cell production is all the rage, reminiscent of the early days of cancer-gene discovery, when researchers raced to identify the first genes and gene combinations that could convert normal cells to an immortal, cancerous state.

The new studies^{1–5} add to the frenzy by decisively showing that inactivation of p53 markedly increases the efficiency of iPS-cell production. Furthermore, Kawamura *et al.*³ (page 1140) show that p53 deficiency simplifies iPS generation by enabling production of iPS cells with only two factors, Oct4 and Sox2. Also, three groups^{1–3} show that p53-deficient iPS cells can give rise to adult tissues when implanted into mouse embryos.

As p53 inactivation promotes genome instability and cancer, the risks of producing iPS cells that lack this essential tumour suppressor may outweigh its benefits. In line with this, Marión *et al.*⁵ (page 1149) reveal that p53-deficient iPS cells are genomically unstable and are not 'fit' enough to efficiently produce mice. And even when mice can be generated partly from iPS cells as in the work by Hong and colleagues¹ (page 1132), they eventually develop tumours. In addressing such safety concerns, Utikal *et al.*⁴ (page 1145) demonstrate that transient, rather than permanent, inhibition of p53 also enhances reprogramming efficiency. Still, for p53-suppressed iPS cells to be used therapeutically, it must be shown that the reconstituted tissues function normally and remain tumour free. Moreover, next-generation sequencing and other genomic technologies must be used to demonstrate that these cells do not acquire deleterious mutations.

Beyond its therapeutic implications, this body of work^{1–5} presents overlapping but contrasting views of the mechanism by which p53 limits reprogramming and, in particular, is inconclusive as to whether interaction between the p53 network and reprogramming pathways is direct or indirect. Li *et al.*² (page 1136) show that the *Ink4a/Arf* locus, which encodes a cell-cycle inhibitor (p16^{Ink4a}) and an indirect p53 activator (p19^{Arf}), is silenced during iPS reprogramming. They argue that this silencing occurs early in reprogramming, implying a direct effect of the reprogramming factors on this locus. There is, however, no consensus about the timing of downregulation of *Ink4a/Arf* expression during reprogramming^{2,4}.

Other observations^{3,4} point to an indirect interaction between reprogramming factors and p53 through activation of a p53-mediated

stress response (for instance, apoptosis or senescence). Accordingly, three groups^{1–3} provide evidence that one key p53 effector in the process is the cell-cycle inhibitor p21. Indeed, Gil and colleagues¹⁰ suggest that senescence represents the primary barrier to reprogramming. It is well established that cells with an intact p53 network are prone to senescence in culture¹¹, and perhaps this alone explains why normal cells are more difficult to reprogram. Accordingly, Utikal *et al.*⁴ show that spontaneously immortalized cells exhibiting unrestricted growth in culture, with or without obvious p53 impairment, are readily reprogrammed into iPS cells.

At face value, the results of these studies are reminiscent of work¹², published 25 years ago, showing that loss of p53 facilitates cellular immortalization — a state of endless self-renewal that is one of the first steps towards cancer. And more recently, p53 has been implicated as a factor that limits the self-renewal capacity of certain stem cells^{13,14}. Even in the iPS field, previous work had shown that the SV40 T antigen — an immortalizing oncogenic protein that disables p53 — or transient inhibition of p53 using small interfering RNAs, enhance reprogramming efficiency^{15,16}. The current studies substantially extend and expand on these findings, and provide new platforms for more effectively studying reprogramming.

Just as the race to find new reprogramming factors is reminiscent of the hunt for cooperating oncogenes, the remarkable similarities between the reprogramming processes and oncogenic transformation may provide insights into cancer (Fig. 1). Indeed, both processes require specific combinations of collaborating genes that can produce a less differentiated cell able to proliferate and self-renew indefinitely. All four factors initially shown to reprogram cells are overexpressed in at least some types of tumour, and at least two of them — *c-myc* and *Klf4* — are established oncogenes. Now we find that p53 — a tumour suppressor whose loss greatly increases the efficiency of oncogene cooperation in transforming normal cells to tumour cells¹⁷ — affects reprogramming similarly. Notably, a gold-standard assay for the formation of iPS cells is in fact a tumorigenesis assay that measures their ability to form germ-cell tumours following transplantation into mice.

If the processes that lead to the production of iPS cells and tumours overlap, one wonders whether so-called cancer stem cells — cells capable of self-renewal that are considered essential for the propagation of some tumour types — might initially arise through a reprogramming-like mechanism. Moreover, not all of the factors required to trigger reprogramming of cells to iPS cells are necessary for their maintenance^{8,9}. If cancer arises through reprogramming-like processes, then perhaps many of the oncogenes that initiate tumour formation might be dispensable for tumour progression and, hence, be poor targets for new cancer

therapies. If this proves to be the case, further studies into reprogramming might eventually point towards new treatments for cancers as well.

Valery Krizhanovsky and Scott W. Lowe are in the Cold Spring Harbor Laboratory and Howard Hughes Medical Institute, Cold Spring Harbor, New York 11724, USA.

1. Hong, H. *et al.* *Nature* **460**, 1132–1135 (2009).
2. Li, H. *et al.* *Nature* **460**, 1136–1139 (2009).
3. Kawamura, T. *et al.* *Nature* **460**, 1140–1144 (2009).
4. Utikal, J. *et al.* *Nature* **460**, 1145–1148 (2009).

5. Marión, R. M. *et al.* *Nature* **460**, 1149–1153 (2009).
6. Takahashi, K. & Yamanaka, S. *Cell* **126**, 663–676 (2006).
7. Nakagawa, M. *et al.* *Nature Biotechnol.* **26**, 101–106 (2008).
8. Okita, K. *et al.* *Science* **322**, 949–953 (2008).
9. Zhou, H. *et al.* *Cell Stem Cell* **4**, 381–384 (2009).
10. Banito, A. *et al.* *Genes Dev.* (in the press).
11. Livingstone, L. R. *et al.* *Cell* **70**, 923–935 (1992).
12. Eliyahu, D., Raz, A., Gruss, P., Givol, D. & Oren, M. *Nature* **312**, 646–649 (1984).
13. Krizhanovsky, V. *et al.* *Cold Spring Harb. Symp. Quant. Biol.* **73**, 513–522 (2008).
14. Lin, T. *et al.* *Nature Cell Biol.* **7**, 165–171 (2005).
15. Mali, P. *et al.* *Stem Cells* **26**, 1998–2005 (2008).
16. Zhao, Y. *et al.* *Cell Stem Cell* **3**, 475–479 (2008).
17. Lowe, S. W. *et al.* *Science* **266**, 807–810 (1994).

EXTRASOLAR PLANETS

Secrets that only tides will tell

Douglas P. Hamilton

Evidence that the most recently discovered extrasolar planet is virtually at the end of its life is a surprise. The odds of that are very low — similar to drawing two consecutive red aces from a well-shuffled deck of cards.

When it was first discovered in 1995, the planet 51 Pegasi b astounded scientists with its 4.3-day orbital period. This placed the Jupiter-sized planet at around 5% of the Earth–Sun distance from its host star (0.05 AU), a sweltering location where no planet had been expected to exist. But now with almost 375 extrasolar planets discovered to date, and nearly 20% of them located within 0.05 AU of their parent stars, a discovery of another ‘hot Jupiter’ is no longer as exciting as it once was. On page 1098 of this issue, however, Hellier *et al.*¹ report the discovery of WASP-18b, a hot Jupiter (Fig. 1) that is sure to generate some buzz: the predicted remaining lifetime of the planet is less than a thousandth of the age of its host star, far shorter than that for any other known planet.

WASP-18b, the eighteenth planet discovered by Britain’s Wide Angle Search for Planets project², is only the second planet found with

an orbital period of less than a day. Proximity to the host star, as well as the planet’s large mass (10.3 times that of Jupiter), lead to strong tidal interactions between the two bodies, which elongate both of them along the line joining their centres. If the bodies spin as well, the tidal bulges can misalign, causing torques that couple their spins to their orbital angular momentum.

For a planet orbiting a star, the tides raised on the smaller object act swiftly to reduce its spin until one face is locked towards the star. The planet’s initially elongated orbit also rapidly becomes circularized by these tides. By contrast, tides raised on the star usually act more slowly, and can either pull the planetary orbit inward (if the planet orbits faster than the star spins) or push it outward (if the stellar spin is faster). WASP-18b should be spiralling inward towards the star, and it is so close and



C. CARREAU/ESA

Figure 1 | The ultimate in global warming. This artist’s impression depicts an exoplanet similar to the newly discovered¹ WASP-18b. As seen from the planet, the host star spans an angle of more than 30° and hovers menacingly at a fixed position in the sky. WASP-18b completes an orbit in 0.94 days, buzzing just 2.5 stellar radii above the star’s surface. That distance may be shrinking surprisingly rapidly.

so massive that the infall timescale is predicted to be well under a million years.

That stings. Planets and stars form together, and Hellier and colleagues¹ find the star to be about a billion years old. So it seems that WASP-18b has lived a billion years and has just a million years left before its fiery demise. The odds of finding a planet so close to the end of its life are low — only about 1 in 1,000. Did Hellier *et al.* really draw the two red aces from the deck? How can this be?

There are a number of possibilities, but none of them is entirely satisfactory. First, 1-in-1,000 odds may not be so bad, considering the roughly 320 planetary systems discovered to date³; effectively, astronomers have had multiple tries at drawing two red aces. Formally, the likelihood of getting a positive result in 320 chances is a respectable 27%. But have we really had 320 chances? The hidden assumption here is that all 320 systems once had a massive planet that was lost to its star. When corrected for the fact that most systems may not have had such a planet, the odds go down considerably. Even more problematic is the fact that there are only three other known planets located within 0.06 AU of their host stars with masses as large as that of WASP-18b. We would probably expect to see many more such objects if this interpretation were correct.

Second, as suggested by Hellier *et al.*, the star may be particularly poor at dissipating tidal energy, which would dramatically increase the planet's lifetime. The tidal-dissipation rate may be loosely parametrized by Q , the quality factor, which depends on properties of the stellar interior. More properly, the dissipation rate is proportional to Q/k_2 , where k_2 is a measure of the star's response to a tidal perturbation. The quantity Q/k_2 is often assumed to be about 10^6 for stars, but is relatively well determined only for colder balls of gas: for example, the values for Uranus⁴ ($Q/k_2 = 2 \times 10^5$) and Neptune⁵ ($Q/k_2 = 4.5 \times 10^4$) are uncertain by about a factor of 2. For Jupiter⁶, the nominal value of Q/k_2 is 8×10^5 , although it could be up to six times higher or lower. Hellier *et al.* show that a Q/k_2 value as high as 10^9 would be required to increase the planet's remaining lifetime towards a billion years; longer-lived planets are much easier to find. If the star's Q/k_2 really is thousands of times above what is measured for either gaseous planets or binary stars, it would be a spectacular finding.

Third, perhaps we are forced to abandon the assumption that the planet has been tidally evolving throughout the billion-year age of its host star. Hot Jupiters are thought to have formed much farther from their stars than where they are found today. A more distant origin gives a planet a far greater supply of raw materials early in its lifetime, allowing growth to Jupiter mass and beyond. After reaching its full size, however, another process, such as interactions with a second planet, must place one planet close to the star, where tidal forces

take over. Perhaps such an event occurred recently in the WASP-18 system. It is impossible to rule this out, and extremely difficult to assess the odds.

Finally, maybe something is holding the planet up against the inward drag of tides. Some poorly understood aspect of stellar convection? An unappreciated subtlety of tides? Another planet? Although these may seem unlikely possibilities, given the existence of the unusual WASP-18 system they should be examined more closely. It is useful here to draw an analogy with the similar situation faced by Mars's largest moon Phobos. Like WASP-18b, Phobos is close to its host, skimming just 1.73 Mars radii above the surface, and its orbit is predicted to decay inward in about 30 million years, a timescale more than 150 times shorter than the age of the Solar System. The past history of Phobos, like that of WASP-18b, is not understood, and possibilities similar to those discussed above

are equally unpalatable. Perhaps we really are missing some key bit of physics.

Relief, however, is on the way. Hellier *et al.*¹ emphasize that if the orbit of WASP-18b is really decaying inward rapidly, the effects will become visible within a decade. Continuous monitoring of this system — as well as others that are predicted to undergo slower, albeit still rapid, tidal evolution⁷ — would be well worth the effort. Only then will tides begin to reveal the secrets of these unusual systems. ■

Douglas P. Hamilton is in the Department of Astronomy, University of Maryland, College Park, Maryland 20742, USA.

e-mail: dphamil@umd.edu

1. Hellier, C. *et al.* *Nature* **460**, 1098–1100 (2009).
2. www.superwasp.org
3. <http://exoplanet.eu/catalog.php>
4. Tittlemore, W. C. & Wisdom, J. *Icarus* **78**, 63–89 (1989).
5. Zhang, K. & Hamilton, D. P. *Icarus* **193**, 267–282 (2008).
6. Yoder, C. F. & Peale, S. J. *Icarus* **47**, 1–35 (1981).
7. Sasselov, D. D. *et al.* *Astrophys. J.* **596**, 1327–1331 (2003).

DEVELOPMENTAL BIOLOGY

Jumping-gene roulette

Sandra L. Martin

Jumping genes, which make DNA copies of themselves through an RNA middleman, provide a stochastic process for generating brain diversity among humans. The effect of their random insertion, however, is a bit of a gamble.

The enormous complexity of the human nervous system is generated by the combined actions of incompletely understood genetic and environmental factors. Coufal *et al.*¹ (page 1127 of this issue) now reveal one remarkable genetic contribution to individual variation in the nervous system. The authors show that normally quiescent 'jumping genes' can be activated in neural progenitor cells. Each hop generates genetic diversity in the nervous system that may or may not affect function or health.

LINE-1 (L1) retrotransposons are the most dynamic force operating in the human genome. These elements are regions of mobile DNA that make copies of themselves by converting their RNA transcript into DNA, which then reinserts into the genome — a process known as retrotransposition. Cleverly, the proteins that convert the L1 RNA transcript into a DNA copy are encoded by the L1 sequence itself. Depending on where the new L1 inserts, its effect on a neighbouring gene can range from nil to destruction².

As selfish mobile elements whose goal it is to make copies of themselves, L1s must be able to retrotranspose in egg and sperm, or in the early embryo, ensuring that new L1 copies are passed on to future generations. That more than 600,000 copies of L1 retrotransposons pepper our genome is proof of the evolutionary success of this strategy. Meanwhile, the human genome has evolved elaborate mechanisms for

repressing L1 retrotransposition³, particularly by blocking transcription, a compulsory first step in the process leading to insertion of a new L1 copy. Methylation of DNA in regulatory regions of genes is a widespread and effective method of transcriptional repression. However, during gamete formation, and in the early embryo, short waves of demethylation in a region of L1 that serves as a promoter of transcription allow the mobile element to temporarily escape transcriptional silencing.

In the body's non-gametes (somatic cells), where new copies of L1 would not be passed on to the next generation but transposition could be harmful, the L1 promoter is methylated and transcription is repressed. Thus, it was surprising to find⁴ that L1 transcription seemed to be increased during the differentiation of neuronal progenitor cells isolated from the hippocampus of adult rat brains. Human L1 also retrotransposed when introduced into these same cells and when expressed in the brain cells of transgenic mice⁴. These results raised the possibility that the genome of individual brain cells could harbour different insertion sites and numbers of L1s (so-called somatic mosaicism), and fuelled speculation that L1 retrotransposition might lead to unique neuronal properties among humans⁴.

Coufal *et al.*¹ provide data to support this suggestion. They show that human neural progenitor cells, whether derived from fetal brains

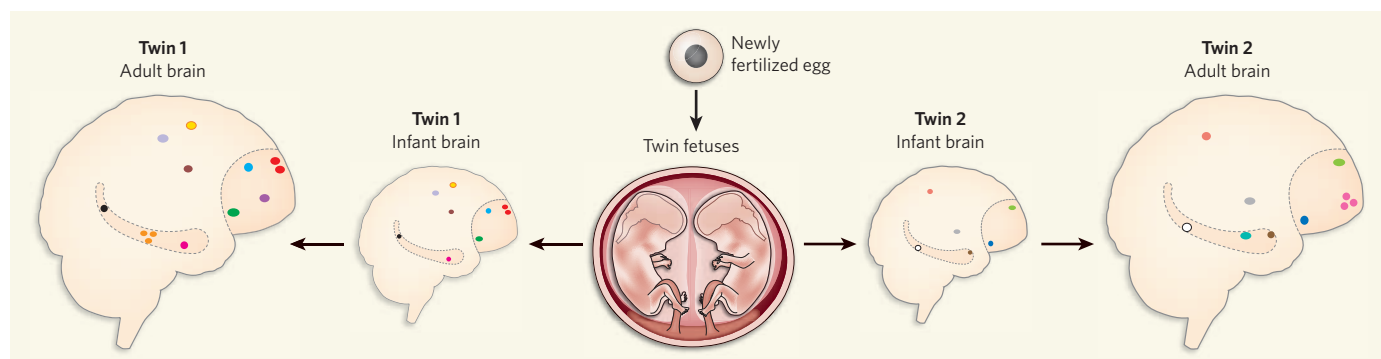


Figure 1 | Human brain variation by retrotransposition. These twins are genetically identical at conception, but at birth their brains differ because of new L1 insertions that take place during the development of the nervous system in the fetus. Ongoing retrotransposition in neural progenitor cells as shown to occur by Coufal *et al.*¹ will further diversify the genetic

make-up of their brains in adulthood. Depending on the target genes and the neurons affected by L1 insertions, the twins may differ in brain function or dysfunction. Each unique insertion is represented by a different colour. Darker-shaded areas highlight regions of the brain where L1 retrotransposition may be more likely to occur after birth.

or from cultured embryonic stem cells, support the retrotransposition of an introduced human L1. Some cells in which L1 had retrotransposed continued to divide, which means that specific new L1 insertions are not necessarily restricted to a single daughter cell. Furthermore, progenitor cells with new L1 insertions generate different types of differentiated cells, including neurons that can conduct electrical impulses. Finally, the authors¹ identified the genomic locations of 19 new L1 insertions by DNA sequencing; 16 of these were located within 100 kilobases of a gene, and many of these genes are expressed in neurons. These data¹ convincingly show that L1s introduced into human neural progenitor cells can jump in the genome, and that these cells can give rise to functional neurons.

Whether native L1s jump in neural progenitor cells *in vivo* is a much more difficult question to answer, but several tantalizing results suggest that they do. Coufal and colleagues¹ show that the native L1 promoter is relatively under-methylated, which allows for increased L1 transcription, and that L1 RNA transcripts are more abundant in fetal brain than in skin. Most provocative, however, are the results of an assay the authors developed to quantify the number of L1s in the brain. As L1 is a retrotransposon, each cycle of transposition adds a new copy of L1 DNA to the genome, and, if L1 is transposing in the brain, it should theoretically be possible to measure the increased numbers of L1 copies in that tissue. It is, however, a substantial challenge to document an increase from 600,000 copies of L1 in every cell to 600,000 plus 1 in one or a few cells of the human brain.

Remarkably, the authors did just that. Using a highly sensitive form of quantitative polymerase chain reaction (PCR), a technique that amplifies and quantifies specific DNA, they detected more L1s in the genome of adult human brain cells than in the genome of liver or heart cells from the same individuals. Cells from all brain regions tested contained more copies of L1 than cells from other tissues, with the highest number found in the dentate gyrus and frontal cortex¹, perhaps reflecting a relatively

greater contribution of the ongoing generation of neurons from precursor cells in these areas of the brain⁵. By adding a known amount of L1-containing DNA to the heart and liver samples before PCR, the authors¹ provided evidence that not only is the apparently lower L1 content in heart and liver not an experimental artefact, but also that each brain cell contained approximately 80 additional copies of L1.

Conclusive evidence that L1 retrotransposons jump in human brain cells will require individual L1 insertions to be characterized by DNA sequencing. Although this is a difficult task, such data will probably soon become available. It is therefore important to ask whether it is reasonable to expect any aspect of brain function to be altered if L1s jump randomly in neuronal precursor cells. Given that changing the firing patterns of single neurons can have marked effects on behaviour^{6,7}, and that single-gene alterations can cause profound effects in subpopulations of neurons⁸, it is

likely that some L1 insertions, in some cells, in some humans⁹, will have significant, if not profound, effects on the final structure and function of the human brain (Fig. 1). These findings challenge the notion of the genome as a constant entity with limited impact on neuronal plasticity, and blur the distinction between genetic and environmental effects on the nervous system.

Sandra L. Martin is in the Department of Cell and Developmental Biology, University of Colorado School of Medicine, Aurora, Colorado 80045, USA. e-mail: sandy.martin@ucdenver.edu

1. Coufal, N. G. *et al.* *Nature* **460**, 1127–1131 (2009).
2. Han, J. S. & Boeke, J. D. *BioEssays* **27**, 775–784 (2005).
3. Goodier, J. L. & Kazazian, H. H. Jr *Cell* **135**, 23–35 (2008).
4. Muotri, A. R. *et al.* *Nature* **435**, 903–910 (2005).
5. Sohur, U. S., Emsley, J. G., Mitchell, B. D. & Macklis, J. D. *Phil. Trans. R. Soc. Lond. B* **361**, 1477–1497 (2006).
6. Houweling, A. R. & Brecht, M. *Nature* **451**, 65–68 (2008).
7. Li, C. Y., Poo, M. M. & Dan, Y. *Science* **324**, 643–646 (2009).
8. Rotenberg, A. *et al.* *Cell* **87**, 1351–1361 (1996).
9. Seleme, M. C. *et al.* *Proc. Natl Acad. Sci. USA* **103**, 6611–6616 (2006).

OPTICS

Ultrafast X-ray photography

Margaret M. Murnane and Jianwei Miao

A super-fast, lensless microscope has been developed that works by decoding the diffraction patterns of bright, laser-like flashes of X-rays. This advance should enable ultrafast events at the nanoscale to be recorded.

Stroboscopic photography has profoundly improved our understanding of both nature and technology, as illustrated by the beautiful snapshots of a milk droplet splashing, or a bullet piercing an apple, produced by the pioneer of the technique, Harold Edgerton. In *Physical Review Letters*, Ravasio *et al.*¹ report that they have captured an image of a nano-object using a single burst of X-rays from the fastest strobe light in existence.

The most rapid natural events occur at the attosecond (10^{-18} seconds) or femtosecond

(10^{-15} seconds) timescale, and must therefore occur in the nanoworld, as even light travels a distance of only 300 nanometres in 1 femtosecond. Because the spatial resolution of any camera or microscope is limited by the wavelength of the illuminating light, short bursts of light at very small wavelengths are needed to see ultrafast motion directly at the nanoscale. Pulses of X-rays would be ideal, for example for directly visualizing how the electrons that bind molecules together adjust as the molecule's structure changes during a chemical

reaction or a conformational change; how the motion of a biological molecule relates to its function; or how rapidly magnetic materials can switch state in data-storage devices. But producing bright bursts of X-rays is technically demanding, so most ultrafast studies have used indirect approaches, such as spectroscopy, to study the fastest events. Furthermore, rapid bursts of electrons in an electron microscope have already been successfully used for ultrafast imaging at the nanoscale^{2,3}.

The past decade, however, has witnessed an exciting convergence of advances that could transform our ability to visualize nanoscale events. First, 'lensless' diffractive imaging enables scientists to use coherent (laser-like and directed) X-ray beams to take pictures of an object, simply by shining a beam on the object and collecting the diffracted photons⁴; sophisticated computational algorithms then process the diffraction pattern to reveal the image. And second, new sources of light can generate coherent, ultrashort pulses of X-rays. For example, X-ray free-electron lasers (XFELs) produce high-energy X-ray beams⁵ that have pulse durations of 100 to 200 femtoseconds. But these stadium-sized facilities are expensive and exclusive: access is limited to one or a few users at a time, and they exist in only a few places worldwide. Moreover, the current pulse repetition rate of XFELs is limited to about 10 to 120 hertz.

On the other hand, table-top lasers can produce femtosecond pulses throughout the visible and infrared regions of the spectrum, and these can be directly converted into ultraviolet and low-energy X-rays using an extreme nonlinear process called high-harmonic generation⁶. In this process, an electron is first ripped from an atom by the laser field, then accelerated away from the resulting ion and back again. The electron accumulates kinetic energy during its journey, which is liberated as an X-ray photon when the electron recombines with the ion. The resulting X-ray beams can be fully coherent under certain conditions, and the pulse duration can span from tens of femtoseconds to less than 100 attoseconds. Although the energy per pulse is a thousand to a million times less than that produced by XFELs, the pulse repetition rate can be very high, ranging from 10 Hz to more than 50 kHz.

Lensless diffractive imaging has succeeded in reconstructing snapshots of virions, cells, nanostructures and plasmas at good resolutions using high-harmonic^{7,8}, synchrotron-radiation^{9,10} and XFEL sources¹¹. With high-harmonic sources⁷, images at a resolution of 50 nanometres have been obtained by exposing a nano-object to a pulsed beam of X-rays for 80 minutes, whereas images at a resolution of 120 nanometres required an exposure of only 30 seconds. In such experiments, data from many pulses must be combined to obtain a single image, because the intensity in each pulse is too low to provide an image on its own. Nevertheless, this approach can be used to

follow nanoscale dynamics simply by varying the delay between a 'pump' laser pulse (which induces the dynamic behaviour) and probe pulses of X-rays.

In some situations, however, it is better to capture diffraction patterns in a single, high-intensity shot of X-rays — for example, if the object under investigation is destroyed by the experimental conditions. To date, single-shot X-ray imaging has been the exclusive realm of large XFEL facilities^{11,12}, because only these sources produce pulses of sufficient intensity. XFELs have been used to capture dynamic motion¹¹: a nano-object is first perturbed by a pump laser pulse, and then probed by single pulses of X-rays at different times afterwards. The resulting series of images, obtained at a resolution of 50 nanometres, show how the object changes over time in response to the pump.

Ravasio *et al.*¹ now report that lensless diffractive imaging can be used to take a picture of a nano-object by means of a single, bright, ultrafast (20 femtoseconds) burst of X-rays

generated using high harmonics (Fig. 1). The authors used a low-energy X-ray beam — which had a photon energy of around 40 electronvolts, corresponding to a wavelength of 32 nanometres — to obtain an image that had a resolution of 120 nanometres. The key to their success was using a bigger laser to generate sufficiently bright X-rays: the lens in the X-ray-production system had a focal length of 5.5 metres. The laser apparatus was therefore relatively large, but it was still much smaller than an XFEL. Furthermore, because the X-ray pulses produced by high harmonics are generated by an optical laser, they are perfectly synchronized to that laser. This makes it much easier to capture dynamically changing images at femtosecond time resolution using a pump-probe procedure than when using an XFEL source, in which the pump laser and the X-rays are not perfectly synchronized.

Ravasio *et al.*¹ have so far obtained pictures only of test objects, but lensless, diffractive X-ray imaging holds much promise as a window into the fast-moving nanoworld. Indeed, ultrafast high-harmonic beams have already been used, for example, to follow indirectly how electrons and atoms couple together as a molecule changes shape¹³, how heat flows in nanostructures, and how electrons move between a catalytic surface and molecules adsorbed to that surface¹⁴.

There are many reasons to expect an explosion in the number of applications of ultrafast X-ray imaging. The energy range over which bright harmonic beams could be generated was previously limited to photon energies of less than 100 electronvolts (wavelengths greater than 13 nanometres). This range severely restricted the variety of objects that could be imaged. Fortunately, recent advances in high-harmonic light sources make it possible to create bright beams that span from the ultraviolet into the high-energy X-ray region of the electromagnetic spectrum (that is, to wavelengths of less than 1 nanometre)¹⁵. This will make it possible not only to substantially increase the variety of objects that can be imaged, but also to obtain much higher spatial resolution (potentially below 10 nanometres), essentially creating a super-resolution microscope that can image thick samples in three dimensions. ■

Margaret M. Murnane is in the Department of Physics and JILA, University of Colorado at Boulder, Colorado 90309-0440, USA.

Jianwei Miao is in the Department of Physics and Astronomy, and the California NanoSystems Institute, University of California, Los Angeles, California 90095-1547, USA.

e-mails: margaret.murnane@colorado.edu; miao@physics.ucla.edu

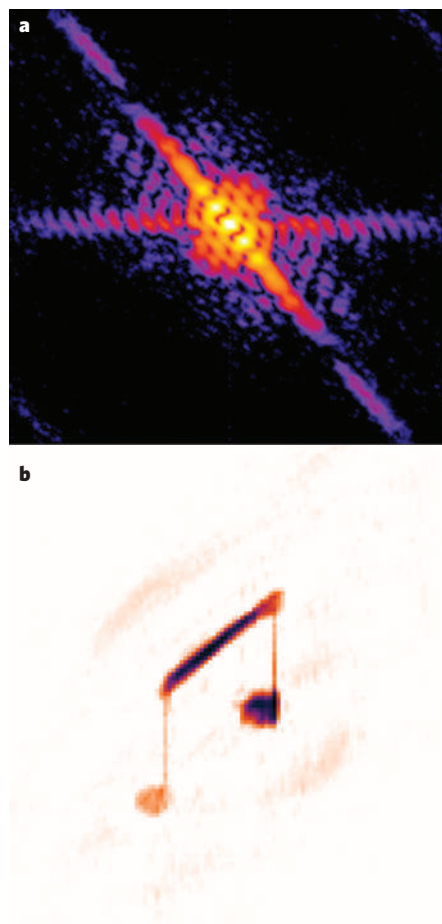


Figure 1 | Decoding the notes. Ravasio *et al.*¹ report a method for obtaining stroboscopic flash images of nanoscale objects. **a**, An ultrafast pulse (exposure time, 20 femtoseconds) of laser-like X-ray beams generates a diffraction pattern when shone on a nanoscale object. **b**, The diffraction pattern is decoded, using computer algorithms, to produce an image of the object — in this case, micrometre-sized 'harmonic notes'. Each pixel is 59 nanometres wide. (Images taken from ref. 1.)

1. Ravasio, A. *et al.* *Phys. Rev. Lett.* **103**, 028104 (2009).

2. Barwick, B. *et al.* *Science* **322**, 1227–1231 (2008).

3. Siwick, B. J., Dwyer, J. R., Jordan, R. E. & Miller, R. J. D. *Science* **302**, 1382–1385 (2003).

4. Miao, J., Charalambous, P., Kirz, J. & Sayre, D. *Nature* **400**, 342–344 (1999).

5. Arthur, J. *et al.* Linac Coherent Light Source (LCLS) Conceptual Design Rep. SLAC-R593 (Stanford, 2002).



50 YEARS AGO

Phoenix Re-born. By Dr. Maurice Burton — For many years anting in birds has held considerable fascination for students of bird behaviour. So, too, has the myth of the Phoenix, and when Maurice Burton saw a tame rook disporting himself on a heap of burning straw it led to an association of ideas which was ultimately responsible for the production of this book ... Burton carried out experiments with his tame rooks and a pet jay to determine their reactions to certain substances and to heat ... Eventually [he] reached certain conclusions which show a clear connexion between Herodotus's account of the Phoenix and the anting of birds. One thing is common to all the substances which cause the anting posture: this is heat or the impression of heat ... Burton comes to the conclusion that anting must be regarded as a posture adopted in moments of unusually intense excitement ... Ant-bathing and thermophily are also shown to be closely related to anting proper and all these are related to such habits as the self-anointing of hedgehogs, the effects of catmint and other odorants on carnivores, as well as numerous idiosyncrasies of behaviour among individual birds and mammals.

From *Nature* 29 August 1959.

100 YEARS AGO

Inaugural address by Prof. Sir J. J. Thomson [to the British Association] — The constant need for thought and action gives to original research in any branch of experimental science great educational value even for those who will not become professional men of science ... I have always been struck by the quite remarkable improvement in judgement, independence of thought and maturity produced by a year's research. Research develops qualities which are apt to atrophy when the student is preparing for examinations, and ... is of the greatest importance as a means of education.

From *Nature* 26 August 1909.

6. Kapteyn, H. C., Murnane, M. M. & Christov, I. P. *Phys. Today* **58** (3), 39–44 (2005).
7. Sandberg, R. L. *et al. Opt. Lett.* **34**, 1618–1620 (2009).
8. Sandberg, R. L. *et al. Proc. Natl Acad. Sci. USA* **105**, 24–27 (2008).
9. Song, C. *et al. Phys. Rev. Lett.* **101**, 158101 (2008).
10. Shapiro, D. *et al. Proc. Natl Acad. Sci. USA* **102**,

- 15343–15346 (2005).
11. Barty, A. *et al. Nature Photon.* **2**, 415–419 (2008).
12. Chapman, H. N. *et al. Nature* **448**, 676–679 (2007).
13. Li, W. *et al. Science* **322**, 1207–1211 (2008).
14. Miaja-Avila, L. *et al. Phys. Rev. Lett.* **101**, 046101 (2008).
15. Popmintchev, T. *et al. Proc. Natl Acad. Sci. USA* **106**, 10516–10521 (2009).

SOLID-STATE PHYSICS

An insulator's metallic side

Joel Moore

Certain insulators have conducting surfaces that arise from subtle chemical properties of the bulk material. The latest experiments suggest that such surfaces may compete with graphene in electronic applications.

Recent progress in solid-state physics has consisted in large part of revelations about the remarkable behaviour of electrons confined to a plane. Every material known to become superconducting above 77 kelvin, the temperature at which nitrogen becomes liquid, contains planes of copper and oxygen atoms from which the superconductivity is believed to originate. The 'quantum dance' of planar electrons in a strong magnetic field underlies their liquid-like behaviour in the quantum Hall effect. Graphene, a single layer of carbon atoms, is arguably the first truly two-dimensional material, and the electrons moving through this layer behave for many purposes as massless. Two papers in this issue^{1,2} add to this list of surprises by showing that the surface of a 'topological insulator' is a novel planar metal. Roushan *et al.*¹ (page 1106) find that, unlike conventional planar metals, the material's surface shows a perfect robustness to impurities. Meanwhile, Hsieh *et al.*² (page 1101) show that its electronic structure can be tuned to a semi-metallic state by chemical manipulation.

According to recent theoretical work^{3,4}, all non-magnetic insulators can be classified as ordinary or topological depending on whether their surfaces are generically insulating or metallic. This classification uses ideas from the branch of mathematics known as topology, which studies properties of objects that are unchanged by smooth modifications to their geometry; smooth changes to a bulk insulator, such as structural modification under strain, cannot shift its topological class except by driving it through a metallic or magnetic state. The metallic surfaces of several topological insulators have been observed previously by using X-rays to knock out their electrons^{5,6}, but this approach alone cannot reveal all of the unusual properties predicted to exist at these surfaces.

Roushan and colleagues¹ observe perhaps the most remarkable such property: topological-insulator surfaces are exceptions to the rule that all planar metals become insulators at low temperature in the presence of impurities or defects. The wave nature of electrons in

quantum mechanics tends to amplify the effects of impurity scattering: an electron bouncing off many impurities often becomes trapped or 'localized', even when a classical particle would continue to diffuse, as first worked out by Philip Anderson 50 years ago⁷. His theory of localization famously predicts that at sufficiently low temperature, and beyond a critical amount of impurity scattering, one- and two-dimensional metals will become insulators — the diffusion of electrons that characterizes the material's conductivity will come to a halt.

However, there is a loophole. In most materials composed of heavy elements, the motion

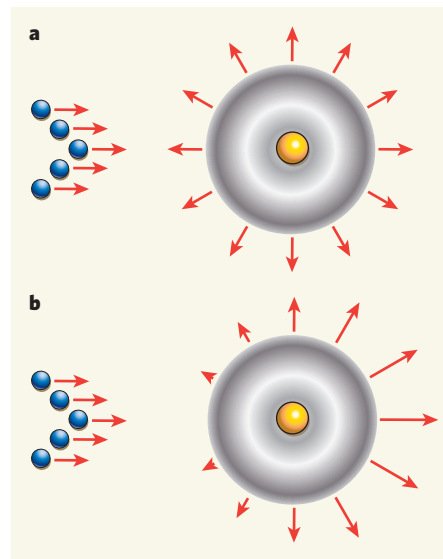


Figure 1 | Electron reflection, or not. **a**, Electrons (blue) in an ordinary planar metal scatter off an impurity (gold) in all directions with equal probability. **b**, At the surface of a topological insulator — one that has a metallic rather than an insulating surface — electrons are preferentially scattered at small angles and have zero probability of being reflected 180° back in the direction of incidence. In reality, electrons scatter as waves rather than as particles at atomic distances, and Roushan *et al.*¹ observe an interference pattern of such waves that indicates the absence of 180° scattering.

of electrons is linked to their spin (intrinsic angular momentum), and this coupling acts to delocalize electrons. Topological-insulator surfaces are effectively at the limit of infinite spin-orbit coupling, and no localization can occur⁸ until the impurity density is so high as to destroy the bulk insulator. The origin of this anti-localization effect is that an electron moving at these surfaces is never perfectly turned back by an impurity, unlike Brave Sir Robin in the film *Monty Python and the Holy Grail*: “When danger reared its ugly head, / He bravely turned his tail and fled.” Although the impurity can change the electron’s direction and the conductivity is finite — not infinite as in a superconductor — a 180° about-face is impossible (Fig. 1). This suppression of perfect backscattering turns out to change the effect of coherence between multiple scattering events from localizing to anti-localizing.

The anti-localization effect is observed by Roushan *et al.*¹ in surface microscopy images of the topological insulator $\text{Bi}_{1-x}\text{Sb}_x$ using the interference of electron waves reflected from a defect or impurity in the material. An intuitive picture for this technique is that the wave pattern from a pebble falling into a pond could be used to study not only the pebble but also the nature of water waves. Recent observation⁹ of a simpler anti-localization effect in the electrical conductance along the one-dimensional edge of a planar insulator was the first evidence for the ‘quantum spin Hall’ phase, which is a topological insulator in two dimensions rather than three.

A weaker form of this anti-localization effect can be observed in graphene if the scattering potential is very smooth, but ultimately electrons in graphene are localized by impurities. Another property of graphene is that it is a semi-metal: unlike in an insulator, graphene has no gap in the energy of electronic states, but the density of metallic electrons vanishes in pure graphene. In most topological insulators, the bulk chemistry leads to a metallic surface rather than a semi-metallic one. But by precise chemical modification of both the bulk and surface of a bismuth-tellurium-based topological insulator, Bi_2Te_3 , Hsieh *et al.*² show that it is possible to bring the surface to the semi-metallic state. They also show that the semi-metallic state retains its strong coupling of orbital motion and spin by examining the spin of electrons moving in each direction along the surface.

Hsieh and colleagues’ discovery suggests that topological-insulator surfaces may compete with graphene in several potential electronic applications. One advantage of tuning the material to the semi-metallic state is that an applied electrical field can create charge carriers of either positive or negative charge (holes and electrons, respectively). This electrical control is possible because, in graphene and the new materials synthesized by Hsieh *et al.*², the semi-metallic electronic structure sits at the boundary between hole-like and electron-like metals. In current silicon-based electronics,

control of the charge of the majority carriers is accomplished permanently by chemical manipulation. Being able to switch electrically between electron and hole carriers leads to new flexibility in device design.

The result of Hsieh *et al.*² also has implications for fundamental science. One example is that using an electrical field to create electrons and holes at the top and bottom surfaces of a thin layer of a topological insulator is predicted to lead to a superconductor-like phase driven by electrostatic binding of electrons and holes¹⁰. The ability to create semi-metals at topological-insulator surfaces and the demonstration¹ of their invulnerability to localization are key steps in unlocking the scientific and technological potential of these remarkable materials. ■

Joel Moore is in the Department of Physics, University of California, and the Materials Sciences Division, Lawrence Berkeley National Laboratory, Berkeley, California 94720, USA. e-mail: jemoore@berkeley.edu

1. Roushan, P. *et al.* *Nature* **460**, 1106–1109 (2009).
2. Hsieh, D. *et al.* *Nature* **460**, 1101–1105 (2009).
3. Fu, L., Kane, C. L. & Mele, E. J. *Phys. Rev. Lett.* **98**, 106803 (2007).
4. Moore, J. E. & Balents, L. *Phys. Rev. B* **75**, 121306(R) (2007).
5. Hsieh, D. *et al.* *Nature* **452**, 970–974 (2008).
6. Xia, Y. *et al.* *Nature Phys.* **5**, 398–402 (2009).
7. Anderson, P. W. *Phys. Rev.* **109**, 1492–1505 (1958).
8. Nomura, K., Koshino, M. & Ryu, S. *Phys. Rev. Lett.* **99**, 146806 (2007).
9. König, M. *et al.* *Science* **318**, 766–770 (2007).
10. Seradjeh, B., Moore, J. E. & Franz, M. *Phys. Rev. Lett.* **103**, 066402 (2009).

GAMMA-RAY BURSTS

Maybe not so old after all

Enrico Ramirez-Ruiz and William Lee

The discovery of a short-lived γ -ray burst at a surprisingly early epoch in the history of the Universe shows how much is still unknown about the evolution of the parent systems of such bursts.

Early on the morning of 14 July 2007, NASA’s Swift spacecraft observed a brief flash of very-high-energy photons, in an event known as a γ -ray burst (GRB). The spacecraft’s wide-field γ -ray monitor established the position of the burst, dubbed GRB 070714B, and within seconds had imaged it with its X-ray telescope, finding a rapidly fading source. Swift’s prompt and highly accurate localization of the GRB allowed a tightly choreographed sequence of observations — performed using ground-based optical telescopes around the world — to follow the progressive dimming, or afterglow, of the source over the next day. These observations enabled Graham and colleagues, who report¹ their study of the GRB in *The Astrophysical Journal*, to firmly identify the galaxy in which the γ -ray explosion took place: it is the most distant galaxy ever detected that harbours a GRB event of the short-lived kind.

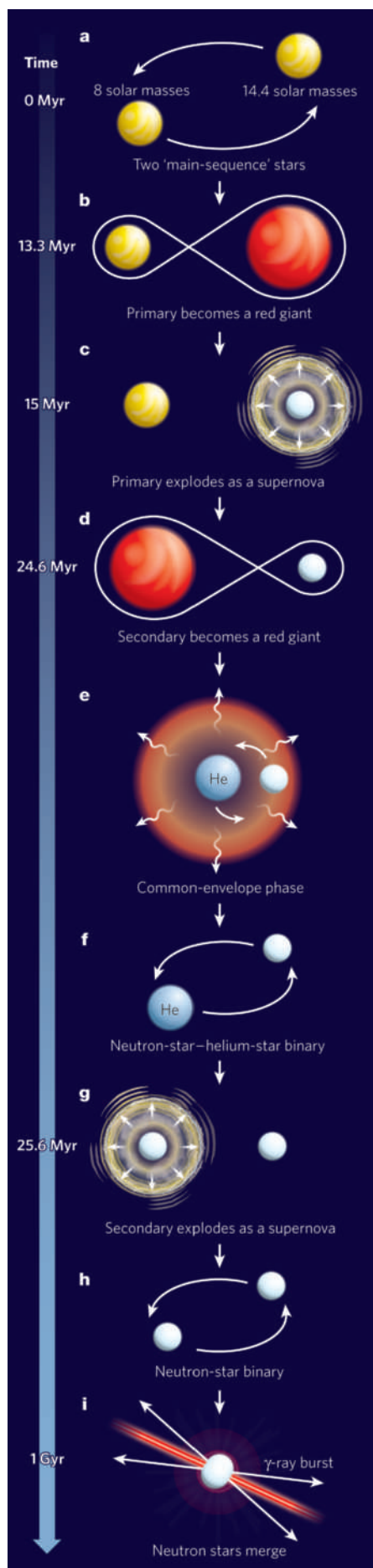
Potentially distant (high-redshift) galaxies can be distinguished from their closer (lower-redshift) counterparts through differences in their spectra. Ultraviolet light given off by hot, young stars in a far-off galaxy excites the surrounding gas clouds from which they were formed, producing strong emission lines in the galaxy’s spectrum. The expansion of the Universe then shifts these lines to longer, redder wavelengths: by the time it reaches us, the wavelength of light from an object at redshift z has been stretched by a factor of $1+z$. Has a spectral signature been unambiguously identified for the host galaxy of GRB 070714B, to claim a redshift record? Graham *et al.*¹ detected

one emission line at optical wavelengths, and, on the basis of the colours of the host galaxy, deduced that it originated from ionized oxygen. But the redshift measurement is not of a quality that can be uncritically accepted as decisive. Traditionally, detection and identification of two spectral features is preferred. That said, Graham and colleagues’ result seems quite robust.

Although each GRB is a unique event, these bursts fall roughly into one of two categories according to the duration of their emission at high energy: events lasting less than about two seconds are termed short, whereas the rest — the majority — are called long. GRB 070714B falls into the short-burst category, and being slightly more than 8 billion parsecs away, turns out to be the most distant explosion of this type found so far. Setting a new record as the farthest short GRB, together with a spectroscopic identification, might seem noteworthy enough, but it is not its distance alone that makes GRB 070714B interesting.

In astronomy, distance and time are inseparable, and because light travels at a finite speed, objects are seen as they were in the past. Distance, or equivalently, look-back time, is generally denoted by the redshift. GRB 070714B is detected at a redshift of $z = 0.923$, which means that it occurred when the Universe was about 40% of its present age, shortly after the time when most stars were being assembled in galaxies.

Swift was designed to answer the mystery of short GRBs, which, despite being known for more than 40 years, have thus far not been



linked to a specific progenitor, or associated with a particular type of galaxy that could be identified as a host. Therefore, constraining models for GRB formation through information about their environments has been challenging. By contrast, long GRBs have been rather firmly associated with the death of massive stars in relatively young galaxies^{2,3}.

The most favoured models for short-GRB formation usually involved old systems, such as highly evolved binary-star progenitors containing neutron stars and/or black holes, which would go through one final cataclysm — hundreds to thousands of millions of years after their formation — before quietly fading away⁴. And indeed, the first few short GRBs detected by Swift after its launch in 2004 seemed to be in general agreement with this picture: the host galaxies seemed to be old rather than young, devoid of much star formation, and generally in the declining phase of their cosmic evolution^{5,6}. However, even at that early stage of Swift's observations, some diversity in host-galaxy type and cosmic epoch was already apparent⁷, and because short bursts are intrinsically less luminous than their long counterparts, they may be prone to observational bias favouring detection at smaller distances, at which old systems are found.

In the years since Swift's first GRB observations, evidence has been steadily mounting for a more diverse landscape of how this class of explosion occurs⁸. Graham and colleagues' observation that GRB 070714B originated at an early epoch in the history of the Universe now strongly indicates that whereas the simple picture most often considered up to now — that short GRBs originate in old systems — may account for a fraction of the events, it surely cannot explain them all. So what does this mean in terms of our understanding of the events themselves, their progenitors, and their hosts and environments?

For one thing, it clearly tells us that we still have much to learn about stellar evolution, particularly in binary systems, where stars live out their lives in very different ways from when they are travelling alone, like the Sun. In such systems, the time delay between progenitor formation and the onset of the burst, if one occurs, is extremely sensitive to the interaction between the stars during what is termed the common-envelope phase⁹, when one star has become a bloated red giant and has essentially

engulfed its ultradense, compact companion (Fig. 1). It has been suggested that this stage in the life of a binary system can lead to both short and long time delays¹⁰, thus producing GRBs at both high and low redshift, respectively. Conversely, that the delays can be so varied as to be able to accommodate either progenitor population is indicative of how much remains to be discovered about binary stars. In this sense, identifying the progenitor of an event such as GRB 070714B would be a way of potentially probing different evolutionary pathways in the lives of stars.

Graham and colleagues' discovery also prompts us to consider other possible short-GRB formation mechanisms that may take place in both old and young galaxies. Among the possible candidates are highly magnetized neutron stars called magnetars¹¹, events involving white dwarfs, and the interaction of compact stellar remnants in very densely populated environments such as stellar clusters. Whatever the mechanism, it is clear that singular events such as GRB 070714B present an exciting opportunity to study new regimes of stellar evolution at an epoch when galaxies were assembling most of their stars.

Over the coming years, space- and ground-based observations should allow us to uncover the detailed nature of these remarkable beasts. Astronomers no longer speak of short GRBs as utter mysteries. But that does not mean the puzzle is completely solved.

Enrico Ramirez-Ruiz is in the Department of Astronomy and Astrophysics, University of California, Santa Cruz, California 95064, USA. William Lee is at the Instituto de Astronomía, Universidad Nacional Autónoma de México, Mexico DF 04510, Mexico.
e-mails: enrico@ucolick.org;
wlee@astroscu.unam.mx

- Graham, J. F. *et al. Astrophys. J.* **698**, 1620–1629 (2009).
- Woosley, S. E. & Bloom, J. S. *Annu. Rev. Astron. Astrophys.* **44**, 507–556 (2006).
- Fruchter, A. S. *et al. Nature* **441**, 463–468 (2006).
- Lee, W. H. & Ramirez-Ruiz, E. *New J. Phys.* **9**, 17 (2007).
- Bloom, J. S. *et al. Astrophys. J.* **638**, 354–368 (2006).
- Gehrels, N. *et al. Nature* **437**, 851–854 (2005).
- Prochaska, J. X. *et al. Astrophys. J.* **642**, 989–994 (2006).
- Berger, E. *et al. Astrophys. J.* **664**, 1000–1010 (2007).
- Taam, R. E. & Sandquist, E. L. *Annu. Rev. Astron. Astrophys.* **38**, 113–141 (2000).
- Belczynski, K. *et al. Astrophys. J.* **648**, 1110–1116 (2006).
- Usov, V. V. *Nature* **357**, 472–474 (1992).

Developmental and species-divergent globin switching are driven by BCL11A

Vijay G. Sankaran^{1*}, Jian Xu^{1,2*}, Tobias Ragoczy³, Gregory C. Ippolito⁴, Carl R. Walkley^{1†}, Shanna D. Maika⁴, Yuko Fujiwara^{1,2}, Masafumi Ito⁵, Mark Groudine^{3,6}, M. A. Bender^{3,7}, Philip W. Tucker⁴ & Stuart H. Orkin^{1,2}

The contribution of changes in *cis*-regulatory elements or *trans*-acting factors to interspecies differences in gene expression is not well understood. The mammalian β -globin loci have served as a model for gene regulation during development. Transgenic mice containing the human β -globin locus, consisting of the linked embryonic (ϵ), fetal (γ) and adult (β) genes, have been used as a system to investigate the temporal switch from fetal to adult haemoglobin, as occurs in humans. Here we show that the human γ -globin (*HBG*) genes in these mice behave as murine embryonic globin genes, revealing a limitation of the model and demonstrating that critical differences in the *trans*-acting milieu have arisen during mammalian evolution. We show that the expression of BCL11A, a repressor of human γ -globin expression identified by genome-wide association studies, differs between mouse and human. Developmental silencing of the mouse embryonic globin and human γ -globin genes fails to occur in mice in the absence of BCL11A. Thus, BCL11A is a critical mediator of species-divergent globin switching. By comparing the ontogeny of β -globin gene regulation in mice and humans, we have shown that alterations in the expression of a *trans*-acting factor constitute a critical driver of gene expression changes during evolution.

The extent to which changes in *cis*-regulatory elements or the *trans*-acting environment account for differences in gene expression in closely related species is the subject of debate^{1,2}. Some studies suggest that changes in *cis*-regulatory elements are largely responsible for many interspecies differences in gene expression^{3,4}. The contribution of alterations in the *trans*-acting milieu is less established. With their temporal switches of globin expression, mammalian β -globin loci serve as a model for developmental gene regulation⁵. To study the regulation of human *cis*-elements in a mouse *trans*-acting environment, we used human β -globin locus transgenic mice (β -locus mice). The regulation of the human β -globin locus has been widely studied using such mouse models^{6–8}. It is generally accepted that these mice provide a valid system for evaluating human developmental globin gene regulation, although some differences have been noted between humans and these mice. For example, the onset of γ -globin expression occurs during the embryonic, yolk sac stage of erythropoiesis in the mouse, whereas high-level expression of this gene occurs during the fetal liver stage in man. Moreover, the switch from γ -globin to adult β -globin occurs during early fetal liver erythropoiesis in these mice^{6–8}, whereas it occurs around the time of birth in humans⁹. Furthermore, differences have been noted in the capacity of the mice to respond to fetal haemoglobin (HbF)-eliciting responses that are active in humans^{10,11}. We began by evaluating whether these mice respond to stimuli that consistently increase the level of HbF in humans¹². We found that these mice have much lower basal levels of γ -globin expression than adult humans, and fail to respond to stimuli that result in increased levels of HbF in humans (Supplementary Fig. 1). Also, in a model of juvenile myelomonocytic leukaemia created in these mice, no increase in γ -globin levels was observed, in contrast to the high levels of γ -globin seen in humans with this syndrome¹³.

Human fetal globin genes behave as mouse embryonic genes

To pursue the underlying basis of these species differences, we re-assessed the ontogeny of human γ -globin expression during mouse development. First we isolated circulating blood from embryos at a time when γ -globin expression is observed (embryonic day (E)13.5)^{6–8}. Using differences in cell size that permit the separation of circulating primitive and definitive lineage cells using flow cytometry^{14,15}, we enriched the erythroid cells in blood from E13.5 β -locus mice (Fig. 1a). As anticipated, the expression of the mouse embryonic gene $\epsilon\gamma$ globin (*Hbb- γ*)—a gene confined to the primitive erythroid lineage along with mouse β h1 globin (*Hbb-bh1*)^{14,15}—was enriched (approximately fivefold) in the primitive population relative to the definitive population (Fig. 1b). Consistent with this distribution, human embryonic ϵ -globin (*HBE*, also known as *HBE1*) transcripts were similarly enriched in the primitive population (Fig. 1b). Surprisingly, no difference was observed between the relative enrichment of the embryonic genes and the degree of enrichment of human γ -globin transcripts in the primitive erythroid population compared to the definitive cells (Fig. 1b). This finding indicates that the human γ -globin genes are not robustly expressed in early definitive erythroid cells in β -locus mice.

We then used immunohistochemistry (IHC) of γ -globin in E13.5 embryos to examine its cellular distribution. IHC of human fetal liver showed positive labelling of all erythroblasts (Fig. 1c). In contrast, most of the erythroblasts present in the murine fetal liver of β -locus mice failed to stain for γ -globin. We observed occasional large nucleated, megaloblastic cells in fetal liver positive for γ -globin (Fig. 1d, e). Morphologically these cells resemble primitive cells that continue to circulate in substantial numbers during this period of gestation⁵. Consistent with this interpretation, the numerous γ -globin-positive cells seen in the circulation were all megaloblastic primitive cells,

¹Division of Hematology/Oncology, Children's Hospital Boston and Department of Pediatric Oncology, Dana-Farber Cancer Institute, Harvard Stem Cell Institute, Harvard Medical School, Boston, Massachusetts 02115, USA. ²Howard Hughes Medical Institute, Boston, Massachusetts 02115, USA. ³Fred Hutchinson Cancer Research Center, Seattle, Washington 98109, USA. ⁴Institute for Cellular and Molecular Biology, The University of Texas at Austin, Austin, Texas 78712, USA. ⁵Department of Pathology, Japanese Red Cross, Nagoya First Hospital, Nagoya, Japan. ⁶Department of Radiation Oncology, and ⁷Department of Pediatrics, University of Washington, Seattle, Washington 98195, USA. [†]Present address: St Vincent's Institute of Medical Research, Fitzroy, Victoria 3065, Australia.

*These authors contributed equally to this work.

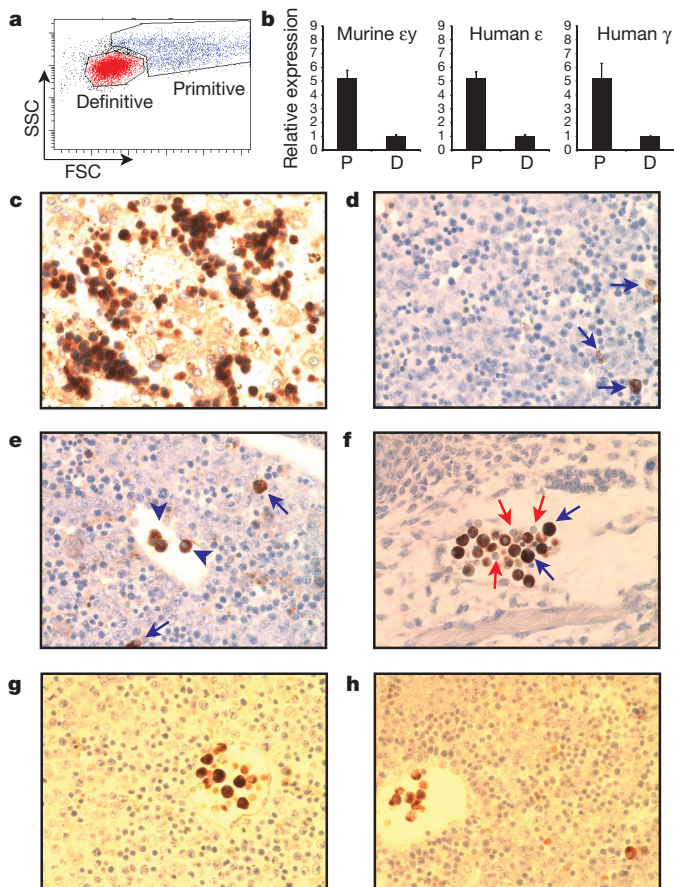


Figure 1 | Human γ -globin is primarily expressed in primitive erythroid cells of β -locus mice. **a**, Representative FACS plot showing forward light scatter (FSC; linear scale) versus side scatter (SSC; log scale) for E13.5 embryonic blood. Gating is shown to allow for the enrichment of primitive (blue population) and definitive (red population) lineages. **b**, The relative expression of the murine $\epsilon\gamma$ globin gene, human embryonic ϵ gene and human γ -globin genes showed similar relative enrichment levels in the primitive population (P) as compared with the definitive population (D). Results are shown as mean and s.d. ($n \geq 3$ per group). $P = 0.98$ for a two-sided t -test comparing the relative enrichment of $\epsilon\gamma$ with γ -globin. **c–h**, Representative IHC staining with an anti-HbF antibody from human and murine E13.5 fetal livers. All images are taken with a $\times 60$ objective. **c**, Human fetal livers contain numerous erythroblasts, which all stain positive for γ -globin expression. **d, e**, In contrast, murine fetal liver definitive erythroblasts do not show major γ -globin staining and only occasional cells with megaloblastic primitive morphology show staining (blue arrows). **e, f**, Many megaloblastic primitive cells in the circulation show highly positive staining (**e**, blue arrowheads; **f**, blue arrows), whereas smaller definitive erythrocytes are negative (**f**, red arrows). **g, h**, Staining performed on the single copy YAC lines A20 and A85 (ref. 8) showed similar staining patterns. Positive staining was determined in comparison with background staining from transgene-negative littermate controls.

whereas enucleate, smaller definitive cells were uniformly negative (Fig. 1e, f). To generalize these findings, we performed similar immunohistochemical staining in other independently derived lines of β -locus mice (Fig. 1g, h)⁸. In all lines, γ -globin expression (as indicated by positive IHC) was confined to circulating megaloblastic cells that were infrequent in fetal liver parenchyma. Because similar observations have been made in independently derived β -locus mice, our findings demonstrate a characteristic feature of β -locus mice.

Divergent behaviour of human β -globin loci in mice

To gain further insight at the single-cell level, we used primary transcript RNA fluorescence *in situ* hybridization (PT-FISH) to examine the relative expression of the endogenous mouse and human globin genes at different stages of ontogeny^{16,17}. First, we examined the relative

expression of human γ - and β -globin (with murine α -globin as a control) in E11.5 primitive erythroid cells from two independent transgenic lines (A20 and A85). Consistent with previous analyses demonstrating high-level expression of γ -globin at the primitive erythroid stage in β -locus mice, we noted relatively high expression of γ -globin by PT-FISH, with low or absent expression of human β -globin (Fig. 2a, b). Among circulating primitive cells from a later stage of development (E13.5) a similar pattern was observed, although more human β -globin expression was seen and an overall reduction in the percentage of cells with a PT-FISH signal (using the murine α -globin control) was noted, with only a fraction of the cells (\sim one-third) showing transcriptionally active loci at a single time point (Fig. 2a, b). Examples of the cells used in this analysis are shown (Fig. 2e–g). An interesting observation made with concomitant PT-FISH analysis of human γ - and β -globin is the extent of cotranscription, which represents the concomitant presence of two primary transcript signals in the same gene locus (Supplementary Fig. 2 and Supplementary Information).

Comparison of mouse embryonic $\epsilon\gamma$ globin with γ -globin showed similar expression levels of the mouse embryonic gene with the human γ -globin in circulating primitive cells from E13.5 (Fig. 2c,

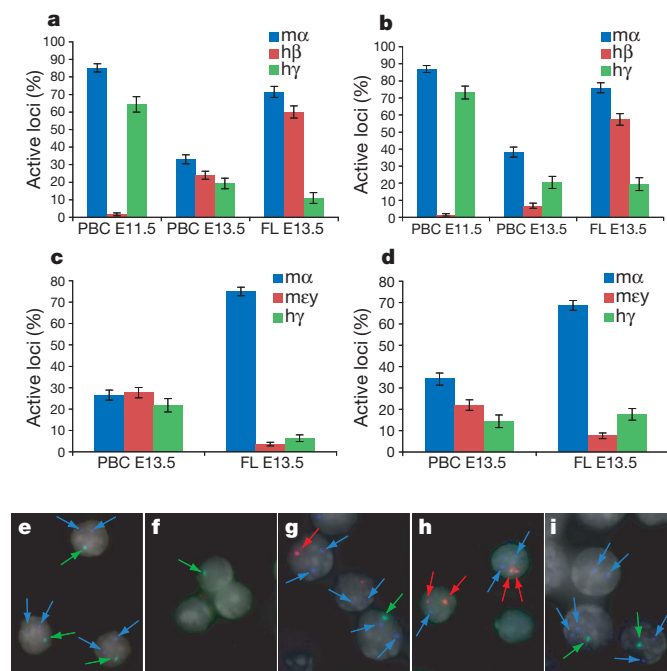


Figure 2 | PT-FISH analysis shows that γ -globin expression parallels the murine embryonic globins in primitive erythroid cells. **a–d**, Two independent lines of transgenic YAC mice, A85 (**a, c**) and A20 (**b, d**), were analysed using four-colour PT-FISH. For the first set of experiments, probes were made to target murine α -globin ($m\alpha$), human β -globin ($h\beta$) and human γ -globin ($h\gamma$). Additionally, 4,6-diamidino-2-phenylindole (DAPI) was used to identify nuclei of cells. Error bars denote the s.d. **a, b**, The expression of γ -globin predominates within the two lines in the primitive populations seen circulating in primitive blood cells (PBC) from embryos E11.5 and E13.5. Minor expression is seen in the mature definitive populations from fetal liver (FL) at E13.5. Many of these cells may represent primitive cells found in the fetal liver parenchyma. **c, d**, Probes were made to target murine α -globin ($m\alpha$), murine $\epsilon\gamma$ globin ($m\epsilon\gamma$) and human γ -globin ($h\gamma$). These data show parallel expression of $m\epsilon\gamma$ and $h\gamma$. **e–g**, Representative images with the staining pattern of **a** and **b** at each developmental time point are shown for PBC at E11.5 (**e**), at E13.5 (**f**), and fetal liver at E13.5 (**g**). **h, i**, Representative images with the staining pattern of **c** and **d** are shown for PBC at E13.5 (**h**) and fetal liver at E13.5 (**i**). The colour of the bars in all graphs (and arrows in images) corresponds to the colours of the probes that were detected for each of these primary transcripts. The graphs depict the percentage of active loci and are measured for ≥ 100 nuclei per probe set at each time point. Original magnification, $\times 100$.

d, h, i). This finding indicates that the expression of the human γ -globin genes parallels that of the mouse embryonic β -like genes in the mouse *trans*-acting environment. Fetal liver cells from E13.5 were analysed in a similar manner, by examining the expression of mouse $\epsilon\gamma$ and human γ -globin by PT-FISH in these cells. Only a low percentage of cells showed staining for either $\epsilon\gamma$ or γ -globin (Fig. 2c, d), compared with robust transcription of human β -globin at the same stage (Fig. 2a, b). Consistent with previous developmental analyses in mice^{14,17}, cells positive for mouse $\epsilon\gamma$ represent circulating primitive cells present in the mouse fetal liver. The cells that are positive for human γ -globin expression are also likely to be primitive erythroid cells, and it is important to recognize that in these cells only a fraction (\sim one-third) of loci are active at any single time point, thereby limiting the degree of concomitant expression seen. Of note, 45% and 54% (in the A85 and A20 lines, respectively) of the primitive cells from E13.5 with γ -globin transcript showed expression of $\epsilon\gamma$ globin, supporting the notion that γ -globin is treated as an embryonic gene in the mouse *trans*-acting environment. Interestingly, an early analysis of very low expressing transgenes lacking critical locus region regulatory sequences had suggested that γ -globin indeed behaved as an embryonic gene, as we have shown for mice containing the entire robustly expressed human β -locus¹⁸.

BCL11A restricts mouse embryonic β -like globin expression

From these results we conclude that the homologous mouse erythroid *trans*-acting environment differs from that of the human, presumably with respect to the composition or regulation of critical transcriptional regulators. We have recently shown that the gene *BCL11A*, which contains genetic variants that affect HbF levels in humans^{19–22}, encodes a developmental-stage-specific repressor of the human γ -globin genes²³. Our previous findings were confined to an analysis of human erythroid cells, in which we found that full-length forms of *BCL11A* were expressed robustly in adult bone marrow erythroblasts, at substantially lower levels in fetal liver, and were absent in primitive erythroblasts. Moreover, shorter variant forms of *BCL11A* are expressed in human primitive and fetal liver erythroblasts, both of which express γ -globin. To investigate potential species differences in *BCL11A* protein expression, we examined stage-matched populations of mouse and human erythroid cells that were subjected to fluorescence-activated cell sorting (FACS). Remarkably, comparison of *BCL11A* expression in mouse and human samples shows notable differences (Fig. 3a and Supplementary Fig. 3). First, *BCL11A* protein and RNA transcripts are absent in primitive erythroid cells of mice. Second, full-length *BCL11A* forms are expressed at similar levels in definitive erythroid cells of both mouse fetal liver and bone marrow, whereas no shorter variant forms could be identified in mice (Fig. 3a). These results highlight important interspecies differences that could potentially have a role in mediating divergent globin gene regulation. A model on the basis of our findings of the developmental expression of the β -like globin genes in humans, mice and β -locus mice is shown, along with a summary of *BCL11A* expression in these two species (Fig. 3b).

We have demonstrated that the expression of the human γ -globin genes strictly parallels that of the mouse embryonic genes, $\epsilon\gamma$ and β h1, in the context of the mouse *trans*-acting environment. Moreover, the pattern of *BCL11A* expression suggests a role throughout definitive erythropoiesis in mice, as opposed to its predominant role after birth in humans. Thus, we propose that changes in *BCL11A* expression may be responsible, at least in part, for the observed interspecies divergent expression of β -like globin genes. To test directly a potential role for *BCL11A* in silencing the endogenous embryonic genes in the definitive erythroid lineage, we examined *BCL11A* knockout mice. As described previously²⁴, *Bcl11a*^{−/−} mice die in the perinatal period from unknown causes. We examined *Bcl11a*^{−/−} mice at E14.5 and E18.5 during gestation when robust definitive erythropoiesis is taking place in the fetal liver (Supplementary Fig. 4). By phenotypic and morphological approaches^{25,26}, erythropoiesis appeared ostensibly

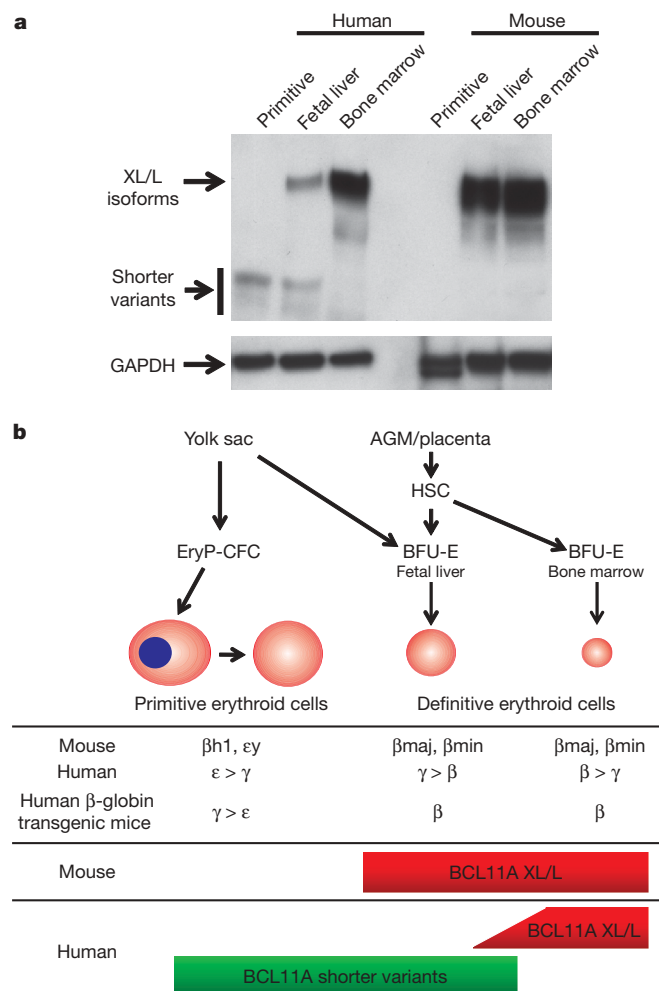


Figure 3 | BCL11A expression varies between humans and mice, suggesting a model for *trans*-acting variation in β -globin gene expression. **a**, In human cells full-length proteins of *BCL11A* (XL/L, full-length isoforms²³) are reduced in cell populations that express high levels of γ -globin, including primitive and fetal liver cells²³. Furthermore, short variant forms are present at these earlier developmental stages. All human cells were sorted for CD235 and CD71 expression. In contrast, in murine cells, full-length *BCL11A* protein expression is evident in all definitive progenitor populations, including sorted stage-matched E13.5 fetal liver and bone marrow erythroid cells (all populations were sorted for TER119⁺ (also known as LY76) and CD71⁺ (also known as TFRC)). No expression of *BCL11A* in murine primitive cell populations was detected. **b**, This model summarizes the ontogeny of β -like globin gene regulation in humans, mice and β -locus mice^{5,9}. The ontogeny of mammalian erythropoiesis and progenitor populations is shown at the top. Progenitor populations, including primitive erythroid populations (EryP-CFC), definitive haematopoietic stem cells (HSC), and definitive erythroid burst-forming unit cells (BFU-E) are depicted. The aorto-gonado-mesonephros (AGM) and the placenta are sites of definitive haematopoiesis. The patterns of β -like globin and *BCL11A* expression seen in the two species are shown below.

normal in these embryos (Fig. 4a and Supplementary Figs 5–7). We then assessed expression of the mouse globin genes. In strong support of our hypothesis, we observed that silencing of the expression of mouse embryonic globin genes fails to occur in E14.5 and E18.5 fetal liver erythroid cells (Fig. 4b–e and Supplementary Fig. 8). Restriction of embryonic globin expression to the primitive lineage is lost. Expression of the $\epsilon\gamma$ and β h1 globin genes was upregulated by 70- and 350-fold, respectively, at E14.5 (Fig. 4b). Together, these embryonic globin genes account for 50% of the total β -like globin genes at this stage, compared with 0.4% in the controls. At E18.5, whereas the contribution of their transcripts to total β -like globin transcripts was reduced, $\epsilon\gamma$ and β h1 globin transcripts were increased

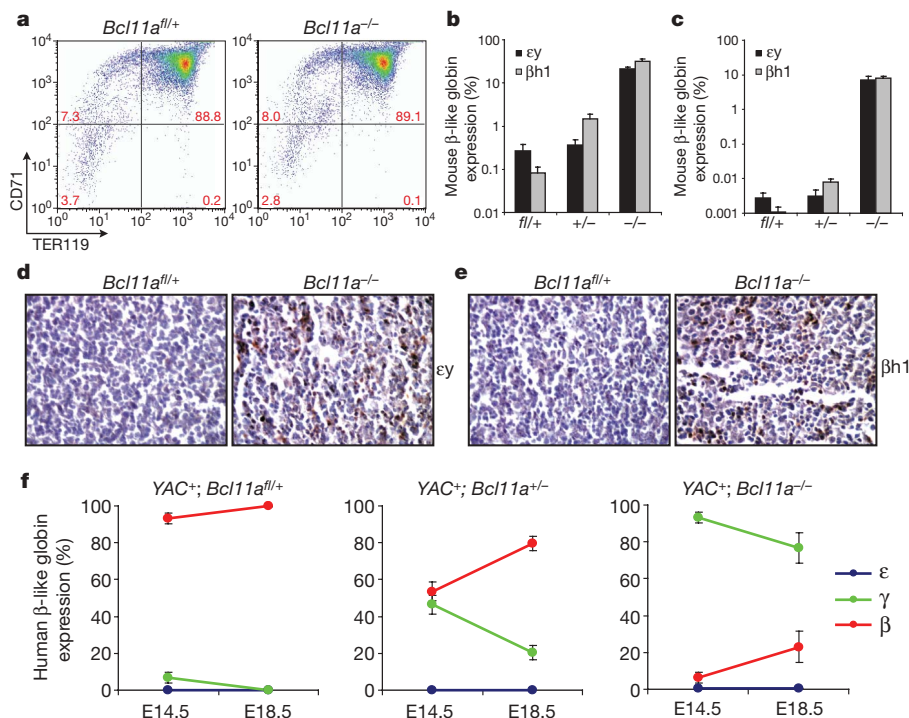


Figure 4 | *Bcl11a*^{-/-} mice fail to silence the expression of mouse embryonic β -like globins and human γ -globin genes. **a**, The CD71 and TER119 expression pattern is shown for fetal liver cells from E14.5 embryos, revealing grossly normal erythropoiesis with these phenotypic markers. The mean percentages for the populations in each quadrant are shown in red ($n = 6$ for *Bcl11a*^{fl/+} controls, $n = 4$ for *Bcl11a*^{-/-} mutants). $P > 0.1$, using a two-sided t -test for all gated populations analysed. **b**, The expression of the embryonic globins is shown as a percentage of total mouse β -like globins for control mice (*fl/+*), *Bcl11a* heterozygous (*+/-*), and null mice (*-/-*) at E14.5 ($n = 10, 14$ and 11 , respectively). **c**, The expression of the embryonic globins is shown as a percentage of the total mouse β -like globins at E18.5 ($n = 9, 9$ and 7 , respectively). **d**, IHC was performed on E14.5 fetal livers

2,600- and 7,600-fold compared to controls (Fig. 4c). To determine the cellular distribution of the mouse embryonic globins, we performed IHC. Using this approach we found that ϵ and β h1 globins were robustly expressed in definitive erythroid cells (Fig. 4d, e and Supplementary Fig. 9), whereas normally these embryonic globins are confined to the primitive erythroid lineage⁵ (Fig. 3b).

Silencing of human γ -globin expression depends on BCL11A

We then examined the consequence of BCL11A loss on the regulation of human globin genes in the β -locus mice. By introducing the β -locus transgene into the knockout environment, we found that in the absence of BCL11A, developmental silencing of the γ -globin genes is markedly impaired in the definitive erythroid lineage (Fig. 4f and Supplementary Fig. 10). In *Bcl11a*^{-/-}, *Bcl11a*^{+/-} and littermate control mice, γ -globin RNA comprised 76%, 20% and 0.24% of total β -like globin gene RNA at E18.5, respectively (Fig. 4f and Supplementary Fig. 10). Relaxation of γ -globin gene silencing in *Bcl11a*^{+/-} heterozygotes is consistent with the genetic association of BCL11A and HbF levels, and extends our previous observations using knockdown approaches in human cells²³ that together point to BCL11A as a quantitative regulator of γ -globin expression. The failure of γ -globin gene silencing in the face of otherwise ostensibly normal erythropoiesis provides compelling evidence that BCL11A is an important regulator of the globin switches in mouse and human ontogeny.

Concluding remarks

Taken together, our findings demonstrate how changes in the expression of a single *trans*-acting factor over the course of evolution may lead to altered developmental gene expression. We have shown that

from *Bcl11a*^{fl/+} and *Bcl11a*^{-/-} animals for the embryonic globin ϵ . Representative sections at $\times 40$ magnification with a $\times 10$ objective lens are shown. **e**, Similar IHC staining was performed for β h1 globin. In both cases robust expression is seen in the scattered erythroblasts of the fetal liver in *Bcl11a*^{-/-} but not control mice. **f**, Expression of human β -globin locus genes is shown for animals with the various *Bcl11a* genotypes in the presence of the β -locus YAC transgene (YAC⁺) at E14.5 ($n = 4, 6$ and 4 for the *Bcl11a*^{fl/+}, *Bcl11a*^{+/-} and *Bcl11a*^{-/-} animals, respectively) and E18.5 ($n = 4, 7$ and 4). All γ - and β -globin levels for the different genotypes are significantly different ($P < 1 \times 10^{-5}$, two-sided t -test). All data are plotted as the mean \pm s.d. of the measurement.

cis-elements in the human β -globin locus are insufficient to recapitulate proper developmental regulation in a mouse context. Previously it has been postulated that the evolution of β -like globin gene expression is largely mediated through changes in *cis*-elements²⁷. Our findings argue persuasively that changes in *trans*-acting factors may exert notable effects on gene switching during development. BCL11A acts to silence the embryonic genes in mouse definitive erythroid cells, in contrast to its role in humans where it acts to silence γ -globin expression after birth. Moreover, we show that BCL11A is a powerful regulator of the species-divergent globin switches by demonstrating that the γ -globin gene escapes proper developmental silencing in a mouse *trans*-acting *Bcl11a*^{-/-} environment. Our findings suggest a model in which one (or more) *trans*-acting silencers of the embryonic globin genes, initially expressed throughout definitive erythropoiesis, have been altered during primate evolution, such that their expression is shifted to a later phase of definitive erythropoiesis, allowing for the evolution of a unique fetal haemoglobin expression stage. We have shown here that BCL11A represents one of the major factors regulating this switch. These findings allow for simplification of molecular models accounting for this critical developmental transition. This work provides not only unique insights into how alterations in gene expression occur in the course of evolution, but also reveals further mechanistic clues to the clinically important fetal-to-adult haemoglobin switch in humans.

METHODS SUMMARY

All experiments performed with the β -locus, K-RasG12D, *Bcl11a*^{-/-}, Gata1-Cre, and Mx1-Cre mice were approved by the Children's Hospital Boston Animal Ethics Committee and the Ethics Committee of the Fred Hutchinson Cancer

Research Center. The analysis of adult and developmental haematopoiesis/erythropoiesis was performed using FACS-based phenotypic and morphological approaches as described^{125,26}. Quantitative PCR and western blotting were carried out as described^{23,25}. RNA primary transcript fluorescence *in situ* hybridization was performed with some modification of published protocols^{16,17}.

Full Methods and any associated references are available in the online version of the paper at www.nature.com/nature.

Received 5 April; accepted 30 June 2009.

Published online 5 August 2009.

- Carroll, S. B. Evo-devo and an expanding evolutionary synthesis: a genetic theory of morphological evolution. *Cell* **134**, 25–36 (2008).
- Hoekstra, H. E. & Coyne, J. A. The locus of evolution: evo devo and the genetics of adaptation. *Evolution* **61**, 995–1016 (2007).
- Wallace, H. A. *et al.* Manipulating the mouse genome to engineer precise functional syntenic replacements with human sequence. *Cell* **128**, 197–209 (2007).
- Wilson, M. D. *et al.* Species-specific transcription in mice carrying human chromosome 21. *Science* **322**, 434–438 (2008).
- McGrath, K. & Palis, J. Ontogeny of erythropoiesis in the mammalian embryo. *Curr. Top. Dev. Biol.* **82**, 1–22 (2008).
- Wijgerde, M., Grosveld, F. & Fraser, P. Transcription complex stability and chromatin dynamics *in vivo*. *Nature* **377**, 209–213 (1995).
- Peterson, K. R., Navas, P. A., Li, Q. & Stamatoyannopoulos, G. LCR-dependent gene expression in β -globin YAC transgenics: detailed structural studies validate functional analysis even in the presence of fragmented YACs. *Hum. Mol. Genet.* **7**, 2079–2088 (1998).
- Porcu, S. *et al.* The human β globin locus introduced by YAC transfer exhibits a specific and reproducible pattern of developmental regulation in transgenic mice. *Blood* **90**, 4602–4609 (1997).
- Peschle, C. *et al.* Haemoglobin switching in human embryos: asynchrony of $\zeta \rightarrow \alpha$ and $\epsilon \rightarrow \gamma$ -globin switches in primitive and definite erythropoietic lineage. *Nature* **313**, 235–238 (1985).
- Sloane-Stanley, J., Roberts, N. A., Olivieri, N., Weatherall, D. J. & Wood, W. G. Globin gene expression in Hb Lepore-BAC transgenic mice. *Br. J. Haematol.* **135**, 735–737 (2006).
- Pace, B., Li, Q., Peterson, K. & Stamatoyannopoulos, G. α -Amino butyric acid cannot reactivate the silenced γ gene of the β locus YAC transgenic mouse. *Blood* **84**, 4344–4353 (1994).
- Papayannopoulou, T., Torrealba de Ron, A., Veith, R., Knitter, G. & Stamatoyannopoulos, G. Arabinosylcytosine induces fetal hemoglobin in baboons by perturbing erythroid cell differentiation kinetics. *Science* **224**, 617–619 (1984).
- Weatherall, D. J. *et al.* Foetal erythropoiesis in human leukaemia. *Nature* **257**, 710–712 (1975).
- Kingsley, P. D. *et al.* “Maturation” globin switching in primary primitive erythroid cells. *Blood* **107**, 1665–1672 (2006).
- Fraser, S. T., Isern, J. & Baron, M. H. Maturation and enucleation of primitive erythroblasts during mouse embryogenesis is accompanied by changes in cell-surface antigen expression. *Blood* **109**, 343–352 (2007).
- Ragoczy, T., Bender, M. A., Telling, A., Byron, R. & Groudine, M. The locus control region is required for association of the murine β -globin locus with engaged transcription factories during erythroid maturation. *Genes Dev.* **20**, 1447–1457 (2006).
- Trimborn, T., Gribnau, J., Grosveld, F. & Fraser, P. Mechanisms of developmental control of transcription in the murine α - and β -globin loci. *Genes Dev.* **13**, 112–124 (1999).
- Chada, K., Magram, J. & Costantini, F. An embryonic pattern of expression of a human fetal globin gene in transgenic mice. *Nature* **319**, 685–689 (1986).
- Uda, M. *et al.* Genome-wide association study shows *BCL11A* associated with persistent fetal hemoglobin and amelioration of the phenotype of β -thalassaemia. *Proc. Natl Acad. Sci. USA* **105**, 1620–1625 (2008).
- Lettre, G. *et al.* DNA polymorphisms at the *BCL11A*, *HBS1L-MYB*, and β -globin loci associate with fetal hemoglobin levels and pain crises in sickle cell disease. *Proc. Natl Acad. Sci. USA* **105**, 11869–11874 (2008).
- Menzel, S. *et al.* A QTL influencing F cell production maps to a gene encoding a zinc-finger protein on chromosome 2p15. *Nature Genet.* **39**, 1197–1199 (2007).
- Sedgewick, A. E. *et al.* *BCL11A* is a major HbF quantitative trait locus in three different populations with β -hemoglobinopathies. *Blood Cells Mol. Dis.* **41**, 255–258 (2008).
- Sankaran, V. G. *et al.* Human fetal hemoglobin expression is regulated by the developmental stage-specific repressor *BCL11A*. *Science* **322**, 1839–1842 (2008).
- Liu, P. *et al.* *Bcl11a* is essential for normal lymphoid development. *Nature Immunol.* **4**, 525–532 (2003).
- Sankaran, V. G., Orkin, S. H. & Walkley, C. R. *Rb* intrinsically promotes erythropoiesis by coupling cell cycle exit with mitochondrial biogenesis. *Genes Dev.* **22**, 463–475 (2008).
- Zhang, J., Socolovsky, M., Gross, A. W. & Lodish, H. F. Role of Ras signaling in erythroid differentiation of mouse fetal liver cells: functional analysis by a flow cytometry-based novel culture system. *Blood* **102**, 3938–3946 (2003).
- Johnson, R. M. *et al.* Phylogenetic comparisons suggest that distance from the locus control region guides developmental expression of primate β -type globin genes. *Proc. Natl Acad. Sci. USA* **103**, 3186–3191 (2006).

Supplementary Information is linked to the online version of the paper at www.nature.com/nature.

Acknowledgements We are grateful to K. Peterson and H. Fedosyuk for providing β -locus mice, K. Gaensler for the A20 and A85 strains of β -locus mice, and T. Jacks for providing the K-RasG12D mice. We thank J. Palis and P. Kingsley for providing mouse embryonic globin antibodies, H. Mikkola and B. Van Handel for providing sorted human samples, and R. Byron and A. Telling for technical support. We thank L. Zon, K. McGrath, P. Kingsley, J. Palis, M. Kowalczyk and T. Menne for advice and discussions. This work was supported by funding from the National Institute of Diabetes and Digestive and Kidney Diseases (NIDDK) and the National Heart, Lung, and Blood Institute (NHLBI) of the National Institutes of Health (NIH) (S.H.O. and M.G.) and the National Cancer Institute (P.W.T.). S.H.O. is an Investigator of the Howard Hughes Medical Institute (HHMI). C.R.W. is a special fellow of the Leukemia & Lymphoma Society. T.R. is supported by a fellowship from the American Society of Hematology. J.X. is an HHMI fellow of the Helen Hay Whitney Foundation. V.G.S. is supported by a Medical Scientist Training Program Award from the NIH and G.C.I. is supported by a NCI postdoctoral fellowship.

Author Contributions V.G.S., J.X. and S.H.O. conceived the study design. V.G.S., J.X., T.R., C.R.W., Y.F., M.I. and M.A.B. performed the experiments. V.G.S., J.X., T.R., C.R.W., M.G., M.A.B. and S.H.O. analysed data. G.C.I., S.D.M. and P.W.T. developed and contributed a new mouse line. V.G.S., J.X. and S.H.O. wrote the paper. All authors read, helped revise, and approved the manuscript.

Author Information Reprints and permissions information is available at www.nature.com/reprints. The authors declare competing financial interests: details accompany the full-text HTML version of the paper at www.nature.com/nature. Correspondence and requests for materials should be addressed to S.H.O. (stuart_orkin@dfci.harvard.edu).

METHODS

Experimental animals. The wild-type β -globin locus YAC transgenic (β -YAC) mouse strains that were used in this study show a similar pattern of human globin gene expression and are representative of the various strains of transgenic mice harbouring the entire human β -globin locus^{7,8,28–31}. One transgenic mouse line was provided by K. Peterson and was created with the insertion of a 213 kilobase (kb) YAC containing the entire intact human β -globin locus and has been described and characterized previously^{7,28,29}. This β -YAC line contains three intact copies of the human β -globin locus integrated at a single genomic locus. Two β -YAC lines (A20 and A85) containing a single copy of a \sim 150-kb β -globin locus YAC were also used in this study and have been described previously⁸ (provided by K. Gaensler). These transgenes were maintained in the hemizygous state. The animals were maintained on a pure C57Bl/6 background for all experiments involving adult haematopoietic analysis. A juvenile myelomonocytic leukaemia-type myeloproliferative disorder was induced by crossing the Mx1-Cre line with the K-RasG12D conditional allele^{32,33}, along with the β -YAC transgene from K. Peterson. Congenic B6.SJL-PtprcaPep3b/BoyJ (Ptprca or CD45.1) mice were purchased from Taconic Farms or The Jackson Laboratory. Mice containing a *Bcl11a* floxed allele (with *loxP* sites flanking exon 1) were created by gene targeting approaches and will be described in future work (G.C.I., S.D.M. and P.W.T., unpublished observations). To obtain the *Bcl11a*-null allele, these mice were crossed with GATA1-Cre mice and screened for germline deletions^{34,35}. All experiments were performed with the approval of the Children's Hospital Boston Animal Ethics Committee and the Ethics Committee of the Fred Hutchinson Cancer Research Center.

Adult haematopoietic analysis. Analyses of adult haematology, bone marrow transplants and 5-fluorouracil induction were performed as described previously^{25,36}. Whole blood was analysed on a Beckman Coulter Act¹⁰ haematological analyser. Recipient (CD45.1) mice were irradiated with a total of 10.5 Gy γ -radiation (5 Gy and 5.5 Gy, 3 h apart) on the day of transplantation. Whole bone marrow was isolated and pooled from β -YAC mice. A total of 2×10^6 cells per mouse were retro-orbitally injected into recipients. RNA was obtained from blood using the QiaAmp Blood Mini Kit (Qiagen), and quantitative reverse transcriptase PCR (qRT-PCR) was performed as described^{23,25} using the human globin gene primers listed or previously reported murine primers¹⁴. The human globin gene primers were: ϵ -globin exon 1 forward, 5'-GAGAGGCAGCAGCA CATATC-3'; ϵ -globin exon 2 reverse, 5'-CAGGGGTAAACAACGAGGAG-3'; γ -globin exon 2 forward, 5'-TGGATGATCTCAAGGCAC-3'; γ -globin exon 3 reverse, 5'-TCAGTGGTATCTGGAGGACA-3'; β -globin exon 1 forward, 5'-CT GAGGAGAAGTCTGCCGTTA-3'; and β -globin exon 2 reverse, 5'-AGCAT CAGGAGTGGACAGAT-3'. The mouse globin gene primers were: $\epsilon\gamma$ globin exon 1 forward, 5'-TGGCCTGTGGAGTAAGGTCAA-3'; $\epsilon\gamma$ globin exon 2 reverse, 5'-GAAGCAGAGGACAAGTTCCCA-3'; β h1 globin exon 2 forward, 5'-TGGACAACCTCAAGGAGACC-3'; β h1 globin exon 3 reverse, 5'-ACCTCT GGGGTGAATTCCTT-3'; β major/ β minor globins exon 2 forward, 5'-TTTA ACGATGGCCTGAATCACTT-3'; and β major/ β minor globins exon 3 reverse, 5'-CAGCACAATCACGATCATATTGC-3'. The mouse *Bcl11a* qRT-PCR primers were forward, 5'-AACCCAGCACTTAAGCAAA-3'; and reverse, 5'-ACAGGTGAGAAGGTCGTGGT-3'.

Developmental haematopoietic analysis. Embryos were obtained from timed matings, bled and TER119-positive cells were sorted on the basis of forward and side scatter, similar to what has been previously described¹⁴. Cells were maintained in PBS with 5% FCS. Unfractionated heparin in PBS was added to this solution to a final concentration of $12.5 \mu\text{g ml}^{-1}$. IHC using an anti-HbF polyclonal antibody was performed on fixed paraffin-embedded sections as described³⁷. The fetal livers of E13.5 murine embryos were dissected and a single-cell suspension was created. Similarly, bone marrow cells were collected as has been described previously from mice²⁵. In both cases, the cells were labelled with TER119 and CD71, as well as with 7-AAD. The TER119⁺/CD71⁺ populations were sorted as described previously²⁵. Stage-matched human samples were obtained and sorted as previously

described²³. These human samples were provided by H. Mikkola and B. Van Handel.

Western blot analysis of BCL11A. Expression of BCL11A was performed using antibody 14B5 (Abcam), as described previously²³. Expression of GAPDH was assessed as a standard using rabbit polyclonal antibody FL-335 (Santa Cruz Biotechnology).

RNA primary transcript FISH. PT-FISH was largely performed as previously described^{6,16} with some modifications. Before hybridization, the slides were equilibrated in 50% formamide, $2\times$ SSC, pH 7.0. Single-stranded DNA probes against the introns of the murine α - and $\epsilon\gamma$ - and human γ - and β -globin genes were generated by *in vitro* transcription of cloned intron fragments, followed by reverse transcription and inclusion of DIG-11-dUTP, biotin-16-dUTP (Roche) or DNP-11-dUTP (Perkin Elmer) in the reactions as described³⁸. Labelled probes were hybridized to the cells in 50% formamide, 10% dextran sulphate, $2\times$ SSC, 5 mM ribonucleotide vanadate complex, 0.05% BSA, 0.1 mg ml⁻¹ Cot-1 DNA, $1 \mu\text{g ml}^{-1}$ *Escherichia coli* tRNA. The probes were heat denatured at 80 °C for 5 min, pre-annealed at 37 °C, and then hybridized overnight at 37 °C in a humid chamber. Slides were washed in 50% formamide, $2\times$ SSC, pH 7 at 37 °C, rinsed in $2\times$ SSC and blocked in 145 mM NaCl, 0.1 M Tris, pH 7.5, 2% BSA, 2 mM ribonucleotide vanadate complex. Primary transcript foci were detected by indirect immunofluorescence with Cy3-, Alexa Fluor 488- and 647-conjugated antibodies including one or two layers of signal amplification, as described¹⁷.

FISH image acquisition and analysis. Image stacks (Z sections spaced 0.25 μm apart) were captured on an Olympus IX71 microscope (Olympus objective $\times 100/1.40$, UPLS Apo) equipped with a cooled CCD camera using Deltavision SoftWorx software (Applied Precision). The presence of the globin gene primary transcripts was determined in two-dimensional projections of the Z stacks using Photoshop (Adobe). Between 100–200 nuclei were analysed for each probe set and maturation stage.

28. Peterson, K. R. *et al.* Transgenic mice containing a 248-kb yeast artificial chromosome carrying the human β -globin locus display proper developmental control of human globin genes. *Proc. Natl Acad. Sci. USA* **90**, 7593–7597 (1993).
29. Harju, S., Navas, P. A., Stamatoyannopoulos, G. & Peterson, K. R. Genome architecture of the human β -globin locus affects developmental regulation of gene expression. *Mol. Cell. Biol.* **25**, 8765–8778 (2005).
30. Gaensler, K. M., Kitamura, M. & Kan, Y. W. Germ-line transmission and developmental regulation of a 150-kb yeast artificial chromosome containing the human β -globin locus in transgenic mice. *Proc. Natl Acad. Sci. USA* **90**, 11381–11385 (1993).
31. Strouboulis, J., Dillon, N. & Grosfeld, F. Developmental regulation of a complete 70-kb human β -globin locus in transgenic mice. *Genes Dev.* **6**, 1857–1864 (1992).
32. Chan, I. T. *et al.* Conditional expression of oncogenic *K-ras* from its endogenous promoter induces a myeloproliferative disease. *J. Clin. Invest.* **113**, 528–538 (2004).
33. Braun, B. S. *et al.* Somatic activation of oncogenic *Kras* in hematopoietic cells initiates a rapidly fatal myeloproliferative disorder. *Proc. Natl Acad. Sci. USA* **101**, 597–602 (2004).
34. Garrick, D. *et al.* Loss of *Atrx* affects trophoblast development and the pattern of X-inactivation in extraembryonic tissues. *PLoS Genet.* **2**, e58 (2006).
35. Jasinski, M., Keller, P., Fujiwara, Y., Orkin, S. H. & Bessler, M. GATA1-Cre mediates *Piga* gene inactivation in the erythroid/megakaryocytic lineage and leads to circulating red cells with a partial deficiency in glycosyl phosphatidylinositol-linked proteins (paroxysmal nocturnal hemoglobinuria type II cells). *Blood* **98**, 2248–2255 (2001).
36. Walkley, C. R., Fero, M. L., Chien, W. M., Purton, L. E. & McArthur, G. A. Negative cell-cycle regulators cooperatively control self-renewal and differentiation of haematopoietic stem cells. *Nature Cell Biol.* **7**, 172–178 (2005).
37. Choi, J. W., Kim, Y., Fujino, M. & Ito, M. A new anti-hemoglobin F antibody against synthetic peptides for the detection of F-cell precursors (F-blasts) in bone marrow. *Int. J. Hematol.* **74**, 277–280 (2001).
38. Bolland, D. J. *et al.* Antisense intergenic transcription in V(D)J recombination. *Nature Immunol.* **5**, 630–637 (2004).

LETTERS

An orbital period of 0.94 days for the hot-Jupiter planet WASP-18b

Coel Hellier¹, D. R. Anderson¹, A. Collier Cameron², M. Gillon^{3,4}, L. Hebb², P. F. L. Maxted¹, D. Queloz³, B. Smalley¹, A. H. M. J. Triaud³, R. G. West⁵, D. M. Wilson¹, S. J. Bentley¹, B. Enoch², K. Horne², J. Irwin⁶, T. A. Lister⁷, M. Mayor³, N. Parley², F. Pepe³, D. L. Pollacco⁸, D. Segransan³, S. Udry³ & P. J. Wheatley⁹

The 'hot Jupiters' that abound in lists of known extrasolar planets are thought to have formed far from their host stars, but migrate inwards through interactions with the proto-planetary disk from which they were born^{1,2}, or by an alternative mechanism such as planet–planet scattering³. The hot Jupiters closest to their parent stars, at orbital distances of only ~ 0.02 astronomical units, have strong tidal interactions^{4,5}, and systems such as OGLE-TR-56 have been suggested as tests of tidal dissipation theory^{6,7}. Here we report the discovery of planet WASP-18b with an orbital period of 0.94 days and a mass of ten Jupiter masses ($10 M_{\text{Jup}}$), resulting in a tidal interaction an order of magnitude stronger than that of planet OGLE-TR-56b. Under the assumption that the tidal-dissipation parameter Q of the host star is of the order of 10^6 , as measured for Solar System bodies and binary stars and as often applied to extrasolar planets, WASP-18b will be spiralling inwards on a timescale less than a thousandth that of the lifetime of its host star. Therefore either WASP-18 is in a rare, exceptionally short-lived state, or the tidal dissipation in this system (and possibly other hot-Jupiter systems) must be much weaker than in the Solar System.

Through monitoring by the WASP-South transit survey⁸, coupled with radial-velocity observations from the Coralie spectrograph, we have discovered a $10 M_{\text{Jup}}$ planet transiting the star WASP-18 (= HD 10069) every 0.94 days (Fig. 1). WASP-18b is the first confirmed hot-Jupiter planet that has a period of less than one day (candidates with periods of less than a day have previously been announced based on photometry alone⁹, though experience shows that less than 10% of such candidates are actual planets¹⁰).

From comparison of the host star to stellar evolutionary tracks^{11,12} (see the Supplementary Information) we find a stellar mass of 1.24 ± 0.04 solar masses, M_{\odot} , and an age of 630^{+950}_{-530} Myr, which is short compared to the approximately 5-Gyr main-sequence lifetime of a star of this mass. A further age constraint is that the observed lithium abundance of WASP-18 is below that typical of F6 stars in the Pleiades (age 120 Myr) but comparable to that in the Hyades¹³ (age 600 Myr). Thus we conclude that WASP-18 has an age of 0.5–1.5 Gyr, making it one of the youngest known planet-hosting stars.

The theory of tidal interaction for hot Jupiters in close orbits^{4,5,14} predicts that the tidal bulge on the star, raised by the planet, exerts a torque that drains angular momentum from the planet's orbit, causing it to spiral inwards (this arises when the planetary orbit is shorter than the stellar rotation, and contrasts with the Earth–Moon system where the longer orbit of the Moon compared to Earth's spin causes it to move away over time). The spiral infall timescale is determined by

the mass and orbital distance of the planet, and by the tidal dissipation parameter of the host star, Q . This quality factor is the ratio of the

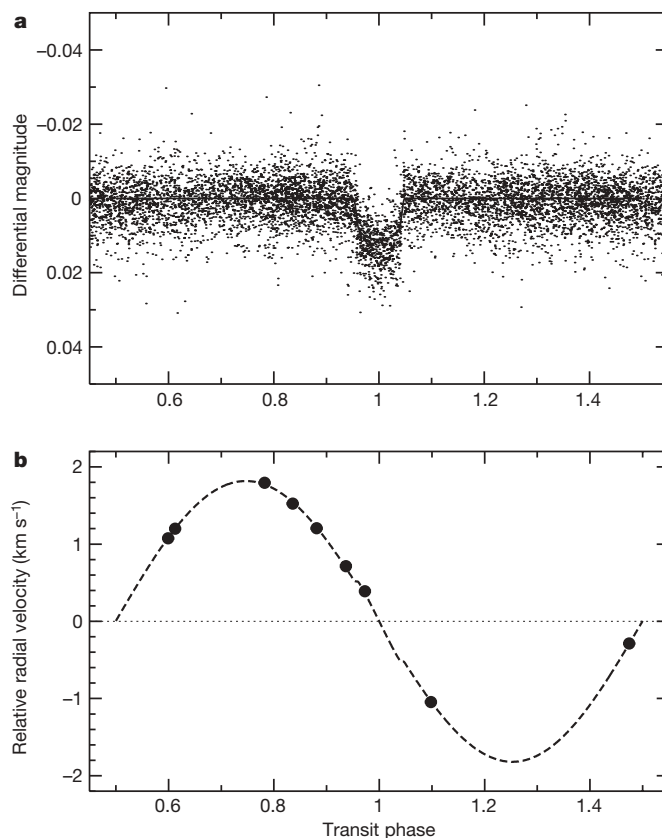


Figure 1 | Discovery data for WASP-18b. **a**, The WASP-South lightcurve folded on the 0.94-day transit period, together with the model curve from the parameters of Table 1. Monitoring from May–December in 2006 and 2007 resulted in 8,235 photometric data points. **b**, Coralie radial-velocity measurements, again with the best-fitting model. The parameters of the system, derived from²⁶ the radial-velocity data, the WASP photometry, and additional transit photometry from the Euler telescope, are given in Table 1. The parameters of the host star in Table 2 were derived independently²⁷ from the stellar spectra. The stellar rotation rate ($v \sin i$) is $11.0 \pm 1.5 \text{ km s}^{-1}$, which (assuming that the spin and orbit are aligned) implies a rotation period of 5.6 days, typical for a young F star.

¹Astrophysics Group, Keele University, Staffordshire, ST5 5BG, UK. ²School of Physics and Astronomy, University of St Andrews, North Haugh, Fife, KY16 9SS, UK. ³Observatoire de Genève, Université de Genève, 51 ch. des Maillettes, 1290 Sauverny, Switzerland. ⁴Institut d'Astrophysique et de Géophysique, Université de Liège, 17 Allée du 6 Août, Batiment B5C, Liège 1, Belgium. ⁵Department of Physics and Astronomy, University of Leicester, Leicester, LE1 7RH, UK. ⁶Department of Astronomy, Harvard University, 60 Garden Street, MS 10, Cambridge, Massachusetts 02138, USA. ⁷Las Cumbres Observatory, 6740 Cortona Dr. Suite 102, Santa Barbara, California 93117, USA. ⁸Astrophysics Research Centre, School of Mathematics and Physics, Queen's University, University Road, Belfast, BT7 1NN, UK. ⁹Department of Physics, University of Warwick, Coventry, CV4 7AL, UK.

Table 1 | System parameters for WASP-18

Parameter	Value
Transit epoch, T_C	BJD 2,454,221.48163 \pm 0.00038
Orbital period, P	0.94145299 \pm 0.00000087 days
Transit duration, T_{14}	0.08932 \pm 0.00068 days
Planet/star area ratio, R_p^2/R_*^2	0.00875 \pm 0.00021
Impact parameter, $b = a \cos i / R_*$	0.25 \pm 0.15
Stellar reflex velocity, K_1	1.8183 \pm 0.0080 km s ⁻¹
Centre-of-mass velocity, γ	3.1961 \pm 0.0033 km s ⁻¹
Orbital semi-major axis, a	0.02026 \pm 0.00068 AU
Orbital inclination, i	86.0 \pm 2.5°
Orbital eccentricity, e	0.0092 \pm 0.0028
Argument of periastron, ω	-96 \pm 10°
Stellar mass, M_*	1.25 \pm 0.13 M_\odot
Stellar radius, R_*	1.216 $^{+0.067}_{-0.054} R_\odot$
Stellar surface gravity, $\log g_*$	4.367 $^{+0.028}_{-0.042}$ (cgs)
Stellar density, ρ_*	0.707 $^{+0.056}_{-0.096} \rho_\odot$
Planet mass, M_p	10.30 \pm 0.69 M_{Jup}
Planet radius, R_p	1.106 $^{+0.072}_{-0.054} R_{Jup}$
Planet surface gravity, $\log g_p$	4.289 $^{+0.027}_{-0.050}$ (cgs)
Planet density, ρ_p	7.73 $^{+0.78}_{-1.27} \rho_{Jup}$
Planet surface temperature, T_p	2,384 $^{+58}_{-30}$ K

BJD, barycentric Julian day. Subscripts P, \odot * and Jup refer to planetary, solar, stellar and Jupiter values, respectively. To convert cgs units to SI units for the gravity values, subtract two.

available energy to the amount dissipated by frictional losses during each orbital forcing cycle.

Q is found to be of the order of 10^5 to 10^6 from studies of binary stars¹⁵ and the gas-giant planets in our Solar System^{16,17} (in which it is often supposed that the Q value of stars and gas-giant planets will be similar). Thus values of $Q = 10^5$ – 10^6 are often applied to the star–planet tides of hot Jupiters^{18–20}. However, for $Q \approx 10^6$ the future lifetime of WASP-18b is only 0.65 Myr (Fig. 2), which is 10^{-4} of the estimated lifetime (~ 5 Gyr) of the host star WASP-18. Thus, either WASP-18 is in an exceptionally short-lived state, or its Q value is much higher. Matching the infall timescale to the current age of WASP-18 gives a Q as high as 10^9 , in line with some previous indications^{7,21,22}.

For comparison, WASP-18b's infall timescale is an order of magnitude shorter than that of the much-discussed OGLE-TR-56b^{6,7} (assuming that Q is the same for both), and gives a current rate of period change of -0.00073 ($10^6/Q$) s yr⁻¹. For low values of Q this would accumulate to a detectable change in transit epoch in less than a decade (for $Q = 10^6$ the transit time shifts by 28 s after 10 yr, which compares with a currently achievable timing accuracy²³ of 5 s). Thus WASP-18b is a diagnostic planet, either (for a low Q) being an exceptionally rare object in which the tidal decay is directly measurable, or forcing a reappraisal to much higher Q values; either way it will help establish the dynamical ages of the class of hot-Jupiter planets. WASP-18 will also help constrain our understanding of stellar interiors, given that the Q value depends on the dissipation of interior waves excited by the tidal forcing⁷.

For all values of Q up to about 10^{10} the planet will spiral inwards to destruction within the star's main-sequence lifetime. The trajectories in Fig. 2 continue until the planet reaches its Roche limit, at which

Table 2 | Stellar parameters of WASP-18

Parameter	Value
Position, J2000	01 h 37 min 25.03 s, -45° 40' 40.3"
Brightness, V mag	9.3
Spectral type	F6
Parallax	10.06 \pm 1.07 mas (ref. 25)
Distance	100 \pm 10 pc
Temperature, T_{eff}	6,400 \pm 100 K
Gravity, $\log g$	4.4 \pm 0.15 (cgs)
Turbulence, ξ_t	1.6 \pm 0.1 km s ⁻¹
Rotation, $v \sin i$	11.0 \pm 1.5 km s ⁻¹
Metallicity, [Fe/H]	0.00 \pm 0.09
Lithium, logN(Li)	2.65 \pm 0.08
Age	0.5–1.5 Gyr

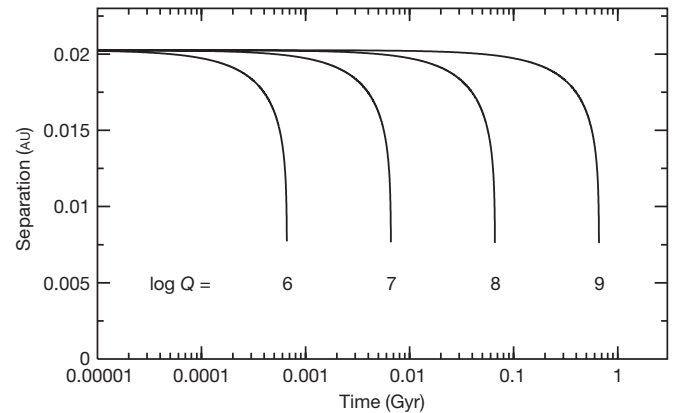


Figure 2 | Future evolution of WASP-18b. The decrease in the orbital semi-major axis for different values of the tidal quality factor Q . The spiral infall timescale is given by (see equation (29) of ref. 14 and equation (5) of ref. 18):

$$t_{\text{remain}} \approx \frac{2Q}{117n} \left(\frac{M_s}{M_p} \right) \left(\frac{a}{R_s} \right)^5$$

where n is the orbital angular frequency, M_s/M_p is the ratio of stellar to planet masses, a/R_s is the ratio of the orbital semi-major axis to the stellar radius, and the star is assumed to rotate slowly. The Q parameter measures the inverse fraction of the available energy dissipated in the star by frictional processes per tidal forcing cycle. It is usually expressed as a dimensionless ratio of the tidal quality factor of the star to the tidal Love number^{14,19}.

point it will be tidally disrupted, and its material will likely feed onto the star through the Lagrangian point (this ignores radiative evaporation, which will be hindered by the relatively high surface gravity of this massive planet). Assuming that the angular momentum is assimilated by the star, it would be spun up from a rotation rate of 5.6 days to about 0.7 days, and thus be reborn as a rapidly rotating star. Heavier elements from the planetary core could contaminate the stellar atmosphere, where, owing to the relatively small convection layer of an F6 star, they might be readily visible. The planet-hosting star HD 82943 shows evidence of planet engulfment²⁴, although it is currently rotating slowly, and thus any engulfment must have occurred long enough ago for magnetic braking to have since slowed the star.

Received 4 March; accepted 26 June 2009.

- Lin, D. N. C., Bodenheimer, P. & Richardson, D. C. Orbital migration of the planetary companion of 51 Pegasi to its present location. *Nature* **380**, 606–607 (1996).
- Tanaka, H., Takeuchi, T. & Ward, W. R. Three-dimensional interaction between a planet and an isothermal gaseous disk. I. Corotation and Lindblad torques and planet migration. *Astrophys. J.* **565**, 1257–1274 (2002).
- Rasio, F. & Ford, E. B. Dynamical instabilities and the formation of extrasolar planetary systems. *Science* **274**, 954–956 (1996).
- Hut, P. Tidal evolution in close binary systems. *Astron. Astrophys.* **99**, 126–140 (1981).
- Eggleton, P. P., Kiseleva, L. G. & Hut, P. The equilibrium tide model for tidal friction. *Astrophys. J.* **499**, 853–870 (1998).
- Sasselov, D. D. The new transiting planet OGLE-TR-56b: orbit and atmosphere. *Astrophys. J.* **596**, 1327–1331 (2003).
- Ogilvie, G. I. & Lin, D. N. C. Tidal dissipation in rotating solar-type stars. *Astrophys. J.* **661**, 1180–1191 (2007).
- Pollacco, D. L. et al. The WASP project and the SuperWASP cameras. *Publ. Astron. Soc. Pac.* **118**, 1407–1418 (2006).
- Sahu, K. C. et al. Transiting extrasolar planetary candidates in the Galactic bulge. *Nature* **443**, 534–540 (2006).
- Pont, F. et al. A transiting planet among 23 new near-threshold candidates from the OGLE survey—OGLE-TR-182. *Astron. Astrophys.* **487**, 749–754 (2008).
- Baraffe, I., Chabrier, G., Allard, F. & Hauschildt, P. H. Evolutionary models for solar metallicity low-mass stars: mass-magnitude relationships and color-magnitude diagrams. *Astron. Astrophys.* **337**, 403–412 (1998).
- Hebb, L. et al. WASP-12b: The hottest transiting planet yet discovered. *Astrophys. J.* **693**, 1920–1928 (2009).
- Boesgaard, A. M. & Tripicco, M. J. Lithium in the Hyades cluster. *Astrophys. J.* **302**, L49–L53 (1986).
- Dobbs-Dixon, I., Lin, D. N. C. & Mardling, R. A. Spin-orbit evolution of short-period planets. *Astrophys. J.* **610**, 464–476 (2004).

15. Meibom, S. & Mathieu, R. D. A robust measure of tidal circularization in coeval binary populations: the solar-type spectroscopic binary population in the open cluster M35. *Astrophys. J.* **620**, 970–983 (2005).
16. Goldreich, P. & Soter, S. Q in the Solar System. *Icarus* **5**, 375–389 (1966).
17. Peale, S. J. Origin and evolution of the natural satellites. *Annu. Rev. Astron. Astrophys.* **37**, 533–602 (1999).
18. Levrard, B., Winisdoerffer, C. & Chabrier, G. Falling transiting extrasolar giant planets. *Astrophys. J.* **692**, L9–L13 (2009).
19. Jackson, B., Greenberg, R. & Barnes, R. Tidal heating of extrasolar planets. *Astrophys. J.* **681**, 1631–1638 (2008).
20. Laughlin, G. *et al.* Rapid heating of the atmosphere of an extrasolar planet. *Nature* **457**, 562–564 (2009).
21. Pätzold, M. & Rauer, H. Where are the massive close-in extrasolar planets? *Astrophys. J.* **568**, L117–L120 (2002).
22. Pätzold, M., Carone, L. & Rauer, H. Tidal interactions of close-in extrasolar planets: The OGLE cases. *Astron. Astrophys.* **427**, 1075–1080 (2004).
23. Gillon, M. *et al.* Improved parameters for the transiting hot Jupiters WASP-4b and WASP-5b. *Astron. Astrophys.* **496**, 259–267 (2009).
24. Israelian, G., Santos, N. C., Mayor, M. & Rebolo, R. Evidence for planet engulfment by the star HD 82943. *Nature* **411**, 163–166 (2001).
25. van Leeuwen, F. Validation of the new Hipparcos reduction. *Astron. Astrophys.* **474**, 653–664 (2007).
26. Collier-Cameron, A. *et al.* WASP-1b and WASP-2b: two new transiting exoplanets detected with SuperWASP and SOPHIE. *Mon. Not. R. Astron. Soc.* **375**, 951–957 (2007).
27. West, R. *et al.* The low density transiting exoplanet WASP-15b. *Astron. J.* **137**, 4834–4836 (2009).

Supplementary Information is linked to the online version of the paper at www.nature.com/nature.

Acknowledgements We thank the South African Astronomical Observatory for hosting WASP-South and the UK's Science and Technology Facilities Council for funding.

Author Contributions WASP-S construction, operation and candidate selection (C.H., D.R.A., D.M.W., P.F.L.M., B.S., S.J.B.); WASP-S design (D.L.P.); WASP observatory software (J.I., D.R.A., P.F.L.M.); WASP-S data processing (D.R.A., D.M.W., B.S.); WASP data pipeline (A.C.C., T.A.L., N.P., K.H.); transit-search code (A.C.C., L.H., B.E.); WASP data archive (R.G.W., P.J.W.); Coralie/EulerCAM data (M.G., A.H.M.J.T., D.S., D.Q.); Euler/Coralie construction and upgrade (D.Q., M.M., S.U., F.P.); planet characterization (A.C.C., D.R.A., M.G.); host star characterization (B.S., L.H.); paper writing (C.H., A.C.C.).

Author Information Reprints and permissions information is available at www.nature.com/reprints. Correspondence and requests for materials should be addressed to C.H. (ch@astro.keele.ac.uk).

A tunable topological insulator in the spin helical Dirac transport regime

D. Hsieh¹, Y. Xia¹, D. Qian^{1,5}, L. Wray¹, J. H. Dil^{6,7}, F. Meier^{6,7}, J. Osterwalder⁷, L. Patthey⁶, J. G. Checkelsky¹, N. P. Ong¹, A. V. Fedorov⁸, H. Lin⁹, A. Bansil⁹, D. Grauer², Y. S. Hor², R. J. Cava² & M. Z. Hasan^{1,3,4}

Helical Dirac fermions—charge carriers that behave as massless relativistic particles with an intrinsic angular momentum (spin) locked to its translational momentum—are proposed to be the key to realizing fundamentally new phenomena in condensed matter physics^{1–9}. Prominent examples include the anomalous quantization of magneto-electric coupling^{4–6}, half-fermion states that are their own antiparticle^{7,8}, and charge fractionalization in a Bose–Einstein condensate⁹, all of which are not possible with conventional Dirac fermions of the graphene variety¹⁰. Helical Dirac fermions have so far remained elusive owing to the lack of necessary spin-sensitive measurements and because such fermions are forbidden to exist in conventional materials harbouring relativistic electrons, such as graphene¹⁰ or bismuth¹¹. It has recently been proposed that helical Dirac fermions may exist at the edges of certain types of topologically ordered insulators^{3,4,12}—materials with a bulk insulating gap of spin–orbit origin and surface states protected against scattering by time-reversal symmetry—and that their peculiar properties may be accessed provided the insulator is tuned into the so-called topological transport regime^{3–9}. However, helical Dirac fermions have not been observed in existing topological insulators^{13–18}. Here we report the realization and characterization of a tunable topological insulator in a bismuth-based class of material by combining spin-imaging and momentum-resolved spectroscopies, bulk charge compensation, Hall transport measurements and surface quantum control. Our results reveal a spin-momentum locked Dirac cone carrying a non-trivial Berry's phase that is nearly 100 per cent spin-polarized, which exhibits a tunable topological fermion density in the vicinity of the Kramers point and can be driven to the long-sought topological spin transport regime. The observed topological nodal state is shown to be protected even up to 300 K. Our demonstration of room-temperature topological order and non-trivial spin-texture in stoichiometric Bi₂Se₃-M_x (M_x indicates surface doping or gating control) paves the way for future graphene-like studies of topological insulators, and applications of the observed spin-polarized edge channels in spintronic and computing technologies possibly at room temperature.

Unlike conventional Dirac fermions as in graphene, helical Dirac fermions possess a net spin and are guaranteed to be conducting because of time-reversal symmetry^{2–5}, allowing the unique possibility of carrying spin currents without heat dissipation. However, the most important difference and a more exciting frontier lies in the topological properties of helical Dirac fermion systems^{3–5,12}, which are expected to manifest in several ways, provided that the system can be tuned to the topological transport regime where the charge density vanishes (analogous to the charge neutrality point in graphene^{10,19}).

These manifestations include an anomalous half-integer quantization of Hall conductance^{3–6}, a realization of Majorana fermions (particles with anyon exchange statistics that differs from the conventional Bose or Fermi–Dirac statistics)^{7,8}, and generation of fractionally charged quantum particles⁹. Helical fermions are believed to exist on the edges of certain types of three-dimensional (3D) topological insulators^{3,4,12}, with material candidates Bi₂X₃ (X = Se, Te)¹⁵ recently proposed on the basis of observations^{15,17} and models^{15,20}. However, these materials cannot be used to detect helical Dirac fermion physics for three reasons. First, the helical properties of the surface electrons are unknown and depend on the materials' class. Second, their electronic structure is not in the topological transport regime, thus not allowing any of the interesting topological insulator experiments to be performed to date. Third, unlike two-dimensional (2D) quantum Hall Dirac systems such as graphene^{10,19}, 3D topological insulators cannot be very easily tuned to this zero carrier density regime through standard electrical gating, which has prevented a revolution like that witnessed for graphene¹⁰ from taking place for topological insulators².

To determine the key helical properties of the edge electrons near the Fermi energy (E_F) in our previously proposed candidate Bi₂X₃ class¹⁵, we performed spin- and angle-resolved photoemission spectroscopy (spin-ARPES) scans using a double Mott detector set-up²¹, which systematically measures all three components of the spin of the electron as a function of its energy and momentum throughout the Brillouin zone (Supplementary Information). Although the surface electrons of both Bi₂Se₃ and Bi₂Te₃ exhibit a finite density of states near E_F (Fig. 1a–d), there is an additional contribution to the density of states around momentum $\bar{\Gamma}$ from the spin-degenerate bulk conduction band in Bi₂Se₃. Therefore, the helical nature of the surface electrons is most clearly resolved in Bi₂Te₃. We analysed the spin-polarization of photoelectrons emitted at a binding energy $E_B = -20$ meV along the k_x ($\parallel \bar{\Gamma} - \bar{M}$) cut in Bi₂Te₃ (Fig. 1e inset). Because the surface state dispersion of Bi₂X₃ exhibits a pronounced time dependence after cleavage (Supplementary Information) related to semiconductor band bending and topological charging effects¹⁷, data collection times were only long enough to ensure a level of statistics sufficient to measure the spin-polarized character of the surface states.

Figure 1e and f shows the measured spin polarization spectra P_i of the $i = x, y$ and z (out-of-plane) components along the $\bar{\Gamma} - \bar{M}$ direction. In the x and z directions, no clear signal can be discerned within the margins of statistical error. In the y direction on the other hand, clear polarization signals of equal magnitude and opposite sign are observed for surface-edge electrons of opposite momentum, evidence that the spin and momentum directions are one-to-one

¹Joseph Henry Laboratories of Physics, Department of Physics, ²Department of Chemistry, ³Princeton Center for Complex Materials, ⁴Princeton Institute for Science and Technology of Materials, Princeton University, Princeton, New Jersey 08544, USA. ⁵Department of Physics, Shanghai Jiao Tong University, Shanghai 200030, China. ⁶Swiss Light Source, Paul Scherrer Institute, CH-5232, Villigen, Switzerland. ⁷Physik-Institute, Universität Zürich-Irchel, 8057 Zürich, Switzerland. ⁸Advanced Light Source, Lawrence Berkeley Laboratory, Berkeley, California 94720, USA. ⁹Department of Physics, Northeastern University, Boston, Massachusetts 02115, USA.

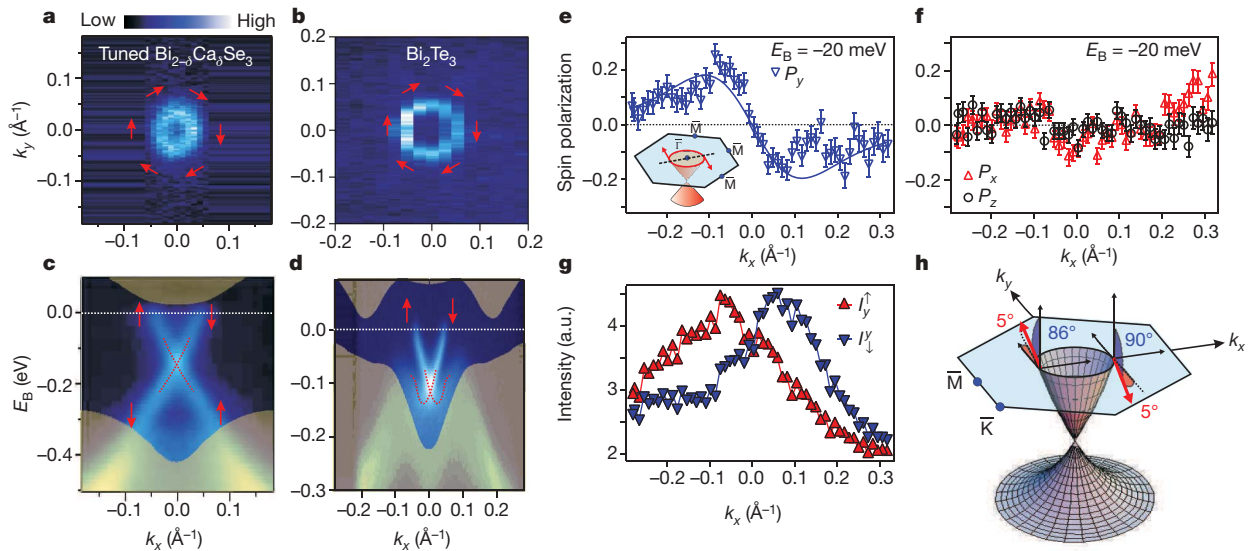


Figure 1 | Detection of spin-momentum locking of spin-helical Dirac electrons in Bi_2Se_3 and Bi_2Te_3 using spin-resolved ARPES. **a, b**, ARPES intensity map at E_F of the (111) surface of tuned stoichiometric $\text{Bi}_{2-\delta}\text{Ca}_\delta\text{Se}_3$ (**a**; see text) and of Bi_2Te_3 (**b**). Red arrows denote the direction of spin projection around the Fermi surface. **c, d**, ARPES dispersion of tuned $\text{Bi}_{2-\delta}\text{Ca}_\delta\text{Se}_3$ (**c**) and Bi_2Te_3 (**d**) along the k_x cut. The dotted red lines are guides to the eye. The shaded regions in **c** and **d** are our projections of the bulk bands of pure Bi_2Se_3 and Bi_2Te_3 , respectively, onto the (111) surface. **e**, Measured y component of spin-polarization along the $\bar{\Gamma}-\bar{M}$ direction at $E_B = -20$ meV, which only cuts through the surface states. Inset, schematic of the cut direction. **f**, Measured x (red triangles) and z (black circles) components of spin-polarization along the $\bar{\Gamma}-\bar{M}$ direction at

$E_B = -20$ meV. Error bars in **e** and **f** denote the standard deviation of $P_{x,y,z}$ where typical detector counts reach 5×10^5 ; solid lines are numerical fits²¹. **g**, Spin-resolved spectra obtained from the y component spin polarization data. The non-Lorentzian lineshape of the I_y^\uparrow and I_y^\downarrow curves and their non-exact merger at large $|k_x|$ is due to the time evolution of the surface band dispersion, which is the dominant source of statistical uncertainty. a.u., arbitrary units. **h**, Fitted values of the spin polarization vector \mathbf{P} (S_x, S_y, S_z) are $(\sin 90^\circ \cos -95^\circ, \sin 90^\circ \sin -95^\circ, \cos 90^\circ)$ for electrons with $+k_x$ and $(\sin 86^\circ \cos 85^\circ, \sin 86^\circ \sin 85^\circ, \cos 86^\circ)$ for electrons with $-k_x$, which demonstrates the topological helicity of the spin-Dirac cone. The angular uncertainties are of the order of $\pm 10^\circ$ and the magnitude uncertainty is of the order of ± 0.15 .

locked due to Z_2 topology. This is most clearly seen in the spin-resolved spectra ($I_y^{\uparrow,\downarrow}$; Fig. 1g), which are calculated from P_y according to $I_y^\uparrow = I_{\text{tot}}(1 + P_y)/2$ and $I_y^\downarrow = I_{\text{tot}}(1 - P_y)/2$, where I_{tot} is the spin-averaged intensity. To extract the spin polarization vectors of the forward ($+k_x$) and backward ($-k_x$) moving electrons, we performed a standard numerical fit (Supplementary Information)²¹. The fit results yield $100(\pm 15)\%$ polarized (Fig. 1h) spins that point along the $(\mathbf{k} \times \mathbf{z})$ direction, which is consistent with its topological spin-orbit coupling origin^{14,21}. Spin-momentum locking is the key to topological order in a topological insulator which cannot be demonstrated without spin sensitive detection. Therefore the existence of the topological insulator state was not established in previous work on Bi_2X_3 . Our combined observations of a spin-orbit origin linear dispersion relation and a one-to-one locking of momentum and spin directions allow us to conclude that the surface electrons of Bi_2X_3 ($\text{X}=\text{Se}, \text{Te}$) are helical Dirac fermions of Z_2 topological-order origin (Fig. 1).

To experimentally access these helical Dirac fermions for research-device applications, the electronic structure must be in the topological transport regime where there is zero charge fermion density⁷⁻⁹. This regime occurs when E_F lies in between the bulk valence band maximum (VBM) and the bulk conduction band minimum (CBM), and exactly at the surface or edge Dirac point, which should in turn lie at a Kramers time-reversal invariant momentum^{3,4}. This is clearly not the case in either Bi_2Te_3 , $\text{Bi}_2(\text{Sn})\text{Te}_3$, Bi_2Se_3 or graphene. Although pure Bi_2X_3 are expected to be undoped semiconductors^{20,22,23}, nominally stoichiometric samples are well known to be n- and p-type semiconductors owing to excess carriers introduced via Se or Te site defects, respectively^{16,17}. To compensate for the unwanted defect dopants, trace amounts of carriers of the opposite sign must be added into the naturally occurring material, which may be easier to achieve in Bi_2Se_3 than in Bi_2Te_3 because the former has a much larger bandgap^{15,24} (around 0.35 eV (ref. 25) compared to 0.18 eV (ref. 26), respectively). To lower the E_F of Bi_2Se_3 into the bulk bandgap, we

substituted trace amounts of Ca^{2+} for Bi^{3+} in as-grown Bi_2Se_3 , where Ca has been previously shown¹⁶ to act as a hole donor by scanning tunnelling microscopy and thermoelectric transport studies¹⁶. Figure 2a shows that as the Ca concentration increases from 0% to 0.5%, the low temperature resistivity sharply peaks at 0.25%, which suggests that the system undergoes a metal to insulator to metal transition. The resistivity peak occurs at a Ca concentration where a change in sign of the Hall carrier density also is observed (Fig. 2b), which shows that for measured Ca concentrations below and above 0.25%, electrical conduction is supported by electron and hole carriers, respectively.

We performed systematic time-dependent ARPES measurements to study the electronic structure evolution of $\text{Bi}_{2-\delta}\text{Ca}_\delta\text{Se}_3$ as a function of Ca doping in order to gain insight into the trends observed in transport (Fig. 2a and b). Early time ARPES energy dispersion maps taken through the $\bar{\Gamma}$ point of the (111) surface Brillouin zone are displayed in Fig. 2c-h for several Ca doping levels. In the as-grown ($\delta = 0$) Bi_2Se_3 samples, a single surface Dirac cone is observed with E_F lying nearly 0.3 eV above the Dirac node forming an electron Fermi surface. We also observe that E_F intersects the electron-like bulk conduction band. When a 0.25% concentration of Ca is introduced, E_F is dramatically lowered to lie near the Dirac node (Fig. 2d), which is consistent with Ca acting as a highly effective hole donor. Because the bulk CBM lies at a binding energy of approximately -0.1 eV for $\delta = 0$ (Fig. 2c), a 0.3 eV shift in E_F between $\delta = 0$ and $\delta = 0.0025$ suggests that for $\delta = 0.0025$, E_F is located 0.2 eV below the CBM. This is consistent with E_F being in the bulk bandgap, because the indirect energy gap between the CBM and the VBM is known from both tunnelling²⁴ and optical²⁵ data and theory²² to be nearly 0.35 eV.

As the Ca concentration is increased further, the position of E_F continues a downward trend such that by $\delta = 0.01$, it is located clearly below the Dirac node (Fig. 2) and intersects the hole-like bulk valence band. The systematic lowering of E_F with increasing δ in $\text{Bi}_{2-\delta}\text{Ca}_\delta\text{Se}_3$ observed in early time ARPES measurements (Fig. 2i-k), which reflect the electronic structure of the sample bulk,

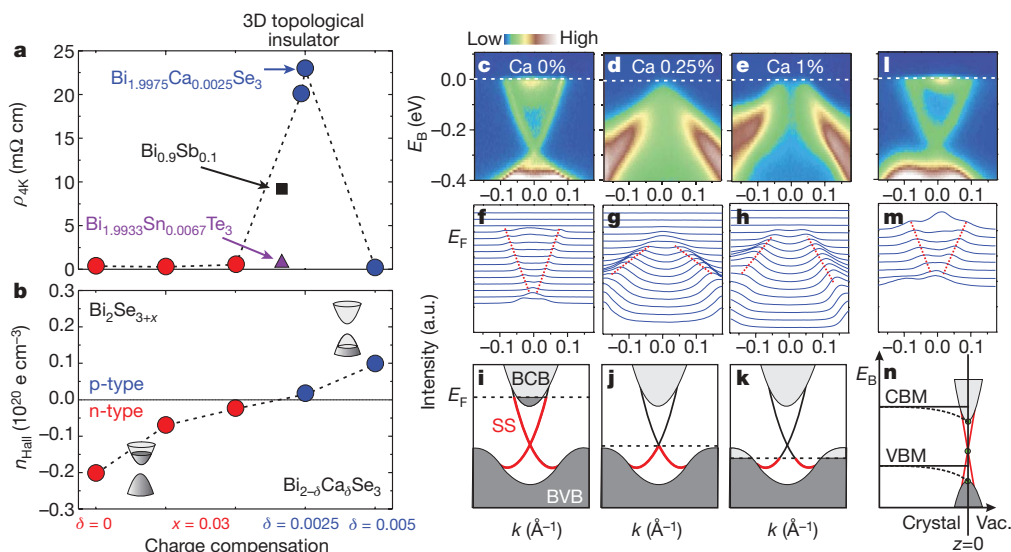


Figure 2 | Tuning the bulk Fermi level through systematic bulk charge compensation monitored through systematic transport and ARPES measurements. **a**, Resistivity at $T = 4$ K measured for samples of Bi_2Se_3 (filled circles, no arrow labels) that are bulk electron doped due to varying concentrations of Se vacancies¹⁶ (x) or bulk hole doped through Ca/Bi substitution (δ). These are compared to analogous values for the topological insulators $\text{Bi}_{0.9}\text{Sb}_{0.1}$ (black square, arrowed; ref. 13) and $\text{Bi}_{1.9933}\text{Sn}_{0.0067}\text{Te}_3$ (purple triangle, arrowed). The stoichiometric Bi_2Se_3 ($\text{Bi}_{1.9975}\text{Ca}_{0.0025}\text{Se}_3$) is found to be the most insulating of these topological insulators. In $\text{Bi}_2(\text{Ca})\text{Se}_3$, bulk resistivity in excess of $75 \text{ m}\Omega \text{ cm}$ is possible, which will be shown elsewhere. The bulk insulating state in $\text{Bi}_{0.9}\text{Sb}_{0.1}$ (ref. 13) is intrinsic and not due to disorder which will also be shown elsewhere. $\text{Bi}_{1.9933}\text{Sn}_{0.0067}\text{Te}_3$ is known to be most metallic-like among the three classes

studied so far. **b**, Hall carrier density of the same samples determined using Hall measurements. Symbols in **a** and **b** coloured red (blue) represent n - (p -) type behaviour. **c–e**, ARPES band dispersion images of $\text{Bi}_{2-\delta}\text{Ca}_\delta\text{Se}_3$ (111) through Γ collected within 20 min after cleavage for $\delta = 0$ (**c**), $\delta = 0.0025$ (**d**) and $\delta = 0.01$ (**e**). **f–h**, Corresponding momentum distribution curves. Red lines are guides to the eye. **i–k**, Schematic downward evolution of E_F with increasing Ca content. The occupied bulk conduction band (BCB) and bulk valence band (BVB) states are shaded dark, and the occupied surface states (SS) are coloured red. **l**, Typical ARPES band dispersion image of **c–e** taken around 18 h after cleavage, and **m**, its corresponding momentum distribution curves. **n**, Schematic of the surface band bending process that is responsible for the observed downward shift in energies over time. Vac., vacuum.

consistently explain the measured transport behaviour. However, we observe that E_F rises back up over time across all samples, such that all spectra relax back to a $\delta = 0$ like spectrum on a typical timescale of 18 h (Fig. 2l). Such a slow upward shift of the surface Fermi level has also been observed in Bi_2Te_3 (ref. 17) and is due to a surface band bending effect commonly observed in many semiconductors (Supplementary Information). Therefore, although bulk Ca doping succeeds in tuning E_F between the bulk valence and conduction bands, it does not change the position of E_F relative to the surface Dirac point in the ground state.

Because the surface Dirac point in the ground state of most insulating compound studied, stoichiometric Bi_2Se_3 or $\text{Bi}_{1.9975}\text{Ca}_{0.0025}\text{Se}_3$, lies $\sim 0.3 \text{ eV}$ below E_F , its electronic structure is still not in the much desired topological quantum transport regime. To bring the surface Dirac point level with E_F in $\text{Bi}_{2-\delta}\text{Ca}_\delta\text{Se}_3$, we demonstrate here that hole carriers can be remarkably systematically introduced into the surface of a large-gap topological insulator by dosing with NO_2 molecules, which has been previously known to work in non-insulating materials^{27,28}. Figure 3 shows that with increasing surface hole donor concentration, the binding energy of the surface Dirac point rises monotonically towards E_F . Starting from $E_B \approx -0.3 \text{ eV}$ at a dose of 0 Langmuir (0 L; refs 27, 28), it rises to -0.15 eV at 0.1 L where the surface bent CBM has completely disappeared, and finally to the charge neutrality point ($E_B = 0 \text{ eV}$) at 2 L. No further changes of the chemical potential are observed with higher dosages. To quantify the surface carrier density (n) dependence on surface hole donor concentration, we mapped the surface state Fermi surface in Fig. 3a–c and performed a Luttinger electron count (number density on the surface) based on Fermi surface area, $n = A_{FS}/A_{BZ}$, where A_{FS} is the area of the Fermi surface and A_{BZ} is the area of the surface Brillouin zone. We find that 0.1 L of NO_2 removes approximately 0.0066 electrons per surface unit cell of $\text{Bi}_{2-\delta}\text{Ca}_\delta\text{Se}_3$ (111), and an excess of 2 L reduces the Fermi surface to a single point within our experimental resolution, which has an additional 0.005 electrons per unit cell

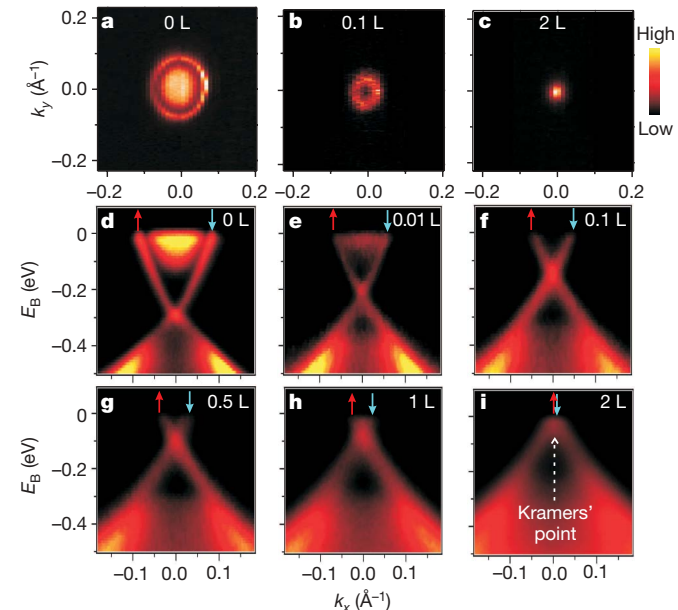


Figure 3 | Tuning the density of helical Dirac electrons to the spin-degenerate Kramers point and topological transport regime. **a**, A high resolution ARPES mapping of the topological surface Fermi surface near Γ of $\text{Bi}_{2-\delta}\text{Ca}_\delta\text{Se}_3$ (111). The diffuse intensity within the ring originates from the bulk-surface resonance state¹⁵. **b**, The Fermi surface after 0.1 L of NO_2 is dosed, showing that the resonance state is removed. **c**, The Fermi surface after a 2 L dosage, which achieves the Dirac charge neutrality point. **d–i**, High resolution ARPES surface band dispersions through Γ after an NO_2 dosage (L) of 0 (**d**), 0.01 (**e**), 0.1 (**f**), 0.5 (**g**), 1 (**h**) and 2 (**i**). The arrows denote the topological spin polarization of the bands. We note that owing to an increasing level of surface disorder with NO_2 adsorption, the measured spectra become progressively more diffuse and the total photoemission intensity from the buried $\text{Bi}_{2-\delta}\text{Ca}_\delta\text{Se}_3$ surface is gradually reduced.

removed. Because surface doping does not affect the carrier density in the bulk (which thus remains insulating), the energy of the Dirac point is lifted above the bulk VBM: a new time independent electronic ground state is realized that lies in the topological transport regime with E_F intersecting the Dirac node.

In order to investigate the thermal stability and strength of topological order of this nodal Dirac ground state (Fig. 4e), temperature dependent ARPES scans were collected on $\text{Bi}_{2-\delta}\text{Ca}_\delta\text{Se}_3$ samples that were first surface hole doped with NO_2 at a temperature $T = 10$ K. Figure 4c and d illustrates that the charge neutral point-like Fermi surface (Fig. 4a) is robust up to room temperature ($T = 300$ K) over measurement times of days. A density of states that decreases linearly to zero at the Dirac point energy at 300 K (Fig. 4f) is further evidence that the low energy properties of stoichiometric Bi_2Se_3 , NO_2 or $\text{Bi}_{1.9975}\text{Ca}_{0.0025}\text{Se}_3$, NO_2 are dominated by a novel topological ground state that features massless helical Dirac fermions with nearly 100% spin polarization. This also confirms a non-trivial π Berry's phase on the surface due to the spin-momentum locking pattern that we observed which is similar to the robust Berry's phase previously observed in the Bi-Sb system¹⁴ (Fig. 1).

Helical nodal Dirac fermions are forbidden from acquiring a mass through bandgap formation because they are located around time-reversal invariant (Kramers') momenta $k_T = \bar{\Gamma}$ or \bar{M} (Fig. 4h). This makes them fundamentally different from chiral Dirac fermions such as those found in graphene, which are located at \bar{K} and not topologically protected (Fig. 4g) and can develop an undesirable mass while in contact with a substrate. The helical nodal Dirac fermion on the surface of Bi_2Se_3 owes its existence to a non-zero topological number ν_0 given by $(-1)^{\nu_0} = \prod_{k_T} \prod_{m=1}^N \xi_{2m}(k_T)$, where $\xi_{2m}(k_T)$ is the parity eigenvalue of the bulk wavefunction at the 3D Kramers' point k_T and N is the number of occupied bulk bands⁴. Because Ca dopants are present in only trace quantities in $\text{Bi}_{1.9975}\text{Ca}_{0.0025}\text{Se}_3$, NO_2 , the values of $\xi_{2m}(k_T)$ do not deviate from those of Bi_2Se_3 , as evidenced by the persistence of a single gapless surface band in both naturally grown Bi_2Se_3 and $\text{Bi}_{1.9975}\text{Ca}_{0.0025}\text{Se}_3$. Both Ca^{2+} and NO_2^- are non-magnetic and so do not break time-reversal symmetry, therefore the same topological quantum number ($\nu_0 = 1$) applies in the Dirac

transport regime (Fig. 4) realized by our method shown here, which is stable with both time and temperature. Our direct demonstration of spin-polarized edge channels and room temperature operability of chemically gated stoichiometric Bi_2Se_3 or $\text{Bi}_{2-\delta}\text{Ca}_\delta\text{Se}_3$, NO_2 , not achieved in purely 2D topological systems such as $\text{Hg}(\text{Cd})\text{Te}$ quantum wells²⁹, enables exciting future room temperature experiments on surface helical Dirac fermions that carry non-trivial π Berry's phase.

Our demonstration of topological order at room temperature opens up possibilities of using quantum Hall-like phenomena and spin-polarized protected edge channels for spintronic or computing device applications without the traditional requirements of high magnetic fields and delicate cryogenics. A direct detection of surface-edge states would be possible in stoichiometric Bi_2Se_3 or $\text{Bi}_{2-\delta}\text{Ca}_\delta\text{Se}_3$, using transport methods which will bear signatures of weak anti-localization and thus exhibit anomalous magneto-optic effects. Here we envisage a few sample experiments that could be carried out by using surface doped or electrically gated $\text{Bi}_{2-\delta}\text{Ca}_\delta\text{Se}_3$. By applying a weak time-reversal breaking perturbation at the helical surface so as to lift the Kramers degeneracy at E_F (a method of gap opening on the surface is shown in Supplementary Information), a half-integer quantized magneto-electric coupling can be realized³⁻⁶, which could be measured by standard quantum Hall probes. This would enable a variety of novel surface quantum Hall physics to be realized. Another class of experiments would be made possible by interfacing the helical topological surface with magnetic and ordinary superconducting films. An interferometer device could be built based on $\text{Bi}_{2-\delta}\text{Ca}_\delta\text{Se}_3$ to create and detect long-sought Majorana fermions^{7,8}. These particles, which have never been observed, possess only half the degrees of freedom of a conventional fermion and constitute the key building block for topological quantum computing that can operate in a fault-tolerant mode. Yet another class of experiments would be made possible by sandwiching a charge neutral topological insulator film made of $\text{Bi}_{2-\delta}\text{Ca}_\delta\text{Se}_3$ within a charged capacitor. In this way, a microchip that supports a topological electron-hole condensate with fractional vortices⁹ could be fabricated, which offers the exciting opportunity to probe

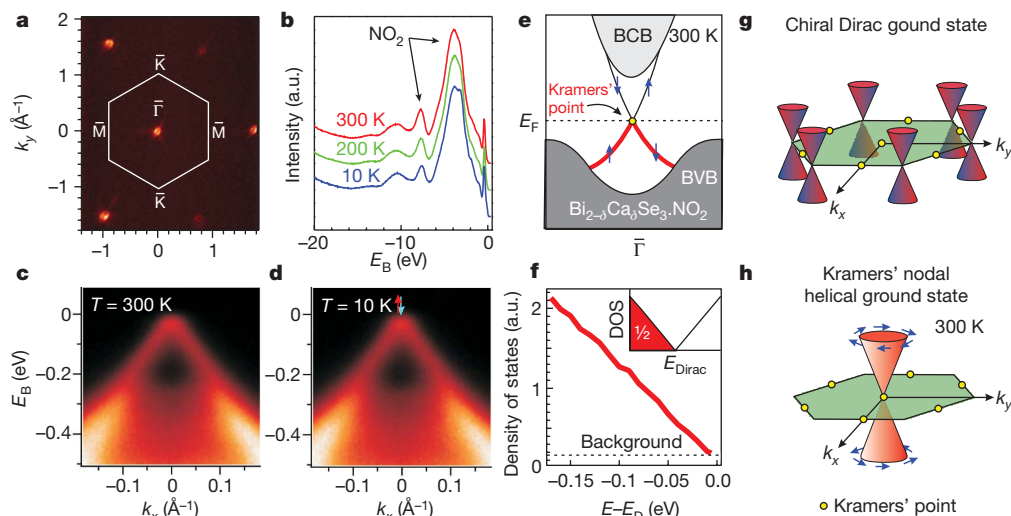


Figure 4 | Topological order of the nodal helical Dirac ground state at 300 K. **a**, Typical ARPES intensity map of the $\text{Bi}_2(\text{Se/Te})_3$ class collected at E_F spanning several Brillouin zones. **b**, Energy distribution curves of the valence bands of $\text{Bi}_{2-\delta}\text{Ca}_\delta\text{Se}_3$ taken at $T = 10$ K, 200 K and 300 K. The peaks around -4 eV and -7.5 eV come from NO_2 adsorption (Supplementary Information). The intensity of these NO_2 core level peaks do not change over this temperature range, indicating no measurable NO_2 desorption during the heating process. **c**, **d**, ARPES intensity map of the surface state band dispersion of $\text{Bi}_{2-\delta}\text{Ca}_\delta\text{Se}_3$ (111) after a 2 L dosage of NO_2 is applied at $T = 10$ K, which is taken at 300 K (**c**) and 10 K (**d**). **e**, Schematic of the surface

and bulk electronic structure of $\text{Bi}_{2-\delta}\text{Ca}_\delta\text{Se}_3$, NO_2 , tuned to the topological transport regime. **f**, Angle-integrated intensity near $\bar{\Gamma}$ (red) shows a linear trend. Inset, the expected density of states (DOS) of a helical Dirac cone, which is 1/2 that of a graphene Dirac cone due to its single spin degeneracy. **g**, Schematic of the chiral Dirac fermion ground state of graphene, which exhibits spin-degenerate Dirac cones that intersect away from the Kramers' points. **h**, Schematic of the helical Dirac fermion ground state of $\text{Bi}_{2-\delta}\text{Ca}_\delta\text{Se}_3$, NO_2 , which exhibits a spin-polarized Dirac cone that intersects at a Kramers' point and guarantees a $\nu_0 = 1$ topological order quantum number for the nodal Dirac ground state.

interactions between Dirac fermions of opposite helicity; this would enable searching for exotic quantum phenomena beyond the standard model of particle physics³⁰.

METHODS SUMMARY

Spin-integrated ARPES data were taken at beamlines 12.0.1 and 7.0.1 of the Advanced Light Source in Lawrence Berkeley National Laboratory with 29-eV to 100-eV photons. Typical energy and momentum resolutions were 15 meV and 1% of the surface Brillouin zone (29-eV photons) and 50 meV and 2% of the surface Brillouin zone (100-eV photons). Spin-resolved ARPES measurements were performed at the SIS beamline at the Swiss Light Source using the COPHEE spectrometer, which consists of two 40-kV classical Mott detectors that measure all three spatial components of spin polarization. Spin-resolved measurements were taken with 20-eV to 22-eV photons with energy and momentum resolutions of 80 meV and 3% of the surface Brillouin zone (all photons). Spin-integrated data were collected on tuned $\text{Bi}_{2-x}\text{Ca}_x\text{Se}_3$ and tuned Bi_2Te_3 single crystals cleaved in ultrahigh vacuum (pressures better than 5×10^{-11} torr) and maintained at a temperature of 10 K unless otherwise specified. Spin-resolved data were collected at 50 K. Adsorption of NO_2 molecules on $\text{Bi}_{2-x}\text{Ca}_x\text{Se}_3$ was achieved via controlled exposures to NO_2 gas (Matheson, 99.5%). The adsorption effects were studied under static flow mode by exposing the cleaved sample surface to the gas for a certain time then taking data after the chamber was pumped down to the base pressure. Spectra of the NO_2 adsorbed surfaces were taken within minutes of opening the photon shutter to minimize photon exposure related effects. The theoretical band calculations were performed with the LAPW method in slab geometry using the WIEN2K package.

Full Methods and any associated references are available in the online version of the paper at www.nature.com/nature.

Received 30 April; accepted 29 June 2009.

Published online 20 July 2009.

- Day, C. Exotic spin textures show up in diverse materials. *Phys. Today* **62**, 12–13 (2009).
- Moore, J. E. Topological insulators: the next generation. *Nature Phys.* **5**, 378–380 (2009).
- Fu, L., Kane, C. L. & Mele, E. J. Topological insulators in three dimensions. *Phys. Rev. Lett.* **98**, 106803 (2007).
- Qi, X.-L., Hughes, T. L. & Zhang, S.-C. Topological field theory of time-reversal invariant insulators. *Phys. Rev. B* **78**, 195424 (2008).
- Schnyder, A. P. *et al.* Classification of topological insulators and superconductors. *Phys. Rev. B* **78**, 195125 (2008).
- Essin, A., Moore, J. E. & Vanderbilt, D. Magnetoelectric polarizability and axion electrodynamics in crystalline insulators. *Phys. Rev. Lett.* **102**, 146805 (2009).
- Fu, L. & Kane, C. L. Probing neutral Majorana fermion edge modes with charge transport. *Phys. Rev. Lett.* **102**, 216403 (2009).
- Akhmerov, A. R., Nilsson, J. & Beenakker, C. W. J. Electrically detected interferometry of Majorana fermions in a topological insulator. *Phys. Rev. Lett.* **102**, 216404 (2009).
- Seradjeh, B., Moore, J. E. & Franz, M. Exciton condensation and charge fractionalization in a topological insulator film. Preprint at (<http://arxiv.org/abs/0902.1147>) (2009).
- Geim, A. K. & Novoselov, K. S. The rise of graphene. *Nature Mater.* **6**, 183–191 (2007).
- Li, L. *et al.* Phase transitions of Dirac electrons in bismuth. *Science* **321**, 547–550 (2008).
- Moore, J. E. & Balents, L. Topological invariants of time-reversal-invariant band structures. *Phys. Rev. B* **75**, 121306(R) (2007).
- Hsieh, D. *et al.* A topological Dirac insulator in a quantum spin Hall phase. *Nature* **452**, 970–974 (2008).
- Hsieh, D. *et al.* Observation of unconventional quantum spin textures in topological insulators. *Science* **323**, 919–922 (2009).
- Xia, Y. *et al.* Observation of a large-gap topological-insulator class with a single Dirac cone on the surface. *Nature Phys.* **5**, 398–402 (2009).

- Hor, Y. S. *et al.* p-type Bi_2Se_3 for topological insulator and low-temperature thermoelectric applications. *Phys. Rev. B* **79**, 195208 (2009).
- Noh, H.-J. *et al.* Spin-orbit interaction effect in the electronic structure of Bi_2Te_3 observed by angle-resolved photoemission spectroscopy. *Europhys. Lett.* **81**, 57006 (2008).
- Nishide, A. *et al.* Direct mapping of the spin-filtered surface bands of a three-dimensional quantum spin Hall insulator. Preprint at (<http://arxiv.org/abs/0902.2251>) (2009).
- Checkelsky, J. G., Li, L. & Ong, N. P. Divergent resistance of the Dirac point in graphene: evidence for a transition in high magnetic field. *Phys. Rev. B* **79**, 115434 (2009).
- Zhang, H. *et al.* Topological insulators in Bi_2Se_3 , Bi_2Te_3 and Sb_2Te_3 with a single Dirac cone on the surface. *Nature Phys.* **5**, 438–442 (2009).
- Meier, F., Dil, J. H., Lobo-Checa, J., Patthey, L. & Osterwalder, J. Quantitative vectorial spin analysis in angle-resolved photoemission: $\text{Bi}/\text{Ag}(111)$ and $\text{Pb}/\text{Ag}(111)$. *Phys. Rev. B* **77**, 165431 (2008).
- Larson, P. *et al.* Electronic structure of Bi_2X_3 ($\text{X} = \text{S}, \text{Se}, \text{T}$) compounds: comparison of theoretical calculations with photoemission studies. *Phys. Rev. B* **65**, 085108 (2001).
- Mishra, S. K., Satpathy, S. & Jepsen, O. Electronic structure and thermoelectric properties of bismuth telluride and bismuth selenide. *J. Phys. Condens. Matter* **9**, 461–470 (1997).
- Urazhdin, S. *et al.* Surface effects in layered semiconductors Bi_2Se_3 and Bi_2Te_3 . *Phys. Rev. B* **69**, 085313 (2004).
- Black, J., Conwell, E. M., Seigle, L. & Spencer, C. W. Electrical and optical properties of some $\text{M}_2^{\text{V-B}}\text{N}_3^{\text{VI-B}}$ semiconductors. *J. Phys. Chem. Solids* **2**, 240–251 (1957).
- Thomas, G. A. *et al.* Large electron-density increase on cooling a layered metal: doped Bi_2Te_3 . *Phys. Rev. B* **46**, 1553–1556 (1992).
- Zhou, S. *et al.* Metal to insulator transition in epitaxial graphene induced by molecular doping. *Phys. Rev. Lett.* **101**, 086402 (2008).
- Schedin, F. *et al.* Detection of individual gas molecules adsorbed on graphene. *Nature Mater.* **6**, 652–655 (2007).
- König, M. *et al.* Quantum spin Hall insulator state in HgTe quantum wells. *Science* **318**, 766–770 (2007).
- Wilczek, F. Remarks on dyons. *Phys. Rev. Lett.* **48**, 1146–1149 (1982).

Supplementary Information is linked to the online version of the paper at www.nature.com/nature.

Acknowledgements We acknowledge the following people for discussions: P. W. Anderson, B. Altshuler, L. Balents, M. R. Beasley, B. A. Bernevig, C. Callan, J. C. Davis, H. Fertig, E. Fradkin, L. Fu, D. Gross, D. Haldane, K. Le Hur, B. I. Halperin, D. A. Huse, C. L. Kane, C. Kallin, E. A. Kim, R. B. Laughlin, D.-H. Lee, P. A. Lee, J. E. Moore, A. J. Millis, A. H. Castro Neto, J. Orenstein, P. Phillips, S. Sachdev, D. C. Tsui, A. Vishwanath, F. Wilczek, X.-G. Wen and A. Yazdani. The spin-resolved and spin-integrated ARPES measurements using synchrotron X-ray facilities and theoretical computations are supported by the Basic Energy Sciences of the US Department of Energy (DE-FG-02-05ER46200, AC03-76SF00098 and DE-FG02-07ER46352) and by the Swiss Light Source, Paul Scherrer Institute. Materials growth and characterization are supported by the NSF through the Princeton Center for Complex Materials (DMR-0819860) and Princeton University. M.Z.H. acknowledges additional support from the A. P. Sloan Foundation, an R. H. Dicke fellowship research grant and the Kavli Institute of Theoretical Physics at Santa Barbara.

Author Contributions D.H., Y.X. and D.Q. contributed equally to the experiment with the assistance of L.W. and M.Z.H.; D.G., Y.S.H. and R.J.C. provided critically important high quality single crystal samples; J.G.C. and N.P.O. performed the transport measurements; J.H.D., F.M., J.O., L.P. and A.V.F. provided beamline assistance; H.L. and A.B. carried out the theoretical calculations; M.Z.H. conceived the design to reach the topological transport regime and was responsible for the overall project direction, planning, and integration among different research units.

Author Information Reprints and permissions information is available at www.nature.com/reprints. Correspondence and requests for materials should be addressed to M.Z.H. (mzhasan@Princeton.edu).

METHODS

Spin-ARPES methods. Spin-integrated angle-resolved photoemission spectroscopy (ARPES³¹) measurements were performed with 29–100 eV linearly polarized photons on beam lines 12.0.1 and 7.0.1 at the Advanced Light Source in Lawrence Berkeley National Laboratory. All endstations were equipped with a Scienta hemispherical electron analyser (see VG Scienta manufacturer website (<http://www.vgscienta.com/>) for instrument specifications). Spin-resolved ARPES measurements were performed at the SIS beam line at the Swiss Light Source using the COPHEE spectrometer³² with two 40-kV classical Mott detectors and linearly polarized photons with energies of 20–22 eV. The COPHEE spectrometer is capable of measuring all three spatial components of the spin polarization vector for any point in reciprocal space, from which a spin-resolved band structure is constructed. The typical energy and momentum resolution was 15 meV and 1% of the surface Brillouin zone respectively at beam line 12.0.1, 50 meV and 2% of the surface Brillouin zone respectively at beam line 7.0.1, and 80 meV and 3% of the surface Brillouin zone respectively at SIS using a pass energy of 3 eV. Spin-integrated data were taken from single crystal Bi_{2–δ}Ca_δSe₃ and Bi₂Te₃ cleaved along its (111) surface in ultrahigh vacuum at pressures better than 5×10^{-11} torr and maintained at a temperature of 10 K unless otherwise specified. Spin-resolved data were collected at 50 K. Adsorption of NO₂ molecules on Bi_{2–δ}Ca_δSe₃ was achieved via controlled exposures to NO₂ gas (Matheson, 99.5%). The adsorption effects were studied under static flow mode by exposing the cleaved sample surface to the gas for a certain time then taking data after the chamber was pumped down to the base pressure. Spectra of the NO₂ adsorbed surfaces were taken within minutes of opening the photon shutter to minimize potential photon induced charge transfer and desorption effects.

Crystal growth methods. To grow single crystals of Bi_{2–δ}Ca_δSe₃, a mixture of elemental Bi (99.999%) and Se (99.999%) was first melted at 800 °C in a quartz tube for 16 h, then cooled to room temperature. Stoichiometric amounts of Ca pieces (99.8%) were then added to the mixture and reheated to 400 °C for 16 h. After an additional day of heating at 800 °C, the crystalline sample was cooled to 550 °C in 24 h. The sample was then annealed for 3 days at 550 °C followed by furnace-cooling to room temperature. Scanning tunnelling microscopy data¹⁶ has shown that Ca addition suppresses Se vacancies to a higher degree than the addition of excess Se alone. Large single crystals of Bi₂Te₃ were grown by melting stoichiometric mixtures of elemental Bi (99.999%) and Te (99.999%) at 800 °C overnight in a sealed vacuum quartz tube. The crystalline sample was cooled over a period of two days to 550 °C, and maintained at the temperature for 5 days. It was then furnace cooled to room temperature.

Sample quality characterization. X-ray diffraction measurements were used to check that the samples were single phase, and confirmed that the single crystals presented in this paper have a rhombohedral crystal structure with space group $D_{3d}^5(R\bar{3}m)$. The X-ray diffraction patterns of the cleaved crystals exhibit only the (*hhh*) peaks showing that the naturally cleaved surface is oriented along the trigonal (111) axis. Room temperature data were recorded on a Bruker D8 diffractometer using Cu K α radiation ($\lambda = 1.54$ Å) and a diffracted beam monochromator. The crystal structure of Bi₂(Te/Se)₃ can be visualized as a stack of hexagonal atomic layers, each consisting of only Bi or Te/Se. Five atomic layers are stacked in a close-packed f.c.c. fashion along the [111] direction in order Te/Se(1)-Bi-Te/Se(2)-Bi-Te/Se(1), in a quintuple layer, and cleavage takes place naturally between such layers. The topmost layer after cleavage is the Te/Se(1) layer as shown by scanning tunnelling microscopy data²⁴. Our ARPES results were reproducible over many different sample batches, although relaxation time scales may vary by up to 10 min and the magnitude of band bending may vary up to 50 meV. The in-plane crystal orientation was determined by Laue X-ray diffraction before insertion into an ultrahigh vacuum environment. Cleaving these samples *in situ* between 10 K and 300 K at chamber pressures less than 5×10^{-11} torr resulted in shiny flat surfaces.

Bulk transport measurements. Resistivity and Hall effect measurements were done in standard four-probe geometries with an AC applied current at 18 Hz. Current was applied in the *a*–*b* plane and magnetic field along the *c*-axis ([111] direction) for Hall effect measurements. Contacts were made with gold wire and silver paint, with resulting contact resistance less than 1 Ω. Measurements were done under vacuum pressures better than 10^{–6} torr.

Theoretical band calculation methods. The calculations were performed with the LAPW method in slab geometry using the WIEN2K package³³. Generalized gradient approximations³⁴ were used to describe the exchange–correlation potential. Spin–orbit coupling was included as a second variational step using scalar-relativistic eigenfunctions as basis. The surface was simulated by placing a slab of six quintuple layers in vacuum using optimized lattice parameters³⁵. A grid of 35 × 35 × 1 points were used in the calculations, equivalent to 120 *k*-points in the irreducible Brillouin zone and 2,450 *k*-points in the first Brillouin zone.

31. Hufner, S. *Photoelectron Spectroscopy* (Springer, 1995).
32. Hoesch, M. *Spin-polarized Fermi Surface Mapping*. PhD thesis, Univ. Zurich (2002).
33. Blaha, P. *et al.* *Computer Code WIEN2k* (Vienna University of Technology, 2001).
34. Perdew, J. P., Burke, K. & Ernzerhof, M. Generalized gradient approximation made simple. *Phys. Rev. Lett.* **77**, 3865–3868 (1996).
35. Wang, G. & Cagin, T. Electronic structure of the thermoelectric materials Bi₂Te₃ and Sb₂Te₃ from first-principles calculations. *Phys. Rev. B* **76**, 075201 (2007).

LETTERS

Topological surface states protected from backscattering by chiral spin texture

Pedram Roushan¹, Jungpil Seo¹, Colin V. Parker¹, Y. S. Hor², D. Hsieh¹, Dong Qian¹, Anthony Richardella¹, M. Z. Hasan¹, R. J. Cava² & Ali Yazdani¹

Topological insulators are a new class of insulators in which a bulk gap for electronic excitations is generated because of the strong spin–orbit coupling^{1–5} inherent to these systems. These materials are distinguished from ordinary insulators by the presence of gapless metallic surface states, resembling chiral edge modes in quantum Hall systems, but with unconventional spin textures. A key predicted feature of such spin-textured boundary states is their insensitivity to spin-independent scattering, which is thought to protect them from backscattering and localization. Recently, experimental and theoretical efforts have provided strong evidence for the existence of both two- and three-dimensional classes of such topological insulator materials in semiconductor quantum well structures^{6–8} and several bismuth-based compounds^{9–13}, but so far experiments have not probed the sensitivity of these chiral states to scattering. Here we use scanning tunnelling spectroscopy and angle-resolved photoemission spectroscopy to visualize the gapless surface states in the three-dimensional topological insulator $\text{Bi}_{1-x}\text{Sb}_x$ and examine in detail the influence of scattering from disorder caused by random alloying in this compound. We show that, despite strong atomic scale disorder, backscattering between states of opposite momentum and opposite spin is absent. Our observations demonstrate that the chiral nature of these states protects the spin of the carriers. These chiral states are therefore potentially useful for spin-based electronics, in which long spin coherence is critical¹⁴, and also for quantum computing applications, where topological protection can enable fault-tolerant information processing^{15,16}.

Angle-resolved photoemission spectroscopy (ARPES) experiments on the (111) surface of $\text{Bi}_{1-x}\text{Sb}_x$ crystals have been used to identify surface states within the bulk bandgap of these compounds^{9,10}. The shape of the Fermi surface for these states shows an odd number of band crossings between time-reversal invariant momentum points in the first Brillouin zone at the Fermi energy, which confirms the identification of $\text{Bi}_{1-x}\text{Sb}_x$ as a strong topological insulator for $x > 0.07$. The odd number of crossings protects the surface states from being gapped, regardless of the position of the chemical potential or the influence of non-magnetic perturbations⁴. Furthermore, spin-sensitive experiments have established that these surface states have a chiral spin structure and an associated Berry's phase¹⁰, which makes them distinct from ordinary surface states with strong spin–orbit coupling¹⁷. All these characteristics suggest that backscattering, or scattering between states of equal and opposite momentum, which results in Anderson localization in typical low-dimensional systems, will not occur for these two-dimensional carriers. Random alloying in $\text{Bi}_{1-x}\text{Sb}_x$, which is not present in other material families of topological insulators found to date, makes this material system an ideal candidate in which to examine the impact of disorder on topological surface states. However, to date there have been no experiments that have

probed whether these chiral two-dimensional states are indeed protected from spin-independent scattering.

We performed our experiments using a home-built cryogenic scanning tunnelling microscope (STM) that operates at 4 K in ultrahigh vacuum. Single-crystal samples of $\text{Bi}_{0.92}\text{Sb}_{0.08}$ were cleaved *in situ* in ultrahigh vacuum at room temperature before STM experiments at low temperatures. The topographic images of the sample are dominated by long wavelength (~ 20 Å) modulations in the local density of states (Fig. 1a). However, atomic corrugation can also be observed in the topography (Fig. 1a inset). Spectroscopic measurements show a general suppression of the density of states near the Fermi level, with spectra appearing for the most part homogeneously across the sample surface (Fig. 1b). ARPES measurements^{9,10} and recent band structure calculations¹³ suggest that within ± 30 meV of the Fermi level, where there is a bulk gap, tunnelling should be dominated by the surface states. While tunnelling spectroscopy measurements do not distinguish between bulk and surface states, energy-resolved spectroscopic maps (Fig. 2a–c) display modulations that are the result of scattering of the surface electronic states. As expected for the scattering and interference of surface states, the observed patterns are not commensurate with the underlying atomic structure. Although we do not have direct information on the identity of the scattering defects, the random distribution of substituted Sb atoms is a likely candidate.

Energy-resolved Fourier transform scanning tunnelling spectroscopy (FT-STS) can be used to reveal the wavelengths of the modulations in the local density of states and to obtain detailed information on the nature of scattering processes for the surface state electrons¹⁸. Previous studies on noble metal surface states^{18,19} and high-temperature superconductors²⁰ have established the link between modulation in the conductance at a wavevector \mathbf{q} and elastic scattering of quasi-particles and their interference between different momentum states (\mathbf{k}_1 and \mathbf{k}_2 , where $\mathbf{q} = \mathbf{k}_1 + \mathbf{k}_2$) at the same energy. The FT-STS maps shown in Fig. 2a–c insets for $\text{Bi}_{0.92}\text{Sb}_{0.08}$ display rich quasi-particle interference (QPI) patterns, which have the six-fold rotational symmetry of the underlying lattice, and evolve as a function of energy. These patterns display the allowed wavevectors \mathbf{q} and the relative intensities for the various scattering processes experienced by the surface state electrons.

Within a simple model of QPI, the interference wavevectors connect regions of high density of states on contours of constant energy (or the Fermi surface at the chemical potential). Therefore the QPI patterns should correspond to a joint density of states (JDOS) for the surface state electrons that can be independently determined from ARPES measurements^{20–23}. Figure 2d and e show contours of constant energy (CCE) in the first Brillouin zone, as measured with ARPES at two energies on $\text{Bi}_{0.92}\text{Sb}_{0.08}$ crystals (following procedures described in ref. 9). The CCE consist of an electron pocket centred on the $\bar{\Gamma}$ point, hole pockets half way to the \bar{M} point, and two electron pockets that occur very close to the \bar{M} point^{9,10}. From these measurements, we can

¹Joseph Henry Laboratories & Department of Physics, ²Department of Chemistry, Princeton University, Princeton, New Jersey 08544, USA.

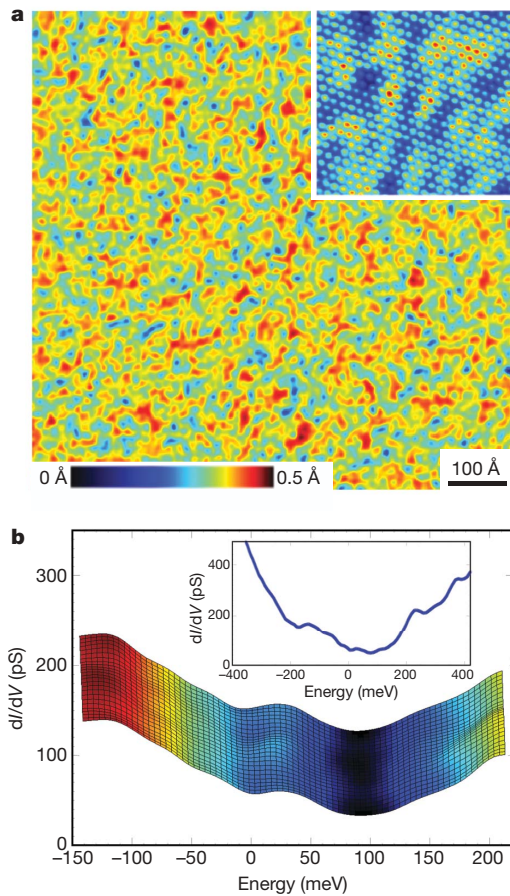


Figure 1 | STM topography and dI/dV spectroscopy of the $\text{Bi}_{0.92}\text{Sb}_{0.08}$ (111) surface. **a**, STM topograph (+50 meV, 100 pA) of the $\text{Bi}_{0.92}\text{Sb}_{0.08}$ (111) surface over an area $800 \text{ \AA} \times 800 \text{ \AA}$. The inset shows an area $80 \text{ \AA} \times 80 \text{ \AA}$ that displays the underlying atomic lattice (+200 mV, 15 pA). **b**, Spatial variation of the differential conductance (dI/dV) measurements across a line of length 250 Å. Inset, a typical differential conductance measurement over larger energy ranges.

determine the JDOS as a function of the momentum difference between initial and final scattering states, \mathbf{q} , using $\text{JDOS}(\mathbf{q}) = \int I(\mathbf{k})I(\mathbf{k}+\mathbf{q})d^2\mathbf{k}$, where $I(\mathbf{k})$ is the ARPES intensity that is

proportional to the surface states' density of states at a specific two-dimensional momentum \mathbf{k} . Figure 3a and d shows the results of computation of the JDOS from ARPES data for two different energies. Contrasting these figures to the corresponding QPI data in Fig. 3b and e, we find a significant suppression of the scattering intensity along the directions equivalent to $\bar{\Gamma}-\bar{M}$ in the first Brillouin zone. Backscattering between various electron and hole pockets around the $\bar{\Gamma}$ point should give rise to a continuous range of scattering wavevectors along the $\bar{\Gamma}-\bar{M}$ direction, a behaviour not observed in the data (see also the expanded view of the JDOS and QPI in Fig. 4a). This discrepancy suggests the potential importance of the surface states' spin texture and the possibility that spin rules are limiting the backscattering for these chiral electronic states.

To include spin effects, we use the results of spin-resolved ARPES studies and assign a chiral spin texture to the electron and hole pockets as shown in Fig. 2f. ARPES studies have resolved the spin structure only for the central electron pocket and the hole pockets near the $\bar{\Gamma}$ point in the first Brillouin zone; however, we assign a similar chiral structure for states near \bar{M} . This assignment is consistent with the presence of a π Berry's phase that distinguishes the spin topology of the $\text{Bi}_{0.92}\text{Sb}_{0.08}$ surfaces states from that of surface state bands that are simply split by spin-orbit coupling. In the latter case, the spin-polarized surface bands come in pairs, while for topological surface states there should be an odd number of spin-polarized states between two equivalent time-reversal points in the band structure^{1,2,11,13}.

To understand scattering and interference for these spin-polarized states, we determine the spin-dependent scattering probability, $\text{SSP}(\mathbf{q}) = \int I(\mathbf{k})T(\mathbf{q},\mathbf{k})I(\mathbf{k}+\mathbf{q})d^2\mathbf{k}$, which in similar fashion to the JDOS uses the ARPES-measured density of states, $I(\mathbf{k})$, but also includes a spin-dependent scattering matrix element $T(\mathbf{q},\mathbf{k})$. This matrix element describes the scattering probability as a function of momentum transfer and spins of states that are connected by the scattering process. Shown in Fig. 3c and f are the calculated $\text{SSP}(\mathbf{q})$ from ARPES data at two different energies using a matrix element of the form $T(\mathbf{q},\mathbf{k}) = |\langle \mathbf{S}(\mathbf{k}) | \mathbf{S}(\mathbf{k}+\mathbf{q}) \rangle|^2$. This simple form of spin-selective scattering reduces scattering between states with non-aligned spins and completely suppresses scattering between states with opposite spin orientations. Comparison of the SSP patterns to the QPI measurements in Fig. 3 shows that including spin effects leads to remarkably good agreement between the scattering wavevectors measured by STM and those expected from the shape of the surface CCE as measured by ARPES (features in the FT-STs and SSP

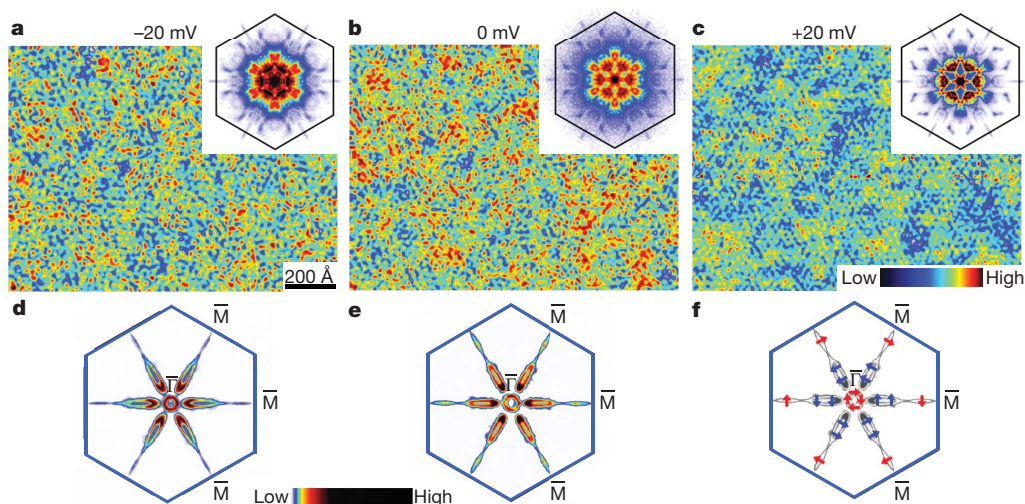


Figure 2 | dI/dV maps, QPI patterns and ARPES measurements on the $\text{Bi}_{0.92}\text{Sb}_{0.08}$ (111) surface. **a–c**, Spatially resolved conductance maps of the $\text{Bi}_{0.92}\text{Sb}_{0.08}$ (111) surface obtained at -20 mV (**a**), 0 mV (**b**) and $+20 \text{ mV}$ (**c**). (Panels show area $1,000 \text{ \AA} \times 1,300 \text{ \AA}$.) Insets, Fourier transforms of the dI/dV maps. The hexagons have the same size as the first Brillouin zone. The

Fourier transforms have been symmetrized in consideration of the three-fold rotation symmetry of the (111) surface. **d**, **e**, ARPES intensity map of the surface state at -20 mV (**d**) and at the Fermi level (**e**). **f**, The spin textures from ARPES measurements are shown with arrows, and high symmetry points are marked ($\bar{\Gamma}$ and three \bar{M}).

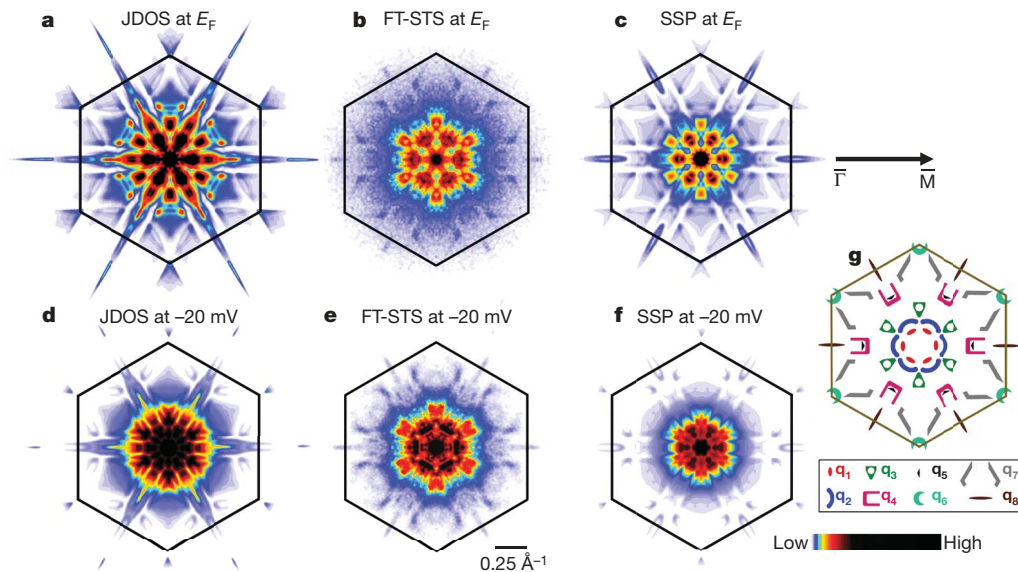


Figure 3 | Construction of JDOS and SSP from ARPES data and their comparison with FT-STs. **a**, The JDOS and SSP calculated at the Fermi energy (E_F), from ARPES data presented in Fig. 2e. **b**, The FT-STs at E_F . **c**, The SSP calculated at E_F . **d**, The JDOS calculated at -20 mV, from ARPES

at different wavevectors are categorized and given labels in Fig. 3g). A quantitative comparison between the QPI from the STM data and JDOS and SSP from ARPES data can be made by computing the cross-correlation between the various patterns. Focusing on the high-symmetry direction, which is shown in Fig. 4a, we find that the QPI (excluding the central $q = 0$ section, which is dominated by the disorder) is 95% correlated with the SSP in the same region. The cross-correlation is found to be 83% between the QPI and JDOS. Therefore, the proposed form of the spin-dependent scattering matrix element is the critical component for understanding the suppression of scattering along the high-symmetry directions in the data.

The proposed scattering matrix elements $T(\mathbf{q}, \mathbf{k})$ and associated spin-scattering rules are further confirmed by a more comprehensive analysis of the QPI patterns. An example of such an analysis is shown in Fig. 4, in which we associate features along the high-symmetry direction in the QPI and SSP with specific scattering wavevectors \mathbf{q} that connect various regions of the CCE. The observed wavevectors in QPI and SSP obey spin rules imposed by $T(\mathbf{q}, \mathbf{k})$, as illustrated schematically in Fig. 4b. We also depict in Fig. 4b examples of scattering processes that, while allowed by the band structure and observed in JDOS, violate the spin scattering rules and are not seen in QPI data in Fig. 4a. A comprehensive analysis of all the features in the QPI data (included in the Supplementary Information) demonstrates that the allowed set of scattering wavevectors \mathbf{q}_1 – \mathbf{q}_8 (Fig. 3g) exclude those that connect states with opposite spin. Finally, in Fig. 5, we show dispersion as a function of energy for some of the wavevectors \mathbf{q} in the QPI and compare their energy dispersion to that expected from ARPES results in the SSP. Remarkably, all the features of the complex QPI patterns and their energy dependence can be understood in detail by the allowed scattering wavevectors based on the band structure of the topological surface states and the spin scattering rule. This agreement provides a precise demonstration that scattering of electrons over thousands of ångströms, which underlies the QPI maps, strictly obeys the spin scattering rules and associated suppression of backscattering.

Other surface states with strong spin–orbit interaction may be expected to show evidence for spin-selective scattering; however, because spin states come in pairs, the QPI patterns can rarely probe these rules²⁴. In some situations there is evidence of such rules^{25,26}, but the precision with which scattering of surface states for $\text{Bi}_{0.92}\text{Sb}_{0.08}$ can be understood using spin-selective scattering is unprecedented.

data presented in Fig. 2d. **e**, The FT-STs at -20 mV. **f**, The SSP calculated at -20 mV. **g**, Schematization of the features associated with scattering wavevectors \mathbf{q}_1 – \mathbf{q}_8 in the FT-STs data.

Unusual scattering of chiral electronic states is also seen in monolayer graphene, where the underlying two-atom basis leads to a pseudospin index for quasi-particles and results in suppression of intravalley scattering^{27,28}. The key difference expected for surface states of a topological insulator is the degree to which they can tolerate disorder. This aspect is clearly demonstrated here for surface states of

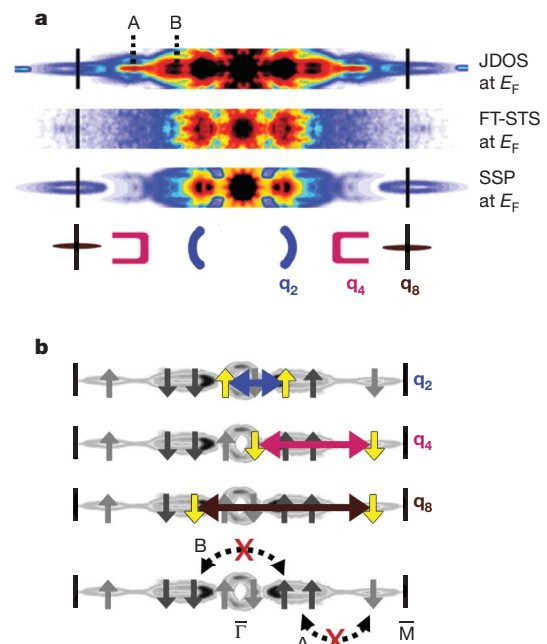


Figure 4 | Comparison of the various parts of the QPI patterns along the Γ – M direction at the Fermi energy. **a**, Close-up view of the QPI pattern from JDOS, FT-STs and SSP at E_F , along the Γ – M direction. The last row shows the schematic representation of \mathbf{q}_2 , \mathbf{q}_4 and \mathbf{q}_8 , which correspond to scatterings shown in **b**. Two high-intensity points which are only seen in JDOS are labelled as A and B. **b**, The Fermi surface along the Γ – M direction, with spin orientation of the quasi-particles shown with arrows. The horizontal colour-coded arrows show the sources of the scatterings seen in the STM data. Note that all highlighted spins have the same orientation. The bottom row depicts the scatterings which involve opposite spins and are present in JDOS, but absent in FT-STs and SSP.

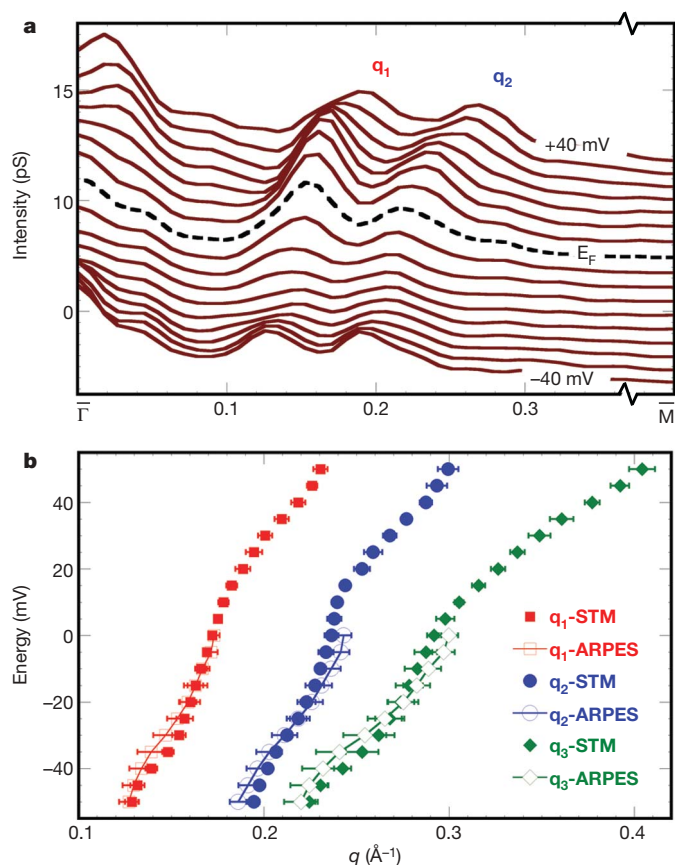


Figure 5 | Dispersion of various peaks from FT-STs and ARPES. **a**, The intensity of the FT-STs maps along the $\bar{\Gamma}$ – \bar{M} direction for various energies. The two peak positions correspond to q_1 and q_2 , which become larger with increasing in energy. Each curve is shifted by 0.6 pS for clarity. **b**, Dispersion of the position of q_1 , q_2 and q_3 from ARPES (open symbols) and STM (filled symbols). The data were obtained from fitting the peak in the intensity of the QPI patterns measured in STM, and calculated from the ARPES CCE. Each STM data point is the averaged value of six independent measurements, and the error bar represents one standard deviation. The systematic error was negligible.

$\text{Bi}_{0.92}\text{Sb}_{0.08}$, where strong alloying causes scattering for the surface state electrons yet the spin-selection scattering rules are strictly obeyed over length scales much longer than that set by the atomic scale disorder. Future experiments with magnetic scattering centres could further probe the spin scattering rules for topological surface states and may provide the setting for the manipulation of these spin-polarized states in device applications.

METHODS SUMMARY

The $\text{Bi}_{0.92}\text{Sb}_{0.08}$ single crystals were grown by melting stoichiometric mixtures of elemental Bi (99.999%) and Sb (99.999%) in 4-mm inner diameter quartz tubes. The samples were cooled over a period of two days, from 650 to 260 °C, and then annealed for a week at 260 °C. The samples were cleaved *in situ* in our home-built cryogenic STM that operates at 4 K in ultrahigh vacuum. The STM topographies were obtained in constant-current mode, and dI/dV spectroscopy was measured by a standard lock-in technique with frequency $f = 757$ Hz, and an a.c. modulation of 3 mV added to the bias voltage. The spatial resolution during the dI/dV mapping (I , current; V , voltage) was about 2 Å, which provided the capability to resolve k -vectors up to twice the first Brillouin zone in momentum space. The spin-resolved ARPES measurements were performed at the SIS beamline at the Swiss Light Source using the COPHEE spectrometer with a single 40 kV classical Mott detector and photon energies of 20 and 22 eV. The typical energy resolution was 80 mV, and momentum resolution was 3% of the surface Brillouin zone. The JDOS formula provides a map of all scatterings by calculating the self-convolution of a given CCE. While JDOS disregards the spin texture of a CCE, the SSP formula considers a weight factor for each possible scattering proportional to the square of the projection of the initial spin state onto the final state.

Full Methods and any associated references are available in the online version of the paper at www.nature.com/nature.

Received 13 May; accepted 21 July 2009.

Published online 9 August 2009.

- Kane, C. L. & Mele, E. J. Z_2 topological order and the quantum spin Hall effect. *Phys. Rev. Lett.* **95**, 146802 (2005).
- Moore, J. E. & Balents, L. Topological invariants of time-reversal-invariant band structures. *Phys. Rev. B* **75**, 121306(R) (2007).
- Fu, L. & Kane, C. L. Topological insulators with inversion symmetry. *Phys. Rev. B* **76**, 045302 (2007).
- Fu, L., Kane, C. L. & Mele, E. J. Topological insulators in three dimensions. *Phys. Rev. Lett.* **98**, 106803 (2007).
- Roy, R. On the Z_2 classification of quantum spin Hall models. Preprint at (<http://arxiv.org/abs/cond-mat/0604211v2>) (2006).
- Bernevig, B. A. & Zhang, S.-C. Quantum spin Hall effect. *Phys. Rev. Lett.* **96**, 106802 (2006).
- Bernevig, B. A., Hughes, T. L. & Zhang, S.-C. Quantum spin Hall effect and topological phase transition in HgTe quantum wells. *Science* **314**, 1757–1761 (2006).
- König, M. *et al.* Quantum spin Hall insulator state in HgTe quantum wells. *Science* **318**, 766–770 (2007).
- Hsieh, D. *et al.* A topological Dirac insulator in a quantum spin Hall phase. *Nature* **452**, 970–974 (2008).
- Hsieh, D. *et al.* Observation of unconventional quantum spin textures in topological insulators. *Science* **323**, 919–922 (2009).
- Teo, J. C. Y., Fu, L. & Kane, C. L. Surface states and topological invariants in three-dimensional topological insulators: application to $\text{Bi}_{1-x}\text{Sb}_x$. *Phys. Rev. B* **78**, 045426 (2008).
- Zhang, H. *et al.* Topological insulators in Bi_2Se_3 , Bi_2Te_3 and Sb_2Te_3 with a single Dirac cone on the surface. *Nature Phys.* **5**, 438–442 (2009).
- Zhang, H.-J. *et al.* Electronic structures and surface states of topological insulator $\text{Bi}_{1-x}\text{Sb}_x$. Preprint at (<http://arxiv.org/abs/0901.2762v2>) (2009).
- Wolf, S. A. *et al.* Spintronics: a spin-based electronics vision for the future. *Science* **294**, 1488–1495 (2001).
- Fu, L. & Kane, C. L. Superconducting proximity effect and Majorana fermions at the surface of a topological insulator. *Phys. Rev. Lett.* **100**, 096407 (2008).
- Leek, P. J. *et al.* Observation of Berry's phase in a solid-state qubit. *Science* **318**, 1889–1892 (2007).
- LaShell, S., McDougall, B. A. & Jensen, E. Spin splitting of an Au(111) surface state band observed with angle resolved photoelectron spectroscopy. *Phys. Rev. Lett.* **77**, 3419–3422 (1996).
- Petersen, L. *et al.* Direct imaging of the two-dimensional Fermi contour: Fourier-transform STM. *Phys. Rev. B* **57**, R6858–R6861 (1998).
- Crommie, M. F., Lutz, C. P. & Eigler, D. M. Imaging standing waves in a two-dimensional electron gas. *Nature* **363**, 524–527 (1993).
- Hoffman, J. E. *et al.* Imaging quasiparticle interference in $\text{Bi}_2\text{Sr}_2\text{CaCu}_2\text{O}_{8+\delta}$. *Science* **297**, 1148–1151 (2002).
- Wang, Q.-H. & Lee, D.-H. Quasiparticle scattering interference in high-temperature superconductors. *Phys. Rev. B* **67**, 20511 (2003).
- Markiewicz, R. S. Bridging k and q space in the cuprates: comparing angle-resolved photoemission and STM results. *Phys. Rev. B* **69**, 214517 (2004).
- McElroy, K. *et al.* Elastic scattering susceptibility of the high temperature superconductor $\text{Bi}_2\text{Sr}_2\text{CaCu}_2\text{O}_{8+\delta}$: a comparison between real and momentum space photoemission spectroscopies. *Phys. Rev. Lett.* **96**, 067005 (2006).
- Petersen, L. & Hedegård, P. A simple tight-binding model of spin-orbit splitting of sp -derived surface states. *Surf. Sci.* **459**, 49–56 (2000).
- Pascual, J. I. *et al.* Role of spin in quasiparticle interference. *Phys. Rev. Lett.* **93**, 196802 (2004).
- Kim, T. K. *et al.* Evidence against a charge density wave on Bi (111). *Phys. Rev. B* **72**, 085440 (2005).
- Brihuega, I. *et al.* Quasiparticle chirality in epitaxial graphene probed at the nanometer scale. *Phys. Rev. Lett.* **101**, 206802 (2008).
- Rutter, G. M. *et al.* Scattering and interference in epitaxial graphene. *Science* **317**, 219–222 (2007).

Supplementary Information is linked to the online version of the paper at www.nature.com/nature.

Acknowledgements We acknowledge K. K. Gomes and A. N. Pasupathy for suggestions about experimental procedure and initial analysis. This work was supported by grants from ONR, ARO, DOE, NSF-DMR and the NSF-MRSEC programme through the Princeton Center for Complex Materials. P.R. acknowledges an NSF graduate fellowship.

Author Contributions Y.S.H. and R.J.C. carried out the growth of the single crystals and characterized them; D.H., D.Q. and M.Z.H. performed the ARPES studies of the samples; STM measurements and data analysis were done by P.R., J.S., C.V.P., A.R. and A.Y.

Author Information Reprints and permissions information is available at www.nature.com/reprints. Correspondence and requests for materials should be addressed to A.Y. (yazdani@princeton.edu).

METHODS

Crystal growth. The $\text{Bi}_{0.92}\text{Sb}_{0.08}$ single crystals were grown by melting stoichiometric mixtures of elemental Bi (99.999%) and Sb (99.999%) in 4-mm inner diameter quartz tubes from a stoichiometric mixture of high purity elements. The samples were cooled over a period of two days, from 650 to 260 °C, and then annealed for a week at 260 °C. The obtained single crystals were confirmed to be single phase and identified as having the rhombohedral A7 crystal structure by X-ray powder diffraction using a Bruker D8 diffractometer with Cu K α radiation and a graphite diffracted beam monochromator.

STM measurement. We performed our experiments using a home-built cryogenic STM that operates at 4 K in ultrahigh vacuum. With our STM, we have examined several crystals of $\text{Bi}_{0.92}\text{Sb}_{0.08}$, grown under the same conditions, and we have not noticed any sample dependence for any of the results we presenting. The typical size of the crystals we used was 1 mm \times 1 mm \times 0.3 mm. Samples were cleaved *in situ* at room temperature in ultrahigh vacuum before STM experiments at low temperatures. The weak bonding between bilayers in this crystal makes the (111) surface the natural cleavage plane. A mechanically sharpened Pt–Ir alloy wire was used as an STM tip, and the quality of the tip apex was examined by scanning an atomically clean Ag(111) surface.

The STM topographies were obtained in constant-current mode, and dI/dV spectroscopy was measured by a standard lock-in technique with $f = 757$ Hz, an a.c. modulation of 3 mV added to the bias voltage, and the feedback loop disabled during the measurement. The spatial resolution during the dI/dV mapping was about 2 Å, which provides the capability to resolve k-vectors up to twice the first Brillouin zone in momentum space. The real space resolution also guarantees inclusion of atomic peaks in FT-STS maps, providing the most accurate calibration. In addition, the deviation of these atomic peaks from a perfect hexagon can be used as a measure of the thermal drift, which for the results presented was negligible, allowing us to symmetrize the FT-STS results without smearing out features or creating artificial ones.

ARPES measurements. High resolution ARPES and spin-resolved ARPES have been measured in different laboratories. High-resolution ARPES data have been

taken at beamlines 12.0.1 and 10.0.1 of the Advanced Light Source at the Lawrence Berkeley National Laboratory, as well as at the PGM beamline of the Synchrotron Radiation Center in Wisconsin, with photon energies ranging from 17 eV to 55 eV and energy resolutions ranging from 9 meV to 40 meV, and momentum resolution better than 1.5% of the surface Brillouin zone. Spin-integrated ARPES measurements were performed with 14 to 30 eV photons on beamline 5-4 at the Stanford Synchrotron Radiation Laboratory, and with 28 to 32 eV photons on beamline 12 at the Advanced Light Source, both endstations being equipped with a Scienta hemispherical electron analyser (see VG Scienta manufacturer website for instrument specifications; <http://www.vgscienta.com/>).

Spin-resolved ARPES measurements were performed at the SIS beamline at the Swiss Light Source using the COPHEE spectrometer with a single 40 kV classical Mott detector and photon energies of 20 and 22 eV. The typical energy and momentum resolution was 15 meV and 1.5% of the surface Brillouin zone respectively at beamline 5-4, 9 meV and 1% of the surface Brillouin zone respectively at beamline 12, and 80 meV and 3% of the surface Brillouin zone respectively at SIS using a pass energy of 3 eV.

JDOS and SSP calculation. Two plausible assumptions were considered for scattering between quasi-particles, spin independent (JDOS) and spin dependent scattering (SSP). The JDOS formula provides a map of all scatterings by calculating the self-convolution of a given CCE, and hence disregards the spin texture of a CCE. The SSP formula considers a weight factor for each possible scattering, proportional to the square of the projection of the initial spin state onto the final state. Therefore, vectors connecting quasi-particles of opposite spins do not contribute to the SSP mapping. The mean subtracted correlation of the FT-STS to the JDOS and SSP was calculated in a rectangular region starting 0.08 \AA^{-1} away from the $\bar{\Gamma}$ point and ending at \bar{M} , and of width 0.22 \AA^{-1} . The calculation of SSP using various subsets of the pockets of the Fermi surface enabled us to identify scattering processes which give rise to the various wavevectors (Supplementary Fig. 1). By using a gaussian fit to the peak of the intensity, we were able to follow the energy evolution of several wavevectors in the FT-STS maps (Fig. 5). A similar fitting procedure was applied to the ARPES intensity maps at fixed energies.

LETTERS

Demonstration of a spaser-based nanolaser

M. A. Noginov¹, G. Zhu¹, A. M. Belgrave¹, R. Bakker², V. M. Shalaev², E. E. Narimanov², S. Stout^{1,3}, E. Herz³, T. Suteewong³ & U. Wiesner³

One of the most rapidly growing areas of physics and nanotechnology focuses on plasmonic effects on the nanometre scale, with possible applications ranging from sensing and biomedicine to imaging and information technology^{1,2}. However, the full development of nanoplasmonics is hindered by the lack of devices that can generate coherent plasmonic fields. It has been proposed³ that in the same way as a laser generates stimulated emission of coherent photons, a 'spaser' could generate stimulated emission of surface plasmons (oscillations of free electrons in metallic nanostructures) in resonating metallic nanostructures adjacent to a gain medium. But attempts to realize a spaser face the challenge of absorption loss in metal, which is particularly strong at optical frequencies. The suggestion^{4–6} to compensate loss by optical gain in localized and propagating surface plasmons has been implemented recently^{7–10} and even allowed the amplification of propagating surface plasmons in open paths¹¹. Still, these experiments and the reported enhancement of the stimulated emission of dye molecules in the presence of metallic nanoparticles^{12–14} lack the feedback mechanism present in a spaser. Here we show that 44-nm-diameter nanoparticles with a gold core and dye-doped silica shell allow us to completely overcome the loss of localized surface plasmons by gain and realize a spaser. And in accord with the notion that only surface plasmon resonances are capable of squeezing optical frequency oscillations into a nanoscopic cavity to enable a true nanolaser^{15–18}, we show that outcoupling of surface plasmon oscillations to photonic modes at a wavelength of 531 nm makes our system the smallest nanolaser reported to date—and to our knowledge the first operating at visible wavelengths. We anticipate that now it has been realized experimentally, the spaser will advance our fundamental understanding of nanoplasmonics and the development of practical applications.

A spaser should have a medium with optical gain in close vicinity to a metallic nanostructure that supports surface plasmon oscillations³. To realize such a structure, we employed a modified synthesis technique for high-brightness luminescent core-shell silica nanoparticles^{19,20}

known as Cornell dots. As illustrated in Fig. 1a, the produced nanoparticles are composed of a gold core, providing for plasmon modes, surrounded by a silica shell containing the organic dye Oregon Green 488 (OG-488), providing for gain.

Transmission and scanning electron microscopy measurements give the diameter of the Au core and the thickness of the silica shell as ~ 14 nm and ~ 15 nm, respectively (Fig. 1b, c). The number of dye molecules per nanoparticle was estimated to be 2.7×10^3 , and the nanoparticle concentration in a water suspension was equal to $3 \times 10^{11} \text{ cm}^{-3}$ (Methods). A calculation of the spaser mode of this system (Fig. 1d) yields a stimulated emission wavelength of 525 nm and a quality (Q)-factor of 14.8 (Methods). We note that in gold nanoparticles as small as the ones used here, the Q -factor is dominated by absorption. But as we show below, the gain in our system is high enough to compensate the loss.

The extinction spectrum of a suspension of nanoparticles shown in Fig. 2 is dominated by the surface plasmon resonance band at ~ 520 nm wavelength and the broad short-wavelength band corresponding to interstate transitions between d states and hybridized s - p states of Au. The Q -factor of the surface plasmon resonance is estimated from the width of its spectral band as 13.2, in good agreement with the calculations. The spectra in Fig. 2 also illustrate that the surface plasmon band overlaps with both the emission and excitation bands of the dye molecules incorporated in the nanoparticles.

As illustrated in Fig. 3, the decay kinetics of the emission at 480 nm were non-exponential. Fitting the data with the sum of two exponentials resulted in two characteristic decay times, 1.6 ns and 4.1 ns. The absorption and emission spectra of OG-488 (Fig. 2) are nearly symmetrical to each other, as expected of dyes, and this allows us to assume that the peak emission cross-section, σ_{em} , is equal to the peak absorption cross-section, $\sigma_{\text{abs}} = 2.55 \times 10^{-16} \text{ cm}^2$, determined from the absorption spectrum of OG-488 in water at known dye concentration. With this value and using the known formula relating the strength and the width of the emission band with the radiative lifetime τ (see ref. 21 and Methods), we obtain an estimated radiative

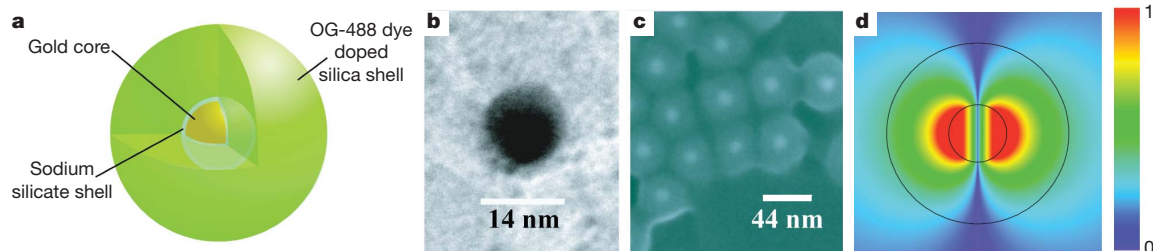


Figure 1 | Spaser design. **a**, Diagram of the hybrid nanoparticle architecture (not to scale), indicating dye molecules throughout the silica shell. **b**, Transmission electron microscope image of Au core. **c**, Scanning electron microscope image of Au/silica/dye core-shell nanoparticles. **d**, Spaser mode

(in false colour), with $\lambda = 525$ nm and $Q = 14.8$; the inner and the outer circles represent the 14-nm core and the 44-nm shell, respectively. The field strength colour scheme is shown on the right.

¹Center for Materials Research, Norfolk State University, Norfolk, Virginia 23504, USA. ²School of Electrical & Computer Engineering and Birck Nanotechnology Center, Purdue University, West Lafayette, Indiana 47907, USA. ³Materials Science and Engineering Department, Cornell University, Ithaca, New York 14850, USA.

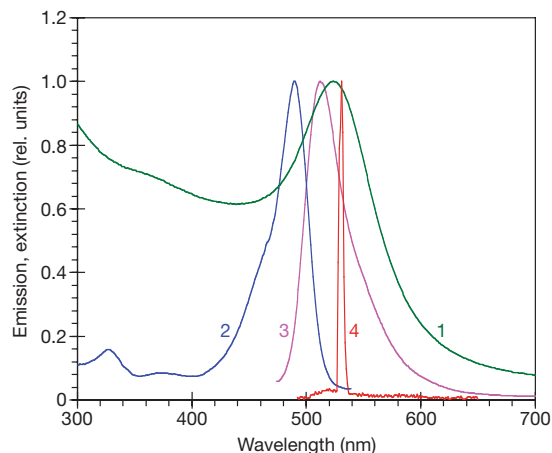


Figure 2 | Spectroscopic results. Normalized extinction (1), excitation (2), spontaneous emission (3), and stimulated emission (4) spectra of Au/silica/dye nanoparticles. The peak extinction cross-section of the nanoparticles is $1.1 \times 10^{-12} \text{ cm}^2$. The emission and excitation spectra were measured in a spectrofluorometer at low fluence.

lifetime of $\tau = 4.3 \text{ ns}$ that is very close to that of the slower component of the experimentally determined emission kinetics. We infer that the decay-time shortening (down to 1.6 ns) seen with the dye molecules in our effective plasmonic nanocavity can be explained by the Purcell effect²².

When the emission was detected in the spectral band $520 \pm 20 \text{ nm}$ (which encompasses the maximum of the emission and gain), it first decayed and then developed a second peak (Fig. 3) that is characteristic of the development of a stimulated emission pulse²³ and consistent with the spaser effect (see below). In fact, both the delay of the stimulated emission pulse relative to the pumping pulse and the oscillating behaviour of the stimulated emission (relaxation oscillations) are known in lasers^{23,24}; and because these phenomena do not depend on the nature of the oscillating mode, they are expected in spasers as well.

To study the stimulated emission, samples were loaded in cuvettes of 2 mm path length and pumped at wavelength $\lambda = 488 \text{ nm}$ with $\sim 5\text{-ns}$ pulses from an optical parametric oscillator lightly focused into a $\sim 2.4\text{-mm}$ spot. Whereas the emission spectra resembled those measured in the spectrofluorometer (Fig. 2) at weak pumping, a narrow peak appeared at $\lambda = 531 \text{ nm}$ (Fig. 4a) once the pumping energy exceeded a critical threshold value. Figure 4b gives the intensity of this peak as a function of pumping energy, yielding an input–output

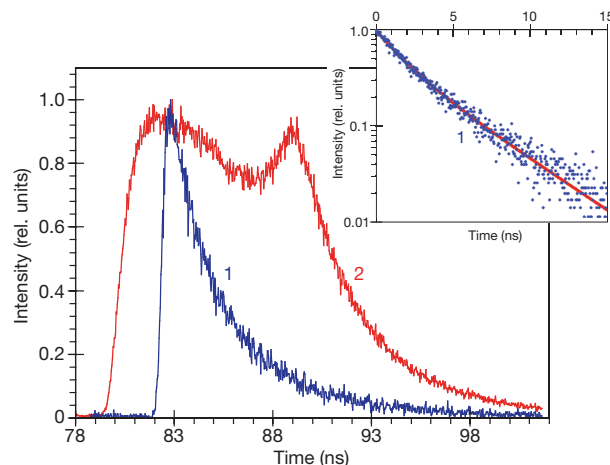


Figure 3 | Emission kinetics. Main panel, emission kinetics detected at 480 nm (1) and 520 nm (2). Inset, trace 1 plotted in semi-logarithmic coordinates (dots) and the corresponding fitting curve. The beginning of each emission kinetic trace coincides with the 90-ps pumping pulse.

curve with a pronounced threshold characteristic of lasers. The ratio of the intensity of this laser peak to the spontaneous emission background increased with increasing pumping energy (Fig. 4b inset). By analogy with lasers, the dramatic change of the emission spectrum above the threshold (from a broad band to a narrow line) suggests that the majority of excited molecules contributed to the stimulated emission mode. As expected, the laser-like emission occurred at a wavelength at which the dye absorption, as evidenced by the excitation spectrum, is practically absent while the emission and the surface plasmon resonance are strong (see Fig. 2).

Diluting the sample more than 100-fold decreased the emission intensity, but did not change the character of the spectral line (Fig. 4a inset) or diminish the ratio of stimulated emission intensity to spontaneous emission background. We conclude from this that the observed stimulated emission was produced by single nanoparticles, rather than being a collective stimulated emission effect in a volume of gain medium with the feedback supported by the cuvette walls.

The spontaneous emission intensity of a 0.235 mM aqueous solution of OG-488 dye was approximately 1,000 times stronger than that of the lasing nanoparticle sample. But under pumping, the dye solution did not show spectral narrowing or superlinear dependence of the emission intensity on pumping power. The dependence of the emission intensity on pumping power was in fact sublinear, which could be a result of dye photo-bleaching. This control result is further

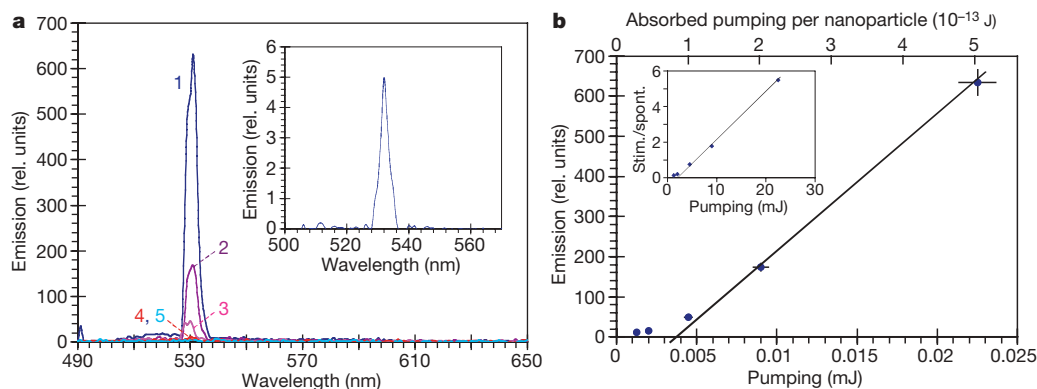


Figure 4 | Stimulated emission. **a**, Main panel, stimulated emission spectra of the nanoparticle sample pumped with 22.5 mJ (1), 9 mJ (2), 4.5 mJ (3), 2 mJ (4) and 1.25 mJ (5) 5-ns optical parametric oscillator pulses at $\lambda = 488 \text{ nm}$. **b**, Main panel, corresponding input–output curve (lower axis, total launched pumping energy; upper axis, absorbed pumping energy per nanoparticle); for most experimental points, $\sim 5\%$ error bars (determined

by the noise of the photodetector and the instability of the pumping laser) do not exceed the size of the symbol. Inset of **a**, stimulated emission spectrum at more than 100-fold dilution of the sample. Inset of **b**, the ratio of the stimulated emission intensity (integrated between 526 nm and 537 nm) to the spontaneous emission background (integrated at $<526 \text{ nm}$ and $>537 \text{ nm}$).

evidence that the stimulated emission occurs in individual hybrid Au/silica/dye nanoparticles, rather than in the macroscopic volume of the cuvette.

The diameter of the nanoparticle (hybrid Cornell dot) is 44 nm—too small to support visible stimulated emission in a purely photonic mode. But modelling of the system predicts that stimulated emission can occur in a much smaller surface plasmon mode if the number of excited dye molecules per nanoparticle exceeds 2.0×10^3 (Methods); this number is smaller than the number of OG-488 molecules available per nanoparticle in the experimental sample, which is $\sim 2.7 \times 10^3$. The pumping photon flux in our measurements ($\sim 10^{25} \text{ cm}^{-2} \text{ s}^{-1}$) exceeds the saturation level for OG-488 dye molecules ($\sim 10^{24} \text{ cm}^{-2} \text{ s}^{-1}$), so almost all the dye molecules were excited. The gain in the system was thus sufficiently large to overcome the overall loss, enabling the first experimental demonstration of a spaser, which we report here and regard as the central finding of the present work. But another important result is that the outcoupling of surface plasmon oscillations to photonic modes (facilitated by the radiative damping of the localized surface plasmon mode) constitutes a nanolaser that is realized by each individual nanoparticle, making it the smallest reported in the literature and the only one to date operating in the visible range.

The demonstrated phenomenon, involving resonant energy transfer from excited molecules to surface plasmon oscillations and stimulated emission of surface plasmons in a luminous mode, is consistent with the original theoretical proposal of a spaser³ and the more recent concept of a 'lasing spaser'²⁵, which share many common features despite their differences in detail. We note that this phenomenon is very different from that exploited in quantum cascade lasers²⁶, in which the surface plasmon mode (almost indistinguishable at the mid-infrared wavelength and the geometry of the experiment from the photonic transverse electromagnetic mode) is used as a guiding mode in an otherwise normal laser cavity. In contrast, in the reported spaser, the oscillating surface plasmon mode provides for feedback needed for stimulated emission of localized surface plasmons. The ability of the spaser to actively generate coherent surface plasmons could lead to new opportunities for the fabrication of photonic metamaterials, and have an impact on technological developments seeking to exploit optical and plasmonic effects on the nanometre scale.

METHODS SUMMARY

The Methods section presents a detailed discussion of the following experimental and theoretical studies: (1) synthesis and cleaning of hybrid Au/silica/dye nanoparticles, (2) theoretical modelling of the spaser effect in hybrid core-shell nanoparticles, (3) emission kinetics measurements, and (4) calculation of the radiative decay lifetime from the emission spectra.

Full Methods and any associated references are available in the online version of the paper at www.nature.com/nature.

Received 15 September 2008; accepted 24 July 2009.

Published online 16 August 2009.

1. Maier, S. A. *Plasmonics: Fundamentals and Applications* (Springer, 2007).

2. Brongersma, M. L. & Kik, P. G. (eds), *Surface Plasmon Nanophotonics* (Springer Series in Optical Sciences, Vol. 131, Springer, 2007).
3. Bergman, D. J. & Stockman, M. I. Surface plasmon amplification by stimulated emission of radiation: quantum generation of coherent surface plasmons in nanosystems. *Phys. Rev. Lett.* **90**, 027402 (2003).
4. Sudarkin, A. N. & Demkovich, P. A. Excitation of surface electromagnetic waves on the boundary of a metal with an amplifying medium. *Sov. Phys. Tech. Phys.* **34**, 764–766 (1989).
5. Nezhad, M. P., Tetz, K. & Fainman, Y. Gain assisted propagation of surface plasmon on planar metallic waveguides. *Opt. Express* **12**, 4072–4079 (2004).
6. Lawandy, N. M. Localized surface plasmon singularities in amplifying media. *Appl. Phys. Lett.* **85**, 5040–5042 (2004).
7. Noginov, M. A. et al. Enhancement of surface plasmons in an Ag aggregate by optical gain in a dielectric medium. *Opt. Lett.* **31**, 3022–3024 (2006).
8. Noginov, M. A. et al. The effect of gain and absorption on surface plasmons in metal nanoparticles. *Appl. Phys. B* **86**, 455–460 (2007).
9. Seidel, J., Grafstroem, S. & Eng, L. Stimulated emission of surface plasmons at the interface between a silver film and an optically pumped dye solution. *Phys. Rev. Lett.* **94**, 177401 (2005).
10. Noginov, M. A. et al. Compensation of loss in propagating surface plasmon polariton by gain in adjacent dielectric medium. *Opt. Express* **16**, 1385–1392 (2008).
11. Noginov, M. A. et al. Stimulated emission of surface plasmon polaritons. *Phys. Rev. Lett.* **101**, 226806 (2008).
12. Dice, G. D., Mujumdar, S. & Elezzabi, A. Y. Plasmonically enhanced diffusive and subdiffusive metal nanoparticle-dye random laser. *Appl. Phys. Lett.* **86**, 131105 (2005).
13. Popov, O., Zilbershtein, A. & Davidov, D. Random lasing from dye-gold nanoparticles in polymer films: enhanced gain at the surface-plasmon-resonance wavelength. *Appl. Phys. Lett.* **89**, 191116 (2006).
14. Kawasaki, M. & Mine, S. Novel lasing action in dye-doped polymer films coated on large pseudotubular Ag islands. *J. Phys. Chem. B* **110**, 15052–15054 (2006).
15. Muhlschlegel, P., Eisler, H.-J., Martin, O. J. F., Hecht, B. & Phol, D. W. Resonant optical antennas. *Science* **308**, 1607–1609 (2005).
16. Gordon, J. & Ziolkowski, R. W. The design and simulated performance of a coated nanoparticle laser. *Opt. Express* **15**, 2622–2653 (2007).
17. Noda, S. Seeking the ultimate nanolaser. *Science* **314**, 260–261 (2006).
18. Hill, M. T. et al. Lasing in metallic-coated nanocavities. *Nature Photon.* **1**, 563–564 (2007).
19. Enüstün, B. V. & Turkevich, J. Coagulation of colloidal gold. *J. Am. Chem. Soc.* **85**, 3317–3328 (1963).
20. Ow, H. et al. Bright and stable core-shell fluorescent silica nanoparticles. *Nano Lett.* **5**, 113–117 (2005).
21. Noginov, M. A. et al. Crystal growth and characterization of a new laser material, Nd:Ba₅(PO₄)₃Cl. *J. Opt. Soc. Am. B* **17**, 1329–1334 (2000).
22. Purcell, E. M. Spontaneous emission probabilities at radio frequencies. *Phys. Rev.* **69**, 681 (1946).
23. Noginov, M. A., Fowlkes, I., Zhu, G. & Novak, J. Neodymium random lasers operating in different pumping regimes. *J. Mod. Opt.* **51**, 2543–2553 (2004).
24. Svelto, O. *Principles of Lasers* 4th edn (Plenum, 1998).
25. Zheludev, N. I., Prosvirnin, S. L., Papasimakis, N. & Fedotov, V. A. Lasing spaser. *Nature Photon.* **2**, 351–354 (2008).
26. Sirtori, C. et al. Long-wavelength ($\lambda \approx 8\text{--}11.5 \mu\text{m}$) semiconductor lasers with waveguides based on surface plasmons. *Opt. Lett.* **23**, 1366–1368 (1998).

Acknowledgements The work was supported by NSF PREM grant DMR 0611430, NSF NCN (EEC-0228390), NASA URC (NCC3-1035), an ARO-MURI award (50342-PH-MUR) and a United States Army award (W911NF-06-C-0124). We thank M. I. Stockman for discussions, and J. Chen and J. Irudayaraj for the assistance with the kinetics measurements. S.S. was a member of the Summer Research Program at the Center for Materials Research, Norfolk State University.

Author Information Reprints and permissions information is available at www.nature.com/reprints. Correspondence and requests for materials should be addressed to M.A.N. (mnoginov@nsu.edu).

METHODS

Particle synthesis and cleaning. Gold cores with a thin sodium silicate shell were prepared according to previously published methods^{19,27} and transferred into a basic ethanol (1 μ l ammonium hydroxide per ml of ethanol) solution via dilution (1:4). Tetraethoxysilane was added (1 μ l per 10 ml of Stöber synthesis solution) to grow a thick silica shell. Ten microlitres of OG-488 isothiocyanate or maleimide (Invitrogen, dissolved to 4.56 mM concentration in dimethylsulphoxide), were conjugated to 3-isocyanatopropyltriethoxysilane (ICPTS) or 3-mercaptopropyltrimethoxysilane (MPTMS), respectively in a 1:50 molar ratio (dye:ICPTS or dye:MPTMS) in an inert atmosphere and added to the aforementioned 10 ml of Stöber synthesis solution. The particles were cleaned by centrifugation and resuspended in water. The concentration of nanoparticles in the suspension, approximately $3 \times 10^{11} \text{ cm}^{-3}$, was calculated from the gold wt% measurements provided by Elemental Analysis, Inc. The number of dye molecules per particle, 2.7×10^3 , was estimated on the basis of the known concentration of nanoparticles, the starting concentration of dye molecules used in the reaction, and the concentration of dye molecules which remained in the solution after the synthesis.

Theoretical model. To calculate the cold-cavity modes in the system, the structure is modelled as a spherical silica shell (refractive index of 1.46) with a gold core, whose frequency-dependent dielectric permittivity is taken from ref. 28 (Fig. 1a). The corresponding three-dimensional wave equation can be solved analytically using Debye potentials²⁹, which yields a sequence of localized plasmon modes with different values of total angular momentum ℓ and its projection m ($m = -\ell, \dots, 0, \dots, \ell$). The experimental wavelength range $\lambda \approx 530 \text{ nm}$ corresponds to the lowest frequency modes of this sequence, $\ell = 1$, which are triply degenerate ($m = -1, 0, 1$). This degeneracy (similar to that in the p state of the hydrogen atom³⁰) can be visualized in relation to a different direction of the mode 'axis' (Fig. 1d) and will be lifted by a deviation from spherical symmetry in the particle geometry. The resulting cold-cavity $\ell = 1$ mode wavelength (calculated with no fitting parameters) is 525 nm, and the Q -factor is 14.8 (where the primary contribution originates from the losses in the gold core).

For the active system, the gain is taken into account in the imaginary part of the refractive index of the silica shell, with the magnitude calculated using standard expressions of refs 24 and 29, and from the known value of the stimulated emission cross-section of OG-488 molecules and their density. In this approach, the

lasing threshold relates to the zero of the imaginary part of the mode frequency (corresponding to infinite lifetime). Assuming that the active molecules are uniformly distributed from the core to the diameter of 24 nm (in the 44-nm-diameter silica shell), we find that the stimulated emission requires $\sim 2,000$ active molecules.

Emission kinetics measurements. Emission decay kinetics were measured using a fluorescence lifetime imaging microscope (Microtime 200). The samples were excited at $\lambda = 466 \text{ nm}$ with $<90 \text{ ps}$ laser pulses at 40 MHz repetition rate. The emission was taken from the side of the pumping in an inverted microscope set-up (an immersion objective lens, a coverslip and a droplet of sample on the coverslip). The diameter and the depth of the focused laser beam were $0.24 \mu\text{m}$ and $1 \mu\text{m}$, respectively, and the pumping power density was $9.8 \times 10^5 \text{ W cm}^{-2}$ ($4.2 \times 10^4 \text{ W cm}^{-2}$) when the emission was detected in the $480 \pm 5 \text{ nm}$ ($520 \pm 20 \text{ nm}$) spectral band. The response time of the detector was shorter than 300 ps. The fit of the emission kinetics detected at 480 nm with the sum of two exponents resulted in $I(t) \propto a_1 \exp(-t/\tau_1) + a_2 \exp(-t/\tau_2)$, with $a_1 = 0.48$, $a_2 = 0.52$, $\tau_1 = 1.6 \text{ ns}$ and $\tau_2 = 4.1 \text{ ns}$. Given the experimental noise, the characteristic decay times are determined with $\pm 10\%$ accuracy.

The observation of the stimulated emission kinetics (Fig. 2, trace 2) from such a tiny volume, which can provide for only very small amplification, is additional proof of the spaser and nanolaser effects occurring in individual nanoparticles.

Radiative lifetime. Evaluation of the radiative lifetime from the emission spectra was performed using the known formula

$$\sigma_{\text{em}}(\lambda) = \frac{\lambda^5 I(\lambda)}{8\pi n^2 c \tau \int \lambda I(\lambda) d\lambda}$$

where λ is the wavelength, $I(\lambda)$ is the emission intensity, n is the index of refraction, and c is the speed of light.

27. Mulvaney, P., Liz-Marzan, L. M., Giersig, M. & Ung, T. Silica encapsulation of quantum dots and metal clusters. *J. Mater. Chem.* **10**, 1259–1270 (2000).
28. Johnson, P. B. & Christy, R. W. Optical constants of the noble metals. *Phys. Rev. B* **6**, 4370–4379 (1972).
29. Born, M. & Wolf, E. *Principles of Optics* 6th edn (Cambridge Univ. Press, 1998).
30. Landau, L. D. & Lifshits, E. M. *Quantum Mechanics: Non-Relativistic Theory* (Pergamon, 1977).

2,000-year-long temperature and hydrology reconstructions from the Indo-Pacific warm pool

Delia W. Oppo¹, Yair Rosenthal² & Braddock K. Linsley³

Northern Hemisphere surface temperature reconstructions suggest that the late twentieth century was warmer than any other time during the past 500 years and possibly any time during the past 1,300 years (refs 1, 2). These temperature reconstructions are based largely on terrestrial records from extra-tropical or high-elevation sites; however, global average surface temperature changes closely follow those of the global tropics³, which are 75% ocean. In particular, the tropical Indo-Pacific warm pool (IPWP) represents a major heat reservoir that both influences global atmospheric circulation⁴ and responds to remote northern high-latitude forcings^{5,6}. Here we present a decadal resolved continuous sea surface temperature (SST) reconstruction from the IPWP that spans the past two millennia and overlaps the instrumental record, enabling both a direct comparison of proxy data to the instrumental record and an evaluation of past changes in the context of twentieth century trends. Our record from the Makassar Strait, Indonesia, exhibits trends that are similar to a recent Northern Hemisphere temperature reconstruction². Reconstructed SST was, however, within error of modern values from about AD 1000 to AD 1250, towards the end of the Medieval Warm Period. SSTs during the Little Ice Age (approximately AD 1550–1850) were variable, and ~ 0.5 to 1°C colder than modern values during the coldest intervals. A companion reconstruction of $\delta^{18}\text{O}$ of sea water—a sea surface salinity and hydrology indicator—indicates a tight coupling with the East Asian monsoon system and remote control of IPWP hydrology on centennial–millennial timescales, rather than a dominant influence from local SST variation.

The IPWP is the largest reservoir of warm surface water on the Earth and the main source of heat for the global atmosphere. Small variations in SST of the IPWP influence the location and strength of convection in the rising limb of the Hadley and Walker circulations, and can thus perturb planetary-scale atmospheric circulation and influence tropical hydrology⁴. However, tropical hydrology is also responsive to high-latitude temperature change^{5,6}. Recent work suggests that SST of the IPWP has varied during the past millennium, with colder SSTs during the peak of the Little Ice Age (LIA) than during the preceding centuries⁷. However, no millennial-length SST reconstructions from the IPWP capture the complete warming out of the LIA or extend into the instrumental era to allow a direct comparison with instrumental data. Therefore, the amplitude of reconstructed SST variations in the context of modern SSTs is still uncertain. Whereas conventional sediment corers—gravity and piston corers—often disturb surface and latest Holocene sediments, multi-corers are lowered gently into ocean sediment and recover the sediment–water interface undisturbed, together with about a half-metre of underlying sediment. Combining records from multi-corers and gravity or piston cores enables the reconstruction of long records that overlap the instrumental record.

We worked on multi-core BJ8-03-31MCA ('31MC') and gravity cores BJ8-03-32GGC ('32GGC') and BJ8-03-34GGC ('34GGC'), recovered from the Makassar Strait, on the Sulawesi margin (Fig. 1). We also use published data from nearby piston core MD98-2160⁷ ('MD60'). Mean annual SSTs in our study area averaged $\sim 29.3^\circ\text{C}$ from 1997 to 2007 (ref. 8) with coldest SSTs (averaging $\sim 28.5^\circ\text{C}$) from July through to the end of September (JAS), the upwelling season. SSTs decrease during El Niño events^{4,8}. Seasonally, surface waters are freshest in boreal winter, when SST is warmest, owing to the combined influence of the northwest monsoon/intertropical convergence zone rainfall^{9,10} and advection of low salinity waters to the site by surface currents (Supplementary Discussion). Boreal summer precipitation is reduced during El Niño events, but rainy season precipitation is unaffected¹⁰. The mean annual weighted $\delta^{18}\text{O}_{\text{ppt}}$ is close to the boreal winter value (about -7‰ versus approximately -4‰ in boreal summer¹¹), reflecting intense vertical convection and heavy rainfall¹². Sediment core chronologies

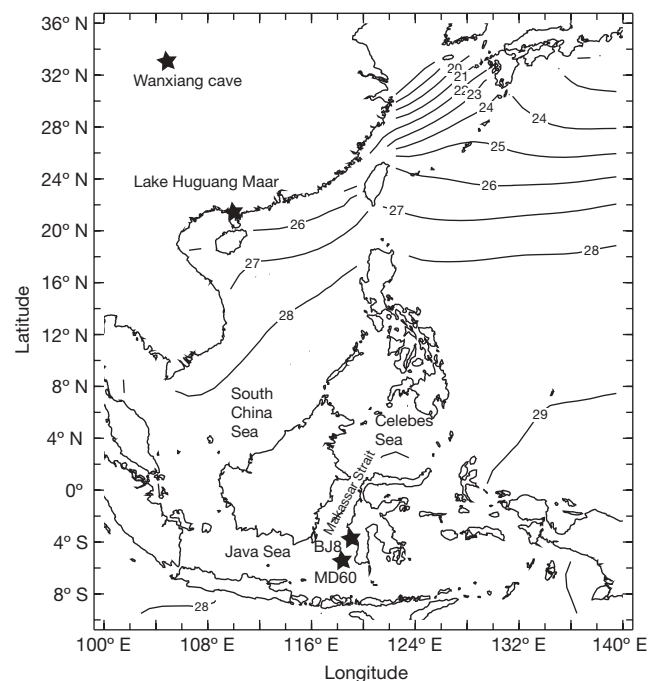


Figure 1 | Mean annual SST of the IPWP. Shown (stars) are locations of sediment cores as follows: multi-core BJ8-03-31MCA (459 m), and gravity cores BJ8-03-34GGC (503 m) and BJ8-03-32GGC (454 m), all at $3^\circ 53' \text{S}$, $119^\circ 27' \text{E}$ ('BJ8'), and piston core MD98-2160 ($5^\circ 12' \text{S}$, $117^\circ 29' \text{E}$, 1,185 m, 'MD60'). Locations of Lake Huguang Maar and Wanxiang cave are also shown (stars). Temperature data from ref. 29.

¹Department of Geology and Geophysics, Woods Hole Oceanographic Institution, Woods Hole, Massachusetts 02543, USA. ²Institute of Marine and Coastal Sciences, and Department of Earth and Planetary Sciences, Rutgers, The State University, New Brunswick, New Jersey 08901, USA. ³Department of Atmospheric and Environmental Sciences, University at Albany–State University of New York, Albany, New York 12222, USA.

are based on ^{210}Pb (31MC), radiocarbon dating, and a correlation to the AD 1815 Mount Tambora ash tentatively identified in MD60⁷ (Supplementary Methods). High sediment accumulation rates ($\sim 100\text{--}200\text{ cm kyr}^{-1}$) enable decadal-scale resolution. To reconstruct $\delta^{18}\text{O}$ of sea water (SST and $\delta^{18}\text{O}_{\text{sw}}$), we generated Mg/Ca and $\delta^{18}\text{O}$ data on the planktonic foraminifera, *Globigerinoides ruber* (sensu stricto morphotype), which inhabits the surface mixed layer (Methods). Sediment trap data indicate that in the tropics, the seasonal preference of *G. ruber* varies among locations, ranging from a cold season (upwelling) preference to a warm season preference^{13–15} (Supplementary Discussion).

We converted Mg/Ca to SST using a calibration, $\text{Mg/Ca} = 0.38\exp(0.09\text{SST})$, based on seasonal Mg/Ca variations in multiple species of planktonic foraminifera from Sargasso Sea sediment trap samples¹⁶ (Fig. 2a). Our reconstructed SSTs generally fall between historical mean annual and JAS SSTs (the National Oceanic and Atmospheric Administration extended SST reconstruction⁸, ERSSTv3; Fig. 2), suggesting that the seasonal flux of *G. ruber* to the sediment (*G. ruber* seasonality) in our study area varied through time, with a greater flux to the sediment in JAS during cooler periods (for example, around AD 1900–50) relative to warm periods, when reconstructed SSTs approach the annual mean.

We applied the Mg/Ca–SST calibration¹⁶ to data from all four cores (Fig. 2b). Following previous studies^{7,17–19}, we also reconstructed

$\delta^{18}\text{O}_{\text{sw}}$ from the $\delta^{18}\text{O}$ of *G. ruber* (Supplementary Data) and our SST estimates (Fig. 2c). The SST reconstruction shows cooler temperatures between about AD 400 and AD 950 than during much of the so-called Medieval Warm Period (about AD 900–1300), a warm period found in many northern high-latitude records but whose global significance is uncertain¹. A gradual SST decrease began at about AD 1300, and culminated at about AD 1700, within the peak of the LIA. Subsequent warming was interrupted by two multi-decadal cold periods, one towards the end of the LIA and one during the early twentieth century. Each was nearly as cold as the coldest LIA peak.

At face value, our reconstruction suggests that peak LIA SSTs were $\sim 1^\circ\text{C}$ and 1.5°C colder than late twentieth century JAS and mean annual SST, respectively. Given the possibility raised by our comparison of reconstructed SST to the instrumental record (Fig. 2a) that the flux of *G. ruber* to the sediment was higher in JAS during the LIA than at present, we favour a conservative interpretation that JAS surface waters were $\sim 1^\circ\text{C}$ colder than late twentieth century JAS SSTs. Considering that from 1856 to 2007⁸, the amplitude of mean annual SST variability averaged $\sim 70\%$ of the amplitude of JAS SSTs variability (Supplementary Discussion), we infer that mean annual SSTs were ~ 0.5 to 1°C colder than the late twentieth century.

Reconstructed SSTs were warmest from AD 1000 to AD 1250 and during short periods of first millennium (Fig. 2b). Given the evidence that *G. ruber* tends to record near mean annual SSTs during warm intervals of the last 150 years (Fig. 2a), reconstructed SSTs during these warm periods probably reflect mean annual SSTs. If this is the case, as we suspect, then SSTs within error of modern SSTs occurred in the IPWP during the Medieval Warm Period and during brief periods of the first millennium AD. If, on the other hand, *G. ruber* calcified preferentially during the JAS upwelling season throughout the study interval, then JAS SSTs as warm as modern also characterized the previous millennium. Regardless of *G. ruber* seasonality in this region, the reconstruction suggests that at least during the Medieval Warm Period, and possibly the preceding 1,000 years, Indonesian SSTs were similar to modern SSTs.

To estimate errors and facilitate comparison to other records, we developed composite records (Fig. 3; Methods Summary). Our averaging scheme reduces the amplitude of the records, but preserves only the most robust features. Considering the age uncertainties in our reconstruction, long-term SST trends are similar to those in Northern Hemisphere temperature reconstructions, especially the 'NH land error-in-variables (EIV) composite'² ($r^2 = 0.5$, $P < 0.00001$; Fig. 3a), consistent with the instrumental record, which suggests that Indonesian SST is correlated to global SST and air temperature on multi-decadal and longer timescales (Supplementary Notes). (Here NH indicates Northern Hemisphere.) Contrary to the Indonesia SST reconstruction, however, the Northern Hemisphere temperature reconstruction does not estimate temperatures as warm as modern at any time during the past two millennia. The hemispheric and global temperature difference between the early AD 1900s and the modern era is similar to the difference in mean annual SST at our core site (Supplementary Notes), so the greater amplitude of Makassar Strait SST than Northern Hemisphere temperature variability (note different axis scaling in Fig. 3a) may be related to the hypothesized changes in *G. ruber* seasonality. We note that the high-amplitude variations resulting from these hypothesized changes in *G. ruber* seasonality also preclude accurate estimates of the rates of SST change in the past and a meaningful comparison to the rate of SST increase during the past decade.

Long-term $\delta^{18}\text{O}_{\text{sw}}$ trends are also similar to Northern Hemisphere temperature trends ($r^2 = 0.3$, $P < 0.0001$) with the lowest values during the coldest peak of the LIA (Fig. 3b). The $\delta^{18}\text{O}_{\text{sw}}$ decrease that began at about AD 1300 was linked to gradual Northern Hemisphere and IPWP cooling, and the subsequent increase in $\delta^{18}\text{O}_{\text{sw}}$ values associated with nineteenth- and twentieth-century warming. This general trend of increasing $\delta^{18}\text{O}_{\text{sw}}$ was punctuated by two multi-decadal $\delta^{18}\text{O}_{\text{sw}}$ minima, each with slightly higher $\delta^{18}\text{O}_{\text{sw}}$ values. By

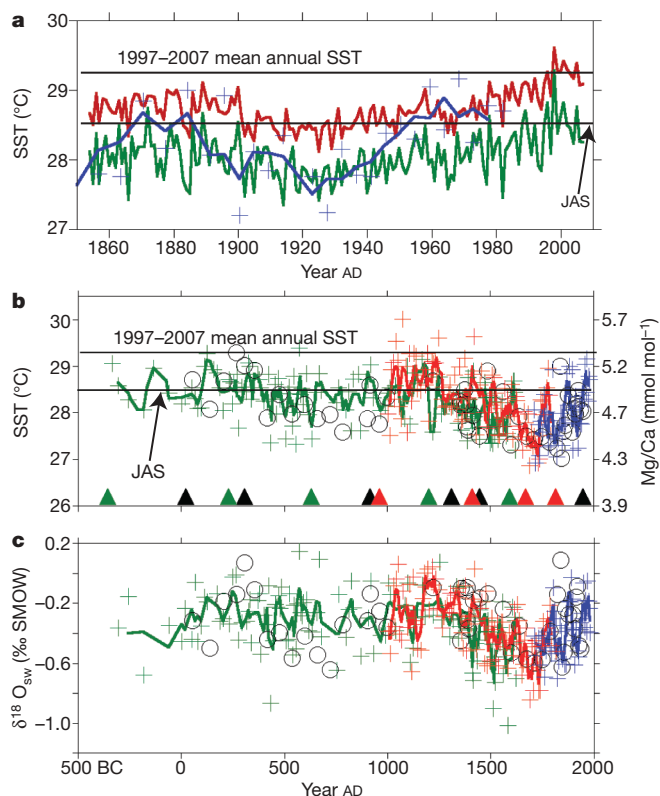


Figure 2 | Sea surface temperature and $\delta^{18}\text{O}_{\text{sw}}$ reconstructions. **a**, ERSSTv3⁸ mean annual (red line) and JAS (green line) SST reconstructions based on the instrumental record for the grid box containing the BJ8 core sites. Blue line, Mg/Ca-based SST estimates using a published calibration¹⁶. Crosses, Mg/Ca-based SST estimates. Lines are three-point running means. **b**, Downcore SST, and **c**, $\delta^{18}\text{O}_{\text{sw}}$ reconstructions (31MC, blue crosses; MD60, red crosses; 34GGC, green crosses; 32GGC black circles). Colour-coded lines are three-point running means. Upper and lower horizontal lines in **a** and **b** are modern (1997–2007) mean annual and JAS SST⁸ at the BJ8 core sites, respectively. Colour-coded triangles in **b** denote radiocarbon age control, except for the most recent red triangle, which denotes the Mt Tambora ash, tentatively identified in MD60 (Supplementary Notes). $\delta^{18}\text{O}_{\text{sw}}$ values are relative to Vienna Standard Mean Ocean Water (VSMOW).

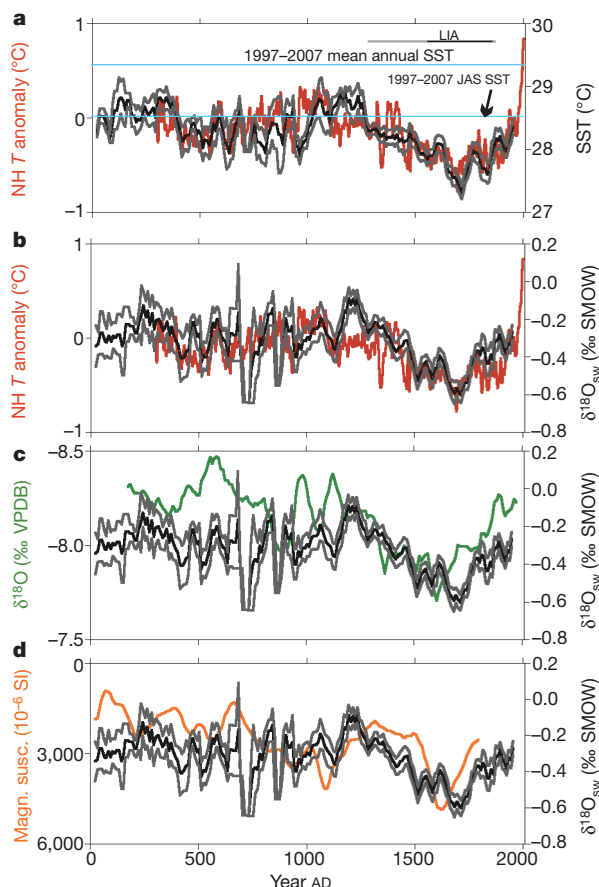


Figure 3 | Comparison of composite Indonesia records to hemispheric and regional records. **a**, Composite SST and **b**, $\delta^{18}\text{O}_{\text{sw}}$ records (black) versus Northern Hemisphere land EIV composite temperature (T) anomaly² (red). **c**, Composite $\delta^{18}\text{O}_{\text{sw}}$ record (black) versus $\delta^{18}\text{O}$ of Wanxiang cave, a summer monsoon record²³ (green) and **d**, Lake Huguang Maar magnetic susceptibility, a winter monsoon record²⁴ (orange). Upper and lower horizontal lines in **a** are modern (1997–2007) mean annual and JAS SST⁸ at the BJ8 core sites, respectively. Composite records were developed by averaging data in 10-year overlapping, 50-year-long bins. Error bars (grey), ± 1 standard error of data in each bin. Wanxiang cave and Lake Huguang Maar data were also averaged in 10-year overlapping 50-year bins for clarity. The approximate time interval of the Little Ice Age (LIA) is denoted by the horizontal bar in **a**.

analogy with the seasonality of modern precipitation^{9,10}, of $\delta^{18}\text{O}_{\text{ppt}}$ values^{11,12}, and of surface currents (Supplementary Discussion), the low $\delta^{18}\text{O}_{\text{sw}}$ values indicate that the Indonesian rainfall regime from about AD 1500 to AD 1900 was more boreal winter-like (stronger boreal winter, weaker boreal summer monsoon) than the preceding centuries.

Additional proxy evidence, discussed below, that the boreal summer monsoon was weaker during the LIA than during the Medieval Warm Period suggests that the colder surface waters implied by our record were not caused by greater monsoon-driven upwelling. El Niño events, as recorded in lake sediments from high-altitude Ecuador²⁰ and Galapagos²¹, may have been subdued during the LIA, suggesting that neither a higher frequency/greater intensity of El Niño events nor a more El Niño-like mean Pacific state caused cold LIA SSTs. Rather, cooling of North Pacific surface water, which enters the southern Makassar Strait in boreal winter via the South China Sea/Java Sea pathway to the west^{4,22}, is the likely proximal cause of LIA cooling.

Our interpretation of a more winter-like rainfall regime during the LIA is substantiated by records from Wanxiang cave, subtropical China²³ ($r^2 = 0.2$, $P \ll 0.0001$) and Lake Huguang Maar, coastal southeast China²⁴ ($r^2 = 0.1$, $P \ll 0.0001$) (Fig. 3c and d), which indicate weaker summer and stronger winter Asian monsoons, respectively, during the LIA. Low Indian summer monsoon rainfall²⁵ also corresponds to low $\delta^{18}\text{O}_{\text{sw}}$ (greater Indonesian rainfall) on

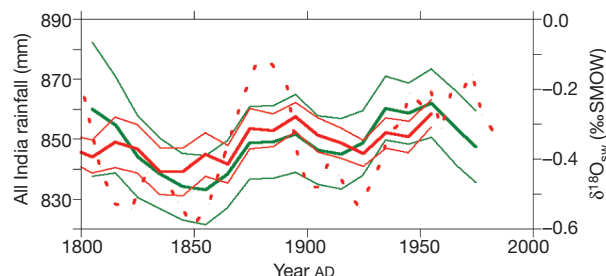


Figure 4 | Comparison of Indonesian $\delta^{18}\text{O}_{\text{sw}}$ and Indian rainfall. Red dashed line, 31MC $\delta^{18}\text{O}_{\text{sw}}$ three-point running mean; red solid lines, composite $\delta^{18}\text{O}_{\text{sw}}$ record (thick line) with ± 1 standard error (thin lines); green, All India Rainfall index²⁵, 10-year overlapping, 50-year long bins (thick line), with ± 1 standard error (thin lines).

multi-decadal timescales (Fig. 4) ($r^2 = 0.6$, $P < 0.0005$). These results, suggesting alternating precipitation maxima in the Northern Hemisphere Asian monsoon regions and over Indonesia, add to a growing body of evidence that monsoon/intertropical convergence zone variations profoundly influenced the tropical hydrology of the past two millennia^{7,23,24,26,27}.

Modern observations and modelling studies indicate that small changes in IPWP SSTs strongly influence the global hydrologic cycle⁴. For example, cooler SSTs in some areas of the IPWP might dampen intense deep atmospheric convection, reducing global precipitation²⁸. However, our finding that $\delta^{18}\text{O}_{\text{sw}}$ was lowest (and by inference, net regional precipitation greatest) when SSTs were cold—during the LIA (Fig. 3) and the early AD 1900s (Fig. 4)—suggests that on multi-decadal through to millennial timescales, IPWP precipitation anomalies are not driven by local SST anomalies, but are remotely forced by the Asian monsoon/intertropical convergence zone.

METHODS SUMMARY

$\delta^{18}\text{O}$ and Mg/Ca were collected on *G. ruber* in the 212–250 μm and 250–300 μm size-fraction, respectively. $\delta^{18}\text{O}$ was measured at WHOI on a Finnigan MAT253 stable isotope mass spectrometer with the Kiel III Carbonate Device. Long-term precision of $\delta^{18}\text{O}$ measurements of standards is 0.07‰. Mg/Ca measurements were made at Rutgers Inorganic Analytical Laboratory using a sector field inductively coupled plasma mass spectrometer (Thermo Element XR). Additional details, including interlaboratory offsets and corrections, are discussed in Methods.

To construct composite records, we binned data from all four cores in 10-year-overlapping 50-year-long bins. We estimated errors in two ways. First, we took the standard error of the SST or $\delta^{18}\text{O}_{\text{sw}}$ in each 50-year bin (grey lines in Fig. 3). Second, we estimated errors by dividing the standard error in the SST and $\delta^{18}\text{O}_{\text{sw}}$ estimate by the square root of the number of data points in each bin. The standard error in the SST calibration is 0.16 °C. The standard error of the $\delta^{18}\text{O}_{\text{sw}}$ is a function of the error in both $\delta^{18}\text{O}$ of calcite and the error in SST. Assuming greater variance for geological samples than standards, we use a 0.2‰ standard deviation for the $\delta^{18}\text{O}$ of calcite, and knowing the standard error in the SST calibration, a standard error of 0.24‰ is estimated for $\delta^{18}\text{O}_{\text{sw}}$. The two methods gave similar error estimates for SST, but the second method (data not shown; <http://www.ncdc.noaa.gov/paleo/>) often suggests larger errors for $\delta^{18}\text{O}_{\text{sw}}$.

To estimate correlation coefficients and P values for the records shown on Figs 3 and 4, we linearly regressed data from each of the two records, already averaged within 10-year-overlapping 50-year-long bins.

Received 6 December 2008; accepted 15 June 2009.

- Jansen, E. et al. in *Climate Change 2007: The Physical Science Basis* (eds Solomon, S. et al.) 466–482 (Cambridge Univ. Press, 2007).
- Mann, M. E. et al. Proxy-based reconstructions of hemispheric and global surface temperature variations over the past two millennia. *Proc. Natl Acad. Sci. USA* **105**, 13252–13257 (2008).
- National Research Council. *Surface Temperature Reconstructions for the Last 2,000 Years* (National Academy Press, 2006); available at (http://www.nap.edu/catalog.php?record_id=11676).
- Qu, T., Du, Y., Strachan, J., Meyers, G. & Slingo, J. Sea surface temperature and its variability in the Indonesian region. *Oceanography* **18**, 50–61 (2005).
- Broccoli, A. J., Dahl, K. A. & Stouffer, R. J. Response of the ITCZ to northern hemisphere cooling. *Geophys. Res. Lett.* **33**, doi:10.1029/2005GL024546 (2006).

6. Chiang, J. C. H. & Bitz, C. M. Influence of high latitude ice cover on the marine Intertropical Convergence Zone. *Clim. Dyn.* **25**, 477–496 (2005).
7. Newton, A., Thunell, R. & Stott, L. Climate and hydrologic variability in the Indo-Pacific Warm Pool during the last Millennium. *Geophys. Res. Lett.* **33**, L19710, doi:10.1029/2006GL0273234 (2006).
8. Smith, T. M., Reynolds, R. W., Peterson, T. C. & Lawrimore, J. Improvements to NOAA's historical merged land-ocean surface temperature analysis (1880–2006). *J. Clim.* **21**, 2283–2296 (2008).
9. Xie, P. & Arkin, P. A. Analyses of global monthly precipitation using gauge observations, satellite estimates, and numerical model predictions. *J. Clim.* **9**, 840–858 (1996).
10. Aldrian, E. & Susanto, R. D. Identification of three dominant rainfall regions within Indonesia and their relationship to sea surface temperature. *Int. J. Clim.* **23**, 1435–1452 (2003).
11. International Atomic Energy Agency/World Meteorological Organization. GNIP programme: resources. (http://www-naweb.iaea.org/naweb/ih/GNIP/IHS_GNIP.html) (2006).
12. Vuille, M., Werner, M., Bradley, R. S. & Keimig, F. Stable isotopes in precipitation in the Asian monsoon region. *J. Geophys. Res.* **110**, D23108, doi:10.1029/2005JD006022 (2005).
13. Kawahata, H., Nishimura, A. & Gagan, M. Seasonal change in foraminiferal production in the western equatorial Pacific warm pool: evidence from sediment trap experiments. *Deep-Sea Res. II* **49**, 2783–2801 (2002).
14. Mohtadi, M. *et al.* Low-latitude control on seasonal and interannual changes in planktonic foraminiferal flux and shell geochemistry off south Java: a sediment trap study. *Paleoceanography* **24**, doi:10.1029/2008PA001636 (2009).
15. Thunell, R. C. & Reynolds, L. A. Sedimentation of planktonic foraminifera: seasonal changes in species in the Panama Basin. *Micropaleontology* **30**, 243–262 (1984).
16. Anand, P., Elderfield, H. & Conte, M. H. Calibration of Mg/Ca thermometry in planktonic foraminifera from a sediment trap time-series. *Paleoceanography* **18**, doi:10.1029/2002PA000846 (2003).
17. Lea, D. W., Pak, D. K. & Spero, H. J. Climate impact of late Quaternary equatorial Pacific sea surface temperature variations. *Science* **289**, 1719–1724 (2000).
18. Stott, L. *et al.* Decline of western Pacific surface ocean salinity and temperature in the early Holocene. *Nature* **431**, 56–59 (2004).
19. Rosenthal, Y., Oppo, D. W. & Linsley, B. K. The amplitude and phasing of climate change during the last deglaciation in the Sulu Sea, western equatorial Pacific. *Geophys. Res. Lett.* **30**, doi:10.1029/2002GL016612 (2003).
20. Moy, C. M., Seltzer, G. O., Rodbell, D. T. & Anderson, D. M. Variability of El Niño/Southern Oscillation activity at millennial timescales during the Holocene epoch. *Nature* **420**, 162–165 (2002).
21. Conroy, J. L., Overpeck, J. T., Cole, J. E., Shanahan, T. M. & Steinitz-Kannan, M. Holocene changes in eastern tropical Pacific climate inferred from a Galapagos lake sediment record. *Quat. Sci. Rev.* **27**, 1166–1180 (2008).
22. Gordon, A. L., Susanto, R. D. & Vranes, K. Cool Indonesian throughflow as a consequence of restricted surface layer flow. *Nature* **425**, 824–828 (2003).
23. Zhang, P. *et al.* A test of climate, sun, and culture relationships from an 1810-year Chinese cave record. *Science* **322**, 940–942 (2008).
24. Yancheva, G. *et al.* Influence of the intertropical convergence zone on the East Asian monsoon. *Nature* **445**, 74–77 (2007).
25. Sontakke, N. A., Pant, G. B. & Singh, N. Construction of all-India summer monsoon rainfall series for the period 1844–1991. *J. Clim.* **6**, 1807–1811 (1993).
26. Haug, G. H. *et al.* Southward migration of the Intertropical Convergence Zone through the Holocene. *Science* **293**, 1304–1308 (2001).
27. Wang, Y. *et al.* The Holocene Asian monsoon: links to solar changes and North Atlantic climate. *Science* **308**, 854–857 (2005).
28. Barsugli, J. J. & Sardeshmukh, P. D. Global atmospheric sensitivity to tropical SST anomalies throughout the Indo-Pacific basin. *J. Clim.* **15**, 3427–3442 (2003).
29. Locarnini, R. A., Mishonov, A. V., Antonov, J. I., Boyer, T. P. & Garcia, H. E. *World Ocean Atlas 2005 Vol. 1, Temperature* (ed. Levitus, S.) (NOAA Atlas NESDIS 61, US Govt Printing Office, 2006).

Supplementary Information is linked to the online version of the paper at www.nature.com/nature.

Acknowledgements We thank the following people and institutions for their support: Y. S. Djajadihardja, F. Syamsudin, the captain and crew of our 2003 RV *Baruna Jaya VIII* cruise, the Indonesian Agency for Assessment and Application of Technology (BPPT), and the Center of Research and Development for Oceanography (LIPI) of Indonesia. This work was financially supported by the US NSF and the Ocean Climate Change Institute of WHOI. We thank L. Zou, D. Ostermann, K. Rose, S. Pike and M. Chong for technical assistance, W. Martin, O. Marchal, C. Saenger and K. Dahl for discussions, and the NOSAMS and Radioanalytical facilities at WHOI for radiocarbon and ^{210}Pb analyses, respectively.

Author Contributions All authors contributed extensively to this work.

Author Information Data are available at ftp://ftp.ncdc.noaa.gov/pub/data/paleo/contributions_by_author/oppo2009/oppo2009.txt. Reprints and permissions information is available at www.nature.com/reprints. Correspondence and requests for materials should be addressed to D.W.O. (doppo@whoi.edu).

Surface hydrophobin prevents immune recognition of airborne fungal spores

Vishukumar Aimanian^{1*}, Jagadeesh Bayry^{2,3,4*}, Silvia Bozza⁵, Olaf Knienmeyer⁷, Katia Perruccio⁶, Sri Ramulu Elluru^{2,3,4}, Cécile Clavaud¹, Sophie Paris¹, Axel A. Brakhage⁷, Srinu V. Kaveri^{2,3,4}, Luigina Romani⁵ & Jean-Paul Latgé¹

The air we breathe is filled with thousands of fungal spores (conidia) per cubic metre, which in certain composting environments can easily exceed 10^9 per cubic metre. They originate from more than a hundred fungal species belonging mainly to the genera *Cladosporium*, *Penicillium*, *Alternaria* and *Aspergillus*^{1–4}. Although these conidia contain many antigens and allergens^{5–7}, it is not known why airborne fungal microflora do not activate the host innate immune cells continuously and do not induce detrimental inflammatory responses following their inhalation. Here we show that the surface layer on the dormant conidia masks their recognition by the immune system and hence prevents immune response. To explore this, we used several fungal members of the airborne microflora, including the human opportunistic fungal pathogen *Aspergillus fumigatus*, in *in vitro* assays with dendritic cells and alveolar macrophages and in *in vivo* murine experiments. In *A. fumigatus*, this surface ‘rodlet layer’ is composed of hydrophobic RodA protein covalently bound to the conidial cell wall through glycosylphosphatidylinositol-remnants. RodA extracted from conidia of *A. fumigatus* was immunologically inert and did not induce dendritic cell or alveolar macrophage maturation and activation, and failed to activate helper T-cell immune responses *in vivo*. The removal of this surface ‘rodlet/hydrophobin layer’ either chemically (using hydrofluoric acid), genetically (Δ rodA mutant) or biologically (germination) resulted in conidial morphotypes inducing immune activation. All these observations show that the hydrophobic rodlet layer on the conidial cell surface immunologically silences airborne moulds.

Dendritic cells are the sentinels of the immune system controlling fungal immunity⁸. Germinating *A. fumigatus* conidia induced significant expression of co-stimulatory molecules (CD80, CD86, CD40 and CD83) and antigen-presenting molecule human leukocyte antigen DR (HLA-DR) on human dendritic cells, and induced the secretion of inflammatory and anti-inflammatory cytokines, indicating that metabolically active germinating conidia provide maturation-associated signals to dendritic cells. On the other hand, dormant conidia did not modify the expression of surface molecules or the secretion of cytokines (Supplementary Fig. 2). These results, in agreement with previous studies^{9–11}, suggest that dormant conidia, in contrast to germinated conidia, are immunologically inert. However, dormant conidia contain many immunogenic molecules¹² so that on cell wall disruption, the intracellular material of dormant conidia could activate dendritic cells (Supplementary Fig. 3).

We then attempted to dissect the reasons for the immunologically inert nature of the dormant conidia. *A. fumigatus* dormant conidia

are covered by a rodlet layer, a thin coating of regularly arranged RodA hydrophobins¹³. The presence of a glycosylphosphatidylinositol (GPI)-anchoring sequence discovered during analysis of the *rodA* gene (*Afu5g09580*; Supplementary Fig. 4a) indicates that RodA is covalently bound to the cell-wall polysaccharides¹⁴. Accordingly, hydrofluoric acid treatment that cleaves phosphodiester bonds of GPI anchors/remnants and releases GPI proteins bound to the cell wall was performed¹⁵. The hydrofluoric acid extract that was completely water soluble accounted for 1.7% of conidial dry weight and resolved into three bands on SDS–PAGE (Fig. 1a). Mass spectrometry (MS) and MS/MS analysis showed that these proteins with an apparent mass of 32, 16 and 14.5 kDa on SDS–PAGE corresponded to the dimeric form of the native RodA, native RodA (consistent with its theoretical mass) and partially degraded or processed RodA (RodA*) (Supplementary Table 1), respectively. We could not observe any RodA released into the culture supernatant when conidia were germinated in various culture media (Fig. 1b, also see ref. 16), indicating the complete degradation of the pre-existing rodlet layer during germination. These observations indicate that the RodA of the outer rodlet layer, covalently bound to the cell wall of the dormant conidia, is degraded during germination, exposing the underlying immunogenic cell wall components usually masked by this rodlet layer.

On the basis of the ability of different morphotypes to induce dendritic cell activation, we surmised that the rodlet layer on the dormant conidia imparts immunological inertness. To examine this, 5×10^5 human dendritic cells were treated with 0.33 μ g of RodA (concentration corresponding to 5×10^5 conidia). Interestingly, RodA did not induce maturation of dendritic cells (Fig. 1c, d). Even at higher concentrations of RodA (up to 1 μ g), there were no changes in the dendritic cell phenotype. Also, RodA neither induced nor altered the basal level of dendritic cell cytokines (Fig. 1e). Thus, the results are reminiscent of interaction of dendritic cells with dormant conidia (Supplementary Fig. 2). Moreover and in contrast to 18-kDa ribonuclease (Aspfl, encoded by the gene *Afu5g02330*), one of the most immunogenic proteins of *A. fumigatus*, RodA was unable to stimulate lymphoproliferation (Fig. 1f, g) or to activate *Aspergillus*-specific human CD4⁺ T-cell clones for cytokine production (Fig. 1h). We verified that the lack of activation by RodA was not due to the hydrofluoric acid treatment because this treatment did not alter the immunogenicity of other *Aspergillus* proteins such as Aspfl (Supplementary Fig. 5). Further, to confirm that RodA does not impart tolerogenic properties and immunological unresponsiveness to dendritic cells on encounter with other immunogenic molecules, we treated dendritic cells with a

¹Unité des Aspergillus, Institut Pasteur, Paris F-75015, France. ²INSERM, U 872, ³Centre de Recherche des Cordeliers, Université Pierre et Marie Curie–Paris 6, UMR S 872, ⁴Université Paris Descartes, UMR S 872, Paris F-75006, France. ⁵Department of Experimental Medicine and Biochemical Sciences, ⁶Clinical Immunology, Department of Clinical and Experimental Medicine, University of Perugia, Perugia 06122, Italy. ⁷Department of Molecular and Applied Microbiology, Leibniz-Institute for Natural Product Research and Infection Biology (HKI) and Friedrich Schiller University, 07745 Jena, Germany.

*These authors contributed equally to this work.

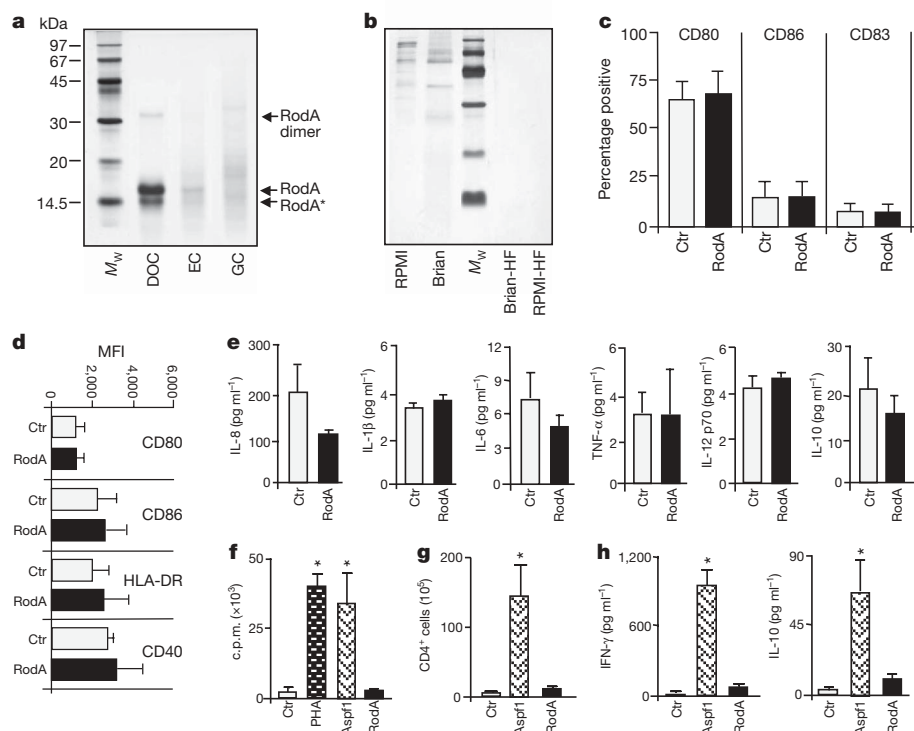


Figure 1 | *Aspergillus fumigatus* conidial surface-hydrophobin, RodA, fails to activate human dendritic cells and CD4⁺ T lymphocytes. **a, b**, SDS-PAGE profiles of hydrofluoric acid extracts from dormant (DOC), enlarged (EC) and germinating (GC) conidia (**a**) and naive or hydrofluoric acid-treated supernatant of the Brian's (5% glucose, 1% asparagine, 1% KH₂PO₄, 0.2% MgSO₄·7H₂O, 0.24% NH₄NO₃, 2.6 × 10⁻³ % ZnSO₄·7H₂O, 2.6 × 10⁻⁴ % CuSO₄·5H₂O, 1.3 × 10⁻⁴ % Co(NO₃)₂·6H₂O and 6.5 × 10⁻³ % CaCl₂, pH 5.4) or RPMI media in which conidia were germinated (**b**). **c-e**, Phenotype markers of human dendritic cells showing the percentage of positive cells (**c**), the mean fluorescence intensities (MFI; **d**) and the cytokine secretion (**e**). **f, g, h**, Lack of lymphoproliferation (**f**, c.p.m.; **g**, frequency) and activation (**h**) of *Aspergillus*-specific human CD4⁺ T-cell clones ($n = 3-7$; means ± s.e.m. are shown; * $P < 0.001$, Mann-Whitney test). Asp1 and PHA (phytohaemagglutinin) were used as positive controls. Ctr, negative control.

mixture of RodA and a recombinant Asp1; RodA did not suppress dendritic cell activation by Asp1 (Supplementary Fig. 6).

To confirm that the RodA layer on the cell wall masks the immunogenicity of dormant conidia, we used $\Delta rodA$ conidia that lack RodA and therefore the rodlet layer¹³. In contrast to the wild-type conidia

and despite being dormant, $\Delta rodA$ conidia induced strong upregulation of costimulatory and antigen-presenting molecules on human dendritic cells (Fig. 2a, b). Additionally, $\Delta rodA$ conidia also induced high amounts of dendritic cell cytokines (Fig. 2c). The hydrofluoric acid-treated dormant wild-type conidia, with exposed immunogenic

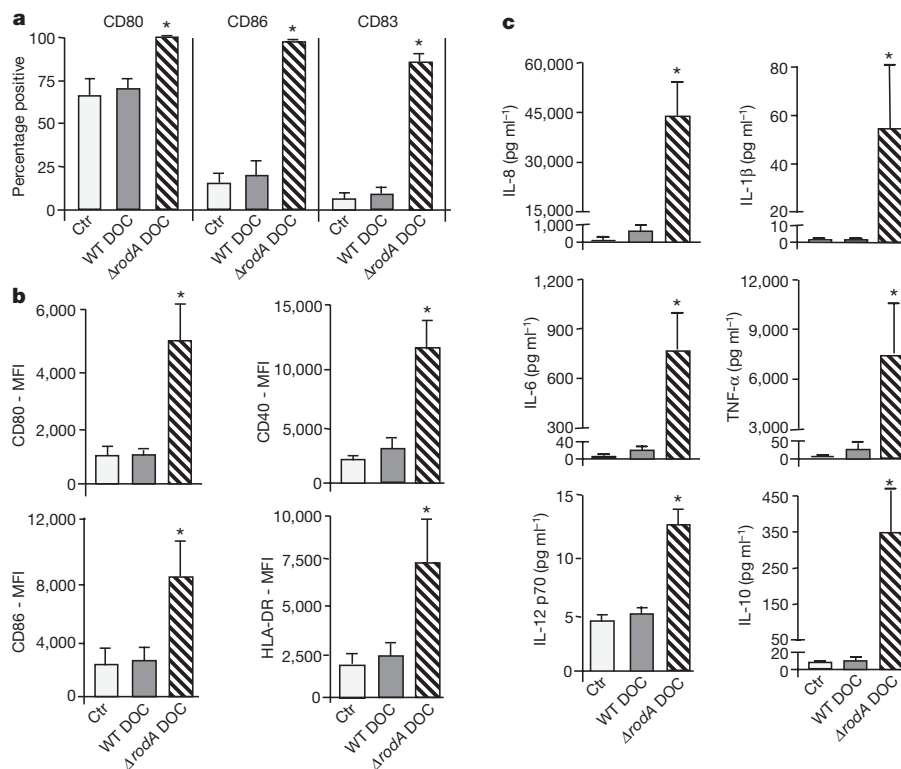


Figure 2 | Dormant conidia of $\Delta rodA$ mutant in contrast to wild-type conidia induce maturation and activation of human dendritic cells. **a-c**, Six-day-old human dendritic cells were cultured with GM-CSF and IL-4 alone (Ctr) or with wild-type dormant conidia (WT DOC) or $\Delta rodA$ dormant

conidia ($\Delta rodA$ DOC). **a**, Percentage of cells expressing the indicated markers; **b**, mean fluorescence intensities (MFI) and **c**, cytokine secretion ($n = 4$; mean ± s.e.m. and statistical significance (* $P < 0.05$ in **a**; $P < 0.001$ in **b** and **c**) determined by the Mann-Whitney test).

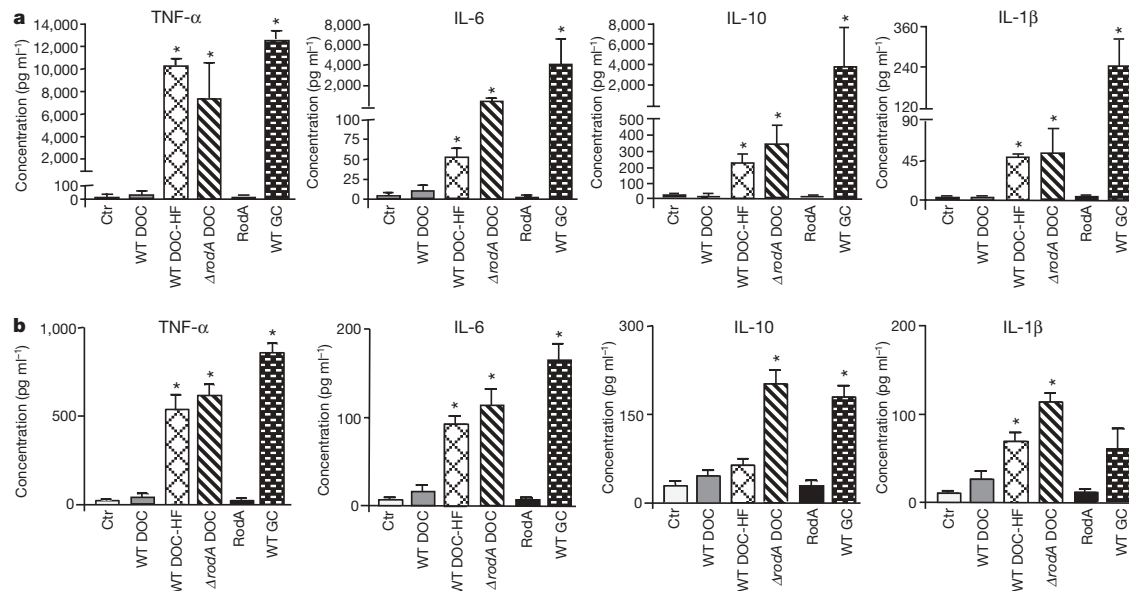


Figure 3 | Biological (conidial germination), chemical (hydrofluoric acid-treatment) or genetic (Δ rodA mutant) removal of RodA from dormant conidia induces activation of human dendritic cells and murine alveolar macrophages *in vitro*. **a**, **b**, Human dendritic cells (**a**) and murine alveolar macrophages (**b**) were incubated with wild-type naive (WT DOC) or hydrofluoric acid-treated dormant conidia (WT DOC-HF), Δ rodA dormant

conidia, RodA and germinated conidia (WT GC). Concentrations (mean \pm s.e.m.) of secreted tumour necrosis factor α (TNF- α), IL-6, IL-10 and IL-1 β are shown. Statistical significance (* P < 0.05) determined by Mann-Whitney test (**a**; n = 4) and paired t -test (**b**; n = 3) compared to unstimulated cells (Ctr) is shown.

determinants after removal of rodlet protein, also stimulated human dendritic cells similarly to germinating conidia (Fig. 3a, Supplementary Figs 2 and 7). Furthermore, when murine alveolar macrophages were exposed *in vitro* to naive or hydrofluoric acid-treated dormant conidia, Δ rodA dormant conidia, RodA and

germinated conidia, all fungal samples except naive dormant conidia and RodA induced inflammatory cytokines, chemokines and reactive oxygen intermediates (ROI) (Fig. 3b and Supplementary Fig. 8). Together, these data show that removal of the surface rodlet layer from conidia either chemically (hydrofluoric acid treatment),

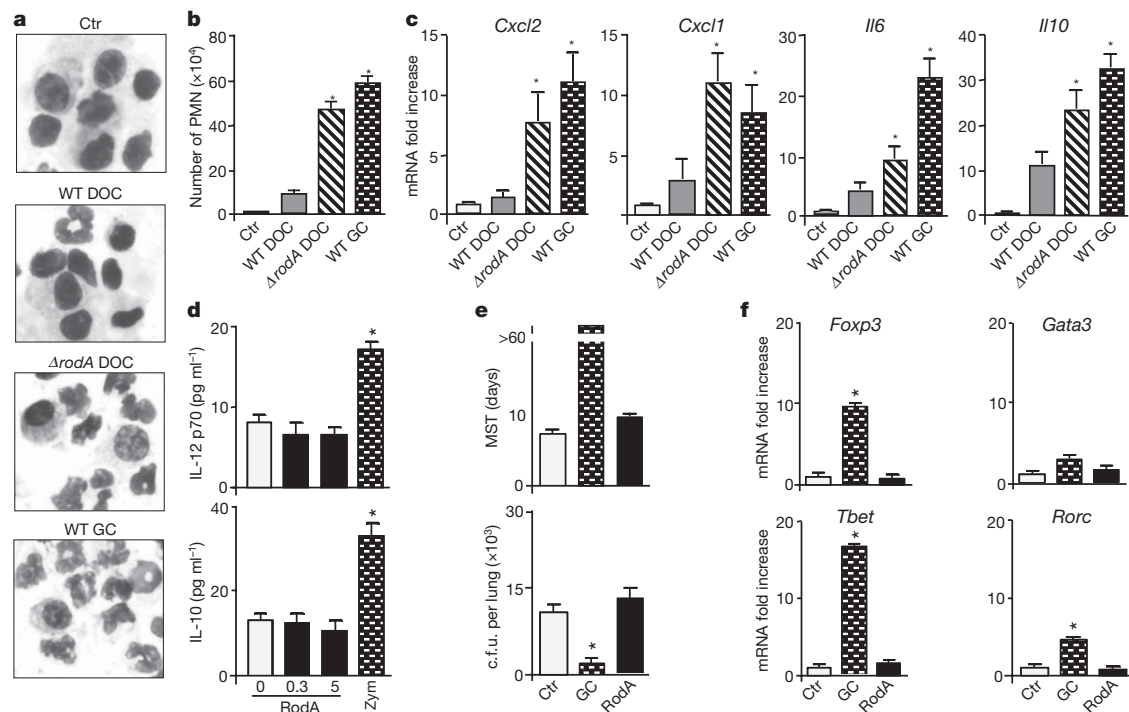


Figure 4 | RodA and wild-type dormant *A. fumigatus* conidia do not activate murine immune system *in vivo*, contrary to Δ rodA-dormant or wild-type-germinated conidia. **a**, Lung cytopsin preparations; **b**, neutrophils (polymorphonuclear cells, PMN) in cytopsin and **c**, *Cxcl2*, *Cxcl1*, *Il6* and *Il10* mRNA in lungs 24 h after conidial inoculation (n = 3; mean \pm s.e.m.; * P < 0.05, paired t -test). WT DOC, wild-type dormant conidia; WT GC, wild-type germinated conidia; Δ rodA DOC, mutant Δ rodA dormant conidia.

d, Cytokine secretion by RodA- and zymosan (Zym.)-stimulated lung CD11c⁺ dendritic cells. **e**, Median survival time (MST) and colony forming units (c.f.u.); **f**, helper T-cell-responses in mice injected with RodA-dendritic cells or germinated conidia-dendritic cells (GC), followed by intranasal inoculation of live conidia (n = 3; mean \pm s.e.m.; * P < 0.001, Mann-Whitney test).

biologically (germinated conidia) or genetically ($\Delta rodA$ mutant) results in an activation of the human or murine innate immune cells.

To confirm that hydrophobins regulate the immune response to conidia *in vivo*, intranasal inoculation of mice was performed with the fungal samples mentioned earlier. First, $\Delta rodA$ dormant conidia or wild-type germinated conidia were highly inflammatory as shown by the massive influx of polymorphonuclear cells in the lungs (Fig. 4a, b) and induction of high levels of chemokines *Cxcl1*, *Cxcl2*, inflammatory *Il6* and anti-inflammatory *Il10* cytokines (Fig. 4c). In contrast, wild-type dormant conidia covered by RodA failed to activate the mouse immune system *in vivo* (Fig. 4a–c). In addition, germinated, hydrofluoric acid-treated dormant and $\Delta rodA$ dormant conidia stimulated alveolar macrophages *in vivo*, but wild-type dormant conidia and RodA did not (data not shown). Second, to assess the biological activity of RodA in a mouse model, we exposed murine lung dendritic cells to RodA, and evaluated their cytokine production and their ability to activate helper T-cell (Th) responses on adoptive transfer *in vivo*. Confirming the human dendritic cell results, RodA neither induced maturation of dendritic cells, even at high concentrations (up to $5 \mu\text{g ml}^{-1}$, data not shown), nor induced secretion of cytokines, in contrast to the positive control (zymosan; Fig. 4d). On adoptive transfer *in vivo* in mice with aspergillosis¹⁷, RodA-pulsed dendritic cells neither increased survival nor decreased fungal growth in the lungs, as opposed to germinated conidia-pulsed dendritic cells (Fig. 4e). This was associated with the failure to activate antigen-specific *Tbet*⁺/Th1, *Gata3*/Th2, *Rorc*⁺/Th17 and *Foxp3*⁺/regulatory T-cell responses (Fig. 4f). In addition, RodA failed to induce antibody responses in mice, despite repeated injections in the presence of Freund's complete/incomplete adjuvants. These results show that the inability of RodA to induce activation of antigen-presenting cells (Figs 1, 3 and 4) is translated into failure to activate antigen-specific adaptive T- and B-cell immune responses *in vivo* in mice. This lack of immune response to RodA may also be due to its resistance to lysosomal proteolytic degradation (Supplementary Fig. 9), resulting in the lack of generation of antigenic peptides and their presentation by dendritic cells.

Rodlet proteins were also extracted using hydrofluoric acid from the conidia of three other moulds of the airborne fungal flora: the food-borne *Penicillium camemberti*, the toxinogenic *Penicillium verrucosum* and the allergenic *Cladosporium cladosporioides* that are known to have rodlets on their aerial conidial surface^{18,19}. The hydrofluoric acid-extracted protein from *P. camemberti*, on single MS and MS/MS analyses, matched exactly with the Q11187 sequence of the *P. camemberti* hydrophobin (data not shown). In addition, sequence analysis of the *P. camemberti* hydrophobin showed an organization similar to RodA of *A. fumigatus* (Supplementary Fig. 4b). We found that dormant conidia or hydrophobins from these three fungal species were also immunologically inert, whereas hydrofluoric acid-treated dormant conidia induced a very strong immune reaction in human dendritic cells (Supplementary Figs 10 and 11), indicating that the lack of recognition of rodlet protein by the immune system is a universal phenomenon.

Taken together, these results demonstrate that the surface rodlet layer of the conidial cell wall makes airborne conidia of filamentous fungi inert to both innate and adaptive immunity. The cell wall of filamentous fungi is a complex structure, rich in many immunologically active components, including either constitutive cell-wall polysaccharides such as β -glucans and galactomannan or secreted (glyco)proteins in transit in the cell wall before being secreted^{14,20}. Activation of dendritic cells and macrophages by these cell-wall immunogenic motifs requires their exposure to the immune cells mentioned earlier^{14,20,21}. *In vivo*, intraphagosomal germination of thermotolerant live conidia or autolysis of fungal species that are sensitive to temperatures above 37°C results in a slow exposure or release of immunologically active molecules after the removal of the surface rodlet layer. Recognition of these exposed molecules by pathogen-recognition-receptors, including dectin-1 (see

Supplementary Fig. 12, the lack of rodlet layer in $\Delta rodA$ dormant conidia exposes β -(1,3)-glucans that are recognized, in a punctuated pattern, by dectin-1), then leads to the activation of a controlled immune response^{9–11,22}. From a pathogen point of view, immunological inertness of the rodlet layer can help dormant conidia to escape the host defence mechanisms and stay dormant in a hidden niche until conditions are suitable for germination. Moreover, considering the fact that airborne conidia are ubiquitous in the atmosphere, the inert nature of hydrophobin rodlet layer makes teleological sense as it prevents undue and exacerbated host response by innate immune cells and hence prevents inflammation and host damage. From a therapeutic point of view, the ability of rodlet proteins to resist degradation could be used to generate rodlet-protein-based nanoparticles containing embedded therapeutic proteins and molecules that have to be slowly released within the host or transported to a specific body location without being recognized by the host immune system²³.

METHODS SUMMARY

A. fumigatus strains were the clinical isolate CBS144-89 (wild type) and the mutant $\Delta rodA$ -47 (ref. 13). *P. camemberti*¹⁸, *P. verrucosum* and *C. cladosporioides* were wild-type strains. Dormant conidia were obtained by growth on 2% malt extract agar. Enlarged and germinating conidia were produced after 4 and 8 h incubation in 2% glucose + 1% mycopeptide medium at 37°C , respectively. Fungal conidia were fixed in 2% *p*-formaldehyde. The rodlet layer was extracted by incubating dry conidia with 48% hydrofluoric acid for 72 h at 4°C . For sequence analysis, protein bands on SDS-PAGE gels were excised manually, trypsin-digested and the peptides obtained²⁴ were subjected to proteomic analyses by matrix-assisted laser desorption/ionization-time of flight/time of flight (MALDI-TOF/TOF; see ref. 25). Immature human dendritic cells were generated by culturing monocytes of healthy donors in the presence of interleukin 4 (IL-4) and granulocyte-macrophage colony-stimulating factor (GM-CSF; see ref. 26). They were incubated for 48 h in the presence of cytokines alone or with RodA or Aspfl²⁷ or with naive or hydrofluoric acid-treated dormant, enlarged and germinating conidia of wild-type *A. fumigatus*, or with $\Delta rodA$ dormant conidia. The surface markers on dendritic cells were analysed by flow cytometry. Cytokines were quantified in cell-free culture supernatants by cytometric bead array assay. Murine alveolar macrophages and dendritic cells from C57BL/6 (*H-2*^b) mice were purified from lungs and stimulated *in vitro* with the same fungal samples as those used for human dendritic cells. Alternatively, mice received 2×10^7 conidia intranasally or the equivalent treated samples. Expression of murine cytokine and chemokines was analysed by polymerase chain reaction with reverse transcription (RT-PCR) and/or enzyme-linked immunosorbent assay (ELISA)²⁸ and helper T-cell-specific transcription factors in CD4⁺ T cells were analysed by RT-PCR²⁸.

Full Methods and any associated references are available in the online version of the paper at www.nature.com/nature.

Received 27 April; accepted 9 July 2009.

- Codina, R., Fox, R. W., Lockett, R. F., DeMarco, P. & Bagg, A. Typical levels of airborne fungal spores in houses without obvious moisture problems during a rainy season in Florida, USA. *J. Investig. Allergol. Clin. Immunol.* **18**, 156–162 (2008).
- de Ana, S. G., Torres-Rodriguez, J. M., Ramirez, E. A., Garcia, S. M. & Belmonte-Soler, J. Seasonal distribution of *Alternaria*, *Aspergillus*, *Cladosporium* and *Penicillium* species isolated in homes of fungal allergic patients. *J. Investig. Allergol. Clin. Immunol.* **16**, 357–363 (2006).
- Kasprzyk, I. Aeromycology—main research fields of interest during the last 25 years. *Ann. Agric. Environ. Med.* **15**, 1–7 (2008).
- Lee, T. et al. Culturability and concentration of indoor and outdoor airborne fungi in six single-family homes. *Atmos. Environ.* **40**, 2902–2910 (2006).
- Glaser, A. G. et al. Molecular and immunological characterization of Asp f 34, a novel major cell wall allergen of *Aspergillus fumigatus*. *Allergy* **64**, 1144–1151 (2009).
- Denning, D. W. Invasive aspergillosis. *Clin. Infect. Dis.* **26**, 781–803 (1998).
- Latge, J. P. *Aspergillus fumigatus* and aspergillosis. *Clin. Microbiol. Rev.* **12**, 310–350 (1999).
- Romani, L. Immunity to fungal infections. *Nature Rev. Immunol.* **4**, 11–24 (2004).
- Hohl, T. M. et al. *Aspergillus fumigatus* triggers inflammatory responses by stage-specific β -glucan display. *PLoS Pathog.* **1**, e30 (2005).
- Steele, C. et al. The β -glucan receptor dectin-1 recognizes specific morphologies of *Aspergillus fumigatus*. *PLoS Pathog.* **1**, e42 (2005).

11. Braedel, S. *et al.* *Aspergillus fumigatus* antigens activate innate immune cells via toll-like receptors 2 and 4. *Br. J. Haematol.* **125**, 392–399 (2004).
 12. Lamarre, C. *et al.* Transcriptomic analysis of the exit from dormancy of *Aspergillus fumigatus* conidia. *BMC Genomics* **9**, 417 (2008).
 13. Thau, N. *et al.* rodletless mutants of *Aspergillus fumigatus*. *Infect. Immun.* **62**, 4380–4388 (1994).
 14. Latge, J. P. The cell wall: a carbohydrate armour for the fungal cell. *Mol. Microbiol.* **66**, 279–290 (2007).
 15. Ferguson, M. A., Homans, S. W., Dwek, R. A. & Rademacher, T. W. Glycosyl-phosphatidylinositol moiety that anchors *Trypanosoma brucei* variant surface glycoprotein to the membrane. *Science* **239**, 753–759 (1988).
 16. Dague, E., Delcorte, A., Latge, J. P. & Dufrene, Y. F. Combined use of atomic force microscopy, X-ray photoelectron spectroscopy, and secondary ion mass spectrometry for cell surface analysis. *Langmuir* **24**, 2955–2959 (2008).
 17. Bozza, S. *et al.* A dendritic cell vaccine against invasive aspergillosis in allogeneic hematopoietic transplantation. *Blood* **102**, 3807–3814 (2003).
 18. Boualem, K. *et al.* Cloning and expression of genes involved in conidiation and surface properties of *Penicillium camemberti* grown in liquid and solid cultures. *Res. Microbiol.* **159**, 110–117 (2008).
 19. Latge, J. P., Bouziane, H. & Diaquin, M. Ultrastructure and composition of the conidial wall of *Cladosporium cladosporioides*. *Can. J. Microbiol.* **34**, 1325–1329 (1988).
 20. Bernard, M. & Latge, J. P. *Aspergillus fumigatus* cell wall: composition and biosynthesis. *Med. Mycol.* **39** (Suppl. 1), 9–17 (2001).
 21. Philippe, B. *et al.* Killing of *Aspergillus fumigatus* by alveolar macrophages is mediated by reactive oxidant intermediates. *Infect. Immun.* **71**, 3034–3042 (2003).
 22. Dubourdeau, M. *et al.* *Aspergillus fumigatus* induces innate immune responses in alveolar macrophages through the MAPK pathway independently of TLR2 and TLR4. *J. Immunol.* **177**, 3994–4001 (2006).
 23. Hektor, H. J. & Scholtmeijer, K. Hydrophobins: proteins with potential. *Curr. Opin. Biotechnol.* **16**, 434–439 (2005).
 24. Shevchenko, A., Wilm, M., Vorm, O. & Mann, M. Mass spectrometric sequencing of proteins from silver-stained polyacrylamide gels. *Anal. Chem.* **68**, 850–858 (1996).
 25. Kniemeyer, O., Lessing, F., Scheibner, O., Hertweck, C. & Brakhage, A. A. Optimisation of a 2-D gel electrophoresis protocol for the human-pathogenic fungus *Aspergillus fumigatus*. *Curr. Genet.* **49**, 178–189 (2006).
 26. Bayry, J., Triebel, F., Kaveri, S. V. & Tough, D. F. Human dendritic cells acquire a semimature phenotype and lymph node homing potential through interaction with CD4⁺CD25⁺ regulatory T cells. *J. Immunol.* **178**, 4184–4193 (2007).
 27. Sarfati, J. *et al.* Recombinant antigens as diagnostic markers for aspergillosis. *Diagn. Microbiol. Infect. Dis.* **55**, 279–291 (2006).
 28. Romani, L. *et al.* Defective tryptophan catabolism underlies inflammation in mouse chronic granulomatous disease. *Nature* **451**, 211–215 (2008).
- Supplementary Information** is linked to the online version of the paper at www.nature.com/nature.
- Acknowledgements** We thank J. Vani, Y. Repesse and C. Galeotti for help with dendritic cell experiments; and R. Winkler, S. Behnken and M. Pötsch for help with the MALDI-TOF/TOF analysis. The research of O.K. and A.A.B. was supported by the Deutsche Forschungsgemeinschaft (DFG) Priority Programme 1160, and the EU-STREP Fungwall LSHB-CT-2004-511952 and MANASP LSGBH37899 were also awarded to J.-P.L., A.A.B. and L.R. J.B. and S.V.K. are supported by INSERM, CNRS and Universities Paris 5 and 6.
- Author Contributions** J.-P.L. initiated the study; V.A., J.B., L.R. and J.-P.L. designed the research; V.A., C.C., S.P. and J.-P.L. prepared and characterized conidia and fungal materials; J.B., S.R.E. and S.V.K. performed experiments with human dendritic cells; S.B., K.P. and L.R. performed experiments with T-cell clones, murine dendritic cells and macrophages; O.K. and A.A.B. performed protein sequence analysis; V.A., J.B., S.B., O.K., K.P., L.R. and J.-P.L. analysed the results; and V.A., J.B., O.K., L.R. and J.-P.L. wrote the paper.
- Author Information** Reprints and permissions information is available at www.nature.com/reprints. Correspondence and requests for materials should be addressed to J.-P.L. (jplatge@pasteur.fr).

METHODS

Mice. Female, 8- to 10-week-old inbred C57BL6 (*H-2^b*) mice were purchased from Charles River Breeding Laboratories. Experiments were performed according to the Italian Approved Animal Welfare Assurance A-3143-01.

Generation of dendritic cells: human dendritic cells. Peripheral blood mononuclear cells were isolated from buffy bags of blood from healthy donors by Ficoll-Hypaque density gradient centrifugation. Monocytes were positively isolated using CD14 beads (Miltenyi Biotec). Immature dendritic cells were generated by culturing monocytes for 6 days in RPMI 1640 containing 10% fetal calf serum, 50 U ml⁻¹ penicillin, 50 U ml⁻¹ streptomycin, IL-4 (500 IU per 10⁶ cells) and GM-CSF (1000 IU per 10⁶ cells)²⁶. Recombinant human GM-CSF and IL-4 were from ImmunoTools. The immature dendritic cells express high levels of CD1a, intermediate levels of HLA-DR, CD80 and CD86, and were negative or low-positive for CD83.

Generation of dendritic cells: murine dendritic cells. Dendritic cells (between 5 and 7% positive for CD8 α and between 30 and 35% positive for Gr-1) from naive mice were purified from collagenase D (Sigma)-treated lungs by magnetic cell sorting with MicroBeads (Miltenyi Biotec) conjugated to hamster anti-mouse CD11c monoclonal antibodies (clone N-418)²⁹.

Isolation of murine alveolar macrophages. Alveolar macrophages were purified from bronchoalveolar lavage fluid of naive or infected mice 6 h after the infection. Alveolar macrophages were collected using a total of 10 ml RPMI-1640 medium containing 0.5 mM EDTA.

Preparation of fungal material. The *A. fumigatus* strains used for this study were CBS144-89, a clinical isolate used as wild-type strain, and a *rodA* minus mutant *Δ rodA-47* (ref. 13). Conidia were harvested from a 1-week-old culture grown at 25 °C on 2% malt extract agar (dormant conidia, DOC). The dormant conidia were germinated for up to 8 h in Sabouraud liquid medium (2% glucose, 1% mycopeptone (Biokar)) at 37 °C. After 4 h, there was iso-diametrical growth and the conidia appeared swollen (enlarged conidia, EC) and after 8 h, growth becomes polarized, leading to the emergence of germ tubes of length <10 μ m (germinating conidia, GC). Conidia at appropriate stage of development were fixed with *p*-formaldehyde (2.5% w/v in phosphate buffered saline (pH 7.4) at 4 °C overnight), neutralized with 0.1 M NH₄Cl, washed and reconstituted in PBS.

The rodlet layer was extracted from the spore surface by incubating dry conidia with 48% hydrofluoric acid for 72 h at 4 °C. The contents were centrifuged (9,000g, 10 min) and the supernatant obtained was dried under N₂. The dried material was reconstituted in H₂O and an aliquot was subjected to SDS-PAGE (15% gel) and visualized by silver nitrate staining following standard protocols. Preliminary assays have shown that the optimum amount of RodA without any contaminants (as proven by SDS-PAGE) could be obtained after 3 days of incubation (0.8, 1.5 and 1.7% RodA was released per dormant conidial dry weight after 1, 2 and 3 days of incubation, respectively). An ultracentrifugation step (100,000g, 40 min) showed that the rodlet hydrophobins were completely soluble in water. The rodlet hydrophobins were also extracted from dry conidia of *Penicillium camemberti* (strain PCENS1, a gift from J.-F. Cavin), *P. verrucosum* (strain IP 1231-80, Institut Pasteur) and *Cladosporium cladosporioides* (strain IP1232-80, Institut Pasteur) using hydrofluoric acid under conditions identical to those used for RodA extraction from *A. fumigatus*. Besides being a food-borne fungus, *P. camemberti* was selected because, similar to *A. fumigatus*, it is one of the few fungal species from which surface hydrophobins were both isolated biochemically and sequenced¹⁸.

The recombinant Asp1 protein (18-kDa RNase) from *A. fumigatus* was produced as described previously²⁷. Asp1 and wild-type conidia also treated with hydrofluoric acid were used as controls to monitor the putative negative effect of the hydrofluoric acid treatment.

Analysis of rodlet hydrophobins by mass spectrometry. Proteins bands of the hydrofluoric acid extract on SDS-PAGE (%T-15, revealed by amido black 10B) were excised manually, followed by tryptic digestion according to an earlier protocol²⁴. Peptides thus obtained were extracted for 1 h with acetonitrile (ACN): trifluoroacetic acid (TFA) 0.1% (1:1 v/v), mixed with saturated α -cyano-4-hydroxycinnamic acid in ACN: TFA 0.1% (1:2 v/v) and allowed to dry on a stainless steel anchor chip target (dry droplet preparation). The samples were measured on an Ultraflex I MALDI-TOF/TOF device using flexControl 3.0 for data collection and flexAnalysis 3.0 for spectra analysis/peak list generation (Bruker Daltonics)²⁵. Up to five peptides of the PMF spectra were chosen for post source decay MS/MS analyses. For identification, peptide mass fingerprint (PMF) and peptide fragmentation fingerprint (PFF) spectra were submitted to the MASCOT server (MASCOT 2.1.02, Matrix Science), searching the NCBI database. Sequences of the rodlet proteins of *A. fumigatus* and *P. camemberti* were already available in databases with reference numbers 70997898 and 94982475, respectively. With respect to the sample preparation, fixed modification of cysteines to S-carbamidomethyl derivatives and variable methionine oxidation

was defined for the database search. Further, no missed cleavage and a peptide mass tolerance of 50 p.p.m. was allowed. Results were regarded as significant with an allowed likelihood for a random hit of $P \leq 0.05$, according to the MASCOT score. Database searches were triggered and archived on a ProteinScape 1.3 database server (Protagen). Accuracy of raw peak lists was improved by automated internal recalibration using known contaminants (Coomassie, trypsin and keratin fragments) and application of the peak rejection filter of the Score Booster tool, implemented into the ProteinScape 1.3 database software.

Assessing the reactivity of conidia to dectin-1-Fc by fluorescence light microscopy. Conidia from wild-type and *Δ rodA* mutant were fixed as described above. After extensive washing with 0.2 M glycine and 1 h post coating in 1% bovine serum albumin buffer, the samples were incubated with dectin-1-human IgGFC chimaeric protein (provided by G. Brown³⁰) at 5 μ g ml⁻¹ in PBS containing 1% bovine serum albumin (BSA) and 0.1% Tween 20. After extensive washing and 1 h incubation in a 1% mock goat serum, the conidia were incubated with a goat anti-human Fc immunoglobulin coupled to fluorescein isothiocyanate (Sigma, diluted 1:100 in PBS containing 1% BSA). Control was either the secondary antibody alone or the dectin-Fc incubated for 1 h in the presence of 10 mg ml⁻¹ laminarin.

Susceptibility of RodA to cathepsins. RodA (2.5 μ g) was treated with 0.125 μ g cathepsin S or L (Sigma) in acetate buffer (100 mM, pH 4.5) containing 0.2 mM dithiothreitol and 0.2 mM EDTA in a final volume of 25 μ l at 25 °C for 30 h. The reaction mixtures were subjected to SDS-PAGE (15% gel) and the protein bands were revealed by silver staining. The recombinant Asp1 protein was taken as a positive control to check the proteolytic actions of cathepsin S and L.

Stimulation of dendritic cells: human dendritic cells. Six-day-old immature human dendritic cells were cultured in medium containing GM-CSF and IL-4 alone (5×10^5 cells ml⁻¹ per well) or with *p*-formaldehyde-inactivated fungal materials for 48 h. Dendritic cells were cultured with dormant (naive or hydrofluoric acid-treated), enlarged and germinated conidia of wild type *A. fumigatus* and *Δ rodA* dormant conidia at a 1:1 ratio (5×10^5 conidia ml⁻¹ per well), 0.33 μ g of RodA (the concentration equivalent to 5×10^5 conidia), 0.6 μ g of intracellular material of dormant conidia or 0.33 μ g of 18-kDa RNase (Asp1), 5×10^5 *Penicillium* and *Cladosporium* dormant conidia (naive or hydrofluoric acid-treated) or 0.33 μ g of *Penicillium* and *Cladosporium* hydrofluoric acid-extracts. It was verified by inverted microscopy that all fungal morphotypes were engulfed by dendritic cells following culture. The surface staining of dendritic cells was performed with fluorochrome-conjugated antibodies to CD83, HLA-DR, CD80 and CD86 (BD Biosciences) and CD40 (Beckman Coulter) and proceeded for flow-cytometry (LSR II, BD Biosciences). Data were analysed by BD FACS DIVA software (BD Biosciences). Cytokines (IL-1 β , IL-6, IL-8, IL-10, IL-12 p70 and TNF- α) were quantified in cell-free culture supernatants using a BD cytometric bead array kit (BD Biosciences).

Stimulation of dendritic cells: murine dendritic cells. Murine dendritic cells were pulsed with live unopsonized *Aspergillus* conidia or RodA before adoptive transfer as described¹⁷. IL-12 p70 (<2.5 pg ml⁻¹, detection limit) and IL-10 (<12 pg ml⁻¹, detection limit) were quantified by ELISA in cell-free culture supernatants of dendritic cells resuspended in serum-free Iscove's medium and pulsed with RodA (0.3–5 μ g ml⁻¹) or 10 μ g ml⁻¹ zymosan from *Saccharomyces cerevisiae* (Sigma) for 24 h.

Stimulation of alveolar macrophages. Alveolar macrophages from naive mice (10⁶) were co-cultured with 10⁶ *A. fumigatus* conidia, 10 μ g RodA or lipopolysaccharide (as positive control) for 2 h at 37 °C, 5% CO₂. Alveolar macrophages from infected mice were immediately used without further stimulation *in vitro*. Secreted cytokines (IL-1 β , IL-6, IL-10 and TNF- α) were measured by ELISA. Transcripts for genes involved in the biosynthesis of chemokines, cytokines and reactive oxygen intermediates (ROI) were measured by RT-PCR.

In vivo mouse experiments. Female, 8- to 10-week-old inbred C57BL6 (*H-2^b*) mice were inoculated intranasally with a homogenous suspension of *p*-formaldehyde-fixed dormant or germinated conidia of wild type conidia and *Δ rodA* or hydrofluoric acid-treated dormant conidia. Anaesthetized mice received 2×10^7 conidia in 20 μ l saline twice intranasally, 6 h apart, before asphyxiation using CO₂ a day after *Aspergillus* conidial inoculation. After perfusion, lungs were collected and neutrophils were counted on May-Grünwald-Giemsa-stained cytospin preparations. At least 200 cells per cytospin preparation were counted. Chemokines and cytokines were quantified by real time polymerase chain reaction with reverse transcription. Increased mouse survival was estimated as median survival time (days) and fungal growth in the lung estimated as c.f.u. during vaccination experiments were performed as described earlier^{17,29}.

Real time RT-PCR. Real time RT-PCR was performed using the iCycler iQ detection system (Bio-Rad) and SYBR Green chemistry (Finnzymes) to analyse chemokines and cytokines. Total lung cells or *in vitro* cultured cells were lysed and total RNA was extracted using an RNeasy Mini Kit (Qiagen). RNA was

reverse transcribed with Sensiscript Reverse Transcriptase (Qiagen) according to the manufacturer's protocol. The PCR primers used were as follows: forward primer 5'-CCGCTCGCTTCTCTGTGC-3' and reverse primer 5'-CTCTGGATGTTCTTGAGGTGAATC-3' for *Cxcl1*; forward primer 5'-CCAACCACAGGCTACAG-3' and reverse primer 5'-CTTCAGGGTCAAGGCAAAC-3' for *Cxcl2*; forward primer 5'-CCCTTTGCTATGGTGTCTT-3' and reverse primer 5'-TGGTTTCTCTTCCCAAGACC-3' for *Il10*; forward primer 5'-CCGGAGAGGAGACTTCACAG-3' and reverse primer 5'-TCCACGATTCCAGAGAAC-3' for *Il6*; forward primer 5'-TGACGGACCCCAAAGATGAAGG-3' and reverse primer 5'-CCACGGGAAAGACACAGGTAGC-3' for *Il1β*; forward primer 5'-CGAGTGACAAGCCTGTAGCC-3' and reverse primer 5'-GAAGAGAACCTGGGAGTAGACAAG-3' for the TNF-α gene (*Tnf*); forward primer 5'-TAGAGACTCCTCCCATGCCT-3' and reverse primer 5'-CACTGCCTCCTCTCATGCTA-3' for *p47^{phox}*. The thermal profile for SYBR Green real-time PCR was at 95 °C for 3 min, followed by 40 cycles of denaturation for 30 s at 95 °C and an annealing/extension step of 30 s at 60 °C. Amplification efficiencies were validated and normalized against *Gapdh*.

Adoptive transfer of dendritic cells. Conidia- or RodA-pulsed dendritic cells (10^5) were administered into recipient mice subcutaneously, 2 and 1 week before the intranasal injection of 2×10^8 *A. fumigatus* conidia. CD4⁺ T cells were purified

(Miltenyi Biotech) from thoracic lymph nodes 3 days post-infection. Total RNA from CD4⁺ T cells was extracted using RNeasy Mini Kit (Qiagen) and reverse transcribed with Sensiscript Reverse Transcriptase (Qiagen) to monitor the expression of transcription factors. The PCR primers for *Tbet*, *Rorc*, *Gata3* and *Foxp3* were as described²⁸. Amplification efficiencies were validated and normalized against *Gapdh*.

Generation of *Aspergillus*-specific human T-cell clones and lymphoproliferation. *Aspergillus*-specific human CD4⁺ T-cell clones were generated on stimulation by conidia-pulsed dendritic cells as described¹⁷. The T-cell clones were assessed for specificity against Aspfl- or RodA-pulsed dendritic cells and 0.5% phytohaemoagglutinin (PHA, Biochrom) (as a positive control) by [³H]-thymidine (Amersham Biosciences) labelling or by measuring cytokine content in supernatants.

Statistical analysis. Statistical significance was determined by using the Mann–Whitney test or paired *t*-test.

29. Bozza, S. *et al.* Dendritic cells transport conidia and hyphae of *Aspergillus fumigatus* from the airways to the draining lymph nodes and initiate disparate Th responses to the fungus. *J. Immunol.* **168**, 1362–1371 (2002).
30. Graham, L. M. *et al.* Soluble Dectin-1 as a tool to detect β-glucans. *J. Immunol. Methods* **314**, 164–169 (2006).

LETTERS

EBI2 mediates B cell segregation between the outer and centre follicle

João P. Pereira¹, Lisa M. Kelly¹, Ying Xu¹ & Jason G. Cyster¹

B cell follicles are specialized microenvironments that support events necessary for humoral immunity^{1–3}. After antigen encounter, activated B cells initially seek T-cell help at the follicle–T-zone boundary and then move to interfollicular and T-zone distal (outer) regions of the follicle^{4–10}. Subsequently, some cells move to the follicle centre, become germinal centre B cells and undergo antibody affinity maturation^{1,2,11}. Although germinal centres within follicles were described in 1885 (ref. 12), the molecular cues mediating segregation of B cells between the outer and centre follicle have remained undefined. Here we present a role for the orphan G-protein-coupled receptor, Epstein-Barr virus induced molecule-2 (EBI2, also known as GPR183)¹³, in this process. EBI2 is expressed in mature B cells and increases in expression early after activation, before being downregulated in germinal centre B cells. EBI2 deficiency in mice led to a reduction in the early antibody response to a T-dependent antigen. EBI2-deficient B cells failed to move to the outer follicle at day 2 of activation, and instead were found in the follicle centre, whereas EBI2 overexpression was sufficient to promote B cell localization to the outer follicle. In mixed bone marrow chimaeras, EBI2-deficient B cells phenocopied germinal centre B cells in preferentially localizing to the follicle centre. When downregulation of EBI2 in wild-type B cells was antagonized, participation in the germinal centre reaction was impaired. These studies identify an important role for EBI2 in promoting B cell localization in the outer follicle, and show that differential expression of this receptor helps position B cells appropriately for mounting T-dependent antibody responses.

The propensity of B cells to migrate to the outer versus centre follicle at different stages of the antibody response, together with the established roles of G-protein-coupled receptors (GPCRs) in controlling lymphocyte positioning events, led us to address whether new GPCRs differentially expressed between early activated and germinal centre B cells may be involved in this subcompartmentalization. These criteria focused our attention on EBI2, a $G\alpha_i$ -coupled orphan receptor^{13,14} abundantly expressed in Epstein-Barr virus (EBV)-infected and activated human B cells, and downregulated in germinal centre B cells^{15,16}. To explore the expression pattern of mouse *Ebi2*, we generated a reporter mouse line carrying the enhanced green fluorescent protein (EGFP) gene inserted in place of the *Ebi2* open reading frame (Supplementary Fig. 1). Analysis of *Ebi2*^{GFP/+} mice showed that EBI2 is upregulated during B cell maturation in the bone marrow, and is expressed in mature recirculating B cells in bone marrow, spleen and lymph nodes (Fig. 1a). The expression of the GFP reporter tracked closely with changes in *Ebi2* transcript abundance (Fig. 1b). GFP levels were further upregulated after B-cell receptor (BCR) engagement with anti-IgM, or combined anti-IgM and anti-CD40 stimulation (Fig. 1c). To examine expression after receipt of T-cell help, we used an adoptive transfer system in which B cells from C57BL/6 (B6) *Ebi2*^{GFP/+} mice were transferred

to the coisogenic strain, bm12, that bears a three amino acid difference in the I-A^b major histocompatibility complex (MHC) class II molecule and contains a high frequency of I-A^b responsive helper T cells^{6,17}. This approach permits tracking of an activated B cell population in non-transgenic mice at early time points after receiving T-cell help. Two days after adoptive transfer of anti-IgM-stimulated B cells, we found higher GFP expression in B cells transferred to bm12 compared to B6 recipients, indicating that interaction with helper T cells promoted EBI2 upregulation (Fig. 1d). EBI2 expression was maintained in plasma cells but was markedly (~25-fold) downregulated in germinal centre B cells (Fig. 1a, b). Most CD4 T cells and a smaller fraction of CD8 T cells also expressed EBI2, although at lower levels than B cells (Fig. 1a, b). In sections, GFP was detectable throughout the follicle and T zone, but was almost undetectable within germinal centres, identified by their expression of GL7 (also known as LY77), making these structures appear as EBI2-deficient islands in a 'sea' of EBI2-expressing cells (Fig. 1e).

An initial analysis of lymphoid tissues from EBI2-deficient mice showed the presence of organized follicles and T-cell compartments, and the mice had normal numbers of B and T cells (Supplementary Fig. 2 and data not shown). Movement of activated B cells to the follicle–T-zone boundary within 6 h of BCR stimulation occurred similarly for EBI2-deficient and wild-type cells (Fig. 2a), suggesting that BCR-mediated EBI2 induction (Fig. 1) is not required for this CCR7-dependent relocation event⁸. We then asked whether the next stage(s) of activated B cell migration that occurs during T-dependent responses, movement to the outer follicle and interfollicular regions, were EBI2-dependent. To permit *in situ* tracking of activated B cells responding to T-cell help, we used the bm12 adoptive transfer approach introduced earlier. Littermate control B cells that had received anti-IgM stimulation were able to respond to T-cell help within bm12 recipients and relocated to the outer follicle at day 2 (Fig. 2b), as did cotransferred wild-type Igh^a B cells (Fig. 2b), consistent with earlier studies using immunoglobulin-transgenic B cells⁶. In contrast, EBI2-deficient B cells were unable to localize to this region and instead favoured the central area of the follicle (Fig. 2b). To determine whether upregulation of EBI2 could be sufficient to control B cell localization to the interfollicular and outer follicle regions within lymphoid tissues, we transduced B cells with *Ebi2*-encoding or control retroviruses and transferred them to wild-type recipients. One day later, the EBI2-overexpressing cells, identified by expression of a human CD4 reporter, were situated in interfollicular regions and in the outer follicle (Fig. 2c). This contrasted with the distribution of B cells transduced with the control retrovirus, where the cells distributed uniformly within the follicle (Fig. 2c). Thus EBI2 seems to be both necessary and sufficient to promote positioning of activated B cells in the outer follicle and interfollicular regions. Consistent with an essential role for EBI2 in the correct positioning of B cells during the early phases of T-dependent humoral responses,

¹Howard Hughes Medical Institute and Department of Microbiology and Immunology, University of California San Francisco, California 94143, USA.

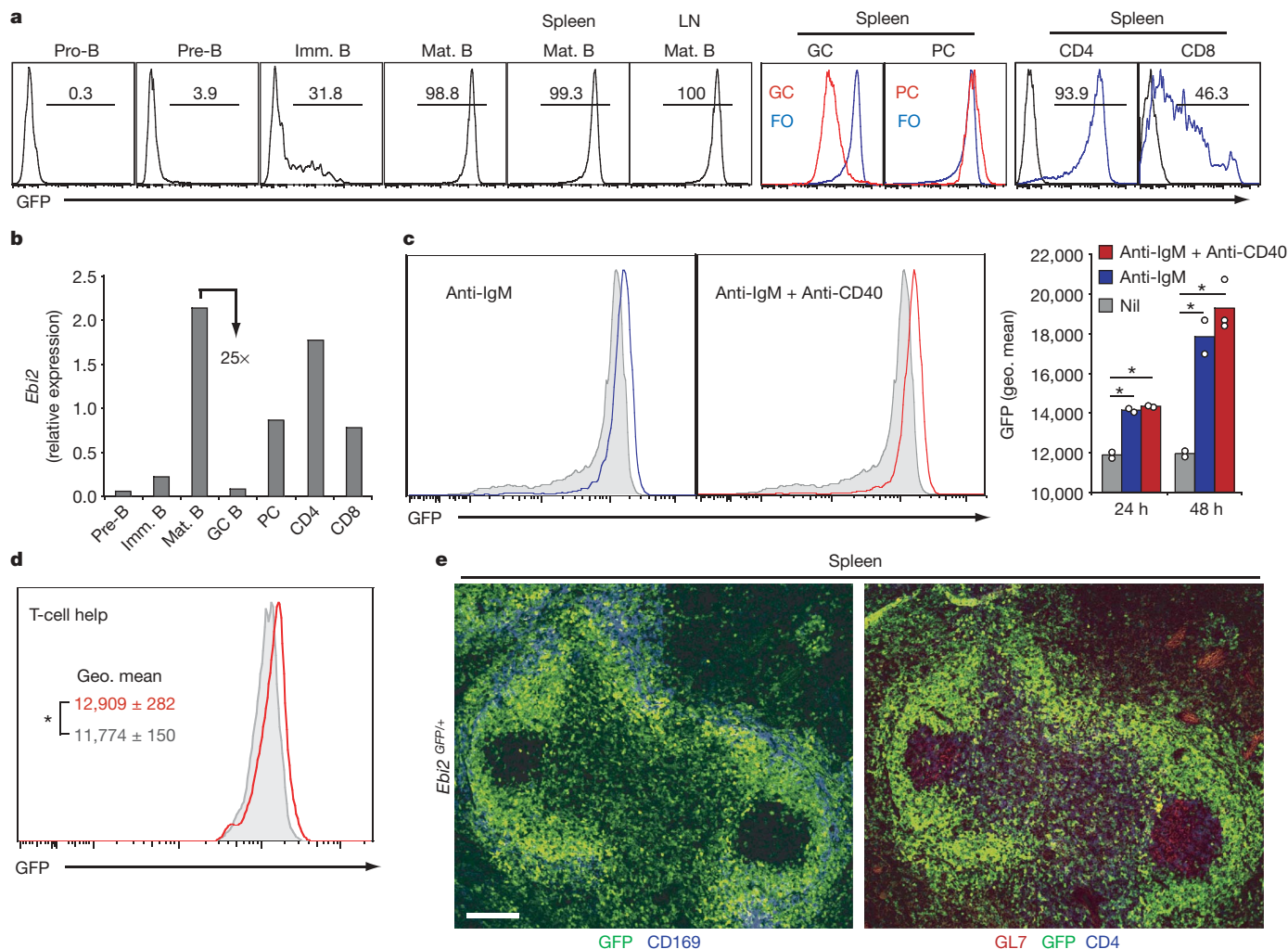


Figure 1 | EBI2 upregulation in activated B cells and downregulation in germinal centres. **a**, Flow cytometric detection of GFP fluorescence in the indicated bone marrow, spleen and lymph node (LN) cell subsets from *Ebi2^{GFP/+}* mice. Numbers indicate the percentage of cells in the gate. FO, follicular B cells; GC, germinal centre; Imm, immature; Mat, mature; PC, plasma cells. **b**, Quantitative PCR analysis of *Ebi2* transcript abundance in the indicated cell populations. Expression is shown relative to *Hprt1*. **c**, **d**, Flow cytometric detection of GFP fluorescence in B cells stimulated for 1 day with anti-IgM or with anti-IgM and anti-CD40 (c), or that were

stimulated for 1 h with anti-IgM and exposed *in vivo* for 2 days to T-cell help (red) or not provided with T-cell help (grey) (d). Grey histograms in c indicate unstimulated cells. The bar graph in c shows the geometric mean GFP fluorescence for 1 and 2 day cultures and summarizes three experiments. * $P < 0.05$, unpaired, two-tailed Student's *t*-test. **e**, Immunofluorescence microscopy of fixed spleen tissue from an *Ebi2^{GFP/+}* mouse, stained to detect GFP⁺ cells (green) and CD169⁺ marginal zone macrophages (blue, left panel) or GL7⁺ germinal centre B cells and CD4 T cells (red and blue, respectively, right panel). Scale bar, 100 μ m.

EBI2-deficient mice mounted a reduced day 7 IgG1 antibody response to nitrophenyl-chicken gamma-globulin (NP-CGG) in alum (Fig. 2d). The IgM response was not affected (Fig. 2d).

As another approach to examine the role of EBI2 in determining B cell localization, we examined cell distribution in 20:80 mixed bone marrow chimaeras that contained a minority of EBI2-deficient cells (20% Igh^b EBI2-deficient or littermate control and 80% Igh^a wild-type). Notably, EBI2-deficient B cells selectively localized in a germinal-centre-like location at the centre of follicles in spleen, lymph nodes and Peyer's patches of the bone marrow chimaeras (Fig. 3a). These foci of cells were not germinal centres as they maintained high expression of IgD and lacked expression of GL7 (Fig. 3a and Supplementary Fig. 3). In contrast, EBI2-deficient and wild-type T cells appeared intermingled throughout the T zone (Supplementary Fig. 4). Analysis of 90:10 mixed bone marrow chimaeras containing mostly EBI2-deficient (or littermate control) cells showed that EBI2-deficient B cells colocalized with the CD35⁺ (also known as CR1⁺) follicular dendritic cell (FDC) network at the centre of follicles, whereas the minor population of wild-type B cells in these mice was partially excluded from this area and enriched in

interfollicular regions or outer follicles (Fig. 3b). Similar findings were made in lymph nodes and Peyer's patches (Supplementary Fig. 5). It seems possible that in mice in which most B cells lack EBI2, there is increased EBI2 ligand availability and wild-type B cells predominate at the sites of ligand production. In control mixed bone marrow chimaeras reconstituted with a minority (20:80) or majority (90:10) of *Ebi2^{+/+}* bone marrow, the two types of wild-type B cells were intermingled in both the follicle centre and periphery (Fig. 3a, b and Supplementary Figs 3 and 5). FDCs are dependent on lymphotoxin (LT) LT α 1 β 2 for their maintenance¹⁸. To test whether the segregation of wild-type and EBI2-deficient B cells was dependent on FDCs, we treated mixed bone marrow chimaeras with LT β R-immunoglobulin, an LT α 1 β 2 antagonist¹⁹, for 2–3 weeks. The CD35⁺ FDC networks were depleted after treatment (Fig. 3c) as expected^{19,20}. Under these conditions, wild-type and EBI2-deficient cells no longer showed a segregated distribution in splenic B cell areas (Fig. 3c), suggesting a role for FDCs or other LT α 1 β 2-dependent cells in this process. In mice that lack CXCL13—a chemokine made broadly by the follicular stromal cell network^{20,21}—B cell localization in the outer splenic white-pulp (where follicles would normally be

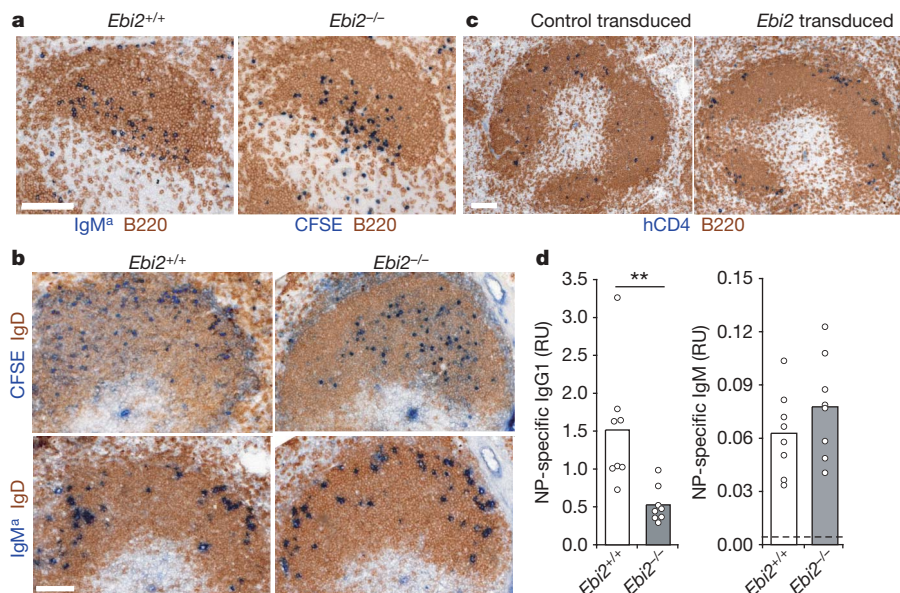


Figure 2 | EBI2 promotes localization of activated B cells in the outer follicle. **a–c**, Immunohistochemical staining of spleen cryosections. **a**, Distribution of wild-type and EBI2-deficient B cells that had been stimulated with anti-IgM *in vitro* for 1 h, and analysed 6 h after being transferred to wild-type hosts. *Ebi2*^{-/-} B cells were CFSE (5 (and 6)-carboxy-fluorescein diacetate succinimidyl ester)-labelled before transfer. Sections were stained with an antibody to detect CFSE (*Ebi2*^{-/-}) or co-transferred wild-type Igh^a (IgM^a, *Ebi2*^{+/+}) B cells (blue) and endogenous B cells (IgD, brown). **b**, Distribution of anti-IgM-treated wild-type and EBI2-deficient B

cells (CFSE, blue), and internal control Igh^a B cells (IgM^a, blue), after 2 days exposure to T-cell help in bm12 hosts. Top and bottom panels are serial sections. Endogenous B cells were detected with anti-IgD (brown). **c**, Distribution of B cells transduced with control or *Ebi2*-expressing retrovirus (human CD4, blue), 1 day after transfer. Endogenous B cells were detected with anti-IgD (brown). Scale bars, 100 μ m. **d**, Anti-nitrophenyl (NP) IgG1 and IgM serum titres in wild-type and EBI2-deficient mice on day 7 after immunization with NP-CGG in alum. RU, relative units. ***P* < 0.005, unpaired, two-tailed Student's *t*-test.

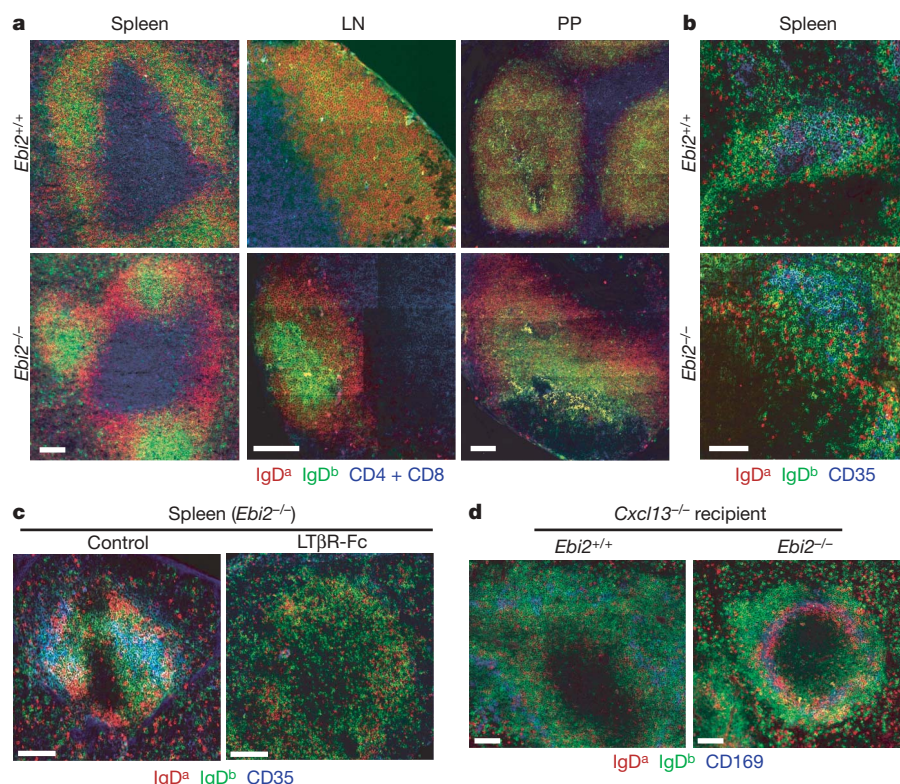


Figure 3 | EBI2-deficient B cells localize to the follicle centre in a LTα1β2- and CXCL13-dependent manner. **a**, Distribution of wild-type (*Ebi2*^{+/+}) and EBI2-deficient (*Ebi2*^{-/-}) B cells in spleen, lymph nodes (LN) and Peyer's patches (PP) of 20:80 mixed bone marrow chimaeras (20% Igh^b *Ebi2*^{+/+} or *Ebi2*^{-/-} and 80% Igh^a wild-type). Sections were stained to detect *Ebi2*^{+/+} or *Ebi2*^{-/-} B cells (IgD^b, green), Igh^a control B cells (IgD^a, red), and T cells (CD4 + CD8, blue). **b**, Spleen sections from 90:10 mixed bone marrow chimaeras (90% Igh^b *Ebi2*^{+/+} or *Ebi2*^{-/-} and 10% Igh^a wild-type) stained to

detect B cells as in **a**, and for CD35 to highlight FDC networks (blue). **c**, Similar analysis to **b** in control or 3 week LTβR-Fc treated 90:10 *Ebi2*^{-/-} mixed bone marrow chimaeras. **d**, Distribution of wild-type and EBI2-deficient B cells in *Cxcl13*^{-/-} hosts reconstituted with 70:30 bone marrow mixtures (70% Igh^b *Ebi2*^{+/+} or *Ebi2*^{-/-} and 30% Igh^a wild-type). Spleen sections stained to detect EBI2-deficient B cells (IgD^b, green), wild-type B cells (IgD^a, red) and marginal zone macrophages (CD169, blue). Scale bars, 100 μ m.

located) is reduced but not completely blocked²² (Fig. 3d). In CXCL13-deficient mice reconstituted with a mixture of EBI2-deficient and wild-type bone marrow, EBI2-deficient B cells were selectively diminished within the white-pulp cords and instead accumulated in the marginal zone that surrounds the white pulp (Fig. 3d). These findings provide further evidence for EBI2-mediated attraction of B cells to the outer white-pulp.

These findings suggested that EBI2 downregulation in germinal centre B cells may promote their positioning at the follicle centre. To test directly the significance of EBI2 downregulation during germinal centre development, we enforced constitutive EBI2 expression in hen egg lysozyme-specific immunoglobulin-transgenic B cells using retroviral gene transduction, and then tested their ability to participate in germinal centre and plasma cell responses after short-term adoptive transfer to hen egg lysozyme-immunized hosts (Fig. 4a). The frequency of *Ebi2* or control-vector transduced B cells among the germinal centre and plasma cell populations was tracked using the CD4 reporter. By flow cytometric analysis, *Ebi2*-transduced cells showed a reduced ability to participate in germinal centre responses compared to vector-transduced cells, while participating with wild-type efficiency in the plasma cell response (Fig. 4a, b). Although some *Ebi2*-transduced cells could take on a germinal centre phenotype (Fig. 4a), the cells were unable to position in germinal centres (Fig. 4c and Supplementary Fig. 6). Cells transduced with the control vector were readily detected within germinal centres (Fig. 4c and Supplementary Fig. 6). *Ebi2*-transduced cells contained *Ebi2* transcripts in amounts within twofold of those present in follicular B cells, and at least 25-fold higher than in germinal centre B cells (Supplementary Fig. 6). These experiments suggest that EBI2 downregulation is necessary for localization of developing germinal centre B cells to the follicle centre.

In summary, we establish that EBI2 is upregulated in B cells after BCR and CD40 engagement and is necessary to promote the positioning of activated B cells to interfollicular regions and the outer follicle. Cognate B cells interact with helper T cells and undergo proliferation in these regions^{7,10}. Defects in these processes are probably responsible for the diminished ability of EBI2-deficient mice to mount an early T-dependent IgG antibody response. Our findings suggest EBI2 is needed within B cells for these events, but we do not exclude that it also has a role in directing activated CD4 helper T cells and possibly other cell types to these regions. Germinal centre B cells markedly downregulate EBI2, a change that seems to be necessary to favour localization of activated B cells at the follicle centre, in association with the antigen-presenting and germinal-centre-supportive²³ FDC network. BCL6, a transcription factor required for germinal centre development, negatively regulates EBI2 expression¹⁵. We suggest that by favouring appropriate niche occupancy, negative regulation of EBI2 represents an important component of the *Bcl6* gene expression program directing germinal centre over plasma cell fate. Although the ligand for EBI2 remains undefined, we speculate that it is more concentrated in the outer compared to centre follicle as well as in interfollicular regions. We propose that although CXCR5 is sufficient to promote B cell localization in follicles^{22,24}, cells expressing EBI2 are more strongly attracted to the outer follicle compared to cells lacking this receptor. A further FDC-derived cue may favour positioning in the centre follicle, and when cells lose responsiveness to EBI2 ligands, positioning in response to this cue is dominant. The activity of EBI2 provides a possible explanation for why CXCR5-deficient B cells continue to localize in interfollicular areas and in regions corresponding to the outer follicle^{22,24}. Our findings may also help explain the niche preferences of certain B cell lymphomas, particularly follicular centre lymphoma²⁵. Indeed, expression array studies demonstrate that EBI2 is downregulated in follicular and germinal centre lymphomas^{16,26}. Moreover, it seems possible that the marked EBI2 induction observed early after EBV infection¹³ serves as a mechanism used by the virus to promote positioning in niches that favour the survival of the infected B cells.

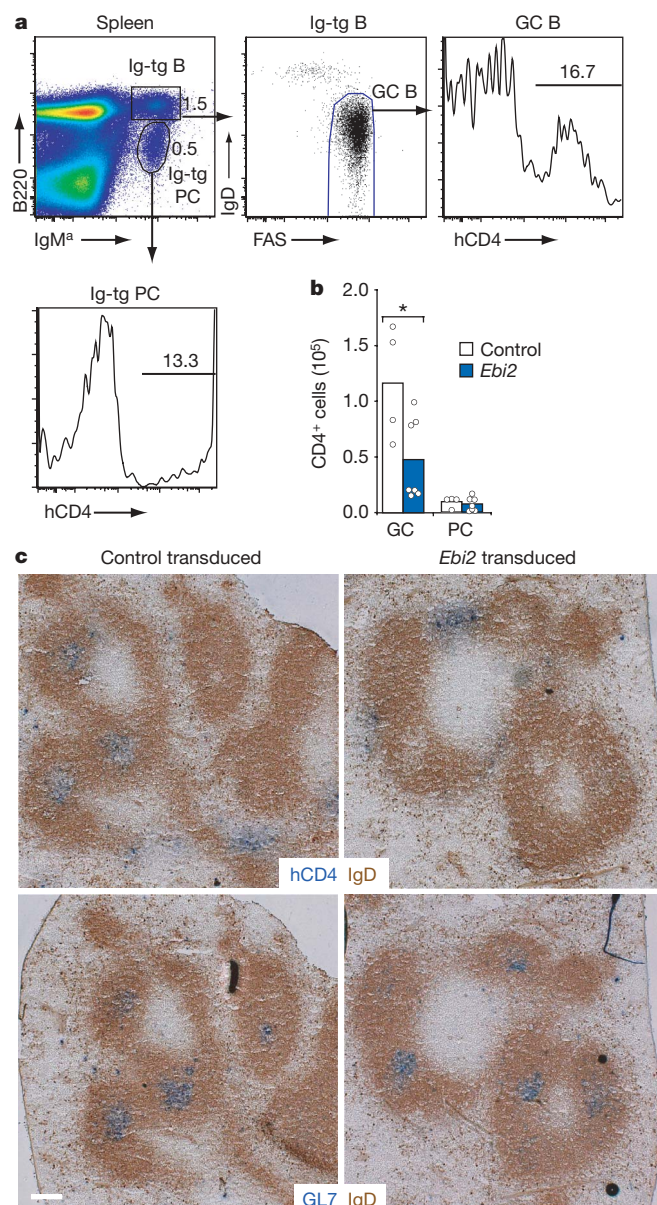


Figure 4 | Maintained *Ebi2* expression impairs participation in germinal centre response. **a**, Flow cytometric analysis of spleen cells from an immunized mouse receiving *Ebi2*-transduced Ig-transgenic (Ig-tg; IgM^a) B cells, 4 days after transfer, showing gating scheme to identify representation of transduced (human CD4⁺) cells among germinal centre (GC) B cells (B220⁺ IgM^a IgD^{lo} Fas^{hi}) and plasma cells (PC; B220^{lo} IgM^a). Numbers indicate frequency of cells in the indicated gate. **b**, Number of transduced (human CD4⁺) B cells having a germinal centre or plasma cell phenotype. **c**, Distribution of transduced B cells (human CD4⁺, blue) in sections of spleen from mice receiving control vector or *Ebi2*-transduced B cells. Endogenous naive B cells are stained brown (IgD) and germinal centres are detected in serial sections using GL7 (blue, lower panels). Scale bar, 100 μm.

METHODS SUMMARY

EGFP was inserted in place of the *Ebi2* open reading frame within E14 (129) embryonic stem cells using standard procedures, and *Ebi2*^{GFP/+} mice were backcrossed to C57BL/6 for six generations. Six-to-twelve-week-old C57BL/6 mice were from either the National Cancer Institute or Jackson Laboratories. B6(C)-H2-Ab1^{bm12}/KhEgJ (bm12) mice and B6.Cg-Igh^aThy1^aGPi1^a/J (IgM^a) mice were from Jackson Laboratories. MD4 mice²⁷ and CXCL13-deficient mice²² were from an internal colony. Bone marrow chimaeras were generated as described¹¹ and analysed after 6–12 weeks. NP-CGG immunizations were performed using 50 μg NP-CGG (Solid Phase Sciences) in Alum (Accurate Chemical & Scientific Corp.). The retroviral construct was made by inserting the mouse *Ebi2* open reading frame, with a preprolactin–Flag leader sequence²⁸ in place of the ATG,

into the MSCV2.2 retroviral vector containing cytoplasmic-domain-truncated human CD4 as an expression marker downstream of the internal ribosomal entry site⁸. B cells were isolated and in some cases labelled with 2.5 μ M 5-(and 6)-carboxy-fluorescein diacetate succinimidyl ester (CFSE, Molecular Probes) as described²⁹. For *in vivo* analysis of EBI2 expression, 5–10 \times 10⁶ purified B cells as described previously¹¹ were transferred into bm12 recipients. Transduced cells were adoptively transferred 1 day after spin-infection for transfers to non-immunized hosts or immediately after spin-infection for transfers to immunized hosts. For germinal centre experiments, B6 mice received 10⁵ MD4 B cells and 10⁵ OTII CD4⁺ T cells at day 1, were intraperitoneally immunized with 50 μ g HEL-OVA in RIBI adjuvant system (Sigma) at day 0, and received approximately 10⁶ Ebi2 or control-vector-transduced cells at day 1. Mice were analysed on day 5. Flow cytometry, ELISA, immunohistochemistry and immunofluorescence microscopy were performed using standard techniques and are detailed in the Methods.

Full Methods and any associated references are available in the online version of the paper at www.nature.com/nature.

Received 28 April; accepted 23 June 2009.

Published online 13 July 2009.

- MacLennan, I. C. M. Germinal centers. *Annu. Rev. Immunol.* **12**, 117–139 (1994).
- Kelsoe, G. The germinal center: a crucible for lymphocyte selection. *Semin. Immunol.* **8**, 179–184 (1996).
- Allen, C. D. & Cyster, J. G. Follicular dendritic cell networks of primary follicles and germinal centers: phenotype and function. *Semin. Immunol.* **20**, 14–25 (2008).
- Liu, Y.-J., Oldfield, S. & MacLennan, I. C. M. Memory B cells in T cell-dependent antibody responses colonize the splenic marginal zones. *Eur. J. Immunol.* **18**, 355–362 (1988).
- Jacob, J., Kassir, R. & Kelsoe, G. *In situ* studies of the primary immune response to (4-hydroxy-3-nitrophenyl)acetyl. I. The architecture and dynamics of responding cell populations. *J. Exp. Med.* **173**, 1165–1175 (1991).
- Cyster, J. G. & Goodnow, C. C. Antigen-induced exclusion from follicles and anergy are separate and complementary processes that influence peripheral B cell fate. *Immunity* **3**, 691–701 (1995).
- Garside, P. *et al.* Visualization of specific B and T lymphocyte interactions in the lymph node. *Science* **281**, 96–99 (1998).
- Reif, K. *et al.* Balanced responsiveness to chemoattractants from adjacent zones determines B-cell position. *Nature* **416**, 94–99 (2002).
- Pape, K. A. *et al.* Visualization of the genesis and fate of isotype-switched B cells during a primary immune response. *J. Exp. Med.* **197**, 1677–1687 (2003).
- Coffey, F., Alabyev, B. & Manser, T. Initial clonal expansion of germinal center B cells takes place at the perimeter of follicles. *Immunity* **30**, 599–609 (2009).
- Allen, C. D. *et al.* Germinal center dark and light zone organization is mediated by CXCR4 and CXCR5. *Nature Immunol.* **5**, 943–952 (2004).
- Nieuwenhuis, P. & Opstelten, D. Functional anatomy of germinal centers. *Am. J. Anat.* **170**, 421–435 (1984).
- Birkenbach, M. *et al.* Epstein-Barr virus induced genes: first lymphocyte-specific G-protein coupled peptide receptors. *J. Virol.* **67**, 2209–2220 (1993).
- Rosenkilde, M. M. *et al.* Molecular pharmacological phenotyping of EBI2. An orphan seven-transmembrane receptor with constitutive activity. *J. Biol. Chem.* **281**, 13199–13208 (2006).
- Shaffer, A. L. *et al.* Signatures of the immune response. *Immunity* **15**, 375–385 (2001).
- Cahir-McFarland, E. D. *et al.* Role of NF- κ B in cell survival and transcription of latent membrane protein 1-expressing or Epstein-Barr virus latency III-infected cells. *J. Virol.* **78**, 4108–4119 (2004).
- Mengle-Gaw, L. *et al.* Gene conversion between murine class II major histocompatibility complex loci. Functional and molecular evidence from the bm 12 mutant. *J. Exp. Med.* **160**, 1184–1194 (1984).
- Fu, Y.-X. & Chaplin, D. D. Development and maturation of secondary lymphoid tissues. *Annu. Rev. Immunol.* **17**, 399–433 (1999).
- Mackay, F. *et al.* Lymphotoxin but not tumor necrosis factor functions to maintain splenic architecture and humoral responsiveness in adult mice. *Eur. J. Immunol.* **27**, 2033–2042 (1997).
- Ngo, V. N. *et al.* Lymphotoxin α/β and tumor necrosis factor are required for stromal cell expression of homing chemokines in B and T cell areas of the spleen. *J. Exp. Med.* **189**, 403–412 (1999).
- Gunn, M. D. *et al.* A B-cell-homing chemokine made in lymphoid follicles activates Burkitt's lymphoma receptor-1. *Nature* **391**, 799–803 (1998).
- Ansel, K. M. *et al.* A chemokine driven positive feedback loop organizes lymphoid follicles. *Nature* **406**, 309–314 (2000).
- Tew, J. G. *et al.* Follicular dendritic cells and presentation of antigen and costimulatory signals to B cells. *Immunol. Rev.* **156**, 39–52 (1997).
- Forster, R. *et al.* A putative chemokine receptor, BLR1, directs B cell migration to defined lymphoid organs and specific anatomic compartments of the spleen. *Cell* **87**, 1037–1047 (1996).
- Lossos, I. S. & Levy, R. Higher grade transformation of follicular lymphoma: phenotypic tumor progression associated with diverse genetic lesions. *Semin. Cancer Biol.* **13**, 191–202 (2003).
- Alizadeh, A. A. *et al.* Distinct types of diffuse large B-cell lymphoma identified by gene expression profiling. *Nature* **403**, 503–511 (2000).
- Goodnow, C. C. *et al.* Altered immunoglobulin expression and functional silencing of self-reactive B lymphocytes in transgenic mice. *Nature* **334**, 676–682 (1988).
- Ishii, K. *et al.* Kinetics of thrombin receptor cleavage on intact cells. Relation to signaling. *J. Biol. Chem.* **268**, 9780–9786 (1993).
- Okada, T. *et al.* Antigen-engaged B cells undergo chemotaxis toward the T zone and form motile conjugates with helper T cells. *PLoS Biol.* **3**, e150 (2005).

Supplementary Information is linked to the online version of the paper at www.nature.com/nature.

Acknowledgements We thank C. Allen for help with microscopy and discussions, J. Green, E. Gray and K. Suzuki for helpful advice and J. An for expert assistance with the mouse colony. We also thank N. Killen and J. Dietrich for help with gene targeting. J.P.P. is an Associate and J.G.C. is an Investigator of the Howard Hughes Medical Institute. This work was supported in part by grants from the National Institutes of Health.

Author Contributions J.P.P. and J.G.C. designed and conceptualized the research; J.P.P., L.M.K. and Y.X. performed the experiments. J.P.P., L.M.K. and J.G.C. analysed the data, prepared the figures and wrote the manuscript.

Author Information Reprints and permissions information is available at www.nature.com/reprints. Correspondence and requests for materials should be addressed to J.G.C. (Jason.Cyster@ucsf.edu).

METHODS

Mice. Six-to-twelve-week-old C57BL/6 were purchased from either the National Cancer Institute or Jackson Laboratories. B6(C)-H2-Ab1^{bm12}/KhEgJ (bm12) mice and B6.Cg-Igh^TThy1^aGPI1^a/J (IgMa) mice were from Jackson Laboratories. MD4 mice²⁷ and CXCL13-deficient mice²² were from an internal colony. Bone marrow chimaeras were generated as described¹¹ and analysed after 6–12 weeks. NP-CGG immunizations were performed using 50 µg NP-CGG (Solid Phase Sciences) in Alum (Accurate Chemical & Scientific Corp.). Treatment with LTβR-Fc (provided by J. Browning, Biogen Idec) was as described²⁰ using 100 µg once a week for 3 weeks. Animals were housed in specific pathogen-free environment in the Laboratory Animal Research Center at UCSF and all experiments conformed to ethical principles and guidelines approved by the UCSF Institutional Animal Care and Use Committee.

Ebi2 gene targeting and retroviral constructs. A 5' homology arm (5.2 kilobases (kb)) and 3' homology arm (3.7 kb) were generated from mouse genomic DNA by PCR and cloned using BD In-Fusion Dry-Down PCR cloning kit into vector EGFP-polyA-loxP-Neo-loxP-DTA-PL452 (provided by N. Killeen) to flank the EGFP-polyA-loxP-Neo-loxP insert. E14 (129) embryonic stem cells were transfected by standard techniques and 350 colonies were screened by long PCR (Roche Long Template PCR system), yielding 22 positive clones. Homologous recombination was confirmed by Southern blotting and three clones were used for microinjection into B6 blastocysts. Chimaeras were bred to B6 mice and germline transmission was confirmed by allele-specific PCR and flow cytometric detection of GFP expression. *Ebi2*^{GFP/+} mice were intercrossed with actin-Cre transgenic mice and deletion of the *loxP*-flanked neomycin-resistance cassette was confirmed by PCR. *Ebi2*^{GFP/+} (neo⁻) mice used in this study were backcrossed to B6 for at least six generations. The retroviral construct was made by inserting the mouse *Ebi2* open reading frame, with a preprolactin-Flag leader sequence²⁸ in place of the ATG, into the MSCV2.2 retroviral vector containing cytoplasmic-domain truncated human CD4 as an expression marker downstream of the internal ribosomal entry site⁸. The control vector contained cytoplasmic domain truncated human nerve growth factor receptor as an irrelevant insert.

Cell isolation, CFSE labelling, retroviral transduction and adoptive transfers. B cells were isolated and in some cases labelled with 2.5 µM 5-(and 6)-carboxy-fluorescein diacetate succinimidyl ester (CFSE, Molecular Probes) as described²⁹. For *in vivo* analysis of *Ebi2* expression, 5–10 × 10⁶ purified B cells as described¹¹, were transferred into bm12 recipients. *In vitro* analysis of *Ebi2* expression was performed by culturing 10⁵ splenocytes from *Ebi2*^{GFP/+} mice with 10–13 µg ml⁻¹ anti-IgM (F(ab')₂ goat anti-mouse IgM, Jackson ImmunoResearch), 10 µg ml⁻¹ anti-CD40 (clone FGK4.5, UCSF Hybridoma Core), or both, for 24 and 48 h. Retroviral supernatant was generated using Phoenix packaging cells. Retroviral transduction of activated B cells was performed as described⁸ using MD4 Ig-transgenic B cells. Transduced cells were adoptively transferred 1 day after spin-infection for transfers to non-immunized hosts, or immediately after spin-infection for transfers to immunized hosts. For germinal centre experiments, B6 mice received 10⁵ MD4 B cells and 10⁵ OTII CD4⁺ T cells at day 1, were intraperitoneally immunized with 50 µg HEL-OVA in RIBI adjuvant system (Sigma) at day 0 and received approximately 10⁶ *Ebi2*- or control-vector-transduced cells at day 1. Mice were analysed on day 5.

Flow cytometry. Bone marrow B cell subsets were analysed as described previously³⁰. Spleen and lymph node cells were isolated and stained as described¹¹. For analysis of germinal centre B cell differentiation, cells were stained with phycoerythrin (PE)-Cy5.5-conjugated anti-B220 (RA3-6B2; BD Biosciences), Pacific blue-conjugated anti-CD45.1, FITC-conjugated anti-IgD (11-26c.2a; BD Biosciences) and PE-Cy7-conjugated anti-Fas (Jo2; BD Biosciences). For analysis of EBI2 expression in T cells, spleens and lymph nodes were stained with allophycocyanin (APC)-conjugated anti-TCRβ (H57-597, eBioscience), PE-Cy5.5-conjugated anti-CD4 (RM4-5, Invitrogen), with PE-conjugated anti-CD8 (CT-CD8a, Invitrogen), and with biotin-conjugated anti-NK1.1 (PK136, BD Biosciences).

ELISA. IgG1 anti-NP ELISA was performed by coating 96-well plates (Immunolon) with 10 µg ml⁻¹ NP(30)BSA (Solid Phase Sciences) in PBS for at least 2 h at 37 °C, and blocked with 5% (w/v) BSA (Calbiochem) for 2 h at ~25 °C. Serum samples were serially diluted (1:2) starting at 1:500 in PBS 0.01% Tween, incubated for 2 h at ~25 °C, and NP-binding IgG1 was detected using biotin-conjugated anti-IgG1 (A85, BD Biosciences), followed by horseradish-peroxidase-conjugated streptavidin (Jackson ImmunoResearch). Colour development was done using ABTS substrate (Southern Biotech) in 55 mM citrate buffer containing 0.03% H₂O₂. Absorbance was measured at 405 nm in a VERSAmax microplate reader using SoftMax pro 5.2 (Molecular Devices). The NP-specific IgG1 concentration was calculated by determining the dilution required to achieve an optical density of 0.5, 1.0 and 1.5 (across these values, the correlation coefficient was >0.99 in all serum samples), averaged, and displayed as relative units to a standard serum sample.

Immunohistochemistry and immunofluorescent microscopy. Cryosections of 5–7 µm were fixed and stained immunohistochemically as described⁸ with combinations of the following antibodies: anti-IgD (11-26c.2a, BD Biosciences), anti-IgMa (DS-1, BD Biosciences), human CD4 (RPA-T4, BD Biosciences) and B220 (RA3-6B2, BD Biosciences). For immunofluorescence, staining with biotin-conjugated anti-IgD^a (AMS9.1, BD Biosciences) was detected with Alexa Fluor488-conjugated streptavidin (Invitrogen), PE-conjugated anti-IgD^b (217-170, BD Biosciences), and Alexa 647-conjugated anti-CD4, and anti-CD8 (UCSF Hybridoma Core). The FDC network was stained using purified anti-CD35 (8C12, BD Biosciences) detected with APC-conjugated anti-rat IgG (Jackson ImmunoResearch). Marginal zone macrophages were stained with an anti-Ser4 antibody (P. Crocker, University of Glasgow) conjugated to Alexa Fluor647. Analysis of T-cell distribution was performed with biotin-conjugated anti-CD90.1 (Thy-1.1, clone HIS51) detected with Alexa Fluor488-conjugated, and with PE-conjugated anti-CD90.2 (Thy-1.2, clone 30-H12). Sections were then blocked with 5% normal rat serum before staining with additional antibodies. FITC-conjugated anti-T- and B-cell activation antigen (GL7; BD Biosciences) was used to detect germinal centres. For detection of GFP, tissues were fixed in 4% paraformaldehyde and prepared as described³¹. Images were obtained with a Zeiss AxioObserver Z1 inverted microscope or a Zeiss AxioImager M1 upright microscope.

30. Pereira, J. P. *et al.* Cannabinoid receptor 2 mediates the retention of immature B cells in bone marrow sinusoids. *Nature Immunol.* **10**, 403–411 (2009).
31. Pappu, R. *et al.* Promotion of lymphocyte egress into blood and lymph by distinct sources of sphingosine-1-phosphate. *Science* **316**, 295–298 (2007).

L1 retrotransposition in human neural progenitor cells

Nicole G. Coufal¹, José L. Garcia-Perez^{2,3}, Grace E. Peng¹, Gene W. Yeo^{1†}, Yangling Mu¹, Michael T. Lovci^{1†}, Maria Morell⁴, K. Sue O'Shea⁴, John V. Moran^{2,5} & Fred H. Gage¹

Long interspersed element 1 (LINE-1 or L1) retrotransposons have markedly affected the human genome. L1s must retrotranspose in the germ line or during early development to ensure their evolutionary success, yet the extent to which this process affects somatic cells is poorly understood. We previously demonstrated that engineered human L1s can retrotranspose in adult rat hippocampus progenitor cells *in vitro* and in the mouse brain *in vivo*¹. Here we demonstrate that neural progenitor cells isolated from human fetal brain and derived from human embryonic stem cells support the retrotransposition of engineered human L1s *in vitro*. Furthermore, we developed a quantitative multiplex polymerase chain reaction that detected an increase in the copy number of endogenous L1s in the hippocampus, and in several regions of adult human brains, when compared to the copy number of endogenous L1s in heart or liver genomic DNAs from the same donor. These data suggest that *de novo* L1 retrotransposition events may occur in the human brain and, in principle, have the potential to contribute to individual somatic mosaicism.

The human nervous system is complex, containing approximately 10¹⁵ synapses with a vast diversity of neuronal cell types and connections that are influenced by complex and incompletely understood environmental and genetic factors². Neural progenitor cells (NPCs) give rise to the three main lineages of the nervous system: neurons, astrocytes and oligodendrocytes. To determine whether human NPCs can support L1 retrotransposition, we transfected human fetal brain stem cells (hCNS-SCNs) (Fig. 1a)³ with an expression construct containing a retrotransposition-competent human L1 (RC-L1) driven from its native promoter (L1_{RP}). The RC-L1 also contains a retrotransposition indicator cassette in its 3' untranslated region (UTR), consisting of a reversed copy of the enhanced green fluorescent protein (EGFP) expression cassette, which is interrupted by an intron in the same transcriptional orientation as the RC-L1 (refs 4–7). The orientation of the cassette ensures that EGFP-positive cells will only arise if the RC-L1 undergoes retrotransposition (Supplementary Fig. 1a).

A low level of L1_{RP} retrotransposition, averaging 8–12 events per 100,000 cells, was observed in three different human fetal brain stem cell lines (BR1, BR3 and BR4; Fig. 1d). By comparison, an L1 containing two missense mutations in the open reading frame 1 (ORF1)-encoded protein (JM111/L1_{RP})^{5,7} did not retrotranspose (Fig. 1b, d). Controls demonstrated precise splicing of the intron from the retrotransposed EGFP gene (Fig. 1b and Supplementary Figs 1 and 4), and indicated that L1 retrotransposition events were detectable by both PCR and Southern blotting 3 months after transfection (Fig. 1c). Moreover, reverse transcriptase PCR (RT-PCR) revealed that hCNS-SCNs express endogenous L1 transcripts and that some transcripts are derived from the human-specific (L1Hs) subfamily^{4,9,10} (Supplementary Fig. 6a, b and Supplementary Tables 4 and 5).

To determine whether L1 retrotransposition occurred in undifferentiated cells, we conducted immunocytochemical localization of cell-type-restricted markers in EGFP-positive hCNS-SCNs. These cells expressed neural stem cell markers, including SOX2, Nestin, Musashi-1 and SOX1 (Fig. 1e and Supplementary Fig. 2a, b), and some co-labelled with Ki-67, indicating that they continued to proliferate (Supplementary Fig. 2c). EGFP-positive hCNS-SCNs could also be differentiated to cells of both the neuronal and the glial lineages (Fig. 1f, g). Notably, L1_{RP} did not retrotranspose using our experimental conditions in primary human astrocytes or fibroblasts, although a low level of endogenous L1 expression was detected in both cell types (Fig. 1d and Supplementary Figs 2d, e and 6a, b).

We next used two different protocols to derive NPCs from five human embryonic stem cell lines (hESCs; Fig. 2a). As in our previous study¹, NPC differentiation led to a ~25-fold increase in L1 promoter activity over a 2-day period, and then a decline (Fig. 2c); there was also a ~250-fold increase in synapsin promoter activity during differentiation (Supplementary Fig. 4b). H13B-derived NPCs expressed both endogenous L1 RNA and ORF1 protein⁸, although the level of ORF1 protein expression was less than in the parental H13B hESC lines (Fig. 2d). HUES6-derived NPCs also expressed endogenous L1 RNA (Supplementary Fig. 6a, b), and sequencing indicated that some transcripts are derived from the L1Hs subfamily (Supplementary Tables 4 and 5). Similar studies performed with fetal brain, liver, and skin samples showed evidence of endogenous L1 transcription (Supplementary Fig. 6c, d and Supplementary Tables 4 and 5).

RC-L1 retrotransposition was readily detected at varying efficiencies in hESC-derived NPC lines (Supplementary Table 1 and Supplementary Figs 1 and 4f, g). Again, we determined that JM111/L1_{RP} could not retrotranspose (Supplementary Table 1), that EGFP-positive NPCs expressed canonical neural stem cell markers (Fig. 2b, e and Supplementary Fig. 3c, d), and that EGFP-positive HUES6-derived NPCs could be differentiated to cells of both the neuronal and glial lineages (Fig. 2f and Supplementary Fig. 3e, f). The variability in retrotransposition efficiencies in hESC-derived NPCs probably depended on several factors (see Supplementary Table 1 for specific details).

Characterization of EGFP-positive neurons showed that some expressed subtype-specific markers (tyrosine hydroxylase (Fig. 2g) and GABA (γ -aminobutyric acid; data not shown)) and whole-cell perforated patch-clamp recording demonstrated that some HUES6-derived NPCs are functional (Fig. 2h–k; $n = 4$ cells). Furthermore, we demonstrated that an RC-L1 tagged with neomycin or blasticidin retrotransposition indicator cassettes could retrotranspose in NPCs (Supplementary Figs 1 and 4c–e)^{5,11}. Some G418-resistant foci also expressed SOX3 and could be differentiated to a neuronal lineage (Fig. 2b).

¹Laboratory of Genetics, The Salk Institute for Biological Studies, 10010 North Torrey Pines Road, La Jolla, California 92037, USA. ²Departments of Human Genetics and Internal Medicine, 1241 East Catherine Street, University of Michigan Medical School, Ann Arbor, Michigan 48109-5618, USA. ³Andalusian Stem Cell Bank, Center for Biomedical Research, Avda Conocimiento s/n, University of Granada, 18100, Spain. ⁴Department of Cell and Developmental Biology, 109 Zina Pitcher, University of Michigan Medical School, Ann Arbor, Michigan 48109-2200, USA. ⁵Howard Hughes Medical Institute, Chevy Chase, Maryland 20815-6789, USA. [†]Present address: Stem Cell Program, Department of Cellular and Molecular Medicine, University of California, San Diego, 9500 Gilman Drive, La Jolla, California 92093-5004, USA.

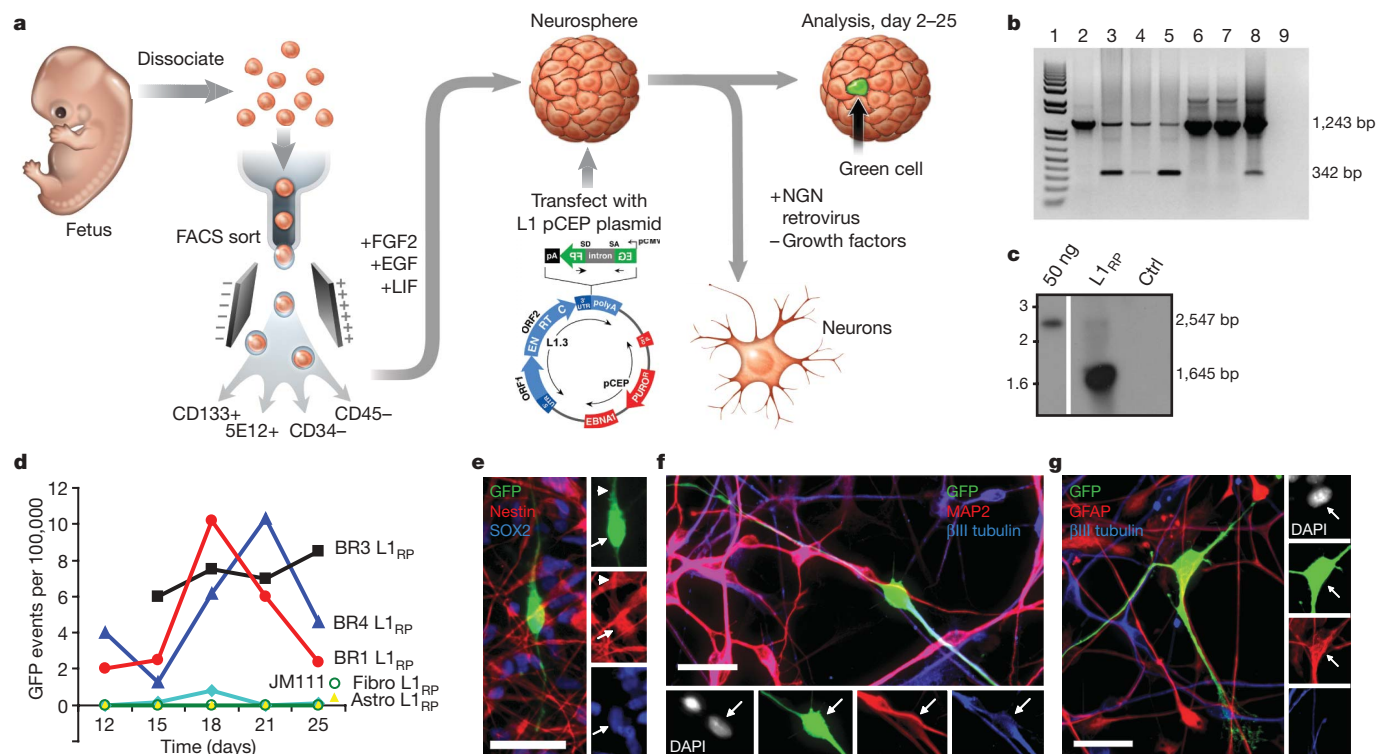


Figure 1 | L1 retrotransposition in hCNS-SCNs. **a**, Experimental rationale. **b**, PCR of genomic DNA. The 1,243-bp product contains the intron, the 342-bp product indicates intron loss and retrotransposition. Lane 1, standards; lane 2, hCNS-SCNs transfected with JM111/L1_{RP}; lanes 3–5, three human fetal brain stem cell lines transfected with L1_{RP}; lanes 6–7, primary astrocytes and fibroblasts transfected with L1_{RP}; lane 8, positive control; lane 9, water. **c**, Southern blot of hCNS-SCNs (line FBR-BR3). The 2,547-bp band

We next characterized 19 retrotransposition events from EGFP-positive NPCs (Supplementary Fig. 7b and Supplementary Table 2). Comparison of the pre- and post-integration sites demonstrated that retrotransposition occurred into an actual or inferred L1 endonuclease consensus cleavage site (5'-TTT/A and derivatives). Five of eight fully characterized events were flanked by target site duplications, and no large deletions were detected at the insertion site^{5,9,12} (Supplementary Fig. 7b and Supplementary Table 2). Interestingly, 16 out of 19 retrotransposition events were fewer than 100 kilobases (kb) from a gene and some occurred in the vicinity of a neuronally expressed gene^{1,12,13}.

Notably, we consistently observed higher L1 retrotransposition efficiencies in hESC-derived NPCs when compared to fetal NPCs. A Euclidian distance map on the basis of exon-array expression analysis¹⁴ indicated that hCNS-SCNs cluster closer to HUES6 cells, whereas HUES6-derived NPCs cluster closer to fetal brain (Supplementary Fig. 11a). Thus, hESC-derived NPCs and hCNS-SCNs may represent different developmental stages in progenitor differentiation. That being stated, we conclude that engineered human L1s can retrotranspose in human NPCs.

Several studies have reported an inverse correlation between L1 expression and the methylation status of the CpG island in their 5' UTRs^{15,16}. Thus, we performed bisulphite conversion analyses on genomic DNAs derived from matched brain and skin tissue samples from two 80–82-day-old fetuses (Fig. 3a, one male/one female sample). We then amplified a portion of the L1 5' UTR containing 20 CpG sites and sequenced the resultant amplicons. Notably, the L1 5' UTR exhibited significantly less methylation in both brain samples when compared to the matched skin sample (two-sample Kolmogorov–Smirnov test, $P \leq 0.0079$ day 80 female, $P \leq 0.0034$ day 82 male; Fig. 3b). The analysis of individual L1 5' UTR sequences demonstrated the greatest variation between the brain and skin at CpG residues

represents plasmid, the 1,645-bp band is diagnostic for genomic insertion. Ctrl, control. **d**, Time course of L1 retrotransposition. Astro, astrocytes; fibro, fibroblasts. **e**, EGFP-positive cells express Nestin and SOX2. Arrows indicate co-labelled cell body, arrowheads indicate co-labelled processes.

f, EGFP-positive cells can differentiate to neurons (βIII tubulin and MAP2ab positive). **g**, EGFP-positive cells can differentiate into glia (GFAP-positive, βIII-tubulin-negative). Scale bars, 25 μm.

located near the 3' end of the amplicon, and six amplicons from the brain samples were unmethylated (Fig. 3e and Supplementary Fig. 8a, b). Restricting this analysis to ten L1s from brain and skin with the highest sequence homology to an RC-L1 showed that 19 out of 20 sequences were derived from the L1Hs subfamily (data not shown), and that one L1Hs element from the brain was completely unmethylated (Fig. 3c). In all cases, control experiments showed that the bisulphite conversion efficiency was >90% (Supplementary Fig. 8c).

Previous data indicated that SOX2 and MECP2 could associate with the L1 promoter and repress L1 transcription under some experimental conditions^{1,17}. Two putative SRY-binding sites are located in the L1 5' UTR immediately 3' to the CpG island (Fig. 3a and Supplementary Fig. 11b)¹⁸. Thus, we performed chromatin immunoprecipitation (ChIP) for SOX2 and MECP2 in hCNS-SCNs, HUES6-derived NPCs, and HUES6-derived neurons. SOX2 associated with the L1 5' UTR in a pattern that correlates with the decrease in SOX2 expression observed during neural differentiation (Fig. 3d and Supplementary Fig. 4h). MECP2 expression was lower in both hCNS-SCNs and HUES6-derived NPCs than in neurons (Supplementary Fig. 4h), and both hCNS-SCNs and HUES6-derived NPCs expressed similar levels and types of L1 transcripts (Supplementary Fig. 6a, b). However, higher levels of MECP2 were detected in association with the L1 promoter in hCNS-SCNs than in HUES6-derived NPCs (Fig. 3d). We propose that less L1 promoter methylation in the developing brain may correlate with increased L1 transcription and perhaps L1 retrotransposition, and the differential interaction of SOX2 and MECP2 with L1 regulatory sequences may modulate L1 activity in different neuronal cell types.

Although NPCs are useful to monitor L1 activity, they only allow monitoring of a single L1 expressed from a privileged context. By comparison, the average human genome contains ~80–100 active L1s, the expression of which may be affected by chromatin structure⁴.

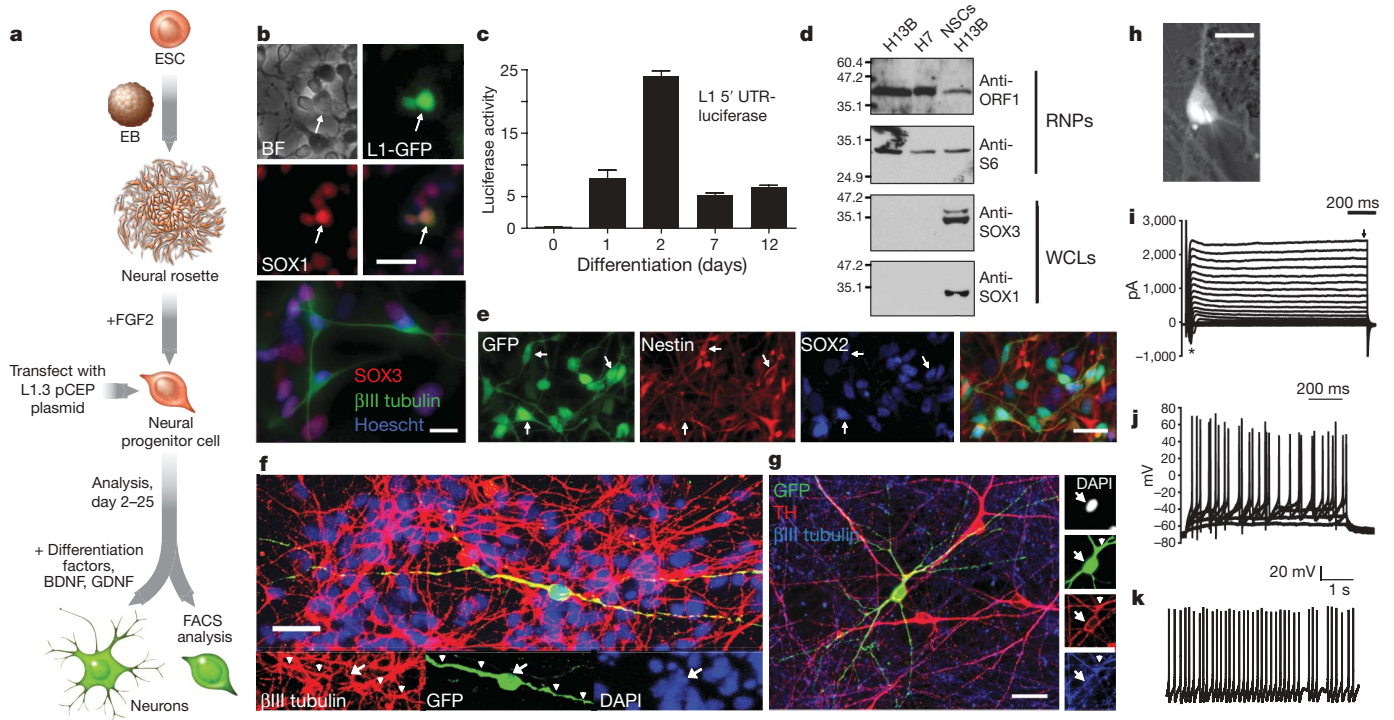
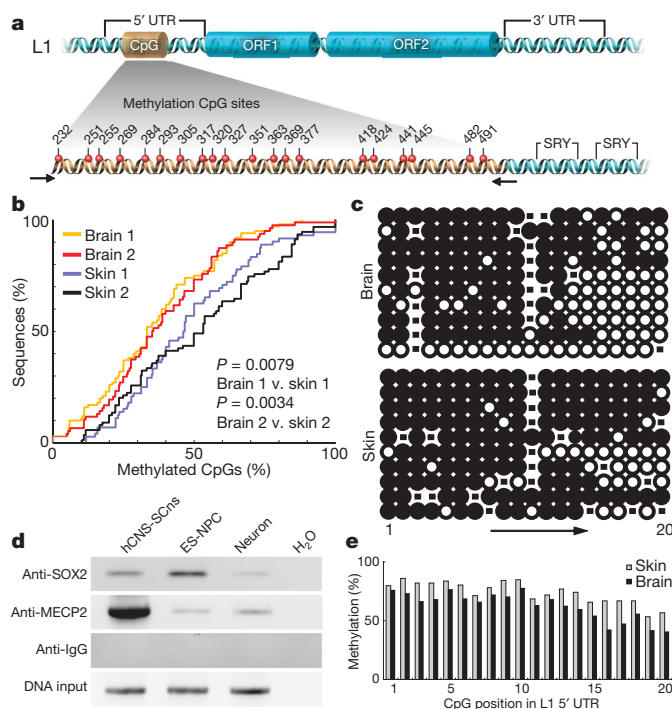


Figure 2 | L1 retrotransposition in hESC-derived NPCs. **a**, Experimental rationale. BDNF, brain-derived neurotrophic factor; EB, embryoid body; GDNF, glial-cell-derived neurotrophic factor. **b**, L1 retrotransposition in H13B (top, LRE3 with EGFP reporter) and H7 (bottom, LRE3 with neomycin reporter)-derived NPCs (BF, bright field). G418-resistant foci can express progenitor (SOX3) and neuronal (β III tubulin) markers. **c**, L1 5' UTR is induced upon differentiation. Error bars denote s.d. **d**, H13B-derived NPCs express endogenous ORF1 protein. RNP, ribonucleoprotein particle samples;

WCL, whole cell lysates. Lane markers denote kDa. **e–g**, EGFP-positive, HUES6-derived NPCs express SOX2 and Nestin and can differentiate to be tyrosine hydroxylase (TH) positive. Arrows indicate cell soma co-localization, arrowheads indicate co-labelled processes. Scale bars, 25 μ m. **h**, An LRE3-EGFP positive neuron. Scale bar, 10 μ m. **i–k**, Data are derived from the neuron in **h**. **i**, Transient Na^+ (asterisk) and sustained K^+ (arrow) currents in response to voltage step depolarizations. **j**, Suprathreshold responses to somatic current injections. **k**, Spontaneous action potentials ($V_m = -50$ mV).

Therefore, we developed a quantitative multiplexing PCR strategy to investigate endogenous L1 activity in the human brain, proposing that active retrotransposition would result in increased L1 content in brain genomic DNA as compared to other tissues (Fig. 4a).



In brief, we designed Taqman probes against a conserved 3' region of ORF2 (conjugated with the VIC fluorophore), as well as several control probes (conjugated with the 6FAM fluorophore). Controls were designed against the L1 5' UTR and other non-mobile DNA sequences in the genome that have copy numbers that are higher (such as α satellite¹⁹) or lower (such as HERVH and the 5S ribosomal DNA (rDNA) gene) than ORF2. Furthermore, because most L1 retrotransposition events are 5' truncated^{9,20,21}, we reasoned that the L1 5' UTR probes should detect a smaller copy number increase than the L1 ORF2 probes. Each probe set amplified a single product of the predicted size (Supplementary Fig. 10b). Moreover, sequencing PCR products derived from both ORF2 probe sets showed enrichment for members of the L1Hs subfamily (Supplementary Table 3).

We next isolated genomic DNA from the hippocampus, cerebellum, liver and heart from three adult humans. We consistently observed a statistically significant increase in L1 ORF2 content in the hippocampus when compared to heart and liver samples from the same individual (Fig. 4b, c and Supplementary Figs 9a and 10a). Notably, two individuals (1079 and 1846) showed more marked copy number differences

Figure 3 | Methylation analysis and ChIP for the endogenous human L1 5' UTR. **a**, Schematic illustrating the L1 CpG island, and SRY-binding sites. **b**, Cumulative distribution function plot, comparing overall methylation and collapsing CpG sites into a single data point (two-sample Kolmogorov–Smirnov test). **c**, Individual methylation of sequences showing highest sequence similarity to consensus RC-L1s. Open and closed circles denote unmethylated and methylated CpG dinucleotides, respectively. Dash indicates mutated CpG site. **d**, ChIP identifying MECP2 and SOX2 occupying the endogenous human L1 promoter, extracts were analysed by PCR towards the L1 5' UTR SRY-binding region (SOX2 immunoprecipitation) or CpG island region (MECP2 immunoprecipitation). **e**, CpG dinucleotides exhibited higher methylation at the 5'-end of the CpG island; higher methylation overall was observed in skin samples.

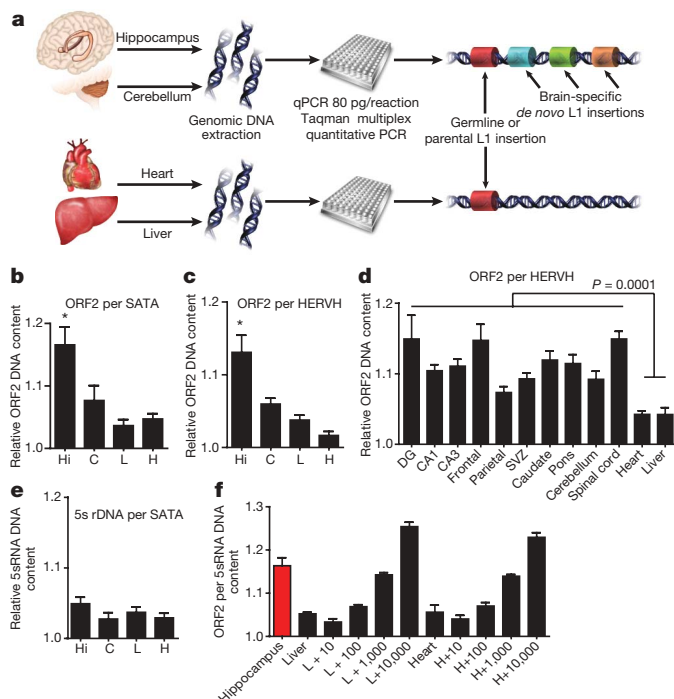


Figure 4 | Multiplex quantitative PCR analyses of L1 copy number in human tissues. **a**, Experimental schematic. **b**, **c**, Relative quantity of L1, standardized such that the lowest liver value was normalized to 1.0. C, cerebellum; H, heart; Hi, hippocampus; L, liver. Further L1 ORF2 assays with other internals controls are shown in Supplementary Figs 9 and 10. All error bars are s.e.m. * $P < 0.05$ (repeated measures one-way analysis of variance (ANOVA) with Bonferroni correction, $n = 3$ individuals, with three repeat samples from each tissue). SATA, α satellite. **d**, Ten samples from various brain regions ($n = 3$ individuals) compared to somatic liver and heart. DG, dentate gyrus; SVZ, subventricular zone. One-way t -test, $P \leq 0.0001$ with 34 degrees of freedom. **e**, Multiplexing of 5S rDNA with α -satellite indicated no significant change, $P \leq 0.5054$. **f**, Hippocampal tissue compared to liver (L) and heart (H) spiked with estimated plasmid copy numbers of L1 (10, 100, 1,000 and 10,000 copies).

than a third individual (4590) (Supplementary Fig. 10a). Controls demonstrated that the ratio of the 5S rDNA gene to α satellite DNA between each tissue remained relatively constant (Fig. 4e).

We extended this analysis to ten brain regions from three other individuals (Fig. 4d and Supplementary Fig. 9b). The samples were derived from the frontal and parietal cortex, spinal cord, caudate, CA1 and CA3 areas of the hippocampus and pons, as well as from the hippocampal dentate gyrus and the subventricular zone²². As described earlier, there was marked variation between different brain areas and between individuals (Supplementary Fig. 9c). However, an unpaired t -test comparing all the grouped brain samples to the heart and liver DNA again showed a small, but statistically significant increase in ORF2 content in the brain (Fig. 4d).

To independently corroborate the observed increase in L1 copy number in the hippocampus and cerebellum samples, we spiked 80 pg of liver and heart genomic DNA (approximately 12 genomes) from individual 1846 with a calculated quantity of L1 plasmid, then we repeated the multiplexing approach to assay ORF2 quantity relative to the 5S rDNA internal control (Fig. 4f). Three replications of this experiment indicated that the hippocampus samples contained approximately 1,000 more L1 copies than the heart or liver genomic DNAs, suggesting a theoretical increase in ORF2 of approximately 80 copies per cell. The spiked L1 copies were in the form of a plasmid, which probably affects the copy number estimates, providing an estimate of relative change and not precise quantification of the absolute number of L1s per cell. Therefore, ultimate proof that endogenous L1s are retrotransposing in the brain requires identification of new retrotransposition events in individual somatic cells.

The large degree of variability in L1-ORF2 copy numbers between brain regions and individuals may represent unsystematic rates of L1 retrotransposition, or another level of regulation that requires further determination. That being stated, our *in vitro* findings in NPCs coupled with the observed L1-ORF2 copy number changes in the brain make it tempting to speculate that somatic retrotransposition events occur during the early stages of human nervous system development. This study contributes to a growing body of evidence indicating that engineered L1s can retrotranspose during early development, and in select somatic cells^{1,6,23–25}. Future experiments will determine whether endogenous L1s truly retrotranspose in the brain and whether these events are simply 'genomic noise' or have the potential to affect neurogenesis and/or neuronal function.

METHODS SUMMARY

Cell culture, transfection and analysis. Fetal hCNS-SCNs lines³ and hESCs^{24,26} were cultured as previously described. Neural progenitors were derived from hESCs as previously described^{14,27}. NPCs were transfected by nucleofection (Amaxa Biosystems), and either maintained as progenitors in the presence of FGF2 or differentiated as previously described¹⁴. Cells were transfected with L1s containing an EGFP retrotransposition cassette in pCEP4 (Invitrogen) that lacks the CMV promoter and contains a puromycin-resistance gene⁷.

Cell lysates. Ribonucleoprotein particles were isolated and analysed as previously described⁸. Luciferase assays were performed as previously described¹. ChIP was performed using primers towards the L1 5' UTR and a ChIP assay kit (Upstate/Millipore) as per the manufacturer's protocol.

Bisulphite analysis. Fetal tissues were obtained from the Birth Defects Research Laboratory at the University of Washington. Bisulphite conversions were performed by manufacturer's instructions using the Epitect kit (Qiagen). BLASTN (<http://blast.ncbi.nlm.nih.gov/Blast.cgi>) was used to align sequences to a database of full-length L1s.

PCR. Adult human tissues were obtained from the NICHD Brain and Tissue Bank for Developmental Disorders (University of Maryland). Taqman probes and primers were designed using L1 Base (<http://l1base.molgen.mpg.de/>) and copy number estimates were based on the UCSC genome browser (<http://genome.ucsc.edu>). Experiments were performed on an ABI Prism 7000 sequence detection system (Applied Biosystems). For each tissue, three separate tissue samples were extracted and considered as repeated measures. Whole genome size was estimated based on the equation: cell genomic DNA content = 3×10^9 (bp) \times 2 (diploid) \times 660 (molecular mass of 1 bp) \times 1.67×10^{12} (weight of 1 Da), (in which bp denote base pairs), resulting in the approximation that one cell contains 6.6 pg genomic DNA²⁸. Therefore, the 80 pg of genomic DNA used per reaction is derived from approximately 12 cells. Inverse PCR was performed as previously described^{1,24}.

Received 31 March; accepted 1 July 2009.

Published online 5 August 2009; corrected 27 August 2009 (see full-text HTML version for details).

- Muotri, A. R. *et al.* Somatic mosaicism in neuronal precursor cells mediated by L1 retrotransposition. *Nature* **435**, 903–910 (2005).
- Tang, Y., Nyengaard, J. R., De Groot, D. M. & Gundersen, H. J. Total regional and global number of synapses in the human brain neocortex. *Synapse* **41**, 258–273 (2001).
- Uchida, N. *et al.* Direct isolation of human central nervous system stem cells. *Proc. Natl Acad. Sci. USA* **97**, 14720–14725 (2000).
- Brouha, B. *et al.* Hot L1s account for the bulk of retrotransposition in the human population. *Proc. Natl Acad. Sci. USA* **100**, 5280–5285 (2003).
- Moran, J. V. *et al.* High frequency retrotransposition in cultured mammalian cells. *Cell* **87**, 917–927 (1996).
- Ostertag, E. M. *et al.* A mouse model of human L1 retrotransposition. *Nature Genet.* **32**, 655–660 (2002).
- Ostertag, E. M., Prak, E. T., DeBerardinis, R. J., Moran, J. V. & Kazazian, H. H. Jr. Determination of L1 retrotransposition kinetics in cultured cells. *Nucleic Acids Res.* **28**, 1418–1423 (2000).
- Kulpa, D. A. & Moran, J. V. Ribonucleoprotein particle formation is necessary but not sufficient for LINE-1 retrotransposition. *Hum. Mol. Genet.* **14**, 3237–3248 (2005).
- Moran, J. & Gilbert, N. *Mammalian LINE-1 Retrotransposons and Related Elements* (ASM Press, 2002).
- Myers, J. S. *et al.* A comprehensive analysis of recently integrated human Ta L1 elements. *Am. J. Hum. Genet.* **71**, 312–326 (2002).
- Morrish, T. A. *et al.* DNA repair mediated by endonuclease-independent LINE-1 retrotransposition. *Nature Genet.* **31**, 159–165 (2002).
- Gilbert, N., Lutz, S., Morrish, T. A. & Moran, J. V. Multiple fates of L1 retrotransposition intermediates in cultured human cells. *Mol. Cell. Biol.* **25**, 7780–7795 (2005).

13. Symer, D. E. *et al.* Human L1 retrotransposition is associated with genetic instability *in vivo*. *Cell* **110**, 327–338 (2002).
14. Yeo, G. W. *et al.* Alternative splicing events identified in human embryonic stem cells and neural progenitors. *PLoS Comput. Biol.* **3**, e196 (2007).
15. Bourc'his, D. & Bestor, T. H. Meiotic catastrophe and retrotransposon reactivation in male germ cells lacking Dnmt3L. *Nature* **431**, 96–99 (2004).
16. Takai, D. & Jones, P. A. The CpG island searcher: a new WWW resource. *In Silico Biol.* **3**, 235–240 (2003).
17. Yu, F., Zingler, N., Schumann, G. & Stratling, W. H. Methyl-CpG-binding protein 2 represses LINE-1 expression and retrotransposition but not Alu transcription. *Nucleic Acids Res.* **29**, 4493–4501 (2001).
18. Tchenio, T., Casella, J. F. & Heidmann, T. Members of the SRY family regulate the human LINE retrotransposons. *Nucleic Acids Res.* **28**, 411–415 (2000).
19. Lee, C., Wevrick, R., Fisher, R. B., Ferguson-Smith, M. A. & Lin, C. C. Human centromeric DNAs. *Hum. Genet.* **100**, 291–304 (1997).
20. Pavlicek, A., Paces, J., Zika, R. & Hejnar, J. Length distribution of long interspersed nucleotide elements (LINEs) and processed pseudogenes of human endogenous retroviruses: implications for retrotransposition and pseudogene detection. *Gene* **300**, 189–194 (2002).
21. Grimaldi, G., Skowronski, J. & Singer, M. F. Defining the beginning and end of KpnI family segments. *EMBO J.* **3**, 1753–1759 (1984).
22. Gage, F. H. Mammalian neural stem cells. *Science* **287**, 1433–1438 (2000).
23. Prak, E. T., Dodson, A. W., Farkash, E. A. & Kazazian, H. H. Jr. Tracking an embryonic L1 retrotransposition event. *Proc. Natl Acad. Sci. USA* **100**, 1832–1837 (2003).
24. Garcia-Perez, J. L. *et al.* LINE-1 retrotransposition in human embryonic stem cells. *Hum. Mol. Genet.* **16**, 1569–1577 (2007).
25. van den Hurk, J. A. *et al.* L1 retrotransposition can occur early in human embryonic development. *Hum. Mol. Genet.* **16**, 1587–1592 (2007).
26. Thomson, J. A. *et al.* Embryonic stem cell lines derived from human blastocysts. *Science* **282**, 1145–1147 (1998).
27. Zhang, S. C., Wernig, M., Duncan, I. D., Brustle, O. & Thomson, J. A. *In vitro* differentiation of transplantable neural precursors from human embryonic stem cells. *Nature Biotechnol.* **19**, 1129–1133 (2001).
28. Forslund, O. *et al.* Nucleotide sequence and phylogenetic classification of candidate human papilloma virus type 92. *Virology* **312**, 255–260 (2003).

Supplementary Information is linked to the online version of the paper at www.nature.com/nature.

Acknowledgements We thank J. Simon for excellent schematic drawings, M. L. Gage, J. Kim and H. Kopera for editorial comments, B. Miller and R. Keithley for cell culture assistance, C. T. Carson for hESC advice, D. Chambers and J. Barrie for flow cytometry assistance, L. Randolph-Moore for molecular advice, B. Aimone for statistics advice, T. Liang for microarray assistance, and Y. Lineu and J. Mosher for helpful comments. We also thank T. Fanning and M. Klymkowsky for the ORF1 protein and SOX3 antibodies, respectively. F.H.G. and N.G.C. are supported by the Picower Foundation, G. Harold and Leila Y. Mathers Charitable Foundation, Lookout Fund (MH082070), and the California Institute for Regenerative Medicine (CIRM). J.L.G.-P. is supported by Plan Estabilizacion Grupos SNS ENCYT 2015 (EMER07/56, Instituto de Salud Carlos III, Spain) and through the IRG-FP7-PEOPLE-2007 Marie Curie program. K.S.O. was supported by grants GM069985 and NS048187 from the National Institutes of Health (NIH). J.V.M. was supported by grants GM082970 and GM069985 from the NIH and by the Howard Hughes Medical Institute. Work in the laboratories of K.S.O. and J.V.M. only used NIH-approved stem cell lines.

Author Contributions N.G.C. and F.H.G. directed the project. J.V.M. and J.L.G.-P. directed aspects of the project conducted at Michigan. N.G.C., J.L.G.-P., J.V.M. and F.H.G. designed experiments and drafted the manuscript. N.G.C., F.H.G., J.L.G.-P. and G.E.P. performed the experiments. G.W.Y. and M.T.L. carried out bioinformatics data analysis. Y.M. performed electrophysiology experiments. M.M. and K.S.O. provided hESC culture and NPC differentiation assistance. All authors commented on or contributed to the current manuscript.

Author Information Reprints and permissions information is available at www.nature.com/reprints. Correspondence and requests for materials should be addressed to F.H.G. (gage@salk.edu).

LETTERS

Suppression of induced pluripotent stem cell generation by the p53–p21 pathway

Hyenjong Hong^{1,2}, Kazutoshi Takahashi¹, Tomoko Ichisaka^{1,3}, Takashi Aoi¹, Osami Kanagawa⁴, Masato Nakagawa^{1,2}, Keisuke Okita¹ & Shinya Yamanaka^{1,2,3,5}

Induced pluripotent stem (iPS) cells can be generated from somatic cells by the introduction of Oct3/4 (also known as Pou5f1), Sox2, Klf4 and c-Myc, in mouse^{1–4} and in human^{5–8}. The efficiency of this process, however, is low⁹. Pluripotency can be induced without c-Myc, but with even lower efficiency^{10,11}. A p53 (also known as TP53 in humans and Trp53 in mice) short-interfering RNA (siRNA) was recently shown to promote human iPS cell generation¹², but the specificity and mechanisms remain to be determined. Here we report that up to 10% of transduced mouse embryonic fibroblasts lacking p53 became iPS cells, even without the Myc retrovirus. The p53 deletion also promoted the induction of integration-free mouse iPS cells with plasmid transfection. Furthermore, in the p53-null background, iPS cells were generated from terminally differentiated T lymphocytes. The suppression of p53 also increased the efficiency of human iPS cell generation. DNA microarray analyses identified 34 p53-regulated genes that are common in mouse and human fibroblasts. Functional analyses of these genes demonstrate that the p53–p21 pathway serves as a barrier not only in tumorigenicity, but also in iPS cell generation.

We used the Nanog–GFP (green fluorescent protein) reporter system for sensitive and specific identification of iPS cells³. When the three factors (Oct3/4, Sox2 and Klf4) devoid of c-Myc were introduced into Nanog–GFP, p53 wild-type (*p53*^{+/+}) mouse embryonic fibroblasts (MEF), we obtained 11 ± 8 (mean ± s.d.; *n* = 4) GFP-positive colonies from 5,000 transduced fibroblasts (Fig. 1a). From Nanog–GFP, p53 heterozygous (*p53*^{+/-}) mutant MEF, we observed 58 ± 56 GFP-positive colonies. In contrast, from Nanog–GFP, p53-null (*p53*^{-/-}) fibroblasts, we obtained significantly more GFP-positive colonies (275 ± 181) than from wild-type MEF.

By using a flow cytometer, we plated one Nanog–GFP cell (*p53* wild-type, heterozygous mutant, or homozygous mutant), which was transduced with the three factors 5 days before the replating, into a well of a 96-well plate. Twenty-three days after the replating, we observed GFP-positive colonies in few wells per 96-well plate with p53 wild-type or heterozygous fibroblasts (Fig. 1b). In contrast, we observed GFP-positive colonies in 7 ± 4 (*n* = 4) wells per 96-well plate with p53-null fibroblasts. These data showed that the loss of p53 function significantly increased the iPS cell induction efficiency, and that up to 10% of transduced cells can become iPS cells even without c-Myc.

We performed the same experiment with the four factors, including c-Myc. We observed GFP-positive colonies in zero or one well per 96-well plate with p53 wild-type fibroblasts (Fig. 1c). In contrast, we observed GFP-positive colonies in 6 ± 7 and 16 ± 10 (*n* = 4) wells per 96-well plate with p53-heterozygous and p53-null fibroblasts, respectively. These data showed that the addition of the Myc retrovirus further increased the efficiency of iPS generation by up to 20%.

We also tested the effect of a dominant-negative p53 mutant Pro275Ser (ref. 13) on iPS cell generation. When Pro275Ser was introduced into Nanog–GFP, p53-heterozygous MEF, we observed a substantial increase in the number of GFP-positive colonies (Fig. 1d). Furthermore, we placed complementary DNAs (cDNAs) encoding the wild-type p53 or transactivation-deficient mutants (Asp278Asn (ref. 14) or Ser58Ala (ref. 15)) into the pMXs retroviral vector¹⁶, and introduced it together with the retroviruses encoding Oct3/4, Sox2 and Klf4 into Nanog–GFP, p53-null MEF. Wild-type p53 significantly decreased the number of GFP-positive colonies (Fig. 1e). The transactivation-deficient p53 mutants, in contrast, did not show significant effects. These data confirmed that the loss of p53 is responsible for the observed increase in the efficiency of direct reprogramming.

We expanded p53-null, GFP-positive clones generated by the three or four factors (six and three clones, respectively). All of the clones showed morphology similar to that of mouse embryonic stem (ES) cells at passage two (Supplementary Fig. 1a). Clones generated by the three factors expressed endogenous Oct3/4, endogenous Sox2, and Nanog at comparable levels to those in ES cells (Supplementary Fig. 1b). The total expression levels of Oct3/4 and Sox2 were also comparable to those in ES cells, indicating that the transgenes were effectively silenced (Supplementary Fig. 1c). When transplanted into nude mice, all six clones gave rise to teratomas containing tissues derived from the three germ layers (Supplementary Fig. 1d). These data confirmed pluripotency of iPS cells generated by the three factors from p53-null MEF.

We found that the expressions of the endogenous Oct3/4 and Sox2 genes were low in p53-null cells generated by the four factors including c-Myc (Supplementary Fig. 1b). In contrast, the total expression levels of Sox2, Klf4 and c-Myc were markedly higher in these cells than in the remaining iPS and ES cells (Supplementary Fig. 1c), indicating that retroviral expression remained active in these cells. Consistent with this observation, tumours derived from these cells in nude mice largely consisted of undifferentiated cells, with only small areas of differentiated tissues (Supplementary Fig. 1d). Furthermore, the p53-null cells generated by the four factors were not able to maintain an ES-cell-like morphology after passage five (Supplementary Fig. 1e). Thus the c-Myc transgene, in the p53-null background, suppresses retroviral silencing and inhibits the acquirement and maintenance of iPS cell identity.

We next tried to generate iPS cells from terminally differentiated somatic cells by the four factors in a p53-null background (Fig. 2a). We isolated T lymphocytes from Nanog–GFP reporter mice that were either p53 wild-type or p53-null. We activated T cells by anti-CD3 and anti-CD28 antibodies and transduced with the four retroviruses.

¹Center for iPS Cell Research and Application (CiRA), Institute for Integrated Cell-Material Sciences, Kyoto University, Kyoto 606-8507, Japan. ²Department of Stem Cell Biology, Institute for Frontier Medical Sciences, Kyoto University, Kyoto 606-8507, Japan. ³Yamanaka iPS Cell Special Project, Japan Science and Technology Agency, Kawaguchi 332-0012, Japan. ⁴Laboratory for Autoimmune Regulation, RIKEN Center for Allergy and Immunology, RIKEN Yokohama Institute, 1-7-22 Suehiro-cho, Tsurumi-ku, Yokohama, Kanagawa 230-0045, Japan. ⁵Gladstone Institute of Cardiovascular Disease, San Francisco, California 94158, USA.

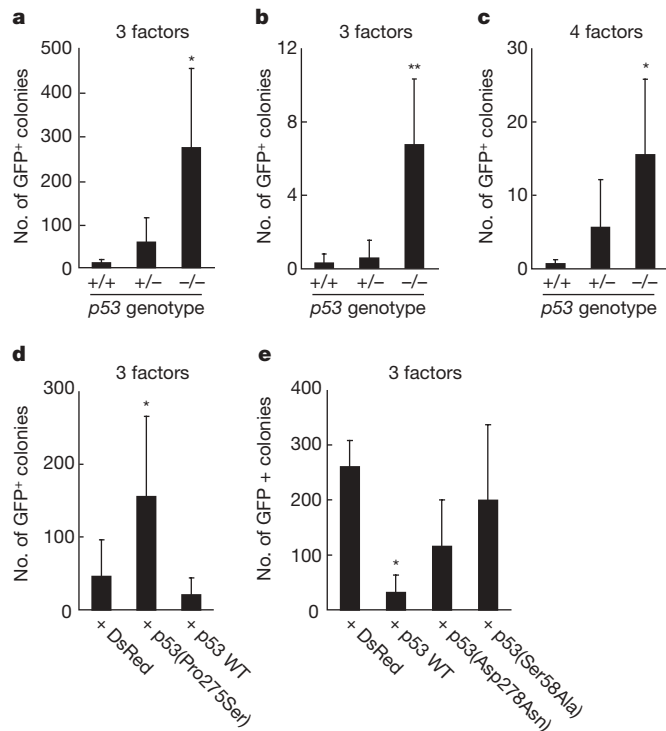


Figure 1 | iPS cell generation from *p53*-null MEF by three or four reprogramming factors. **a**, iPS cells were generated from Nanog-GFP reporter MEF, which were either *p53* wild-type (+/+), heterozygous (+/-), or homozygous (-/-), by the three reprogramming factors (Oct3/4, Sox2 and Klf4). After retroviral transduction, 5,000 live cells were collected by a flow cytometer, and GFP-positive colonies were counted 28 days after transduction. * $P < 0.05$ compared to wild-type ($n = 4$). **b**, iPS cells were generated by the three factors from single-sorted cells in wells of 96-well plates. GFP-positive colonies were counted 28 days after transduction. ** $P < 0.01$ compared to wild-type ($n = 4$). **c**, iPS cells were generated by the four factors, including *c-Myc*, from single-sorted cells in wells of 96-well plates. GFP-positive colonies were counted 21 days after transduction. * $P < 0.05$ compared to wild-type ($n = 4$). **d**, Retroviruses expressing either the dominant-negative *p53*(Pro275Ser) mutant or wild-type (WT) *p53* were co-transduced with the three factors into Nanog-GFP, *p53* heterozygous MEF. After retroviral transduction, 5,000 cells were collected and GFP-positive colonies were counted 28 days after the transduction. As a control, retrovirus for a red fluorescent protein (DsRed) was transduced. * $P < 0.05$ compared to DsRed control ($n = 3$). **e**, Retroviruses expressing either wild-type or mutant *p53* were co-transduced with the three factors into Nanog-GFP, *p53*-null MEF. After retroviral transduction, 5,000 live cells were collected and GFP-positive colonies were counted 28 days after transduction. * $P < 0.05$ compared to DsRed control ($n = 3$). Error bars, s.d.

From *p53* wild-type T lymphocytes, we did not obtain any GFP-positive colonies. In contrast, we obtained 11 GFP-positive colonies from *p53*-null T cells (2×10^6 cells), from which three iPS cell lines were established.

These GFP-positive cells were expandable and showed similar morphology to mouse ES cells (Fig. 2b). They were positive for alkaline phosphatase and SSEA1—markers of mouse ES cells (Fig. 2b)—and they expressed ES cell marker genes, including *Rex1* (also known as *Zfp42*) and *Nanog* (Fig. 2c). In contrast, they did not express T-cell-specific genes such as *Fas*, *Gzma*, *Gzmb* and *Ifng*. As was the case in iPS cells derived from *p53*-null MEF, silencing of the transgenes in these cells was not complete. Nevertheless, we obtained four adult chimaeric mice from these iPS cells (Fig. 2d). As we predicted from the *p53*-null background and incomplete silencing of the *c-Myc* retroviruses, three of the four chimaeric mice died within seven weeks. We confirmed the rearrangement of the T-cell receptors in these iPS cells, various tissues from the chimaeras, and the tumour observed in the chimaeras (Fig. 2e). The intensity of the rearranged bands in

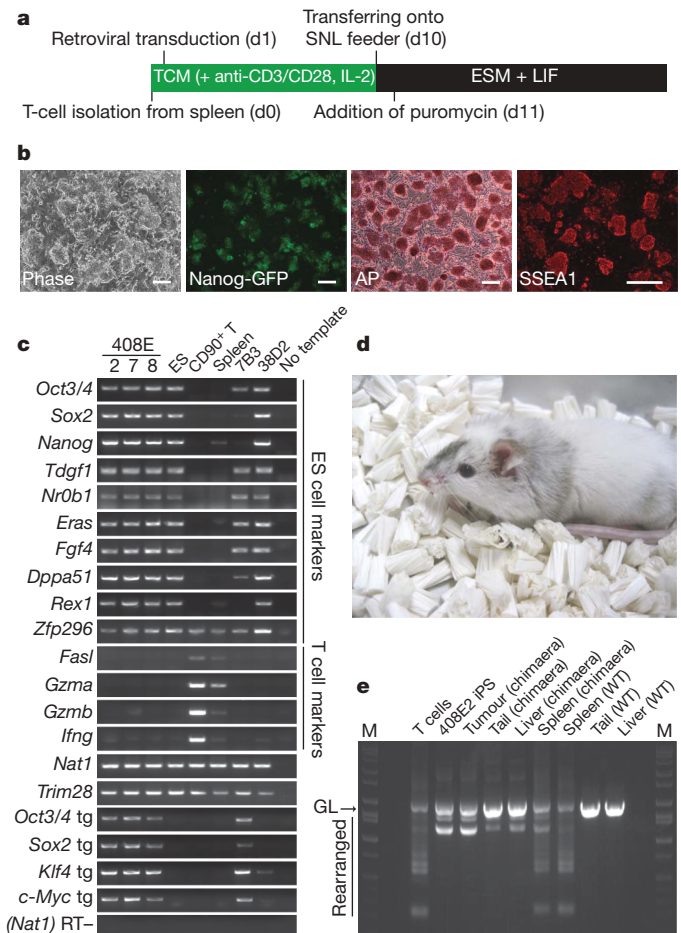


Figure 2 | T-lymphocyte-derived iPS cells. **a**, Protocol for iPS cell generation from mouse T-lymphocytes. **b**, day; ESM, ES cell medium; TCM, T cell medium. **c**, A phase-contrast image, Nanog-GFP expression, alkaline phosphatase (AP) staining, and SSEA1 staining of T-cell-derived iPS cells (clone 408E2) are shown. Scale bars, 100 μ m. **d**, Expression of marker genes was examined by PCR with reverse transcription (RT-PCR) in T-cell-derived iPS cells (clones 408E2/7/8), RF8 ES cells, T cells, spleen, Fbxo15-selected iPS cells from *p53* wild-type MEF (clone 7B3), and Nanog-selected iPS cells from *p53* wild-type MEF (clone 38D2). Tg, transgene. RT—denotes absence of reverse transcriptase as a control. **e**, A chimaera mouse derived from clone 408E2. iPS cells were microinjected into blastocysts from ICR mice. **e**, The variable, diversity and joining (V(D)J) DNA rearrangement of the *Tcrb* gene was confirmed by genomic PCR in iPS cells and a chimaeric mouse. GL, germline band; M denotes lane markers.

tumours was as strong as in iPS cells, indicating that the tumour was derived from iPS cells. These data demonstrated that the four factors could generate iPS cells even from terminally differentiated T cells, when *p53* is inactivated.

We then examined whether *p53* deficiency increased the efficiency of human iPS cell generation. To this end, we introduced the dominant-negative mutant Pro275Ser or a *p53* carboxy-terminal dominant-negative fragment (*p53*DD; ref. 17) into adult human dermal fibroblasts (HDF), together with three or four reprogramming factors. We found that the numbers of iPS cell colonies markedly increased with the two independent *p53* dominant-negative mutants (Supplementary Fig. 2a, b). In another experiment, we examined the effects of shRNA against human *p53* (shRNA-2)¹⁸. We confirmed that the shRNA effectively suppressed the *p53* protein levels in HDF (Supplementary Fig. 2c). When co-introduced with the four reprogramming factors, the *p53* shRNA markedly increased the number of human iPS cell colonies (Supplementary Fig. 2d). Similar results were obtained in the experiments with three reprogramming factors (Supplementary Fig. 2e). In contrast, suppression of the retinoblastoma protein (RB)

did not enhance iPS cell generation. A control shRNA containing one nucleotide deletion in the antisense sequence (shRNA-1) did not show such effects (Supplementary Fig. 2d, e). Co-introduction of the mouse *p53* suppressed the effect of the shRNA. When transplanted into the testes of severe combined immunodeficient (SCID) mice, these cells developed teratomas containing various tissues of three germ layers (Supplementary Fig. 2f). These data demonstrated that *p53* suppresses iPS cell generation not only in mice, but also in human.

To determine *p53* target genes that are responsible for the observed enhancement of iPS cell generation, we compared gene expression between *p53* wild-type MEF and *p53*-null MEF by DNA microarrays, and between control HDF and *p53* knockdown HDF. In MEF, 1,590 genes were increased and 1,485 genes were decreased >fivefold in *p53*-null MEF. In HDF, 290 genes were increased and 430 genes were decreased >fivefold by *p53* shRNA. Between mouse and human, there were eight increased genes in common, including *v-myb* myeloblastosis viral oncogene homologue (*MYB*) and a RAS oncogene family member, *RAB39B* (Supplementary Table 1). There were 27 decreased genes in common between the two species, including *p53*, cyclin-dependent kinase inhibitor 1A (*p21*, also known as *CDKN1A* and *CIP1*), BTG family, member 2 (*BTG2*), zinc finger, matrin type 3 (*ZMAT3*), and *MDM2*.

We transduced four of the increased genes and seven of the decreased genes by retroviruses into HDF, together with either the four reprogramming factors alone or the four factors plus *p53* shRNA. Among the four increased genes, none mimicked the effect of *p53* suppression (Fig. 3a), whereas among the seven decreased genes, *MDM2*, which binds to and degrades the *p53* proteins, mimicked *p53* suppression. Two genes, *p53* derived from mouse and *p21*, effectively counteracted the effect of the *p53* shRNA (Fig. 3b). Forced expression of *p21* markedly decreased iPS cell generation from *p53*-null MEF (data not shown). In wild-type MEF, the combination of the four factors markedly increased *p21* protein levels (Fig. 3c). When c-Myc was omitted, *p21* protein levels still increased, but to a lesser extent than with the four factors together. In *p53*-null MEF, these increases in *p21* protein by either the three or the four factors were not observed. These data highlighted the importance of *p21* as a *p53* target during iPS cell generation.

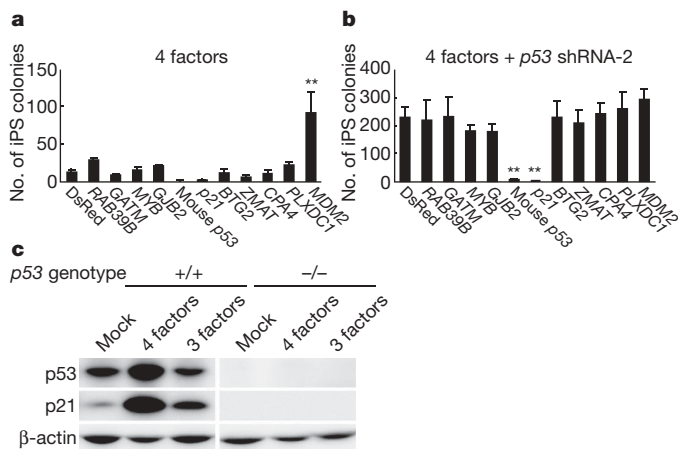


Figure 3 | *p21* as a target of *p53* during iPS cell generation. **a**, Genes regulated by *p53* were introduced into HDF together with the four reprogramming factors. On day 24 after transduction, the numbers of iPS cell colonies were counted. **b**, Genes regulated by *p53* were introduced into HDF together with the four reprogramming factors and the *p53* shRNA. On day 28 after transduction, the numbers of iPS cell colonies were counted. **c**, Induction of *p21* proteins during iPS cell generation. MEF, either wild-type or *p53*-null, were transduced with the three or four reprogramming factors. Three days after transduction, *p21* and *p53* protein levels were determined by western blot analyses.

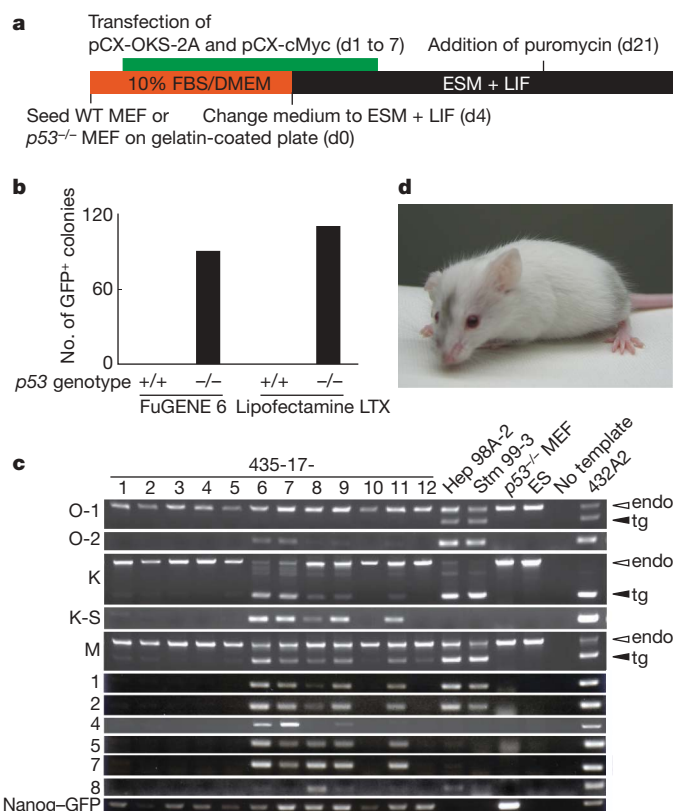


Figure 4 | Effect of *p53* suppression on plasmid-mediated mouse iPS cell generation. **a**, Protocol for mouse iPS cell generation by plasmid transfection. **b**, Number of GFP-positive colonies. Shown are results of experiment with different transfection reagents. **c**, Detection of plasmid integration by genomic PCR. endo, endogenous transcripts only; tg, transgene transcripts only. O-1, O-2, K, K-S, M and 1–8 represent primer sets described in ref. 19. **d**, A chimaera mouse derived from integration-free iPS cells. iPS cells were microinjected into blastocysts from ICR mice.

Moreover, we generated iPS cells from wild-type or *p53*-null MEF, both containing the Nanog–GFP reporter, by repeated transfection of two expression plasmids, one containing the cDNAs of *Oct3/4*, *Klf4* and *Sox2* connected with the 2A polypeptides, and the other one with the *c-Myc* cDNA¹⁹ (Fig. 4a). We plated 1.3×10^5 MEF and transfected the two plasmids together daily for seven days. Twenty-eight days after the initial transfection, we did not observe any Nanog–GFP-positive colonies from wild-type cells (Fig. 4b). In contrast, ~100 GFP-positive colonies emerged from *p53*-null cells. We randomly picked 12 colonies, and found that seven of them did not contain plasmid integrations (Fig. 4c). By microinjecting these integration-free iPS cells, we obtained adult chimaeric mice (Fig. 4d). It remains to be determined whether germline transmission can be obtained.

Our data showed that *p53* and *p21* suppress iPS cell generation. The suppressive effects of these tumour suppressor gene products on cell proliferation, survival or plating efficiency should contribute to the observed effect (Supplementary Fig. 3). In addition, they may have direct effects on reprogramming²⁰. Permanent suppression of *p53* would lower the quality of iPS cells and cause genomic instability. Nevertheless, transient suppression of *p53* by siRNA or other methods may be useful in generating integration-free iPS cells for future medical applications²¹.

METHODS SUMMARY

Effect of *p53* suppression in iPS cell generation. Mice deficient in *p53* (Taconic Farms, Inc.) were crossed with Nanog–GFP reporter mice³. HDF from facial dermis of a 36-year-old Caucasian female were purchased from Cell Application, Inc. The generation and analyses of mouse iPS cells with retroviruses were performed as previously described^{3,10,22}. Human iPS cells were generated and

evaluated as described⁵. Various p53 mutants were constructed as described in the full Methods. Retroviral vectors for shRNA were purchased from Addgene. The p53 mutants and shRNAs were co-transduced with the reprogramming factors.

Microarray analyses. Total RNAs were analysed with oligonucleotide microarrays (Agilent) and GeneSpring software (Agilent). Microarray data are available from Gene Expression Omnibus (GEO, <http://www.ncbi.nlm.nih.gov/geo/>) with the accession number GSE13365.

Statistical analyses. Data are shown as average \pm standard deviation. Statistical analyses were performed with one-way repeated-measures analysis of variance (ANOVA) and Bonferroni post-hoc test, using KaleidaGraph 4 (HULINKS).

Full Methods and any associated references are available in the online version of the paper at www.nature.com/nature.

Received 8 September 2008; accepted 30 June 2009.

Published online 9 August 2009.

1. Takahashi, K. & Yamanaka, S. Induction of pluripotent stem cells from mouse embryonic and adult fibroblast cultures by defined factors. *Cell* **126**, 663–676 (2006).
2. Maherali, N. *et al.* Directly reprogrammed fibroblasts show global epigenetic remodelling and widespread tissue contribution. *Cell Stem Cell* **1**, 55–70 (2007).
3. Okita, K., Ichisaka, T. & Yamanaka, S. Generation of germ-line competent induced pluripotent stem cells. *Nature* **448**, 313–317 (2007).
4. Wernig, M. *et al.* *In vitro* reprogramming of fibroblasts into a pluripotent ES cell-like state. *Nature* **448**, 318–324 (2007).
5. Takahashi, K. *et al.* Induction of pluripotent stem cells from adult human fibroblasts by defined factors. *Cell* **131**, 861–872 (2007).
6. Yu, J. *et al.* Induced pluripotent stem cell lines derived from human somatic cells. *Science* **318**, 1917–1920 (2007).
7. Lowry, W. E. *et al.* Generation of human induced pluripotent stem cells from dermal fibroblasts. *Proc. Natl Acad. Sci. USA* **105**, 2883–2888 (2008).
8. Park, I. H. *et al.* Reprogramming of human somatic cells to pluripotency with defined factors. *Nature* **451**, 141–146 (2008).
9. Yamanaka, S. Strategies and new developments in the generation of patient-specific pluripotent stem cells. *Cell Stem Cell* **1**, 39–49 (2007).
10. Nakagawa, M. *et al.* Generation of induced pluripotent stem cells without Myc from mouse and human fibroblasts. *Nature Biotechnol.* **26**, 101–106 (2008).
11. Wernig, M., Meissner, A., Cassidy, J. P. & Jaenisch, R. c-Myc is dispensable for direct reprogramming of mouse fibroblasts. *Cell Stem Cell* **2**, 10–12 (2008).
12. Zhao, Y. *et al.* Two supporting factors greatly improve the efficiency of human iPSC generation. *Cell Stem Cell* **3**, 475–479 (2008).
13. de Vries, A. *et al.* Targeted point mutations of p53 lead to dominant-negative inhibition of wild-type p53 function. *Proc. Natl Acad. Sci. USA* **99**, 2948–2953 (2002).
14. Shinmura, K., Bennett, R. A., Tarapore, P. & Fukasawa, K. Direct evidence for the role of centrosomally localized p53 in the regulation of centrosome duplication. *Oncogene* **26**, 2939–2944 (2007).
15. Cecchinelli, B. *et al.* Ser58 of mouse p53 is the homologue of human Ser46 and is phosphorylated by HIPK2 in apoptosis. *Cell Death Differ.* **13**, 1994–1997 (2006).
16. Morita, S., Kojima, T. & Kitamura, T. Plat-E: an efficient and stable system for transient packaging of retroviruses. *Gene Ther.* **7**, 1063–1066 (2000).
17. Bowman, T. *et al.* Tissue-specific inactivation of p53 tumor suppression in the mouse. *Genes Dev.* **10**, 826–835 (1996).
18. Stewart, S. A. *et al.* Lentivirus-delivered stable gene silencing by RNAi in primary cells. *RNA* **9**, 493–501 (2003).
19. Okita, K., Nakagawa, M., Hyenjong, H., Ichisaka, T. & Yamanaka, S. Generation of mouse induced pluripotent stem cells without viral vectors. *Science* **322**, 949–953 (2008).
20. Yamanaka, S. Elite and stochastic models for induced pluripotent stem cell generation. *Nature* **460**, 49–52 (2009).
21. Yamanaka, S. A fresh look at iPS cells. *Cell* **137**, 13–17 (2009).
22. Aoi, T. *et al.* Generation of pluripotent stem cells from adult mouse liver and stomach cells. *Science* **321**, 699–702 (2008).

Supplementary Information is linked to the online version of the paper at www.nature.com/nature.

Acknowledgements We thank D. Srivastava for critical reading of the manuscript; M. Narita, A. Okada, N. Takizawa, H. Miyachi and S. Kitano for technical assistance; and R. Kato, S. Takeshima, Y. Ohtsu and E. Nishikawa for administrative assistance. We also thank Y. Sasai and T. Tada for technical advices, T. Kitamura for Plat-E cells and pMXs retroviral vectors, R. Farese for RF8 ES cells, and B. Weinberg and W. Hahn for shRNA constructs. This study was supported in part by a grant from the Leading Project of MEXT, Grants-in-Aid for Scientific Research of JSPS and MEXT, and a grant from the Program for Promotion of Fundamental Studies in Health Sciences of NIBIO (to S.Y.). H. H. is a research student under the Japanese Government (MEXT).

Author Contributions H.H. conducted most of the experiments in this study. K.T. generated iPS cells from T cells and also performed the shRNA experiments. T.I. performed manipulation of mouse embryos, teratoma experiments, and mouse line maintenance. T.A. and O.K. optimized retroviral transduction into T cells. M.N. generated iPS cells with plasmids. K.O. generated the Nanog–GFP reporter mice and the plasmids for iPS cell generation. K.O. and K.T. supervised H.H. S.Y. designed and supervised the study, and prepared the manuscript.

Author Information Microarray data are available at the Gene Expression Omnibus (GEO, <http://www.ncbi.nlm.nih.gov/geo/>) public database under accession number GSE13365. Reprints and permissions information is available at www.nature.com/reprints. Correspondence and requests for materials should be addressed to S.Y. (yamanaka@frontier.kyoto-u.ac.jp).

METHODS

Generation of p53 retroviral vectors. cDNA of mouse *p53* gene was amplified by RT-PCR with p53-1S (CACCAGGATGACTGCCATGGAGGAGTC) and p53-1223AS (GTGTCTCAGCCCTGAAGTCATAA), and subcloned into pENTR-D-TOPO (Invitrogen). After sequencing verification, cDNA was transferred to pMXs-gw by Gateway cloning technology (Invitrogen). Retroviral vectors for p53 mutants were generated by two-step PCR. For the Pro275Ser mutant, the first PCR was performed with two primer sets, p53-Pro275Ser-S (TGTTTGTGCCTGCTCTGGGAGAGACCGC) and p53-1223AS, and p53-Pro275Ser-AS (GCGGTCTCTCCAGAGCAGGCACAAACA) and p53-1S. For the DD mutant, the first PCR was performed with two primer sets, p53-DD-S (CGGATATCAGCCTCAAGAGAGCGCTGCC) and p53-1223AS, and p53-DD-AS (GGCAGCGCTCTCTTGAAGGCTGATATCCG) and p53-1S. For the Asp278Asn mutant, the first PCR was performed with two primer sets, p53-Asp278Asn-S (TGCCCTGGGAGAAACCGCCGTACAGAA) and p53-1223AS, and p53-Asp278Asn-AS (TTCTGTACGGCGGTTTCTCCAGGGCA) and p53-1S. For the Ser58Ala mutant, the first PCR was performed with two primer sets, p53-Ser58Ala-S (TTTGAAGGCCAGCTGAAGCCCTCCGA) and p53-1223AS, and p53-S58A-AS (TCGGAGGGCTTCAGCTGGGCCTTCAAA) and p53-1S. The two PCR products of each first PCR were mixed and used as a template for the secondary PCR with the primer set p53-1S and p53-1223AS. These mutants were cloned into pENTR-D-TOPO, and then transferred to pMXs-gw by Gateway cloning technology.

Effect of p53 suppression in iPS cell generation from MEF. Wild type, *p53*^{+/-} or *p53*^{-/-} MEF, which also contain the Nanog-GFP reporter, were seeded at 1×10^5 cells per well of 6-well plates. Retroviral transduction was performed the next day (day 0) with retrovirus made from Plat-E¹⁶. On day 5, cells were reseeded either at one cell per well of a 96-well plate using a cell sorter (FACS Aria, Beckton Dickinson) or 5,000 cells per 100-mm dish. Puromycin selection ($1.5 \mu\text{g ml}^{-1}$) was initiated on day 13 in the four-factor protocol, and on day 19 in the three-factor protocol. The numbers of GFP-positive colonies were determined on day 21 for the four-factor protocol, and on day 28 in the three-factor protocol. In addition to the targeted disruption, p53 was suppressed in MEF by a dominant-negative mutant, Pro275Ser.

Effect of p53 suppression in iPS cell generation from HDF. Function of p53 was suppressed in HDF either by the dominant-negative mutants (Pro275Ser or DD) or by shRNAs (pMKO.1-puro, pMKO.1-puro p53 shRNA-1, or pMKO.1-puro p53 shRNA-2 from Addgene). Retrovirus for the dominant-negative mutants, shRNAs, and the four reprogramming factors were produced in Plat-E cells. For iPS cell generation, we plated 2×10^5 cells per well of a 6-well plate 1 day before transduction. The next day, HDF were transduced overnight with equal amounts of Plat-E supernatants containing each retrovirus, supplemented with $4 \mu\text{g ml}^{-1}$ polybrene.

In assays with dominant-negative mutants, 6 days after infection, transduced HDF were collected and replated at 5×10^3 (with the four reprogramming factors) or 4×10^4 (with the three factors) per 100-mm dish on mitomycin-C-treated SNL feeder cells. The next day, the medium was replaced with Primate ES cell medium (ReproCELL) supplemented with 4 ng ml^{-1} bFGF. The medium was changed every other day. We counted the number of iPS cell colonies at day 30 after transduction (with the four factors) or day 40 (with the three factors).

In the experiments with shRNA-mediated knockdown, 6 days after infection, the transduced cells were replated at 5×10^4 cells per 100-mm dish onto mitomycin-C-treated SNL feeder. The next day, we started cultivation of the cells with the human ES cell culture condition. Twenty-four days after transduction, we counted the number of iPS colonies, isolated them, and used them for functional analyses.

Generation of iPS cells from T cells. Spleen from *p53*-null, Nanog-GFP male mouse was dissected, minced and suspended in T cell medium consisting of DMEM containing 10% heat-inactivated fetal bovine serum (FBS; Thermo). T lymphocytes were isolated using mouse CD90 microbeads (Miltenyi biotec) and plated at 1×10^6 cells per well of RetroNectin ($50 \mu\text{g ml}^{-1}$; Takara)-coated 24-well plates in T cell medium supplemented with Dynabeads CD3/CD28 T cell Expander ($10 \mu\text{l}$ for 1×10^6 cells; Invitrogen) and 10 units ml^{-1} of IL-2.

Retroviruses were prepared as described previously^{1,3,5}. We added $8 \mu\text{g ml}^{-1}$ of polybrene (Nacalai tesque) and 10 units ml^{-1} of IL-2 to virus-containing supernatant. The four reprogramming factors or DsRed were introduced by retroviral transduction with centrifugation ($1,580g$ for 30 min), and then incubated in a 37°C , 5% CO_2 incubator. Twenty-four hours after transduction, the medium was replaced, and then half of the medium was changed every other day. Two weeks after transduction, the cells were plated at 5×10^4 cells per 100-mm dish onto mitomycin-C-treated puromycin-resistant SNL feeder in ES medium, which consisted of DMEM (Nacalai tesque) supplemented with 15% FBS, 2 mM L-glutamine (Invitrogen), 1×10^{-4} M non-essential amino acids (Invitrogen), 1×10^{-4} M 2-mercaptoethanol (Invitrogen) and 0.5% penicillin and streptomycin (Invitrogen). The next day, selection was started with $1.5 \mu\text{g ml}^{-1}$ puromycin for 5 days.

V(D)J DNA rearrangements of the *Tcrb* gene were confirmed by PCR with primers D β 2 (GTAGGCACCTGTGGGAAGAAACT) and J β 2 (TGAGAGCTGTCTCCTACTATCGATT)²³. PCR products were separated on a 1.2% agarose gel.

Functional analyses of p53 target genes. Open reading frames of p53 target genes were amplified by PCR and subcloned into pENTR-D-TOPO. Some target genes were obtained from National Institute of Technology and Evaluation (NITE, Japan). These cDNAs were transferred to pMXs-gw using the gateway cloning system. We transduced retroviruses of each of the p53 target genes along with the reprogramming factors, either with or without the p53-knockdown construct. Six days after infection, cells were collected and replated at 5×10^4 cells per 100-mm dish on mitomycin-C-treated SNL feeder cells. The next day, we started cultivation of the cells with human ES cell culture condition. We counted the number of iPS cell colonies at day 24 (with the four factors) or 28 (with the three factors) after transduction.

Generation of integration-free mouse iPS cells from p53-null MEF by plasmid transfection. Generation of integration-free mouse iPS cells was performed as previously described¹⁹, with some modifications. In brief, wild type or *p53*^{-/-} Nanog-GFP MEF were seeded at 1.3×10^5 cells per well of gelatin-coated 6-well plates (day 0). Co-transfection of pCX-OKS-2A and pCX-cMyc using FuGENE6 (Roche) or Lipofectamine LTX (plus reagent) (Invitrogen) was done once a day from days 1 to 7. The cells were cultivated with ES medium containing LIF from day 4. From day 21, puromycin ($1.5 \mu\text{g ml}^{-1}$) was added to the medium. On day 34, several GFP-positive colonies were picked up for expansion. Integration of plasmids into host chromosomes was examined with genomic PCR¹⁹.

23. Tada, M., Takahama, Y., Abe, K., Nakatsuji, N. & Tada, T. Nuclear reprogramming of somatic cells by in vitro hybridization with ES cells. *Curr. Biol.* 11, 1553–1558 (2001).

LETTERS

The *Ink4/Arf* locus is a barrier for iPS cell reprogramming

Han Li¹, Manuel Collado¹, Aranzazu Villasante¹, Katerina Strati², Sagrario Ortega³, Marta Cañamero⁴, Maria A. Blasco² & Manuel Serrano¹

The mechanisms involved in the reprogramming of differentiated cells into induced pluripotent stem (iPS) cells by the three transcription factors Oct4 (also known as Pou5f1), Klf4 and Sox2 remain poorly understood¹. The *Ink4/Arf* locus comprises the *Cdkn2a–Cdkn2b* genes encoding three potent tumour suppressors, namely p16^{Ink4a}, p19^{Arf} and p15^{Ink4b}, which are basally expressed in differentiated cells and upregulated by aberrant mitogenic signals^{2–4}. Here we show that the locus is completely silenced in iPS cells, as well as in embryonic stem (ES) cells, acquiring the epigenetic marks of a bivalent chromatin domain, and retaining the ability to be reactivated after differentiation. Cell culture conditions during reprogramming enhance the expression of the *Ink4/Arf* locus, further highlighting the importance of silencing the locus to allow proliferation and reprogramming. Indeed, the three factors together repress the *Ink4/Arf* locus soon after their expression and concomitant with the appearance of the first molecular markers of 'stemness'. This downregulation also occurs in cells carrying the oncoprotein large-T, which functionally inactivates the pathways regulated by the *Ink4/Arf* locus, thus indicating that the silencing of the locus is intrinsic to reprogramming and not the result of a selective process. Genetic inhibition of the *Ink4/Arf* locus has a profound positive effect on the efficiency of iPS cell generation, increasing both the kinetics of reprogramming and the number of emerging iPS cell colonies. In murine cells, *Arf*, rather than *Ink4a*, is the main barrier to reprogramming by activation of p53 (encoded by *Trp53*) and p21 (encoded by *Cdkn1a*); whereas, in human fibroblasts, *INK4a* is more important than *ARF*. Furthermore, organismal ageing upregulates the *Ink4/Arf* locus^{2,5} and, accordingly, reprogramming is less efficient in cells from old organisms, but this defect can be rescued by inhibiting the locus with a short hairpin RNA. All together, we conclude that the silencing of *Ink4/Arf* locus is rate-limiting for reprogramming, and its transient inhibition may significantly improve the generation of iPS cells.

The *Ink4/Arf* tumour suppressor locus encodes three important tumour suppressors (p16^{Ink4a} and p19^{Arf} from *Cdkn2a*, and p15^{Ink4b} from *Cdkn2b*; see scheme in Supplementary Fig. 1) that activate two critical anti-proliferative pathways, namely, the Rb and p53 pathways, the activation of which prevents the propagation of aberrant cells, either by apoptosis or by senescence (see scheme in Supplementary Fig. 1)⁴. In brief, the paralogues p16^{Ink4a} and p15^{Ink4b} bind and inhibit the cyclin-D-dependent kinases Cdk4 and Cdk6, which in turn are important to relieve the cell-cycle inhibitory activity of the Rb tumour suppressor. On the other hand, p19^{Arf} binds and inhibits Mdm2, which is the main destabilizing enzyme of the tumour suppressor p53. Given the relevance of the *Ink4/Arf* locus in cancer protection, it is important to understand its behaviour after reprogramming in relation to the 'safety' of iPS cells.

We began by measuring the expression levels of the three genes present in the locus (*Ink4a*, *Arf*, *Ink4b*) in the parental mouse embryo fibroblasts (MEFs), in the resulting iPS cells after three-factor-reprogramming, and in ES cells. The transcripts of the three genes of the locus were significantly repressed in iPS/ES cells compared to MEFs (Fig. 1a). In accordance with a previous report¹, we observed a similar reduction in the levels of *p21* in iPS/ES cells, whereas the stemness markers *Nanog* and *Esg1* (also known as *Dppa5a*) were abundantly expressed (Fig. 1a). To understand the epigenetic basis of the silencing of the locus in iPS/ES cells, we first examined the DNA methylation of the *Ink4a* promoter in iPS/ES

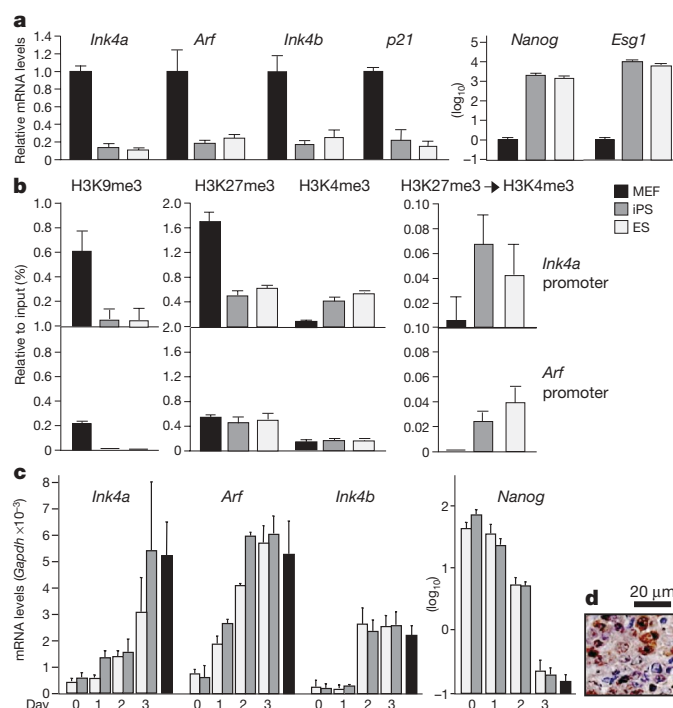


Figure 1 | Functional reprogramming of the *Ink4/Arf* locus. **a**, Expression of the indicated genes in iPS cells compared with their parental MEFs and with ES cells measured by quantitative reverse transcription PCR (qRT-PCR). **b**, Epigenetic marks present at the indicated promoters. Sequential ChIP, first of H3K27me3 and then of H3K4me3, is in the right panel. Data correspond to the average and s.d. of a representative assay from at least two independent assays. **c**, Expression of the indicated genes in iPS and ES cells undergoing differentiation by the addition of retinoic acid and in the absence of LIF. Data correspond to the average and s.d. of at least two independent assays. **d**, Re-expression of p19^{Arf} in a teratoma developed by a chimaeric-iPS-cell mouse and detected by immunohistochemistry.

¹Tumor Suppression Group, ²Telomeres and Telomerase Group, ³Transgenic Mice Unit, ⁴Comparative Pathology Unit, Spanish National Cancer Research Centre (CNIO), 3 Melchor Fernandez Almagro Street, Madrid E-28029, Spain.

cells, but there was no evidence of promoter methylation (Supplementary Fig. 2). When histone marks were examined by chromatin immunoprecipitation (ChIP), we found that the repressive mark histone H3 lysine 9 trimethylation (H3K9me3) essentially disappeared in iPS/ES cells compared to MEFs (Fig. 1b). In the case of the *Ink4a* promoter, the repressive mark H3K27me3 also decreased, whereas the active mark H3K4me3 was increased (Fig. 1b). Although none of the histone marks taken alone explain the silencing of the locus, when taken together they are reminiscent of the silent chromatin configuration characteristic of ES cells and known as 'bivalent' in which repressive (H3K27me3) and active (H3K4me3) marks coexist in the same molecule^{6–8}. Bivalent chromatin has been proposed to be present at the *Ink4a/Arf* locus in ES cells⁹, and to directly assess this, we performed sequential ChIP assay pulling down first H3K27me3 and then H3K4me3. We found that the *Ink4a* and *Arf* promoters are bivalent in iPS/ES cells (Fig. 1b; positive and negative controls are shown in Supplementary Fig. 3). About half of the bivalent domains in ES cells are associated with binding sites for Oct4, Sox2 or Nanog⁶. However, we could not detect the binding of these proteins, nor of Klf4, to the three promoter regions of the *Ink4a/Arf* locus (Supplementary Fig. 4). To test the functionality of the *Ink4a/Arf* locus in iPS cells, we tested whether the locus is normally re-expressed after differentiation. Addition of retinoic acid and removal of leukaemia inhibitory factor (LIF)¹⁰ resulted in a similar pattern of re-expression of the locus in iPS and ES cells (Fig. 1c). As another proof of the functionality of the locus, we observed re-expression of p19^{Arf} in a teratoma spontaneously developed by an iPS-chimaeric mouse (Fig. 1d). Together, these results indicate that the *Ink4a/Arf* locus is epigenetically re-programmed in iPS cells, adopting a bivalent, silent, configuration and retaining its ability to be re-expressed upon differentiation.

Culture conditions *in vitro* generally entail mitogenic hyperstimulation, which in most primary cells results in upregulation of the *Ink4a/Arf* locus¹¹. Detailed kinetic analyses indicated that the locus is highly induced merely by the culture conditions used for reprogramming (that is, in the absence of the three factors or 'mock') (Fig. 2a, b). Notably, the upregulation of the locus is prevented by the presence of the three factors, and this is clearly noticeable as early as days 4–5 (Fig. 2b and Supplementary Fig. 5). In contrast, single factors or double combinations only partially prevented the induction of the locus (Supplementary Fig. 6). We wondered whether the silencing of the locus is intrinsic to reprogramming, and therefore whether it occurs even under conditions in which the locus is not functional. To test this, we performed three-factor-reprogramming in MEFs previously infected with a retrovirus expressing SV40 large-T (MEF-LT cells). Cells carrying SV40 large-T lack functional Rb and p53, rendering the *Ink4a/Arf* locus functionally irrelevant despite its high levels of expression¹². Interestingly, the high levels of expression of the *Ink4a/Arf* locus in MEF-LT cells began to decrease soon (day 3) after introduction of the three factors (Fig. 2c and Supplementary Fig. 7). These observations dissociate the silencing of the *Ink4a/Arf* locus from its anti-proliferative capacity, and suggest that three-factor-reprogramming, rather than selecting rare pre-existing cells with a silent *Ink4a/Arf* locus, enforces a process that includes the silencing of the *Ink4a/Arf* locus regardless of its functionality.

Next, we wondered whether the silencing of the *Ink4a/Arf* locus was rate-limiting for reprogramming. For this, we scored the 'yield' of alkaline-phosphatase-positive colonies between days 10 and 12, when colonies are first visible. The yield of colonies was corrected by the efficiency of retroviral infection measured in parallel infections with the three factors plus green fluorescence protein (GFP), all at equal proportions (see Methods). The efficiency of three-factor-reprogramming in a series ($n = 10$) of independent wild-type MEF cultures was $0.54\% \pm 0.26$ (mean \pm s.d.) (see primary data in Supplementary Table 1). MEFs deficient in *Ink4a/Arf* were re-programmed with an efficiency that was on average 15-fold higher than in wild-type MEFs (Fig. 3a and Supplementary Fig. 8). We

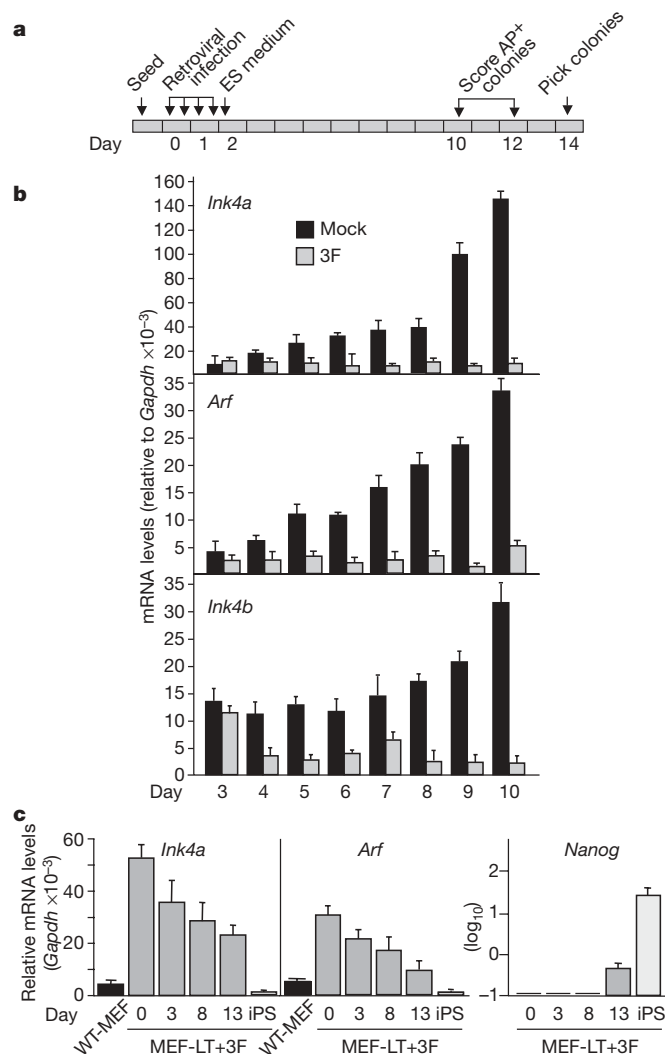


Figure 2 | Silencing of the *Ink4a/Arf* locus during reprogramming. **a**, Experimental layout and day numbering. **b**, Kinetics of expression of the *Ink4a/Arf* locus in mock-infected (mock) and three-factor-infected (3F) MEFs, measured by qRT-PCR. **c**, Repression of *Ink4a* and *Arf* during three-factor-reprogramming of MEFs expressing large-T (MEF-LT + 3F), measured by qRT-PCR. Data correspond to the average and s.d. of at least two independent assays.

confirmed the functionality of the *Ink4a/Arf*-null iPS cells by demonstrating that they are chromosomally stable (Supplementary Fig. 9), produce teratomas with representation of the three developmental layers (Supplementary Fig. 10), and generate chimaeras (Supplementary Fig. 11). Deficiency of *Arf* alone also increased reprogramming efficiency by a factor of sevenfold, an effect that was quantitatively similar to that observed in *p53*-null MEFs (Fig. 3a), which is in agreement with the concept that *p53* is the main target of *Arf*¹³ and also with previous data indicating that *p53* inhibition increases reprogramming¹⁴. The cell-cycle inhibitor *p21* mediates part, but not all, of the anti-proliferative effects of *p53* (ref. 15), and interestingly, reprogramming efficiency increased by a factor of fourfold in *p21*-null MEFs (Fig. 3a). Addition of *c-Myc* to the reprogramming cocktail (four-factor-reprogramming) improved the reprogramming efficiency of wild-type MEFs, and the absence of *Ink4a/Arf* still had a clear positive effect on reprogramming (Fig. 3a). To prove further the implication of *Ink4a* and *Arf* on reprogramming, we performed assays in wild-type cells adding to the three factors a retrovirus expressing a short hairpin RNA (shRNA) against *Ink4a* (targeted to exon 1a), *Arf* (to exon 1b), or both (to the common exon 3) (see Supplementary Fig. 1). Notably, the single inhibition of *Ink4a*

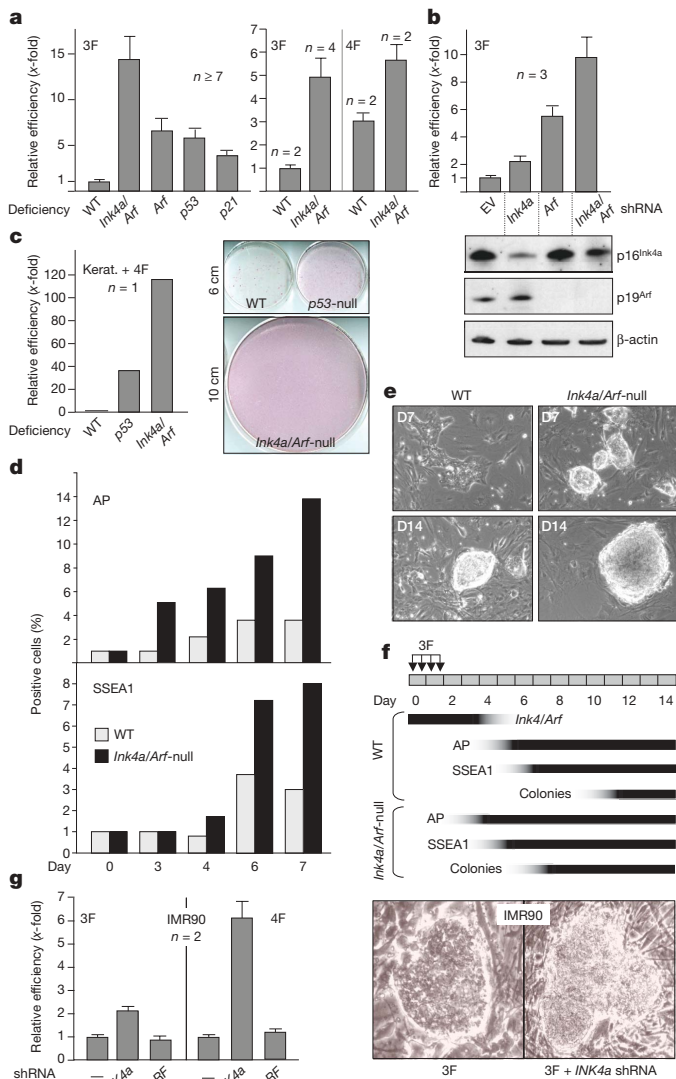


Figure 3 | Effect of *Ink4a/Arf* on reprogramming efficiency.

a, Reprogramming efficiencies of MEFs of the indicated genotypes relative to wild-type (WT) MEFs. Data correspond to the average and s.e.m.; n = independent assays with different MEF isolates. 3F, three factors; 4F, four factors. **b**, Fold change of reprogramming efficiency of primary wild-type MEFs retrovirally infected with three factors plus empty vector (EV) or the indicated shRNAs. Data correspond to the average and s.d. Protein levels were analysed 48 h after infection. **c**, Fold change of reprogramming efficiency measured in newborn keratinocytes (kerat.) of the indicated genotypes. Tissue culture plate diameters are indicated. **d**, Kinetics of expression of pluripotency markers alkaline phosphatase (AP) and SSEA1 during three-factor-reprogramming, measured by FACS. **e**, Representative images of colonies at days (D) 7 and 14. Original magnification, $\times 20$. **f**, Schematic representation of the kinetics of *Ink4a/Arf* locus suppression and marker expression during reprogramming. **g**, Reprogramming efficiencies of human diploid fibroblasts IMR90-TERT using three or four factors plus the indicated shRNAs. Data correspond to the average and s.d. The right panels show representative iPS cell colonies. Original magnification, $\times 20$.

or *Arf* had a beneficial effect on reprogramming, which was more prominent in the case of *Arf* shRNA (Fig. 3b and Supplementary Fig. 12a). Simultaneous inhibition of *Ink4a* and *Arf* had the maximal effect, close to that observed in cells genetically null for these genes (Fig. 4a, b). In agreement with the concept that retroviral vectors are only transiently expressed during reprogramming and then become permanently silenced in iPS/ES cells¹⁶, we observed that after retinoic-acid differentiation of *Ink4a/Arf* shRNA iPS cells, the levels of expression of *Ink4a* and *Arf* were normally induced (Supplementary Fig. 12b).

Furthermore, we wanted to extend the earlier observations to cell types other than fibroblasts. Remarkably, when using mouse keratinocytes from newborn mice, the absence of *Ink4a/Arf* increased the yield of iPS cell colonies more than 100-fold, and, as in the case of MEFs, the absence of *Ink4a/Arf* had a more pronounced effect than the absence of *p53* (Fig. 3c).

In addition to the effect of the *Ink4a/Arf* locus on the yield of iPS cell colonies, we noted that *Ink4a/Arf*-null iPS cell colonies appear significantly faster than wild-type iPS cell colonies. For example, at day 7, wild-type MEFs showed 'pre-iPS cell' micro-colonies characterized by being flat, lacking smooth borders, and having cells with a fibroblast morphology (Fig. 3e); in contrast, *Ink4a/Arf*-null MEFs at this time already presented colonies with bona fide iPS/ES cell morphology (Fig. 3e). To document this further, we observed that the early reprogramming markers alkaline phosphatase and SSEA1 (refs 17, 18) appear earlier in *Ink4a/Arf*-null MEFs compared to wild-type MEFs, with alkaline phosphatase being detectable as early as day 3 (Fig. 3d). Notably, in wild-type MEFs, the appearance of alkaline phosphatase and SSEA1 occurred after day 4, and this timing is coincident with our first detectable evidence of repression of the locus by the three factors (see Fig. 2). A summary of these data is shown in Fig. 3f. The faster kinetics of reprogramming of *Ink4a/Arf*-null MEFs can be due, at least in part, to their faster proliferation rate during the initial stages of reprogramming (Supplementary Fig. 13a). Once reprogramming is completed, both wild-type iPS cells and *Ink4a/Arf*-null iPS cells proliferate at similar rates (Supplementary Fig. 13b), in agreement with the fact that wild-type iPS cells have a silent *Ink4a/Arf* locus. We conclude that inhibition of the *Ink4a/Arf* locus has a dual effect on reprogramming: accelerating the process and also increasing the number of successfully reprogrammed cells.

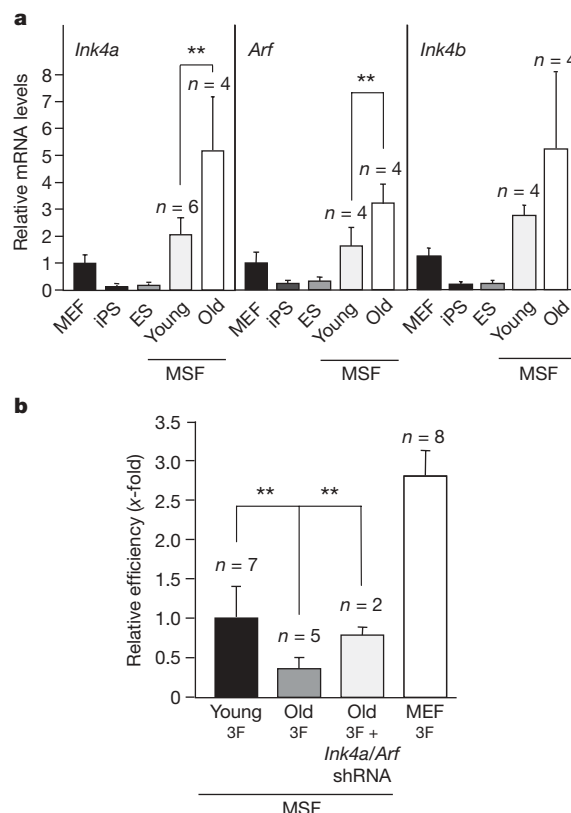


Figure 4 | Association between age of the parental cells, expression of the *Ink4a/Arf* locus and reprogramming efficiency. **a**, Expression of the *Ink4a/Arf* locus in MSFs from 2-month-old (young) or 2-year-old (old) mice, compared to MEFs, iPS and ES cells, measured by qRT-PCR. **b**, Reprogramming efficiencies of old MSFs by three factors plus or minus *Ink4a/Arf* shRNA. Data correspond to the average and s.d. $**P < 0.01$.

We extended the earlier concepts to the reprogramming of human cells. In particular, we performed three- and four-factor-reprogramming of 'telomerized' human IMR90 fibroblast cells, carrying ectopically expressed human TERT (IMR90-TERT). Interestingly, supplementation of three or four factors with a retrovirus expressing *INK4a* shRNA had a positive effect on the efficiency of reprogramming (Fig. 3g). In contrast, *ARF* shRNA had no effect on the reprogramming of human fibroblasts (Fig. 3g), which is in agreement with the modest role of *ARF* in these cells¹⁹. The human *INK4a* shRNA iPS cells expressed endogenous SOX2, NANOG, alkaline phosphatase and SSEA3, and formed teratomas (Supplementary Figs 14 and 15). When comparing the human and mouse data, a theme emerges that is extensively reported in other biological contexts²⁰, namely, that *Arf* dominates over *Ink4a* in murine cells, whereas *INK4a* dominates over *ARF* in human cells.

The expression of the *Ink4a/Arf* locus is progressively upregulated at old age^{2,5}. On the basis of this, we proposed that ageing should decrease reprogramming efficiency and that this should be rescued, at least in part, by inhibition of the locus. Murine skin fibroblasts (MSFs) from ear punches of old (≥ 2 years) mice had a significantly increased expression of the locus compared to MSFs from young (2 months) mice, and this was accompanied by a lower reprogramming efficiency of the old MSFs (Fig. 4a, b). Notably, the addition of *Ink4a/Arf* shRNA to the old MSFs rescued their low reprogramming efficiency to the same levels as young MSFs (Fig. 4b), thus suggesting that the *Ink4a/Arf* locus is partly responsible for the decreased reprogramming associated with ageing.

Collectively, our data indicate that the *Ink4a/Arf* locus constitutes a main barrier to reprogramming in different cell types (fibroblasts and keratinocytes) and in different species (mouse and human). Experimental inhibition of the *Ink4a/Arf* locus improves reprogramming efficiency, both accelerating the process and increasing the number of successfully reprogrammed cells. Also, transitory inhibition of the locus could be of particular practical advantage when reprogramming cells from aged individuals. Finally, recent data have pointed out similarities between malignant cells and embryonic stem cells^{21,22} and, in this context, there is a parallelism between the known activity of *Ink4a/Arf* locus as a barrier to malignancy and the new activity reported here as a barrier to de-differentiation.

METHODS SUMMARY

Primary MEFs were reprogrammed following modifications of a previous protocol²³. Human fibroblasts were reprogrammed as previously described^{24,25}. For quantification of iPS cell generation efficiency, retroviral transduction was measured in parallel infections containing the reprogramming factors plus a GFP retroviral plasmid, followed by FACS analysis at day 3 (see day numbering at Fig. 2a). The total number of iPS cell colonies was counted after staining plates for alkaline phosphatase activity (AP detection kit, Chemicon International) following the manufacturer's instructions. All statistical analyses correspond to unpaired two-tailed Student's *t*-tests.

Full Methods and any associated references are available in the online version of the paper at www.nature.com/nature.

Received 3 April; accepted 20 July 2009.

Published online 9 August 2009.

1. Takahashi, K. & Yamanaka, S. Induction of pluripotent stem cells from mouse embryonic and adult fibroblast cultures by defined factors. *Cell* **126**, 663–676 (2006).
2. Collado, M., Blasco, M. A. & Serrano, M. Cellular senescence in cancer and aging. *Cell* **130**, 223–233 (2007).

3. Serrano, M., Lin, A. W., McCurrach, M. E., Beach, D. & Lowe, S. W. Oncogenic ras provokes premature cell senescence associated with accumulation of p53 and p16INK4a. *Cell* **88**, 593–602 (1997).
4. Sharpless, N. E. *INK4a/ARF*: a multifunctional tumor suppressor locus. *Mutat. Res.* **576**, 22–38 (2005).
5. Krishnamurthy, J. et al. *Ink4a/Arf* expression is a biomarker of aging. *J. Clin. Invest.* **114**, 1299–1307 (2004).
6. Bernstein, B. E. et al. A bivalent chromatin structure marks key developmental genes in embryonic stem cells. *Cell* **125**, 315–326 (2006).
7. Azuara, V. et al. Chromatin signatures of pluripotent cell lines. *Nature Cell Biol.* **8**, 532–538 (2006).
8. Mikkelsen, T. S. et al. Genome-wide maps of chromatin state in pluripotent and lineage-committed cells. *Nature* **448**, 553–560 (2007).
9. Ohm, J. E. et al. A stem cell-like chromatin pattern may predispose tumor suppressor genes to DNA hypermethylation and heritable silencing. *Nature Genet.* **39**, 237–242 (2007).
10. Savatier, P., Lapillonne, H., van Grunsven, L. A., Rudkin, B. B. & Samarut, J. Withdrawal of differentiation inhibitory activity/leukemia inhibitory factor up-regulates D-type cyclins and cyclin-dependent kinase inhibitors in mouse embryonic stem cells. *Oncogene* **12**, 309–322 (1996).
11. Sharpless, N. E. *Ink4a/Arf* links senescence and aging. *Exp. Gerontol.* **39**, 1751–1759 (2004).
12. Hara, E. et al. Regulation of p16^{CDKN2} expression and its implications for cell immortalization and senescence. *Mol. Cell. Biol.* **16**, 859–867 (1996).
13. Sherr, C. J. Divorcing ARF and p53: an unsettled case. *Nature Rev. Cancer* **6**, 663–673 (2006).
14. Zhao, Y. et al. Two supporting factors greatly improve the efficiency of human iPSC generation. *Cell Stem Cell* **3**, 475–479 (2008).
15. Sherr, C. J. & Roberts, J. M. CDK inhibitors: positive and negative regulators of G1-phase progression. *Genes Dev.* **13**, 1501–1512 (1999).
16. Cherry, S. R., Binischewicz, D., van Parijs, L., Baltimore, D. & Jaenisch, R. Retroviral expression in embryonic stem cells and hematopoietic stem cells. *Mol. Cell. Biol.* **20**, 7419–7426 (2000).
17. Brambrink, T. et al. Sequential expression of pluripotency markers during direct reprogramming of mouse somatic cells. *Cell Stem Cell* **2**, 151–159 (2008).
18. Stadtfeld, M., Maherali, N., Breault, D. T. & Hochedlinger, K. Defining molecular cornerstones during fibroblast to iPS cell reprogramming in mouse. *Cell Stem Cell* **2**, 230–240 (2008).
19. Wei, W., Hemmer, R. M. & Sedivy, J. M. Role of p14^{ARF} in replicative and induced senescence of human fibroblasts. *Mol. Cell. Biol.* **21**, 6748–6757 (2001).
20. Evan, G. I. & d'Adda di Fagagna, F. Cellular senescence: hot or what? *Curr. Opin. Genet. Dev.* **19**, 25–31 (2009).
21. Wong, D. J. et al. Module map of stem cell genes guides creation of epithelial cancer stem cells. *Cell Stem Cell* **2**, 333–344 (2008).
22. Ben-Porath, I. et al. An embryonic stem cell-like gene expression signature in poorly differentiated aggressive human tumors. *Nature Genet.* **40**, 499–507 (2008).
23. Blöchl, R., Venere, M., Yen, J. & Ramalho-Santos, M. Generation of induced pluripotent stem cells in the absence of drug selection. *Cell Stem Cell* **1**, 245–247 (2007).
24. Takahashi, K. et al. Induction of pluripotent stem cells from adult human fibroblasts by defined factors. *Cell* **131**, 861–872 (2007).
25. Park, I. H. et al. Reprogramming of human somatic cells to pluripotency with defined factors. *Nature* **451**, 141–146 (2008).

Supplementary Information is linked to the online version of the paper at www.nature.com/nature.

Acknowledgements We thank S. Lowe and R. Agami for reagents. We are grateful to M. Muñoz, O. Dominguez, D. Megias and H. Schonthaler. H.L. is the recipient of a 'Juan de la Cierva' contract from the Spanish Ministry of Science (MICINN). M.Co. is the recipient of a 'Ramon y Cajal' contract (MICINN). Work in the laboratory of M.S. is funded by the CNIO and by grants from the MICINN (SAF and CONSOLIDER), the Regional Government of Madrid, the European Union, the European Research Council (ERC), and the 'Marcelino Botin' Foundation.

Author Contributions H.L. performed most of the experimental work. M.Co. and A.V. made critical experimental contributions. K.S., S.O. and M.Ca. contributed experimentally. H.L., M.Co., M.A.B. and M.S. designed the experimental plan, analysed and interpreted the data. M.S. directed the project and wrote the paper.

Author Information Reprints and permissions information is available at www.nature.com/reprints. Correspondence and requests for materials should be addressed to M.S. (mserrano@cnio.es).

METHODS

Culture conditions. Primary MEFs (passage 2) and keratinocytes of the indicated genotypes were obtained from pure inbred C57BL/6 background mice, as described previously^{26,27}. MSFs were obtained from the ears of young (2 months) or old (2 years) wild type C57BL/6 mice as described before²⁸. Primary murine fibroblasts (MEFs and MSFs) were cultured in standard DMEM medium with 10% FBS (Gibco). Murine keratinocytes were cultured in basal keratinocyte medium (CellNtec). Human foreskin fibroblasts IMR90 stably expressing TERT (IMR90-TERT) were cultured in standard DMEM medium with 10% FBS. Murine ES and iPS cells were cultured in 'complete KSR medium' composed of DMEM (high glucose) supplemented with serum replacement (KSR, 15%, Invitrogen), LIF (1,000 U ml⁻¹), non-essential amino acids, glutamax and β -mercaptoethanol. C57BL/6 ES cells were derived at the Transgenic Mice Unit of the CNIO from C57BL/6 blastocysts. Human iPS cells were cultured in 'human ES medium' composed of DMEM/F12 supplemented with serum replacement (KSR, 20%, Invitrogen), non-essential amino acids, glutamax, β -mercaptoethanol and bFGF (4 ng ml⁻¹).

Generation of mouse iPS cells. Reprogramming of primary (passage 2–4) MEFs was performed following modifications of a previous protocol²³. In brief, retroviral supernatants were produced in HEK-293T cells (5×10^6 cells per 100-mm-diameter dish) transfected with the ecotropic packaging plasmid pCL-Eco (4 μ g) together with one of the following retroviral constructs (4 μ g): pMXs-Klf4, pMXs-Sox2, pMXs-Oct4 or pMXs-c-Myc (obtained from Addgene and previously described¹). The retroviral vector expressing mouse shRNA against *Ink4a*, *Arf* and *Ink4a/Arf*, and the corresponding empty vector LMP were provided by S. Lowe²⁹. Transfections were performed using Eugene-6 transfection reagent (Roche) according to the manufacturer's protocol. Two days later, retroviral supernatants (10 ml) were collected serially during the subsequent 48 h, at 12-h intervals, each time adding fresh medium to the cells (10 ml). The recipient MEFs had been seeded the previous day (2.5×10^5 cells per 100-mm-diameter dish) and received 1.5 ml of each of the corresponding retroviral supernatants (amounting in the case of the three factors to 4.5 ml, and in the cases of the three factors plus shRNA or the four factors to 6 ml, and in the case of the four factors plus shRNA to 7.5 ml). This procedure was repeated every 12 h for 2 days (a total of four additions). After infection was completed, medium was replaced by complete KSR medium (see earlier). Cultures were maintained in the absence of drug selection with daily medium changes²³. From days 10 to 12 (according to the day numbering in Fig. 2a), colonies with ES-cell-like morphology became visible and were scored after alkaline phosphatase staining. Colonies were picked at day 14 and expanded on feeder fibroblasts using standard procedures.

For reprogramming of murine keratinocytes, cells were freshly isolated from neonates (days 1–4 post-partum)²⁷, and were reprogrammed at passage 5. Virus was produced in HEK-293T cells as described earlier, and 3×10^5 keratinocytes were plated per 60-mm collagen-coated plate. On the 2 days after cell seeding, infections were performed twice daily. The keratinocytes were exposed to the cocktail of viral supernatants for 1-h intervals to prevent differentiation and then allowed to recover in basal keratinocyte media (CellNtec) between infections. The day after infection, media were changed to a 'mixture medium' containing basal keratinocyte medium supplemented with serum replacement (KSR, 15%, Invitrogen), LIF (1,000 U ml⁻¹), non-essential amino acids, glutamax and β -mercaptoethanol. Medium was changed daily and cellular changes in plates were monitored. Clones were picked and amplified in conventional complete KSR medium.

Generation of human iPS cells. Reprogramming of IMR90-TERT cells was done as previously described^{24,25}. In brief, retroviral supernatants were produced in HEK-293T cells (5×10^6 cells per 100-mm-diameter dish) transfected with the ecotropic packaging plasmid pCL-Ampho (4 μ g) together with one of the following retroviral constructs (4 μ g): pMXs-hKlf4, pMXs-hSox2, pMXs-hOct4 and pMXs-hc-Myc (obtained from Addgene and previously described²⁴). The retroviral vectors expressing human shRNA pRetroSuper-ARF and pRetroSuper-INK4a were provided by R. Agami³⁰. Transfections and infections were performed the same as mouse iPS cell reprogramming described earlier. IMR90-TERT fibroblasts had been seeded the previous day (2×10^5 cells per well in 6-well gelatin-coated plates) and received 1.5 ml of each of the corresponding retroviral supernatants (either a total of three or four—the fourth factor being the *INK4a* shRNA or *ARF* shRNA, see later). This procedure was repeated every 12 h for 2 days (a total of four additions). The day after infection was completed, medium was replaced, and kept for three more days (days 2, 3 and 4, according to the numbering scheme in Fig. 2a). At day 5, cells were trypsinized and reseeded on feeder plates. At day 6, medium was changed to human ES cell medium. Cultures were maintained in the absence of drug selection with daily medium changes. At day 17, colonies with ES-cell-like morphology became visible at the microscope. Colonies were picked after 3 weeks and expanded on feeder fibroblasts using standard procedures.

Reprogramming efficiency. For quantification of iPS cell generation efficiency, retroviral transduction was measured in parallel infections containing all the retroviruses used for reprogramming plus a GFP retrovirus (pBabe-PURO-GFP) (equal volumes of each retrovirus). The efficiency of infection was measured by FACS analysis at day 3 (see day numbering in Fig. 2a). The total number of iPS cell colonies was counted after staining plates for alkaline phosphatase activity (AP detection kit, Chemicon International) following the manufacturer's instructions.

Chimaera formation. The capacity of the iPS cell clones to generate chimaeras *in vivo* was tested by microinjection into C57BL/6J-Tyr^{C-2J}/J (albino) blastocysts, or by aggregation with CD1 (albino) morulae.

Differentiation with retinoic acid. Differentiation with retinoic acid was performed essentially as described¹⁰. Cultures were grown to near confluency in complete KSR medium with LIF (day 0), and then trypsinized and seeded at a lower density in the absence of LIF for 1 day (day 1). During the next 2 days (days 2 and 3), retinoic acid was added at a concentration of 10^{-6} M.

Teratoma formation. *Ink4/Arf*-null (three factors) iPS cells or human iPS cells (four factors plus *INK4a* shRNA, or four factors plus *INK4a* shRNA and *ARF* shRNA) (2×10^6 cells) were subcutaneously injected into irradiated (4 Gy) nude mice (injections were performed 1 day after irradiation). Teratomas were surgically removed after 3 weeks in the case of murine iPS cells, or after 9 weeks in the case of human iPS cells. Tissue was fixed in formalin at 4 °C, embedded in paraffin wax, and sectioned at a thickness of 5 μ m. Sections were stained with haematoxylin and eosin for pathological examination, or processed for immunohistochemical analysis with antibodies against mouse p19^{Arf} (SantaCruz 5-C3-1) or for markers of differentiation. In the case of murine teratomas: anti-neuronal nuclei (NeuN, MAB377, Chemicon) for neuroectoderm, cytokeratin-19 (CK-19, Developmental Studies Hybridoma Bank) for ectoderm, common-muscle actin (HHF-35, M0635, Dako) for mesoderm, and chymotrypsin (2100-0657, Serotec) for endoderm. In the case of human teratomas: synaptophysin (SY38 Dako) for ectoderm marker, smooth muscle actin (SMA, 1A4, Dako) for mesoderm, and cytokeratins (AE1/AE3, Dako) for endoderm.

Quantitative real-time PCR. Total RNA from cells was extracted with Trizol (Life Technologies). Samples were treated with DNase I before reverse transcription using random priming and Superscript Reverse Transcriptase (Life Technologies), according to the manufacturer's protocols. Quantitative real-time PCR was performed using an ABI PRISM 7700 (Applied Biosystems), using DNA Master SYBR Green I mix (Applied Biosystems). All values were obtained at least in duplicate, and in a total of at least two independent assays.

The primers used were: *mInk4a*-F, 5'-CGTACCCGATTGAGTGAT-3'; *mInk4a*-R, 5'-TTGAGCAGAAGAGCTGCTACGT-3'; *mInk4b*-F, 5'-AGATCCC AACGCCCTGAAC-3'; *mInk4b*-R, 5'-CCCATCATCATGACCTGGATT-3'; *mArf*-F, 5'-GCCGCACCGGAATCCT-3'; *mArf*-R, 5'-TTGAGCAGAAGAGCT GCTACGT-3'; *mp21*-F, 5'-GTGGGTCTGACTCCAGCCC-3'; *mp21*-R, 5'-CC TTCTCTGTGAGACGCTTAC-3'; *mNanog*-F, 5'-AGGGTCTGCTACTGAGATG CTCTG-3'; *mNanog*-R, 5'-CAACCACCTGGTTTCTGCCACCG-3'; *mEsg1*-F, 5'-GAAGTCTGGTTCCTTGGCAGGATG-3'; *mEsg1*-R, 5'-ACTCGATACAC TGGCCTAGC-3'; *Gapdh*-F, 5'-TTACCACCATGGAGAAGGC-3'; *Gapdh*-R, 5'-CCCTTTTGGCTCCACCCT-3'; *hEndo-SOX2*-F, 5'-GGGAAATGGGAG GGGTGCAAAAGAGG-3'; *hEndo-SOX2*-R, 5'-TTGCGTGAGTGTGGATG GGATGGTG-3'; *hNANOG*-F, 5'-TTTCAGAGACAGAAATACCTCAGC-3'; *hNANOG*-R, 5'-TCACACCATGCTATTCTTCG-3'; *hACTB*-F, 5'-CAAGGCC AACCGCAGAGAAGAT-3'; and *hACTB*-R, 5'-CCAGAGGCGTACAGGGA TAGCAC-3'. Calculations for the values were made using the $\Delta\Delta C_t$ method, as previously described³¹.

FACS. FACS was performed as previously described¹⁷. In brief, cells were trypsinized and washed once in PBS. For APC-conjugated SSEA1 (R&D), 1×10^5 cells were washed once in PBS and 0.5% BSA, and incubated with 10 μ l of SSEA1 in 50 μ l of PBS, 0.5% BSA for 30 min at 4 °C. Afterwards, cells were washed by PBS and 0.5% BSA once to remove antibody, and resuspended in 300 μ l PBS for FACS analysis. For alkaline phosphatase staining, cells were washed once in PBS and fixed/permeabilized using an intracellular staining kit (eBioscience). After permeabilization, cells were treated with 500 μ l of alkaline phosphatase substrate (Vector Red substrate kit, Vector Laboratories) and stained according to the manufacturer's protocol for 20 min. Cells were washed once and resuspended in PBS for FACS analysis. FACSCanto II (BD Biosciences) was used for all FACS analysis. Mock-infected cells were stained and analysed in parallel to set the thresholds.

Western blot. Cell extracts were prepared using RIPA buffer, resolved on NuPAGE 4–12% gradient Bis-Tris gels, transferred to nitrocellulose and hybridized using antibodies against Oct4 (1:250; H-134, SantaCruz), Sox2 (1:250; ab5603, Chemicon) and Klf4 (1:250; SantaCruz).

Immunofluorescence. MEF-LT cells were grown on chamber slides and infected with or without the three factors using the same reprogramming protocol as for the rest of the experiments. At days 3 and 8, cells were fixed with 2% paraformaldehyde for 15 min at room temperature, washed with PBS and permeabilized with PBS

containing 0.02% Tween-20 for 20 min. Cells were blocked in PBS with 4% BSA for 1 h and incubated with antibodies against mouse p19^{Arf} (SantaCruz; 1:250 in PBS and 4% BSA) for 2 h, washed with PBS and further incubated with secondary anti-rat antibodies conjugated with Cy3 (1:1,000 in PBS and 4% BSA). For NANOG immunofluorescence of human iPS cells, cells were seeded in 2-well chamber slides with feeders, fixed in 4% paraformaldehyde for 15 min, permeabilized (PBS and 0.1% Triton X-100) for 15 min and blocked (PBS and 5% BSA) for 1 h at room temperature. NANOG antibody (1:500; Chemicon) was added and incubated in PBS and 2% BSA overnight. The next day, cells were washed by PBS and incubated with Alexa Fluor 488 secondary antibodies against mouse (1:1,000 in PBS and 4% BSA). For SSEA3 immunofluorescence of human iPS cells, cells were grown on 6-well plates with feeders, and fixed with 4% paraformaldehyde for 15 min at room temperature. Wells were washed with PBS before blocking in PBS with 4% BSA for 1 h and incubated with antibody against human SSEA3 (R&D, 25 µg ml⁻¹) overnight at 4 °C. Cells were washed with PBS and further incubated with a secondary antibody as explained before for NANOG staining.

Chromatin immunoprecipitation. Cells were crosslinked with 1% formaldehyde for 15 min at room temperature. Crosslinking was stopped by the addition of glycine to a final concentration of 0.125 M. Fixed cells were lysed in lysis buffer (1% SDS, 10 mM EDTA, 50 mM Tris-HCl, pH 8.0) and sonicated. An aliquot of 60 µg was reserved as input. For immunoprecipitation, 600 µg of protein were diluted in dilution buffer (1% Triton X-100, 2 mM EDTA, 150 mM NaCl and 20 mM Tris-HCl, pH 8.0, containing protease inhibitors), and precleared with 60 µl of A/G plus-agarose (SantaCruz). The antibodies used for the immunoprecipitation were histone H3 trimethyl Lys4 (Abcam), histone H3 trimethyl Lys27 (Upstate), and histone H3 trimethyl Lys9 (Upstate). Immune complexes were precipitated with A/G plus-agarose and washed sequentially with low-salt immune complex wash buffer (0.1% SDS, 1% Triton X-100, 2 mM EDTA, 20 mM Tris-HCl, pH 8.1, 150 mM NaCl), high-salt immune complex wash buffer (0.1% SDS,

1% Triton X-100, 2 mM EDTA, 20 mM Tris-HCl, pH 8.1, 500 mM NaCl), LiCl immune complex wash buffer (0.25 M LiCl, 1% NP-40, 1% deoxycholate-Na, 1 mM EDTA, 10 mM Tris-HCl, pH 8.1), and TE buffer, and then eluted in elution buffer (1% SDS, 0.1 M NaHCO₃). All samples, including inputs, were de-crosslinked, treated with proteinase K, and DNA was extracted with phenol-chloroform and resuspended in TE buffer. Sequential ChIP experiments were carried out essentially as described earlier with modifications previously reported⁶.

The primers used for detection of promoters after ChIP were: m*Irx2*-F, 5'-TAACACGGCCTGAAATCTTCTC-3'; m*Irx2*-R, 5'-GCATCCCACTTCTACAGTCTC-3'; m*Tcf4*-F, 5'-CGGATGTGAATGGATTACAATG-3'; m*Tcf4*-R, 5'-ATTGTTCTTCGGTCTTGTTGGT-3'; m*Ink4a*-F, 5'-CAGATTGCCCTCCGATGACTTC-3'; m*Ink4a*-R, 5'-TGGACCCGCACAGCAAAGAAGT-3'; m*Arf*-F, 5'-GCCTCGCGGATCTTCCTATTTTCT-3'; m*Arf*-R, 5'-CCCATCGCGGTGACAGC-3'; m*Ink4b*-F, 5'-ACCAAGCGAAGGAACATACTGC-3'; and m*Ink4b*-R, 5'-GGCACCTGGCTTCCTTAAGA-3'.

26. Palmero, I. & Serrano, M. Induction of senescence by oncogenic Ras. *Methods Enzymol.* **333**, 247–256 (2001).
27. Munoz, P., Blanco, R., Flores, J. M. & Blasco, M. A. XPF nuclease-dependent telomere loss and increased DNA damage in mice overexpressing TRF2 result in premature aging and cancer. *Nature Genet.* **37**, 1063–1071 (2005).
28. Li, H., Vogel, H., Holcomb, V. B., Gu, Y. & Hastay, P. Deletion of Ku70, Ku80, or both causes early aging without substantially increased cancer. *Mol. Cell. Biol.* **27**, 8205–8214 (2007).
29. Dickins, R. A. *et al.* Probing tumor phenotypes using stable and regulated synthetic microRNA precursors. *Nature Genet.* **37**, 1289–1295 (2005).
30. Voorhoeve, P. M. & Agami, R. The tumor-suppressive functions of the human *INK4A* locus. *Cancer Cell* **4**, 311–319 (2003).
31. Yuan, J. S., Reed, A., Chen, F. & Stewart, C. N. Jr. Statistical analysis of real-time PCR data. *BMC Bioinformatics* **7**, 85 (2006).

LETTERS

Linking the p53 tumour suppressor pathway to somatic cell reprogramming

Teruhisa Kawamura^{1,2*}, Jotaro Suzuki^{1,3*}, Yunyuan V. Wang¹, Sergio Menendez⁴, Laura Batlle Morera⁴, Angel Raya^{4,5,6}, Geoffrey M. Wahl¹ & Juan Carlos Izpisua Belmonte^{1,4}

Reprogramming somatic cells to induced pluripotent stem (iPS) cells has been accomplished by expressing pluripotency factors and oncogenes^{1–8}, but the low frequency and tendency to induce malignant transformation⁹ compromise the clinical utility of this powerful approach. We address both issues by investigating the mechanisms limiting reprogramming efficiency in somatic cells. Here we show that reprogramming factors can activate the p53 (also known as Trp53 in mice, TP53 in humans) pathway. Reducing signalling to p53 by expressing a mutated version of one of its negative regulators, by deleting or knocking down p53 or its target gene, *p21* (also known as *Cdkn1a*), or by antagonizing reprogramming-induced apoptosis in mouse fibroblasts increases reprogramming efficiency. Notably, decreasing p53 protein levels enabled fibroblasts to give rise to iPS cells capable of generating germline-transmitting chimaeric mice using only Oct4 (also known as Pou5f1) and Sox2. Furthermore, silencing of p53 significantly increased the reprogramming efficiency of human somatic cells. These results provide insights into reprogramming mechanisms and suggest new routes to more efficient reprogramming while minimizing the use of oncogenes.

The p53 pathway reduces cancer initiation by inducing apoptosis or cell cycle arrest in response to a variety of stress signals, including overexpressed oncogenes such as c-Myc. Klf4 can either activate or antagonize p53, depending on the cell type used and expression level¹⁰. Consequently, reprogramming efficiency is probably reduced through oncogene-mediated activation of the p53 pathway. This is consistent with previous results showing that germ cells can be spontaneously reprogrammed in the absence of p53 (ref. 11), and a combination of p53 short interfering RNA (shRNA) and Utl1 expression increased iPS cell formation¹².

We first determined whether the reprogramming factors, individually or in combination, activate the p53 pathway in mouse embryo fibroblasts (MEFs). Relative to the green fluorescent protein (GFP)-retroviral control, c-Myc considerably increased p53 abundance and activity, manifested by increased expression of the cyclin-dependent kinase inhibitor p21 (Fig. 1a). This was achieved by induction of p19^{Arf}, an antagonist of Mdm2, the E3-ubiquitin ligase principally responsible for p53 degradation¹³. Increased p21 protein levels were also observed in MEFs infected with Klf4 alone, with Oct4 and Sox2 (two factors) or with Oct, Sox2 and Klf4 (three factors) (Fig. 1a). Because introducing reprogramming factors increased γ -H2ax (also known as γ -H2afx) foci (Supplementary Fig. 1), we infer that the expression of reprogramming factors may induce p53 activity by DNA damage. We also compared p53 and p21 expression in a variety of mouse and human cell lines previously used for iPS cell production

(Supplementary Fig. 2). Interestingly, keratinocytes, which have higher reprogramming efficiency, display lower p53 and p21 protein levels than other cell types. Moreover, p21 induction in keratinocytes is lower than in fibroblasts after infection with the three factors (Supplementary Fig. 3). Together, these data indicate that the p53 pathway is one determinant of reprogramming efficiency.

We therefore tested the effects of reducing p53 signalling by determining reprogramming efficiencies in cells in which p53 function was reduced by shRNA or ablated by homologous recombination. Most cells were infected with shRNA (Supplementary Fig. 4), p53 messenger RNA and protein levels were reduced by 60–80% (Fig. 1c and Supplementary Fig. 5), and iPS cell colony formation was increased by 2–4-fold using two different shRNAs (Fig. 1b, c). This probably underestimates p53 suppressive capacity, because functional p53 protein clearly remained present, as indicated by the ability of the p53 activating agent Nutlin-3a (ref. 14) to dose-dependently reduce iPS cell formation in MEFs treated with the most effective p53 shRNA (Fig. 1d). In contrast, reprogramming efficiency was increased by at least tenfold in p53-null MEFs, and this was not reduced by Nutlin-3a (Supplementary Table 1 and Fig. 1e, g). p53^{+/-} heterozygous MEFs also exhibited higher three-factor-reprogramming efficiency than wild-type MEFs. Although culture stress can induce cellular senescence and activate p53, which would reduce reprogramming, less than 1% of the cells of all p53 genotypes stained with the senescence marker β -galactosidase (Supplementary Fig. 6). Because we did not detect loss of heterozygosity of the p53 gene in iPS cell colonies derived from p53^{+/-} MEFs (Supplementary Fig. 7), the data suggest a p53 dosage-sensitivity to reprogramming (Fig. 1e). We were concerned that because p53-null MEFs are genetically unstable, increased reprogramming efficiency might result from expression of the three factors in variant cells. However, we found that re-expressing p53 protein in the p53-null MEFs markedly reduced reprogramming efficiency (Fig. 1f).

Reducing factors downstream of p53 also increased reprogramming efficiency. For example, p21 shRNA increased reprogramming by approximately threefold (Fig. 1h). This probably underestimates the magnitude to which p21 induction suppresses reprogramming as p21-shRNA-expressing cells still responded to Nutlin-3a treatment as discussed earlier. We also noted a modest induction of the pro-apoptotic factor Bax, another p53-inducible gene¹⁵, in three-factor experiments (data not shown). Consistent with a limiting role of the p53-induced apoptotic response during reprogramming, overexpression of the Bax antagonist Bcl2 suppressed apoptosis in two, three and four factor experiments, and increased the frequency of colonies expressing the pluripotency factor Nanog by fourfold

¹Gene Expression Laboratory, Salk Institute for Biological Studies, 10010 North Torrey Pines Road, La Jolla, California 92037, USA. ²Career-Path Promotion Unit for Young Life Scientists, Kyoto University, Kyoto 606-8501, Japan. ³Drug Discovery Research, Astellas Pharma Inc., Tsukuba, Ibaraki 305-8585, Japan. ⁴Center of Regenerative Medicine in Barcelona, Dr. Aiguader 88, 08003 Barcelona, Spain. ⁵Institució Catalana de Recerca i Estudis Avançats (ICREA), Passeig Lluís Companys 23, 08010 Barcelona, Spain. ⁶Networking Center of Biomedical Research in Bioengineering, Biomaterials and Nanomedicine (CIBER-BBN), Dr. Aiguader 88, 08003 Barcelona, Spain.

*These authors contributed equally to this work.

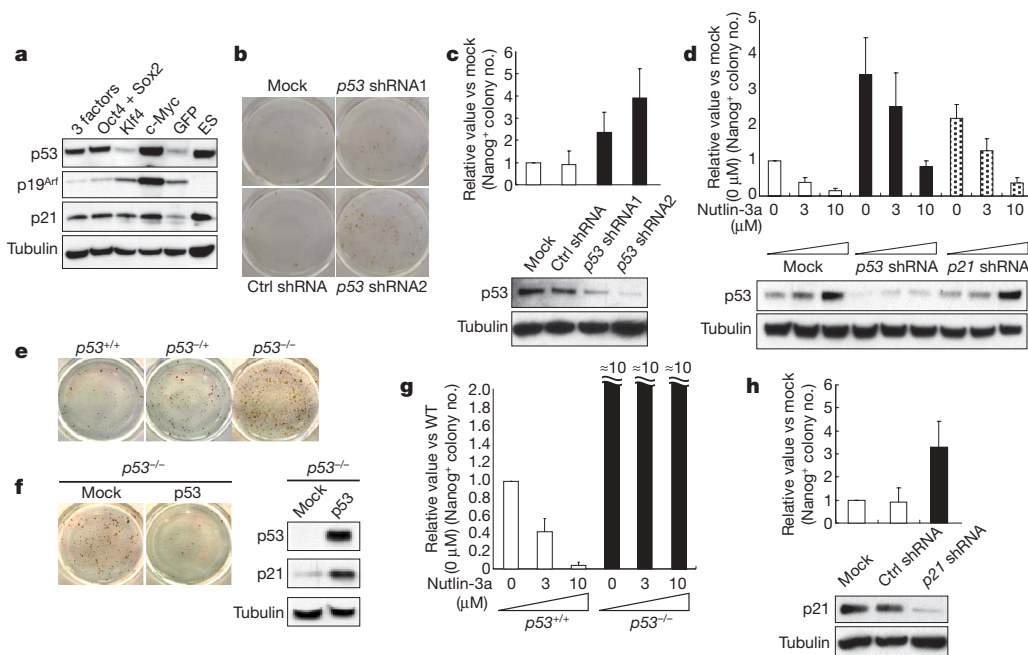


Figure 1 | Increased generation of iPS cells by blocking p53 and p21.

a, MEFs were infected by retroviruses encoding three factors (Oct4, Sox2 and Klf4), two factors (Oct4 and Sox2), Klf4, c-Myc or GFP. Four days after infection, the protein levels of p53, p19^{Arf} and p21 were analysed by western blotting. α -tubulin was used as a loading control. **b**, MEFs were infected by three factors in combination with mock, control (Ctrl) shRNA (GFP) and p53 shRNA (1 and 2). Emerging colonies of iPS cells were visualized by immunostaining with an anti-Nanog antibody using an avidin-biotin complex method. **c**, The fold-change in the number of Nanog-positive colonies compared to mock ($n = 4$) (top). p53-knockdown efficiency was examined by western blot (bottom). **d**, MEFs were infected by three factors in combination with mock, p53 shRNA and p21 shRNA. Four days later, half

the cells were treated with Nutlin-3a (0, 3 and 10 μ M) and analysed for p53 levels. The remainder were stained for Nanog-positive colonies.

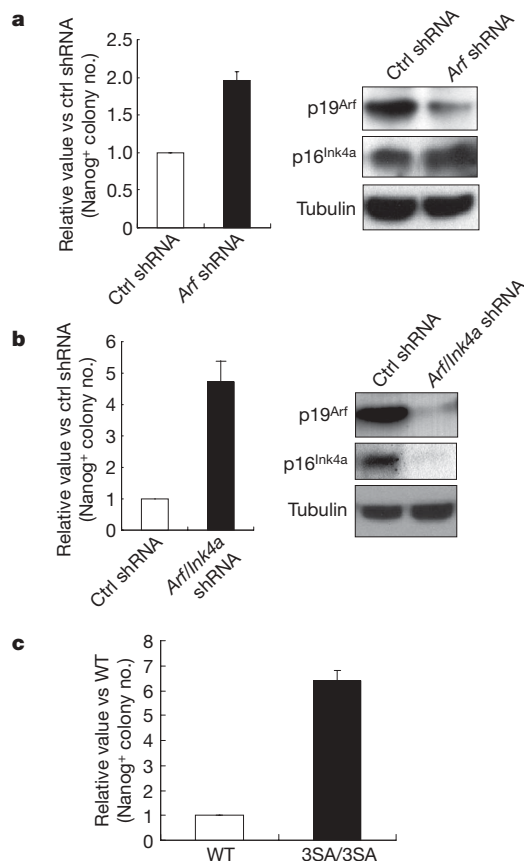
e, Immunostaining of Nanog-positive colonies generated from p53^{+/+}, p53^{+/-} and p53^{-/-} MEFs by three-factors showed p53 dose-dependent decrease of colony number. **f**, Retroviral infection of p53 into p53^{-/-} MEFs decreased the number of Nanog-positive colonies induced by three factors. p53 and p21 levels on day 3 after infection were analysed. **g**, Nutlin-3a markedly reduced reprogramming of p53^{+/+} MEFs, but not of p53^{-/-} MEFs. **h**, Fold change in the number of Nanog-positive colonies by p21 shRNA ($n = 4$). p21-knockdown efficiency was examined by western blot. All error bars indicate s.d.

(Supplementary Fig. 8). The three-factor-transduced colonies exhibit the characteristics of iPS cells, with mouse embryonic stem (ES) cell morphology, high levels of alkaline phosphatase activity and expression of pluripotency-associated transcription factors and surface markers, and ability to differentiate into derivatives of all three embryonic germ layers *in vitro* (Supplementary Figs 9–11). Taken together with the genetic and shRNA studies described earlier, these data show that complete loss of p53 function markedly increases reprogramming efficiency, and that even low levels of p53 activity are all that is needed to compromise somatic cell reprogramming.

The ability of the three factors to increase p53 abundance suggests that controlling its stability might be crucial for p53-mediated reprogramming suppression. Thus we determined whether reducing p19^{Arf} levels using *Arf* shRNA increases reprogramming efficiency, as lower *Arf* levels should decrease p53 stability^{16–18}. Reducing p19^{Arf} levels by 2–4-fold (Fig. 2a) engendered an approximately twofold increase in three-factor-reprogramming (Fig. 2a). Reducing p19^{Arf} and p16^{Ink4a} (both encoded by alternative reading frames of the *Ink4a/Arf* locus, also known as *Cdkn2a* locus) together increased iPS cell formation even more than p19^{Arf} alone (4–5-fold; Fig. 2b), indicating that compromising retinoblastoma (Rb) tumour suppressor¹⁹ function by antagonizing p16^{Ink4a} can collaborate with diminished p53 activity to improve reprogramming efficiency.

Figure 2 | Modulation of p53 activity alters reprogramming efficiency.

a, **b**, Fold changes in the number of three-factor-induced Nanog-positive colonies by *Arf* shRNA (**a**) or by *Arf/Ink4a* shRNA (**b**) compared to control shRNA ($n = 3$) (left). Protein knockdown efficiency was examined by western blot (right). **c**, Three-factor-induced Nanog-positive colonies from wild type (+/+; WT) and homozygous (3SA/3SA) MEFs ($n = 3$). Error bars, s.d.



We next genetically modulated the activity of the E3 ligase that regulates p53 stability by generating a mouse encoding a mutant version of Mdmx (also known as Mdm4), a critical negative regulator of p53. We substituted three serine residues with alanines (Mdmx Ser 341, Ser 367 and Ser 402, hereafter called Mdmx3SA) to prevent its phosphorylation and degradation in response to DNA damage or activated oncogenes^{20,21}. Notably, MEFs or thymocytes derived from homozygous Mdmx3SA mice exhibited lower basal expression of p21, lower DNA damage induced p21 levels (Supplementary Fig. 12 and ref. 21) and an impaired ability of c-Myc to activate p53 *in vivo*²¹. Three-factor-reprogramming increased ~7-fold in Mdmx3SA MEFs, in agreement with their reduced sensitivity to activated oncogenes and DNA damage signalling (Fig. 2c).

Because Klf4 has been reported to have oncogenic properties when overexpressed²², and we showed that it alone can activate p53, we investigated whether cells with reduced p53 expression could be converted into iPS cells using only two factors, Oct4 and Sox2. We tested this hypothesis by transducing MEFs with a lentivirus expressing p53 shRNA plus retroviruses encoding Oct4 and Sox2 (hereafter designated as 2F-p53KD-iPS cells; Supplementary Fig. 13). Cells that developed into colonies exhibiting ES-cell-like morphology were obtained by week 4 after infection. Of six colonies selected for analysis, four grew using standard mouse ES cell culturing methods (Fig. 3a), and all were alkaline-phosphatase-positive (Fig. 3b) and expressed genes and cell surface markers characteristic of mouse ES cells, including the pluripotency marker Nanog (Fig. 3c and Supplementary Fig. 14). 2F-p53KD-iPS cells and mouse ES cell lines had indistinguishable gene expression patterns when maintained under similar conditions. Bisulphite sequencing of the Oct4 and Nanog promoters showed nearly complete demethylation in 2F-p53KD-iPS cells when compared to MEFs (Supplementary Fig. 14). Consistent with this, we observed expression of the pluripotency-associated transcription factors Oct4 and Sox2 from the endogenous loci in 2F-p53KD-iPS cells, at levels that were comparable to those of ES cells (Supplementary Fig. 15).

Also, like ES cells, most (70–80%) cells were in S-phase (Supplementary Fig. 16). We tested the pluripotency of three 2F-p53KD-iPS clones in assays of embryoid body formation *in vitro* and/or teratoma induction *in vivo*. The tested cell lines differentiated into the three germ layer derivatives, as shown by immunostaining and mRNA expression *in vitro* (Fig. 3d and Supplementary Fig. 17). Furthermore, these cells differentiated with high efficiency into beating cardiomyocytes (Supplementary Fig. 18 and Supplementary Movies 1–3). After injection into immunocompromised mice, two independent 2F-p53KD-iPS lines generated complex intratesticular and subcutaneous teratomas containing structures and tissues representative of the three embryonic germ layers (Fig. 3e). Microarray analyses demonstrate that gene expression patterns of these clones are similar to mouse ES cells (Supplementary Fig. 19). We also tested whether 2F-p53KD-iPS cells contribute to the formation of chimaeric mice when injected into mouse blastocysts. One line (clone 6) contributed almost 100% to chimaera formation, and the other line (clone 1) contributed 30–50%, as judged by coat colour (Fig. 3f and Supplementary Fig. 20). We finally used the highest contribution chimaera to test for germline competence by crossing it with wild-type C57BL/6J mice. Notably, the offspring of such crosses included agouti pups (Fig. 3g), indicating germline transmission of the two-factor-iPS genome. Taken together, these results demonstrate that MEFs can be reprogrammed to pluripotency by the forced expression of only two factors, Oct4 and Sox2, when p53 levels are reduced.

We next tested whether downregulating p53 activity had any effect on the reprogramming of human embryonic fibroblasts (HEFs) and juvenile epidermal keratinocytes. We could not obtain Nanog-positive colonies from HEFs with either three or four factors combined with control shRNA under our reprogramming conditions after up to 4 weeks. In contrast, cell reprogramming occurred rapidly (after 2 weeks) with high efficiency when p53 expression was reduced by shRNA (Fig. 4a and Supplementary Figs 22, 23 and Supplementary Table 2). p53 shRNA induced ES-cell-like colonies, expressed human

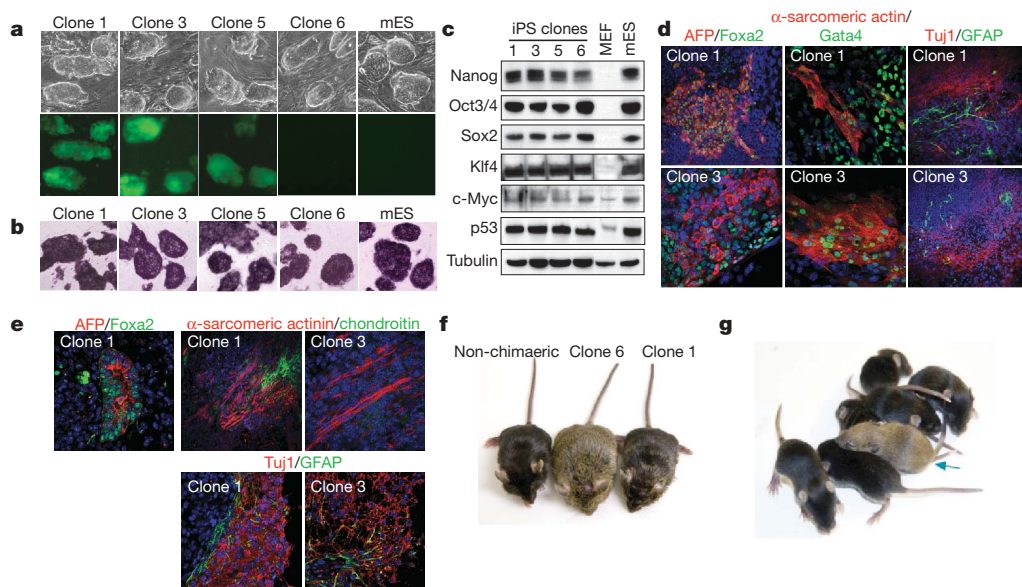


Figure 3 | Generation and characterization of 2F-p53KD-iPS cells by p53 downregulation. **a**, Morphology and GFP fluorescence of 2F-p53KD-iPS cell lines. GFP expression is silenced in clone 6. mES, mouse ES cells. **b**, Alkaline phosphatase staining of 2F-p53KD-iPS cell lines. DAPI (4,6-diamidino-2-phenylindole) was used to visualize cell nuclei. Original magnification (**a**, **b**), $\times 200$. **c**, Protein levels of Nanog, Oct4, Sox2, Klf4, c-Myc and p53 in 2F-p53KD-iPS cell lines are shown. α -tubulin was used as loading control. **d**, Embryoid bodies of 2F-p53KD-iPS cell clones on day 6 of differentiation. Embryoid bodies were transferred to gelatinized dishes on days 3 to 5 for further differentiation. On day 14, embryoid bodies were subjected to immunofluorescence for α -fetoprotein (AFP) and Foxa2 (endoderm),

α -sarcomeric actinin and Gata4 (mesoderm) and Tuj1 and GFAP (ectoderm). **e**, Immunofluorescence of teratoma from 2F-p53KD-iPS cells using antibodies against AFP and Foxa2 (endoderm), sarcomeric α -actinin and chondroitin (mesoderm), and Tuj1 and GFAP (ectoderm) showed spontaneous differentiation into all three germ layers. Original magnification (**d**, **e**), $\times 400$. **f**, Adult chimaeric mice obtained from 2F-p53KD-iPS cell lines (1 and 6) and non-chimaeric mouse in C57BL/6J host blastocysts. **g**, As of the date of submission, the mating of offspring from clone 6 chimaera to a C57BL/6J female generated 1 agouti pup (blue arrow), that together with PCR analysis (not shown) indicate germline transmission of the two-factor iPS genome.

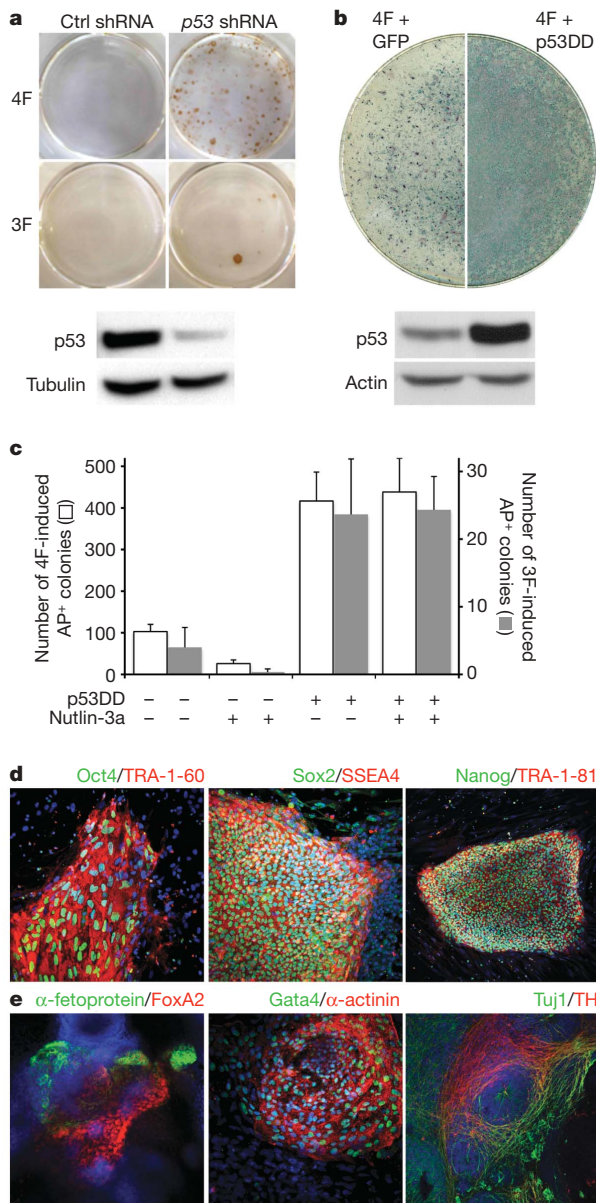


Figure 4 | Downregulation of p53 activity increases reprogramming efficiency of human somatic cells. **a**, HEFs were infected with retroviruses encoding Oct4, Sox2 and Klf4 (three factors, or 3F) or Oct4, Sox2, Klf4 and c-Myc (four factors, or 4F) in combination with lentiviruses expressing control or p53 shRNA. Emerging colonies of iPS cells were immunostained with anti-Nanog antibody (top). p53-knockdown efficiency was examined by western blot (bottom). **b**, Human primary keratinocytes were co-infected with four factors and retroviruses expressing GFP or p53DD. After 2 weeks, cells were stained for alkaline phosphatase activity (top). Expression of p53DD resulted in stabilization of wild-type p53 (bottom). Actin was used as a loading control. **c**, The average number of iPS-cell-like colonies obtained from 10^4 keratinocytes reprogrammed with three or four factors and retroviruses encoding GFP or p53DD, in the absence or presence of Nutlin-3a ($n = 3$). iPS-cell-like colonies were scored as having human ES-cell-like morphology and positive alkaline phosphatase activity (top). Owing to the numerous colonies generated in four-factor p53DD keratinocytes, quantification was done using 10^4 cells. Error bars, s.d. **d**, **e**, Colonies of human keratinocyte-derived iPS cells generated by three factors and p53DD show strong immunoreactivity for pluripotency-associated transcription factors (Oct4, Sox2, and Nanog) and surface markers (TRA-1-60 and TRA-1-81) (**d**) and differentiate *in vitro* into cell types that express markers of endoderm (α -fetoprotein, FoxA2), mesoderm (Gata4, sarcomeric α -actinin), and ectoderm (Tuj1, tyrosine hydroxylase (TH)) (**e**).

ES cell marker genes, could be successfully cloned and expanded, exhibited ES-cell-like morphology, and differentiated *in vitro* in embryoid body formation assays (Supplementary Figs 24 and 25). We also obtained two-factor-induced iPS cell colonies from HEFs infected with p53 shRNA, although with lower efficiency (two iPS cell colonies resulted from six independent attempts, Supplementary Fig. 26). Consistently, reprogramming efficiency was increased using either three or four factors in human primary keratinocytes when p53 activity was downregulated using a dominant negative mutant of p53 (p53DD)²³ (Fig. 4b, c) that inhibited p53 activity more effectively than p53 shRNA, because Nutlin-3a did not reduce reprogramming of three-factor or four-factor p53DD expressing iPS cells (Fig. 4c). 3F-p53DD-iPS cells grew robustly and strongly expressed pluripotency-associated transcription factors and surface markers (Fig. 4d and data not shown). Furthermore, 3F-p53DD-iPS cells readily differentiated *in vitro* into derivatives of the three embryonic germ layers as judged by cell morphology and specific immunostaining (Fig. 4e). These results show that p53 activity limits reprogramming of both mouse and human cells.

Oct4, Sox2 and Nanog interact with each other to enable the genome-wide chromatin remodelling required for induction of pluripotency. None of these factors are expressed at detectable levels in somatic cells. Previous work showed that p53 represses Nanog in response to DNA damage in ES cells²⁴, raising the possibility that p53 might prevent Nanog expression in MEFs. However, we observed that *Nanog* mRNA was not expressed at detectable levels in either p53 wild-type or p53-null MEFs (Supplementary Fig. 11a and data not shown). On the other hand, the oncogene Klf4 has been reported to induce Nanog²⁵. It is possible that in the absence of Klf4 in two-factor iPS cells, p53 elimination allowed Oct4 and Sox2 to remodel the chromatin to a threshold required for expression of sufficient Nanog to drive the subsequent events involved in iPS cell generation.

Our data show that reprogramming somatic cells to iPS cells is associated with activation of the p53 pathway, which acts as a barrier to reprogramming. The mechanisms by which p53 antagonizes reprogramming seem to involve both its ability to limit cell cycling by induction of the cyclin-dependent kinase inhibitor p21 and its ability to induce apoptosis. This suggests that direct chemical inhibition of the apoptotic cascade may provide a useful tool for enhancing reprogramming efficiency without direct genetic manipulation of tumour suppressors. We also show that reprogramming in the absence of oncogenes such as c-Myc and Klf4 will require inactivating the p53 and Rb tumour suppressors. Although p53 pathway inactivation will be key, this cannot be done on a permanent basis, as this would increase the probability of malignant transformation and the generation of unstable genomes that would mitigate their use for understanding many diseases. Rather, transient inhibition using chemical antagonists or reversible approaches that avoid genetic disruption will be required^{12,26}. As Oct4 and Sox2 are oncogenic when overexpressed, using small molecules or proteins to transiently mimic their reprogramming functions^{27–29} may enable oncogene-free iPS cells to be obtained at acceptable frequencies. The mechanistic insights we provide (Supplementary Fig. 27) should shorten the road to developing clinically useful iPS cells.

METHODS SUMMARY

MEFs were isolated from embryonic day (E) 13.5 embryos obtained from wild-type, p53-deficient, or Mdmx-mutant mice. Retroviral and lentiviral viruses were produced in HEK293 cells, and 12 to 14 days after infection MEFs were fixed for immunofluorescence. Reprogramming of HEFs (IMR90) and keratinocytes was done as previously described^{2,3,6}. Around two to three weeks after infection, cells were fixed for immunofluorescence studies. As for two-factor iPS cell formation, after a minimum of 4 weeks, colonies derived from infected MEFs or IMR90 cells were fixed for immunostaining or picked up for clonal expansion. Protein, mRNA, promoter methylation, microarray and immunofluorescence analyses were performed by standard methods³⁰. *In vitro* differentiation of mouse iPS cells was established by the hanging-drop method, whereas human iPS cells were differentiated by suspension culture. Teratomas were induced by

injecting iPS cells subcutaneously and into the testicles, and analysed three to four weeks after injection. Chimaeric mice were obtained by injecting iPS cells into C57BL/6J hosts. High-contribution chimaeras were mated to C57BL/6J mice to test for germline transmission.

Full Methods and any associated references are available in the online version of the paper at www.nature.com/nature.

Received 6 March; accepted 23 July 2009.

Published online 9 August 2009.

1. Takahashi, K. & Yamanaka, S. Induction of pluripotent stem cells from mouse embryonic and adult fibroblast cultures by defined factors. *Cell* **126**, 663–676 (2006).
2. Takahashi, K. *et al.* Induction of pluripotent stem cells from adult human fibroblasts by defined factors. *Cell* **131**, 861–872 (2007).
3. Yu, J. *et al.* Induced pluripotent stem cell lines derived from human somatic cells. *Science* **318**, 1917–1920 (2007).
4. Park, I. H. *et al.* Reprogramming of human somatic cells to pluripotency with defined factors. *Nature* **451**, 141–146 (2008).
5. Lowry, W. E. *et al.* Generation of human induced pluripotent stem cells from dermal fibroblasts. *Proc. Natl Acad. Sci. USA* **105**, 2883–2888 (2008).
6. Aasen, T. *et al.* Efficient and rapid generation of induced pluripotent stem cells from human keratinocytes. *Nature Biotechnol.* **26**, 1276–1284 (2008).
7. Nakagawa, M. *et al.* Generation of induced pluripotent stem cells without Myc from mouse and human fibroblasts. *Nature Biotechnol.* **26**, 101–106 (2008).
8. Wernig, M., Meissner, A., Cassady, J. P. & Jaenisch, R. c-Myc is dispensable for direct reprogramming of mouse fibroblasts. *Cell Stem Cell* **2**, 10–12 (2008).
9. Okita, K., Ichisaka, T. & Yamanaka, S. Generation of germline-competent induced pluripotent stem cells. *Nature* **448**, 313–317 (2007).
10. Rowland, B. D., Bernards, R. & Peeper, D. S. The KLF4 tumour suppressor is a transcriptional repressor of p53 that acts as a context-dependent oncogene. *Nature Cell Biol.* **7**, 1074–1082 (2005).
11. Kanatsu-Shinohara, M. *et al.* Generation of pluripotent stem cells from neonatal mouse testis. *Cell* **119**, 1001–1012 (2004).
12. Zhao, Y. *et al.* Two supporting factors greatly improve the efficiency of human iPSC generation. *Cell Stem Cell* **3**, 475–479 (2008).
13. Cleveland, J. L. & Sherr, C. J. Antagonism of Myc functions by Arf. *Cancer Cell* **6**, 309–311 (2004).
14. Vassilev, L. T. *et al.* In vivo activation of the p53 pathway by small-molecule antagonists of MDM2. *Science* **303**, 844–848 (2004).
15. Miyashita, T. & Reed, J. C. Tumor suppressor p53 is a direct transcriptional activator of the human *bax* gene. *Cell* **80**, 293–299 (1995).
16. Kamijo, T. *et al.* Functional and physical interactions of the ARF tumor suppressor with p53 and Mdm2. *Proc. Natl Acad. Sci. USA* **95**, 8292–8297 (1998).
17. Pomerantz, J. *et al.* The *Ink4a* tumor suppressor gene product, p19^{Arf}, interacts with MDM2 and neutralizes MDM2's inhibition of p53. *Cell* **92**, 713–723 (1998).
18. Zhang, Y., Xiong, Y. & Yarbrough, W. G. ARF promotes MDM2 degradation and stabilizes p53: ARF-*INK4a* locus deletion impairs both the Rb and p53 tumor suppression pathways. *Cell* **92**, 725–734 (1998).
19. Knudsen, E. S. & Knudsen, K. E. Tailoring to RB: tumour suppressor status and therapeutic response. *Nature Rev. Cancer* **8**, 714–724 (2008).
20. Marine, J. C., Dyer, M. A. & Jochemsen, A. G. MDMX: from bench to bedside. *J. Cell Sci.* **120**, 371–378 (2007).
21. Wang, Y. V. *et al.* Increased radioresistance and accelerated B cell lymphomas in mice with Mdmx mutations that prevent modifications by DNA-damage-activated kinases. *Cancer Cell* **16**, 33–43 (2009).
22. Foster, K. W. *et al.* Oncogene expression cloning by retroviral transduction of adenovirus E1A-immortalized rat kidney RK3E cells: transformation of a host with epithelial features by c-MYC and the zinc finger protein GKLf. *Cell Growth Differ.* **10**, 423–434 (1999).
23. Shaulian, E., Zauberman, A., Ginsberg, D. & Oren, M. Identification of a minimal transforming domain of p53: negative dominance through abrogation of sequence-specific DNA binding. *Mol. Cell. Biol.* **12**, 5581–5592 (1992).
24. Lin, T. *et al.* p53 induces differentiation of mouse embryonic stem cells by suppressing *Nanog* expression. *Nature Cell Biol.* **7**, 165–171 (2005).
25. Jiang, J. *et al.* A core Klf circuitry regulates self-renewal of embryonic stem cells. *Nature Cell Biol.* **10**, 353–360 (2008).
26. Komarov, P. G. *et al.* A chemical inhibitor of p53 that protects mice from the side effects of cancer therapy. *Science* **285**, 1733–1737 (1999).
27. Shi, Y. *et al.* Induction of pluripotent stem cells from mouse embryonic fibroblasts by Oct4 and Klf4 with small-molecule compounds. *Cell Stem Cell* **3**, 568–574 (2008).
28. Huangfu, D. *et al.* Induction of pluripotent stem cells from primary human fibroblasts with only Oct4 and Sox2. *Nature Biotechnol.* **26**, 1269–1275 (2008).
29. Kim, D. *et al.* Generation of human induced pluripotent stem cells by direct delivery of reprogramming proteins. *Cell Stem Cell* **4**, 472–476 (2009).
30. Gonzalez, F. *et al.* Generation of mouse-induced pluripotent stem cells by transient expression of a single nonviral polycistronic vector. *Proc. Natl Acad. Sci. USA* **106**, 8918–8922 (2009).

Supplementary Information is linked to the online version of the paper at www.nature.com/nature.

Acknowledgements We are grateful to the CMRB Histology & Bioimaging and Cell culture Platforms for assistance, S. Boue for microarray analysis, S. Kim for help with maintenance of mouse colonies, Y. Richaud for technical assistance, M. Nagao for preparation of mouse neural stem cells, K. Brennand and F. Gage for preparation of human neural stem cells, I. Verma and A. Consiglio for advice and help with lentiviral transduction, Y. Dayn for chimaeric mouse production, and all members of the Gene Expression Laboratory and CMRB for discussions and M. Serrano for sharing unpublished results. J.S. was partially supported by Astellas Pharma Inc. T.K. was partially supported by Japan Society for the Promotion of Science. Work in the laboratory of G.M.W. was supported by NIH grants (5 R01 CA061449 and CA100845). Work in the laboratory of J.C.I.B. was supported by grants from the NIH, Tercel, Marato, G. Harold and Leila Y. Mathers Charitable Foundation and Fundacion Cellex.

Author Contributions T.K. and J.S. contributed to the experimental work, project planning, data analysis and writing the manuscript and contributed equally to this work. Y.V.W. contributed to the experimental work, data analysis, writing the manuscript and established Mdmx mutant mice. S.M., L.B.M. and A.R. contributed to the experimental work, data analysis and writing the manuscript. G.M.W. and J.C.I.B. contributed to project planning and writing the manuscript, and supervised all the work. G.M.W. and J.C.I.B. are co-contributing corresponding authors.

Author Information Reprints and permissions information is available at www.nature.com/reprints. Correspondence and requests for materials should be addressed to J.C.I.B. (belmonte@salk.edu) or G.M.W. (wahl@salk.edu).

METHODS

Reagents. Reagents were obtained from the following sources: Nutlin-3a (Cayman Chemical); anti-Oct-3/4 (sc-5279), anti-GKLF (sc-20691), anti-p53 (sc-6243), anti-p21 (sc-53870), anti-p16^{Ink4a} (sc-1207), anti-c-Myc (sc-764) and anti-Gata4 (sc-9053) (Santa Cruz Biotechnology); anti-Sox2 (AB5603) (Chemicon); anti-p53 antibody (1C12), anti-phospho-Histone H2A.X (Ser139) antibody (20E3) (Cell Signaling); anti-p19^{Arf} (ab80) and anti-Nanog (ab21603) (Abcam); anti-Nanog (SC1000) and anti-p53 (DO-1) (Calbiochem); anti-Tuj1 antibody (MMS-435P-0) (Covance); anti- α -tubulin (T5168), anti- α -actinin sarcomeric (A7811), anti- α -actin sarcomeric (A2172), anti-actin (A2066) and anti-chondroitin (C8035) (Sigma); anti-Foxa2 antibody (AF2400) (R&D systems); anti-alpha-1-fetoprotein (A008) and anti-GFAP (Z0334) (Dako); anti-TRA-1-81 antibody (Millipore).

Mice. Wild-type MEFs used for iPS cell production were derived from embryos obtained by mating BDF1/ICR and ICR strains. p53-knockout mice were purchased from Taconic Farms, Inc. p53^{-/-} MEFs were obtained by heterozygous versus heterozygous mating. For genotyping, PCR primers are available on the company website. Mdmx-mutant mice were generated from ES cells of 129Sv origin by homologous recombination²¹.

Plasmids. Mouse p53 and GFP complementary DNAs were cloned into pMXs retroviral vectors³¹. The cDNA of mouse Bcl2 was cloned into HIV pBOBI lentiviral vector³². Human p53DD (a gift from M. Oren) is in pLXSN (Clontech). The cDNAs of mouse p53 and p21, pMXs-Oct4, -Sox2, -Klf4 and -c-Myc were purchased from Addgene^{1,33,34}. Human pMSCV-Oct4, -Sox2, -Klf4 and -c-Myc were constructed as previously described⁶. The shRNA sequences against p53, p21, Arf and Ink4a were inserted into pLVTHM lentiviral vectors³⁶. Sequences for shRNA are shown in Supplementary Table 3.

Production of retroviruses and lentiviruses and iPS cell formation. VSV-G viruses were produced in HEK293T cells. For pMX-based and pMSCV-based retroviruses, vectors were transfected using CaPO₄ or lipofectamine, following the manufacturers' directions. One day after transfection, culture medium was changed to new medium. For lentivirus, pBOBI-based³² or pLVTHM-based³⁶ vectors were transfected by Lipofectamine 2000 (Invitrogen) according to the manufacturer's protocol. Six hours after transfection, the DNA-lipofectamine complex was removed and the medium was replaced the next day. Two days after transfection, the supernatant containing viruses was collected and filtered through a 0.45- μ m filter. Mouse iPS cells were induced as previously described^{35,37}. In brief, MEFs (passage 3–5) were infected (day 0) with pMX-based retroviruses together with pLVTHM-based lentivirus for shRNAs or pBOBI-based lentivirus for Bcl2. On day 2, cells were passed onto new gelatin-coated plates. Medium was changed every 2 days. On days 12 to 14, cells were fixed for immunofluorescence study. For the Nutlin-3a experiments, cells were treated starting from day 4. Reprogramming of HEFs (IMR90) was done as previously described^{2,3}. In brief, IMR90 fibroblasts (passage 7–9) were infected (day 0) with pMSCV-based retroviruses plus pLVTHM-based lentiviruses for p53 shRNA. On day 4 or 5, cells were passed onto feeder MEFs. Medium was changed every other day. Around 3 weeks after infection, cells were fixed for immunofluorescence studies. Reprogramming of human primary keratinocytes was carried out essentially as described⁶. Cells were co-infected with retroviral supernatants containing 3 or 4 reprogramming factors and p53DD or GFP at a 1:2 ratio. To assess the reprogramming efficiency, cells were trypsinized 3 days after retroviral infection and 10⁴ cells were plated onto 6-cm tissue culture dishes on top of irradiated human foreskin fibroblasts with human ES cell medium. After 2 weeks, the dishes were stained for alkaline phosphatase activity and colonies that displayed strong staining and showed human ES-cell-like

morphology were scored positive. As for two-factor iPS cell formation, MEFs or IMR90 cells were co-infected with retroviral supernatants containing two factors (Oct4 and Sox2) and lentivirus supernatants (p53 shRNA) at a 1:1:3 ratio. Infected cells were passed onto new gelatin-coated plates at day 2 (MEFs) or onto feeder MEFs at day 5 (IMR90). Medium was changed every other day, and after a minimum of 4 weeks, colonies were fixed for immunostaining or picked up for clonal expansion.

Protein and mRNA analysis. Cells were washed once in PBS and lysed in 2 \times SDS-PAGE sample buffer without 2-mercaptoethanol and glycerol. Lysates were briefly sonicated and cleared by centrifugation. The protein concentration was determined by a BCA Protein Assay Kit (Thermo Scientific). Lysates were then mixed with 2-mercaptoethanol, bromophenol blue and glycerol, and boiled. Equal amounts of proteins were subjected to SDS-PAGE. Total RNA was isolated using Trizol (Invitrogen) followed by cDNA synthesis using Superscript II Reverse Transcriptase (Invitrogen). Quantitative PCR was performed using SYBR Green PCR Master Mix (Applied Biosystems). Primer sequences are available on request.

Promoter methylation analysis. Genomic DNA was isolated and bisulphite modification performed using the EZ DNA Methylation-Direct Kit (Zymo Research). The promoter regions of *Nanog* and *Oct4* were amplified by nested PCR using primer sets previously described³⁸. The amplified PCR products were ligated into pCRII-TOPO (Invitrogen) and sequenced. Data was analysed using Lasergene (Dnastar).

In vitro and in vivo differentiation. For *in vitro* differentiation of mouse iPS cells, after dissociation with trypsin/EDTA, cells were cultured in suspension by the hanging-drop method. For *in vivo* differentiation, cells were trypsinized, and injected subcutaneously into severe combined immunodeficient (SCID) mice. After 3 weeks, teratomas were dissected, fixed and analysed. Detailed methods for *in vitro* differentiation, teratoma formation and immunostaining are described in Supplementary Methods. *In vitro* differentiation of HEF-derived human iPS cells was induced by culturing cells in suspension and then transferring onto gelatine-coated dishes. *In vitro* differentiation of keratinocytes-derived human iPS cells was carried out as previously described⁶.

Blastocyst injections for chimaeric mice. iPS cells were injected into C57BL/6J hosts blastocysts and transferred into 2.5 days post-coitum ICR pseudopregnant recipient females. Chimaerism was ascertained after birth by the appearance of agouti coat colour (from iPS cells) in black host pups. High-contribution chimaeras were mated to C57BL/6J mice to test for germline transmission.

31. Kitamura, T. *et al.* Retrovirus-mediated gene transfer and expression cloning: powerful tools in functional genomics. *Exp. Hematol.* **31**, 1007–1014 (2003).
32. Miyoshi, H., Blömer, U., Takahashi, M., Gage, F. H. & Verma, I. M. Development of a self-inactivating lentivirus vector. *J. Virol.* **72**, 8150–8157 (1998).
33. Sherley, J. L. Guanine nucleotide biosynthesis is regulated by the cellular p53 concentration. *J. Biol. Chem.* **266**, 24815–24828 (1991).
34. Huppi, K. *et al.* Molecular cloning, sequencing, chromosomal localization and expression of mouse p21 (Waf1). *Oncogene* **9**, 3017–3020 (1994).
35. Takahashi, K., Okita, K., Nakagawa, M. & Yamanaka, S. Induction of pluripotent stem cells from fibroblast cultures. *Nature Protocols* **2**, 3081–3089 (2007).
36. Wiznerowicz, M. & Trono, D. Conditional suppression of cellular genes: lentivirus vector-mediated drug-inducible RNA interference. *J. Virol.* **77**, 8957–8961 (2003).
37. Blelloch, R., Venere, M., Yen, J. & Ramalho-Santos, M. Generation of induced pluripotent stem cells in the absence of drug selection. *Cell Stem Cell* **1**, 245–247 (2007).
38. Blelloch, R. *et al.* Reprogramming efficiency following somatic cell nuclear transfer is influenced by the differentiation and methylation state of the donor nucleus. *Stem Cells* **24**, 2007–2013 (2006).

Immortalization eliminates a roadblock during cellular reprogramming into iPS cells

Jochen Utikal^{1,2,3*}, Jose M. Polo^{1,2*}, Matthias Stadtfeld^{1,2}, Nimet Maherali^{1,2,4}, Warakorn Kulalert^{1,2}, Ryan M. Walsh^{1,2}, Adam Khalil^{1,2}, James G. Rheinwald⁵ & Konrad Hochedlinger^{1,2}

The overexpression of defined transcription factors in somatic cells results in their reprogramming into induced pluripotent stem (iPS) cells^{1–3}. The extremely low efficiency and slow kinetics of *in vitro* reprogramming suggest that further rare events are required to generate iPS cells. The nature and identity of these events, however, remain elusive. We noticed that the reprogramming potential of primary murine fibroblasts into iPS cells decreases after serial passaging and the concomitant onset of senescence. Consistent with the notion that loss of replicative potential provides a barrier for reprogramming, here we show that cells with low endogenous p19^{Arf} (encoded by the *Ink4a/Arf* locus, also known as *Cdkn2a* locus) protein levels and immortal fibroblasts deficient in components of the *Arf–Trp53* pathway yield iPS cell colonies with up to threefold faster kinetics and at a significantly higher efficiency than wild-type cells, endowing almost every somatic cell with the potential to form iPS cells. Notably, the acute genetic ablation of *Trp53* (also known as *p53*) in cellular subpopulations that normally fail to reprogram rescues their ability to produce iPS cells. Our results show that the acquisition of immortality is a crucial and rate-limiting step towards the establishment of a pluripotent state in somatic cells and underscore the similarities between induced pluripotency and tumorigenesis.

The possibility to generate patient-specific pluripotent cells may enable the study and treatment of several degenerative diseases and therefore has enormous therapeutic potential. A major limitation of inducing pluripotency, however, is its low efficiency, which ranges between 0.01% and 0.2% when using direct viral infection of adult cells with vectors expressing the four reprogramming factors—Oct4 (also known as Pou5f1), Sox2, Klf4 and c-Myc^{2,4–6}—and reaches up to ~5% when using optimized ‘secondary systems’^{7–9}. Secondary systems are based on somatic cells that already carry all four reprogramming transgenes in their genome under the control of doxycycline-inducible elements, thus enabling homogeneous factor expression (Supplementary Fig. 1). The low efficiency of reprogramming secondary cells suggests that other molecular events are required that restrict the conversion of somatic cells into iPS cells¹. Identifying these restrictions is critical for understanding the mechanisms of induced pluripotency as well as for its potential clinical applications.

We noticed that secondary murine embryonic fibroblasts (MEFs) at early passages generate iPS cells more efficiently than MEFs at later passages, consistent with the notion that a high replicative potential of somatic cells is critical for successful reprogramming into iPS cells (Fig. 1a, top row). The accumulation of β -galactosidase-positive senescent cells in late passage cultures further suggests that molecular

changes associated with cellular senescence provide a roadblock for the conversion of somatic cells into iPS cells (Fig. 1a, bottom row). The loss of replicative potential is often the consequence of culture-induced upregulation of the cell-cycle-dependent kinase inhibitors p16^{Ink4a}, p19^{Arf} (which are encoded by alternative reading frames of the *Ink4a/Arf* locus), p21^{Cip1} (*Cdkn1a*), as well as activation of *Trp53* (ref. 10). Indeed, we observed a progressive upregulation of *Ink4a*,

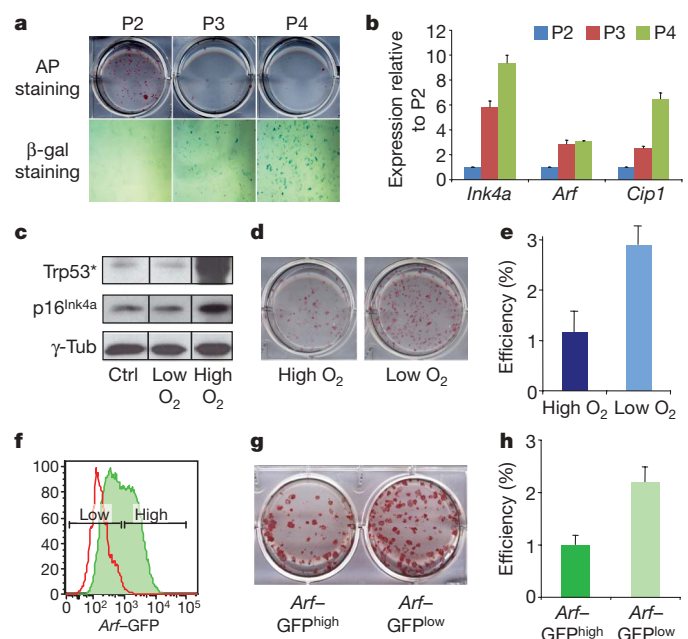


Figure 1 | Reprogramming efficiency of fibroblasts is influenced by replicative potential and *Arf* expression status. **a**, Alkaline phosphatase (AP) staining (top) of iPS cell colonies derived from secondary murine embryonic fibroblasts (MEFs) at different passages (P). Senescence associated β -galactosidase activity (bottom) of MEFs at the same passages. Original magnification, $\times 200$. **b**, Expression levels of *Ink4a*, *Arf* and *Cip1* in MEFs at the same passages as shown in **a** ($n = 2$). **c**, Western blot analysis of p16^{Ink4a} and phosphorylated-Trp53 (Trp53*) in MEFs grown at low (4%) or high (21%) oxygen for 6 days. Ctrl, control MEFs at day 1. **d**, **e**, Secondary MEFs grown under low O₂ give rise to iPS cells more efficiently ($n = 3$). **f**, *Arf*-GFP reporter MEFs (green line) at passage 3 show heterogeneous expression levels. Shown in red are wild-type MEFs. **g**, **h**, *Arf*-GFP^{low} MEFs give rise to iPS cell colonies more efficiently than *Arf*-GFP^{high} cells ($n = 2$). See Methods for details on measuring efficiencies. All error bars depict the s.e.m.

¹Massachusetts General Hospital Cancer Center and Center for Regenerative Medicine, Harvard Stem Cell Institute, 185 Cambridge Street, Boston, Massachusetts 02114, USA.

²Department of Stem Cell and Regenerative Biology, Harvard University, Cambridge, Massachusetts 02138, USA. ³Department of Dermatology, Venerology and Allergology, University Medical Center Mannheim, Ruprecht-Karl-University of Heidelberg, Theodor-Kutzer-Ufer 1-3, 68135 Mannheim, Germany. ⁴Department of Molecular and Cellular Biology, Harvard University, 7 Divinity Avenue, Cambridge, Massachusetts 02138, USA. ⁵Department of Dermatology, Brigham and Women's Hospital and Harvard Skin Disease Research Center, 77 Avenue Louis Pasteur, Boston, Massachusetts 02115, USA.

*These authors contributed equally to this work.

Arf and *Cip1* transcript levels in serially passaged MEFs (Fig. 1b). Growth of MEFs in low oxygen (4%) can counteract culture-induced upregulation of p16^{Ink4a}, p19^{Arf} and activation of Trp53, thereby extending replicative lifespan (Fig. 1c)¹¹. We detected a threefold increase in reprogramming efficiency in secondary MEFs cultured in low oxygen (Fig. 1d, e), in agreement with the notion that p16^{Ink4a} and activated Trp53 inhibit reprogramming.

To test directly whether the expression status of the *Ink4a/Arf* locus in the starting cell population has an influence on reprogramming, we analysed cells derived from an *Arf*-green fluorescent protein (GFP) knock-in reporter mouse¹². *Arf*-GFP MEFs at passage 3 contained a population of *Arf*-GFP^{high} and *Arf*-GFP^{low} cells, consistent with previous observations¹² (Fig. 1f). Interestingly, fluorescence-activated cell sorting (FACS)-purified *Arf*-GFP^{low} MEFs yielded iPS cell colonies twice as efficiently as *Arf*-GFP^{high} MEFs, indicating that reduced *Arf* levels in the starting cell population are beneficial for reprogramming (Fig. 1g, h).

Notably, *Arf*-GFP expression was undetectable and endogenous *Ink4a* and *Arf* transcript levels were downregulated in established iPS cells (Fig. 2a and Supplementary Fig. 2a), further indicating that inactivation of this key senescence pathway by the reprogramming factors may be critical for the acquisition of pluripotency. In agreement, expression of the four reprogramming factors for 6 days resulted in efficient downregulation of the *Arf*-GFP allele (Fig. 2a). However, no single reprogramming factor alone was sufficient to silence *Arf*-GFP expression (Fig. 2a), suggesting that the synergistic action of at least two of the factors is required to inhibit *Arf* transcription.

To examine how silencing of the *Ink4a/Arf* locus correlates with other markers that change during reprogramming, we followed the expression of *Arf*-GFP in intermediate cell populations previously identified by surface markers^{13,14}. Notably, *Arf* expression was downregulated specifically in the Thy1⁺ and SSEA1⁺ fractions, which are enriched for cells poised to become iPS cells, but not in the Thy1⁺

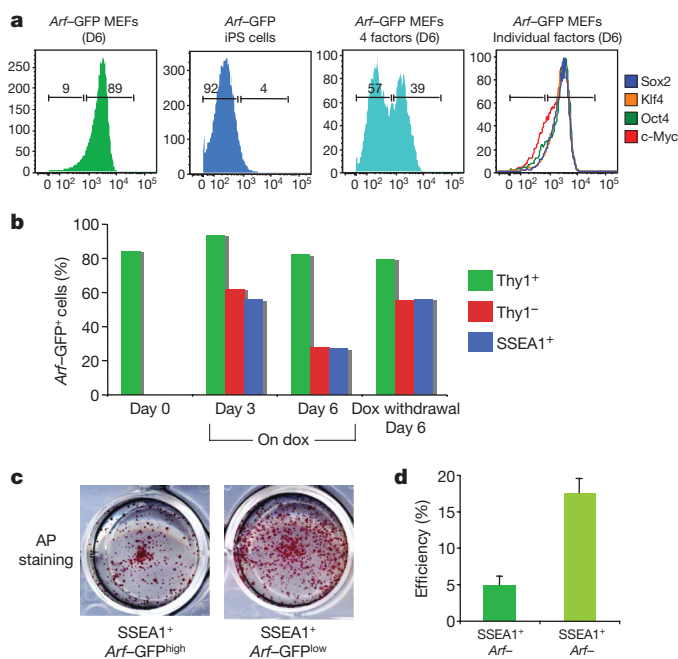


Figure 2 | Transcription-factor-induced downregulation of *Ink4a/Arf* expression in cells undergoing reprogramming. **a**, FACS plots of sorted *Arf*-GFP^{high} MEFs (left), established iPS cells from *Arf*-GFP MEFs (left middle), *Arf*-GFP^{high} MEFs expressing all four reprogramming factors (right middle) or each factor individually (right). Cells withdrawn from doxycycline (dox) on day 6 were analysed 3 days later. D6, day 6. **b**, Time course of *Arf*-GFP expression in subpopulations of cells undergoing reprogramming. **c**, **d**, *Arf*-GFP^{low} SSEA1⁺ cells at 6 days of transgene expression give rise to more transgene-independent alkaline phosphatase (AP)⁺ iPS cell colonies than *Arf*-GFP^{high} SSEA1⁺ cells ($n = 3$). Error bars depict the s.e.m.

fraction, which fails to give rise to iPS cells (Fig. 2b). *Ink4a* RNA and protein levels followed a similar trend as the *Arf*-GFP expression during reprogramming (Supplementary Fig. 3). Of note, SSEA1⁺ *Arf*-GFP^{low} cells had a threefold higher reprogramming potential than SSEA1⁺ *Arf*-GFP^{high} cells, indicating that low *Arf* expression is a useful prospective marker to further enrich for intermediate cells poised to become iPS cells (Fig. 2c, d). Together, these results show that downregulation of the *Ink4a/Arf* locus correlates well with, and further refines previously identified subpopulations of cells undergoing reprogramming.

Using a published PCR-based assay¹⁵, we found that iPS cells and ES cells, in contrast to MEFs, show *Ink4a/Arf* promoter methylation, consistent with stable transcriptional silencing of *Ink4a/Arf* in pluripotent cells (Supplementary Fig. 2b). However, the downregulation of *Arf*-GFP expression at day 6 of reprogramming as seen by FACS (Fig. 2b) was not yet accompanied by detectable promoter methylation, suggesting that stable silencing of the *Ink4a/Arf* locus is a late event during reprogramming that requires further molecular changes. In agreement with a transient decrease in *Arf* expression, the withdrawal of doxycycline from day 6 cultures resulted in the rapid re-appearance of *Arf*-GFP expression and the failure to recover stable iPS cell colonies (Fig. 2b and data not shown). Promoter methylation first became detectable at day 9 of reprogramming in the SSEA1⁺ fraction (Supplementary Fig. 2b), which contains most stably reprogrammed cells¹³. This observation indicates that the stable silencing of the *Ink4a/Arf* locus is achieved by epigenetic modifications and occurs specifically in late intermediate cells that are poised to become iPS cells.

Because genetic deletion of the entire *Ink4a/Arf* locus in fibroblasts results in their immortalization¹⁶, we wondered whether immortalized somatic cells are more amenable to reprogramming than primary cells. We first assessed the reprogramming potential of a spontaneously immortalized melanocyte line¹⁷ (designated 'Melan A'). Melan A cells gave rise to iPS cells four times more efficiently than primary melanocytes, yielding efficiencies close to 1% (Fig. 3a and Supplementary Fig. 4a–d). Injection of these iPS cells into severe combined immunodeficient (SCID) mice gave rise to well-differentiated teratomas, and introduction into blastocysts yielded chimaeric mice that showed contribution to different tissues (Fig. 3b, c and Supplementary Fig. 4e). These results document that an established cell line remains permissive for reprogramming into a pluripotent state. Spontaneous immortalization of cultured cells is usually accompanied by mutations of components of the *Arf*-*Trp53* pathway¹⁸. Indeed, western blot analysis showed the absence of p16^{Ink4a} protein in Melan A cells (Supplementary Fig. 4f) even though sequence analysis of the *Ink4a* and *Arf* exons did not reveal any mutations (data not shown).

To assess more accurately reprogramming frequencies of immortalized versus primary melanocytes, we established secondary cells by *in vitro* differentiation of iPS cells^{7,8} (Supplementary Figs 1 and 5a). Secondary cells obtained from primary melanocytes converted into iPS cells at an average efficiency of 1.5%, consistent with previous observations^{7–9,19} (Fig. 3d, clones 1–3). Remarkably, however, Melan A-derived secondary cells gave rise to iPS cells at efficiencies of up to ~65%, indicating that immortalization endows almost two in three cells with the potential to form iPS cells (Fig. 3d, clones 57–61 and Supplementary Fig. 5b). Moreover, single-cell sorting of one subclone (clone 59.3) generated iPS cells at 100% efficiency, demonstrating that most, if not all, of the cells are endowed with the potential to give rise to pluripotent colonies (Fig. 3e). Secondary MEFs obtained from Melan A-iPS cells at embryonic day (E) 14.5 gave rise to iPS cell colonies at an efficiency of ~40%, which is comparable to *in vitro*-derived secondary cells (Fig. 3d, clones M4 and M7).

We next tested whether deletion of *Trp53* or *Ink4a/Arf* in fibroblasts mimics the phenotype of spontaneously immortalized cells. Indeed, we observed a 30–40-fold increase in the number of iPS cell colonies in *Trp53*, compound *Ink4a/Arf* and single *Arf* mutant cells compared with wild-type control cells, demonstrating that inactivation of these pathways is probably responsible for the increased reprogramming efficiencies of spontaneously immortalized cells (Fig. 3f,

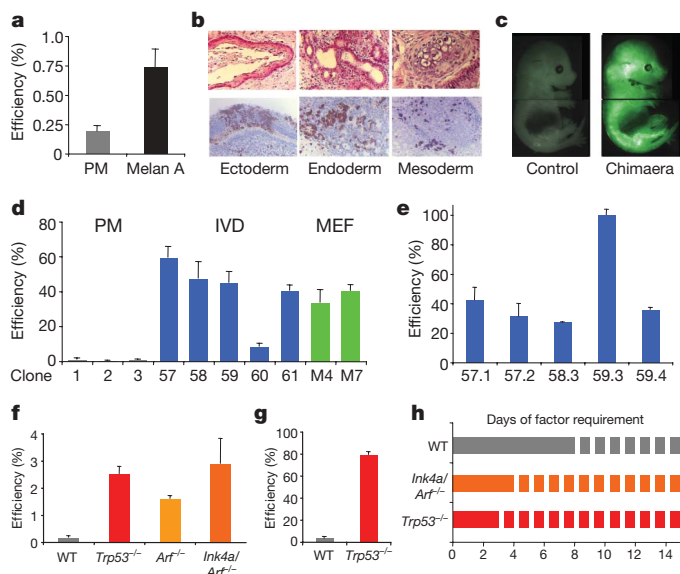


Figure 3 | Cellular immortalization enhances reprogramming potential and kinetics. **a**, The spontaneously immortalized Melan A cell line yields iPS colonies 3–4 times more efficiently than primary melanocytes (PM) after direct viral infection ($n = 3$). **b, c**, Melan A-derived iPS cells show differentiation into ectodermal, mesodermal and endodermal derivatives in teratomas (**b**, top) and in chimaeras produced from iPS cells labelled with a lentivirus constitutively expressing GFP (**b**, bottom, and **c**). Original magnification, $\times 400$. **d**, iPS cell formation efficiency of secondary cells derived from primary melanocytes (grey bars), Melan A-derived *in vitro*-differentiated (IVD) cells (blue bars) or Melan A-derived MEFs (green bars) ($n = 3$). **e**, iPS cell formation efficiency of subclones of Melan A-derived IVD secondary cells ($n = 3$). **f**, Reprogramming efficiency of wild-type (WT), *Trp53*^{-/-}, *Arf*^{-/-} and *Ink4a/Arf*^{-/-} MEFs after direct viral infection ($n = 3$). **g**, Reprogramming potential of secondary *Trp53*^{-/-} iPS cell-derived E14.5 MEFs ($n = 2$). **h**, Evaluation of minimal temporal transgene requirement (solid lines) in wild-type, *Ink4a/Arf*^{-/-} and *Trp53*^{-/-} MEFs to form stable iPS cell colonies. All error bars depict s.e.m.

Supplementary Fig. 6 and Supplementary Table 1). Moreover, *Trp53*^{-/-} iPS-cell-derived E14.5 secondary MEFs gave rise to iPS cell colonies at an efficiency of $\sim 80\%$, similar to results obtained with spontaneously immortalized cells (Fig. 3g). Collectively, these observations provide strong functional evidence that the inactivation of key pathways controlling replicative potential and senescence substantially enhance the reprogramming potential of somatic cells into iPS cells.

To exclude the possibility that an altered growth rate of immortal cells rather than their long-term proliferation potential influences their increased reprogramming potential, we compared the iPS cell formation efficiencies of *Trp53*^{-/-} and wild-type MEFs grown under low (0.5% FBS) and high (15% FBS) serum conditions. *Trp53*-deficient MEFs cultured in low serum exhibited a significantly reduced growth rate compared with MEFs cultured in high serum (Supplementary Fig. 7a). Despite this growth disadvantage, *Trp53*-mutant cells gave rise to iPS cells more efficiently than wild-type MEFs, suggesting that the long-term proliferation potential of immortal cells is responsible for their enhanced reprogramming potential (Supplementary Fig. 7b, c). Given that the acquisition of immortality by downregulation of *Arf* or *Trp53* seems to eliminate a roadblock during the reprogramming of somatic cells into iPS cells, inactivation of these pathways might also affect the kinetics of reprogramming. Indeed, although wild-type cells required 8 days of transgene expression to produce stable iPS cells, which is consistent with a previous report¹³, *Trp53* and *Ink4a/Arf* mutant cells gave rise to iPS cell colonies after only 3 and 4 days of transgene expression, respectively, demonstrating that the acquisition of cellular immortality is not only an efficiency-limiting but also a rate-limiting step during induced pluripotency (Fig. 3h).

Surprisingly, we failed to detect a correlation between the relative numbers of *Thy1*⁻ and *SSEA1*⁺ intermediate cells and

reprogramming efficiency in *Trp53*^{-/-} compared with wild-type cultures (Supplementary Fig. 8). This suggests that immortal cells undergoing reprogramming pass through the same roadblocks as control cells but that immortality endows those cells that otherwise fail to reprogram with the potential to form iPS cells. To test this hypothesis further, we plated FACS-purified *Thy1*⁺, *Thy1*⁻ and *SSEA1*⁺ cells isolated from wild-type or *Trp53*-deficient secondary cells on feeders in the presence or absence of doxycycline (Fig. 4a). In wild-type cells, iPS cells appeared predominantly from the *SSEA1*⁺ population at all time points and to a lesser degree from the *Thy1*⁻ and *Thy1*⁺ fractions in the continuous presence of doxycycline (Fig. 4a, left). However, when doxycycline was withdrawn after the sorting of these populations, only the *SSEA1*⁺ fraction at day 9 gave rise to stable iPS cells, consistent with previous observations^{13,14} (Fig. 4a, right). This result is in accordance with the earlier finding that the methylation of the *Ink4a/Arf* locus becomes detectable specifically in the *SSEA1*⁺ population in wild-type cells (Supplementary Fig. 2b). In contrast, *Trp53*-deficient secondary cells continuously treated with doxycycline gave rise to iPS cells at high efficiency and regardless of the *Thy1* and *SSEA1* expression status (Fig. 4a, left). Moreover, when doxycycline treatment was discontinued after sorting, iPS cell colonies emerged from *Thy1*⁺, *Thy1*⁻ and *SSEA1*⁺

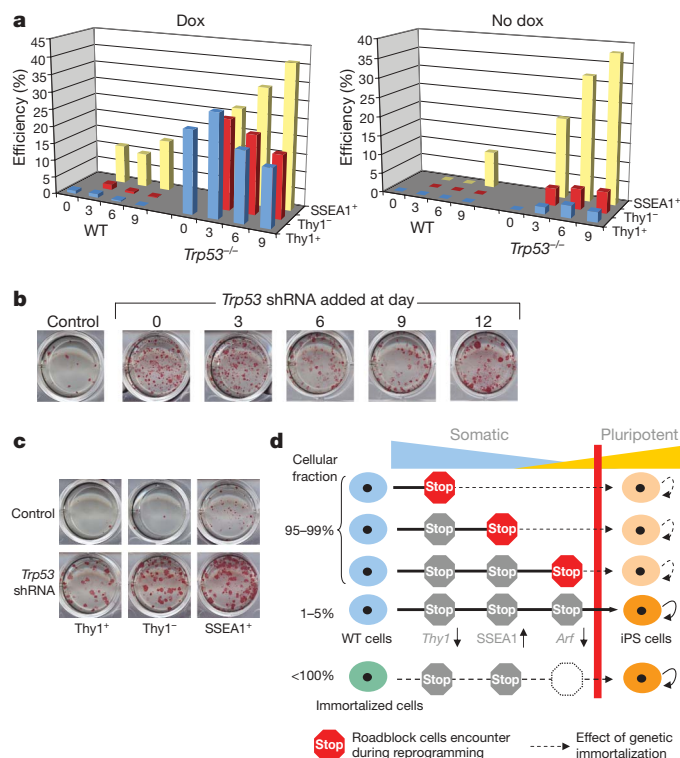


Figure 4 | *Trp53* deficiency rescues reprogramming potential in cells that normally fail to form iPS cells. **a**, Comparison of reprogramming potentials of sorted *Thy1*⁺, *Thy1*⁻ and *SSEA1*⁺ subpopulations in wild-type and *Trp53*^{-/-} cells at different time points (in days) during reprogramming in the presence or absence of doxycycline (dox). **b**, Acute inactivation of *Trp53* by lentivirus expressing *Trp53* shRNA in secondary cells increases reprogramming efficiency at all time points. **c**, Knockdown of *Trp53* by *Trp53* shRNA rescues the potential of *Thy1*⁻ and *Thy1*⁺ subpopulations to generate iPS cells. **d**, Model summarizing the presented data. During factor-induced reprogramming, cells encounter different roadblocks, such as the successful silencing of somatic genes (for example, *Thy1*), the activation of pluripotency genes (for example, *SSEA1*) and eventually the acquisition of immortality (for example, silencing of *Arf*). The low efficiency of the process is probably due to the capacity of rare cells to overcome these roadblocks. In immortal fibroblasts, however, almost every cell is endowed with the potential to produce iPS cells. Moreover, cells that have already encountered a roadblock can be rescued by acute inactivation of *Trp53* (indicated by dashed black lines). Red bar illustrates the transition point between the somatic (blue) and the pluripotent (yellow) state.

cells as early as 3 days after induction of transgenes. These findings confirm that reprogramming kinetics are up to three times faster in immortal cells than primary cells, and demonstrate that *Trp53* deficiency confers reprogramming potential to cells that normally fail to form iPS cells.

Because continuous *Trp53* deficiency in MEFs may select for genomic aberrations that favour reprogramming into iPS cells, we acutely inhibited *Trp53* expression by infecting secondary wild-type cells with a lentiviral construct expressing a short hairpin RNA (shRNA) against *Trp53* (*Trp53* shRNA)²⁰. We found that MEFs treated with *Trp53* shRNA at any time point during reprogramming gave rise to iPS cell colonies at higher efficiency than control cells (Fig. 4b). Furthermore, infection of Thy1^+ and Thy1^- cells with *Trp53* shRNA yielded iPS cells at similar efficiencies as the SSEA1⁺ population, demonstrating that the acute inactivation of *Trp53* is sufficient to confer the ability to undergo reprogramming on cells that would otherwise fail to form iPS cells (Fig. 4c). Likewise, the treatment of senescent cultures, which appear refractory to reprogramming, with *Trp53* shRNA rescued their ability to produce iPS cells (Supplementary Fig. 9). Notably, we demonstrate a continuous requirement for the absence of *Trp53* to elicit an enhanced effect on reprogramming using a Cre-reactivable allele of *Trp53* (Supplementary Fig. 10).

Furthermore, we sought to determine whether human immortalized cells are equally amenable to reprogramming as murine cells. To this end, we compared the reprogramming abilities of primary and TERT-immortalized human keratinocyte cell lines, which show comparable growth rates but obvious differences in their long-term proliferation potential²¹. Indeed, TERT-immortalized keratinocyte lines gave rise to iPS-cell-like colonies ~20 times more efficiently than early passage cultures of the primary keratinocyte line, from which they were derived (strain N)²¹, indicating that overcoming replicative senescence may be critical during the reprogramming of both murine and human somatic cells into iPS cells (Supplementary Fig. 11).

Our results indicate that the acquisition of immortality by epigenetic silencing of the *Ink4a/Arf* locus provides a bottleneck for the conversion of somatic cells into iPS cells, thus contributing to the low efficiency and delayed kinetics of *in vitro* reprogramming. After immortalization of fibroblasts, however, almost every somatic cell (or its clonal offspring) is endowed with the potential to generate iPS cells (Fig. 4d). Our findings are consistent with previous reports showing a more subtle effect of genetically interfering with immortalization pathways on iPS cell formation efficiency in human cells^{22,23}. Because *Trp53* and *p19^{Arf}* are guardians of chromosomal stability, however, their manipulation in a therapeutic setting should be approached with caution. Primary cell populations with low endogenous levels of active *Trp53* or *p16^{Ink4a}* and *p19^{Arf}* (refs 24–26) or cells with a high endogenous proliferative potential, such as somatic stem and progenitor cells²⁷, might provide an alternative and safer source for producing iPS cells at high efficiency.

METHODS SUMMARY

To generate iPS cells, primary and immortalized cell populations were infected with lentiviral vectors expressing Oct4, Sox2, Klf4 and c-Myc from a polycistronic construct under the control of a doxycycline-inducible promoter, together with a lentivirus constitutively expressing the M2 reverse tetracycline transactivator (M2-rtTA). Secondary cells were derived either by *in vitro* differentiation of iPS cells or after blastocyst injection and isolation of fibroblasts from chimaeras. The developmental potential of iPS cells was assessed by teratoma formation after subcutaneous injection into immunocompromised mice and by chimaera formation after blastocyst injection. Intermediate cell populations were isolated by flow cytometry.

Full Methods and any associated references are available in the online version of the paper at www.nature.com/nature.

Received 25 February; accepted 15 July 2009.

Published online 9 August 2009.

1. Hochedlinger, K. & Plath, K. Epigenetic reprogramming and induced pluripotency. *Development* **136**, 509–523 (2009).

2. Takahashi, K. *et al.* Induction of pluripotent stem cells from adult human fibroblasts by defined factors. *Cell* **131**, 861–872 (2007).
3. Takahashi, K. & Yamanaka, S. Induction of pluripotent stem cells from mouse embryonic and adult fibroblast cultures by defined factors. *Cell* **126**, 663–676 (2006).
4. Maherali, N. *et al.* Directly reprogrammed fibroblasts show global epigenetic remodeling and widespread tissue contribution. *Cell Stem Cell* **1**, 55–70 (2007).
5. Okita, K., Ichisaka, T. & Yamanaka, S. Generation of germline-competent induced pluripotent stem cells. *Nature* **448**, 313–317 (2007).
6. Wernig, M. *et al.* *In vitro* reprogramming of fibroblasts into a pluripotent ES-cell-like state. *Nature* **448**, 318–324 (2007).
7. Hockemeyer, D. *et al.* A drug-inducible system for direct reprogramming of human somatic cells to pluripotency. *Cell Stem Cell* **3**, 346–353 (2008).
8. Maherali, N. *et al.* A high-efficiency system for the generation and study of human induced pluripotent stem cells. *Cell Stem Cell* **3**, 340–345 (2008).
9. Wernig, M. *et al.* A drug-inducible transgenic system for direct reprogramming of multiple somatic cell types. *Nature Biotechnol.* **26**, 916–924 (2008).
10. Collado, M., Blasco, M. A. & Serrano, M. Cellular senescence in cancer and aging. *Cell* **130**, 223–233 (2007).
11. Parrinello, S. *et al.* Oxygen sensitivity severely limits the replicative lifespan of murine fibroblasts. *Nature Cell Biol.* **5**, 741–747 (2003).
12. Zindy, F. *et al.* Arf tumor suppressor promoter monitors latent oncogenic signals *in vivo*. *Proc. Natl Acad. Sci. USA* **100**, 15930–15935 (2003).
13. Stadtfeld, M., Maherali, N., Breault, D. T. & Hochedlinger, K. Defining molecular cornerstones during fibroblast to iPS cell reprogramming in mouse. *Cell Stem Cell* **2**, 230–240 (2008).
14. Brambrink, T. *et al.* Sequential expression of pluripotency markers during direct reprogramming of mouse somatic cells. *Cell Stem Cell* **2**, 151–159 (2008).
15. Sharpless, N. E. *et al.* Loss of p16^{Ink4a} with retention of p19^{Arf} predisposes mice to tumorigenesis. *Nature* **413**, 86–91 (2001).
16. Serrano, M. *et al.* Role of the INK4a locus in tumor suppression and cell mortality. *Cell* **85**, 27–37 (1996).
17. Bennett, D. C., Cooper, P. J. & Hart, I. R. A line of non-tumorigenic mouse melanocytes, syngeneic with the B16 melanoma and requiring a tumour promoter for growth. *Int. J. Cancer* **39**, 414–418 (1987).
18. Kamijo, T. *et al.* Tumor suppression at the mouse INK4a locus mediated by the alternative reading frame product p19^{ARF}. *Cell* **91**, 649–659 (1997).
19. Hanna, J. *et al.* Direct reprogramming of terminally differentiated mature B lymphocytes to pluripotency. *Cell* **133**, 250–264 (2008).
20. Ventura, A. *et al.* Cre-lox-regulated conditional RNA interference from transgenes. *Proc. Natl Acad. Sci. USA* **101**, 10380–10385 (2004).
21. Dickson, M. A. *et al.* Human keratinocytes that express hTERT and also bypass a p16^{Ink4a}-enforced mechanism that limits life span become immortal yet retain normal growth and differentiation characteristics. *Mol. Cell. Biol.* **20**, 1436–1447 (2000).
22. Mali, P. *et al.* Improved efficiency and pace of generating induced pluripotent stem cells from human adult and fetal fibroblasts. *Stem Cells* **26**, 1998–2005 (2008).
23. Zhao, Y. *et al.* Two supporting factors greatly improve the efficiency of human iPS cell generation. *Cell Stem Cell* **3**, 475–479 (2008).
24. Molofsky, A. V. *et al.* Increasing p16^{Ink4a} expression decreases forebrain progenitors and neurogenesis during ageing. *Nature* **443**, 448–452 (2006).
25. Krishnamurthy, J. *et al.* p16^{Ink4a} induces an age-dependent decline in islet regenerative potential. *Nature* **443**, 453–457 (2006).
26. Janzen, V. *et al.* Stem-cell ageing modified by the cyclin-dependent kinase inhibitor p16^{Ink4a}. *Nature* **443**, 421–426 (2006).
27. Eminli, S. *et al.* Differentiation stage determines reprogramming potential of hematopoietic cells into iPS cells. *Nature Genet.* (in the press).

Supplementary Information is linked to the online version of the paper at www.nature.com/nature.

Acknowledgements We thank M. Roussel and C. Sherr for providing us with *Arf*-GFP cells, D. C. Bennett and E. Sviderskaya for sharing Melan A cells, and A. Ventura and T. Jacks for tail biopsies of conditional *Trp53*-mutant mice. We also thank A. Tzatsos and N. Bardeesy for suggestions, for critical reading of the manuscript and for providing *Ink4a/Arf*^{-/-} MEFs. We are grateful to P. Follett for blastocyst injections and L. Prickett and K. Folz-Donahue for assistance with FACS. J.U. was supported by a postdoctoral fellowship from the Mildred Scheel Foundation, J.M.P. by an ECOR fellowship, and M.S. by a fellowship from the Schering Foundation. J.G.R. was supported by an NIH Skin Disease Research Center Grant. N.M. was supported by a graduated scholarship from the Natural Sciences and Engineering Council of Canada. Support to K.H. came from the NIH Director's Innovator Award, the Harvard Stem Cell Institute, the Kimmel Foundation and the V Foundation.

Author Contributions J.U., J.M.P. and K.H. conceived the study, interpreted results and wrote the manuscript, J.U. and J.M.P. performed most of the experiments with help from W.K., R.M.W. and A.K. M.S., N.M. and J.G.R. provided essential study material and helped with interpretation of results.

Author Information Reprints and permissions information is available at www.nature.com/reprints. Correspondence and requests for materials should be addressed to K.H. (khochedlinger@helix.mgh.harvard.edu).

METHODS

Viral vectors and production. The generation and structure of replication-defective doxycycline-inducible lentiviral vectors and a lentiviral vector constitutively expressing the reverse tetracycline-controlled transactivator (rtTA) has been described in detail elsewhere^{13,28}. Viral supernatant was concentrated approximately 100-fold by ultracentrifugation at 50,000g for 1.5 h at 4 °C, resuspended in 300 µl PBS, and stored at -80 °C. Infections were carried out in 1 ml medium using 5 µl of each viral concentrate per 35-mm plate. Downregulation of Trp53 expression was performed by infecting cells with a lentiviral construct expressing an shRNA against *Trp53* (GTAAGTCTCTCC CCTCAAT) as previously described²⁰.

Cell culture and *in vitro* differentiation of iPS cells. Melan A cells were grown in RPMI medium containing 10% FCS and 200 nM 12-*O*-tetradecanoylphorbol-13-acetate (TPA)¹⁷. Melan A cells were single-cell cloned and only one subclone was used for subsequent experiments. Fibroblast cultures containing a reactivatable *Trp53* allele as well as the ROSA26-CreER allele²⁹ were obtained from the tail of an adult mouse as described previously¹³. *Trp53*^{-/-} fibroblasts and *Ink4a*/*Arf*^{-/-} MEFs were cultured in DMEM containing 10% FCS. Primary melanocytes were purchased from the Skin Diseases Research Center, Yale School of Medicine, and were grown like Melan A cells. For lentiviral vector infections, cells were seeded in 6-well plates at a density of 1×10^5 cells per well and infected on three consecutive days. Medium changes were performed 12–24 h after infection. One day after the last infection, ES cell medium containing $1 \mu\text{g ml}^{-1}$ doxycycline was added. Fresh ES cell medium with doxycycline was added every other day until iPS cell colonies developed. Five days later, cell culture conditions were switched to ES cell medium in the absence of doxycycline. iPS cell colonies were picked into 96-well plates containing PBS without magnesium and calcium using a 10-µl pipette. Trypsin was added to each well, incubated for 5 min and single-cell suspension was transferred into 24-well dishes containing MEF feeder layers. Picked iPS cells were grown on MEFs in standard ES cell conditions. For blastocyst injections, iPS cells were marked with a FUGW lentiviral vector constitutively expressing GFP. For *in vitro* differentiation assays, iPS cells were grown in the absence of leukaemia inhibitory factor (LIF) on uncoated plates to induce embryoid body formation. Embryoid bodies were explanted on gelatinized plates and outgrowths were dissociated by trypsinization and expanded for FACS purification (see flow cytometry).

Human cell culture and generation of human iPS cells. The human epidermal keratinocyte lines strain N, N/TERT-1, and N/TERT-2G were grown in keratinocyte serum-free medium (KSFM) medium as previously described²¹. STEMCCA lentiviral vector²⁸ infections were carried out with human keratinocytes in 6-well plates at a density of 100,000 cells per well on two subsequent days. The infection efficiency of primary human keratinocytes after two subsequent infections with tetO-GFP lentiviral vector in the presence of the rtTA expressing lentiviral vector was 40%. Medium changes were performed 12 h after infections, and 1 day after infection human keratinocytes were transferred to MEFs. Media containing 50% keratinocyte medium and 50% human ES cell medium containing $0.5 \mu\text{g ml}^{-1}$ doxycycline was added 1 day later. Medium changes were performed every other day in the presence of $0.5 \mu\text{g ml}^{-1}$ doxycycline until colonies developed. After the appearance of human ES-cell-like colonies, medium was switched to human ES cell culture conditions and human iPS cells were picked and further expanded as described previously⁸.

Calculation of reprogramming efficiencies. For cells directly infected with lentivirus (LV-tetO-Oct4, -Sox2, -Klf4 and -c-Myc¹³ plus FUGW-rtTA¹³, or LV-tetO-STEMCCA²⁸ plus FUGW-rtTA), reprogramming efficiencies were calculated on the basis of the infection efficiency of somatic cells with a single control virus expressing EGFP (FUGW-GFP) or by performing immunofluorescence staining for Oct4 and Sox2. For secondary cells, equal numbers of cells were plated in the absence or presence of doxycycline on 100-mm dishes coated with gelatin or containing a layer of irradiated MEF feeders. Efficiencies were determined on average 20 days later by dividing the number of iPS cell colonies that grew after the withdrawal of doxycycline by the number of seeded cells, or alternatively, by the number of colonies that adhered to the control plate in the absence of doxycycline. ES cell character of iPS cell colonies was validated by immunofluorescence staining for Nanog. For some experiments, we FACS-sorted single secondary cells (previously marked with a lentiviral vector expressing td-Tomato) into wells of a 96-well plate. Reprogramming was induced by treatment of cells with doxycycline for 15 days, followed by doxycycline-independent growth for another 7 days. The number of wells with ES cell-like transgene-independent colonies was then scored by morphology and alkaline phosphatase staining; ES cell phenotype of these colonies was further verified by immunofluorescence staining for Nanog and Sox2. Efficiencies were calculated

on the basis of the number of wells containing colonies, normalized by the seeding efficiency, which was determined at day 3 by the presence of at least one td-Tomato cell in the well.

Alkaline phosphatase staining. Alkaline phosphatase staining was performed using an Alkaline Phosphatase substrate kit (Vector laboratories) according to manufacturer's recommendations.

Immunofluorescence. iPS cells were cultured on pretreated coverslips, fixed with 4% PFA, and permeabilized with 0.5% Triton X-100. The cells were then stained with primary antibodies against mouse Oct4 (sc-8628, Santa Cruz), mouse Sox2 (AB5603, Chemicon), and mouse Nanog (ab21603, Abcam). Respective secondary antibodies were conjugated to Alexa Fluor 546 (Invitrogen). Nuclei were counterstained with 4,6-diamidino-2-phenylindole (DAPI; Invitrogen). Cells were imaged with a Leica DMI4000B inverted fluorescence microscope equipped with a Leica DFC350FX camera. Images were processed and analysed with Adobe Photoshop software.

Flow cytometry. Collected cells were incubated with antibodies against Thy1.2 (phycoerythrin (PE)-conjugated, 53-2.1, eBiosciences), SSEA1 (mouse IgM, MC-480, Developmental Hybridoma Bank) and Flk1 (biotinylated, Aves 12a1, eBiosciences) for 20 min. Cells were washed in PBS and then incubated for 20 min with allophycocyanin (APC)-conjugated anti mouse IgM (eBioscience) and Pacific Blue-conjugated streptavidin (Invitrogen). The cells were washed in PBS, resuspended in propidium iodide 5% FBS/PBS solution, and passed through a 40-µm cell strainer to achieve single-cell suspension. Cells positive for Thy1 and Flk1 and negative for SSEA1 were sorted on a FACSaria (BD Biosciences). For analysis and/or sorting of intermediates, cells were stained with Thy1.2 and SSEA1 antibodies and sorted or analysed as indicated.

PCR analysis. For quantitative PCR (qPCR) analysis, RNA was isolated from cells with TRIzol reagent (Invitrogen). For strongly pigmented cells, an extra phenol-chloroform purification step was performed before RNA clean up with the RNeasy Minikit (Qiagen). Complementary DNA was produced with the Super Script III kit (Invitrogen). Real-time quantitative PCR reactions were set up in triplicate with the Brilliant II SYBR Green QPCR Master Mix (Stratagene), and run on a Mx3000P QPCR System (Stratagene). Primer sequences are listed in Supplementary Table 2. Genotyping for the *Trp53*^{-/-} allele was performed by PCR using the following three primer pairs: P53K_A: 5'-CAAACGTGTTCTACCTCAAGAGCC-3', P53K_B: 5'-AGCTAGCCACCATG GCTTGAGTAAGTCTGCA-3', and P53K_C: 5'-CTTGGAGACATAGCCACA CTG-3' (provided by A. Ventura).

Western blot analysis. Cell extracts were run in 15% SDS-PAGE gels. The gels were run at 90 V until proteins were separated (~2 h) and transferred to PVDF membranes (Bio-Rad) by running overnight at 20 V, 4 °C in transfer apparatus (Bio-Rad). The membranes were washed in PBS-T (PBS + 0.1% Tween) and blocked in 5% milk in PBS-T for 1 h. The membranes were then incubated with anti-p16^{Ink4a}, anti-Trp53 (phospho s15) (abcam) and γ-tubulin antibody overnight at 4 °C, washed and incubated in horseradish-peroxidase-conjugated anti-rabbit antibodies for 1 h at room temperature. Immunoblots were visualized using ECL reagent (Santa Cruz).

Cellular senescence detection. Cellular senescence was detected using a cellular senescence detection kit (Millipore) on the basis of β-galactosidase staining according to manufacturer's recommendations.

Bisulphite sequencing. Bisulphite treatment of DNA was performed with the EpiTect Bisulfite Kit (Qiagen) according to manufacturer's instructions. Primer sequences were as previously described for *Oct4* and *Nanog*⁸. Amplified products were purified by using gel filtration columns, cloned into the pCR4-TOPO vector (Invitrogen), and sequenced with M13 forward and reverse primers.

Generation of teratomas and chimaeras. For teratoma induction, 2×10^6 cells of each iPS cell line were injected subcutaneously into the dorsal flank of isoflurane-anaesthetized SCID mice. Teratomas were recovered 3–5 weeks after injection, fixed overnight in 10% formalin, paraffin embedded, and processed with haematoxylin and eosin. For chimaera production, female BDF1 mice were superovulated with PMS (pregnant mare serum) and hCG (human chorion gonadotropin) and mated to BDF1 stud males. Zygotes were isolated from plugged females 24 h after hCG injection. After 3 days of *in vitro* culture in KSOM media, blastocysts were injected with iPS cells, and transferred into day 2.5 pseudopregnant recipient females. Caesarean sections were performed 17 days later and pups were fostered with lactating females.

28. Sommer, C. A. *et al.* iPS cell generation using a single lentiviral stem cell cassette. *Stem Cells* 27, 543–549 (2008).

29. Ventura, A. *et al.* Restoration of p53 function leads to tumour regression *in vivo*. *Nature* 445, 661–665 (2007).

A p53-mediated DNA damage response limits reprogramming to ensure iPS cell genomic integrity

Rosa M. Marión^{1*}, Katerina Strati^{1*}, Han Li², Matilde Murga³, Raquel Blanco¹, Sagrario Ortega⁴, Oscar Fernandez-Capetillo³, Manuel Serrano² & Maria A. Blasco¹

The reprogramming of differentiated cells to pluripotent cells (induced pluripotent stem (iPS) cells) is known to be an inefficient process. We recently reported that cells with short telomeres cannot be reprogrammed to iPS cells despite their normal proliferation rates^{1,2}, probably reflecting the existence of 'reprogramming barriers' that abort the reprogramming of cells with uncapped telomeres. Here we show that p53 (also known as Trp53 in mice and TP53 in humans) is critically involved in preventing the reprogramming of cells carrying various types of DNA damage, including short telomeres, DNA repair deficiencies, or exogenously inflicted DNA damage. Reprogramming in the presence of pre-existing, but tolerated, DNA damage is aborted by the activation of a DNA damage response and p53-dependent apoptosis. Abrogation of p53 allows efficient reprogramming in the face of DNA damage and the generation of iPS cells carrying persistent DNA damage and chromosomal aberrations. These observations indicate that during reprogramming cells increase their intolerance to different types of DNA damage and that p53 is critical in preventing the generation of human and mouse pluripotent cells from suboptimal parental cells.

Nuclear reprogramming of differentiated cells into pluripotent stem cells is thought to be a possible source of patient-specific cells for transplantation therapies. Several strategies have been used to achieve nuclear reprogramming, including nuclear transplantation and cellular fusion³. Recently, the generation of iPS cells from differentiated cells was achieved by the overexpression of four transcription factors^{4–6}. These factors are Oct4 (also known as Pou5f1), Sox2, Klf4 and c-Myc, although some of them are dispensable to reprogram certain cell types^{4–11}.

Notably, only a small proportion of cells become pluripotent iPS cells (less than 1% (ref. 3); Supplementary Table 1). Several models have been proposed to explain the low efficiency of reprogramming³. Here we reasoned that a further explanation may be related to the presence of DNA damage in the cells undergoing reprogramming.

This notion is on the basis of our observations that murine fibroblasts with increased DNA damage owing to the presence of critically short telomeres (third generation (G3) telomerase-deficient mouse embryonic fibroblasts (MEFs), or G3 *Terc*^{−/−} MEFs) cannot be reprogrammed to iPS cells^{1,2}, despite the fact that the cells have normal proliferation rates¹² (Supplementary Fig. 1) and are able to spontaneously immortalize and be transformed by oncogenes¹². iPS cell generation from G3 *Terc*^{−/−} MEFs can be restored after re-elongation of the shortest telomeres by telomerase^{1,2}, indicating that damaged/uncapped telomeres are responsible for their failure to reprogram. These observations suggest that an important impediment for reprogramming is the existence of reprogramming barriers

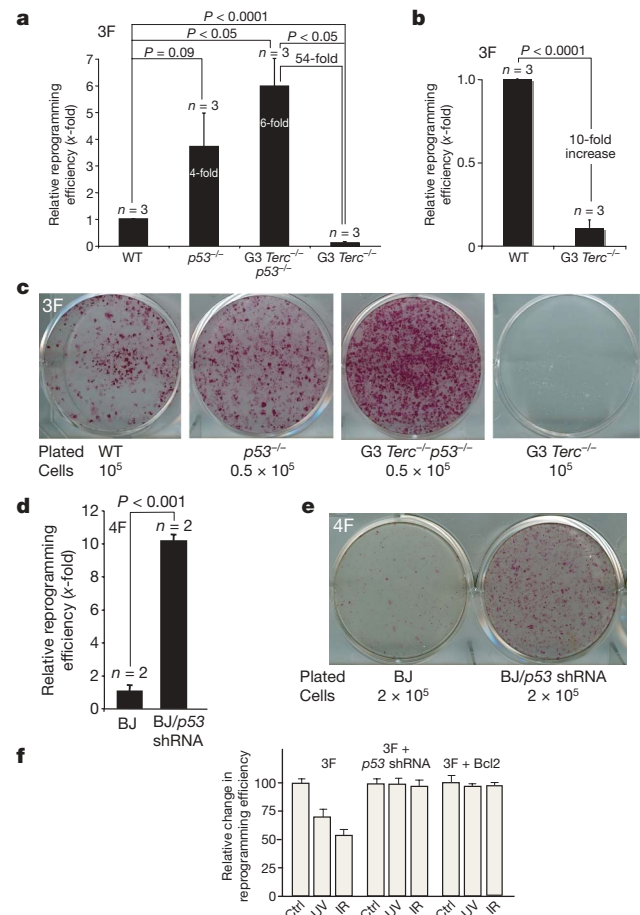


Figure 1 | p53-deficiency allows reprogramming of MEFs with short telomeres. **a, b**, Relative reprogramming efficiencies are shown, with the fold changes indicated. Student's *t*-test (two-tailed) is used for statistics. Error bars, standard error. *n* = experiments with independent MEFs. 3F, three factors; WT, wild type. **c**, Reprogramming plates stained with alkaline phosphatase. The number of parental cells used is indicated. **d**, Reprogramming of BJ human fibroblasts with four factors (4F) together with a human shRNA against the human p53 gene. Fold changes relative to BJ + 4F (BJ) are indicated. **e**, Reprogramming plates stained with alkaline phosphatase. **f**, Relative reprogramming efficiencies of wild-type MEFs exposed to UVC (UV) or ionizing radiation (IR), and expressing three factors together with a retrovirus expressing mouse p53 shRNA or Bcl2. Error bars, standard deviation. Ctrl, control.

¹Telomeres and Telomerase Group, ²Tumor Suppression Group, ³Genetic Instability Group, Molecular Oncology Program, Spanish National Cancer Research Centre (CNIO), Melchor Fernández Almagro 3, Madrid E-28029, Spain. ⁴Transgenic mice Unit, Biotechnology Program, Spanish National Cancer Research Centre (CNIO), Melchor Fernández Almagro 3, Madrid E-28029, Spain.

*These authors contributed equally to this work.

that abort reprogramming of DNA-damaged cells, such as those with uncapped telomeres.

p53 has a crucial involvement in preventing the propagation of DNA-damaged cells, including those containing short/dysfunctional telomeres^{13,14}. We began to test the role of p53 by reprogramming cells with critically short telomeres (G3 *Terc*^{-/-} MEFs) in the presence or absence of p53. We used three reprogramming factors (Oct4, Klf4 and Sox2) following methods previously shown to reprogram wild-type MEFs into bona fide pluripotent iPS cells¹. The efficiency of reprogramming of wild-type MEF cultures was 0.72% ± 0.05% (mean ± s.e.m.) (Supplementary Table 1)^{1,9}. p53-null MEFs were reprogrammed with an efficiency that was on average fourfold higher than the wild-type MEFs (Fig. 1a–c and Supplementary Table 1), suggesting that p53 limits reprogramming of wild-type MEFs. We extended these findings to the reprogramming of BJ human foreskin fibroblasts with four factors (Oct4, Sox2, Klf4 and c-Myc). The

simultaneous infection with a retrovirus expressing short hairpin RNA (shRNA) against p53 (p53 shRNA) resulted in a tenfold increase in reprogramming efficiency compared to BJ fibroblast controls (Fig. 1d, e). Furthermore, p53-null iPS cell colonies appeared 3 days earlier than in the p53-proficient controls. G3 *Terc*^{-/-} MEFs showed a tenfold decrease in reprogramming efficiency compared to wild-type MEFs (Fig. 1a–c and Supplementary Table 1)¹, and G3 *Terc*^{-/-} iPS cells colonies appeared 2–3 days later. Notably, p53 abrogation in G3 *Terc*^{-/-} p53^{-/-} restored their reprogramming efficiency to similar levels seen in p53-null cells, which represented a 54-fold increase in reprogramming efficiency compared with the G3 *Terc*^{-/-} controls, and a sixfold increase compared with wild-type cells (Fig. 1a–c and Supplementary Table 1). We extended these results to other sources of DNA damage, such as low doses of γ -irradiation and ultraviolet light. In both cases, irradiated MEFs showed lower reprogramming efficiencies than the non-irradiated controls (Fig. 1f). Co-infection of

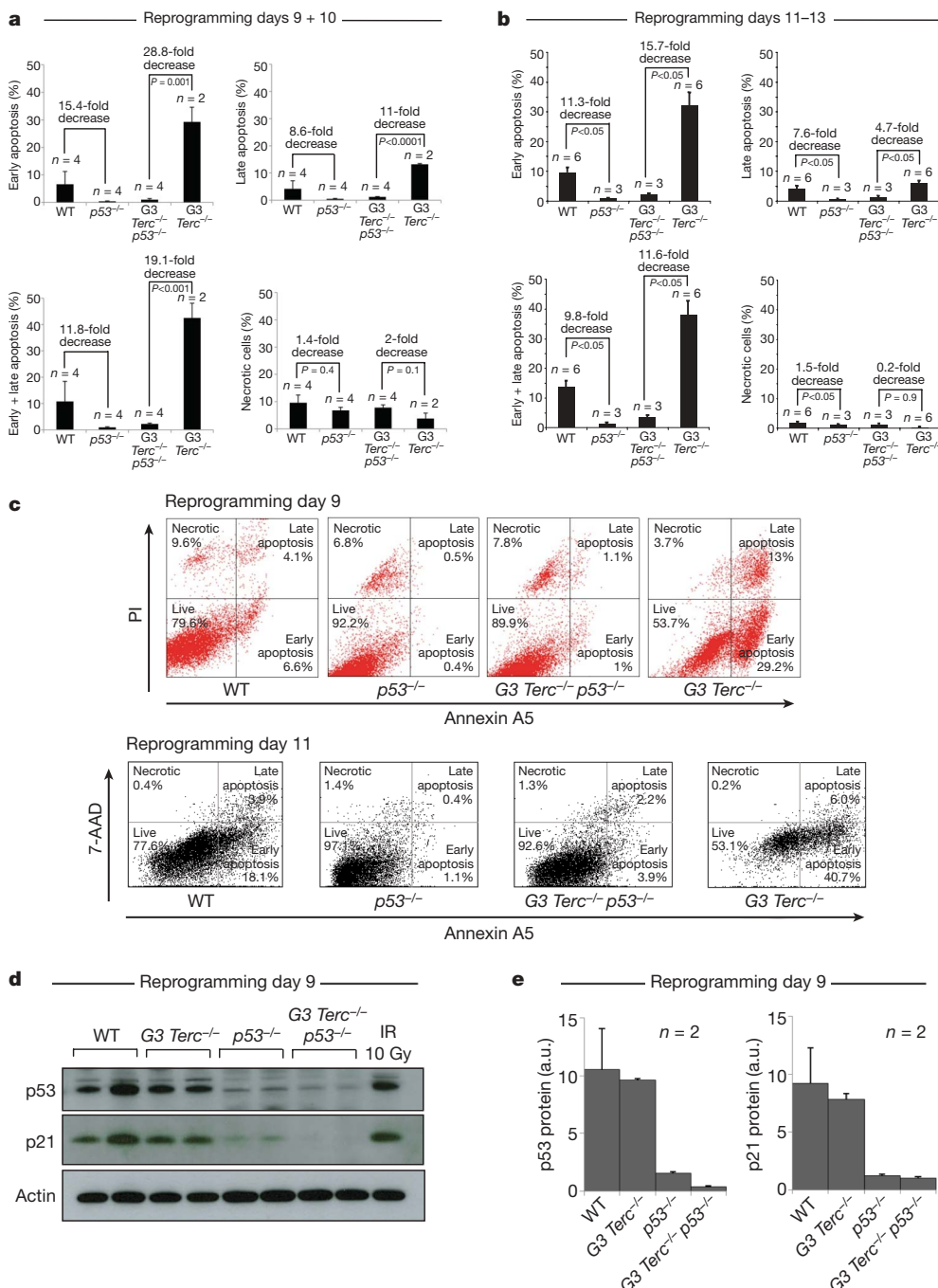


Figure 2 | p53-deficiency abrogates apoptosis at the onset of iPS cell formation. **a, b**, Apoptosis and necrosis are determined on days 9 and 10 (**a**) and 11–13 (**b**) post-infection. Data are mean and s.e.m. A Student's *t*-test is used for statistics. **c**, Representative FACS profiles at day 9 of reprogramming. PI, propidium iodide. 7-AAD, 7-amino-actinomycin D. **d**, Western blots of p53 and p21 protein levels at day 9 post-infection. As a control, wild-type MEFs were γ -irradiated (10 Gy). Two reprogramming experiments per genotype are shown. **e**, Quantification of p53 and p21 westerns shown in **d**. Values are in arbitrary units (a.u.). Error bars, standard error.

wild-type MEFs with the three factors together with a retrovirus expressing *p53* shRNA or the anti-apoptotic protein Bcl2, rendered the reprogramming of these cells essentially insensitive to these doses of DNA damage (Fig. 1f). Together, these findings indicate that *p53* limits reprogramming of mouse and human cells by restricting conversion of DNA-damaged cells into iPS cells, probably by the elimination of these cells by apoptosis^{13,15}. This effect is exacerbated in cells containing a higher proportion of DNA-damaged cells owing to their dysfunctional telomeres or after infliction of exogenous DNA damage.

Our data indicates that *p53* becomes sensitized to DNA damage once cells engage the iPS cell program. We sought to find direct evidence of *p53* activity at early times during iPS cell formation before the appearance of typical iPS cell colonies. For this, we quantified the percentage of cells undergoing apoptosis at days 9–10 and 11–13 after infection, at the time of induction of pluripotency^{8,9}. A significant proportion (10% and 15%) of wild-type cells undergo apoptosis at days 9–10 and 11–13 after infection, respectively (Fig. 2a–c). This is further increased to 40% in G3 *Terc*^{−/−} cultures at 9–13 days after infection (Fig. 2a–c), in agreement with their lower iPS cell yields (Fig. 1a–c). Notably, apoptosis was essentially abrogated in *p53*^{−/−}

and G3 *Terc*^{−/−} *p53*^{−/−} cells at 9–13 days after infection (Fig. 2a–c), whereas no differences in necrosis were observed (Fig. 2a–c). The increased apoptosis in wild-type and G3 *Terc*^{−/−} cultures at day 9 of reprogramming was accompanied by *p53* and *p21* (also referred as *Cdkn1a*) protein levels similar to those of γ -irradiated wild-type MEFs, while this was not observed in the *p53*-null cultures (Fig. 2d, e). These results indicate that *p53* limits reprogramming by inducing apoptosis of suboptimal cells at the time of pluripotency induction, in agreement with Bcl2-overexpression allowing normal reprogramming of cells with exogenously inflicted DNA damage (Fig. 1f). The activity of *p53* restricting reprogramming of suboptimal cells is readily observed in wild-type cells and it is further exacerbated in G3 *Terc*^{−/−} cells, which contain a higher proportion of damaged cells¹.

If *p53*-deficiency is allowing the conversion of DNA-damaged cells into iPS cells, we should expect to see persistent activation of the DNA damage response (DDR) in the *p53*-null genotypes, both during reprogramming and in the resulting iPS cell clones, while this should be less apparent in *p53*-proficient cells in which damaged cells are being eliminated by apoptosis. DDR activation was evidenced by the presence of γ H2ax (also known as γ H2afx) and

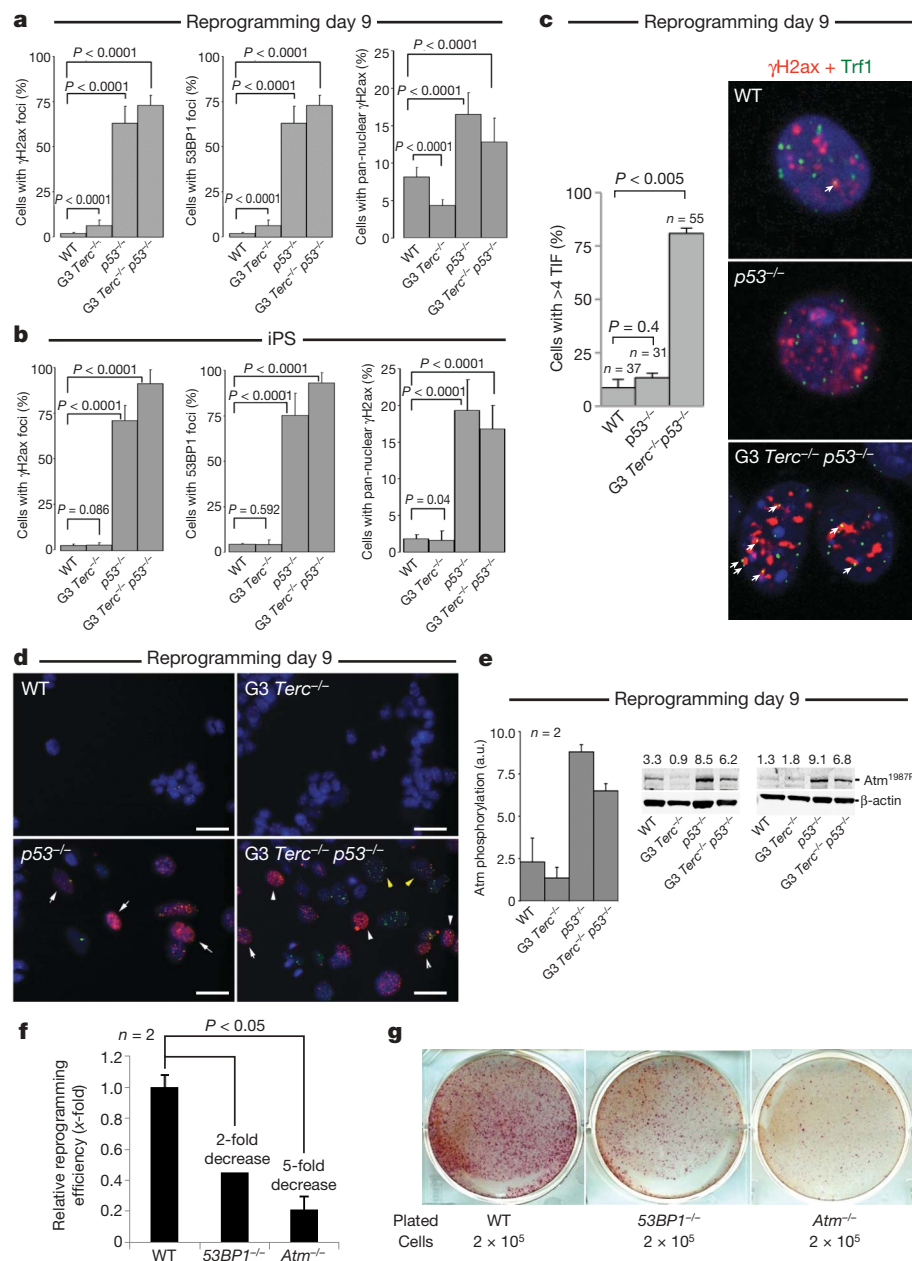


Figure 3 | DDR activation during reprogramming.

a, b, γ H2ax and 53BP1 foci 9 days after infection (**a**) and in iPS cell clones (**b**). Results are the mean of two experiments. Two-hundred cells were analysed per genotype/experiment. Error bars, s.d. **c**, Left, telomere-induced DNA damage foci (TIF) 9 days after infection. n = cells with γ H2ax foci analysed. Values correspond to two reprogramming experiments. Error bars, standard error. Student's *t*-test was used for statistics. Right, representative images of γ H2ax (red) and Trf1 (green) staining. Arrows indicate co-localization events (yellow). Original magnification, $\times 63$. **d**, Representative images that are quantified in **a**. White arrows, pan-nuclear γ H2ax; yellow arrows, co-localization of γ H2ax and 53BP1. Scale bars, 10 μ m. **e**, Western blot (right) showing Atm phosphorylation 9 days after infection. Atm^{1987P} denotes Atm protein phosphorylated at Ser 1987. Numbers above each lane represent the relative quantification of Atm levels. Two western blots were used for quantification (left). Error bars, standard deviation. **f**, Relative reprogramming efficiencies of *53BP1*^{−/−} and *Atm*^{−/−} MEFs compared to wild-type MEFs. Fold changes are indicated. Student's *t*-test is used for statistics. Error bars, standard error. n = experiments performed with independent MEF cultures. **g**, Reprogramming plates stained with alkaline phosphatase.

53BP1 (also known as Trp53bp1) foci at day 9 after infection in $p53^{-/-}$ and G3 $Terc^{-/-} p53^{-/-}$ cultures (Fig. 3a), which persisted in the isolated iPS cell clones (Fig. 3b) and the teratomas derived from them (Supplementary Fig. 4d). γ H2ax and 53BP1 foci showed frequent co-localization, indicating a robust DDR activation (Fig. 3d, yellow arrows). Furthermore, in the G3 $Terc^{-/-} p53^{-/-}$ cultures, a significant proportion of cells with γ H2ax foci (>75%) showed co-localization with the Trf1 (also known as Terf1) telomeric protein forming the so-called telomere-induced DNA damage foci (TIF) (Fig. 3c), indicative of telomere dysfunction. Cells with pan-nuclear γ H2ax staining were also increased in the $p53$ -null cultures at day 9 after infection and in the corresponding iPS cell clones (Fig. 3a, b and white arrows in Fig. 3d). Pan-nuclear γ H2ax staining is associated with replication-induced DNA damage¹⁶, suggesting generation of this type of endogenous DNA damage during the reprogramming process¹⁶. Finally, we detected Atm phosphorylation in the $p53$ -null cultures at day 9 after infection (Fig. 3e), a hallmark of Atm activation¹⁷ and further indicating DDR activation during reprogramming of these cells.

To test the unique role of p53 in the elimination of DNA-damaged cells during reprogramming, we considered the effect of Atm and 53BP1 deficiencies on reprogramming. These two proteins participate in the repair of DNA breaks and, consequently, their absence increases the endogenous levels of DNA damage^{18,19}. Furthermore,

the two proteins participate in the signalling of DNA damage to p53 (refs 18, 19). MEFs deficient in either Atm or 53BP1 showed a decreased reprogramming efficiency compared to wild-type controls (Fig. 3f, g), which might reflect increased endogenous DNA damage in these cultures^{18,19}. These results are in agreement with the central role of p53 as the integrator of several and redundant DNA damage signalling pathways, whereas other upstream components of the DDR, such as Atm or 53BP1, are not essential to prevent the reprogramming of DNA-damaged cells.

We wondered whether reprogramming of $p53$ -null cultures in the face of DNA damage was accompanied by increased chromosomal damage. Short/uncapped telomeres are known to lead to chromosome end-to-end fusions¹². $p53^{-/-}$ iPS cells showed sixfold more end-to-end fusions than wild-type iPS cells (Fig. 4a, c), and this was increased by 40- and 37-fold in G3 $Terc^{-/-} p53^{-/-}$ and G3 $Terc^{-/-}$ iPS cells, respectively (Fig. 4a, c). Of note, G3 $Terc^{-/-}$ iPS cells represent rare reprogramming events (Fig. 1a) after widespread apoptotic death (Fig. 2a–c), which may explain the high levels of fusions in the face of functional p53. Chromosomal breaks/fragments were also increased in $p53^{-/-}$ iPS cells compared to wild-type iPS cells (sixfold), and further increased in G3 $Terc^{-/-}$ and G3 $Terc^{-/-} p53^{-/-}$ iPS cells (13- and 10-fold, respectively) (Fig. 4b). Increased fusions in G3 $Terc^{-/-} p53^{-/-}$ and G3 $Terc^{-/-}$ iPS cells were coincidental with a high percentage (30% and 42%, respectively) of chromosome ends with

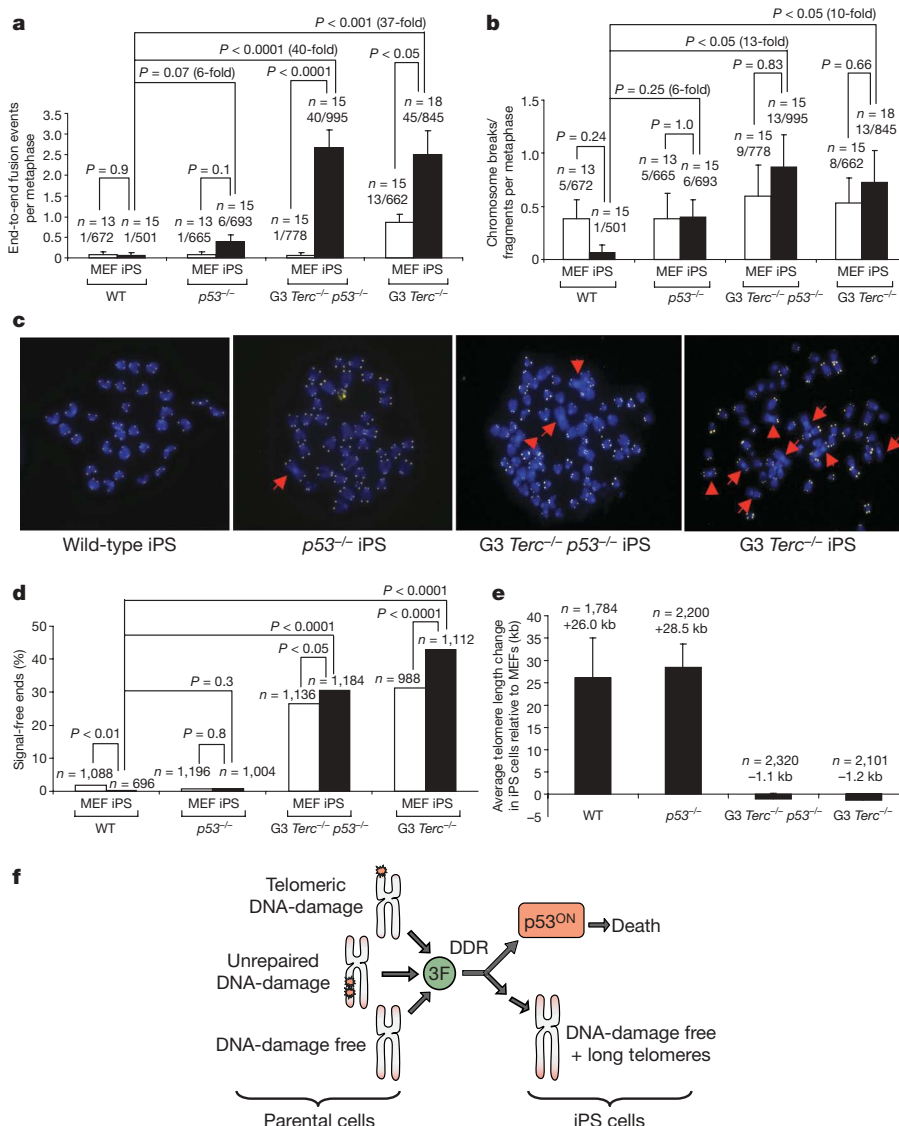


Figure 4 | $p53$ -null iPS cells show chromosomal instability. **a, b**, Frequency of end-to-end fusions (**a**) and breaks/fragments (**b**) in the indicated cells. n = metaphase number. The number of aberrations out of the chromosomes scored is indicated. Student's t -test was used for statistics. Error bars, s.e.m. **c**, Representative metaphases. Red arrows, end-to-end fusions. Original magnification, $\times 100$. **d**, Percentage of signal-free ends. n = telomeres used for the analysis. Chi-square test is used for statistics. **e**, Average telomere elongation (kilobase (kb)) in iPS cell clones compared to parental MEFs. n = telomeres used for the analysis. At least two independent iPS cell clones were used per genotype. MEF passage number = 3; iPS cell passage number = 4–6. Error bars, s.e.m. **f**, Summary illustrating that p53 constitutes a main barrier to reprogramming of cells with increased DNA damage by preventing that they become iPS cells.

undetectable telomere signals or 'signal-free ends', compared to only 0.29% of signal-free ends in wild-type iPS cells (Fig. 4d).

Telomeres undergo telomerase-dependent elongation during reprogramming—a process that continues after reprogramming until iPS cells clones acquire the typically long telomeres of embryonic stem (ES) cells^{1,2}. Telomeres were similarly elongated in wild-type and *p53*-null iPS cells compared with the parental MEFs, but suffered further shortening in the telomerase-deficient *G3 Terc*^{-/-} and *G3 Terc*^{-/-} *p53*^{-/-} iPS cells (Fig. 4e). These results indicate that the *p53*-deficiency allows reprogramming of *G3 Terc*^{-/-} cells independently of telomere length.

Furthermore, we tested whether *p53*-abrogation in *p53*^{-/-} and *G3 Terc*^{-/-} *p53*^{-/-} iPS cells had an effect on their ability to contribute to mouse chimaerism and teratomas. Although some of the *p53*^{-/-} and *G3 Terc*^{-/-} *p53*^{-/-} iPS cell clones lost the typical rounded iPS cell morphology after expansion (Supplementary Fig. 2), we were able to obtain chimaeras from *p53*^{-/-} and *G3 Terc*^{-/-} *p53*^{-/-} iPS cells by picking individual iPS cell colonies with robust Nanog and Oct4 expression (Supplementary Table 2 and Supplementary Figs 3 and 4a). *p53*^{-/-} chimaeras were able to contribute to the germ line, however, the only *G3 Terc*^{-/-} *p53*^{-/-} chimaera obtained died at 14 days of age with severe intestinal atrophy (Supplementary Table 2). All of the *p53*^{-/-} and *G3 Terc*^{-/-} *p53*^{-/-} iPS cell clones tested were able to form teratomas (Supplementary Fig. 4b, c). Notably, teratomas derived from *G3 Terc*^{-/-} *p53*^{-/-} iPS cells showed abundant γ H2ax staining and anaphase bridges concomitant with lower p21 and apoptosis levels than wild-type teratomas (Supplementary Fig. 4d), indicating that DDR activation persists during the differentiation of *p53*-null iPS cell clones.

In summary, these data indicate that *p53* constitutes a main barrier to reprogramming of wild-type cells, which is exacerbated in cells with pre-existing DNA damage (that is, cells with short telomeres or deficient for Atm and 53BP1) and in cells in which DNA damage has been exogenously inflicted (irradiated cells). In this manner, suboptimal cells carrying DNA damage are eliminated by *p53*-dependent apoptosis and prevented from becoming iPS cells (Fig. 4f). These results agree with previous findings showing that *p53* downregulation improves reprogramming efficiency²⁰. A *p53*-dependent counterselection of DNA-damaged cells during reprogramming is shown by increased Atm phosphorylation and increased DNA damage foci both in *p53*^{-/-} and *G3 Terc*^{-/-} *p53*^{-/-} cultures. Given that some of the reprogramming factors promote tumorigenesis *in vivo*²¹, it is tempting to propose that the observed DDR in *p53*^{-/-} cultures might be equivalent to the oncogene-induced DDR reported in the context of malignant transformation^{22,23}. In both models, reprogramming and transformation, *p53* is critical to control the spreading of damaged cells.

METHODS SUMMARY

MEFs from the indicated genotypes were reprogrammed as described¹. Human foreskin fibroblasts (BJ) were reprogrammed as described⁵. For quantification of iPS cell generation efficiency, retroviral transduction was measured in parallel infections containing the reprogramming factors plus a green fluorescent protein (GFP) retroviral plasmid, followed by FACS analysis at day 3. The total number of iPS cell colonies was counted after staining plates for alkaline phosphatase activity (AP detection kit, Chemicon International) following the manufacturer's instructions. Supplementary Table 1 shows a summary of the different reprogramming efficiencies.

Apoptosis was determined by annexin A5 staining and quantified using a FACS Canto. Analysis of the DDR was performed by high-throughput microscopy and western blotting as described before¹⁶. Analyses of telomere length and chromosomal aberrations were performed as described¹. Chimaeras were derived from iPS cells as described¹. For teratoma generation (nu/nu) mice were subcutaneously injected with 1×10^6 cells of each iPS cell clone. Protein and RNA analyses were performed following standard procedures.

Full Methods and any associated references are available in the online version of the paper at www.nature.com/nature.

Received 15 May; accepted 17 July 2009.

Published online 9 August 2009.

1. Marion, R. M. *et al.* Telomeres acquire embryonic stem cell characteristics in induced pluripotent stem cells. *Cell Stem Cell* **4**, 141–154 (2009).
2. Davy, P. & Allsopp, R. Balancing out the ends during iPSC nuclear reprogramming. *Cell Stem Cell* **4**, 95–96 (2009).
3. Jaenisch, R. & Young, R. Stem cells, the molecular circuitry of pluripotency and nuclear reprogramming. *Cell* **132**, 567–582 (2008).
4. Takahashi, K. & Yamanaka, S. Induction of pluripotent stem cells from mouse embryonic and adult fibroblast cultures by defined factors. *Cell* **126**, 663–676 (2006).
5. Takahashi, K. *et al.* Induction of pluripotent stem cells from adult human fibroblasts by defined factors. *Cell* **131**, 861–872 (2007).
6. Wernig, M. *et al.* *In vitro* reprogramming of fibroblasts into a pluripotent ES-cell-like state. *Nature* **448**, 318–324 (2007).
7. Wernig, M., Meissner, A., Cassady, J. P. & Jaenisch, R. c-Myc is dispensable for direct reprogramming of mouse fibroblasts. *Cell Stem Cell* **2**, 10–12 (2008).
8. Stadtfeld, M., Maherali, N., Breault, D. T. & Hochedlinger, K. Defining molecular cornerstones during fibroblast to iPS cell reprogramming in mouse. *Cell Stem Cell* **2**, 230–240 (2008).
9. Meissner, A., Wernig, M. & Jaenisch, R. Direct reprogramming of genetically unmodified fibroblasts into pluripotent stem cells. *Nature Biotechnol.* **25**, 1177–1181 (2007).
10. Nakagawa, M. *et al.* Generation of induced pluripotent stem cells without Myc from mouse and human fibroblasts. *Nature Biotechnol.* **26**, 101–106 (2008).
11. Kim, J. B. *et al.* Oct4-induced pluripotency in adult neural stem cells. *Cell* **136**, 411–419 (2009).
12. Blasco, M. A. *et al.* Telomere shortening and tumor formation by mouse cells lacking telomerase RNA. *Cell* **91**, 25–34 (1997).
13. Collado, M., Blasco, M. A. & Serrano, M. Cellular senescence in cancer and aging. *Cell* **130**, 223–233 (2007).
14. Chin, L. *et al.* p53 deficiency rescues the adverse effects of telomere loss and cooperates with telomere dysfunction to accelerate carcinogenesis. *Cell* **97**, 527–538 (1999).
15. Vousden, K. H. & Lane, D. P. p53 in health and disease. *Nature Rev. Mol. Cell Biol.* **8**, 275–283 (2007).
16. Toledo, L. I., Murga, M., Gutierrez-Martinez, P., Soria, R. & Fernandez-Capetillo, O. ATR signaling can drive cells into senescence in the absence of DNA breaks. *Genes Dev.* **22**, 297–302 (2008).
17. Bakkenist, C. J. & Kastan, M. B. DNA damage activates ATM through intermolecular autophosphorylation and dimer dissociation. *Nature* **421**, 499–506 (2003).
18. Xu, Y. *et al.* Targeted disruption of ATM leads to growth retardation, chromosomal fragmentation during meiosis, immune defects, and thymic lymphoma. *Genes Dev.* **10**, 2411–2422 (1996).
19. Ward, I. M., Minn, K., van Deursen, J. & Chen, J. p53 Binding protein 53BP1 is required for DNA damage responses and tumor suppression in mice. *Mol. Cell Biol.* **23**, 2556–2563 (2003).
20. Zhao, Y. *et al.* Two supporting factors greatly improve the efficiency of human iPS cell generation. *Cell Stem Cell* **3**, 475–479 (2008).
21. Hochedlinger, K., Yamada, Y., Beard, C. & Jaenisch, R. Ectopic expression of Oct-4 blocks progenitor-cell differentiation and causes dysplasia in epithelial tissues. *Cell* **121**, 465–477 (2005).
22. Bartkova, J. *et al.* DNA damage response as a candidate anti-cancer barrier in early human tumorigenesis. *Nature* **434**, 864–870 (2005).
23. Di Micco, R. *et al.* Oncogene-induced senescence is a DNA damage response triggered by DNA hyper-replication. *Nature* **444**, 638–642 (2006).

Supplementary Information is linked to the online version of the paper at www.nature.com/nature.

Acknowledgements We thank R. Serrano for mouse colony management, and M. Cañamero and the Comparative Pathology Unit at the CNIO for teratoma analysis. K.S. is recipient of a contract from the Spanish Association Against Cancer (AECC). Work in the laboratory of M.A.B. is funded by grants from the MICINN (CONSOLIDER), the Regional Government of Madrid, the European Union, the European Research Council (ERC), the AECC, and the Korber European Research Award.

Author Contributions R.M.M. and K.S. performed most of the experimental work. H.L., M.M., R.B. and S.O. made critical experimental contributions. R.M.M., K.S., O.F.-C., M.S. and M.A.B. designed the experimental plan, analysed and interpreted the data. M.A.B. directed the project and wrote the paper.

Author Information Reprints and permissions information is available at www.nature.com/reprints. Correspondence and requests for materials should be addressed to M.A.B. (mblasco@cnio.es).

METHODS

Mice, cells and culture conditions. *Terc*^{+/-} and *p53*^{+/-} mice were first intercrossed to generate *Terc*^{+/-} *p53*^{+/-} double heterozygous mice and then mated to generate first generation (G1) *Terc*^{-/-} *p53*^{+/-} littermates. G1 *Terc*^{-/-} *p53*^{+/-} littermates were interbred for successive generations to obtain late generation G3 *Terc*^{-/-} *p53*^{-/-} double mutant mice, as well as their G3 *Terc*^{-/-} littermate controls, as previously described^{14,24}. The genetic background for all genotypes was a pure C57BL/6 background.

Primary MEFs (passage 2) were obtained from embryos of the indicated *Terc* and *p53* genotypes as described previously^{14,24}. *Atm*^{-/-} and *53BP1*^{-/-} MEFs and their corresponding wild-type controls were obtained from the null-mouse strains described before^{19,25}.

MEFs were cultured in standard DMEM medium with 10% FBS (Gibco). ES and iPS cells were cultured in DMEM (high glucose) supplemented with serum replacement (KSR, Invitrogen), Lif (1,000 U ml⁻¹), non-essential amino acids, glutamax and β-mercaptoethanol. C57BL/6 ES cells were derived at the Transgenic Mouse Unit of the CNIO from C57BL/6 blastocysts.

Generation of mouse iPS cells. Reprogramming of primary (passage 2–4) MEFs was performed as previously described¹ following modifications of a previous protocol²⁶. In brief, primary MEFs of the indicated genotypes in a pure C57BL/6 background were seeded in 6-well plates (0.25–1 × 10⁵ cells per well). They were infected four times in the next two days with a cocktail of the retroviral constructs pMXsOct3/4, pMXsKlf4 and pMXsSox2 as described¹. Reprogramming was assessed 2 weeks after infection by counting alkaline-phosphatase-positive colonies. Alkaline phosphatase staining was performed according to manufacturer's instructions (Alkaline Phosphatase Detection kit; Millipore). The results were normalized to the respective efficiencies of retroviral transduction as assessed by transducing with the three retroviruses pMXsOct3/4, pMXsKlf4 and pMXsSox2, plus a retrovirus expressing GFP. Absolute reprogramming efficiencies are shown in Supplementary Table 1. The efficiency of reprogramming was also calculated as the relative change compared to that of wild-type MEFs (Fig. 1). Colonies were picked after 2 weeks and expanded on feeder fibroblasts using standard procedures.

Generation of human iPS cells. Reprogramming of BJ human foreskin fibroblasts (passage 15; obtained from the American Type Culture Collection (ATCC)) was done as previously described^{5,27}. In brief, retroviral supernatants were produced in HEK-293T cells (5 × 10⁶ cells per 100-mm-diameter dish) transfected with the ecotopic packaging plasmid pCL-Ampho (4 μg) together with one of the following retroviral constructs (4 μg): pMXs-hKlf4, pMXs-hSox2 or pMXs-hOct4 (obtained from Addgene and previously described⁵). The retroviral construct expressing human shRNA against *p53*, pRETRO-Super, was provided by R. Bernards. Transfections and infections were performed the same as the mouse iPS cell reprogramming described earlier. Twenty-thousand BJ fibroblasts had been seeded the previous day (2 × 10⁵ cells per 60-mm-diameter gelatin-coated dish) and received 1.5 ml of each of the corresponding retroviral supernatants (a total of either three or four—the fourth being the *p53* shRNA retroviral supernatant). This procedure was repeated every 12 h for 2 days (a total of four additions). The day after infection was completed, media was replaced by human fibroblast media, and kept for a further 2 days. At day 8, cells were trypsinized and reseeded on feeder plate. At day 9, media was changed to human ES cell media. Cultures were maintained in the absence of drug selection with daily medium changes. At day 20, colonies with ES-like morphology became visible at the microscope. Colonies were picked after 3 weeks and expanded on feeder fibroblasts using standard procedures.

Reprogramming of irradiated cells. Primary wild-type MEFs were exposed to UVC (2 J m⁻²) or ionizing radiation (2 Gy), and 24 h later cells were infected with the three factors together with a fourth retrovirus expressing *p53* shRNA or Bcl2, as indicated. Bcl2 was overexpressed using retroviral pBabe-PURO-Bcl2 (provided by A. Carnero). *p53* shRNA against murine *p53* was expressed using retroviral pRetro-SUPER (provided by R. Bernards).

Analysis of the DDR. γH2ax (Upstate Biotechnology) and 53BP1 (Novus Biologicals), as well as secondary antibodies conjugated with Alexa 488 or Alexa 594 (Molecular Probes), were used. Image acquisition was done with high-throughput-microscopy. In brief, cells were grown on gelatinized mCLEAR bottom 96-well dishes (Greiner Bio-One), and analysed on a BD Pathway 855 BioImager (Beckton Dickinson). All of the images used for quantitative analyses were acquired under non-saturating exposure conditions. Western analyses were performed on the LICOR platform (Biosciences) with β-actin (Sigma) and *Atm*^{1987P} (gift from A. Nussenzweig) antibodies.

Analysis of telomere damage-induced foci. Reprogramming with the three factors was performed in the indicated MEFs. At days 9 and 10 after infection, cells were collected and plated in gelatinized coverslips. Once attached to the coverslips, cells were rinsed with PBS and incubated with Triton X-100 buffer

(20 mM Tris-HCl, pH 8, 50 mM NaCl, 3 mM MgCl₂, 0.5% Triton X-100 and 300 mM sucrose) at room temperature for 5 min. Cells were then fixed in PBS-buffered 4% paraformaldehyde for 10 min at room temperature, followed by permeabilization in PBS-0.1% Triton X-100 for 10 min. Cells were then blocked with 2% BSA (Sigma) for 1 h. The samples were incubated overnight at 4 °C with the primary antibodies. Phosphorylated γH2ax and Trf1 foci were detected using a mouse monoclonal anti-phospho-histone γH2ax (Ser 139) antibody (1:500; from Upstate Biotechnology) and an anti-Trf1 antibody (1:500). After washing with 0.1% Tween-20 buffer for 30 min at room temperature, the samples were incubated with Cy3-goat anti-mouse and Alexa 488-goat anti-rabbit antibody (1:400; Jackson ImmunoResearch Laboratories), for 1 h at room temperature. Slides were mounted in Vectashield with 4',6-diamino-2-phenylindole (DAPI). Images were obtained using a confocal microscope (Leica TCS-SP5 (Acousto-optical beamsplitter)).

iPS cell chimaeras. The capacity of the *p53*^{-/-} and G3 *Terc*^{-/-} *p53*^{-/-} iPS cell clones to generate chimaeras *in vivo* was tested by microinjection into C57BL/6J-Tyr(C-2J)/J (albino) blastocysts and the assessment of hair colour in the resulting progeny (Supplementary Table 2 and Supplementary Fig. 4a). Wild-type iPS cell clones were previously described to produce chimaeras and to contribute to the germ line¹. Late generation *Terc*^{-/-} iPS cells were previously described to fail to produce any viable chimaeras¹.

Teratoma formation. The indicated number of mice (nu/nu) was subcutaneously injected with 1 × 10⁶ cells of each iPS cell clone. All injected clones showed high expression of the pluripotency genes *Nanog* and *Oct4* (Supplementary Fig. 3). Tumour growth was measured at the indicated days post-injection with a calibre, and tumour volume was calculated according to the formula: long diameter × (short diameter)² × 0.51.

Apoptosis assay. Reprogramming with the three factors was performed in the indicated MEFs. At days 9 and 10 after infection, cells were collected, washed in PBS, resuspended in 1 × annexin A5 binding buffer, and stained with annexin-A5-FITC (BD Pharmingen) and propidium iodide (Sigma). After a 15-min incubation in the dark at room temperature, annexin-A5-positive cells were quantified using a FACS Canto within 1 h. Similarly, at days 11, 12 and 13 after infection, cells were collected, washed in PBS, resuspended in 1 × annexin A5 binding buffer (BD Biosciences), and stained with annexin-A5-APC (BD Biosciences) and the viability marker 7-amino-actinomycin D (BD Biosciences). After a 15-min incubation in the dark at room temperature, annexin-A5-positive cells were quantified using a FACS Canto within 1 h.

EdU proliferation assay. Proliferation assay was performed using a Click-it EdU Proliferation kit (Invitrogen) according to manufacturer's instructions. In brief, MEFs were allowed to incorporate EdU (5-ethynyl-2'-deoxyuridine) overnight and then collected and fixed. Fixed cells were stained with Click-it EdU detection reagent, and EdU-positive cells were visualized using a FACS Canto.

Western blots. Cell extracts were prepared using RIPA buffer, resolved on NuPAGE 4–12% gradient Bis-Tris gels, transferred to nitrocellulose and hybridized using antibodies against *Nanog* (1:5,000; Chemicon), *Oct4* (1:500; SantaCruz), *p53* (1:500; Cell Signaling), *p21* (1:500; Santa Cruz), *actin* (1:10,000; Sigma) and *tubulin* (1:10,000; Sigma).

Quantitative FISH analysis. We prepared metaphases and performed quantitative FISH (Q-FISH) hybridization as previously described^{28,29}. To correct for lamp intensity and alignment, images from fluorescent beads (Molecular Probes, Invitrogen) were analysed in parallel, using the TFL-Telo program (a gift from P. Lansdorp). Telomere fluorescence values were extrapolated from the telomere fluorescence of lymphoma cell lines LY-R (R cells) and LY-S (S cells) with known telomere lengths of 80 and 10 kb, respectively. There was a linear correlation ($r^2 = 0.999$) between the fluorescence intensity of the R and S telomeres. We captured the images using a CCD camera (FK7512; COHU) on a fluorescence microscope (DMRB; Leica). We captured the images using Q-FISH software (Leica) in a linear acquisition mode to prevent the over-saturation of fluorescence intensity. TFL-Telo software³⁰ was used to quantify the fluorescence intensity of telomeres from at least six metaphases for each data point.

Chromosomal aberrations. FISH hybridization was performed as described before^{28,29}. At least 15 metaphases per genotype and from at least two independent cultures per genotype were scored for chromosomal aberrations by superimposing the telomere image on the DAPI chromosomes image using the TFL-Telo software.

Histopathology and immunohistochemistry. After mice excision, the specimens were fixed in 10% buffered formalin (Sigma) and embedded in paraffin. For histopathological analysis of teratomas, tumours were serially sectioned (3 μm) to find the different germ-layer components, and every tenth section was stained with haematoxylin and eosin. Remaining sections were used for immunohistochemical studies with the primary antibodies mouse monoclonal anti-phospho-Histone H2A.X (Ser139) (clone JBW30) (1:350; Millipore), goat polyclonal anti-p21 (1:2,000; Santa Cruz Biotechnology), and TUNEL kit (ApopTag, Chemicon)

following manufacturer instructions. Following incubation with the primary antibodies, positive cells were visualized using 3,3'-diaminobenzidine tetrahydrochloride plus (DAB⁺) as a chromogen. Counterstaining was performed with nuclear haematoxylin. Images were captured with a DP-10 digital camera in an Olympus Vanox microscope at the indicated magnifications.

Anaphase bridges in teratomas. For detection of anaphase bridges in the teratomas, samples were fixed in 10% buffered formalin, dehydrated, and embedded in paraffin. Four-micrometre sections were deparaffinized and stained with DAPI. Images were captured using a CCD camera (FK7512; COHU) on a fluorescence microscope (DMRB; Leica).

24. Herrera, E. *et al.* Disease states associated with telomerase deficiency appear earlier in mice with short telomeres. *EMBO J.* **18**, 2950–2960 (1999).
25. Barlow, C. *et al.* *Atm*-deficient mice: a paradigm of ataxia telangiectasia. *Cell* **86**, 159–171 (1996).
26. Blelloch, R., Venere, M., Yen, J. & Ramalho-Santos, M. Generation of induced pluripotent stem cells in the absence of drug selection. *Cell Stem Cell* **1**, 245–247 (2007).
27. Park, I. H. *et al.* Reprogramming of human somatic cells to pluripotency with defined factors. *Nature* **451**, 141–146 (2008).
28. Blasco, M. A. *et al.* Telomere shortening and tumor formation by mouse cells lacking telomerase RNA. *Cell* **91**, 25–34 (1997).
29. Samper, E., Goytisolo, F. A., Slijepcevic, P., van Buul, P. P. & Blasco, M. A. Mammalian Ku86 protein prevents telomeric fusions independently of the length of TTAGGG repeats and the G-strand overhang. *EMBO Rep.* **1**, 244–252 (2000).
30. Zijlmans, J. M. *et al.* Telomeres in the mouse have large inter-chromosomal variations in the number of T2AG3 repeats. *Proc. Natl Acad. Sci. USA* **94**, 7423–7428 (1997).

LETTERS

Initiation of myoblast to brown fat switch by a PRDM16-C/EBP- β transcriptional complexShingo Kajimura^{1,2}, Patrick Seale^{1,2}, Kazuishi Kubota², Elaine Lunsford³, John V. Frangioni³, Steven P. Gygi² & Bruce M. Spiegelman^{1,2}

Brown adipose cells are specialized to dissipate chemical energy in the form of heat, as a physiological defence against cold and obesity¹. PRDM16 (PR domain containing 16) is a 140 kDa zinc finger protein that robustly induces brown fat determination and differentiation². Recent data suggests that brown fat cells arise *in vivo* from a *Myf5*-positive, myoblastic lineage by the action of PRDM16 (ref. 3); however, the molecular mechanisms responsible for this developmental switch is unclear. Here we show that PRDM16 forms a transcriptional complex with the active form of C/EBP- β (also known as LAP), acting as a critical molecular unit that controls the cell fate switch from myoblastic precursors to brown fat cells. Forced expression of PRDM16 and C/EBP- β is sufficient to induce a fully functional brown fat program in naive fibroblastic cells, including skin fibroblasts from mouse and man. Transplantation of fibroblasts expressing these two factors into mice gives rise to an ectopic fat pad with the morphological and biochemical characteristics of brown fat. Like endogenous brown fat, this synthetic brown fat tissue acts as a sink for glucose uptake, as determined by positron emission tomography with fluorodeoxyglucose. These data indicate that the PRDM16-C/EBP- β complex initiates brown fat formation from myoblastic precursors, and may provide opportunities for the development of new therapeutics for obesity and type-2 diabetes.

Because of the importance of brown adipose tissue (BAT) as a natural defence against hypothermia and obesity¹, and its demonstrated presence in adult humans^{4–7}, understanding its formation in mechanistic detail may open new avenues to the development of new therapeutics for metabolic diseases such as obesity and type-2 diabetes. Several transcriptional regulators have been identified that positively or negatively control BAT development including RB1 (ref. 8), p107 (also known as RBL1)⁹, RIP140 (NRIP1)¹⁰ and FOXC2 (ref. 11). Most recently, we have shown that PRDM16, a 140-kDa zinc finger protein, functions as a bidirectional switch in brown fat cell fate by stimulating the development of brown fat cells from white preadipocytes^{12,13} and from *Myf5*-positive myoblastic precursors³ *in vitro* and *in vivo*. At a molecular level, PRDM16 works as a transcriptional co-regulatory protein by co-activating PPAR γ (peroxisome proliferator-activated receptor γ), which is considered the 'master' gene of fat cell differentiation^{14,15}, and this is almost certainly an important event in the conversion of myoblasts to brown adipocytes³. However, both isoforms of PPAR γ are expressed at very low levels in primary and immortalized myoblasts, whereas they are abundantly expressed in white and brown preadipocytes (Supplementary Fig. 1). Hence, it is very likely that PRDM16 initiates the process of myoblast to brown fat conversion by complexing with other DNA-binding factors, well before the co-activation of PPAR γ .

We therefore devised a strategy to address this, as illustrated in Fig. 1a. In brief, we performed proteomic analyses of transcriptional

complexes formed with wild-type PRDM16 or different mutant alleles that were differentiation-competent or -incompetent. Transcription factors that co-purified preferentially with differentiation-competent PRDM16 proteins were identified; their expression in white and brown fat was then analysed and compared to that of PRDM16. Subsequently, we examined their function in the process of myoblast to brown fat conversion through PRDM16.

As shown in Fig. 1b, wild type PRDM16 and a mutant protein lacking the PR (PRD1-BF1-RIZ1 homologous) domain (Δ PR; amino acids 91–223) that shares homology to the SET chromatin remodelling domain^{16,17}, induced brown fat cell differentiation from myoblasts. In

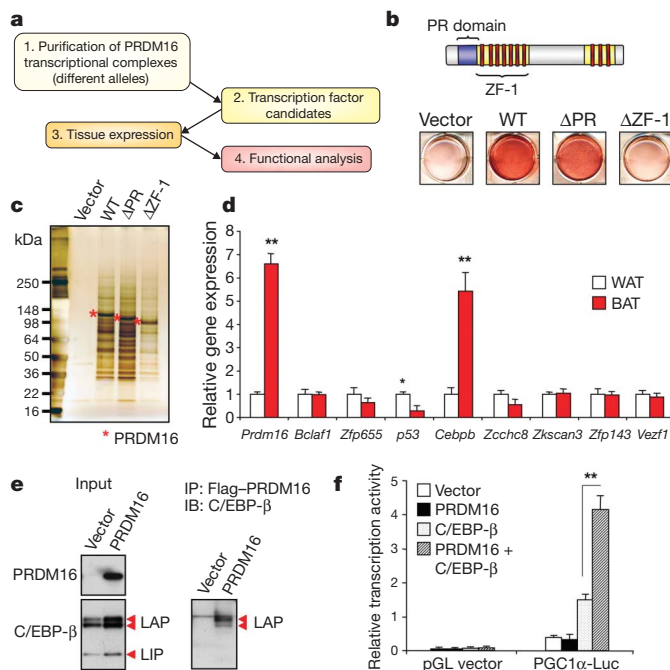


Figure 1 | Identification of C/EBP- β as a critical binding partner in the PRDM16 transcriptional complex. **a**, Strategy to identify key PRDM16 binding partners. **b**, C2C12 myoblasts expressing indicated viral vectors were stained with Oil Red O 6 days after inducing adipocyte differentiation. **c**, PRDM16 transcriptional complex was immunopurified from brown fat cells expressing full-length or deletion mutants of PRDM16. **d**, Gene expression of known or predicted transcription factors identified in the PRDM16 complex in BAT and WAT. $n = 6$. **e**, Endogenous C/EBP- β was detected in the PRDM16 complex by western blotting. Input is shown to the left. IB, immunoblot; IP, immunoprecipitate. **f**, Transcriptional activity of the *Pgc1 α* promoter in response to PRDM16 and/or C/EBP- β . $n = 3$; all error bars are s.e.m.; * $P < 0.05$, ** $P < 0.01$.

¹Dana-Farber Cancer Institute, ²Department of Cell Biology, Harvard Medical School, 44 Binney Street, Boston, Massachusetts 02115, USA. ³Division of Hematology/Oncology, Beth Israel Deaconess Medical Center, 330 Brookline Avenue, Boston, Massachusetts 02215, USA.

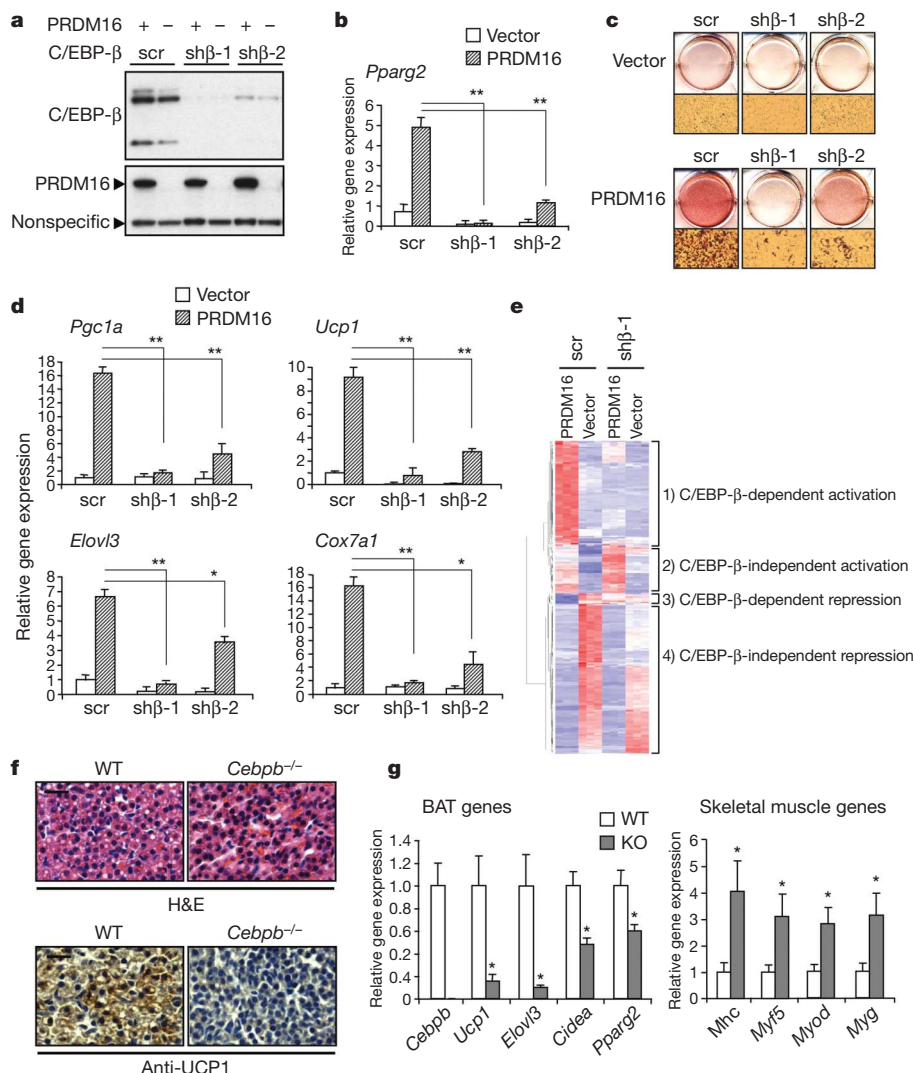


Figure 2 | C/EBP- β is required for initiation of the myoblast to brown fat conversion by PRDM16. **a**, Western blot analysis for C/EBP- β and PRDM16 in C2C12 myoblasts expressing scr, sh β -1 or sh β -2, with PRDM16 or vector. **b**, *Pparg2* gene expression. **c**, The cells were stained with Oil Red O 6 days after inducing adipocyte differentiation. **d**, BAT-selective gene expression. **e**, Microarray analysis of undifferentiated C2C12

contrast, a mutant allele lacking zinc finger domain-1 (Δ ZF-1; amino acids 224–447) completely lost its adipogenic function. The brown fat gene program was also induced by both wild-type and Δ PR, but not by Δ ZF-1 (Supplementary Fig. 2). To avoid comparing proteomic analyses of complexes from cells of very different phenotypes, we expressed all three PRDM16 forms in bona fide brown fat cells. PRDM16 complexes were then immunopurified to apparent homogeneity (Fig. 1c), and subjected to high-resolution ‘shotgun’ sequencing by liquid chromatography with tandem mass spectrometry (LC–MS/MS)¹⁸. In total, 49 proteins were identified in differentiation-competent PRDM16 complexes, but only eight of these (*Bclaf1*, *Zfp655*, *p53* (also known as *Trp53*), *Cebpb*, *Zcchc8*, *Zkscan3*, *Zfp143* and *Vezf1*) are known or predicted transcription factors (Supplementary Table 1). Because we have assumed that the expression of a key initiating transcription factor would not be extinguished during the brown fat cell adipogenesis, and as PRDM16 is highly enriched in BAT relative to white adipose tissue (WAT)¹³, we asked whether any of these factors were similarly enriched in BAT. As shown in Fig. 1d, the expression of only *Cebpb* (C/EBP- β) was co-enriched with PRDM16 in BAT versus WAT. In addition, C/EBP- β protein was enriched in BAT, and further induced by cold exposure (Supplementary Fig. 3). Notably, both primary and immortalized myoblasts express C/EBP- β at similar levels to those seen in

myoblasts expressing scr or sh β -1 with PRDM16 or vector. **f**, Top, haematoxylin and eosin (H&E) staining of BAT from wild-type (WT) and C/EBP- β knockout (KO) mice. Bottom, immunohistochemistry to detect UCP1 expression. Scale bars, 20 μ m. **g**, mRNA expression of BAT and skeletal-muscle-selective genes in BAT from E17.5 embryos. **n** = 5–8; all error bars are s.e.m.; * P < 0.05, ** P < 0.01.

preadipocytes (Supplementary Fig. 4), where this factor is thought to have a very important role in adipogenesis^{19,20}. Our analyses have therefore been focused on C/EBP- β and its function in complex with PRDM16.

Brown fat cells express three forms of C/EBP- β , two active forms, named LAP (liver-enriched transcriptional activator protein) and a dominant-negative form, LIP (liver-enriched transcriptional inhibitory protein)²¹ (Fig. 1e, left). Notably, PRDM16 preferentially bound to LAP, but not to LIP (Fig. 1e, right and Supplementary Fig. 5). Independent co-expression assays in HEK293 cells confirmed the physical binding of PRDM16 and C/EBP- β . Furthermore, PRDM16 interacts with other C/EBP family members, C/EBP- α and - δ (Supplementary Fig. 6). This interaction is likely to be direct through the two zinc finger domains, because the zinc finger domains of the purified glutathione S-transferase (GST)-fused PRDM16 bound to *in vitro* translated C/EBP- β (Supplementary Fig. 7). We also addressed whether PRDM16 could affect the transcriptional activity of C/EBP- β . Because C/EBP- β is known to induce *Pgc1a* (also known as *Pparg1a*) gene expression²², we performed a luciferase reporter assay using the –2 kilobase (kb) *Pgc1a* promoter where the C/EBP-binding sites have been characterized²². As shown in Fig. 1f, the expression of PRDM16 and C/EBP- β synergistically stimulated *Pgc1a* promoter activity. These

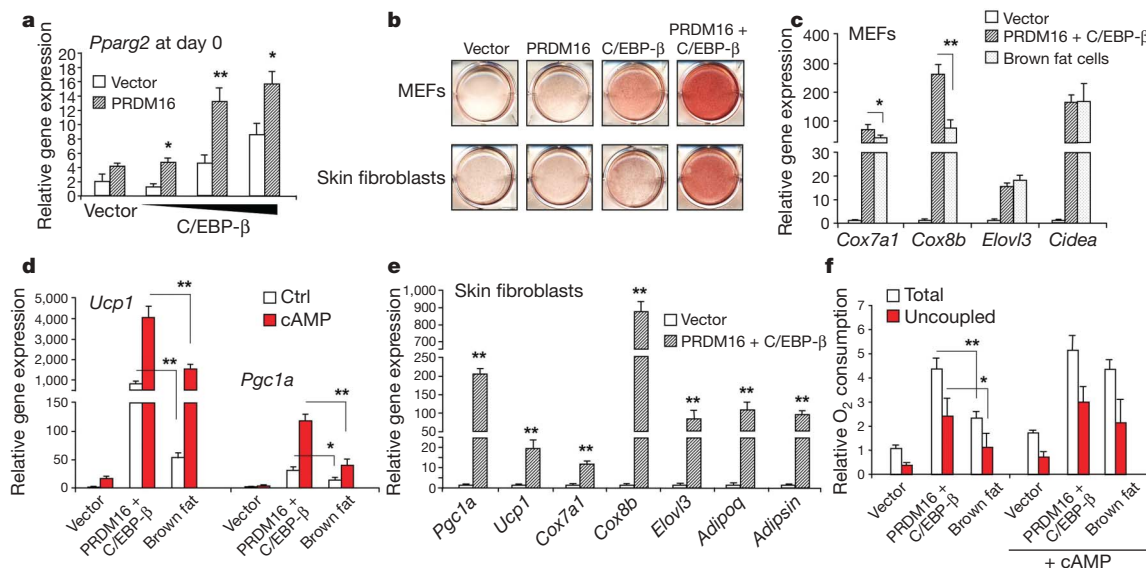


Figure 3 | Reconstitution of the brown fat gene program in fibroblasts by PRDM16 and C/EBP- β . **a**, *Pparg2* expression in undifferentiated MEFs expressing indicated viral vectors. $n = 3$. **b**, Immortalized MEFs or skin fibroblasts expressing indicated viral vectors were stained with Oil Red O 6–8 days after inducing adipocyte differentiation. **c**, BAT-selective gene expression. **d**, Thermogenic gene expression. The cells were treated with

cAMP for 4 h. $n = 4$; ctrl, control. **e**, BAT-selective gene expression in primary skin fibroblasts expressing vector or PRDM16 and C/EBP- β . $n = 3$. *Adipsin* is also known as *Cfd*. **f**, Total and uncoupled cellular respiration in differentiated brown fat cells and the MEFs expressing vector or PRDM16 and C/EBP- β . The cells were treated with dibutyryl-cAMP for 12 h. $n = 3$; all error bars are s.e.m.; * $P < 0.05$, ** $P < 0.01$.

data suggest that PRDM16 forms a transcriptional complex with active forms of C/EBP- β by direct interaction, and regulates their transcriptional activity.

To examine the functional role of the interaction between PRDM16 and C/EBP- β in the myoblast to brown fat conversion, retroviruses expressing a short hairpin (sh) scrambled control RNA (scr), or shRNAs targeting C/EBP- β (sh β -1 and sh β -2) were transduced together with PRDM16 or an empty vector into C2C12 myoblasts (Fig. 2a). As shown in Fig. 2b, knockdown of C/EBP- β significantly blunted the induction of *Pparg2* expression by PRDM16 in undifferentiated C2C12 myoblasts. Consistent with this result, Oil Red O staining showed that depletion of C/EBP- β blunted the adipogenesis induced by PRDM16 (Fig. 2c). Furthermore, induction of brown-fat-selective genes including *Pgc1a*, *Ucp1*, *Elovl3* and *Cox7a1* were completely or partially blocked by knockdown of C/EBP- β , correlating with the knockdown efficacy (Fig. 2d). In addition, we ectopically expressed LIP, a dominant-negative form of C/EBP- β , and this also significantly blunted PRDM16-induced adipogenesis and brown-fat-selective gene expression (Supplementary Fig. 8).

Next, we took a systematic approach to determine what fraction of the PRDM16-regulated genes requires C/EBP- β at the initiating step of the myoblast to brown fat conversion. To this end, RNAs from undifferentiated C2C12 myoblasts expressing PRDM16 or control together with scr or sh β -1, maintained under conditions non-permissive for differentiation, were subjected to Affymetrix microarray analysis. As shown in Fig. 2e, 316 genes were significantly increased or reduced by PRDM16 (>twofold, $P < 0.05$), which were clustered into four groups: (1) genes increased by PRDM16 in a C/EBP- β -dependent manner, (2) genes increased by PRDM16 in a C/EBP- β -independent manner, (3) genes repressed by PRDM16 in a C/EBP- β -dependent manner, and (4) genes repressed by PRDM16 in a C/EBP- β -independent manner. The expression of a subset of genes identified by microarray analyses was validated by PCR with reverse transcription (RT-PCR) (Supplementary Fig. 9). Notably, most genes activated by PRDM16 before differentiation (62 out of 95, 65.3%) indeed required C/EBP- β , whereas most of the repressed genes (210 out of 221, 95.0%) were not grossly altered by C/EBP- β depletion.

We explored further the genetic requirement for C/EBP- β in brown fat development by analysing C/EBP- β -deficient embryos. Defects in BAT of C/EBP- β -null newborn or adult mice have been described, although the reported phenotype was inconsistent^{23,24}. Because a large number of these embryos died within the first 24 h after birth^{23,25}, we have re-examined this issue in late gestation (stage embryonic day (E)18.5). This should permit a clearer separation of developmental changes in the BAT, as opposed to those that might occur secondarily to abnormalities in other tissues after birth. As shown in Fig. 2f, haematoxylin and eosin staining showed that brown fat cells in knockout embryos contained significantly less lipid droplets than those in wild-type embryos, suggesting defects in brown fat development per se (Fig. 2f, top). Moreover, UCP1 expression was severely reduced in knockout embryos (Fig. 2f, bottom), consistent with the results described previously²³. We also conducted a definitive molecular characterization of the BAT from wild-type and knockout embryos. Notably, BAT from C/EBP- β -knockout mice nearly phenocopied that from PRDM16-knockout mice at the gene expression level; that is, a broad reduction of BAT-selective gene expression, and a broad induction of the skeletal muscle gene expression (Fig. 2g). Together, these data indicate that the PRDM16–C/EBP- β transcriptional complex specifically has a critical role in the initiation of myoblast to brown fat switch. This strongly suggests that PRDM16 acts in *Myf5*-positive myoblastic precursors, at least in part, by co-activation of C/EBP- β to induce the expression of *Pparg* and *Pgc1a*. Subsequently, PRDM16 co-activates PPAR γ and PGC-1 α by direct binding events, which drives a complete brown fat differentiation program (Supplementary Fig. 10).

This mechanistic model suggests a critical question: are the two factors sufficient to reconstitute a brown fat program in naive cells? To this end, PRDM16 and C/EBP- β were ectopically expressed in mouse embryonic fibroblasts (MEFs) or primary skin fibroblasts with no inherent adipose or brown fat character. As shown in Fig. 3a, *Pparg2* messenger RNA expression was synergistically induced by PRDM16 and C/EBP- β in a dose-dependent manner in undifferentiated fibroblasts. After 6–8 days under adipogenic conditions, both MEFs and skin fibroblasts expressing these two factors uniformly differentiated into lipid-filled adipocytes, as shown by Oil Red O staining (Fig. 3b). The single factors alone were not sufficient

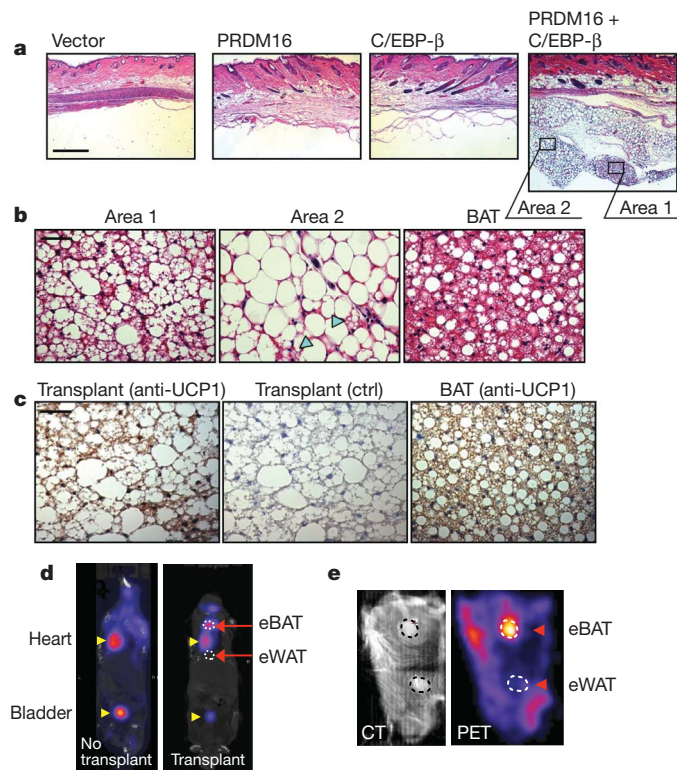


Figure 4 | Generation of functional brown adipose tissue *in vivo* by expression of PRDM16 and C/EBP- β . **a**, Fat pads from transplanted MEFs expressing indicated viral vectors were stained by H&E. Scale bar, 500 μ m. **b**, High magnification images of H&E staining in the transplants expressing PRDM16 and C/EBP- β , and endogenous BAT. Arrowheads show multilocular fat cells. Scale bar, 50 μ m. **c**, Immunohistochemistry to detect UCP1 expression in the transplant (left, anti-UCP1; middle, negative control) and BAT (right). Scale bar, 50 μ m. **d**, PET/computed tomography image of mice with engineered BAT (eBAT) and engineered WAT (eWAT). **e**, Computed tomography (CT) image (left) and PET image (right) of mouse skin with the eBAT and eWAT.

to robustly stimulate the differentiated state. Gene expression studies showed that PRDM16 and C/EBP- β powerfully induced mRNA levels of brown fat genes including *Cox7a1* (70-fold), *Cox8b* (260-fold), *Elovl3* (16-fold) and *Cidea* (170-fold) to levels comparable with or even higher than those seen in bona fide immortalized brown fat cells (Fig. 3c). Notably, as in authentic brown fat cells, mRNA level of thermogenic genes such as *Pgc1a* and *Ucp1* were further enhanced by cyclic AMP treatment (Fig. 3d). The mechanism underlying the augmentation of cAMP effects in the engineered brown fat cells remains unknown. To our surprise, the mRNA levels of those genes at the basal state were activated to levels seen in cAMP-stimulated brown fat cells. Furthermore, the two factors were able to induce the brown fat gene program from primary mouse skin fibroblasts (Fig. 3e) and human skin fibroblasts isolated from newborn foreskin (Supplementary Fig. 11).

An important characteristic of brown fat cells is their extraordinarily high rates of respiration, particularly uncoupled respiration in response to cAMP. As shown in Fig. 3f, engineered brown fat cells induced by these two factors have significantly higher levels of total and uncoupled respiration than control cells, by 4.4- and 6.5-fold, respectively, at the basal state. It is notable that the engineered cells have greater basal respiration, both total and uncoupled, than bona fide brown fat cells. However, whereas the bona fide brown fat cells can increase both total and uncoupled respiration further (by 85% and 90%, respectively) in response to cAMP, engineered brown fat cells already seem to be at their maximal respiration. That these cells are responsive to cAMP is shown by the fact that expression of thermogenic genes, such as *Pgc1a* and *Ucp1*, are induced by cAMP

treatment (Fig. 3d). Hence, some other aspect of the respiratory apparatus, unknown at this point, seems to be limiting in the engineered brown fat cells.

The finding that the combination of PRDM16 and C/EBP- β is sufficient to reconstitute a near complete brown fat program offers an opportunity for controlling brown fat levels and function *in vivo*. We conducted transplantation studies, as originally developed by Green and Kehinde²⁶, using undifferentiated MEFs expressing vector, PRDM16, C/EBP- β , or a combination of the two factors. As shown by haematoxylin and eosin staining (Fig. 4a), the cells expressing vector or PRDM16 or C/EBP- β alone did not form visible fat tissues. In contrast, the cells expressing both PRDM16 and C/EBP- β formed very distinct fat pads *in vivo*. Notably, at high magnification, the engineered fat tissue induced by the two factors contained 'multilocular' fat cells, a morphological characteristic of brown fat *in vivo* (Fig. 4b). The population of multilocular fat cells (area 1) is mixed with regions of 'unilocular' fat cells (area 2). Notably, immunohistochemical analyses showed that the engineered adipose tissue was UCP1-positive in both the multilocular and unilocular fat cells (Fig. 4c).

To characterize the activity of engineered brown fat tissue *in vivo* further, we used positron emission tomography (PET) with fluoro-deoxyglucose (¹⁸FDG), which has recently been used to detect active BAT in adult humans⁴⁻⁷. This technique measures glucose uptake, with brown fat functioning *in vivo* as an active 'sink' for glucose. To this end, we engineered two adipose tissues with similar sizes in the same nude mice: a 'brown' fat tissue induced by PRDM16 and C/EBP- β , and a 'white' fat tissue induced by PPAR γ alone as a control (Supplementary Fig. 12a). The induction of BAT-selective genes by PRDM16 and C/EBP- β was confirmed in the cultured cells by RT-PCR (Supplementary Fig. 12b). As shown in Fig. 4d, PET scanning detected a signal in mice from the engineered BAT. To enhance the sensitivity and specificity of the PET signal from the engineered fat tissues, the skin with these fat tissues attached was removed and scanned. The combination of computed tomography image (Fig. 4e, left) and PET image (Fig. 4e, right) clearly showed that the PET signal was detected from the engineered BAT, but not from the engineered WAT. These results indicate that the engineered brown fat cells function as a sink for active glucose disposal. Given the incredible capacity of BAT to dissipate stored chemical energy and thus counteract obesity, we are optimistic that the PRDM16 pathway can be used to drive brown fat development *in vivo* in a therapeutic setting. Certainly natural or synthetic compounds that can induce PRDM16 in white fat precursors or in myoblastic cells could have great value in human metabolic disease. Alternatively, as shown here, autologous transplantation of engineered brown fat induced by PRDM16 and C/EBP- β in amounts that are both clinically acceptable and therapeutically useful may well be possible. Future experiments must define the optimal conditions to achieve maximal angiogenesis, innervation and resulting energy expenditure from autologous transplants.

METHODS SUMMARY

Cell culture. Immortalized brown fat cells have been described previously²⁷. Mouse embryonic fibroblasts were isolated from E13.5 C57/Bl6 embryos, and immortalized according to the established methods²⁸. R2F primary skin fibroblasts isolated from human newborn foreskin were a gift from J. G. Rheinwald and cultured following the methods described elsewhere²⁹. Adipocyte differentiation in fibroblasts was induced with medium containing 5 μ M dexamethasone, 850 nM insulin, 1 nM T3 and 1 μ M rosiglitazone.

Identification of the PRDM16 transcriptional complex. Immortalized brown fat cells stably expressing Flag-tagged PRDM16 were homogenized to prepare nuclear extracts. The nuclear extracts were incubated with Flag M2 agarose (Sigma), washed in a binding buffer, and eluted by incubating with Flag peptide¹². The immunoprecipitated proteins were digested by trypsin and subjected to reverse-phase LC-MS/MS, using a high-resolution hybrid mass spectrometer (LTQ-Orbitrap, Thermo Scientific) with TOP10 method¹⁸.

Animal experiments. All animal experiments were performed according to procedures approved by Beth Israel Deaconess Medical Center Institutional Animal Care and Use Committee. C/EBP- β -null mice (Cebpb^{tm1Vpo/J}) were obtained from the Jackson Laboratory. For transplantation studies, immortalized

MEFs, transduced with retroviral PRDM16 and/or C/EBP- β , were implanted subcutaneously into 7–9-week-old male nude mice (NCR-*Foxn1*tm)^{13,26}. For PET scanning studies, MEFs expressing retroviral PPAR γ were implanted as control. After 4–6 weeks, fat pads were dissected for histological analysis. MicroPET/computed tomography (CT) scanning was performed using the Mosaic HP microPET in conjunction with the microCT of the NanoSPECT/CT (Philips), 60 min after the injection of ¹⁸F-FDG.

Full Methods and any associated references are available in the online version of the paper at www.nature.com/nature.

Received 1 June; accepted 13 July 2009.

Published online 29 July 2009.

- Cannon, B. & Nedergaard, J. Brown adipose tissue: function and physiological significance. *Physiol. Rev.* **84**, 277–359 (2004).
- Seale, P., Kajimura, S. & Spiegelman, B. M. Transcriptional control of brown adipocyte development and physiological function—of mice and men. *Genes Dev.* **23**, 788–797 (2009).
- Seale, P. *et al.* PRDM16 controls a brown fat/skeletal muscle switch. *Nature* **454**, 961–967 (2008).
- Nedergaard, J., Bengtsson, T. & Cannon, B. Unexpected evidence for active brown adipose tissue in adult humans. *Am. J. Physiol. Endocrinol. Metab.* **293**, E444–E452 (2007).
- Cypess, A. M. *et al.* Identification and importance of brown adipose tissue in adult humans. *N. Engl. J. Med.* **360**, 1509–1517 (2009).
- van Marken Lichtenbelt, W. D. *et al.* Cold-activated brown adipose tissue in healthy men. *N. Engl. J. Med.* **360**, 1500–1508 (2009).
- Virtanen, K. A. *et al.* Functional brown adipose tissue in healthy adults. *N. Engl. J. Med.* **360**, 1518–1525 (2009).
- Hansen, J. B. *et al.* Retinoblastoma protein functions as a molecular switch determining white versus brown adipocyte differentiation. *Proc. Natl Acad. Sci. USA* **101**, 4112–4117 (2004).
- Scime, A. *et al.* Rb and p107 regulate preadipocyte differentiation into white versus brown fat through repression of PGC-1 α . *Cell Metab.* **2**, 283–295 (2005).
- Leonardsson, G. *et al.* Nuclear receptor corepressor RIP140 regulates fat accumulation. *Proc. Natl Acad. Sci. USA* **101**, 8437–8442 (2004).
- Cederberg, A. *et al.* FOXO2 is a winged helix gene that counteracts obesity, hypertriglyceridemia, and diet-induced insulin resistance. *Cell* **106**, 563–573 (2001).
- Kajimura, S. *et al.* Regulation of the brown and white fat gene programs through a PRDM16/CtBP transcriptional complex. *Genes Dev.* **22**, 1397–1409 (2008).
- Seale, P. *et al.* Transcriptional control of brown fat determination by PRDM16. *Cell Metab.* **6**, 38–54 (2007).
- Tontonoz, P., Hu, E. & Spiegelman, B. M. Stimulation of adipogenesis in fibroblasts by PPAR γ , a lipid-activated transcription factor. *Cell* **79**, 1147–1156 (1994).
- Tontonoz, P. & Spiegelman, B. M. Fat and beyond: the diverse biology of PPAR γ . *Annu. Rev. Biochem.* **77**, 289–312 (2008).
- Mochizuki, N. *et al.* A novel gene, MEL1, mapped to 1p36.3 is highly homologous to the MDS1/EVI1 gene and is transcriptionally activated in t(1;3)(p36;q21)-positive leukemia cells. *Blood* **96**, 3209–3214 (2000).
- Shing, D. C. *et al.* Overexpression of sPRDM16 coupled with loss of p53 induces myeloid leukemias in mice. *J. Clin. Invest.* **117**, 3696–3707 (2007).
- Haas, W. *et al.* Optimization and use of peptide mass measurement accuracy in shotgun proteomics. *Mol. Cell. Proteomics* **5**, 1326–1337 (2006).
- Wu, Z., Xie, Y., Bucher, N. L. & Farmer, S. R. Conditional ectopic expression of C/EBP β in NIH-3T3 cells induces PPAR γ and stimulates adipogenesis. *Genes Dev.* **9**, 2350–2363 (1995).
- Farmer, S. R. Transcriptional control of adipocyte formation. *Cell Metab.* **4**, 263–273 (2006).
- Descombes, P. & Schibler, U. A liver-enriched transcriptional activator protein, LAP, and a transcriptional inhibitory protein, LIP, are translated from the same mRNA. *Cell* **67**, 569–579 (1991).
- Wang, H. *et al.* CCAAT/enhancer binding protein- β is a transcriptional regulator of peroxisome-proliferator-activated receptor- γ coactivator-1 α in the regenerating liver. *Mol. Endocrinol.* **22**, 1596–1605 (2008).
- Tanaka, T., Yoshida, N., Kishimoto, T. & Akira, S. Defective adipocyte differentiation in mice lacking the C/EBP β and/or C/EBP δ gene. *EMBO J.* **16**, 7432–7443 (1997).
- Carmona, M. C. *et al.* Defective thermoregulation, impaired lipid metabolism, but preserved adrenergic induction of gene expression in brown fat of mice lacking C/EBP β . *Biochem. J.* **389**, 47–56 (2005).
- Scrapanti, I. *et al.* Lymphoproliferative disorder and imbalanced T-helper response in C/EBP β -deficient mice. *EMBO J.* **14**, 1932–1941 (1995).
- Green, H. & Kehinde, O. Formation of normally differentiated subcutaneous fat pads by an established preadipose cell line. *J. Cell. Physiol.* **101**, 169–171 (1979).
- Uldry, M. *et al.* Complementary action of the PGC-1 coactivators in mitochondrial biogenesis and brown fat differentiation. *Cell Metab.* **3**, 333–341 (2006).
- Todaro, G. J. & Green, H. Quantitative studies of the growth of mouse embryo cells in culture and their development into established lines. *J. Cell Biol.* **17**, 299–313 (1963).
- Rheinwald, J. G. *et al.* A two-stage, p16(INK4A)- and p53-dependent keratinocyte senescence mechanism that limits replicative potential independent of telomere status. *Mol. Cell. Biol.* **22**, 5157–5172 (2002).

Supplementary Information is linked to the online version of the paper at www.nature.com/nature.

Acknowledgements We are grateful to S. R. Farmer, J. Rheinwald and P. F. Johnson for providing cells and other reagents, R. Gupta for his critical comments on the manuscript, and J. Y. Choi and E. Naseri for their assistance. S.K. is supported by AHA scientist development grant (0930125N). P.S. is supported by a National Institutes of Health (NIH) grant (DK081605). This work was supported by grants from the Picower Foundation and the NIH (DK31405) to B.M.S., NIH HG3456 and GM67945 to S.P.G., and NIH/NCRR shared instrumentation grant S10-RR-023010.

Author Contributions S.K. and B.M.S. conceived and designed the experiments. S.K., K.K. and E.L. performed the experiments. All of the authors analysed the data. S.K. and B.M.S. wrote the paper.

Author Information Microarray data has been deposited in the Gene Expression Omnibus (GEO) public database under accession GSE15895. Reprints and permissions information is available at www.nature.com/reprints. Correspondence and requests for materials should be addressed to B.M.S. (bruce_spiegelman@dfci.harvard.edu).

METHODS

Cell culture. Immortalized brown fat cells have been described previously²⁷. Mouse embryonic fibroblasts were isolated from E13.5 C57/Bl6 embryos (Jackson Laboratory), and immortalized according to the methods previously described²⁸. Mouse dermal fibroblasts were obtained from Millipore. R2F primary skin fibroblasts isolated from human newborn foreskin were a gift from J. G. Rheinwald, and were cultured as per methods described elsewhere²⁹. HEK293 cells and C2C12 cells were obtained from ATCC. Adipocyte differentiation in C2C12 cells was induced by treating confluent cells in DMEM containing 10% FBS, 0.5 mM isobutylmethylxanthine, 125 nM indomethacin, 5 μ M dexamethasone, 850 nM insulin, 1 nM T3 and 1 μ M rosiglitazone. Two days after induction, cells were switched to the maintenance medium containing 10% FBS, 850 nM insulin, 1 nM T3 and 1 μ M rosiglitazone. Adipocyte differentiation in fibroblasts was induced with medium containing 5 μ M dexamethasone, 850 nM insulin, 1 nM T3 and 1 μ M rosiglitazone. For cAMP treatment, cells were incubated with 10 μ M forskolin or 0.5 mM dibutyryl-cAMP. All chemicals for cell culture were obtained from Sigma unless otherwise indicated.

DNA constructs and viruses production. Deletion mutants of Flag-tagged PRDM16 were amplified by PCR using full-length PRDM16 as a template, and subcloned into pMSCV-puro retroviral vector (Stratagene). Various fragments of GST-fused PRDM16 fragments (1–223, 224–454, 455–680, 680–880, 881–1038 and 1039–1176) were described previously¹². Myc-tagged C/EBP- β constructs³⁰ were gifts from S. R. Farmer. The sequences used for retroviral shRNA expression vectors targeting C/EBP- β were 5'-GCCCTGAGTAATCACTTAAAG-3' (sh β -1) and 5'-CCGGGCCCTGAGTAATCAC-3' (sh β -2). The corresponding double-stranded DNA sequences were ligated into pSUPER-Retro (Oligoengine) for retroviral expression. For retrovirus production, Phoenix packaging cells³¹ were transfected at 70% confluence by calcium phosphate method with 10 μ g retroviral vectors. After 48 h, the viral supernatant was collected and filtered. Cells were incubated overnight with the viral supernatant, supplemented with 8 μ g ml⁻¹ polybrene. Subsequently, puromycin (PRDM16), hygromycin (C/EBP- β) or G418 (shRNAs) were used for selection. Fibroblasts expressing both PRDM16 and C/EBP- β were selected by puromycin and hygromycin to ensure expression of both constructs.

Affinity purification of PRDM16 transcriptional complex. Immortalized brown fat cells stably expressing Flag-tagged wild-type, PRA mutant, and ZF-1A mutant of PRDM16 or an empty vector were grown to confluence. The cells were homogenized to prepare nuclear extracts¹². The nuclear extracts were incubated overnight with Flag M2 agarose (Sigma), washed in a binding buffer (180 mM KCl), and then eluted by incubating with 1 \times Flag peptide (0.2 mg ml⁻¹). The eluted materials were TCA precipitated, separated in a 4–20% acrylamide gradient gel, and visualized by silver staining, as described previously¹².

Mass spectrometry. The immunoprecipitated proteins were precipitated with methanol and chloroform, and precipitates were dissolved in 50 mM Tris-HCl, pH 7.5, containing 8 M urea, 50 mM EDTA and 0.005% *n*-dodecyl β -D-maltoside (DDM). Proteins were reduced with dithiothreitol (DTT) and alkylated with iodoacetamide. After diluting urea concentration to 1 M with 50 mM Tris-HCl, pH 7.5, containing 0.005% DDM, trypsin was added and proteins were digested in solution at 37 °C for 12 h. The reaction was stopped with formic acid, and the resultant peptides were desalted with StageTips³². Desalted peptides were subjected to reverse-phase LC-MS/MS using a high-resolution hybrid mass spectrometer (LTQ-Orbitrap, Thermo Scientific) with TOP10 method, as described previously¹⁸. The obtained data were searched against the International Protein Index (IPI) mouse database³³. Proteins were identified with at least two unique valid peptides, and the false discovery rate was estimated to be 0% using target-decoy approach³⁴.

Protein interaction analysis. HEK293 cells expressing PRDM16 or C/EBPs were collected 24 h after transfection. Total cell lysates were incubated overnight at 4 °C with Flag M2 agarose, washed and eluted with Flag peptide. The eluted materials were analysed by western blot using antibodies against C/EBP- α , C/EBP- β and C/EBP- δ (Santa Cruz). For *in vitro* binding assays, various fragments of the GST-fusion PRDM16 fragments were purified as described previously¹². [³⁵S]-labelled proteins were made with a TNT reticulocyte lysate kit (Promega). Equal amounts of GST-fusion proteins (2 μ g) were incubated overnight at 4 °C with *in vitro* translated proteins in a binding buffer containing 20 mM HEPES, pH 7.7, 300 mM KCl, 2.5 mM MgCl₂, 0.05% NP40, 1 mM

DTT and 10% glycerol. The sepharose beads were then washed five times with the binding buffer. Bound proteins were separated by SDS-PAGE and analysed by autoradiography.

Gene expression analysis. Total RNA was isolated from cells or tissues using Trizol (Invitrogen). Reverse transcriptase reactions were performed using a cDNA reverse transcription kit (Applied Biosystems). The sequences of primers used in this study are found in Supplementary Table 2. Quantitative real-time PCR was performed with SYBR green fluorescent dye using an ABI9300 PCR machine. TATA-binding protein acted as an internal control.

Microarray analysis. Total RNA was isolated from undifferentiated C2C12 cells transduced with scr or sh β together with PRDM16 or vector control. Array hybridization and scanning were performed by the Dana-Farber Cancer Institute Core Facility using Affymetrix GeneChip Mouse Genome 430 2.0 arrays according to established methods³⁵. The array data were analysed using the DNA-Chip Analyser software³⁶. The statistical significance of differences in gene expression was assessed using an unpaired *t*-test ($P < 0.05$).

Reporter gene assay. The *PGC1A* (–2 kb) promoter linked to a luciferase reporter was transiently co-transfected with PRDM16 and/or C/EBP- β expression plasmids in brown preadipocytes using Lipofectamine 2000 (Invitrogen). Forty-eight hours after the transfection, cells were collected and reporter gene assays were carried out using the Dual Luciferase Kit (Promega). Transfection efficiency was normalized by measuring expression of *Renilla* luciferase.

Cellular respiration assay. Immortalized brown fat cells or MEFs transduced with retroviral PRDM16 and C/EBP- β or an empty vector were grown to confluence and induced to differentiate. At day 6 or 7 of differentiation, oxygen consumption was measured as described previously^{12,13}. For cAMP-induced respiration assays, fully differentiated fat cells were incubated with 0.5 mM dibutyryl-cAMP for 12 h before measuring oxygen consumption.

Animals. All animal experiments were performed according to procedures approved by Beth Israel Deaconess Medical Center Institutional Animal Care and Use Committee. C/EBP- β -null mice (Cebpb^{tm1Vpo/J}) were obtained from the Jackson Laboratory. For transplantation studies, male NCR-nude mice (NCR-*Foxn1*^{nu/nu}) were obtained from Taconic.

Cell transplantations. Immortalized MEFs (3×10^7) were transduced with retroviral PRDM16, C/EBP- β , vector control, or a combination of PRDM16 and C/EBP- β , and implanted subcutaneously into 7–9-week-old male nude mice ($n = 6$ mice per group), according to the methods described previously^{13,26}. For PET scanning studies, MEFs expressing retroviral PPAR γ alone were implanted as a control. After 4–6 weeks, fat pads were carefully dissected and fixed in 4% paraformaldehyde for histological analysis. For immunohistochemistry, paraffin-embedded sections were incubated with anti-UCP1 antibody (Chemicon), followed by detection using the ABC Vectastain-Elite kit (Vector Labs) according to the manufacturer's instructions.

PET/CT imaging. ¹⁸FDG (100 μ Ci) was injected intravenously to animals acclimated for at least 48 h to room temperature. Animals were imaged or euthanized at 1 h after injection in the Longwood small animal imaging facility of Harvard Medical School. PET/CT imaging was performed using a Minerve anaesthesia bed moved between a Philips Mosaic HP small animal scanner and a Bioscan CT scanner, and co-registered using custom fiducial markers. The acquired data was reconstructed by InVivoScope software (Bioscan).

30. Bezy, O., Vernochet, C., Gesta, S., Farmer, S. R. & Kahn, C. R. TRB3 blocks adipocyte differentiation through the inhibition of C/EBP β transcriptional activity. *Mol. Cell. Biol.* **27**, 6818–6831 (2007).
31. Kinsella, T. M. & Nolan, G. P. Episomal vectors rapidly and stably produce high-titer recombinant retrovirus. *Hum. Gene Ther.* **7**, 1405–1413 (1996).
32. Rappsilber, J., Mann, M. & Ishihama, Y. Protocol for micro-purification, enrichment, pre-fractionation and storage of peptides for proteomics using StageTips. *Nature Protocols* **2**, 1896–1906 (2007).
33. Kersey, P. J. *et al.* The International Protein Index: an integrated database for proteomics experiments. *Proteomics* **4**, 1985–1988 (2004).
34. Elias, J. E. & Gygi, S. P. Target-decoy search strategy for increased confidence in large-scale protein identifications by mass spectrometry. *Nat. Methods* **4**, 207–214 (2007).
35. Lockhart, D. J. *et al.* Expression monitoring by hybridization to high-density oligonucleotide arrays. *Nature Biotechnol.* **14**, 1675–1680 (1996).
36. Li, C. & Wong, W. H. Model-based analysis of oligonucleotide arrays: expression index computation and outlier detection. *Proc. Natl Acad. Sci. USA* **98**, 31–36 (2001).

Riboflavin kinase couples TNF receptor 1 to NADPH oxidase

Benjamin Yazdanpanah^{1,2}, Katja Wiegmann¹, Vladimir Tchikov⁴, Oleg Krut^{1,2}, Carola Pongratz¹, Michael Schramm¹, Andre Kleinriders³, Thomas Wunderlich³, Hamid Kashkar^{1,2,5}, Olaf Utermöhlen^{1,2}, Jens C. Brüning^{2,3,5}, Stefan Schütze⁴ & Martin Krönke^{1,2,5}

Reactive oxygen species (ROS) produced by NADPH oxidase function as defence and signalling molecules related to innate immunity and various cellular responses^{1,2}. The activation of NADPH oxidase in response to plasma membrane receptor activation depends on the phosphorylation of cytoplasmic oxidase subunits, their translocation to membranes and the assembly of all NADPH oxidase components³. Tumour necrosis factor (TNF) is a prominent stimulus of ROS production, but the molecular mechanisms by which TNF activates NADPH oxidase are poorly understood. Here we identify riboflavin kinase (RFK, formerly known as flavokinase⁴) as a previously unrecognized TNF-receptor-1 (TNFR1)-binding protein that physically and functionally couples TNFR1 to NADPH oxidase. In mouse and human cells, RFK binds to both the TNFR1-death domain and to p22^{phox}, the common subunit of NADPH oxidase isoforms. RFK-mediated bridging of TNFR1 and p22^{phox} is a prerequisite for TNF-induced but not for Toll-like-receptor-induced ROS production. Exogenous flavin mononucleotide or FAD was able to substitute fully for TNF stimulation of NADPH oxidase in RFK-deficient cells. RFK is rate-limiting in the synthesis of FAD, an essential prosthetic group of NADPH oxidase. The results suggest that TNF, through the activation of RFK, enhances the incorporation of FAD in NADPH oxidase enzymes, a critical step for the assembly and activation of NADPH oxidase.

TNFR1 was recently shown to activate NADPH oxidase 1 (Nox1), resulting in ROS production and necrotic cell death⁵. TNF-induced Nox1 activation was suggested to occur through TRADD⁵, a crucial signalling adaptor binding to the death domain (DD) of TNFR1 to serve as an assembly platform for binding further TNF-receptor-associated factors signalling cell death and many cellular TNF responses^{6–8}. However, direct interaction of Nox1 with TNFR1 has not yet been demonstrated⁵, and the molecular mechanism of NADPH oxidase activation by the TNFR1 DD remained ill defined. Our previous work revealed DD-binding sites not only for TRADD but also for other proteins⁹. Because binding site IV (Supplementary Fig. 1) overlapped only partly with TRADD binding (M.K., unpublished observation), we performed a yeast two-hybrid screen using as a bait binding site IV, whose amino-acid sequences represent α -helices 1–3 of the TNFR1 DD¹⁰. The hypothetical protein Flj11149 (GenBank, gi145199238) bound selectively to the TNFR1 DD but not to the cytoplasmic tails of TNFR2 or CD95 (Supplementary Fig. 1b). Flj11149 was later shown to be homologous to yeast RFK¹¹ (Supplementary Fig. 2a). Human recombinant RFK expressed in, and purified from, *Escherichia coli* phosphorylated riboflavin to produce flavin mononucleotide (FMN), indicating that the human homologue of RFK is a genuine RFK (Supplementary Fig. 2b).

To demonstrate that RFK interacts with TNFR1 under physiological conditions, TNFR1 receptosomes were prepared from HeLa cells by magnetic membrane fractionation¹² and analysed by immunoblotting. RFK was detected in TNFR1 receptosomes within 10 min after TNFR1 ligation (Fig. 1a). Moreover, RFK co-immunoprecipitated with TNFR1, indicating a physical interaction of endogenous proteins. To confirm the binding of RFK to the TNFR1 DD in intact cells, TNF receptosomes were prepared from murine embryonic fibroblasts (MEFs) derived from TNFR1/TNFR2 doubly deficient mice, retransfected with either the human wild-type TNFR1 or a mutant human TNFR1 lacking the DD (TNFR1^{ΔDD})¹². As in HeLa cells, endogenous RFK was detected in TNF receptosomes within 10 min after the stimulation of wild-type TNFR1-expressing MEFs by TNF (Fig. 1b). In contrast, MEFs expressing TNFR1^{ΔDD} showed a complete lack of association of RFK, indicating that the co-occurrence of RFK in TNFR1 receptosomes is strictly dependent on the TNFR1 DD. Because TRADD is crucially involved in the formation of the TNFR1 DD complex, we next analysed its possible interaction with RFK. In lysates from TNFR1-deficient MEFs, endogenous TRADD but not receptor interacting protein 1 (RIP1) co-immunoprecipitated with RFK (Fig. 1c), indicating that RFK binds to TRADD in the absence of TNFR1. In comparison with wild-type MEFs, RFK expression was markedly decreased in TNF receptosomes prepared from *Tradd*^{−/−} MEFs¹³ (Fig. 1d). Correspondingly smaller amounts of RFK were found in TNFR1 immunoprecipitates from *Tradd*^{−/−} TNFR1 receptosomes (Fig. 1e), suggesting that the interaction of RFK with TNFR1 is supported by TRADD.

In intact cells, FAD synthetase converts FMN to FAD, which is an important prosthetic group for many enzymes involved in redox reactions, including the flavoprotein cytochrome *b*₅₅₈ consisting of the p22^{phox} and Nox2 subunits of NADPH oxidase¹. To address the general functional role of RFK in NADPH oxidase activation, HeLa cell lines were generated that stably express RFK-specific shRNA (HeLa^{shRFK}) to downmodulate RFK. The efficacy and specificity of the RFK-directed shRNA is shown in Supplementary Fig. 3a–c. Parental HeLa cells, HeLa cells expressing scrambled control shRNA (HeLa^{shScr}) and HeLa^{shRFK} cells were treated with TNF and analysed for ROS production. As shown in Fig. 2a, TNF readily induced ROS production in HeLa and HeLa^{shScr} cells, which was inhibited by the antioxidant *N*-acetyl-L-cysteine. In contrast, markedly decreased ROS production was detected in TNF-treated HeLa^{shRFK} cells. Two short interfering RNA (siRNA)-resistant RFK mutants were generated for reconstitution experiments, one containing the intact open reading frame (RFK^{WT/siR}), and the other harbouring an additional point mutation, E86Q (ref. 11), destroying the kinase domain of RFK

¹Institute for Medical Microbiology, Immunology and Hygiene, ²Center of Molecular Medicine Cologne, ³Institute for Genetics, University of Cologne, 50935 Cologne, Germany.

⁴Institute for Immunology, University of Kiel, 24105 Kiel, Germany. ⁵Cologne cluster of excellence on cellular stress responses in aging-associated diseases, (CECAD), 50674 Cologne, Germany.

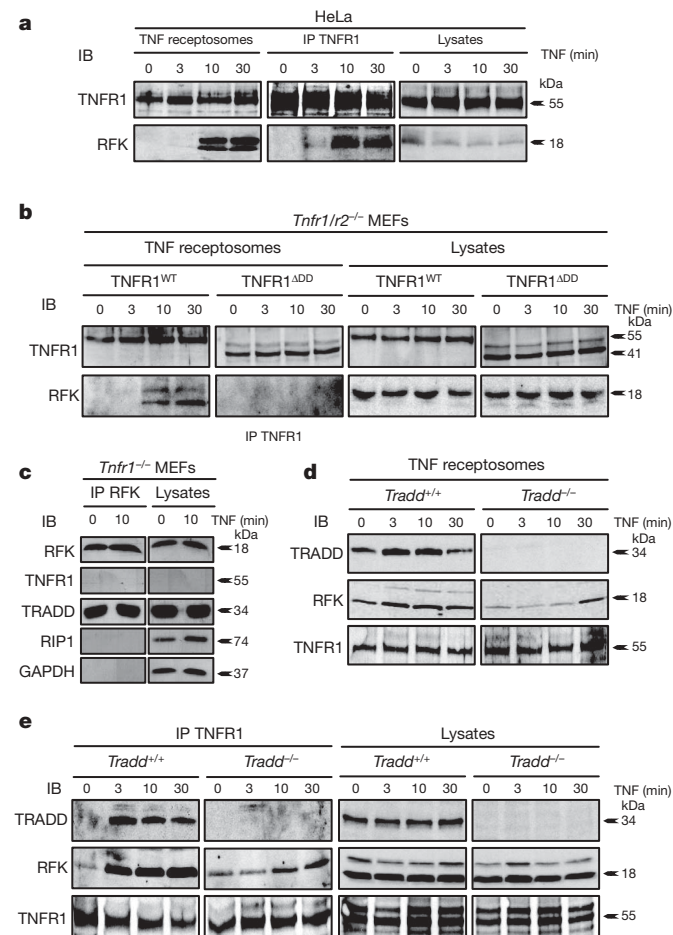


Figure 1 | Interaction of endogenous RFK with TNFR1. **a**, TNFR1 receptosomes, TNFR1 immunoprecipitates (IP) from TNF receptosomes, and cellular extracts were prepared from HeLa cells and immunoblotted (IB) with antibodies specific for RFK and TNFR1. **b**, Immunoblots of TNF receptosomes from TNFR1 and TNFR2 doubly deficient MEFs previously transfected with either wild-type (TNFR1^{WT}) or mutant (TNFR1^{ADD}) TNFR1. **c**, Interaction of RFK with TNFR1 and TRADD. Cellular lysates from *Tnfr1*^{-/-} MEFs were immunoprecipitated with anti-RFK antibody and immunoblotted with antibodies specific for RFK, TNFR1, TRADD, RIP1 and glyceraldehyde-3-phosphate dehydrogenase (GAPDH). **d, e**, TNF receptosomes (**d**) and cell lysates and TNFR1 immunoprecipitates of TNF receptosomes (**e**) from *Tradd*^{+/+} and *Tradd*^{-/-} MEFs were immunoblotted with antibodies specific for TRADD, RFK and TNFR1. Results are representative of at least three independent experiments.

(RFK^{E86Q/siR}, Supplementary Fig. 2b). The RFK^{E86Q} mutant bound equally efficiently not only to TNFR1 but also to p22^{phox} in comparison with wild-type RFK (Supplementary Fig. 4). RFK^{WT/siR}, but not the kinase-dead siRNA-resistant RFK^{E86Q/siR}, rescued TNF-induced ROS production in HeLa^{shRFK} cells (Fig. 2b), suggesting an essential function of enzymatically active RFK in TNF-induced ROS production.

The complete RFK knockout obtained by crossbreeding *Rfk*^{lox/lox} mice (Supplementary Fig. 5) with the transgenic Cre-deleter strain of mice¹⁴ produced an embryonic-lethal phenotype (Supplementary Fig. 6) that manifested before day 7.5 of gestation. In general, RFK deficiency is expected to impair the activity of any flavoprotein that uses FMN and/or FAD as prosthetic groups, such as mammalian nitric oxide synthases, whose reductase domains bind FMN, FAD and NADPH¹⁵. Indeed, macrophages from poly(I)•poly(C)-treated *Rfk*^{lox/lox}-Mx-cre mice showed markedly decreased NO production in response to interferon (IFN)- γ , and to combinations of TNF/IFN- γ , TNF/lipopolysaccharide or IFN- γ /lipopolysaccharide (Supplementary Fig. 7). Although relative RFK deficiency is associated with selective preservation of critical flavoenzyme-dependent metabolic pathways¹⁶,

complete knockout of RFK also affects flavoproteins of the electron transport chain that are critically involved in energy generation, which explains early lethality. RFK-deficient MEFs were generated instead from *Rfk*^{lox/lox} mice and the *Rfk* gene was excised by transduction with a membrane-permeable Cre recombinase fusion protein (HTN-Cre)¹⁷. Excision of the *Rfk* gene impaired TNF-induced ROS production (Fig. 2c), confirming the requirement of RFK for TNF-induced ROS production.

In accordance with its essential function in providing FMN/FAD, RFK deficiency was expected to impair NADPH oxidase activation by other stimuli. Indeed, poly(I)•poly(C), the agonist of Toll-like receptor (TLR)3, failed to stimulate ROS production in RFK-deficient MEFs but not in wild-type, *Tnfr1*^{-/-} or *Tradd*^{-/-} MEFs (Fig. 2d), indicating that the TLR3-induced generation of ROS depends on RFK but not on TNFR1 or TRADD. Similar results were obtained with the TLR2 and TLR9 agonists Pam₃CSK₄ and CpG, respectively (Fig. 2e). Furthermore, the TLR3 ligand poly(I)•poly(C) failed to induce ROS production *in vivo* in *Rfk*^{lox/lox}-Mx-cre mice (Supplementary Fig. 6c), in which the floxed *Rfk* gene is deleted as a consequence of poly(I)•poly(C)-induced interferon induction¹⁸, indicating that RFK is also critically involved in TLR3-induced ROS production *in vivo*. The question of whether RFK-mediated physical bridging of TNFR1 to NADPH oxidase is of functional relevance was addressed by binding competition experiments with a TNFR1-derived peptide, pep^{TNFR1}, encompassing the RFK binding site (amino-acid residues 331–363) fused to an HIV-TAT-derived protein transduction-competent domain with enhanced transduction potential¹⁹. Peptide pep^{TNFR1} competed specifically with the binding of RFK to TNFR1 but left the interaction of TNFR1 with TRADD unaffected; furthermore, it did not interfere with TRADD-mediated activation of NF- κ B (Fig. 2g, h). Peptide pep^{TNFR1}, but not control peptides, dose-dependently diminished TNF-induced ROS production in THP-1 cells, whereas TLR-induced ROS production was not impeded (Fig. 2f). These findings underscore the unique requirement of RFK binding to TNFR1 for TNF-induced NADPH oxidase activation.

To assess a possibly specific impact of RFK binding to TNFR1 on further physical interactions, we analysed TNF receptosomes for the presence of NADPH oxidase components. Within 10 min after TNF stimulation of HeLa cells, p22^{phox}, Nox1 and Nox2 were recruited to the TNFR1 receptosome (Fig. 3a). In TNFR1 receptosomes of TNF-treated cells, the GTPase Rac1 was also detected, which is a component of the NADPH oxidase activation complex²⁰. In contrast, TNF failed to recruit p22^{phox}, Nox1, Nox2 or Rac1 in RFK-deficient HeLa^{shRFK} cells (Fig. 3a). As shown in Fig. 3b, p22^{phox}, Nox1, Nox2 and Rac1 immunoprecipitated together with TNFR1 and RFK in HeLa^{shScr} cells but not in HeLa^{shRFK} cells, indicating that the physical interaction of TNFR1 with the NADPH oxidase complex is dependent on RFK. Reciprocally, immunoblotting analysis of anti-RFK immunoprecipitates from HeLa cell lysates confirmed the interaction of RFK with p22^{phox} as well as with TNFR1 and TRADD, but not with RIP1 (Fig. 3c). p22^{phox} immunoprecipitated together with RFK in unstimulated cells and also in *Tnfr1*^{-/-} MEFs (Fig. 3d), suggesting that RFK interaction with p22^{phox} can occur independently of TNFR1. The presence of both Nox1 and Nox2 in TNFR1 receptosomes raised the question of which Nox enzyme mediated TNF-induced ROS production. siRNAs specific for Nox1 and Nox2 were transfected into HeLa cells to selectively downregulate the expression of either isoenzyme (Supplementary Fig. 8). siNox1 as well as siNox2 markedly, but not completely, decreased TNF-induced ROS production. The combination of siNox1 and siNox2 resulted in an almost complete elimination of ROS generation, indicating additive functions of Nox1 and Nox2 in ROS production (Supplementary Fig. 8b).

When considering the possible mechanism by which TNF activates NADPH oxidase, it is important to note that the Nox enzymes are not fully saturated with the FAD coenzyme under unstimulated conditions^{16,21}. We therefore tested whether the TNF-induced activation of NADPH oxidase relies on RFK-dependent FAD generation, which is a

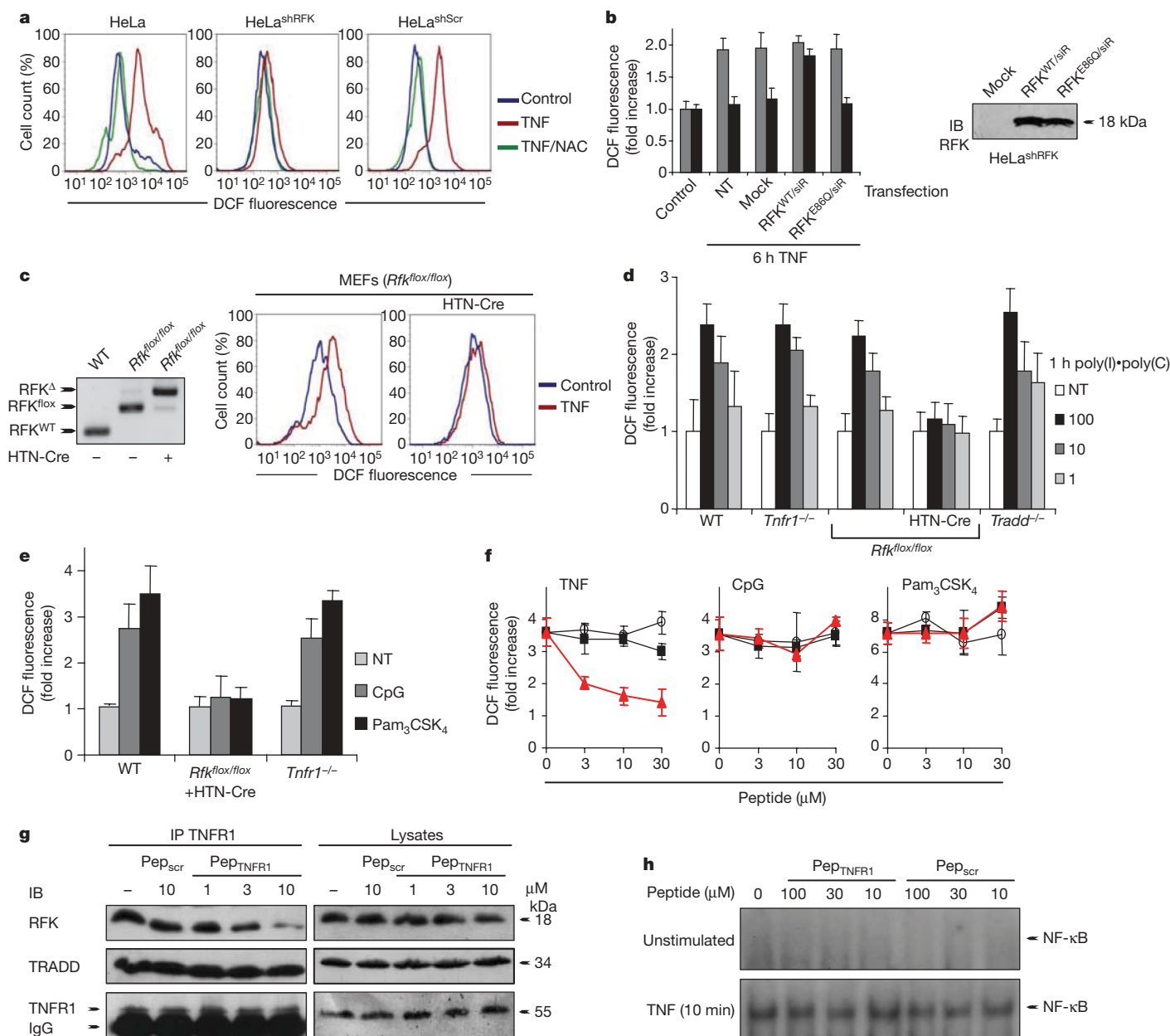


Figure 2 | TNF-induced generation of ROS in HeLa cells depends on binding of enzymatically active RfK to TNFR1. **a**, TNF-induced ROS production was assayed in HeLa, HeLa^{shScr} and HeLa^{shRfK} cells, using 20 μM dichlorofluorescein 5-(and 6-) carboxy-2',7'-dichlorodihydrofluorescein diacetate (carboxy-H₂DCF-DA). Before stimulation with TNF, cells were left untreated or were pretreated for 30 min with 25 mM *N*-acetyl-L-cysteine. DCF, dichlorofluorescein. **b**, Reconstitution of RfK deficiency by siRNA-resistant (RfK^{siR}) mutants. HeLa^{shScr} (grey columns) or HeLa^{shRfK} (black columns) cells were transfected with RfK^{WT/siR} or kinase-deficient enhanced green fluorescent protein (EGFP)-tagged RfK^{E86Q/siR} constructs and analysed for TNF-induced ROS production. Expression of RfK rescue constructs was controlled by immunoblotting. NT, non-treated. **c**, HTN-Cre-mediated deletion of floxed RfK alleles in MEFs from *RfK*^{WT/WT} or *RfK*^{flox/flox} mice was monitored by PCR, and MEFs were analysed for TNF-induced ROS production. **d**, **e**, MEFs of the indicated genotypes were

prerequisite for saturation of Nox with FAD. Treatment of murine RAW264.7 cells with TNF increased the conversion of riboflavin to FMN and FAD (Supplementary Fig. 9), indicating that RfK is a TNF-responsive enzyme. If TNF-induced NADPH oxidase activation is brought about by targeting FAD production to Nox, TNF action should be mimicked in RfK-deficient cells by exogenous FMN or FAD. Indeed, exogenous FMN and FAD reconstituted ROS production in permeabilized²² RfK-deficient HeLa^{shRfK} cells, with an amplitude

stimulated for 60 min with poly(I)•poly(C) at the indicated concentrations (μg ml⁻¹) (**d**) or with CpG (10 μg ml⁻¹) or Pam₃CSK₄ (1 μg ml⁻¹) (**e**), and intracellular ROS levels were measured. **f**, Peptide competition reveals the functional significance of RfK–TNFR1 interaction. THP-1 cells were preincubated for 30 min with Pep_{TNFR1} (red triangles) or control peptides, Pep_{TRADD} (black squares) or Pep_{scr} (black circles) (Methods). THP-1 cells were stimulated with TNF (10 ng ml⁻¹) or the TLR2 and TLR9 agonists PAM₃CSK₄ (1 μg ml⁻¹) and CpG (10 μg ml⁻¹), respectively, and analysed for ROS production. **g**, HeLa cells were treated with Pep_{TNFR1} and anti-TNFR1 immunoprecipitates were analysed for possible interference of Pep_{TNFR1} with TRADD binding to TNFR1. **h**, HeLa cells were treated as in **g**, and NF-κB activation was determined by electrophoretic mobility-shift assay as described in Methods. Error bars indicate s.d.; results are representative of at least three independent experiments.

comparable to that in TNF-stimulated control HeLa and HeLa^{shScr} cells (Fig. 4a–h). Exogenous FMN/FAD did not add to TNF-induced ROS production in wild-type HeLa cells, suggesting that TNF stimulates NADPH oxidase solely through FMN/FAD generation, supposedly leading to greater FAD saturation of Nox enzymes. Synergistic NADPH oxidase activation pathways have been postulated in neutrophils, in which the model of priming and activation of NADPH oxidase was established, whereby priming brings NADPH oxidase into a state

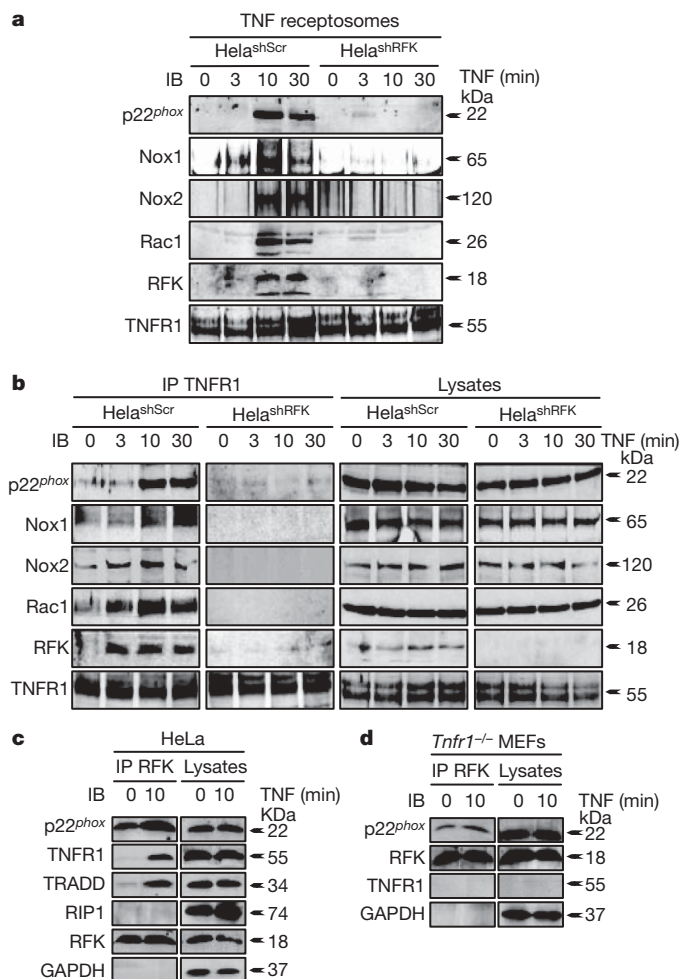


Figure 3 | RFK-dependent recruitment of p22^{phox}, Nox1 and Nox2 to TNFR1. **a, b**, HeLa^{shScr} and HeLa^{shRFK} cells were stimulated with TNF (10 ng ml⁻¹) for the indicated durations. TNF receptor complexes (**a**) or TNFR1 immunoprecipitates from TNF receptor complexes or whole cellular lysates (**b**) were analysed by immunoblotting with antibodies specific for p22^{phox}, Nox1, Nox2, Rac1, TNFR1 and RFK. **c**, Lysates from HeLa cells left untreated or stimulated with TNF (10 ng ml⁻¹) for 10 min were immunoprecipitated with anti-RFK and immunoblotted with antibodies specific for p22^{phox}, TNFR1, TRADD, RIP1, RFK and GAPDH. **d**, Lysates from Tnfr1^{-/-} MEFs were immunoprecipitated with anti-RFK and immunoblotted with antibodies specific for p22^{phox}, RFK, TNFR1 or GAPDH. Results are representative of at least three independent experiments.

of enhanced responsiveness to a second stimulus^{23,24}. TNF is considered a weak activation agent yet a strong priming agent, whereas 12-O-tetradecanoylphorbol-13-acetate (TPA) is a strong activator of NADPH oxidase^{23,24}. To test whether RFK-mediated FMN/FAD generation also accounts for the NADPH oxidase priming effect of TNF, HeLa, HeLa^{shScr} and HeLa^{shRFK} cells were incubated for 6 h with TNF followed by stimulation with TPA. TPA induced ROS production in wild-type HeLa and HeLa^{shScr} cells, and this was synergistically enhanced in TNF-pretreated cells (compare Fig. 4i with Fig. 4m). In contrast, TPA only marginally induced ROS production in RFK-deficient HeLa^{shRFK} cells, confirming the critical function of RFK in NADPH oxidase activity. As expected, riboflavin, the substrate of RFK, did not correct for RFK deficiency in HeLa^{shRFK} cells (Fig. 4j, n). In contrast, FMN and FAD not only fully substituted for the absence of RFK in RFK-deficient HeLa^{shRFK} cells but also led to enhanced, maximal TPA-induced NADPH oxidase activation, as observed in HeLa cells primed with TNF (compare Fig. 4k, l with Fig. 4i, m, o, p). These data suggest that RFK-mediated bridging of TNFR1 to NADPH oxidase is critical for TNF-induced FAD generation in close proximity

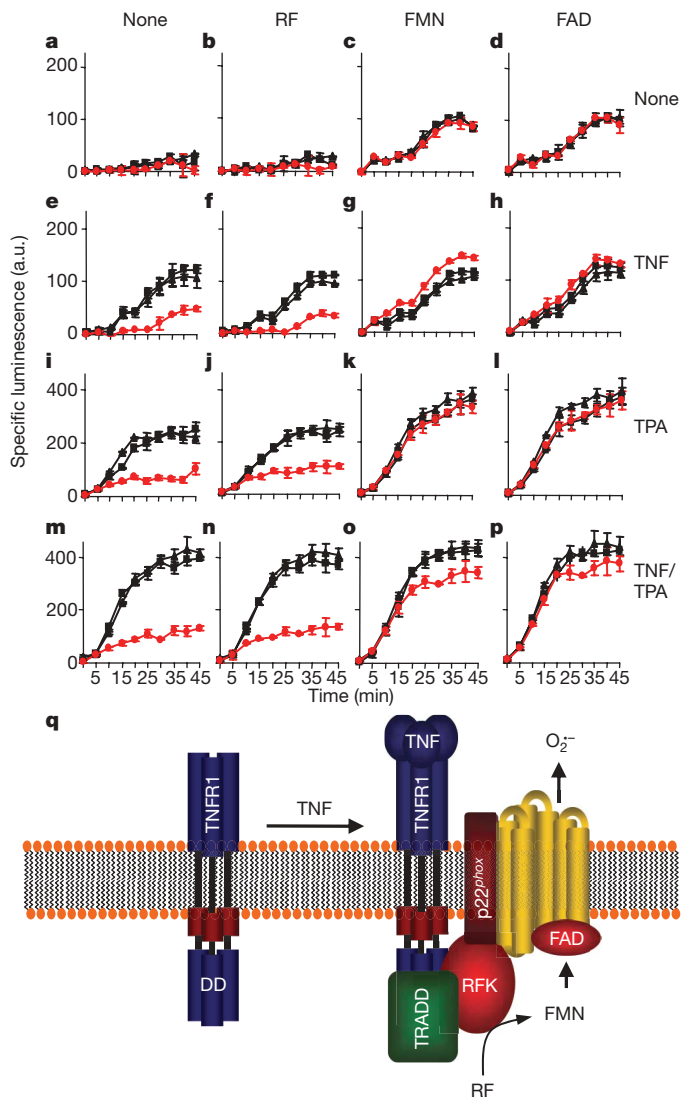


Figure 4 | Substitution of RFK deficiency and TNF activation and priming of NADPH oxidase by FMN/FAD. **a–h**, Wild-type HeLa (black triangles), HeLa^{shScr} (black squares) and HeLa^{shRFK} (red circles) cells were permeabilized with 0.05% sodium deoxycholate²² and stimulated with TNF in the presence or absence of riboflavin (RF), FMN or FAD. Flavins were applied at a final concentration of 25 nM. Superoxide anion production was measured by 2-methyl-6-(4-methoxyphenyl)-3,7-dihydroimidazol[1,2-a]pyrazin-3-one (MCLA). **i–p**, Wild-type HeLa, HeLa^{shScr} and HeLa^{shRFK} cells were left untreated (**i–l**) or preincubated for 6 h with 10 ng ml⁻¹ TNF (**m–p**). Cells were stimulated with TPA in the presence or absence of riboflavin, FMN or FAD and analysed for superoxide anion production. Error bars reflect s.d. Results are representative of at least three independent experiments. **q**, A schematic model illustrating the functional coupling of TNFR1 to NADPH oxidase by RFK.

to Nox. A model of the proposed function of RFK in the TNFR1-induced activation and priming of NADPH oxidase is shown in Fig. 4q.

ROS are important in TNF-induced apoptotic and necrotic cell death^{5,25,26}. As expected, RFK-deficient HeLa^{shRFK} cells proved resistant to TNF-induced cell death (Supplementary Figs 10 and 11). However, ROS also function as signalling molecules mediating TNF responses such as sustained JNK activation by inhibiting mitogen-activated protein (MAP) kinase phosphatases²⁷. ROS react nonspecifically and rapidly with DNA, proteins, lipids and carbohydrates, causing molecular damage such as DNA mutation, protein oxidation and lipid peroxidation. The discovery of RFK as an integral component of the TNFR1 receptor complex regulating NADPH oxidase assembly and activation provides a new cue for the investigation of spatially and temporally controlled ROS production, which is likely

to determine the specificity of ROS action in cellular TNF responses related to signal transduction, innate immunity, inflammatory diseases and atherosclerosis.

METHODS SUMMARY

Yeast two-hybrid screening was performed as described previously⁹. The preparation and analysis of TNFR1 receptosomes and TNFR1 magnetic membrane fractions were performed as described previously¹².

Full Methods and any associated references are available in the online version of the paper at www.nature.com/nature.

Received 22 April; accepted 10 June 2009.

Published online 29 July 2009.

- Lambeth, J. D. NOX enzymes and the biology of reactive oxygen. *Nature Rev. Immunol.* **4**, 181–189 (2004).
- Bedard, K. & Krause, K. H. The NOX family of ROS-generating NADPH oxidases: physiology and pathophysiology. *Physiol. Rev.* **87**, 245–313 (2007).
- Vignais, P. V. The superoxide-generating NADPH oxidase: structural aspects and activation mechanism. *Cell. Mol. Life Sci.* **59**, 1428–1459 (2002).
- Merrill, A. H. Jr & McCormick, D. B. Preparation of flavin 5'-phosphates using immobilized flavokinase. *Methods Enzymol.* **66**, 287–290 (1980).
- Kim, Y. S., Morgan, M. J., Choksi, S. & Liu, Z. G. TNF-induced activation of the Nox1 NADPH oxidase and its role in the induction of necrotic cell death. *Mol. Cell* **26**, 675–687 (2007).
- Hsu, H., Xiong, J. & Goeddel, D. V. The TNF receptor 1-associated protein TRADD signals cell death and NF- κ B activation. *Cell* **81**, 495–504 (1995).
- Zhang, S. Q., Kovalenko, A., Cantarella, G. & Wallach, D. Recruitment of the IKK signalosome to the p55 TNF receptor: RIP and A20 bind to NEMO (IKK γ) upon receptor stimulation. *Immunity* **12**, 301–311 (2000).
- Micheau, O. & Tschoop, J. Induction of TNF receptor 1-mediated apoptosis via two sequential signaling complexes. *Cell* **114**, 181–190 (2003).
- Adam-Klages, S. *et al.* FAN, a novel WD-repeat protein, couples the p55 TNF-receptor to neutral sphingomyelinase. *Cell* **86**, 937–947 (1996).
- Tsao, D. H., Hum, W. T., Hsu, S., Malakian, K. & Lin, L. L. The NMR structure of the TRADD death domain, a key protein in the TNF signaling pathway. *J. Biomol. NMR* **39**, 337–342 (2007).
- Karthikeyan, S. *et al.* Crystal structure of human riboflavin kinase reveals a β barrel fold and a novel active site arch. *Structure* **11**, 265–273 (2003).
- Schneider-Brachert, W. *et al.* Compartmentalization of TNF receptor 1 signaling: internalized TNF receptosomes as death signaling vesicles. *Immunity* **21**, 415–428 (2004).
- Ermolaeva, M. A. *et al.* Function of TRADD in tumor necrosis factor receptor 1 signaling and in TRIF-dependent inflammatory responses. *Nature Immunol.* **9**, 1037–1046 (2008).
- Rodriguez, C. I. *et al.* High-efficiency deleter mice show that FLPe is an alternative to Cre-loxP. *Nature Genet.* **25**, 139–140 (2000).
- Stuehr, D. J. Mammalian nitric oxide synthases. *Biochim. Biophys. Acta* **1411**, 217–230 (1999).
- Ross, N. S. & Hansen, T. P. Riboflavin deficiency is associated with selective preservation of critical flavoenzyme-dependent metabolic pathways. *Biofactors* **3**, 185–190 (1992).
- Peitz, M., Pfannkuche, K., Rajewsky, K. & Edenhofer, F. Ability of the hydrophobic FGF and basic TAT peptides to promote cellular uptake of recombinant Cre recombinase: a tool for efficient genetic engineering of mammalian genomes. *Proc. Natl Acad. Sci. USA* **99**, 4489–4494 (2002).
- Kuhn, R., Schwenk, F., Aguet, M. & Rajewsky, K. Inducible gene targeting in mice. *Science* **269**, 1427–1429 (1995).
- Ho, A., Schwarze, S. R., Mermelstein, S. J., Waksman, G. & Dowdy, S. F. Synthetic protein transduction domains: enhanced transduction potential *in vitro* and *in vivo*. *Cancer Res.* **61**, 474–477 (2001).
- Hordijk, P. L. Regulation of NADPH oxidases: the role of Rac proteins. *Circ. Res.* **98**, 453–462 (2006).
- Hashida, S. *et al.* Binding of FAD to cytochrome *b*₅₅₈ is facilitated during activation of the phagocyte NADPH oxidase, leading to superoxide production. *J. Biol. Chem.* **279**, 26378–26386 (2004).
- Tsunawaki, S. & Nathan, C. F. Enzymatic basis of macrophage activation. Kinetic analysis of superoxide production in lysates of resident and activated mouse peritoneal macrophages and granulocytes. *J. Biol. Chem.* **259**, 4305–4312 (1984).
- El-Benna, J., Dang, P. M. & Gougerot-Pocidalo, M. A. Priming of the neutrophil NADPH oxidase activation: role of p47phox phosphorylation and NOX2 mobilization to the plasma membrane. *Semin. Immunopathol.* **30**, 279–289 (2008).
- Sheppard, F. R. *et al.* Structural organization of the neutrophil NADPH oxidase: phosphorylation and translocation during priming and activation. *J. Leukoc. Biol.* **78**, 1025–1042 (2005).
- Lin, Y. *et al.* Tumor necrosis factor-induced nonapoptotic cell death requires receptor-interacting protein-mediated cellular reactive oxygen species accumulation. *J. Biol. Chem.* **279**, 10822–10828 (2004).
- Fiers, W., Beyaert, R., Declercq, W. & Vandenabeele, P. More than one way to die: apoptosis, necrosis and reactive oxygen damage. *Oncogene* **18**, 7719–7730 (1999).
- Kamata, H. *et al.* Reactive oxygen species promote TNF α -induced death and sustained JNK activation by inhibiting MAP kinase phosphatases. *Cell* **120**, 649–661 (2005).

Supplementary Information is linked to the online version of the paper at www.nature.com/nature.

Acknowledgements We thank M. Pasparakis for TRADD-deficient and TNFR1-deficient MEFs, R. Brandes for gp91-deficient mice and helpful discussions, and D. Männel for TNFR1 and TNFR2 doubly deficient MEFs and for recombinant TNF. This work was supported by grants from the Deutsche Forschungsgemeinschaft (DFG; SFB670 to O.K., J.C.B., O.U. and M.K., and SFB415 to S.S.), DFG grant 733/7-1 to S.S., and a grant from the DFG Leibniz programme to J.C.B. and M.K.

Author Contributions Experiments were performed by B.Y. (Figs 2 and 4, and Supplementary Figs 2b, 3a, b, 5, 6a, b and 8–11). K.W. originally cloned the RFK cDNA (Figs 1c, 2f–h and 3c, d, and Supplementary Figs 2b, 4, 7 and 9). V.T. and S.S. analysed TNF receptosomes (Figs 1a–e and 3a, b, and Supplementary Fig. 3c). O.K. planned experimental approaches (Supplementary Fig. 1). C.P. (Fig. 2c), M.S. and O.U. (Supplementary Figs 6c and 7) performed ROS and NO measurements in RFK-deficient cells. H.K. supervised the apoptosis assays. A.K., T.W. and J.C.B. contributed to the knockout strategy for the generation of RFK-deficient strain of mice. M.K. conceived the study, evaluated the experimental results and wrote the paper.

Author Information Reprints and permissions information is available at www.nature.com/reprints. Correspondence and requests for materials should be addressed to M.K. (m.kroenke@uni-koeln.de).

METHODS

Cell culture and transfection. HeLa and MEF cells were grown in DMEM medium (Biochrom) supplemented with 10% FBS, penicillin (100 U ml⁻¹) and streptomycin (100 µg ml⁻¹); HEK293FT cells were grown in DMEM supplemented with 10% FBS, penicillin (100 U ml⁻¹), streptomycin (100 µg ml⁻¹) and G418 (400 µg ml⁻¹). RAW264.7 cells were cultured in RPMI medium (Biochrom) supplemented with 10% FBS, penicillin (100 U ml⁻¹) and streptomycin (100 µg ml⁻¹). All cell lines were cultured at 37 °C and 5% CO₂. Cells were transfected with Lipofectamine 2000 (Invitrogen) in DMEM without penicillin or streptomycin. Murine embryonic stem (ES) cells (Bruce4) were cultured in DMEM without Glutamax (Gibco; Invitrogen) supplemented with 15% FBS, penicillin (100 U ml⁻¹) and streptomycin (100 µg ml⁻¹), non-essential amino acids, 100 µM 2-mercaptoethanol and 1.6 ml of leukaemia inhibitory factor (LIF), at 37 °C and 9% CO₂ on a monolayer of MEFs. ES cells were transfected with 40 µg of linearized pΔmRFK by electroporation at 200 Ω, 500 µF and 240 V.

The following siRNAs against NOX1, NOX2 and TRADD were used: siNOX1 (Ambion; siRNA ID no. 42157, target sequence 5'-GAAGCCGACAAA TACTAC-3', and siRNA ID no. 42294, target sequence 5'-GAAAAA TCCTTGGGTCAAC-3'), siNOX2 (Ambion; siRNA ID no. s3787, target sequence 5'-CCCTAATACCAGAATAGGA-3', and siRNA ID no. s3789, target sequence 5'-CCGGGTTTATGATATTTCCA-3') and siTRADD (target sequence 5'-AGGATGCGCTGCGAATTT-3'). The AllStars Negative Control siRNA (Qiagen) was used as a control.

Expression and purification of recombinant RFK. RFK^{WT} and its mutated derivatives RFK^{N36D} and RFK^{E86Q} were cloned into pGEX-4T-3 (GE Healthcare) and purified as C-terminal glutathione S-transferase (GST) fusion proteins from *Escherichia coli* BL-21—pLysS (DE3). Luria-Bertani medium supplemented with 150 µg ml⁻¹ ampicillin was inoculated, incubated at 37 °C with shaking (250 r.p.m.) and induced at a *D*₆₀₀ of 0.6 by the addition of 300 µM isopropyl β-D-thiogalactoside for 3 h. Cultures were harvested by centrifugation at 4 °C, resuspended in PBS and lysed by the addition of 1% Triton X-100 and 200 µg ml⁻¹ lysozyme for 1 h and subsequent ultrasonication at 4 °C. Lysates were centrifuged at 15,000g at 4 °C for 20 min, and supernatants were used for the purification of GST fusion proteins. GST fusion proteins were bound to glutathione-Sepharose 4B (GE Healthcare) and eluted as described by the manufacturer in a buffer containing 50 mM Tris-HCl pH 8 and 10 mM reduced glutathione.

The anti-RFK antibody was raised in rabbits by using a recombinant GST-RFK fusion protein. GST was removed by on-column digestion with thrombin. The antibody was purified by affinity chromatography with RFK bound to HiTrap (GE Healthcare).

Riboflavin kinase assay. To determine riboflavin kinase activity, recombinant GST-RFK fusion proteins were subjected to a riboflavin kinase assay in 50 µl of 1 × RFK buffer (25 mM Tris-HCl pH 8, 5 mM MgCl₂, 1 mM ATP, 50 µM riboflavin). Supernatants after trichloroacetic acid precipitation were separated on equilibrated thin-layer chromatography plates in butan-1-ol/acetic acid/water (12:3:5) as described²⁸. Standards (riboflavin, FMN and FAD) were used to identify the different flavins, which were detected with ultraviolet (365 nm) and a charge-coupled device camera.

ROS production. DCF fluorescence: cells were loaded at 37 °C for 30 min with 20 µM dichlorofluorescein 5-(and 6-) carboxy-2',7'-dichlorodihydrofluorescein diacetate (carboxy-H₂DCF-DA) in Hanks balanced salt solution (HBSS). DCF fluorescence was detected on a FACSCalibur flow cytometer with an excitation wavelength of 488 nm and a fluorescein isothiocyanate filter (530 ± 20 nm). Alternatively, cells were plated overnight on black microtitre plates and labelled as described above. Quantitative DCF fluorescence was measured with a fluorescence plate reader at 485 nm (excitation) and 535 nm (emission).

Detection of superoxide anions with 2-methyl-6-(4-methoxyphenyl)-3,7-dihydroimidazo[1,2-a]pyrazin-3-one (MCLA). Production of superoxide anions by macrophages and HeLa cells was measured with MCLA. Cells were stimulated with 10 ng ml⁻¹ TNF or left untreated, and production of superoxide anions was measured with 5 µM MCLA in HBSS at 37 °C at the indicated time points. For flavin reconstitution experiments, HeLa cells were treated with 0.05 mM sodium deoxycholate in PBS as described previously²². In brief, superoxide anion production was initiated by the addition of 0.5 mM NADPH and 100 ng ml⁻¹ TPA. Riboflavin, FMN and FAD were each used at a concentration of 25 nM. Specific luminescence was measured with a microtitre luminometer.

Induction and quantification of cell death. For staining with crystal violet, 10⁴ cells were seeded on a 96-well plate 24 h before the induction of cell death with H₂O₂, cycloheximide/TNF or staurosporine (STS) for 16–24 h. Adherent cells were stained with crystal violet (0.2% in 2% ethanol) for 10 min, and excess colour was removed by several washings with doubly distilled water. Plates were

dried, bound dye was dissolved with 0.2% sodium citrate in 50% ethanol, and the attenuation was measured at 595 nm (*D*₅₉₅).

Western blot analysis. Cells were harvested, washed twice with PBS and lysed for 20 min at 4 °C in 0.2 ml of lysis buffer (0.01 M Tris base, 1 mM EDTA, 200 mM NaCl, 1% Nonidet P40 pH 7.4 plus protease inhibitor mix (Complete; Roche)). Cell lysates were fractionated by 12.5% SDS-PAGE and transferred to Protan NC filters (Whatman). Filters were blocked for 30 min at room temperature (about 21 °C) in Tris-buffered saline containing 0.1% (v/v) Tween-20, 5% milk powder and 1% BSA. After incubation for 1 h at room temperature with anti-p22^{phox} antibody (Sanguin), anti-Rac1 antibody (Upstate) and anti-β-actin antibody (Sigma), filters were washed with Tris-buffered saline containing 0.1% (v/v) Tween-20 and incubated with a 1:5,000 dilution of goat anti-mouse horseradish peroxidase conjugate (Sigma) in blocking buffer for 1 h at RT. Filters were washed and developed with ECL detection reagent (Thermo).

Pull-down assay. A GST-RFK expression vector was constructed by the insertion of wild-type RFK into pRK 5 vector (originally provided by D. V. Goeddel). HEK-293 cells (3 × 10⁷) were transiently transfected with the pRK GST-RFK construct. After 24 h, cells were stimulated with TNF (10 ng ml⁻¹) for 10 or 30 min or left untreated, then lysed in TNE buffer (0.01 M Tris base, 1 mM EDTA, 200 mM NaCl, 1% Nonidet P40 and protease inhibitor mix (Complete; Roche) at pH 7.4, and centrifuged for 30 min at 20,000g. Supernatants were incubated with 50 µl of glutathione-Sepharose beads for 2 h at 4 °C. Beads were washed extensively, resuspended in SDS sample buffer and analysed by SDS-PAGE and immunoblotting.

Preparation and analysis of TNFR1 receptosomes. TNFR1 magnetic membrane fractions were prepared as described previously¹². In brief, TNF receptors were magnetically labelled with biotin-TNF (Fluorokine; R&D Systems) and 50-nm MACS streptavidin-microbeads (Miltenyi Biotec). Cells were incubated in a total volume of 250 µl of cold DMEM with 100 µl (400 ng) of biotin-TNF for 1 h at 4 °C, followed by incubation with 200 µl of MACS streptavidin-microbead solution for 1 h at 4 °C. Formation of magnetized TNF-TNFR1 complexes was achieved by incubation at 37 °C for the periods indicated and stopped by chilling to 4 °C. Cells were pelleted by centrifugation at 300g and washed with 0.25 M sucrose buffer supplemented with 0.015 M HEPES, 100 mg l⁻¹ MgCl₂ pH 7.4 and Protease Inhibitors Set (Roche Diagnostics). Cells were mechanically homogenized with steel beads in 250 µl of supplemented sucrose buffer at 4 °C, and post-nuclear supernatants containing intact membrane vesicles were subjected to magnetic separation of TNFR1 fractions in a high-gradient magnetic field. Proteins were separated by SDS-PAGE and analysed by immunoblotting with antibodies against RFK, TNFR1 (H5, sc8436; Santa Cruz Biotech Inc.), TRADD (556496; BD Pharmingen), Rac1 (clone 23A8, lot 27666; Upstate) and p22^{phox} (monoclonal antibody 449; Sanguin).

Generation of *Rfk*^{lox/lox} mice. To generate a conditional floxed *Rfk* allele, a targeting vector based on the vector pRAPID-Flirt (provided by A. Waisman) spanning 6.6 kilobases (kb) of the murine *Rfk* locus was constructed. First, a 1.6-kb genomic region encoding the 5' upstream region and exons 1 and 2 was used to introduce two *loxP* sites (floxed region). The 5'-*loxP*-site was placed into the 5'-upstream region (nucleotide position -517) of the *Rfk* gene. The 3'-*loxP*-site was introduced into a branch-site free position in intron 2 (nucleotide position +1080). The floxed region was cloned into the unique SbfI and Sall restriction sites of the targeting vector. Second, the long homology arm consisting of a 2.6-kb intronic stretch (intron 2) was cloned downstream of the 3'-*loxP* site and upstream of the herpes simplex virus thymidine kinase gene for negative selection with gancyclovir, with the use of the unique XhoI site. Last, the short homology arm (2.5 kb) was cloned upstream of the neomycin resistance cassette and the 5'-*loxP* site into the ClaI and BamHI restriction sites. ES cell transfection, selection and screening were performed with Bruce4 ES cells. Homologously targeted clones were identified by Southern blotting of EcoRV-digested genomic DNA with 5', 3' and *neo* probes, respectively. ES cell clones were injected into blastocysts of C57BL/6 mice, and the resulting germline transmitting chimaeras were mated to C57BL/6 mice to generate heterozygous floxed *Rfk* mice and wild-type F₁ mice. *Rfk*^{lox/lox} mice show no obvious phenotype. To excise the *neo* selection cassette, targeted mice were crossed with a Flp-deleter strain¹⁴. For the deletion of the floxed region, *Rfk*^{lox/lox} mice were mated either to a Cre-deleter line or to the interferon type I inducible MxCre mice and deletion was induced by intraperitoneal treatment with poly(I)•poly(C) as described¹⁸.

Southern blot and PCR analyses: wild-type and mutant alleles were assessed by Southern blot hybridization and/or PCR from DNA isolated from ES cells, mouse tail biopsies or from yolk sacs of embryos or whole embryos as described. In brief, genomic DNA was digested with EcoRV or HindIII and analysed with radiolabelled 5' probe (250 base pairs (bp); primers P3/P4), a 3' probe (250 bp; primers P9/P10) or a *neo* probe (500 bp; primers Neo-5/Neo-3), respectively. For genotyping the wild-type (WT) and floxed *Rfk* allele (flox) as well as the Cre-mediated knockout allele, PCR amplifications with genomic DNA and the specific primer set (see below) were performed. The positions of the primers are

located in close vicinity to the *loxP* sites. The allele-specific primer sequences, pairs and orientation (forward, Fw; reverse, Rev), the primer pairs and their corresponding PCR-product sizes are as follows: WT- and floxed allele (S1; 5'-TG GATCTCTGATATTCAAGG-3', α -S1; 5'-AACATGGAGAAAACATATCCC-3' (210 bp and 270 bp respectively), knockout allele (23; 5'-AAGAATGTTCCC AACATAGA-3' and α -S1 (330 bp), neo cassette (23 and ftrR; 5'-TGCTCAC AAGATAACTTAAG-3', 156 (WT) and 285 bp (flox)). Primers for Southern 5' probe: P3; 5'-GCCGGTATCCAATTACCACC-3', P4; 5'-TGCTATTGGG ACGTAAGGTG-3', the 3' probe: P9; 5'-GTACAAAATAGATCTGTGGC-3', P10; 5'-ATGCCTGCAAACATTCAGAC-3' and the neo probe Neo-5; 5'-TGA ATGAAGTGCAGGACGAGGCA-3', Neo-3; 5'-GCCGCCAAGCTCTTCAGCA ATAT-3'.

HTN-Cre transduction. Bacteria carrying an inducible HTN-Cre-expressing plasmid were provided by F. Edenhofer. HTN-Cre was purified as described previously¹⁷ and concentrated to 100 μ M through a 30-kDa cut-off filter (Amicon). HTN-Cre (3 μ M) in PBS/DMEM was used to transduce MEFs or ES cells overnight. Cells were analysed 3–5 days after replacement of medium.

Quantification of reactive nitrogen intermediates. Peritoneal macrophages were enriched from peritoneal exudate cells by magnetic cell sorting with CD11b-specific monoclonal antibodies conjugated to paramagnetic beads (CD11b MicroBeads; Miltenyi Biotec) in accordance with the instructions of the manufacturer. Peritoneal macrophages were incubated at a density of 10^6 cells ml^{-1} in DMEM supplemented with 5% FCS. Recombinant murine IFN- γ (10 ng ml^{-1}), TNF (1 ng ml^{-1}) or lipopolysaccharide from *E. coli* serotype 0111:B4 (10 ng ml^{-1}) were added in the indicated combinations. After 24, 48 or 72 h, cell-free supernatant was harvested and the concentration of nitrite in the

supernatant was determined as a stable surrogate for nitric oxide by using the Griess reagent as described²⁹.

Peptide competition experiments. To compete for RFK binding to TNFR1, a TNFR1-derived peptide, $\text{Pep}_{\text{TNFR1}}$ was synthesized encompassing the death domain fragment IV (Supplementary Fig. 1a) fused to an enhanced protein transduction domain of HIV-1 TAT¹⁹ (amino-acid sequence YARAAARQARAP-YAVVENVPPLRWKEFVRLGLSDHEIDRLQLN (molecular mass 5,275.97 Da). The following peptides were used as controls: TRADD-derived peptide, ($\text{Pep}_{\text{TRADD}}$, YARAAARQARAP-TFARSVGLKWRKVGRSLQRCRALRDPALDSLAYE, molecular mass 5,261.03 Da) and Pep_{scr} (amino-acid sequence YARAAARQARAP-AEPDEPVVDRLNVVLYRLGQFSKRRLNIWLH, molecular mass 5,275.97 Da). HEK293 cells previously transfected with pGST-TNFR1 and pRK-CrmA were incubated for 30 min with graded concentrations of peptides (3–30 μ M). For ROS production, cells were treated with the peptides for 30 min before stimulation with TNF or TLR agonists; for binding experiments, lysates were prepared in the presence of peptides, and TNFR1 interaction with RFK was analysed by pull-down experiments. Analysis of NF- κ B activation by electrophoretic mobility-shift assays was performed as described³⁰.

28. White, D. J., Merod, R., Thomasson, B. & Hartzell, P. L. GidA is an FAD-binding protein involved in development of *Myxococcus xanthus*. *Mol. Microbiol.* **42**, 503–517 (2001).
29. Kruisbeek, A. M. & Vogel, S. N. in *Current Protocols in Immunology* Vol. 3 (ed. Coligan, J. E. et al.) p. 14.5.1 (John Wiley, 1999).
30. Wiegmann, K. et al. Requirement of FADD for tumor necrosis factor-induced activation of acid sphingomyelinase. *J. Biol. Chem.* **274**, 5267–5270 (1999).

CORRIGENDUM

doi:10.1038/nature08352

Liquid water on Enceladus from observations of ammonia and ^{40}Ar in the plume

J. H. Waite Jr, W. S. Lewis, B. A. Magee, J. I. Lunine, W. B. McKinnon, C. R. Glein, O. Mousis, D. T. Young, T. Brockwell, J. Westlake, M.-J. Nguyen, B. D. Teolis, H. B. Niemann, R. L. McNutt Jr, M. Perry & W.-H. Ip

Nature 460, 487–490 (2009)

In this Letter, the address for author J. Westlake was listed incorrectly. The correct address is: Department of Physics and Astronomy, University of Texas at San Antonio, San Antonio, Texas 78249-1644, USA.

CORRIGENDUM

doi:10.1038/nature08360

CBP/p300-mediated acetylation of histone H3 on lysine 56

Chandrima Das, M. Scott Lucia, Kirk C. Hansen & Jessica K. Tyler

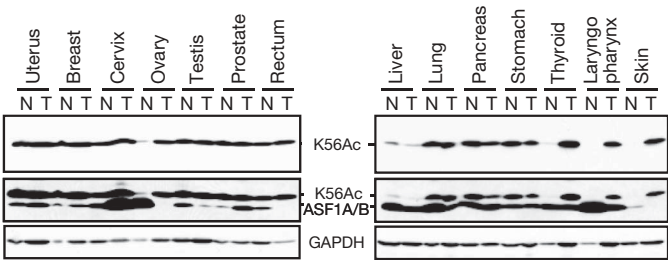
Nature 459, 113–117 (2009)

In Fig. 4e of this Letter, one band was incorrectly labelled. We thank B. Lüscher for drawing this to our attention. The correctly labelled version of the figure is provided below. As such, the statement that there is “a notable correlation between levels of H3K56 acetylation and ASF1A but not ASF1B in a wide variety of normal and cancerous human tissues” is no longer accurate. However, the main purpose of Fig. 4e is still valid, which was to show by western blotting analysis that the level of H3K56ac is much higher in some tumours as compared to the matching normal tissue.

We also note that although the fractionation of the total stained proteins in Figs 1f and 4d did not show obvious differences, the fractionation of histones and tubulin was effective between the supernatant and pellet fractions (see Supplementary Figure).

We also omitted to state that the ultraviolet light used in our analysis was 312 nm UVB, which causes 1% of the amount of DNA damage as 254 nm UVC.

Supplementary Information is linked to the online version of the paper at www.nature.com/nature.



PROSPECTS

A sequence for success

The next generation of DNA sequencers could create more genomics jobs, says **Paul Smaglik**.

Bioengineer Stephen Quake and his colleagues at Stanford University, California, reported earlier this month that they had sequenced Quake's own genome in 4 weeks for less than US\$50,000, leading to predictions that physicians will soon be able to sequence patients' DNA in their offices (D. Pushkarev, N. Neff and S. Quake *Nature Biotechnol.* doi:10.1038/nbt.1561; 2009). Yet such predictions may be premature — the machine used by Quake costs around \$1 million, and sequencing one patient's genome currently yields little clinical benefit. Still, the next-generation sequencing technology the group reports could boost careers in three areas of genetics and genomics.

First, it is likely to prompt the development of even cheaper, better and faster sequencing technologies. Companies such as Helicos Biosciences in Cambridge, Massachusetts, which developed the sequencing technology used by Quake, and others will race to generate improved instruments. That should mean jobs for biomedical engineers and computational biologists who can develop and test new sequencers and bioinformatics approaches.

Second, this technology can be used with bioinformatics to unearth the complex multiple-gene variants that drive many diseases, such as cancer, and will enable cheaper and faster genomic sequencing of individuals with the same disorders. Bioinformaticians and biostatisticians will be needed to compare genomes directly to



Rapid-sequencing technologies are getting a boost.

reveal the multiple genes or variants that cause a particular disease.

Third, an improved understanding of these variants should help move drug development into the era of personalized medicine, requiring pharmacogeneticists who can tailor drug therapies to individuals that have different genetic variants.

Another stimulus for genomics jobs comes from funding. The US economic recovery act is already channelling money into two Department of Energy labs to purchase faster sequencing equipment and to develop better bioinformatics software. And with Francis Collins confirmed as the new director of the National Institutes of Health, the former leader of the Human Genome Project is in a strong position to advocate funding of the latest rapid-sequencing technologies. ■

Paul Smaglik is a freelance writer based in Milwaukee, Wisconsin.

POSTDOC JOURNAL

A strong idea

Last weekend was fun. I didn't get to bed before midnight either night. Sometimes work is like that.

On Friday afternoon, while fine-tuning a paper about a model of intramolecular interactions in myosin, a protein integral to muscle contraction, I found a paper about an experiment with a related protein.

At first, I was excited to find that my model predicted the experimental results. But my excitement evaporated when I read the authors' simple, logical and elegant explanation — an explanation

that completely contradicted my results. I felt sick thinking about what seemed to be wasted effort.

I thought about another time when my work had disintegrated at the final moment. Several years ago, while finishing a manuscript, I found a paper that had been published 30 years earlier. This paper presented 'my' idea and explained it 'my' way. I had felt a mix of emotions. Although it was nice to know I'd been right, I had nothing to show for it.

But on Friday evening, after a few hours of frantic thinking, I hit on an idea that explained

why my model was correct. As the weekend passed, my excitement mounted and the idea gained clarity. I went to bed late Sunday night, calm and happy. The paper had survived the moment of doubt and had emerged stronger. Weekends like this make me glad to be a scientist. In science, sometimes you work hard and fail, but sometimes you work hard and succeed. The failures are what make success so sweet. ■

Sam Walcott is a postdoc in theoretical biophysics at Johns Hopkins University in Baltimore, Maryland.



IN BRIEF

UK grants in refund threat

A inflation rate lower than that predicted may force some UK research scientists to refund research allocations. The UK government has asked the nation's seven research councils, which distribute government research funding, to come up with about £100 million (US\$165 million) in cuts.

The government had forecast an annual inflation rate of 2.7%, and had based its funding levels on that figure, but the actual rate has averaged 1.5%. The councils say that they are deciding how to come up with the funds they must repay the government. Asking researchers to return allocations could help them to reach their goal but could also alienate scientists.

College salaries put on ice

Two-thirds of independent US colleges and universities polled in a recent survey said they plan to freeze employee salaries. Of those respondents, 80% said the freeze would be imposed across the institution; 15% said it would affect only the president and top executives; and 6% said only the president's salary would be capped.

Yet 24% of all respondents said they plan compensation increases, with 87% of that group expecting to raise salaries across the board. Nine per cent of respondents predicted they would make pay cuts, with 64% of those saying the reduction would be institution-wide. The survey, conducted in June by consultants Yaffe & Company of Towson, Maryland, produced responses from 259 institutions in 39 states.

A guide for policy work

Those considering a career in public policy now have a new edition of an existing resource to help guide their path. The American Association for the Advancement of Science (AAAS) has updated and expanded its 1985 *Guide to Graduate Education in Science, Engineering and Public Policy*.

The fourth edition of the guide is now available for free online at www.aaas.org/spp/sepp. Albert Teich, the AAAS's director of science and policy programmes, says that science and technology have taken on more important roles in public policy since the guide was first published. "The need for people educated in this field has grown proportionately," Teich says.

The Gower Street cuckoos

It's a growing problem.

Joe Dunckley

Charles Quackenbush is a prodigy. He doesn't look his 39 years, and already *The Daily Mail* has credited him with seven miracle cures for cancer, one for each of his years as professor at the Midwiche Institute. He looks up from his computer to sigh in unison with his 460 fellow travellers, as a crackly voice announces that all Crossrail services have been suspended, and that the train will terminate at Tottenham Court Road. Thank God the tunnel has Wi-Fi.

Charles adjusts the bag between his feet, and presses himself to the carriage wall, in an attempt to gain some working space among those standing. All he can do is return to the device before him, and the online lab notebook that he is searching for clues. He is *still* trying to solve the problems that his graduate student has been having, and is furious with his lack of success.

Let me explain. Charles's student is trying to treat some glioma cells with a drug that should inhibit the cell cycle. This treatment is just a preliminary step in a bigger experiment, and the activity of the drug on the cells has been known for decades. The pesky cells, however, are showing utter disregard for orthodox science, and stubbornly reproduce like rabbits.

The student did not need Charles's prompting to try the experiment with a new stock of drug from the concentrate, with fresh culture media, and finally with new cells from the frozen stock. None had made the slightest difference. It was at this point that Charles came in. He had bought a new set of media ingredients, had his pipettes calibrated and the tissue culture incubators serviced, and treated the cells to glass Petri dishes begged and borrowed from a colleague. Finally, two weeks ago, he had actually attempted to perform the experiment himself. After his inevitable failure he was at least consoled by issuing the order that the pests be disposed of. Stumped, he had sent a vial of frozen cells to colleagues in Sweden, and

another to the department's sequencing guys, in the hope that somebody else might solve the problem for him.

Charles *had* hoped that the matter would all go away after Sarah had left. It had been a blow having to dismiss his technician: she was skilled, hardworking and thorough. But towards the end, he had received ever more frequent reports of infractions — flooding the laboratory by leaving the water purifier on over night; allowing a fungal contamination to wipe out all the flasks of neuroblastoma cells; and finally, Charles had found her at the tissue culture hood, glassy eyed and filling an incubator with nearly 60 flasks of glioma cells.

Charles moves on, and the uneasy feeling that has been competing with anger for space in his head grabs a lead. Either one of his students has totally destroyed his records, or something is very wrong with his inventory of liquid-nitrogen frozen cells. The page should list first- and

second-generation stocks of a dozen different cell types going back to the start of Charles's 10 years as a lab leader, but instead lists four dozen vials of glioma cells. Like the 'regular save' function on his notebook, five vials had been frozen consistently at three-day intervals for a month.

Charles clicks through to a batch that had been frozen on a Sunday two weeks ago. A student who had only been in the laboratory to

prepare an overnight antibody incubation, and who

did not even use glioma cells in his work, had archived five vials of the cells. Charles checks the rest of the entries. At one time or another, each of his two postdocs and four students had frozen five vials of glioma cells, at or after 3 p.m. on the allotted day.

Charles is even more disturbed to note that nine of the vials have already been plucked from their sleep and moved on. One, Charles supposes, is now in Sweden, and another — one that Charles had believed to be seven years old, but that he now finds to be just seven days old — had gone for genome sequencing. This left seven that Charles couldn't account for. And somebody better be able to account

for them by the time health and safety made their next audit.

The train jerks back into life and grinds into the station. An incomplete but disturbing hypothesis forming in his mind, Charlie pockets the computer and alights, just in time to miss a message from a postdoc.

*<esther> hi chuck, we've got a *big* problem here. someone has filled the incubators with glioma, and the whole lot are duds anyway. no one even admits to doing it. i think i know what the problem is. it looks like you're gonna have to start from scratch. i'll keep some for troubleshooting, but i'm gonna have to start clearing out these incubators.*

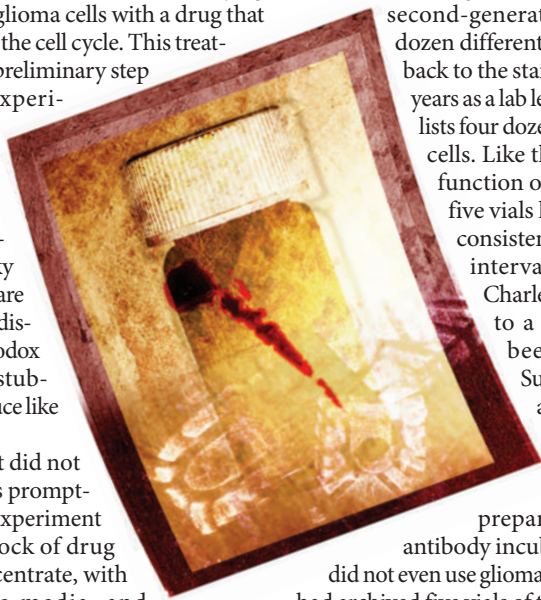
Now blinking in the sunlight, Charles ignores the cyclist gesturing at him as, still distracted, he shuffles across Oxford Street. On Tottenham Court Road he pushes a straight trajectory through the tourists. He trips in Bedford Square, taking the skin off one hand on the gravel, but does not stop to feel embarrassed.

At the Midwiche Institute on Gower Street, Charles is soon through the reception and up the concrete stairwell. He fumbles with his security card and crashes through the heavy doors to the lab, down a corridor cluttered with trolleys, tanks and barrels. He is too late. Charles has to push hard against the tissue culture room door to shift it, and the body behind. Esther, in a spreading pool of blood, two flasks in her left hand, a blade in the right.

Charles kneels in the vain hope of finding something he can do. Rising to leave and raise the alarm, he does not even notice himself step over the body, pry the flasks of glioma cells from the dead woman's hand, and place them neatly back in the crowded incubator, beside the dishes that he had ordered be destroyed two weeks earlier, closing the air-tight door behind them. So he was unable to explain to the court the presence of his footprint in the pool. Charles was loud and disruptive in court, but he settled into the routine at Broadmoor. After all, eight vials had got out. Soon the world would *have* to believe him.

Joe Dunckley once worked in cancer-cell biology, where he was never affected by cell-culture contamination. He blogs at Cotch.net and is excited about being paid to make stuff up.

Join the discussion of Futures in Nature at <http://tinyurl.com/kkh3kt>



JACEY